CFD Open Series
Patch 2.23

Aerodynamic Basics

Edited by :
Ideen Sadrehaghighi, Ph.D.

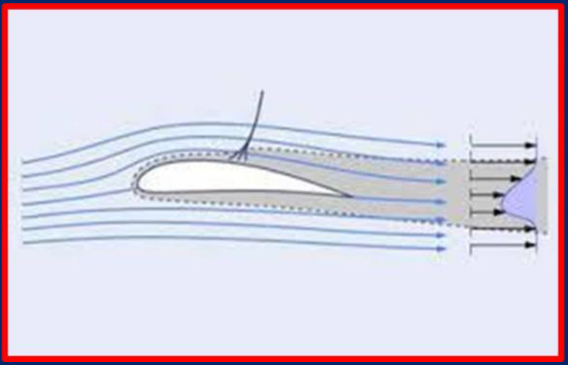

Airfoil Aerodynamics

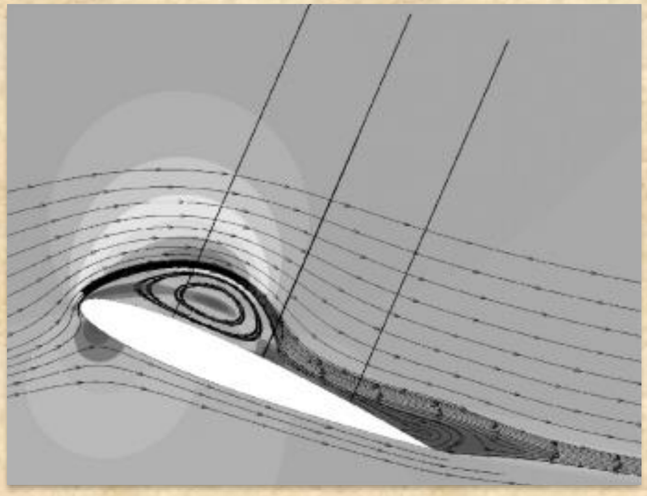

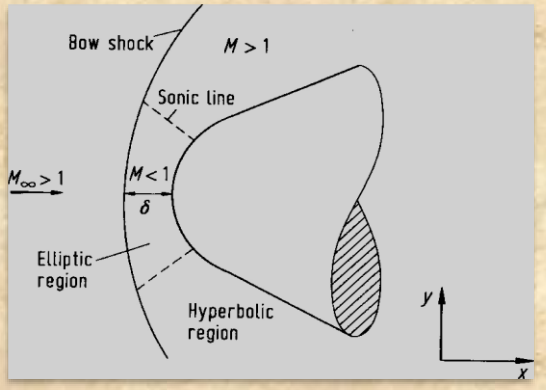

Flow Over a
Supersonic Blunt Body

Annapolis, MD

Contents

List of Tables

List of Figures

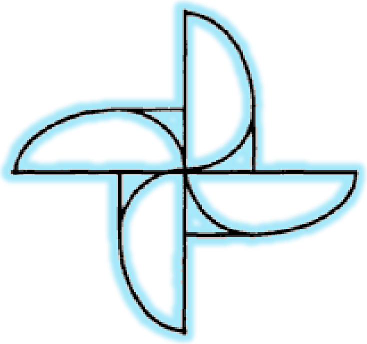

Preface

This note is intended for all undergraduate, graduate, and scholars of Fluid Mechanics. It is not completed and never claims to be as such. Therefore, all the comments are greatly appreciated. In assembling that, I was influenced with sources from my textbooks, papers, and materials that I deemed to be important. At best, it could be used as a reference. I also would like to express my appreciation to several people who have given thoughts and time to the development of this article. Special thanks should be forwarded to the authors whose papers seemed relevant to topics, and consequently, it appears here©. Finally I would like to thank my wife, *Sudabeh* for her understanding and the hours she relinquished to me. Their continuous support and encouragement are greatly appreciated.

Ideen Sadrehaghighi
June 2018

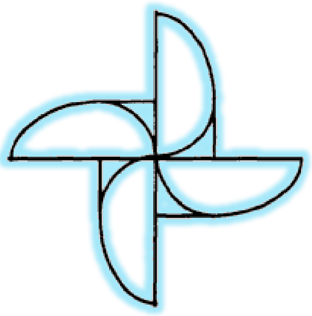

1 Introduction

1.1 Definitions

Aerodynamics is the study of how gases interact with moving bodies. Because the gas that we encounter most is air, aerodynamics is primarily concerned with the forces of drag and lift, which are caused by air passing over and around solid bodies[1]. Engineers apply the principles of aerodynamics to the designs of many different things, including buildings, bridges and even soccer balls; however, of primary concern is the aerodynamics of aircraft and automobiles. Aerodynamics comes into play in the study of flight and the science of building and operating an aircraft, which is called ***aeronautics***. Aeronautical engineers use the fundamentals of aerodynamics to design aircraft that fly through the Earth's atmosphere.

In another similar definition from ***Wikipedia***, aerodynamics is defined as the study of motion of air, particularly as interaction with a solid object, such as an airplane wing. It is a sub-field of fluid dynamics and gas dynamics, and many aspects of aerodynamics theory are common to these fields. The term aerodynamics is often used synonymously with gas dynamics, the difference being that "***gas dynamics***" applies to the study of the motion of all gases, and is not limited to air. The formal study of aerodynamics began in the modern sense in the eighteenth century, although observations of fundamental concepts such as aerodynamic drag were recorded much earlier. Most of the early efforts in aerodynamics were directed toward achieving heavier-than-air flight, which was first demonstrated by *Otto Lilienthal in 1891*. Since then, the use of aerodynamics through mathematical analysis, empirical approximations, wind tunnel experimentation, and computer simulations has formed a rational basis for the development of heavier-than-air flight and a number of other technologies. Recent work in aerodynamics has focused on issues related to compressible flow, turbulence, and boundary layers and has become increasingly computational in nature.

1.2 Motivation

Imagine that you are an aeronautical engineer in the later 1950s. You have been given the task of designing an atmospheric entry vehicle in those days it would have been an intercontinental ballistic missile[2]. You are well aware of the fact that such vehicles will enter the earth's atmosphere at very high velocities, about 7.9 km/s for entry from earth orbit and about 11.2 km/s for entry after returning from a lunar mission. At these extreme hypersonic speeds, aerodynamic heating of the entry vehicle becomes very severe, and is the dominant concern in the design of such vehicles. Therefore, you know that your task involves the design of a ***blunt body*** for hypersonic speed. Moreover, you know from supersonic wind tunnel experiments that the flow field over the blunt body is qualitatively like that sketched in **Figure 1.2.1**. You know that a strong curved bow shock wave sits in front of the blunt nose, detached from the nose by the distance δ, called the shock detachment distance. You know that the gas temperatures between the shock and the body can be as high as 7000K for an ICBM, and 11000K for entry from a lunar mission.

And you know that you must understand some of the details of this flow field in order to intelligently design the entry vehicle. So, your first logical step is to perform an analysis of the aerodynamic flow over a blunt body in order to provide detailed information on the pressure and heat transfer distributions over the body surface, and to examine the properties of the high-temperature shock layer between the bow shock wave and the body. You ask such questions as: what is the shape of the bow shock wave; what is the detachment distance δ; what are the velocity, temperature and pressure distributions throughout the shock layer, etc.? However, much to your dismay, you find that no

---

[1] ***Live Science*** Web Page.

[2] John D. Anderson Jr., Joris Degroote, G´erard Degrez, Erik Dick, Roger Grundmann and Jan Vierendeels, "*Computational Fluid Dynamics - An Introduction*", 3rd Edition, ISBN: 978-3-540-85055-7, 2009.

reliable, accurate aerodynamic theory exists to answer your questions. You quickly discover that an accurate and practical analysis of supersonic blunt body flows is beyond your current state-of-the-art. As a result, you ultimately resort to empirical information along with some simplified but approximate theories (such as Newtonian theory) in order to carry out your designated task of designing the entry vehicle.

The above paragraph illustrates one of the most important, yet perplexing, aerodynamic problems of the 1950s and early 1960s. The application of blunt bodies had become extremely important due to the advent of ICBMs, and later the manned space program. Yet, no aerodynamic theory existed to properly calculate the flow over such bodies. Indeed, entire sessions of technical meetings (such as meetings of the Institute for Aeronautical Sciences in the USA, later to become the American Institute for Aeronautics and Astronautics) were devoted exclusively to research on the supersonic blunt body problem. Moreover, some of the best aerodynamicists of that day spent their time on this problem, funded and strongly encouraged by the NACA (later NASA), the US Air Force and others. What was causing the difficulty? Why was the flow field over a body moving at supersonic and hypersonic speeds so hard to calculate? The answer rests basically in the sketch shown in **Figure 1.2.1,** which illustrates the steady flow over a supersonic blunt body. The region of steady flow near the nose region behind the shock is locally subsonic, and hence is governed by elliptic partial differential equations. In contrast, the flow further downstream of the nose becomes supersonic, and this locally steady supersonic flow is governed by hyperbolic partial differential equations. (What is meant by ***'elliptic'*** and ***'hyperbolic'*** equations, and the mathematical distinction between them, will be discussed them later). The dividing line between the subsonic and supersonic regions is called the sonic line, as sketched in **Figure 1.2.1**.

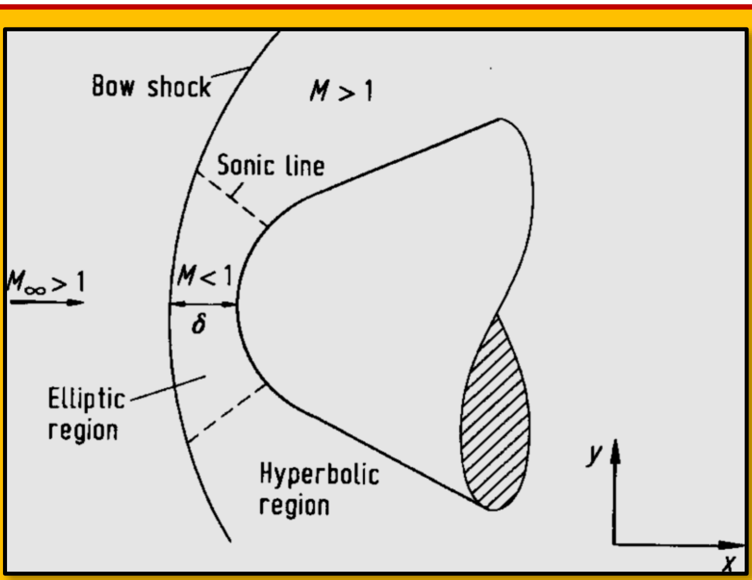

Figure 1.2.1 Flow over a Supersonic Blunt Body

The change in the mathematical behavior of the governing equations from elliptic in the subsonic region to hyperbolic in the supersonic region made a consistent mathematical analysis, which included both regions, virtually impossible to obtain. Techniques were developed for just the subsonic portion, and other techniques (such as the standard '***method of characteristics'***) were developed for the supersonic region. Unfortunately, the proper patching of these different techniques through the transonic region around the sonic line was extremely difficult. Hence, as late as the mid-1960s, no uniformly valid aerodynamic technique existed to treat the entire flow field over the blunt body. This situation was clearly noted in the classic textbook by [Liepmann and Roshko][3] published in 1957, where in a discussion of blunt body they state: ***The shock shape and detachment distance cannot, at present, be theoretically predicted.*** The purpose of this lengthy discussion on the status of the blunt body problem in the late 1950s is to set the background for the following important point. In 1966, a breakthrough occurred in the blunt body problem. Using the developing power of

---

[3] Liepmann, H.W. and Roshko, A., "*Elements of Gas dynamics*", Wiley, New York, 1957.

Computational Fluid Dynamics (CFD) at that time, and employing the concept of a '***time-dependent'*** approach to the steady state, [Moretti and Abbett][4] developed a numerical, finite-difference solution to the supersonic blunt body problem which constituted the first practical, straightforward engineering solution for this flow. After 1966, the blunt body problem was no longer a real problem. Industry and government laboratories quickly adopted this computational technique for their blunt body analyses. Perhaps the most striking aspect of this comparison is that the supersonic blunt body problem, which was one of the most serious, most difficult, and most researched theoretical aerodynamic problems of the 1950s and 1960s, is today assigned as a *homework problem* in a computational fluid dynamics graduate course at the University of Maryland. Therein lies an example of the power of ***Computational Fluid Dynamics (CFD)***. The above example concerning blunt body flows serves to illustrate the importance of computational fluid dynamics to modern aerodynamic applications. Here is an important problem which was impossible to solve in a practical fashion before the advent of computational fluid dynamics (CFD), but which is now tractable and straightforward using the modern techniques of CFD. Indeed, this is but one example out of many where CFD is revolutionizing the world of aerodynamics.

1.3 From Subsonic to Hypersonic Wings

The aerodynamic characteristics of an aircraft are closely related to its flight speed range[5]. As shown in **Figure 1.3.1** and **Figure 1.3.2** [6], the optimized aerodynamic configurations are quite different in different speed ranges. Therefore, combining the configuration characteristics of the aircraft in different flight speed ranges can be used as a development idea to find the optimal wide speed range wave rider configuration. To this end, a good understanding of the non-linear behavior of the vortex generated lift as discussed in is very important. As discussed in Ref. [7], the aerodynamic performance of the wave rider is closely related to the aerodynamic state of its leading edge, that is, to the average aspect ratio of the wave rider. When the leading edge of the wave rider is subsonic, the flow field exhibits typical characteristics of a subsonic

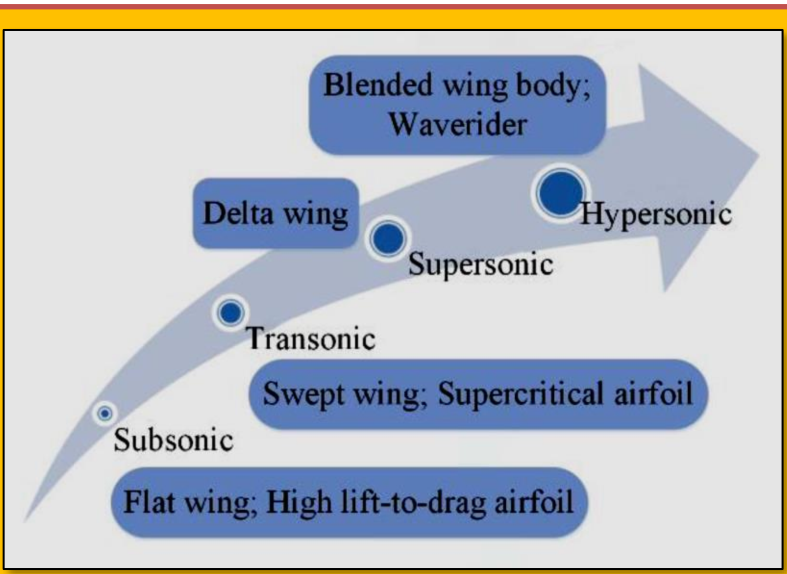

Figure 1.3.1 Optimal Aerodynamic Configuration At Different Speed Ranges

---

[4] Moretti, G. and Abbett, M., '*A Time-Dependent Computational Method for Blunt Body Flows*,' AIAA Journal, Vol. 4, No. 12, December 1966, pp. 2136–2141.

[5] Zhen-tao Zhao, Wei Huang,Li Yan, Yan-guang Yang,, "*An overview of research on wide-speed range wave rider configuration*", Article *in* Progress in Aerospace Sciences · February 2020.

[6] Küchemann D. *The aerodynamic design of aircraft*. Pergamon Press, 1978.

[7] Li WD, Ding H H, Wang F M. *Research on aerodynamic characteristics of wave rider-based vehicles flying at low-Mach states*. Journal of Astronautics, 2010, 31(5): 1283-1288 (in Chinese).

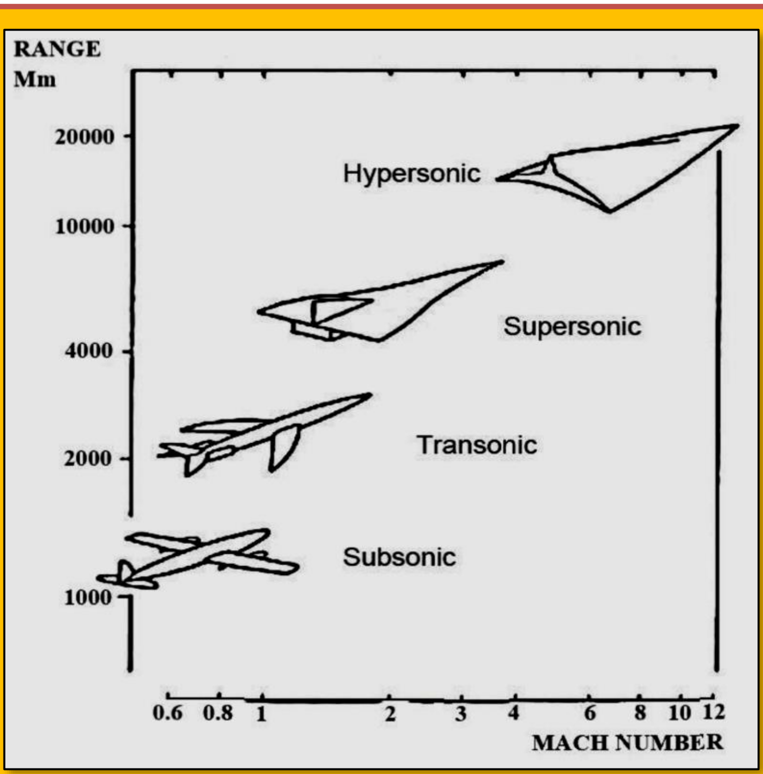

Figure 1.3.2 The Aircraft Pedigree (Courtesy of Küchemann)

flow field, and its lift is mainly derived from leading edge vortices near the leading edge of the upper surface. On the other hand, when the leading edge is supersonic, the compression effect of the shock near the leading edge becomes the main source of the lift of the wave rider. Therefore, another development idea of the wide-speed range wave rider is to analyze and study the characteristics of vortex flow around the wave rider, and then design a wave rider which can effectively employ the vortex effect to improve the subsonic performance and the shock effect to improve the super/hypersonic erformance, respectively. For example, the study in Ref.[8] is a design that combines vortex lift and compression lift to improve the aerodynamic performance of the wave rider over a wide-speed range.

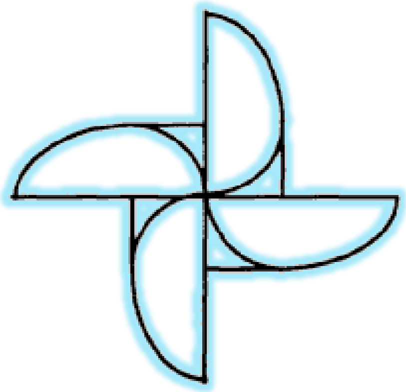

---

[8] Liu C Z, Liu Q, Bai P, et al. *Planform-customized wave rider design integrating with vortex effect*. Aerospace Science and Technology, 2019,86: 438-443.

2 Viscous Flow

2.1 Qualitative Aspects of Viscous Flow

Viscous flow could be defined as a flow where the effects of viscous dissipation, thermal conductivity, and mass diffusion are important and could not be ignored[9]. All are consequence of assuming a viscous surface where the effects of friction, creating ***shear stress***, on the surface are pronounced. There are number of interesting and important conditions associated with viscous effect that should be analyzed separately. In general, two regions to consider, even the divisions between not very sharp:

- A very thin layer in the intermediate neighborhood of the body, δ, in which the velocity gradient normal to the wall, ∂u/∂y, is very large (***Boundary Layer***). In this region the very small viscosity of μ of the fluid exerts an essential influence in so far as the shearing stress $\tau = \mu\ (\partial u/\partial y)$ may assume large value.
- In the remaining region no such a large velocity gradient occurs and the influence of viscosity is unimportant. In this region the flow is ***frictionless and potential.***

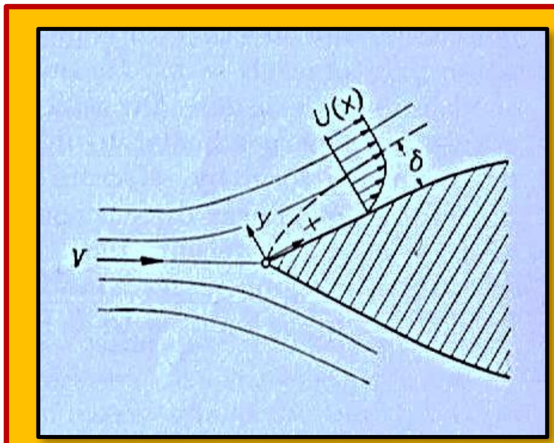

Figure 2.1.1 Boundary Layer Flow along a Wall

The general form on boundary layer equations, shown in **Figure 2.1.1**, and their characteristic will be discussed later.

2.1.1 No-Slip Wall Condition

Due to influence of friction, the velocity approaches zero on the surface and this is dominant factor in viscous flows which could easily be observed. Or more precisely:

$$V_{\text{fluid}} = V_{\text{solid}} \quad \& \quad T_{\text{fluid}} = T_{\text{solid}}$$

Eq. 2.1.1

2.1.2 Flow Separation

Figure 2.1.2 Airflow Separating from a Wing at a High Angle of Attack

Another contribution due to friction and shear stress is the effects of flow separation or adverse pressure gradient. If the flow over a body is turbulent, it is less likely to separate from the body surface, and if flow separation does occur, the separated region will be smaller (see **Figure 2.1.2**). As a result, the pressure drag due to flow separation D_p will be smaller for turbulent flow. This discussion points out one of the great compromises in aerodynamics. For the flow over a body, is laminar or turbulent flow preferable? There is no pat answer; it depends on the shape of the body. In general, if the body is slender, as sketched in **Figure 2.1.3-a**, the friction drag D_f is much greater than D_p. For this case, because D_f is smaller for laminar than for turbulent flow, laminar flow is desirable for slender bodies.

---

[9] White, Frank M. 1974: *Viscous Fluid Flow*, McGraw-Hill Inc.

In contrast, if the body is blunt, as sketched in **Figure 2.1.3-b**, D_p is much greater than D_f. For this case, because D_p is smaller for turbulent than for laminar flow, turbulent flow is desirable for blunt bodies.

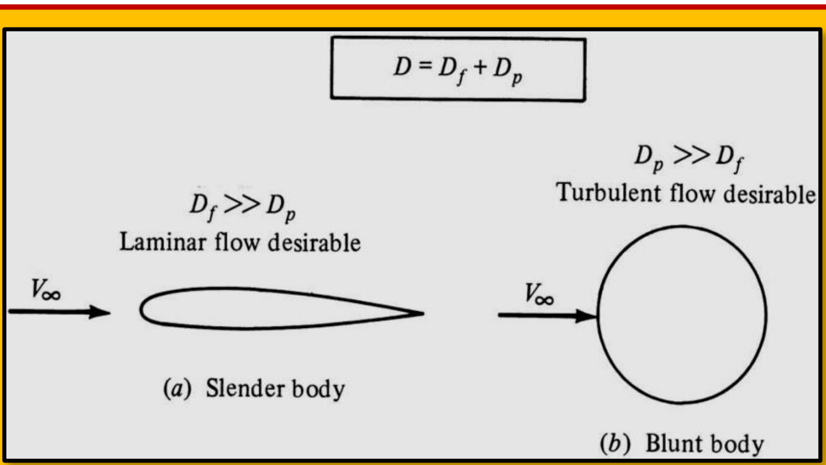

Figure 2.1.3 Drag on Slender & Blunt Bodies

The above comments are not all-inclusive; they simply state general trends, and for any given body, the aerodynamic virtues of laminar versus turbulent flow must always be assessed. Although, from the above discussion, laminar flow is preferable for some cases, and turbulent flow for other cases, in reality we have little control over what actually happens. Nature makes the ultimate decision as to whether a flow when left to itself, will always move toward its state of maximum disorder. To bring order to the system, we generally have to exert some work on the system or expend energy in some manner. (This analogy can be carried over to daily life; a room will soon become cluttered and disordered unless we exert some effort to keep it clean.) Since turbulent flow is much more "disordered" than laminar flow, nature will always favor the occurrence of turbulent flow. Indeed, in the vast majority of practical aerodynamic problems, turbulent flow is usually present[10].

2.1.2.1 Supersonic Laminar Flow

In recent years, there was a tendency to achieve laminar flow in supersonic speeds, without violating **Figure 2.1.4**. The goal was to investigate active and passive ***Laminar Flow Control (LFC)*** as a potential technology for a future ***High Speed Civil Transport (HSCT)***[11]. The computation of boundary-layer properties and laminar-to-turbulent transition location is a complex problem generally not undertaken in the context of aircraft design[12]. Yet this is just what must be done if an aircraft designer is to exploit the advantages of laminar flow while making the proper trade-offs

Figure 2.1.4 The Porous Titanium LFC Glove is Clearly seen on the Left Wing of test aircraft - NASA Photo EC96-43548-7

---

[10] John D. Anderson, Jr., "*Fundamentals of Aerodynamics*", 5th Edition, McGraw-Hill Companies, 2007.

[11] NASA TF-2004-12 DFRC.

[12] Peter Sturdza, "*An Aerodynamic Design Method For Supersonic Natural Laminar Flow Aircraft*", a dissertation submitted to the department of aeronautics and astronautics and the committee on graduate studies of Stanford university, December 2003.

between inviscid drag, structural weight and skin friction. Potential benefits of laminar flow over an aircraft's wings include increased range, improved fuel economy, and reduced aircraft weight. These benefits add up to improved economic conditions, while also reducing the impact of exhaust emissions in the upper atmosphere where a supersonic transport would normally operate.

Laminar conditions are hard to achieve and maintain. There are two basic techniques to achieve laminar conditions: ***passive*** (without mechanical devices), and ***active*** (using suction devices). Passive laminar flow can be achieved in the wing design process, but the laminar condition is normally very small in relation to the wing's cord and is usually confined to the leading edge region. Passive laminar flow can also be created on an existing wing by altering the cross-sectional contour of the lifting surface to change the pressure gradient. Both of these laminar conditions are called natural laminar flow. Active control LFC must be used to achieve laminar flow across larger distances from the leading edge. The main means of achieving active LFC is to remove a portion of the turbulent boundary layer with a suction mechanism that uses porous material, slots in the wing, or tiny perforations in the wing skin. **Figure 2.1.4** displays the active mode of LFC with a suction system beneath the wing's surface was used to achieve laminar flow over 46 percent of the glove's surface while flying at a speed of Mach 2 in a successful demonstration of laminar flow at supersonic speeds. Other methods include the boundary-layer analyses which are computationally inexpensive, as well as, sufficiently accurate to provide guidance for advanced design studies. The boundary-layer solver could be based on an enhanced quasi-3D sweep/taper theory which is revealed to agree well with 3D Navier-Stokes results[13]. The transition calculation scheme is implemented within the boundary-layer solver and automatically triggers a turbulence model at the predicted transition front. transition for a supersonic flight test.

2.1.3 Skin Friction and Skin Friction Coefficient

When the boundary layer equations are integrated, the velocity distribution can be deduced, and point of separation can be determined. This in turn, permits us to calculate the viscous drag (skin friction) around a surface by a simple process of integrating the shearing stress at the wall and viscous drag for a 2D flow becomes:

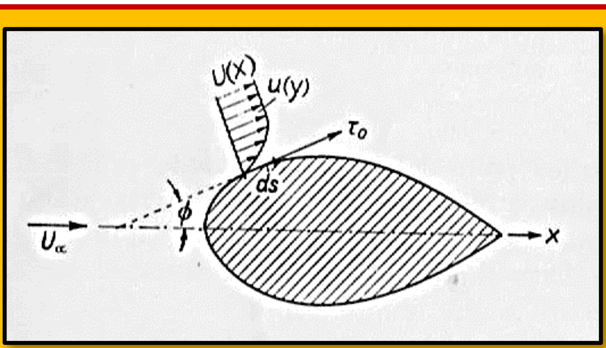

Figure 2.1.5 Illustrating the calculation of Skin Friction – Courtesy of John D. Anderson Jr.

$$T_w = \mu \left(\frac{\partial u}{\partial y}\right)_{y=0}$$

$$D_f = b \int_{s=o}^{L} \tau_w \cos\ \varphi\ ds$$

Eq. 2.1.2

Where *b* denotes the height of cylindrical body, φ is the angle between tangent to the surface and the free-stream velocity U_∞, and *s* is the coordinate measured along the surface, as shown in **Figure 2.1.5**. The dimensionless ***friction coefficient C_f, is commonly referred to the free-stream dynamic pressure*** as:

$$C_f = \frac{2\tau_w}{\rho U_\infty^2}$$

Eq. 2.1.3

---

[13] See Previous.

2.1.3.1 Case Study - Image-Based Modelling of the Skin-Friction Coefficient

We develop a model of the skin-friction coefficient based on scalar images in the compressible, spatially evolving boundary-layer transition [Zheng et al.][14]. The multi-scale and multi-directional geometric analysis is applied to characterize the averaged inclination angle of spatially evolving filtered component fields at different scales ranging from a boundary-layer thickness to several viscous length scales. The prediction of the skin-friction coefficient C_f in compressible boundary layers is critically important for the design of high-speed vehicles and propulsion systems. The boundary-layer transition has a strong influence on ***aerodynamic drag*** and ***heating,*** because much higher friction and heating can be generated on the surface of aerospace vehicles in turbulent flows than those in laminar flows. Despite considerable efforts in theoretical, experimental and numerical studies, the reliable prediction of the skin friction coefficient in compressible boundary layers is still very challenging [Zhong & Wang].

The theoretical study of the empirical formula of C_f in compressible boundary layers, in general, is restricted to the laminar or fully developed turbulent state. The empirical formulae of C_f for compressible laminar and turbulent boundary layers are transformed from their counterparts in incompressible boundary layers.

In general, the averaged inclination angles increase along the streamwise direction, and the variation of the angles for large-scale structures is smaller than that for small-scale structures. Inspired by the coincidence of the increasing averaged inclination angle and the rise of the skin-friction coefficient, The evolutionary geometry of coherent structures with different scales and inclination angles in the laminar–turbulent transition is sketched in **Figure 2.1.6**, along with the rise of C_f . The superposition of hierarchies of attached and inclined vortical structures is also suggested by the models (e.g. Perry & Chong 1982; Marusic & Monty) based on the attached eddy hypothesis (Townsend).

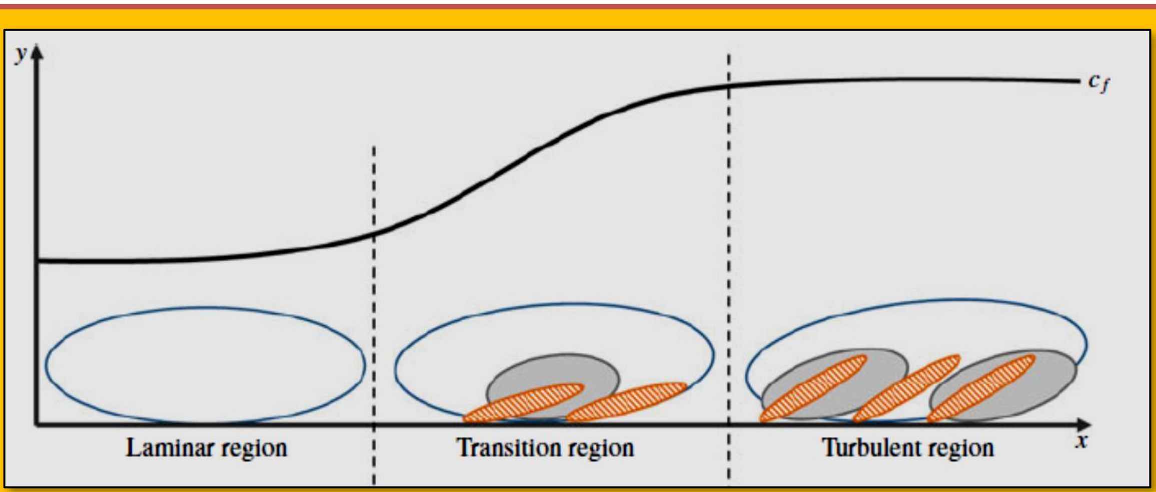

Figure 2.1.6 Evolutionary geometry of vortical or scalar structures, sketched by the ellipses with different scales and inclination angles, in the boundary-layer transition, along with the rise of the skin-friction coefficient C_f

2.1.3.1.1 Inclined Structures and Drag Production

The relatively accurate prediction of C_f in the image-based model indicates that the generation of inclined small-scale flow structures is closely related to the drag production. As sketched in **Figure 2.1.7,** one possible reason is that the lifts of material surfaces during the transition, which are good surrogates of vortex surfaces consisting of vortex lines, can generate strong inclined shear layers

---

[14] Wenjie Zheng1, Shanxin Ruan, Yue Yang, Lin He and Shiyi Chen, "*Image-based modelling of the skin-friction coefficient in compressible boundary-layer transition*", J. Fluid Mech. (2019), vol. 875, pp. 1175_1203.

[Zhao et al.] to increase C_f. Assume the flow field is filled with wall-parallel material surfaces in the laminar state with all the surface normal $\mathbf{n}_\phi=\nabla\phi/|\nabla\phi|$ pointing to the wall-normal direction.

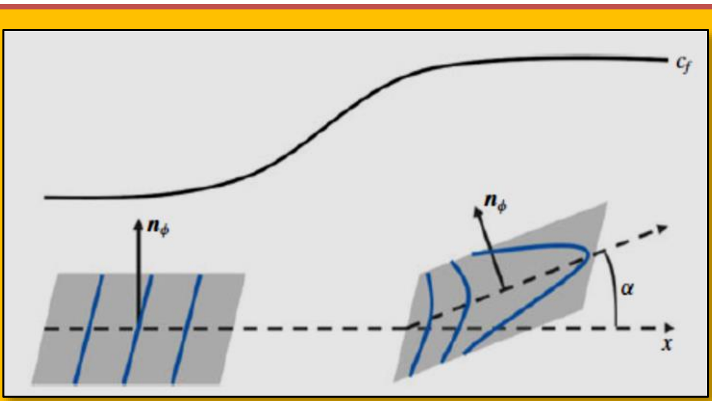

Figure 2.1.7 Diagram of the geometry of material surfaces and typical vortex lines near the surfaces, along with the rise of cf . Solid lines denote vortex lines, and solid vectors n_ denote the normal of material surfaces.

In the transitional region, the near-wall material surfaces are lifted due to the growing streamwise vorticity. This elevation event is quantified by the wall-normal Lagrangian displacement where Y is the wall-normal location of a fluid particle on a material surface. The displacement ΔY quantifies the scalar transport in the wall-normal direction within a time interval of interest, and [Zhao et al.] define the Lagrangian events 'elevation' with $\Delta Y > 0$ and 'descent' with $1Y < 0$. The contour of ΔY and the contour lines of high shear $\partial u/\partial y$ in the transitional region are shown in **Figure 2.1.8**.

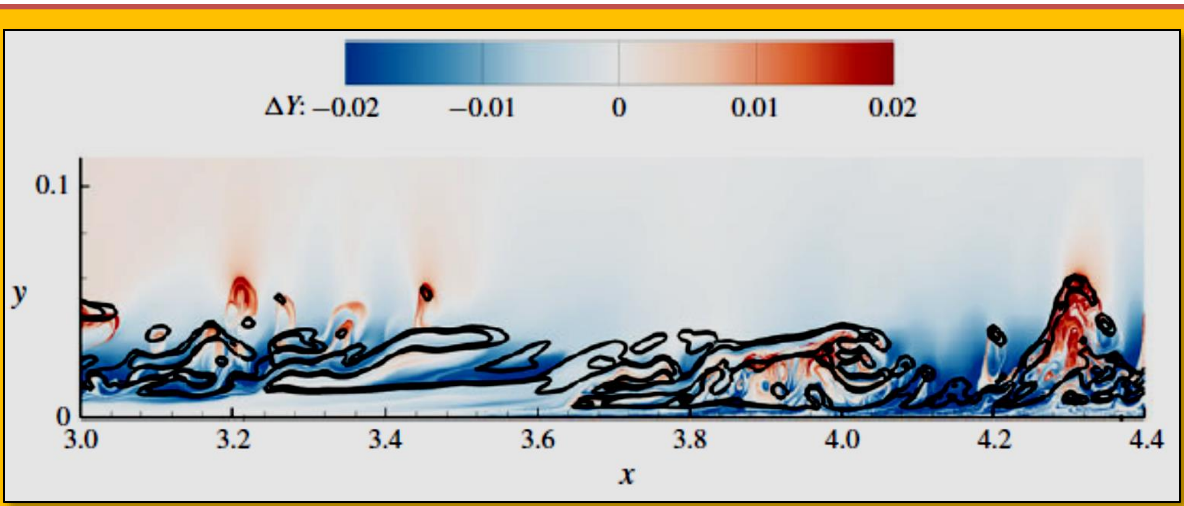

Figure 2.1.8 The contour of the Lagrangian wall-normal displacement ΔY and contour lines for the strong shear layers on the x–y plane in the transitional region at $M_\infty = 6$.

In general, the inclined high shear layers cover the region with $\Delta Y > 0$, which is similar to the observation in an incompressible temporal transitional channel flow in [Zhao et al.], because the strong shear layer can be generated between the elevated low-speed fluid and the surrounding high-speed fluid. Furthermore, the region with $\Delta Y > 0$, which also corresponds to the inclined scalar structure with n_ϕ, deviates from the wall-normal direction as sketched in **Figure 2.1.7**, which can be characterized as a finite $< \alpha >$ in the multi-directional analysis. Thus the inclined high shear layers accelerate the momentum transport and produce the large Reynolds shear stress [Zhao et al.], which can increase C_f implied by the relation between the Reynolds shear stress and C_f [Fukagata et al.; Gomez, Flutet & Sagaut].

2.1.3.1.2 Reference

- Zhong, X. & Wang, X. 2012 *Direct numerical simulation on the receptivity, instability, and transition of hypersonic boundary layers.* Annual Rev. Fluid Mech. 44, 527–561.
- Perry, A. E. & Chong, M. S. 1982 *On the mechanism of wall turbulence*. J. Fluid Mech. 119.
- Marusic, I. & Monty, J. P. 2019 *Attached eddy model of wall turbulence*. Annual Rev. Fluid Mech. 51, 49–74.
- Townsend, A. A. 1976 *The Structure of Turbulent Shear Flow*, 2nd ed. Cambridge University Press.
- Zhao, Y., Xiong, S., Yang, Y. & Chen, S. 2018 *Sinuous distortion of vortex surfaces in the lateral growth of turbulent spots.* Phys. Rev. Fluids 3, 074701.
- Zhao, Y., Yang, Y. & Chen, S. 2016 *Evolution of material surfaces in the temporal transition in channel flow*. J. Fluid Mech. 793, 840–876.
- Fukagata, K., Iwamoto, K. & Kasagi, N. 2002 *Contribution of Reynolds stress distribution to the skin friction in wall-bounded flows*. Phys. Fluids 14, L73–76.
- Gomez, T., Flutet, V. & Sagaut, P. 2009 *Contribution of Reynolds stress distribution to the skin friction in compressible turbulent channel flows*. Phys. Rev. E 79, 035301.

2.1.4 Aerodynamic Heating

Another overall physical aspect of viscous flow is the influence of thermal conduction. On a fluid over a surface, the moving fluid elements have certain amount of kinetic energy. As the flow velocity decreases under influence of friction, the kinetic energy decreases[15]. This lost kinetic energy reappears in the form on internal energy of the fluid, hence, causing temperature to rise. This phenomenon is called viscous dissipation within the fluid. This temperature gradient between fluid and surface would cause the transfer of heat from fluid to surface. This is called ***Aerodynamic Heating*** of a body. Aerodynamic heating becomes more severe as the flow velocity increase, because more kinetic energy is dissipated by friction, and hence, the temperature gradient increases. In fact it is one of the dominant aspects of hypersonic flows. The block diagram of **Figure 2.1.9,**

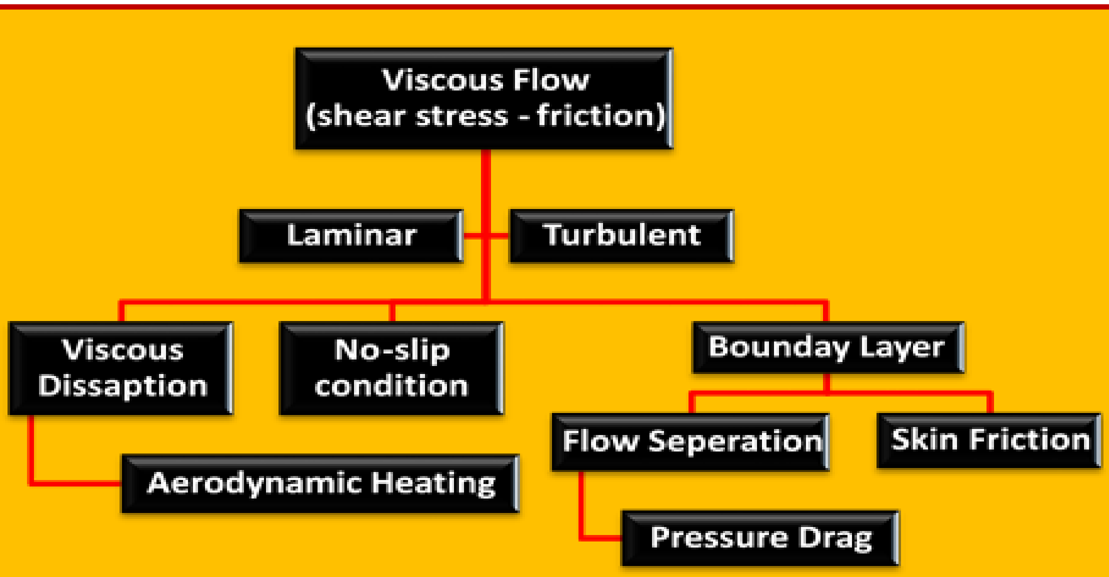

Figure 2.1.9 Quantitate Aspects of Viscous Flow

---

[15] Anderson, John D. 1984: "*Fundamentals of Aerodynamics*", McGraw Hills Inc.

summarizes these finding for viscous flow.

2.1.5 Reynolds Number

The Reynolds number is a measure of ratio of inertia forces to viscous forces,

$$Re = \frac{\rho UL}{\mu} = \frac{UL}{\nu}$$

Eq. 2.1.4

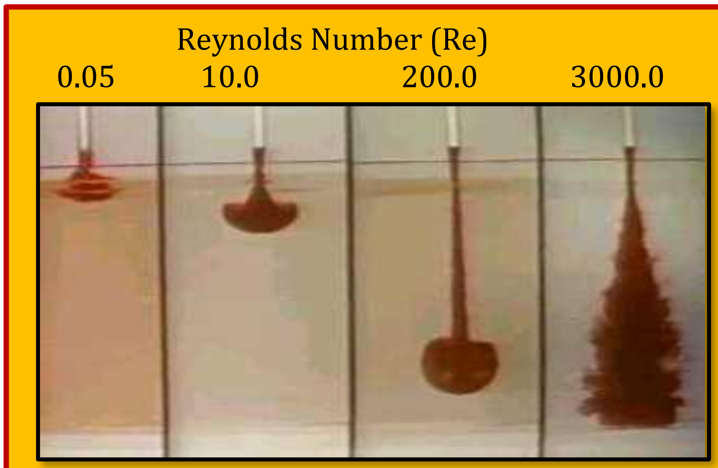

Figure 2.1.10 Effects of Reynolds Number in Inertia vs Viscosity

Where U and L are local velocity and characteristic length. This is a very important scaling tool for fluid flow equations as to be seen later. Additionally, it could be represents using dynamic viscosity $\nu = \mu/\rho$. This is a really is measure or scaling of inertia vs viscous forces as shown in **Figure 2.1.10** and has great importance in Fluid Mechanics. It can be used to evaluate whether viscous or inviscid equations are appropriate to the problem. The Reynolds Number is also valuable tool and guide to the in a particular flow situation, and for the scaling of similar but different-sized flow situations, such as between an aircraft model in a wind tunnel and the full size version[16].

2.1.6 Reynolds Number Effects in Reduced Model

The kinematic similarity between full scale and scaled tests has to be maintained for reduced model testing (wind-tunnels). In order to maintain this kinematic similarity, all forces determining a flow field must be the same for both cases. For incompressible flow, only the forces from inertia and friction need to be considered (i.e., Reynold Number). Two flow fields are kinematically similar if the following condition is met

$$\frac{U_1 L_1}{\nu_1} = \frac{U_2 L_2}{\nu_2}$$

Eq. 2.1.5

To recognize Reynolds number effects a dependency test should be done[17]. Results from such a dependency study are presented in **Figure 2.1.11**. At high Reynolds numbers, the drag coefficient is almost constant, and the values for the full scale vehicle are slightly lower than those for the scaled model. Below a certain Reynolds number, however, the drag coefficient from the scaled test noticeably deviates from the full scale results. That is due to the fact, that in this range, individual components of the car go through their critical Reynolds number. Violating Reynolds' law of similarity can cause considerable error. On the other hand, for small scales, sometimes it is hard to maintain the same Reynolds number. That is for two main reasons. Wind tunnels have limited top speed. At the same time, increasing speed in model testing also has its limits in another perspective.

---

[16] From Wikipedia, the free encyclopedia.

[17] Bc. Lukáš Fryšták, "Formula SAE Aerodynamic Optimization", Master's Thesis, BRNO 2016.

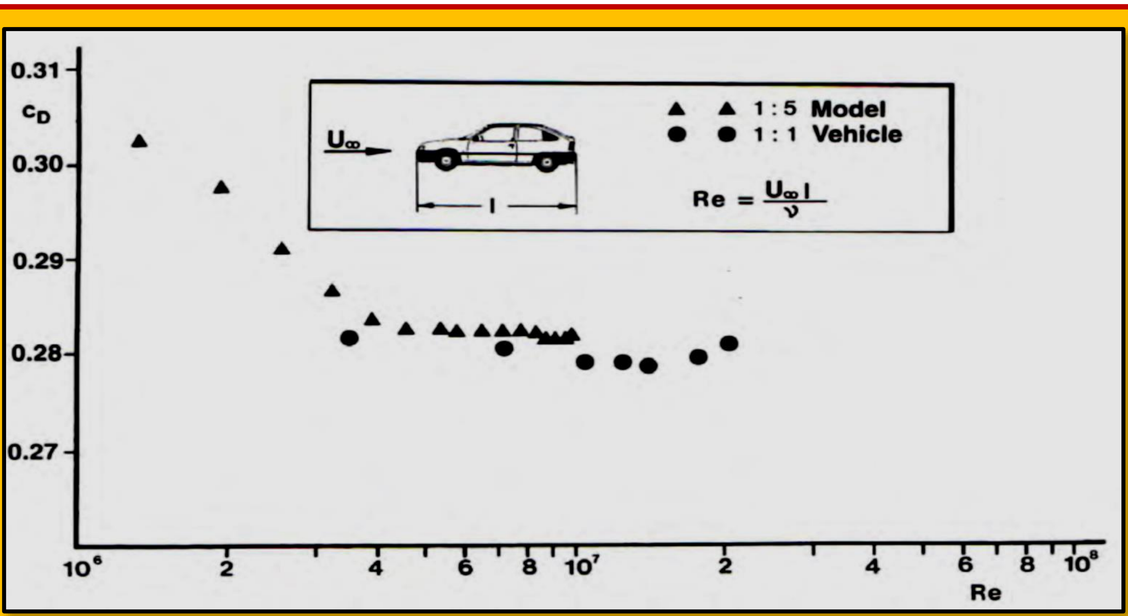

Figure 2.1.11 Drag Coefficient versus Reynolds Number for a 1:5 Model and a Car (Courtesy of [35])

2.1.7 Case Study - Scaling and Skin Friction Estimation in Flight using Reynold Number

Now that we familiar ourselves with some concepts if viscous flow, such as Reynolds Number, separation, boundary layer and skin friction, it is time to see their effects in real life situation. The purpose here is to conduct a brief review of skin-friction estimation over a range of Reynolds numbers, as this is one of the key parameters in performance estimation and Reynolds number scaling. These are among the most important in Aerodynamic performance. The flow around modern aircraft can be highly sensitive to Reynolds number and its effects when they move significantly the design of an aircraft as derived from sub-scale wind tunnel testing as investigated by [Crook][18]. For a transport aircraft, the wing is the component most sensitive to Reynolds number change. **Figure**

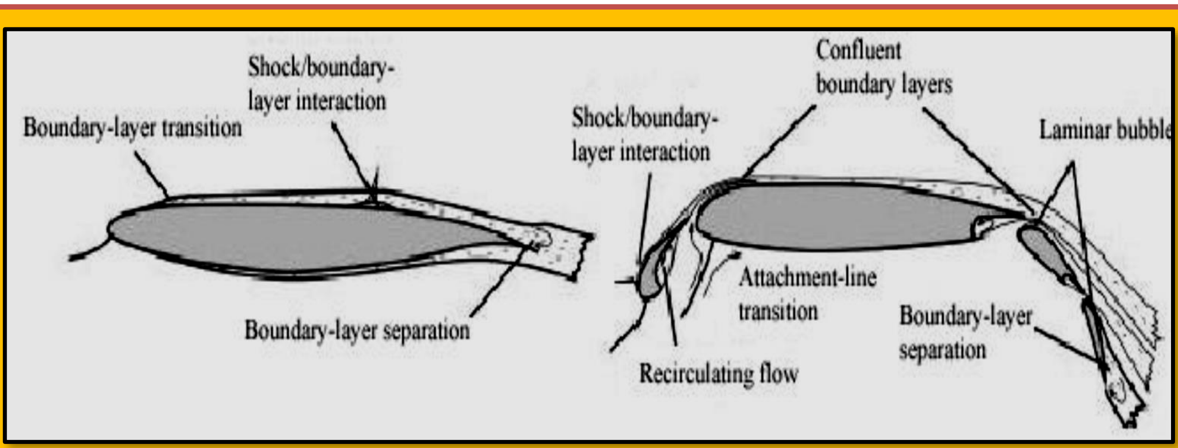

Figure 2.1.12 Flow features sensitive to Reynolds number for a cruise condition on a wing section

---

[18] A. Crook, "*Skin-friction estimation at high Reynolds numbers and Reynolds-number effects for transport aircraft*", Center for Turbulence Research Annual Research Briefs, 2002.

2.1.12 shows the flow typically responsible for such sensitivity, which includes boundary layer transition, shock/boundary layer interaction and trailing-edge boundary layer.

2.1.7.1 Interaction Between Shock Wave and Boundary Layer

The nature of the interaction between a shock wave and an attached boundary layer depends largely upon whether the boundary layer is laminar or turbulent at the foot of the shock. For a laminar boundary layer, separation of the boundary layer will occur for a relatively weak shock and upstream of the freestream position of the shock. The majority of the pressure rise in this type of shock /boundary layer interaction, generally described as a ¸ shock, occurs in the rear leg. The interaction of the rear leg with the separated boundary layer causes a fan of expansion waves that tend to turn the flow toward the wall, and hence re-attach the separated boundary layer. This is in contrast to the interaction between a turbulent boundary layer and a shock wave, in which the majority of the pressure rise occurs in the front leg of the shock wave. The expansion fan that causes reattachment of the laminar separated boundary layer is therefore not present, and the turbulent boundary layer has little tendency to re-attach. Here lies the problem of predicting the flight performance of an aircraft when the methods used to design the aircraft have historically relied upon wind tunnels operating below flight Reynolds number, together with other tools such as (CFD), empirical and semi-empirical methods and previous experience of similar design aircraft. Industrial wind tunnels can only achieve a maximum chord Reynolds number of between $3 \times 10^6 < Re_c < 16 \times 10^6$, compared with a typical value of 45×10^6 for cruise conditions. Therefore historically, results from wind tunnels have to ***be extrapolated*** to flight conditions in a process known as ***Reynolds Number Scaling***. Wind tunnel models are generally supported free flying. As flow around them is constrained by the tunnel walls, and therefore support and wall interference must be accounted for correctly. The freestream flow may also have a different turbulent length scale, turbulence intensity and spectrum to that occurring in the atmosphere. Other effects which can be wrongly interpreted as Reynolds number effects include the tunnel calibration, buoyancy effects, thermal equilibrium and humidity, as discussed by [Haines][19]

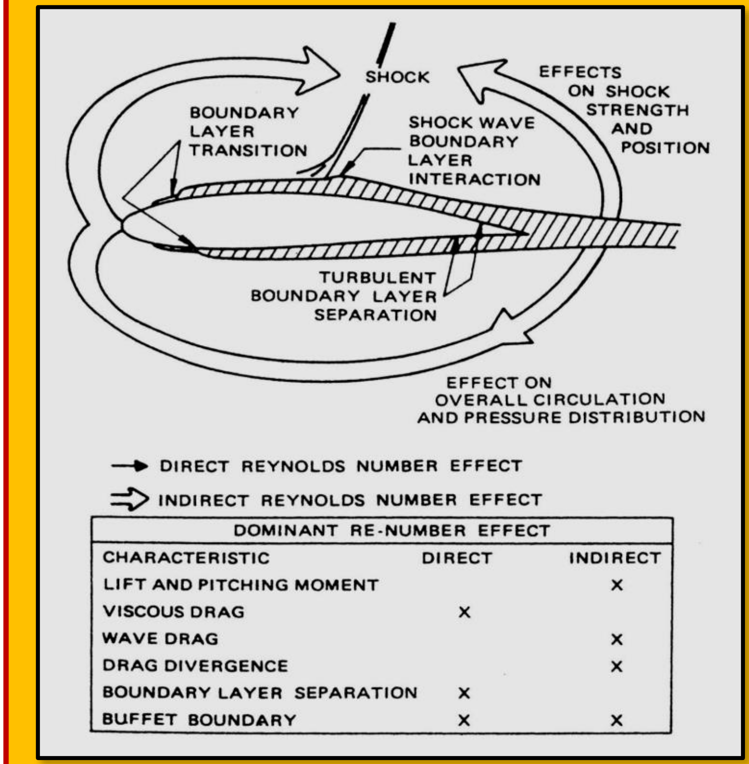

DOMINANT RE-NUMBER EFFECT		
CHARACTERISTIC	DIRECT	INDIRECT
LIFT AND PITCHING MOMENT		X
VISCOUS DRAG	X	
WAVE DRAG		X
DRAG DIVERGENCE		X
BOUNDARY LAYER SEPARATION	X	
BUFFET BOUNDARY	X	X

Figure 2.1.13 Schematic representation of direct and indirect Reynolds number effects

2.1.7.2 Reynolds Number Scaling

Rendering to [Haines & Elsenaar][20], there are two types of scale effect: ***Direct*** and ***Indirect***, which is based upon the definition by Hall[21] of scale effects being the complex of

---

[19] Haines, A. B., "Scale *Effects On Aircraft and Weapon Aerodynamics*", AGARDograph AG-323, 1994.

[20] Haines, A. B. & Elsenaar, A., "*An outline of the methodology Boundary layer simulation and control in wind tunnels*", AGARD Advisory Report AR-224, 96-110-1988.

[21] Hall, M. G., "*Scale Effects In Flows Over Swept Wings*", AGARD CP 83-71, 1971.

interactions between the boundary layer development and the external inviscid flow. *Direct* and *Indirect* Reynolds number effects are represented schematically in **Figure 2.1.13** and defined as:

1. ***Direct Reynolds Number*** effects occur as a consequence of a change in the boundary layer development for a fixed (frozen) pressure distribution. Examples of direct effects range from the well-known variation of skin friction with Reynolds number for a given transition position to complex issues such as changes in the length of a shock-induced separation bubble for a given pressure rise through a shock.
2. ***Indirect Reynolds number*** properties are associated with changes in the pressure distribution arising from changes with Reynolds number in the boundary layer and wake development. An example of an indirect effect is when changes in the boundary layer displacement thickness with Reynolds number lead to changes in the development of supercritical flow, and hence in shock position and shock strength. Therefore, a change in wave drag with Reynolds number at a given C_L or incidence, can appear as an indirect Reynolds number effect[22].

2.1.7.3 Discrepancy in Flight Performance and Wind Tunnel Testing

[Haines][23] provides a historical review of scale effects and gives examples of aircraft where direct properties dominated the wing flow, and indirect effects were probably small. The examples given are those of the VC-10 and X-1 aircraft, and correlation between wing pressure distributions in the wind tunnel and in flight are good. It is observed that the shock position in flight is slightly aft of that found in the tunnel test for these test conditions, when the flow is attached, with little or no trailing edge separation, and is turbulent. The reason for this behavior in these two cases is the thinning of the boundary layer with increasing Reynolds number, with the displacement thickness being roughly proportional to $Re^{-1/5}$. The effective thickness of the wing therefore decreases and the effective camber increases with increasing Reynolds number. The shock wave will move downstream with reduced viscous effects until the limiting case of inviscid flow is reached. If however, C_L is kept

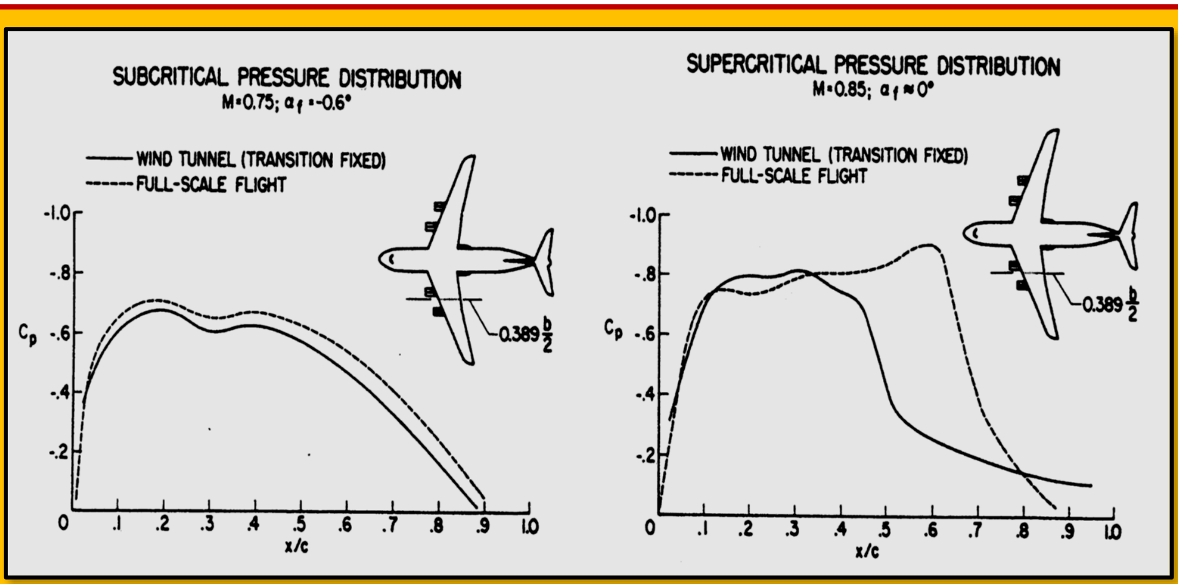

Figure 2.1.14 Comparison of C-141 Wing Pressure Distributions Between Wind Tunnel and Flight

---

[22] A. Crook, "*Skin-friction estimation at high Reynolds numbers and Reynolds-number effects for transport aircraft*", Center for Turbulence Research Annual Research Briefs, 2002.

[23] Haines, A. B., "*Lanchester Memorial Lecture: Scale Effect in Transonic Flow*", Aeronautical J., August-September 1987, 291-313, 1987.

constant for a given Mach number, and the Reynolds number varied, the increased aft loading must be compensated by a decrease in the load over the front of the airfoil. This is generally accomplished by a decrease in the angle of incidence, which normally results in the forward movement of the shock wave. The final outcome of these opposing efforts will depend upon their relative strength. When the flow is attached or mostly attached, indirect Reynolds-number effects appear to be small. However, when the flow is separated large variations in the pressure distribution can result with varying Reynolds number i.e. indirect effects can be large as demonstrated in **Figure 2.1.14** where the comparison of C-141 wing pressure distributions between wind tunnel and flight for regions of subcritical (a) and Supercritical flow (b) is made. Aside from the separation that can occur due to an adverse pressure gradient at the trailing edge, shock-boundary layer interaction is one of the primary causes of separation in transonic flight.

2.1.7.4 Flow Separation Type (A - B)

Following the work of [Pearcey][24] such flow separations are classed as either type *A* or *B*. [Elsenaar][25] describes the differences between type A and type B separation, and states that the final state is the same both, namely a boundary-layer separation from the shock to the trailing edge. However, the mechanism by which this final state is achieved, differs for the two. For a type A separation, the bubble that forms underneath the foot of the shock grows until it reaches the trailing-edge. The type B separation has three variants, with the common feature being a trailing edge separation that is present before the final state is reached. The final state is reached when the separation bubble and Trailing-edge separation merge. The type B separation is considered to be more sensitive to Reynolds number than type A. This is partly because the trailing-edge separation is dependent upon the boundary layer parameters such as its thickness and displacement thickness. Furthermore, it was shown by [Pearcey & Holder][26] that the supersonic tongue that exists in a shock- boundary interaction is the dominant factor in the development of the separation bubble, and that the incoming boundary layer is less important. Moreover, the local shock Mach number that causes shock-induced separation is a weak function of the freestream Mach number. Relevant to wind tunnel-to-flight scaling is the possibility that at sufficiently high Reynolds numbers, the trailing edge separation will disappear and the type B flow that is observed in wind tunnels becomes a type A separation at flight conditions.

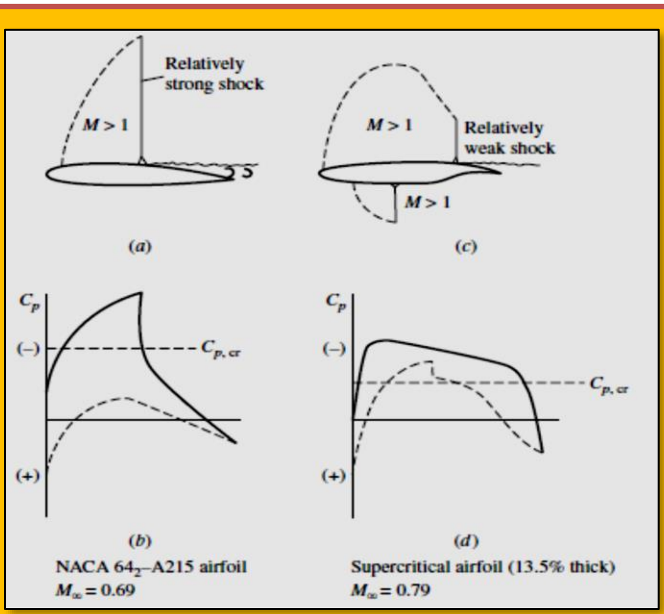

Figure 2.1.15 Standard NACA 64-series airfoil compared with a supercritical airfoil at cruise lift conditions

---

[24] Pearcey, H. H., Osborne, J. & Haines, A. B.," *The interaction between local effects at the shock and rear separation - a source of significant scale effects in wind tunnel tests on airfoils and wings*", AGARD CP 35, 1968.

[25] Elsenaar, A. Introduction. Elsenaar, A., Binion, T. W. & Stanewsky, E.,"*Reynolds number effects in transonic flow*", AG-303, 1-6, 1988.

[26] Pearcey, H. H. & Holder, D. W., "*Examples of shock induced boundary layer separation in Transonic flight*", Aeronautical Research Council Technical Report R & M No. 3012, 1954.

The behavior of the trailing-edge separation and that of the separation bubble are highly coupled, with the trailing-edge separation amplified by the upstream effects of the shock-boundary layer interaction. The trailing-edge separation will modify the pressure distribution in a Reynolds-number-dependent manner, and this in turn will alter the shock strength and the conditions for separation at the foot of the shock. This will then affect the boundary layer at the trailing edge. The sensitivity to Reynolds number of this interaction process will be dependent upon the pressure distribution and hence the type of airfoil. It is also argued that most pre-1960 airfoils show a rapid increase in shock strength with increasing Mach number and angle of incidence. By implication viscous effects would be small, and the dominant effect would be lengthening of the shock-induced separation bubble. By contrast, modern ***supercritical airfoils***[27] (see **Figure 2.1.15**) are designed to limit the variation in shock-wave strength and have higher aft loading and hence greater pressure gradients over the rear of the airfoil. Viscous effects will therefore be more important for these airfoils and there performance more sensitive to Reynolds number.

2.1.7.5 Over-Sensitive Prediction in Flight Performance

As demonstrated by **Figure 2.1.14**, estimation of aircraft performance and characteristics based upon data from wind-tunnel tests at low Reynolds number can lead to flight performance that is worse than that predicted. In the case of the C-141, the wing pressure distribution in flight shows that the shock is further aft than predicted by the wind tunnel tests. This increased aft loading meant that the pitch characteristics of the wing were very different in flight to that predicted and this necessitated a complete re-design of the wing. There are many examples of where flight performance is worse than predicted using wind tunnel tests at lower Reynolds numbers. Examples include higher than expected interference drag of the F-111 airframe, the lack of performance benefit for the DC-10 and recently the wing- drop phenomenon of the F/A-18E/F Super Hornet. The flight performance need not be worse than predicted from wind tunnel data. The fact that the flight performance is better than predicted means that the design point was calculated incorrectly and raises the possibility that the design is overly conservative. The financial incentives for designing and predicting the flight than predicted using wind tunnel tests at lower Reynolds numbers. Examples include higher than performance of an aircraft at high Reynolds numbers are large. [Mack & McMasters][28] reported that a 1% reduction in drag equates to several million dollars in savings per year for a typical aircraft. [Bocci][29] examined what performance might be lost by designing an airfoil at a typical test Reynolds number of 6 x 10^6 instead of a typical full-scale Reynolds number of 35 x 10^6. The results were gained by calculating the 2D transonic flow over an airfoil section, and it was found that:

- The C_L for the section designed (using CFD) to operate at Re = 6 x 10^6, but simulated at Re_c = 35x10^6 is 4% higher for the same Mach number and shock strength on the upper surface.
- For the airfoil section designed (using CFD) for a Reynolds number of 35x10^6, the improvement in C_L is 13% over the section designed and simulated at a Re_c = 6 x 10^6.

The accurate prediction of flight performance would also save time in the development process by reducing the number of wind-tunnel hours, flight-test hours and design iterations. The use of CFD has helped reduce the upward trend in the number of wind-tunnel hours required to develop an aircraft, although approximately 20,000 wind tunnel hours were still required to develop the Boeing 777-200. Differences between predicted and flight performance have led to many different methods of simulating the flight Reynolds number flow using low Reynolds number testing facilities. In flight,

---

[27] The supercritical airfoil for commercial aircraft allows airplanes to fly faster without the increase in fuel consumption. This was due to the increase in the critical Mach number, which allowed commercial aircraft to fly faster without the impact of transonic effects or wave drag.

[28] Mack, M. D. & McMasters, J. H.," *High Reynolds number testing in support of transport airplane development*", AIAA Paper 92-3982.

[29] Bocci, A. J., "*Airfoil design for full scale Reynolds number*", ARA Memo 211, 1979.

transition normally occurs near the leading edge of the wing, and the boundary layer interacting with the shock wave is therefore turbulent. In wind tunnels, it is possible for the boundary layer to remain laminar over a large percentage of the chord, and therefore a laminar boundary layer-shock interaction may occur. These two types of interaction are vastly different in their nature, and therefore the flow is generally tripped.

2.1.7.6 Aerodynamic Prediction

The current status of Reynolds-number scaling can be assessed from a number of recent publications. The full details are too long to discuss in this brief, but an attempt at a summary is provided herein.

- Angle of incidence at cruise, drag-rise Mach number, C_L and C_M are all functions of Reynolds Number.
- The effect of Reynolds Number on drag can be predicted if the empirical relationship is matched to drag measured at a Reynolds number of 8-10 M or above.
- The shape of drag polar varies with Reynolds number up to flight Reynolds numbers of approximately 40 million, although vortex generators reduce the variation slightly.
- Drag-rise Mach number is increased with increasing Reynolds number, indicating that higher Reynolds number testing would predict a higher cruise Mach number than that achieved using a tunnel such as the Boeing Transonic Wind Tunnel (BTWT).
- The effect of vortex generators on drag at cruise varies with Reynolds number, causing a higher drag at low Reynolds numbers and having very little or a slightly beneficial effect at flight Reynolds numbers. Vortex generators also have little effect on span wise loading at flight Reynolds numbers, compared with a large effect at low Reynolds numbers. This indicates that if wing loads were developed from low Reynolds number data, an unnecessary structural weight penalty would be paid.
- Buffet onset is very difficult to predict, and is often difficult to measure in a wind tunnel because the model dynamics and that of the aircraft are very different.

As Reynolds number scaling remains a topic that receives a great deal of attention 50 years after such effects were first observed. The advent of high Reynolds number tunnels such as the NTF and ETW has not lessened the need for good Reynolds number scaling techniques, but has provided the facilities in which to test new methods and aircraft designs before their first flight, helping to reduce risk. Comparison of flight data with that taken in such tunnels is good for cruise conditions. However, buffet onset is still very difficult to predict, due primarily to the fact that the wind tunnel model and support dynamics are very different to the real aircraft.

2.1.7.7 Skin Friction Estimation

Drag estimation is an important part of the design process, and involves the prediction of wave drag, vortex-induced drag and viscous drag, with the latter contributing approximately 50% to the total drag during cruise [Thibert][30]. A simple estimate of the scaled viscous drag is often gained by using a combination of formula and flat plate skin friction formulae once the transition location is known. This method relies upon an accurate description of the skin friction coefficient, C_f from low Reynolds numbers found in wind tunnels to flight Reynolds numbers. The accurate prediction of drag at flight Reynolds number using low Reynolds number wind tunnels remains a challenge, and it appears that a $Re = 8 - 10 \times 10^6$ or above is required if empirical methods are to be used for extrapolation to flight conditions. The error in the extrapolation is likely to be higher than the variation of C_f with Reynolds number predicted by the best empirical methods discussed. It is therefore concluded that the measurements of skin friction taken in the NTF over a very large range of Reynolds number match

---

[30] Thibert, J. J., Reneaux, J. & Schmitt, R. V., "*ONERA activities on drag reduction*", Proceedings of the 17th Congress of the ICAS. 1053-1059, 1990.

the predictions of [Spalding] [31] and [Karman-Schoenherr] [32] well enough for skin friction extrapolation purposes.

The direct and accurate measurement of skin friction however remains very challenging, although micro fabricated skin friction devices are promising. The relationships of Spalding and Karman-Schoenherr[34] are used for comparison with the data taken in the *National Transonic Facility (NTF)* at NASA Langley in 1996. Although a flat-plate experiment was originally proposed by [Saric & Peterson] [33], it posed too many problems in the high-dynamic, environment of the NTF. An axisymmetric body, 17ft long, for which transverse-curvature effects are small ($\delta/R = 0.25$) was therefore tested at Mach numbers between 0.2 and 0.85 and unit $6x10^6 < Re < 94\ x10^6$ per foot. Skin friction was measured using three different techniques: ***a skin friction balance, Preston tubes*** and ***velocity profiles*** from which the skin friction was inferred by the ***Clauser method***. The last method relies upon the validity of the logarithmic law and the constants used, which have been a subject of debate over the last decade, and one that is still not settled. [Hites et al.][34] compared the skin friction velocity u_τ measured by a near-wall hot wire, a micro fabricated hot wire on the wall, and a conventional hot wire on the wall to that obtained by measuring the velocity profile using a hot wire and applying the Clauser technique. In all cases, the measured u_τ is higher than that predicted by the Clauser technique. The prediction of u_τ is also sensitive to the values of log-law. The comparison of the measured values of u_τ to that predicted by the Clauser method should however be treated with care as significant errors can occur, even for micro fabricated devices, due to thermal conduction to the substrate and connecting wires. More recently, Watson[35] carried out a comparison of the semi-empirical relationships of [Ludwieg & Tillmann][36], [Spalding][37], [Schoenherr][38] and [Fernholz][39]. The methods of Karman-Schoenherr and Spalding show opposite trends at low and high Reynolds numbers with the inter section point at $6000 < Re_\theta < 7000$. The relationship of [Fernholz][41] consistently under-predicts the skin friction compared to the other methods. The skin friction predicted by [Ludwieg-Tillmann][38] matches that of Karman-Schoenherr for $3000 < Re_\theta < 20000$. Both the methods of [Spalding and Fernholz][41] rely upon the logarithmic law and hence the von Karman constant κ and the additive constant, B. Watson report that the method of Spalding incorrectly predicts the skin friction if the usual value of κ is used. This is because the relationship relies upon Spalding's sub layer-buffer-log profile which does not take the wake region into account correctly. Despite this, the relationships of [Karman-Schoenherr][40] and [Spalding][39] are observed to be the best fit to the data of [Coles][40] and [Gaudet][41].

---

[31] Spalding, D. B.,"*A new analytical expression for the drag of a °at plate valid for both turbulent and laminar regimes*", Int. Journal Heat and Mass Transf. 5, 1133-1138, 1962.

[32] Schoenherr, K. E.,"*Resistance of flat surfaces moving through a fluid Trans*", SNAME. 40, 279-313, 1932.

[33] Saric, W. S. & Peterson, J. B., Jr.," *Design of high Reynolds number flat plate experiments in the NTF*", AIAA, 1984.

[34] Hites, M., Nagib, H. & Wark, C.," *Velocity and wall shear stress measurements in high Reynolds number turbulent boundary layers*", AIAA Paper 97-1873, 1997.

[35] Watson, R. D., Hall, R. M. & Anders, J. B., "*Review of skin friction measurements including recent high Reynolds number results from NASA Langley NTF*", AIAA Paper 2000-2392, 2000.

[36] Ludwieg, H. & Tilmann, W., "*Investigations of the wall shearing stress in turbulent boundary layers*", NACA TM-1285. National Advisory Committee for Aeronautics, 1950.

[37] See 48.

[38] Schoenherr, K. E., "*Resistance of °at surfaces moving through a fluid*", Trans. SNAME. 40, 279-13, 1932.

[39] Fernholz, H. H., Ein halbempirisches Gesetz fÄur die Wandreibung in kompressiblen turbulenten renzschichten bei isothermer and Adiabater Wand. ZAMM. 51, 149-149-1971.

[40] Coles, D.,"*The turbulent boundary layer in a compressible fluid*", R-403-PR, Rand Corp, 1962.

[41] Gaudet, L.,"*Experimental investigation of the turbulent boundary layer at high Reynolds Number and a Mach number of 0.8*", TR 84094, Royal Aircraft Establishment, 1984.

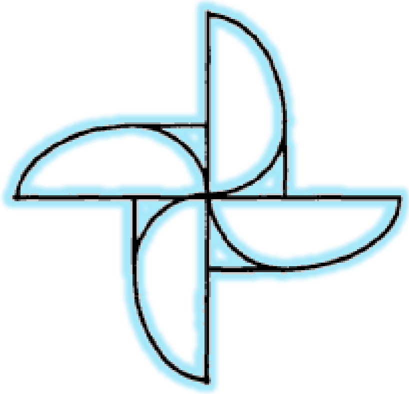

3 Aerodynamics Distinction

A distinction between ***solids, liquids***, and ***gases*** can be made in a simplistic sense as follows. Put a solid object inside a larger, closed container. The solid object will not change; its shape and boundaries will remain the same. Now put a liquid inside the container. The liquid will change its shape to conform to that of the container and will take on the same boundaries as the container up to the maximum depth of the liquid. Now put a gas inside the container. The gas will completely fill the container, taking on the same boundaries as the container. The word ***fluid*** is used to denote either a liquid or a gas. A more technical distinction between a solid and a fluid can be made as follows. When a force is applied tangentially to the surface of a solid, the solid will experience a *finite* deformation, and the tangential force per unit area the shear stress will usually be proportional to the amount of deformation. In contrast, when a tangential shear stress is applied to the surface of a fluid, the fluid will experience a ***continuously increasing*** deformation, and the shear stress usually will be proportional to the rate of change of the deformation[42]. ***The most fundamental distinction between solids, liquids, and gases is at the atomic and molecular level.*** In a solid, the molecules are packed so closely together that their nuclei and electrons form a rigid geometric structure, "glued" together by powerful intermolecular forces. In a liquid, the spacing between molecules is larger, and although intermolecular forces are still strong they allow enough movement of the molecules to give the liquid its "***fluidity***." In a gas, the spacing between molecules is much larger (for air at standard conditions, the spacing between molecules is, on the average, about 10 times the molecular diameter). Hence, the influence of intermolecular forces is much weaker, and the motion of the molecules occurs rather freely throughout the gas. This movement of molecules in both gases and liquids leads to similar physical characteristics, the characteristics of a fluid quite different from those of a solid. Therefore, it makes sense to classify the study of the dynamics of both liquids and gases under the same general heading, called ***fluid dynamics***. On the other hand, certain differences exist between the flow of liquids and the flow of gases; also, different species of gases (say, N2, He, etc.) have different properties. Therefore, fluid dynamics is subdivided into three areas as follows:

- ***Hydrodynamics - flow of liquids***
- ***Gas dynamics - flow of gases***
- ***Aerodynamics - flow of air***

These areas are by no means mutually exclusive; there are many similarities and identical phenomena between them. Also, the word ***aerodynamics*** has taken on a popular usage that sometimes covers the other two areas.

3.1 Aerodynamic Practical Application

Acceding to [Anderson][43], aerodynamics is an applied science with many practical applications in engineering. No matter how elegant an aerodynamic theory may be, or how mathematically complex a numerical solution may be, or how sophisticated an aerodynamic experiment may be, all such efforts are usually aimed at one or more of the following practical objectives:

1. The prediction of forces and moments on, and heat transfer to, bodies moving through a fluid (usually air). For example, we are concerned with the generation of lift, drag, and moments on airfoils, wings, fuselages, engine nacelles, and most importantly, whole airplane configurations. We want to estimate the wind force on buildings, ships, and other surface vehicles. We are concerned with the hydrodynamic forces on surface ships, submarines, and torpedoes. We need to be able to calculate the aerodynamic heating of flight vehicles ranging

---

[42] John D. Anderson, Jr., "*Fundamentals of Aerodynamics*", 5th Edition, McGraw-Hill Companies, 2011.

[43] John D. Anderson, Jr., "*Fundamentals of Aerodynamics*", 5th Edition, McGraw-Hill Companies, 2011

from the supersonic transport to a planetary probe entering the atmosphere of Jupiter. These are but a few examples.

2. Determination of flows moving internally through ducts. We wish to calculate and measure the flow properties inside rocket and air-breathing jet engines and to calculate the engine thrust. We need to know the flow conditions in the test section of a wind tunnel. We must know how much fluid can flow through pipes under various conditions. A recent, very interesting application of aerodynamics is high-energy chemical and gas-dynamic lasers, which are nothing more than specialized wind tunnels that can produce extremely powerful laser beams.

The applications in item 1 come under the heading of ***external aerodynamics*** since they deal with external flows over a body. In contrast, the applications in item 2 involve ***internal aerodynamics*** because they deal with flows internally within ducts. In external aerodynamics, in addition to forces, moments, and aerodynamic heating associated with a body, we are frequently interested in the details of the flow field away from the body. For example is the flow associated with the strong vortices trailing downstream from the wing tips of large subsonic airplanes such as the Boeing 747. What are the properties of these vortices, and how do they affect smaller aircraft which happen to fly through them? The above is just a sample of the countless applications of aerodynamics. There are three major fluid forces of interest:

- Drag
- Lift
- Buoyancy which is closely related to the concept of density

From those, The ***drag force*** acts in a direction that is opposite of the relative flow velocity.

- Affected by cross-section area (form drag)
- Affected by surface smoothness (surface drag)

And the ***lift force*** acts in a direction that is perpendicular to the relative flow.

- The lift force is not necessarily vertical.

3.2 Physics of Aerodynamic Lift

Author : Ed Regis has written 10 science books, including *Monsters: The Hindenburg Disaster and the Birth of Pathological Technology* (Basic Books, 2015). He has also logged 1,000 hours flying time as a private pilot. *Credit: Nick Higgins.*
Original Appearance : This article was originally published with the title "*The Enigma of Aerodynamic Lift*" in Scientific American 322, 2, 44-51 (February 2020).
Source : doi:10.1038/scientificamerican0220-44

3.2.1 Do Recent Explanations Solve The Mysteries of Aerodynamic Lift?

In Brief

- **On a strictly** mathematical level, engineers know how to design planes that will stay aloft. But equations don't explain why aerodynamic lift occurs.
- **There are two** competing theories that illuminate the forces and factors of lift. Both are incomplete explanations.
- **Aerodynamicists** have recently tried to close the gaps in understanding. Still, no consensus exists.

In December 2003, to commemorate the 100th anniversary of the first flight of the Wright brothers, the *New York Times* ran a story entitled "*Staying Aloft; What Does Keep Them Up There*?" The point of the piece was a simple question: What keeps planes in the air? To answer it, the *Times* turned to John D. Anderson, Jr., curator of aerodynamics at the National Air and Space Museum and author of several textbooks in the field.

What Anderson said, however, is that there is actually no agreement on what generates the aerodynamic force known as lift. "There is no simple one-liner answer to this," he told the *Times*. People give different answers to the question, some with "religious fervor." More than 15 years after that pronouncement, there are still different accounts of what generates lift, each with its own substantial rank of zealous defenders. At this point in the history of flight, this situation is slightly puzzling. After all, the natural processes of evolution, working mindlessly, at random and without any understanding of physics, solved the mechanical problem of aerodynamic lift for soaring birds eons ago. Why should it be so hard for scientists to explain what keeps birds, and airliners, up in the air?

Adding to the confusion is the fact that accounts of lift exist on two separate levels of abstraction: the technical and the nontechnical. They are complementary rather than contradictory, but they differ in their aims. One exists as a strictly mathematical theory, a realm in which the analysis medium consists of equations, symbols, computer simulations and numbers. There is little, if any, serious disagreement as to what the appropriate equations or their solutions are. The objective of technical mathematical theory is to make accurate predictions and to project results that are useful to aeronautical engineers engaged in the complex business of designing aircraft.

But by themselves, equations are not explanations, and neither are their solutions. There is a second, nontechnical level of analysis that is intended to provide us with a physical, commonsense explanation of lift. The objective of the nontechnical approach is to give us an intuitive understanding of the actual forces and factors that are at work in holding an airplane aloft. This approach exists not on the level of numbers and equations but rather on the level of concepts and principles that are familiar and intelligible to non-specialists.

It is on this second, nontechnical level where the controversies lie. Two different theories are commonly proposed to explain lift, and advocates on both sides argue their viewpoints in articles, in books and online. The problem is that each of these two nontechnical theories is correct in itself. But neither produces a complete explanation of lift, one that provides a full accounting of all the basic forces, factors and physical conditions governing aerodynamic lift, with no issues left dangling, unexplained or unknown. Does such a theory even exist?

3.2.2 Two Competing Theories

By far the most popular explanation of lift is Bernoulli's theorem, a principle identified by Swiss mathematician ***Daniel Bernoulli*** in his 1738 treatise, *Hydrodynamica*. Bernoulli came from a family of mathematicians. His father, Johann, made contributions to the calculus, and his Uncle Jakob coined the term "integral." Many of Daniel Bernoulli's contributions had to do with fluid flow: Air is a fluid, and the theorem associated with his name is commonly expressed in terms of fluid dynamics. Stated simply, Bernoulli's law says that the pressure of a fluid decreases as its velocity increases, and vice versa. Bernoulli's theorem attempts to explain lift as a consequence of the curved upper surface of an airfoil, the technical name for an airplane wing. Because of this curvature, the idea goes, air traveling across the top of the wing moves faster than the air moving along the wing's bottom surface, which is flat. Bernoulli's theorem says that the increased speed atop the wing is associated with a region of lower pressure there, which is lift.

3.2.3 The Flawed Classics[44]

On a commonsense, everyday basis, two theories have been advanced to explain what keeps an airplane aloft. One is **Bernoulli's theorem***, which associates lift with the area of higher speed and lower pressure atop the wing. The other is the* **Newtonian principle of action and reaction***, which explains lift as an upward push on the wing from the moving air below. Each of these theories is correct in its way, and neither one contradicts the other, although proponents of each theory argue their viewpoints with a zeal bordering on mania. Still, neither theory by itself provides a complete explanation of lift, nor do both of them together, because each leaves something out. A complete explanation must account for all the forces and factors acting on the wing, with no issue, major or minor, left dangling.*

3.2.3.1 Bernoulli's Theorem

As applied to an airplane wing, technically called an airfoil **Bernoulli's theorem** *attempts to explain lift as a consequence of the wing's curved upper surface. The idea is that because of this curvature, the air traveling across the top of the wing moves faster than the air moving along the wing's bottom surface, which is flat. Bernoulli's theorem says that the increased speed atop the wing is associated with a region of lower pressure there, which is lift.*
BUT...
Although Bernoulli's theorem is largely correct, there are several reasons that the principle does not constitute a complete explanation of lift. It is a fact of experience that air moves faster across a curved surface, but the theorem alone does not explain why this is so or why the higher velocity atop the wing brings lower pressure along with it. And practically speaking, an airplane with wings that have a curved upper surface, or even flat surfaces on top and bottom, is capable of flying inverted, so long as the airfoil meets the oncoming wind at an appropriate angle.

3.2.3.2 Newton's 3rd Law

Air has mass. Therefore, Newton's third law would say that the wing's downward push results in an equal and opposite push back upward. This Newtonian account of lift applies to wings of any shape, curved or flat, symmetrical or not, and it holds for aircraft flying inverted or right-side up (the critical feature being a suitable angle of attack). For these reasons, it is a more comprehensive and universally applicable explanation of lift than Bernoulli's.
BUT...
Taken by itself, the principle of action and reaction still fails to explain the lower pressure atop the wing, which exists in that region irrespective of whether the airfoil is cambered or not.

Mountains of empirical data from streamlines (lines of smoke particles) in wind-tunnel tests, laboratory experiments on nozzles and Venturi tubes, and so on provide overwhelming evidence that as stated, Bernoulli’s principle is correct and true. Nevertheless, there are several reasons that Bernoulli’s theorem does not by itself constitute a *complete* explanation of lift. Although it is a fact of experience that air moves faster across a curved surface, Bernoulli’s theorem alone does not explain why this is so. In other words, the theorem does not say how the higher velocity above the wing came about to begin with.

3.2.4 New Ideas of Lift[45]

Today's scientific approaches to aircraft design are determined by computational fluid dynamics (CFD) simulations, as well as equations that take full account of the actual viscosity of real air. Although we still do not have a singular and satisfying physical, qualitative explanation of lift, some recent attempts may have gotten us a bit closer.

---

[44] L-Dopa
[45] See Previous

3.2.4.1 Co-Dependency of Lift's Four Elements

As applied to an airplane wing technically called an airfoil Bernoulli's theorem attempts to explain lift as a consequence of the wing's curved upper surface. The idea is that because of this curvature, the air traveling across the top of the wing moves faster than the air moving along the wing's bottom surface, which is flat. Bernoulli's theorem says that the increased speed atop the wing is associated with a region of lower pressure there, which is lift.

BUT...

Although McLean says the reduced pressure above and increased pressure below result from the airfoil being "completely surrounded by flowing air," this doesn't explain how the reduced pressure up top got there initially.

3.2.4.2 How Low Pressure Forms Above The Wing

[Mark Drela], *an expert on fluid dynamics, has attempted to address what evaded Newton and Bernoulli: how the low-pressure zone, or partial vacuum, above the wing comes into existence. The air above the wing momentarily flows straight back forming a void or vacuum. This vacuum will then strongly pull the air back down , filling in and thus eliminating most but not all of the vacuum. Just enough vacuum remains to pull the air into the curved path that follows the wing.*

There are plenty of bad explanations for the higher velocity. According to the most common one the “equal transit time” theory parcels of air that separate at the wing’s leading edge must rejoin simultaneously at the trailing edge. Because the top parcel travels farther than the lower parcel in a given amount of time, it must go faster. The fallacy here is that there is no physical reason that the two parcels must reach the trailing edge simultaneously. And indeed, they do not: the empirical fact is that the air atop moves much faster than the equal transit time theory could account for. There is also a notorious “demonstration” of Bernoulli’s principle, one that is repeated in many popular accounts, YouTube videos and even some textbooks. It involves holding a sheet of paper horizontally at your mouth and blowing across the curved top of it. The page rises, supposedly illustrating the Bernoulli effect. The opposite result ought to occur when you blow across the bottom of the sheet: the velocity of the moving air below it should pull the page downward. Instead, paradoxically, the page rises.

The lifting of the curved paper when flow is applied to one side “is not because air is moving at different speeds on the two sides,” says [Holger Babinsky], a professor of aerodynamics at the University of Cambridge, in his article “How Do Wings Work?” To demonstrate this, blow across a straight piece of paper, for example, one held so that it hangs down vertically and witness that the paper does not move one way or the other, because “the pressure on both sides of the paper is the same, despite the obvious difference in velocity.”

The second shortcoming of Bernoulli’s theorem is that it does not say how or why the higher velocity atop the wing brings lower pressure, rather than higher pressure, along with it. It might be natural to think that when a wing’s curvature displaces air upward, that air is compressed, resulting in increased pressure atop the wing. This kind of “bottleneck” typically slows things down in ordinary life rather than speeding them up. On a highway, when two or more lanes of traffic merge into one, the cars involved do not go faster; there is instead a mass slowdown and possibly even a traffic jam. Air molecules flowing atop a wing do not behave like that, but Bernoulli’s theorem does not say why not.

The third problem provides the most decisive argument against regarding Bernoulli’s theorem as a complete account of lift: An airplane with a curved upper surface is capable of flying inverted. In inverted flight, the curved wing surface becomes the bottom surface, and according to Bernoulli’s theorem, it then generates reduced pressure *below* the wing. That lower pressure, added to the force of gravity, should have the overall effect of pulling the plane downward rather than holding it up. Moreover, aircraft with symmetrical airfoils, with equal curvature on the top and bottom or even with flat top and bottom surfaces are also capable of flying inverted, so long as the airfoil meets the oncoming wind at an appropriate angle of attack. This means that Bernoulli's theorem alone is insufficient to explain these facts.

The other theory of lift is based on Newton's third law of motion, the principle of action and reaction. The theory states that a wing keeps an airplane up by pushing the air down. Air has mass, and from Newton's third law it follows that the wing's downward push results in an equal and opposite push back upward, which is lift. The Newtonian account applies to wings of any shape, curved or flat, symmetrical or not. It holds for aircraft flying inverted or right-side up. The forces at work are also familiar from ordinary experience for example, when you stick your hand out of a moving car and tilt it upward, the air is deflected downward, and your hand rises. For these reasons, ***Newton's 3rd law*** is a more universal and comprehensive explanation of lift than Bernoulli's theorem. But taken by itself, the principle of action and reaction also fails to explain the lower pressure atop the wing, which exists in that region irrespective of whether the airfoil is cambered. It is only when an airplane lands and comes to a halt that the region of lower pressure atop the wing disappears, returns to ambient pressure, and becomes the same at both top and bottom. But as long as a plane is flying, that region of lower pressure is an inescapable element of aerodynamic lift, and it must be explained.

3.2.5 Historical Understanding

Neither Bernoulli nor Newton was consciously trying to explain what holds aircraft up, of course, because they lived long before the actual development of mechanical flight. Their respective laws and theories were merely repurposed once the Wright brothers flew, making it a serious and pressing business for scientists to understand aerodynamic lift.

Most of these theoretical accounts came from Europe. In the early years of the 20th century, several British scientists advanced technical, mathematical accounts of lift that treated air as a perfect fluid, meaning that it was incompressible and had zero viscosity. These were unrealistic assumptions but perhaps understandable ones for scientists faced with the new phenomenon of controlled, powered mechanical flight. These assumptions also made the underlying mathematics simpler and more straightforward than they otherwise would have been, but that simplicity came at a price: however successful the accounts of airfoils moving in ideal gases might be mathematically, they remained defective empirically.

In Germany, one of the scientists who applied themselves to the problem of lift was none other than ***Albert Einstein***. In 1916 Einstein published a short piece in the journal *Die Naturwissenschaften* entitled "*Elementary Theory of Water Waves and of Flight*," which sought to explain what accounted for the carrying capacity of the wings of flying machines and soaring birds. "There is a lot of obscurity surrounding these questions," Einstein wrote. "Indeed, I must confess that I have never encountered a simple answer to them even in the specialist literature." Einstein then proceeded to give an explanation that assumed an incompressible, frictionless fluid that is, an ideal fluid. Without mentioning Bernoulli by name, he gave an account that is consistent with Bernoulli's principle by saying that fluid pressure is greater where its velocity is slower, and vice versa. To take advantage of these pressure differences, Einstein proposed an airfoil with a bulge on top such that the shape would increase airflow velocity above the bulge and thus decrease pressure there as well.

Einstein probably thought that his ideal-fluid analysis would apply equally well to real-world fluid flows. In 1917, on the basis of his theory, Einstein designed an airfoil that later came to be known as a cat's-back wing because of its resemblance to the humped back of a stretching cat. He brought the design to aircraft manufacturer LVG (Luftverkehrsgesellschaft) in Berlin, which built a new flying machine around it. A test pilot reported that the craft waddled around in the air like "a pregnant duck." Much later, in 1954, Einstein himself called his excursion into aeronautics a "youthful folly." The individual who gave us radically new theories that penetrated both the smallest and the largest components of the universe nonetheless failed to make a positive contribution to the understanding of lift or to come up with a practical airfoil design.

3.2.6 Toward a Complete Theory of Lift

Contemporary scientific approaches to aircraft design are the province of computational fluid dynamics (CFD) simulations and the so-called Navier-Stokes equations, which take full account of the actual viscosity of real air. The solutions of those equations and the output of the CFD simulations yield pressure-distribution predictions, airflow patterns and quantitative results that are the basis for today's highly advanced aircraft designs. Still, they do not by themselves give a physical, qualitative explanation of lift. In recent years, however, leading aerodynamicist Doug McLean has attempted to go beyond sheer mathematical formalism and come to grips with the physical cause-and-effect relations that account for lift in all of its real-life manifestations. McLean, who spent most of his professional career as an engineer at Boeing Commercial Airplanes, where he specialized in CFD code development, published his new ideas in the 2012 text *Understanding Aerodynamics: Arguing from the Real Physics*.

Considering that the book runs to more than 500 pages of fairly dense technical analysis, it is surprising to see that it includes a section entitled "*A Basic Explanation of Lift on an Airfoil, Accessible to a Nontechnical Audience*." Producing these 16 pages was not easy for McLean, a master of the subject; indeed, it was "probably the hardest part of the book to write," the author says. "It saw more revisions than I can count. I was never entirely happy with it." McLean's complex explanation of lift starts with the basic assumption of all ordinary aerodynamics: the air around a wing acts as "a continuous material that deforms to follow the contours of the airfoil." That deformation exists in the form of a deep swath of fluid flow both above and below the wing. "The airfoil affects the pressure over a wide area in what is called a ***pressure field***," McLean writes. "When lift is produced, a diffuse cloud of low pressure always forms above the airfoil, and a diffuse cloud of high pressure usually forms below. Where these clouds touch the airfoil they constitute the pressure difference that exerts lift on the airfoil."

The wing pushes the air down, resulting in a downward turn of the airflow. The air above the wing is sped up in accordance with Bernoulli's principle. In addition, there is an area of high pressure below the wing and a region of low pressure above. This means that there are four necessary components in McLean's explanation of lift: a downward turning of the airflow, an increase in the airflow's speed, an area of low pressure and an area of high pressure.

But it is the interrelation among these four elements that is the most novel and distinctive aspect of McLean's account. "They support each other in a reciprocal cause-and-effect relationship, and none would exist without the others," he writes. "The pressure differences exert the lift force on the airfoil, while the downward turning of the flow and the changes in flow speed sustain the pressure differences." It is this interrelation that constitutes a fifth element of McLean's explanation: the reciprocity among the other four. It is as if those four components collectively bring themselves into existence, and sustain themselves, by simultaneous acts of mutual creation and causation.

There seems to be a hint of magic in this synergy. The process that McLean describes seems akin to four active agents pulling up on one another's bootstraps to keep themselves in the air collectively. Or, as he acknowledges, it is a case of "circular cause-and-effect." How is it possible for each element of the interaction to sustain and reinforce all of the others? And what causes this mutual, reciprocal, dynamic interaction? McLean's answer: ***Newton's 2nd law of motion***.

Newton's second law states that the acceleration of a body, or a parcel of fluid, is proportional to the force exerted on it. "Newton's 2nd law tells us that when a pressure difference imposes a net force on a fluid parcel, it must cause a change in the speed or direction (or both) of the parcel's motion," McLean explains. But reciprocally, the pressure difference depends on and exists because of the parcel's acceleration. Aren't we getting something for nothing here? McLean says no: If the wing were at rest, no part of this cluster of mutually reinforcing activity would exist. But the fact that the wing is moving through the air, with each parcel affecting all of the others, brings these co-dependent elements into existence and sustains them throughout the flight.

3.2.7 Turning on the Reciprocity of Lift

Soon after the publication of *Understanding Aerodynamics*, McLean realized that he had not fully accounted for all the elements of aerodynamic lift, because he did not explain convincingly what causes the pressures on the wing to change from ambient. So, in November 2018, McLean published a two-part article in *The Physics Teacher* in which he proposed “a comprehensive physical explanation” of aerodynamic lift.

Although the article largely restates McLean’s earlier line of argument, it also attempts to add a better explanation of what causes the pressure field to be nonuniform and to assume the physical shape that it does. In particular, his new argument introduces a mutual interaction at the flow field level so that the nonuniform pressure field is a result of an applied force, the downward force exerted on the air by the airfoil.

Whether McLean’s section 7.3.3 and his follow-up article are successful in providing a complete and correct account of lift is open to interpretation and debate. There are reasons that it is difficult to produce a clear, simple and satisfactory account of aerodynamic lift. For one thing, fluid flows are more complex and harder to understand than the motions of solid objects, especially fluid flows that separate at the wing’s leading edge and are subject to different physical forces along the top and bottom. Some of the disputes regarding lift involve not the facts themselves but rather how those facts are to be interpreted, which may involve issues that are impossible to decide by experiment.

Nevertheless, there are at this point only a few outstanding matters that require explanation. Lift, as you will recall, is the result of the pressure differences between the top and bottom parts of an airfoil. We already have an acceptable explanation for what happens at the bottom part of an airfoil: the oncoming air pushes on the wing both vertically (producing lift) and horizontally (producing drag). The upward push exists in the form of higher pressure below the wing, and this higher pressure is a result of simple Newtonian action and reaction.

Things are quite different at the top of the wing, however. A region of lower pressure exists there that is also part of the aerodynamic lifting force. But if neither Bernoulli’s principle nor Newton’s third law explains it, what does? We know from streamlines that the air above the wing adheres closely to the downward curvature of the airfoil. But why must the parcels of air moving across the wing’s top surface follow its downward curvature? Why can’t they separate from it and fly straight back?

Mark Drela, a professor of fluid dynamics at the Massachusetts Institute of Technology and author of *Flight Vehicle Aerodynamics*, offers an answer: “If the parcels momentarily flew off tangent to the airfoil top surface, there would literally be a vacuum created below them,” he explains. “This vacuum would then suck down the parcels until they mostly fill in the vacuum, i.e., until they move tangent to the airfoil again. This is the physical mechanism which forces the parcels to move along the airfoil shape. A slight partial vacuum remains to maintain the parcels in a curved path.”

This drawing away or pulling down of those air parcels from their neighboring parcels above is what creates the area of lower pressure atop the wing. But another effect also accompanies this action: the higher airflow speed atop the wing. “The reduced pressure over a lifting wing also ‘pulls horizontally’ on air parcels as they approach from upstream, so they have a higher speed by the time they arrive above the wing,” Drela says. “So the increased speed above the lifting wing can be viewed as a side effect of the reduced pressure there.”

But as always, when it comes to explaining lift on a nontechnical level, another expert will have another answer. Cambridge aerodynamicist Babinsky says, “I hate to disagree with my esteemed colleague Mark Drela, but if the creation of a vacuum were the explanation, then it is hard to explain why sometimes the flow does nonetheless separate from the surface. But he is correct in everything else. The problem is that there is no quick and easy explanation.”

Drela himself concedes that his explanation is unsatisfactory in some ways. “One apparent problem is that there is no explanation that will be universally accepted,” he says. So where does that leave us? In effect, right where we started: with John D. Anderson, who stated, “There is no simple one-liner answer to this.”

3.3 Drag Estimation

Accurate drag estimation is critical in making computational design studies[46]. Drag may be estimated thousands of times during a multidisciplinary design optimization, and computational fluid dynamics is not yet possible in these studies. The current model has been developed as part of an air-vehicle conceptual-design multidisciplinary design optimization framework. Its use for subsonic and transonic aircraft configurations is presented and validated. We present our parametric geometry definition, followed by the drag model description. The drag model includes induced, friction, wave, and interference drag. The model is compared with subsonic and transonic isolated wings, and a wing/body configuration used previously in drag prediction workshops. The agreement between the predictions of the drag model and test data is good, but lessens at high lift coefficients and high transonic Mach numbers. In some cases the accuracy of this drag estimation method exceeds much more elaborate analyses. It is common to divide a configuration's total drag into two components: induced and parasite. Several nomenclatures can be found for the parasite-drag breakdown, whereas the current research uses three components: friction/form, interference, and wave drag. **Figure 3.3.1** displays the drag breakdown into its various components. Each of the parasite-drag components include the influence of lift; thus, the parasite drag cannot be defined as the zero-lift drag. Still, the influence of lift on the total parasite drag is generally small.

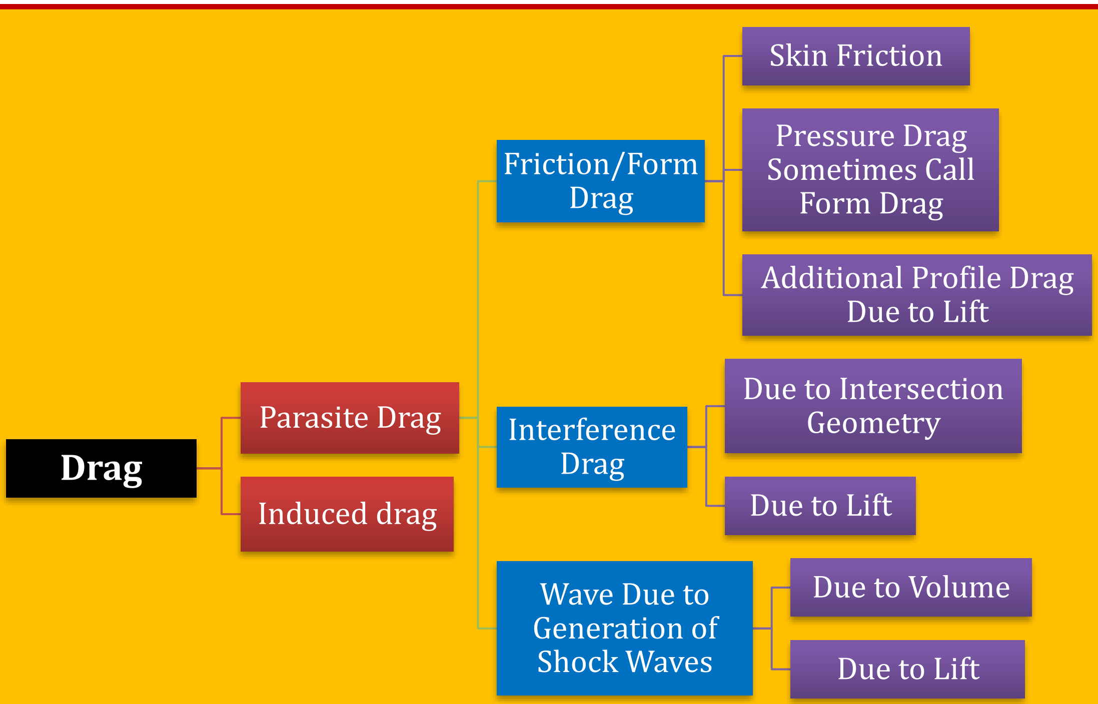

Figure 3.3.1 Typical Drag Breakdown Terminology

---

[46] Ohad Gur, William H. Mason, and Joseph A. Schetz, "*Full-Configuration Drag Estimation*", Journal of Aircraft Vol. 47, No. 4, July–August 2010.

3.3.1 Induced Drag

Induced drag often contributes about half of the entire vehicle drag, and thus accurate induced-drag modeling is essential. Several induced-drag models exist, such as the *Trefftz plane*[47], Prandtl's lifting-line theory[48], and the vortex lattice method[49]. The current research uses a ***Weissinger nonlinear lifting-line model***. This method takes advantage of two-dimensional lift data, and thus the viscosity and compressibility effects can be included, although the model was originally developed for linear aerodynamics and incompressible flow. The airfoil two-dimensional lift data only contributed at high-lift conditions, well away from most conditions of interest. Thus, a linear 2D lift model can be used at low-lift conditions, and in some cases, the theoretical lift-slope value 2π can be used. Note that the current model does not make use of the two-dimensional airfoil drag data. These data are sometimes of low reliability, as demonstrated in for the NACA-0012 airfoil. The airfoil drag is calculated using the friction/form drag model. A detailed description of the method that is used in the current model is given in[50].

3.3.2 Friction/Form Drag

According to the drag breakdown shown in **Figure 3.3.1**, the friction/form drag can be divided into three components: ***skin friction, pressure***, and ***lift-related profile drag***. The current model neglects the third component, which is small, and the remaining two components are addressed simultaneously. The friction/form drag coefficient $C_{D,F}$ is calculated using the following relation for each component:

$$C_{D,F} = C_F FF \frac{S_{wet}}{S_{ref}}$$

Eq. 3.3.1

where C_F is a flat-plate skin-friction coefficient, FF is the form factor of the component, and S_{wet} and S_{ref} are the wetted and reference areas, respectively. The full configuration is divided into components, and **Eq. 3.3.1** is used separately for each component. Finally, the total friction/form drag is found by summing the contributions of these components. For each component, the reference area and wetted areas are well defined, but the flat-plate skin-friction coefficient and the form factor are estimated based on semi-empirical models. Various skin-friction and form-factor models exist in the literature. Comparison of these models reveals small differences, and thus we chose the most well-known and validated models for the current method. For laminar flow, the Eckert reference temperature method is used, and for turbulent flow, the Van Driest II method (based on the von Kármán–Schoenherr model) is used. The total skin friction coefficient is based on a composition of the laminar/turbulent flow. Similar to the skin-friction models, several composition formulas are available, and Schlichting's composition formula is used for the current research[51].

---

[47] Blackwell, J., "*Numerical Method To Calculate the Induced Drag or Optimal Span Loading for Arbitrary Non-Planar Aircraft*," NASA SP-405, May 1976.

[48] Prandtl, L., "Tragfliigeltheorie," Nachrichten von der Gesellschaft der Wissenschaften zu Göttingen, 1918.

[49] Falkner, V., "*The Solution of Lifting-Plane Problems by Vortex-Lattice Theory*," Aeronautical Research Council Reports and Memoranda No. 2591, London, 1943.

[50] Ohad Gur, William H. Mason, and Joseph A. Schetz, "*Full-Configuration Drag Estimation*", Journal of Aircraft Vol. 47, No. 4, July–August 2010.

[51] Ohad Gur, William H. Mason, and Joseph A. Schetz, "*Full-Configuration Drag Estimation*", Journal of Aircraft Vol. 47, No. 4, July–August 2010

3.3.3 Drag - A Major Concern for Car Manufacturers and Beyond

In the past, the external shape of cars has evolved particularly for safety reasons, comfort improvement and also aesthetic considerations [Dumas][52]. Consequences of these guidelines on car aerodynamics were not of major concern for many years. However, this situation changed in the 70's with the emergence of the oil crisis. To promote energy conservation, studies were carried out and it was discovered that the amount of the aerodynamic drag in the fuel consumption ranges between 30% during an urban cycle and 75% at a 120 km/h cruise speed. Since then, decreasing the drag force acting on road vehicles and thus their fuel consumption, became a major concern for car manufacturers.

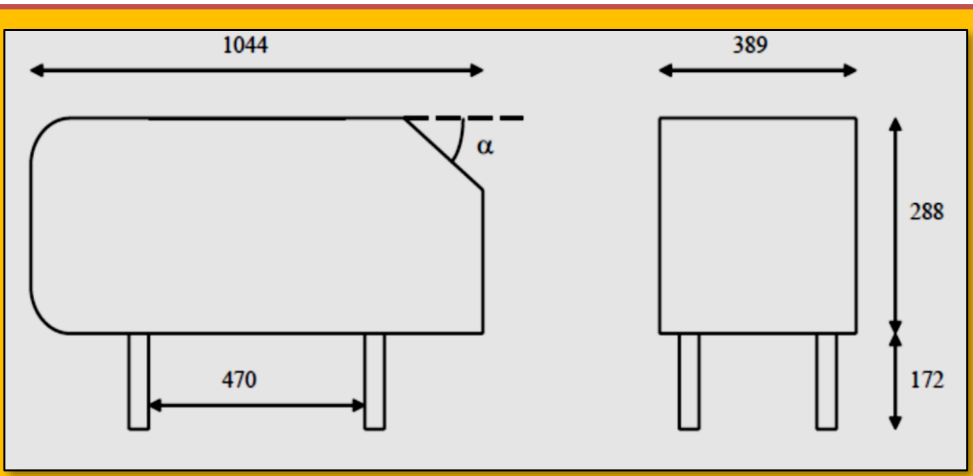

Figure 3.3.2 The Ahmed bluff body

Growing ecological concerns within the last decade further make this a critically relevant issue in the automotive research centers. The process of drag creation and the way to control it was first discovered experimentally. In particular, it was found that the major amount of drag was due to the emergence of flow separation at the rear surface of cars. Unfortunately, unlike in aeronautics where it can be largely excluded from the body surface, this aerodynamic phenomenon is an inherent problem for ground vehicles and cannot be avoided. Moreover, the associated three-dimensional flow in the wake behind a car exhibits a complex 3D behavior and is very difficult to control because of its unsteadiness and its sensitivity to the car geometry. The pioneering experiments of *Morel and Ahmed* done in the late 70's on simplified geometries also called bluff bodies, are now described in **3.3.3.2-3.3.3.3**.

3.3.3.1 Experiments on Bluff Bodies

Two major experiments have been done on bluff bodies, the first one by [Morel][53] and the second by [Ahmed][54]. The objective was to study the flow behavior around cars with a particular type of rear shape called hatchback or fastback. These experiments are even now used as a reference in many numerical studies. The bluff body used by *Ahmed*, similar to the one used by *Morel,* is illustrated in **Figure 3.3.2**. It has the same proportions as a realistic car but with sharp edges. More precisely, the ratio of length/width/height is equal to 3.33/1.5/1. In both cases, the rear base is interchangeable by modifying the slant angle denoted here as α. The Reynolds numbers are taken equal to 1.4×10^6 and 4.29×10^6 in the Morel and Ahmed experiments, respectively.

---

[52] Laurent Dumas, "*Chapter 7- CFD-based Optimization for Automotive Aerodynamics*", Optimization and Computational Fluid Dynamics, ISBN 978-3-540-72152-9, 2008.

[53] Morel, T.: *Aerodynamic drag of bluff body shapes characteristic of hatch-back cars*. SAE Paper 7802670 (1978)

[54] Ahmed, S.R., Ramm, R., Faltin, G.: *Some salient features of the time averaged ground vehicle wake*. SAE Paper 840300 (1984).

3.3.3.2 Wake Flow Behind a Bluff Body

The most difficult flow region to predict is located at the wake of the car where recirculation and separation occur. It is also the region which is responsible for most of the car drag (see 3.3.3.3).

In a time-averaged sense, two distinct regimes depending on the slant angle α , called Regime I and II, have been observed in the experiments done by Morel and Ahmed. The value of the critical angle α_c between both regimes is approximately equal to 30 degrees in each experiment but can slightly change depending on the Reynolds number and the exact geometry.

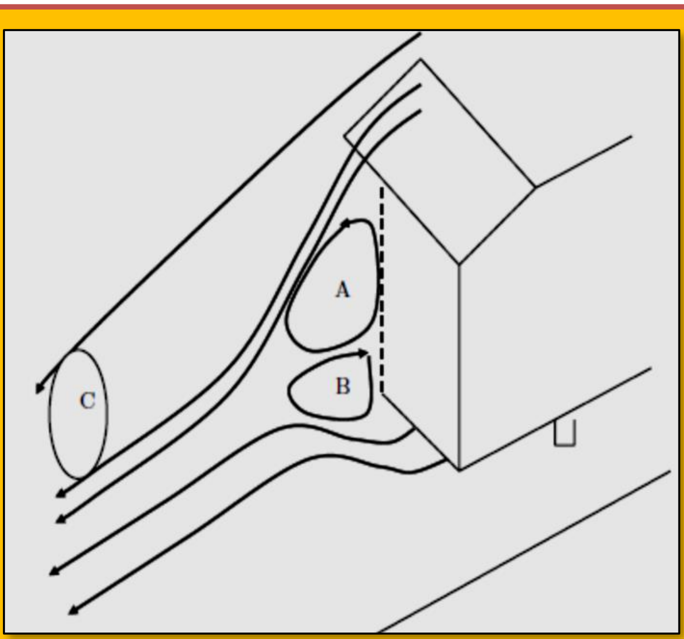

Figure 3.3.3 Wake flow behavior behind Ahmed's bluff body

- Regime I $(\alpha_c < \alpha < 90^\circ)$: In this case, the flow exhibits a full 3D behavior with a separation area including the whole slant and base area. The recirculation zones, coming from the four parts of the car (roof, floor and the two base sides) gather and form a pair of horseshoe vortices situated one above another in a separation bulb (see zones A and B in **Figure 3.3.3**). Vortices, coming off the slant side edges are also present (zone C in **Figure 3.3.3**).
- Regime II $(0 < \alpha < \alpha_c)$: For low values of α, the flow remains two dimensional and separates only at the rear base. Two counter-rotating vortices appear from the roof and the floor similar to what happens around airfoils. When increases up to α_c, the flow becomes three-dimensional because of the appearance of two longitudinal vortices issued from the side walls of the car.

The critical value of C_{Lc} corresponds to an unstable configuration associated with a peak in the drag coefficient (see 3.3.3.3). In this case, a slight change can generate a high modification of the wake flow. For these reasons, it is essential to avoid such angle value in the design of real cars.

3.3.3.3 Drag Variation with the Slant Angle

A dimensionless coefficient, called drag coefficient and related to the drag force acting on the bluff body, is defined as follows:

$$C_D = \frac{\mathbf{F}_D}{\frac{1}{2}\rho V_\infty{}^2 S}$$

Eq. 3.3.2

In this expression, ρ represents the air density, V_∞ is the freestream velocity, S is the cross section area and $\mathbf{F}_d$ is the total drag force acting on the car projected on the longitudinal direction. Note that the drag force $\mathbf{F}_d$ can be decomposed into a sum of a ***viscous drag force and a pressure drag force***. A first striking result observed by *Morel* is that the slant surface and the rear base are responsible for more than 90% of the pressure drag force. Moreover, the latter represents more than 70% of the total drag force. These observations have been confirmed by the Ahmed experiment where only 15% to 25% of the drag is due to the viscous drag.

3.3.3.4 Case Study 1 – Nature Aerodynamic Lift From the Tail Reduces Drag as Relates to Birds

---

Authors : *James R. Usherwood, Jorn A. Cheney, Jialei Song, Shane P. Windsor, Jonathan P. J. Stevenson, Uwe Dierksheide, Alex Nila and Richard J. Bomphrey*
Title : *High Aerodynamic Lift From The Tail Reduces Drag In Gliding Raptors*
Appeared in : *Published by The Company of Biologists Ltd | Journal of Experimental Biology (2020)*
Source : *doi:10.1242/jeb.214809*
Citation : *(Usherwood, et al., 2020)*
Bibliography : *Usherwood, J. R., Cheney, J. A., Song, J., Windsor, S. P., Stevenson, J. P., Dierksheide, U., . . . Bomphrey, R. J. (2020). High Aerodynamic Lift From The Tail Reduces Drag In Gliding Raptors.*

3.3.3.5 Abstract

Many functions have been postulated for the aerodynamic role of the avian tail during steady-state flight. By analogy with conventional aircraft, the tail might provide passive pitch stability if it produced very low or negative lift. Alternatively, aeronautical principles might suggest strategies that allow the tail to reduce inviscid, induced drag: if the wings and tail act in different horizontal planes, they might benefit from biplane-like aerodynamics; if they act in the same plane, lift from the tail might compensate for lift lost over the fuselage (body), reducing induced drag with a more even downwash profile. However, textbook aeronautical principles should be applied with caution because birds have highly capable sensing and active control, presumably reducing the demand for passive aerodynamic stability, and, because of their small size and low flight speeds, operate at Reynolds numbers two orders of magnitude below those of light aircraft. Here, by tracking up to 20,000, 0.3 mm neutrally buoyant soap bubbles behind a gliding barn owl, tawny owl and goshawk, we found that downwash velocity due to the body/tail consistently exceeds that due to the wings. The downwash measured behind the centerline is quantitatively consistent with an alternative hypothesis: that of constant lift production per planform area, a requirement for minimizing viscous, profile drag. Gliding raptors use lift distributions that compromise both inviscid induced drag minimization and static pitch stability, instead adopting a strategy that reduces the viscous drag, which is of proportionately greater importance to lower Reynolds number fliers.

3.3.3.5.1 Introduction

Bird tails clearly perform many roles, both in terms of display and as aerodynamically active surfaces. The potential aerodynamic roles performed by bird tails can be divided into maneuverability, stability, lift production and drag reduction through a variety of mechanisms (Thomas, 1996; Maybury and Rayner, 2001; Huyssen et al., 2012). These functions often have opposing demands: it is difficult to enhance both maneuverability and static stability; lift production often comes at the cost of increased drag. Conventional aircraft tails act as rudders, elevators and stabilizers, providing moments about the center of mass to initiate and maintain turns, and restoring moments that correct perturbations from trimmed, level flight. Bird tails have a quite different form, lacking the vertical fin of typical aircraft. Further, tails are not a requirement for competent, maneuverable flight for flapping animals: birds without tails are still able to achieve some – albeit ungainly – level of control, and many bats are functionally tailless.

Flying animals differ markedly from traditional fixed wing aircraft in a number of ways: they flap, they have rapid sensing and complex control capability, and they are, at least in some gliding cases, aerodynamically unstable (Durston et al., 2019; Durston, 2019). They are also smaller and slower, so potentially operate under quite different aerodynamic regimes. How, then, should the aerodynamic role of the bird tail be understood?

In order to explore the aerodynamics of gliding in a range of raptors, we measured the flow field through particle tracking of neutrally buoyant 0.3 mm helium bubbles (**Figure 3.3.4**; M1: https://youtu.be/utV-UM27COM). Application of automated Lagrangian particle tracking velocimetry (M2: https://youtu.be/HlBEZv0sRf0) to the study of bird flight is novel, though seeding the air with helium bubbles builds upon the early studies of animal flight (Spedding et al., 1984; Spedding, 1987); and wakes have been measured using smoke and particle image velocimetry for a range of considerably smaller flapping (Spedding et al., 2003;Warrick et al., 2005; Van Griethuijsen et al., 2006; Tobalske et al., 2009; Altshuler et al., 2009; Johansson et al., 2018) and gliding (Henningsson and Hedenström, 2011; Henningsson et al., 2014; Klein Heerenbrink et al., 2016) birds.

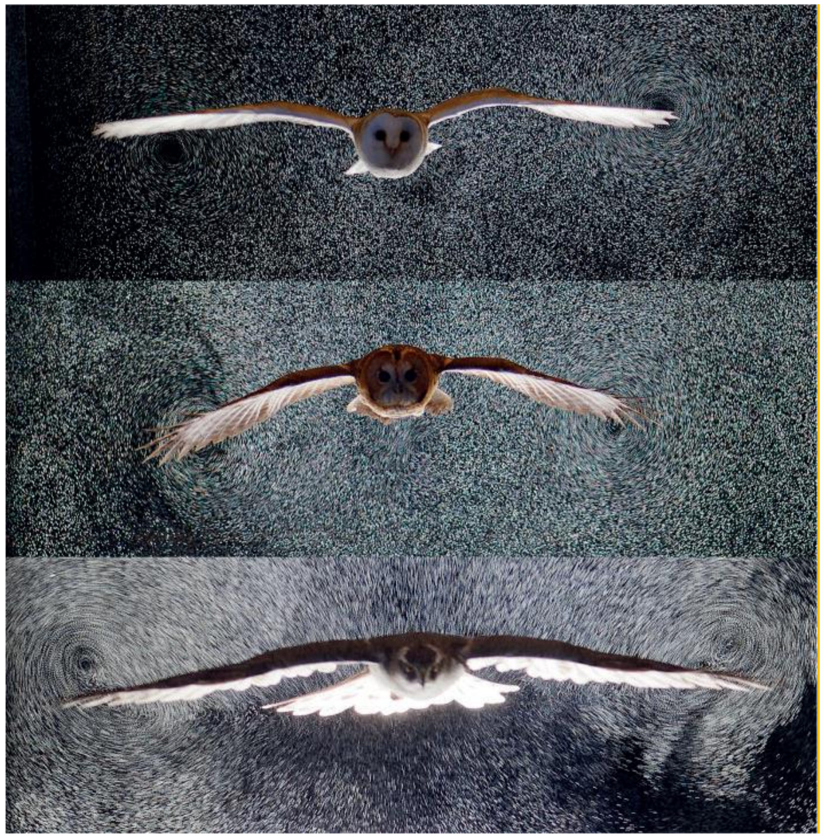

Figure 3.3.4 Air motions caused by gliding raptors visualized with bubbles. Photographs of a gliding barn owl (top), tawny owl (middle) and goshawk (bottom) as, or narrowly after, they passed through a 0.1 m light sheet seeded with neutrally buoyant 0.3 mm soap bubbles. See also M1

Following initial inspection of the bubble motions, interpretations for various wake structures were developed. These can be presented here as hypotheses, though their post hoc nature should be acknowledged. The rotational sense and initial relative position of trailing vortices behind wing tips and body/tail section distinguish certain potential tail actions (**Figure 3.3.5**). Many traditional aircraft make use of negative lift from the tail, resulting in 'longitudinal dihedral' to improve stability in pitch; this would result in upwash from the tail, and trailing vortices following the wing/body of opposite sense to those following the wing tips on the same side (**Figure 3.3.5 A**). A tail/body section that does not disrupt the downwash would result in the absence of trailing vortices behind the tail (**Figure 3.3.5 B**). Drag reduction through biplane aerodynamics (Thomas, 1996) would require wing tip and body/tail trailing vortices of the same sense each side, but with vertical offset (**Figure 3.3.5 C**). Vortices with the same sense each side but without the offset **(Figure 3.3.5 D**)

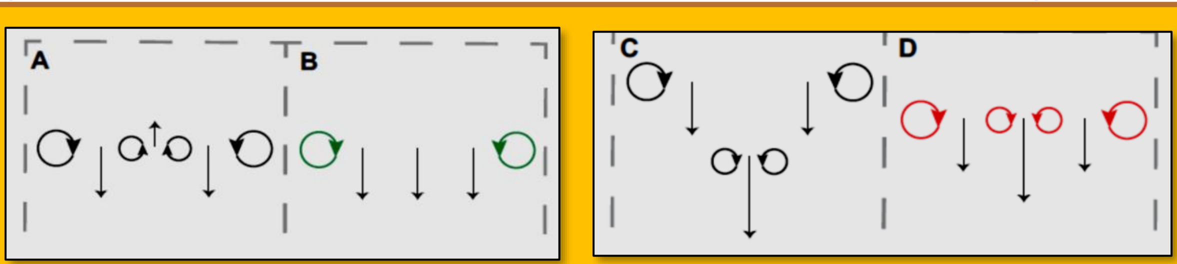

Figure 3.3.5 Post hoc hypotheses for competing models of tail function in steady gliding – [see 103]

indicate an increased lift across the body/tail section, detrimental to induced drag minimization but potentially consistent with drag reduction at low Reynolds numbers[55].

3.3.3.5.2 Materials and Methods as Relates to Birds

Three captive and mature raptors were used in this study: a female Linnaeus 1758) and a female northern goshawk [Accipiter gentilis (Linnaeus 1758)]. All individuals were trained to fly between handlers on command and were experienced at operating in brightly illuminated and unusual environments, such as film sets. Work was approved by the *Ethics and Welfare Committee of the Royal Veterinary College (URN 2018 1836-3).*

3.3.3.5.3 Experimental Setup

Experiments were conducted within a purpose-built indoor flight corridor at the Royal Veterinary College (Hatfield, UK). The corridor was constructed to (1) prevent ambient air flow from introducing noise to the measured flow fields; (2) prevent dispersal of the helium-filled soap bubble tracer particles; and (3) create a dark background for maximizing image signal (bubbles) to noise (background). The corridor was roofed and black on all inner surfaces. It was contained within a larger room, with the end of the flight path open to the room, allowing ambient light to illuminate the receiving handler. The measurement volume was not illuminated until after the birds entered it; otherwise, birds reacted to the illuminated volume of bubbles as if it were a wall. The corridor was approximately 1.8 m wide×1.8 m tall×14 m long. Results from three trials each for the three birds are reported here.

For each trial, bubbles were injected into the volume and allowed to quiesce prior to the flight. Bubbles were generated with 40 nozzles, and a fluid supply unit (LaVision GmbH) regulated soap, helium and air content to maintain neutral buoyancy. Bubbles were approximately 300 μm in diameter and, because of their large size and light scattering properties, were approximately 10,000 times brighter than standard-use aerosol particles for particle image velocimetry (Caridi, 2018), allowing LED lights to provide sufficient illumination, rather than high-power laser light sources that could potentially be damaging to birds' vision. During each recorded flight, the bird flapped along the corridor, gaining speed before entering a smooth, steady glide just before the measurement volume. Initiation of LED illumination of the measurement volume was controlled using a hand trigger.

3.3.3.5.4 Imaging

The measurement volume was constrained to the region illuminated by the LEDs. Four high-power LED units (LED-Flashlight 300, LaVision GmbH) illuminated the bubbles. Each LED unit consisted of an array of 72 CoB LEDs arranged over an active area of 300×100 mm2, with each CoB LED subunit focused with a lens to a divergence of 10 deg. Four units were placed side by side pointing upward, and a concave mirror on the corridor roof reflected light back down. Because of divergence and reflection, the four LED light units covered an effective measurement region slightly greater than 1.2 m×0.1 m. LEDs strobed in synchrony with the video frame capture and with the same 10:1 duty cycle, thereby maximizing useful illumination while minimizing electrical power demand and the brightness perceived by the birds.

The illuminated volume was captured using four high-speed cameras recording at 700 Hz (VEO 640L, Phantom Inc.; and Fastcam SA3, Photron Inc.). Cameras were positioned principally along the flight path, facing the bird as it entered the illuminated volume. Cameras and LED lights were synchronized and controlled with a timing unit (PTU X, LaVision GmbH). Further cameras (Nikon D3, Nikon

---

[55] Negative lift from the tail (A) might improve pitch stability; induced drag might be low (B) if the tail counteracted loss of lift over the body; or induced drag might be reduced through biplane aerodynamics (C). A step increase in lift over the body/tail section would be evident from trailing vortices following behind the tail of the same sense as those following the wingtips on the same side (D), associated with an increase in downwash velocity, and would be inconsistent with simple pitch stability or minimization of induced drag.

Corporation; Red Epic Dragon, Red.com, LLC, at 120 Hz,) situated behind the receiving handler provided context images (**Figure 3.3.4**).

3.3.3.5.5 Camera Calibration

A two-stage iterative camera calibration process was used, followed by the unusual step of estimating projected bubble shape as a function of position. We first calibrated using a standard target (a dot grid), then improved the calibration by minimizing reprojection error of images of bubbles at moderate seeding density. Because imaging is diffraction limited, bubbles project onto the sensor as diffraction-induced airy disc patterns, with disc shape a function of position due to optical aberrations. Using the same bubble images at moderate seeding density, an optical transfer function was estimated for the modified airy disc shape as a function of position, which improved our capacity to resolve bubble location, and better accounted for overlapping bubbles.

Particle tracking: 'shake-the-box' The 'shake-the-box' (STB) algorithm (Schanz et al., 2013, 2016) is a 4D particle tracking algorithm that identifies particle positions in 3D space by triangulation and follows individual particles over time. The output from STB consists of individual particle tracks, from which velocities and accelerations are derived. This contrasts to the output from Tomo-PIV, which is a regular grid of velocity vectors. After a bubble is located in space, its projection onto the image is subtracted to yield residual images showing only the remaining particles yet to be located. The STB algorithm makes use of the particle track information from previous time steps to predict the new particle position in subsequent time steps. This predicted 3D position is prioritized in the search for matching 2D particle images on the camera frames. Finally, this particle position is subsequently 'shaken' to maximize the match with the camera images.

3.3.3.5.6 Image Processing

Prior to volume self-calibration, and in addition to all dataset processing, image sets were pre-processed to optimize image quality. A combination of time-based and spatial filters was used to remove image artefacts such as background noise and image noise. The time based filter removes stationary artefacts by means of subtracting the minimum recorded value at each pixel from a set of images for a camera. Spatial image filters reduce image noise and normalize image intensity. Image noise was reduced using a sliding window to subtract minimum intensity contained in a 7×7 pixel window, larger than twice the particle image diameter (which here was on average 3–4 pixels). Particle intensity, which varies as a result of scattering angle, was standardized across the image by normalizing the values using a local average based on a 300×300 sliding pixel window.

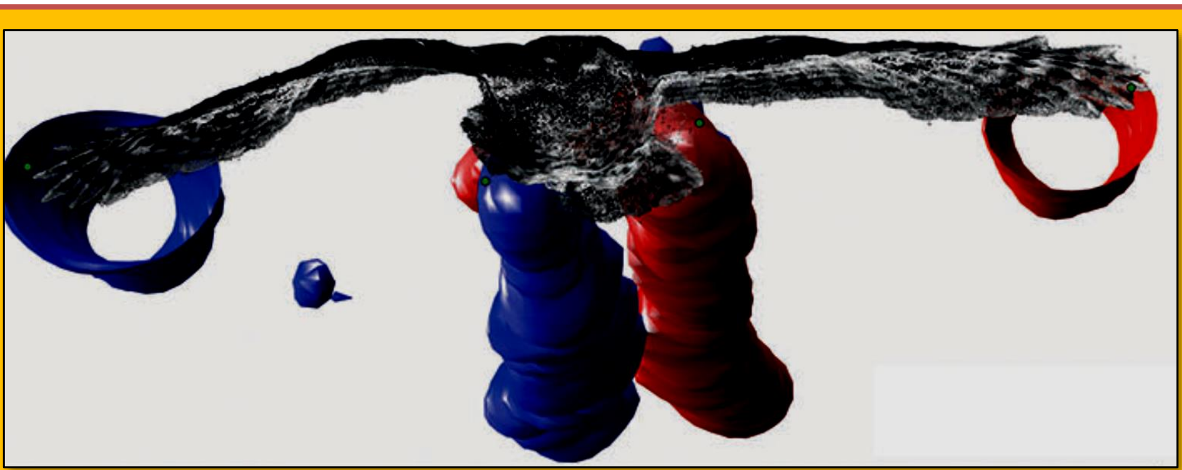

Figure 3.3.6 An example reconstruction of vortex structures behind a gliding tawny Owl

3.3.3.5.7 Vortex Structure Identification Using the Q-Criterion

The Q-criterion aims to capture the fluid ‘particles’ for which rotation predominates over shear strain, with the additional condition that pressure is lower than the ambient value (Jeong and Hussain, 1995). In our implementation, we considered the flow to be incompressible (Mach number ~0.03), and solved the Q-value as:

$$Q = -\frac{1}{2}u_{i,j}u_{j,i}$$

Eq. 3.3.3

where $u_{i,j}$ describes the partial derivative of the flow along axis i, taken in the j direction, and i, j=1,2,3 as in the Einstein summation. Critical Q-values were selected to highlight the dominant vortex structures (**Figure 3.3.6**)[56].

3.3.3.5.8 Downwash Calculation

To compute downwash, particle velocities were placed into a uniform 3D grid using the Fine scale reconstruction (or VIC#) module in DaVis 10. Fine scale reconstruction is a PTV interpolation method similar to the ‘vortex in cell plus (VIC+) method which interpolates flow using the instantaneous spatial and temporal information from each bubble, linking the two with the Navier–Stokes equations (Schneiders and Scarano, 2016). The approach is grid based, and here we selected a 16×16×16 voxel window to form the grid. Window size was selected based on the observation that flow speed was maintained when compared with smaller windows, but with substantially less noise. To estimate wake evolution, the middle, frontal plane for each time step in the flight direction was extracted and stacked. The time axis was converted to a spatial axis based on average forward flight speed, which was estimated from digitization of the birds passing through the volume.

3.3.3.5.9 Bird Planform

We could not comprehensively resolve bird planform from our camera views, but made use of relevant 3D reconstruction data collected from an earlier series of observations. To ensure appropriate planform selection, we digitized wing- and tail-tip position from images of the birds in the measurement volume, and selected planforms that best matched the spans and span ratio in this study. Planforms are from the same barn owl and goshawk individuals, but a different tawny owl. We then calculated planform from the boundary of the projected point clouds, from which chord profiles and derivative metrics were calculated (**Table 3.3.1**).

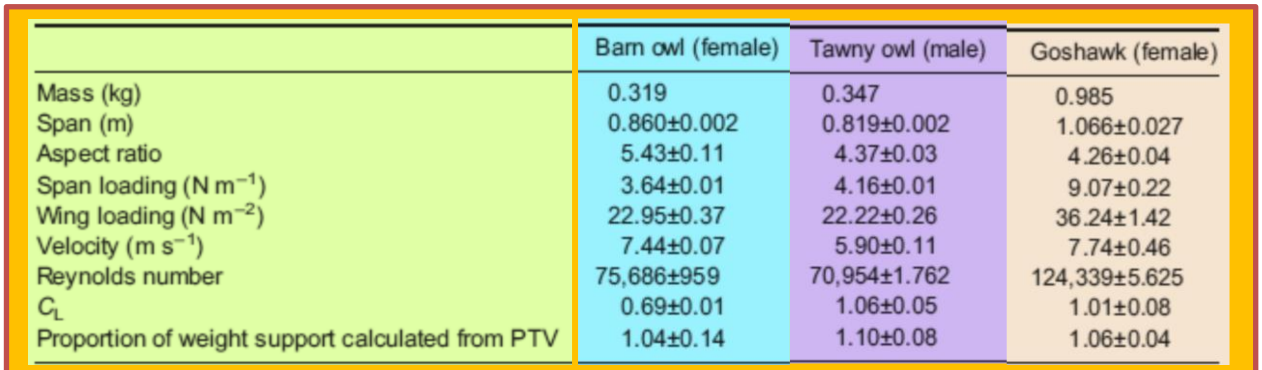

	Barn owl (female)	Tawny owl (male)	Goshawk (female)
Mass (kg)	0.319	0.347	0.985
Span (m)	0.860±0.002	0.819±0.002	1.066±0.027
Aspect ratio	5.43±0.11	4.37±0.03	4.26±0.04
Span loading (N m^{-1})	3.64±0.01	4.16±0.01	9.07±0.22
Wing loading (N m^{-2})	22.95±0.37	22.22±0.26	36.24±1.42
Velocity (m s^{-1})	7.44±0.07	5.90±0.11	7.74±0.46
Reynolds number	75,686±959	70,954±1.762	124,339±5.625
C_L	0.69±0.01	1.06±0.05	1.01±0.08
Proportion of weight support calculated from PTV	1.04±0.14	1.10±0.08	1.06±0.04

Table 3.3.1 Mean (±s.d.) morphology, flight and Aerodynamic parameters for the three study individuals, each for three flights

---

[56] Iso surfaces of the wake displayed using the Q-criterion highlight two discrete pairs of trailing vortices: an outer pair behind the wing tips and a narrower pair trailing the body/tail section (blue – clockwise facing the bird; red – anticlockwise)

3.3.3.5.10 Results

Flights selected for analysis were steady, broadly level glides at relatively low speeds (**Table 3.3.1**). Motion of the seeding bubbles revealed trailing vortices in the wake of the wingtips, clearly visible in the photographs (**Figure 3.3.4**). These vortices were tracked and quantified are displayed using iso surfaces of the wake Q-value (**Figure 3.3.6**). Trailing vortices behind the wing tips associated with downwash following the birds – and the momentum flux resulting in weight support – are not surprising, and entirely match expectations from aerodynamic theory and experience from aeronautics. What is more noteworthy is that discrete trailing vortices were also consistently observed in the wake behind the body and tail (**Figure 3.3.4 - Figure 3.3.6**).

3.3.3.5.11 Discussion

The trailing vortices following the tail, and the associated downwash near the bird centerline, demonstrate that the body/tail section produces greater aerodynamic lift per span than the wings. This positive lift is opposite to that required for tails producing stability through longitudinal dihedral: the tails of conventional, passively stable aircraft produce negative lift and accelerate air in the opposite direction – upwards – which would be associated with trailing vortices of the opposite sense. If not used for passive pitch stability, it might be expected that the bird tails contribute to weight support during slow flight, and this is consistent with balancing of pitch moments in hawks (Tucker, 1992), visualization of gliding swift (Henningsson and Hedenström, 2011; Henningsson et al., 2014) and jackdaw (KleinHeerenbrink et al., 2016) wakes, and direct pressure measurements through pigeon tails (Usherwood et al., 2005). However, the observed trailing vortices behind the tail indicate that lift contribution of the central section is considerably in excess of simply filling in the lift distribution between the wings. The lift coefficients calculated for the tawny owl and goshawk were high for raptor wings (Withers, 1981; Van Oorschot et al., 2016), close to 1, so there is the possibility that tail lift is merely allowing slow gliding while preventing stall, analogous to the flaps deployed by landing aircraft (Pennycuick, 1975). However, the barn owl operated with a mean lift coefficient close to 0.7 – well below the maximum lift coefficient measured for isolated raptor wings (Withers, 1981; Van Oorschot et al., 2016) – yet also displayed the step increase in downwash behind the tail, meaning that a simple account based on stall avoidance is insufficient.

The apparently excessive aerodynamic lift produced by the body/tail is significant because it affects the drag experienced by the gliding bird. To understand its implications in terms of overall drag, we adapted classical approaches (Tucker, 1987; Spedding and McArthur, 2010) to model the drag D produced by wings of aspect ratio AR and area S through air of density ρ at flight speed V with wings at lift coefficient C_L. In this presentation, total drag due to the wings can be separated into three components:

$$D = \left(\frac{{C_L}^2}{\pi A R e_i} + \frac{k{C_L}^2}{{e_v}^2} + C_{D,0}\right)\frac{\rho}{2}\,SV^2$$

Eq. 3.3.4

where e_i and e_v are inviscid and viscous efficiency factors, respectively. An e value of 1 is ideal, and the factors reducing efficiency from unity form the basis of the analysis developed here. The first term is the inviscid or induced drag coefficient – that associated with accelerating air downward in order to provide weight support. The second and third terms together combine to give the profile drag coefficient, with $C_{D,0}$ the minimum drag coefficient (assumed here to occur close to zero lift). It is important to highlight that the second term increases with the square of lift coefficient, denoting the C-shape of a lift–drag polar for a generic pre-stall airfoil (2D); the curvature of the polar relates to the constant k that expresses the quadratic rise of this drag term with lift (Spedding and McArthur, 2010), and tends to be more extreme at lower Reynolds numbers (Abbott and Doenhoff, 1949). This dependency on lift can present some confusion as it is sometimes convenient to combine it with the inviscid induced drag term (Houghton et al., 2016; Spedding and McArthur, 2010), which also varies with C^2_L.

It is, however, a form of viscous drag and is therefore of proportionally greater magnitude at lower Reynolds numbers. Relating drag minimization predictions to downwash profiles In order to compare the predictions from minimization of inviscid and viscous (or induced and profile) drag

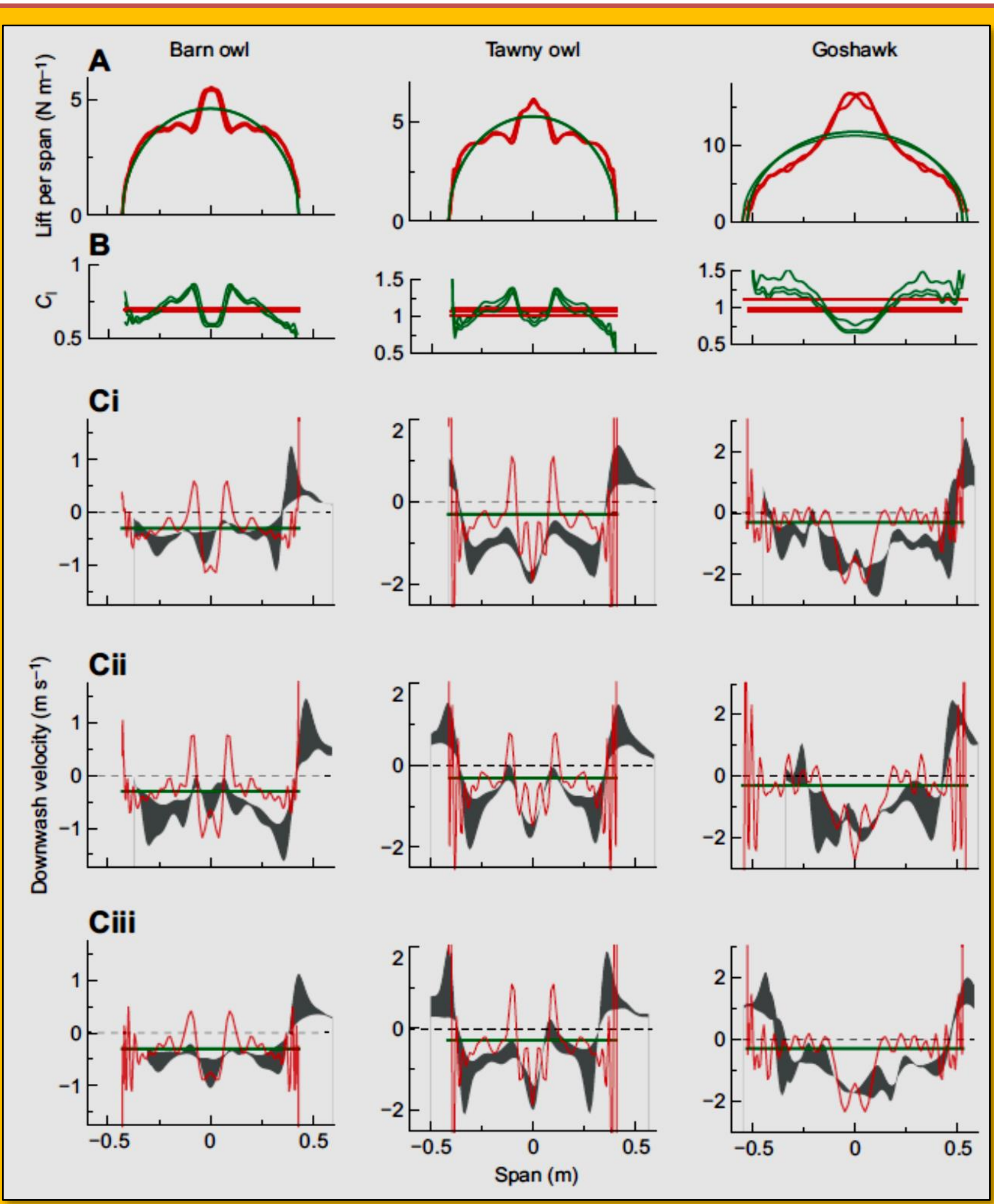

Figure 3.3.7 Comparison of Competing Models of Drag Minimization (see 105)

separately, the downwash profiles minimizing each were calculated and compared with measured profiles for gliding barn owl, tawny owl and goshawk (**Figure 3.3.7**)[57].

Inviscid or induced drag is classically minimized with an elliptical lift distribution across the span (Prandtl, 1921; Munk, 1923) (**Figure 3.3.7 A,** green lines), leading to a constant downwash velocity of sufficient magnitude to support body weight, but resulting in lift coefficients that vary across the planform (**Figure 3.3.7 C,** green lines). Viscous, profile drag, in contrast, is minimized (**Figure 3.3.7**, red lines) if the lift coefficient is constant for every section :

$$e_v = \frac{C_L{}^2}{C_l{}^2}$$

Eq. 3.3.5

for wings of sectional lift coefficient C_l and near-constant airfoil section shape. This requires that lift is evenly distributed across the planform area, and so spanwise lift profile matches the aerodynamic chord profile – in which case $C^2_l = C^2_L$ and $e_v = 1$. Minimization of inviscid, induced drag and viscous, profile drag cannot both be met simultaneously without an elliptical planform.

Spanwise chord profiles matching the wing and tail spans of the measured glides were calculated from point clouds, excluding the head, from earlier glides using high-speed video photogrammetric methods, and were fitted with 50 Fourier terms to provide a close –though constrained to be symmetrical about the center line – representation of the chord profile. This technique allows classical aerodynamic methods (Munk, 1923; Prandtl, 1921; Houghton et al., 2016, Phillips et al., 2019) to be applied to determine the associated downwash profiles given the assumption that profile drag is minimized if all sections operate at constant lift coefficient (and the lift coefficient is sufficient to support body weight).

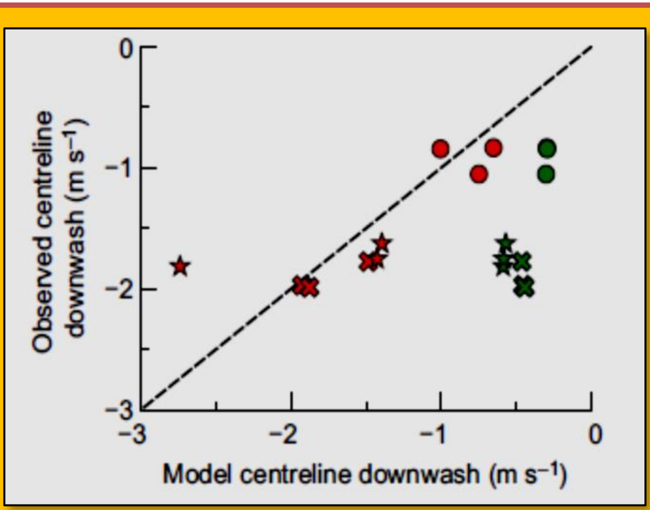

Figure 3.3.8 Measured downwash quantitatively agrees with a significant role for viscous drag minimization and qualitatively refutes alternative hypotheses of tail function in gliding

3.3.3.5.12 Derived Downwash Results and Discussion

Downwash velocity fields for each trial were measured for a transverse plane closely after the passage of the tail trailing edge, but also dependent on good bubble seeding coverage. As these planes we're not exactly at the 'lifting line'

---

[57] Hypothetical spanwise lift profiles (A) and associated sectional lift coefficients (C_l; B), and their modelled consequences in terms of downwash profiles (colored lines) for three glides per species (Ci–iii). Green lines indicate the hypothetical inviscid or induced-drag minimizing case, with elliptical spanwise lift distribution, variable lift coefficient and constant downwash velocity across the span. Red lines indicate the theoretical viscous or profile-drag minimizing strategy, with lift distribution matching the chord profile of the wings/body planform resulting in a constant spanwise lift coefficient and – because the planform is not elliptical – varying downwash velocity. The deviation in planform from elliptical, largely due to the projecting central tail area, is evident from A, in which the loading profile is either elliptical or in direct proportion to chord (excluding the head). Grey shading indicates measurements spanning the maximum to minimum downwash velocities across horizontal transects of transverse planes after passage of the bird, located level with the wingtips, and 50 and 100 mm below the wingtips.

aerodynamic abstraction (a concept underlying the simplest 3D wing theory – Prandtl, 1921; see Abbott and Doenhoff, 1949), downward convection, though gradual (**Figure 3.3.6**), meant that no single horizontal transect across the plane provided an adequate measurement of downwash profile; instead, we show the range between maximum and minimum downwash values for transects at 0, 50 and 100 mm below the wingtips (**Figure 3.3.7**).

Downwash values at the centerline did not match the prediction of constant downwash from inviscid induced drag minimization. Instead, they provide a good quantitative match (**Figure 3.3.8**)[58] with predictions based on constant spanwise lift coefficient and minimized profile drag. The success of the second model, and contrast with aircraft-based postulations, may reflect both the relatively large contribution of viscous effects at the low Reynolds numbers (~100,000) experienced by birds and a low cost to birds for their moderate deviation from perfect induced drag minimization. Indeed, using the constant-C_l theoretical downwash profiles, e_i is only reduced to 0.8–0.9.

We can therefore reject the action of the tail – at least under the conditions measured – as: (1) passive pitch stabilizer, which would require negative lift from the tail, upwash and associated trailing vortices of opposite sense from those we observed behind the body/tail (**Figure 3.3.5 A**); (2) downwash compensator, restoring lift lost over the body and minimizing inviscid induced drag (Huyssen et al., 2012), as this would result in constant downwash and only wingtip vortices being manifest in the wake (**Figure 3.3.5 B**); or (**Figure 3.3.6**) a functional biplane (Thomas, 1996) (**Figure 3.3.5 C**), because the wing and tail tips and their trailing vortices initially lie in the same horizontal plane. We found that the body/tail section contributes lift proportional to chord, thereby spreading the load across a greater surface and reducing the profile drag. We conclude, therefore, that the tail does not contribute to passive pitch stability with a longitudinal dihedral mechanism but, in addition to its role in moment generation when maneuvering Downwash velocity (e.g. Gillies et al., 2011), acts as an aerodynamic wing 'flap', expanding the aerodynamic planform area. However, whereas aircraft flaps are required for stall avoidance and increase drag, bird tails produce aerodynamic lift even when not near a stall limit, and act to reduce overall drag at low Reynolds numbers.

3.3.3.5.13 Further Caveats and Comments

3.3.3.5.14 Note on Passive Longitudinal Stability

We do not present here a full stability analysis for the birds of this study; this would require measurement or modelling of the inertial properties of each bird in gliding posture. See [Durston (2019)] for such an analysis of two raptors, which demonstrates a high degree of longitudinal instability. Positive lift from an aft airfoil does not necessarily preclude the possibility that static longitudinal stability is obtained; indeed, this is a feature of certain airplane styles such as the 'canard' design, which has a smaller pair of wings ahead of the main, often delta, wing. However, the traditional airplane design appears to be a better initial analogue, with the larger lifting surface ahead of the smaller. In this case, a large upward lift from the tail is inconsistent with longitudinal static stability. The observed strong downwash and positive lift from the tail does therefore suggest that

---

[58] Measurements of downwash following the body/tail centerline section (A) (three species, three trials each) show close agreement (24% root mean square error, RMSE) with a profile drag minimizing (red) role for the tail; whereas, the induced drag minimizing (green) model consistently underpredicts downwash (247% RMSE). Treating each glide as an independent sample (while acknowledging the issues with this assumption), Mann–Whitney U-tests on the residuals indicate that the two models deviate from observation to different degrees ($P < 0.05$): the induced drag minimizing model deviates significantly from observation ($P < 0.005$) but the profile drag minimizing model does not ($P = 0.25$). The profile drag minimizing, constant spanwise lift coefficient hypothesis with increased lift over and downwash behind the broader body/tail section is supported both qualitatively, with the presence of discrete tail tip vortices associated with positive lift (**Figure 3.3.4-Figure 3.3.6**; M1, 2; contrast with **Figure 3.3.5**), and quantitatively through downwash modelling. Circles: barn owl; crosses: tawny owl; stars: goshawk.

the tail is not contributing to static longitudinal stability, at least by the mechanism of longitudinal dihedral as exploited in traditional airplane designs.

3.3.3.5.15 Note on Non-Elliptical Loading for Induced Drag Minimization

While an elliptical loading distribution provides the theoretical minimum induced drag for a constrained wing span, other loading distributions are optimal given different constraints. Various structural, geometrical and weight considerations, along with passive yaw stability, may be important in aircraft design, leading to a range of non-elliptical loading distributions providing theoretical optima for minimizing induced drag (Prandtl, 1933; Phillips et al., 2019). The optimal loading distributions with such constraints tend to be more 'bell shaped', with a bias in loading towards central sections of the vehicle. However, the question of relevance in the current case is not 'how can induced drag be minimized given certain constraints to do with stress, deflection or bending moment?' but 'how would induced drag be minimized given the wings available?', i.e. given their maximum span. Induced drag is only reduced with bell-shaped loading distributions if the wing span is unconstrained. The spans of the birds in this study were certainly constrained, and so the theoretical minimum induced drag prediction remains that of elliptical spanwise loading and perfectly constant downwash velocity in the immediate wake.

Despite this, the conceptual basis behind the advantages of bell-shaped loading distributions may have some relevance to the case of birds. High weight support by the central sections would indeed reduce the bending moment demanded at the wing roots – corresponding to torque around the shoulders – reducing at least some degree of muscle action and associated physiological costs. Bell-shaped loading distributions therefore have the potential to reduce the metabolic demands of gliding with a mechanism other than drag reduction. Consequently, while the viscous drag minimizing account proposed here provides a reasonable and quantitatively sufficient reasoning for the action of the tail during gliding, some alternative options cannot be rejected without further study.

3.3.3.5.16 References

Abbott, I. H. and von Doenhoff, A. E. (1949). *Theory of Wing Sections*. NY: Dover Publications Inc.

Altshuler, D. L., Princevac, M., Pan, H. and Lozano, J. (2009). *Wake patterns of the wings and tail of hovering hummingbirds*. Exp. Fluids 46, 835-846. doi:10. 1007/s00348-008-0602-5

Caridi, G. C. A. (2018). *Development and application of helium-filled soap bubbles: For large-scale PIV experiments in aerodynamics*. PhD thesis, Delft University of Technology.

Durston, N. E. (2019). Quantifying the flight stability of free-gliding birds of prey. PhD Thesis, University of Bristol. https://research-information.bris.ac.uk/files/ 198573023/thesis_c.pdf.

Durston, N. E., Wan, X., Liu, J. G. and Windsor, S. P. (2019). *Avian surface reconstruction in free flight with application to flight stability analysis of a barn owl and peregrine falcon*. J. Exp. Biol. 222, jeb185488. doi: 10.1242/jeb.185488

Gillies, J. A., Thomas, A. L. R. and Taylor, G. K. (2011). *Soaring and maneuvering flight of a steppe eagle Aquila nipalensis*. J. Avian Biol. 42, 377-386. doi:10.1111/j. 1600-048X.2011.05105.x

Henningsson, P. and Hedenstro¨ m, A. (2011). *Aerodynamics of gliding flight in common swifts*. J. Exp. Biol. 214, 382-393. doi:10.1242/jeb.050609

Henningsson, P., Hedenstro¨ m, A. and Bomphrey, R. J. (2014). *Efficiency of lift production in flapping and gliding flight of swifts*. PLoS ONE 9, e90170. doi:10. 1371/journal.pone.0090170

Houghton, E. L., Carpenter, P. W., Collicott, S. H. and Valentine, D. T. (2016). A*erodynamics for Engineering Students.* 7th edn.: Elsevier. ISBN: 978-0-08- 100194-3.

Huyssen, R. J., Spedding, G. R., Mathews, E. H. and Liebenberg, L. (2012). *Wing-body circulation control by means of a fuselage trailing edge*. J. Air. 49, 1279-1289. doi:10.2514/1.C031543

Jeong, J. and Hussain, F., (1995). *On the identification of a vortex*. J. Fluid Mech. 285, 69-94. doi:10.1017/S0022112095000462

Johansson, L. C., Maeda, M., Henningsson, P. and Hedenstro¨ m, A. (2018). *Mechanical power curve measured in the wake of pied flycatchers indicates modulation of parasite power across flight speeds*. J. R. Soc. Interface 15,20170814. doi:10.1098/rsif.2017.0814

KleinHeerenbrink, M., Warfvinge, K. and Hedenstro¨ m, A. (2016). *Wake analysis of aerodynamic components for the glide envelope of a jackdaw (Corvus monedula*). J. Exp. Biol. 219, 1572-1581. doi:10.1242/jeb.132480

Maybury, W. J. and Rayner, J. M. V. (2001). *The avian tail reduces body parasite drag by controlling flow separation and vortex shedding*. Proc. R. Soc. London B 268, 1405-1410. doi:10.1098/rspb.2001.1635

Munk, M. M. (1923). *The minimum induced drag of aerofoils*. NACATR-121. NACA Technical Report 121. https://ntrs.nasa.gov/search.jsp?R=19930091456

Pennycuick, C. J. (1975). *Mechanics of flight. In Avian Biology*, Vol. 5 (ed. D. S. Farner and J. R. King) pp. 1-75. London: Academic Press.

Phillips,W. F., Hunsaker, D. F. and Joo, J. J. (2019). *Minimizing induced drag with lift distribution and wingspan*. J. Air. 56, 431-441. doi:10.2514/1.C035027

Prandtl, L. (1921). *Applications of modern hydrodynamics to aeronautics*. NACATR 116. NACA Technical Report 121. https://ntrs.nasa.gov/search.jsp? R=19930091180

Prandtl, L. (1933). *Über tragflu ¨gel kleinsten induzierten widerstandes*. Z. Flugtech. Motorluftschiffahrt 24, 305-306.

Schanz, D., Schro¨ der, A., Gesemann, S., Michaelis, D. and Wieneke, B. (2013). '*Shake The Box': a highly efficient and accurate Tomographic Particle Tracking Velocimetry (TOMO-PTV) method using prediction of particle positions*. PIV13; 10th International Symposium on Particle Image Velocimetry.

Schanz, D., Gesemann, S. and Schro¨ der, S. (2016). *Shake-The-Box: lagrangian particle tracking at high particle image densities. Exp*. Fluids 57, 70. doi:10.1007/s00348-016-2157-1

Schneiders, J. R. G. and Scarano, R. (2016). *Dense velocity reconstruction from tomographic PTV with material derivatives.* Exp. Fluids 57, 139. doi:10.1007/s00348-016-2225-6

Spedding, G. R. (1987). *The wake of a kestrel (Falco tinnunculus) in gliding flight*. J. Exp. Biol. 127.

Spedding, G. R. and McArthur, J. (2010). *Span efficiencies of wings at low Reynolds Numbers*. J. Aircr. 47, 120-128. doi:10.2514/1.44247

Spedding, G. R., Rayner, J. M. V. and Pennycuick, C. J. (1984). *Momentum and energy in the wake of a pigeon (Columba livia) in slow flight*. J. Exp. Biol. 111, 81-102. Spedding, G. R., Rose´ n, M. and Hedenstro¨ m, A. (2003). *A family of vortex wakes generated by a thrush nightingale in free flight in a wind tunnel over its entire natural range of flight speeds*. J. Exp. Biol. 206, 2313-2344. doi:10.1242/jeb. 00423

Thomas, A. L. R. (1996). *Why do birds have tails? The tail as a drag reducing flap, and trim control*. J. theorical Biol. 183, 247-253. doi:10.1006/jtbi.1996.0218

Tobalske, B. W., Hearn, J. W. D. and Warrick, D. R. (2009). *Aerodynamics of intermittent bounds in flying birds*. Exp. Fluids 46, 963-973. doi:10.1007/s00348- 009-0614-9

Tucker, V. A. (1987). *Gliding birds: the effect of variable wing span*. J. Exp. Biol. 133, 33-58.

Tucker, V. A. (1992). *Pitching equilibrium, wing span and tail span in a gliding Harris' hawk*, Parabuteo unicinctus. J. Exp. Biol. 165, 21-41.

Usherwood, J. R., Hedrick, T. L., McGowan, C. P. and Biewener, A. A. (2005). *Dynamic pressure maps for wings and tails of pigeons in slow, flapping flight, and their energetic implications.* J. Exp. Biol. 208, 355-369. doi:10.1242/jeb.01359

Van Griethuijsen, L., Rosen, M., Hedenstro¨ m, A. and Spedding, G. R. (2006). *Vortex wakes of birds: recent developments using digital particle image velocimetry in a wind tunnel*. Anim. Biol. 56, 535-549. doi:10.1163/ 157075606778967856

Van Oorschot, B. K., Mistick, E. A. and Tobalske, B. W. (2016). *Aerodynamic consequences of wing morphing during emulated take-off and gliding in birds*. J. Exp. Biol. 219, 3146-3154. doi:10.1242/jeb.136721 Warrick, D. R., Tobalske, B. W. and Powers, D. R. (2005). *Aerodynamics of the*

hovering hummingbird. Nature 435, 1094-1097. doi:10.1038/nature03647 Withers, P. C. (1981). An aerodynamic analysis of bird wings as fixed airfoils. J. Exp. Biol. 90, 143-1.

3.4 Aerodynamic Forces and Moments

The aerodynamic forces and moments on a body are due to only two basic sources: ***Pressure*** and ***Shear Stress*** distributions over the body. Both have dimensions of force per unit area where pressure acts normal to surface and shear tangential. The net effect of P and τ distributions integrated over the complete body surface is a resultant aerodynamic force R and moment M on the body. Lift is the perpendicular component of R w.r.t. free stream while Drag represents the parallel[59]. Therefore, source of aerodynamic Lift, Drag, and Moments on the body are the pressure and shear stress distributions integrated over the body. To better represent these forces, dimensionless coefficients of Lift, C_L, drag, C_D, and moment, C_M, introduced as

$$C_L = \frac{L}{q_\infty S} \quad , \quad C_D = \frac{D}{q_\infty S} \quad , \quad C_M = \frac{M}{q_\infty SL}$$

Eq. 3.4.1

Where q_∞ is the previously defined dynamic pressure, ½ ρV^2 , and reference area S and reference length L are chosen to pertain to given geometric shape; for different shapes , S and L may be different things. For example, for an airplane wing S is the plan form area and L the mean chord length. However for a sphere, S would be the cross-section area while L is the diameter. More information such as lifting airfoil and finite wing theory, and other relevant topics, can be obtained in any aerodynamic specific text books such as [Anerson][60]. Generic variations for C_L and C_D versus angle of attack (α) are sketched in **Figure 4.1.1**. Note that C_L increases linearly with α until an angle of attack is reached when the wing stalls, the lift coefficient reaches a peak value, and then drops off as C_L is further increased. The maximum value of the lift coefficient is denoted by $C_{L,max}$, as illustrated.

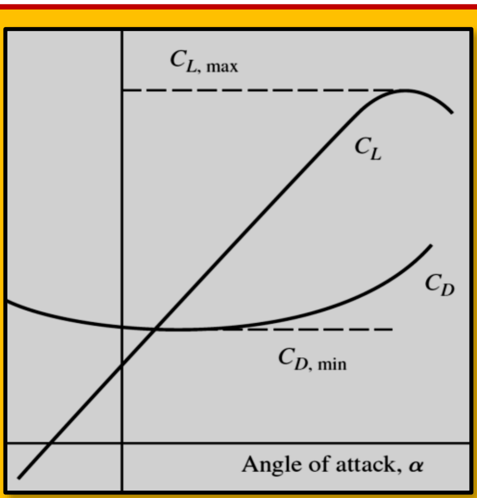

Figure 3.4.1 Schematic of Lift and Drag Coefficients vs Angle of Attack on a Airfoil (Courtesy of Anderson)

3.5 Leading-Edge Flow as a Governing Factor in Leading-Edge Vortex (LEV) Initiation in Unsteady Airfoil Flows

A leading-edge suction parameter (LESP) that is derived from potential flow theory as a measure of suction at the airfoil leading edge is used to study initiation of ***Leading Edge Vortex (LEV)*** formation by [Ramesh et al.][61]. The LESP hypothesis is presented, which states that LEV formation in unsteady flows for specified airfoil shape and Reynolds number occurs at a critical constant value of LESP, regardless of motion kinematics. The hypothesis is seen to hold except in cases with slow-rate kinematics which evince significant trailing-edge separation. Low-Reynolds-number flows at low speeds and small scales, despite being incompressible and non-thermodynamic, are rife with complexity owing to the effects of viscosity and flow separation. Much research on this topic in the

---

[59] Anderson, John D. 1984: "*Fundamentals of Aerodynamics*", McGraw Hills Inc.

[60] John D. Anderson, Jr., "*Fundamentals of Aerodynamics*", 5th Edition, McGraw-Hill Companies, 2011.

[61] Kiran Ramesh, Kenneth Granlund, Michael V. Ol, Ashok Gopalarathnam, Jack R. Edwards, "*Leading-edge flow criticality as a governing factor in leading-edge vortex initiation in unsteady airfoil flows*", Theoretical Computational Fluid Dynamics, 2017.

twenty-first century has been driven by interest in ***Micro-Air Vehicle (MAV)*** design, a problem at the interface between low *Re* fluid mechanics and flight vehicle engineering. The design problem in this regime has been driven by seeking bio-inspiration from insects which employ flapping flight at high dimensionless rates of motion (reduced frequencies) to achieve remarkable flying prowess. It has been shown that the single most important aerodynamic phenomenon largely responsible for the success of flapping flight at low Reynolds numbers is the leading-edge vortex (LEV). The conditions under which such LEVs develop on rounded-leading-edge airfoils form the subject of this study and are investigated with a large set of unsteady test cases using experiments, computations, and theoretical methods. Two-dimensional problems without additional complexity involving span-wise flow and wingtip vortices are considered here and serve as a starting point for more complex investigations. LEV formation is initiated by reversed flow at the airfoil surface in the vicinity of the leading edge, followed by the formation of a free shear layer. The free shear layer then builds up into a vortex, which traverses the airfoil chord and convects into the wake. Research contributions on LEV formation have largely arisen from the rotorcraft community and the more recent low-Re/MAV community.

3.5.1 Identification of LEV Initiation From CFD Data

The procedure used in this research for identifying the initiation of LEV formation from CFD skin friction information is illustrated here with the baseline case listed. **Figure 3.5.1** presents results from experiments and CFD for the baseline case at four instants during the motion. The upper surface skin friction (C_f) distributions from CFD (on the third row of the figure) are examined at various time instants of the motion to identify several key steps that lead to the formation of the LEV. The flow features leading to LEV formation have been discussed by several authors. The four time instants at (a)–(d), are used to highlight the following flow features:

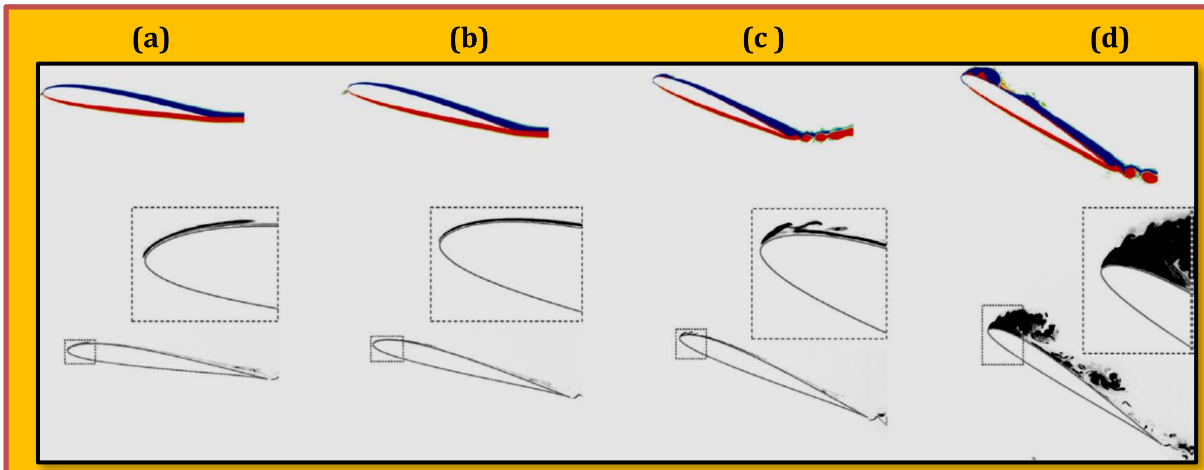

Figure 3.5.1 Vorticity Plots from CFD (*first row*), Flow Visualization from Experiment (*second row*)

(a) *Attached flow* - Before the initiation of the LEV formation, the flow is attached at the leading edge. The attached boundary layer is thin and the C_f is positive.

(b) *Onset of reversed flow* - LEV formation is first preceded by the formation of a small region of reversed flow near the leading edge of the airfoil, signaled by appearance of counterclockwise vorticity near the surface and a small region of negative C_f.

(c) *Initiation of LEV formation* - Next, a small region of clockwise vorticity starts to develop at the surface within the region of counterclockwise vorticity seen in (b). This manifests as a spike in the negative C_f distribution that reaches up to zero and subsequently becomes a region of positive C_f within the region of negative C_f distribution. This flow feature signals the formation of the shear layer in which there is an eruption of surface flow into the mainstream. As in previous work, the instant when the spike in the negative C_f region first reaches the zero value is taken as the time corresponding to initiation of LEV formation.

(d) *Formation and feeding of the LEV -* The eruption of surface flow, initiated in (c), results in a plume of clockwise vorticity flowing into the mainstream. During these time instants, there are several spikes in the C_f distribution corresponding to positive-C_f regions embedded within a larger negative-C_f region.

3.6 Measure of Compressibility & Compressible vs. Incompressible Flows

A flow is classified as being compressible or incompressible depending on the level of variation of density during flow. Physically, compressibility is the fractional change in volume of the fluid element per unit change in pressure or isothermal compressibility

$$\tau = -\frac{1}{v}\left(\frac{dv}{dp}\right)_T \quad \text{for } v = \frac{1}{\rho} \quad \Rightarrow \quad \tau = \frac{1}{\rho}\frac{d\rho}{dp} \quad \text{where} \quad \rho = \rho\,(p\,,T)$$

Eq. 3.6.1

Therefore, for incompressible flow or constant ρ, the compressibility of gas ($\tau = 0$). In contrast, if $\rho = \rho\,(p, T)$, then flow is considered compressible. There are number of aerodynamic problems that could be considered incompressible without any determinable loss of accuracy. For example flow for liquids could be considered incompressible, and hence most hydrodynamic problem assume ρ = constant. Also the flow of gases at low Mach number ($M_\infty < 0.3$) is essentially incompressible. This is not true for high speed flow when the density fluctuations are apparent and must be treated as compressible[62].

3.7 Speed of Sound

The speed of sound, a molecular phenomenon, in a calorically perfect gas is given by

$$a = \sqrt{\gamma R T}$$

Eq. 3.7.1

This is a function of temperature only and related to the average molecular velocity. It is also relates to compressibility of gas, τ by

$$a = \sqrt{\frac{1}{\rho\tau}}$$

Eq. 3.7.2

The lower the compressibility, the higher the speed of sound. For an incompressible flow, $\tau = 0$, then speed of sound is theoretically infinite. The Mach number $M = (V/a)$ is therefore, zero. Hence, the incompressible flow could be theoretically characterized as zero Mach number flow.

3.8 Sonic Boom

A sonic boom is the sound associated with the shock waves created by an object traveling through the air faster than the speed of sound. Sonic booms generate significant amounts of sound energy, sounding much like an explosion to the human ear[63]. The crack of a supersonic bullet passing overhead or the crack of a bullwhip are examples of a sonic boom in miniature. Contrary to popular

---

[62] Anderson, John D. 1984: "*Fundamentals of Aerodynamics*", McGraw Hills Inc.

[63] Wikipedia.

belief, a sonic boom does not occur only at the moment an object crosses the speed of sound; and neither is it heard in all directions emanating from the speeding object. Rather the boom is a continuous effect that occurs while the object is travelling at supersonic speeds. But it only affects observers that are positioned at a point that intersects an imaginary geometrical cone behind the object. As the object moves, this imaginary cone also moves behind it and when the cone passes over the observer, they will briefly experience the ***boom***. When an aircraft passes through the air it creates a series of pressure waves in front of it and behind it, similar to the bow and stern waves created by a boat. These waves travel at the speed of sound and, as the speed of the object increases, the waves are forced together, or compressed, because they cannot get out of the way of each other. Eventually they merge into a single shock wave, which travels at the speed of sound, a critical speed known as Mach 1, and is approximately 1,235 km/h (767 mph) at sea level and 20 °C (68 °F). In smooth flight, the shock wave starts at the nose of the aircraft and ends at the tail. Because the different radial directions around the aircraft's direction of travel are equivalent (given the "smooth flight" condition), the shock wave forms a Mach cone, similar to a vapor cone, with the aircraft at its tip (see **Figure 3.8.1**). As a reference, a systematic grid resolution and time step resolution studies made by [Yang et al.][64] using the high-order scheme for supersonic flows and for sonic boom prediction problems. Considerable improvements in accuracy are found when using the new 3rd order U-MUSCL[65] scheme.

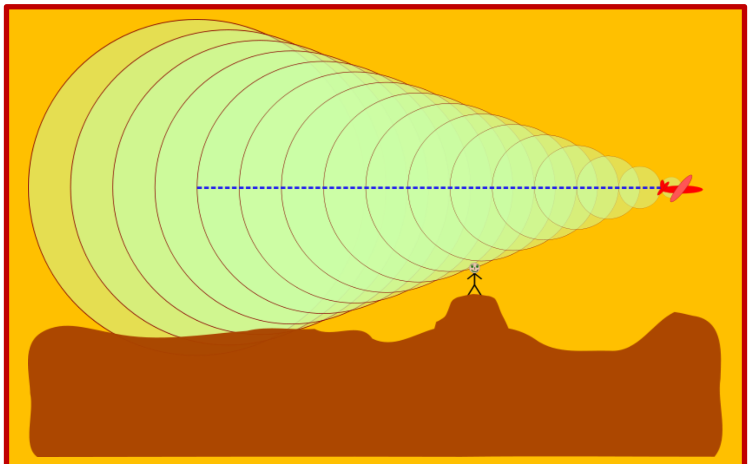

Figure 3.8.1 Illustration of a Sonic Boom as Received by Human Ears

3.9 Mach Number

In fluid dynamics, the Mach number (M or Ma) is a dimensionless quantity representing the ratio of flow velocity past a boundary to the local speed of sound [66]-[67],

$$M = \frac{V}{c}$$

Eq. 3.9.1

Where M is the Mach number, V is the local flow velocity with respect to the boundaries (either internal, such as an object immersed in the flow, or external, like a channel), and c is the speed of

---

[64] Simon Yang, H. Q. Yang, and Robert E. Harris, "*Sonic Boom Prediction Using FUN3D High-Order U-MUSCL Schemes*", 2018 AIAA/CEAS Aeroacoustics Conference.

[65] A variable extrapolation formulation for unstructured finite volume codes developed by [Burg] has been implemented in FUN3D. This scheme is called U-MUSCL and closely resembles the MUSCL scheme used within structured flow solvers. The formulation is based on information currently available to the unstructured flow solvers, namely the variable information and the gradient information, and as such, it is trivial to implement within finite volume flow solvers.

[66] Young, Donald F.; Bruce R. Munson; Theodore H. Okiishi; Wade W. Huebsch (2010). A Brief Introduction to Fluid Mechanics (5 Ed.). John Wiley & Sons. p. 95.

[67] Graebel, W.P. (2001). Engineering Fluid Mechanics. Taylor & Francis. p. 16.

Figure 3.9.1 An F/A-18 Hornet Creating a Vapor Cone at Transonic Speed

sound in the medium. The local speed of sound, and thereby the Mach number, depends on the surrounding medium, in particular the temperature and pressure. **Figure 3.9.1** shows an F/A-18 creating a vapor cone at transonic speed just before reaching Mach 1 (By Ensign John Gay, U.S. Navy). The Mach number is primarily used to determine the approximation with which a flow can be treated as an incompressible flow. The medium can be a gas or a liquid. While the terms "***subsonic***" and "***supersonic***," in the purest sense, refer to speeds below and above the local speed of sound respectively, aerodynamicists often use the same terms to talk about particular ranges of Mach values. This occurs because of the presence of a "transonic regime" around M = 1 where approximations of the Navier-Stokes equations used for subsonic design actually no longer apply; the simplest explanation is that the flow locally begins to exceed M = 1 even though the freestream Mach number is below this value. Meanwhile, the "***supersonic regime***" is usually used to talk about the set of Mach numbers for which linearized theory may be used, where for example the (air) flow is not chemically reacting, and where heat-transfer between air and vehicle may be reasonably neglected in calculations. In the following table (see **Table 3.9.1**), the "***regimes***" or "***ranges*** of Mach values" are referred to, and not the "pure" meanings of the words "***subsonic***" and "***supersonic***". Generally, NASA defines "***high" hypersonic*** as any Mach number from 10 to 25, and re-entry speeds as anything greater than Mach 24. Aircraft operating in this regime include the Space Shuttle and various space planes in development. Further details regarding the Mach number regimes can be obtained from [Anderson][68].

Regime	Mach	knots	mph	Km/h	m/s
Subsonic	< 0.8	< 530	< 609	< 980	< 273
Transonic	0.8 - 1.2	530-794	609-914	980-1470	273-409
Supersonic	1.2 - 5.0	794-3308	915-3806	1470-6126	410-1702
Hypersonic	5.0 - 10.0	3308-6615	3806-7680	6125-12251	1702-3403
High-Hypersonic	10.0 -24.0	6615-16537	7680-19031	12251-30626	3403-8508
Re-Entry Speeds	> 24.0	> 16537	> 19031	> 30626	> 8508

Table 3.9.1 Classification of Mach Number

---

[68] John D. Anderson, "*Fundamentals of Aerodynamics*", McGraw Hill Inc. pp.37-39, 1976.

In summary, we attempt to organize our study of aerodynamic flows according to one or more of the various categories discussed in this section[69]. The block diagram in **Figure 3.9.2** is presented to help emphasize these categories and to show how they are related.

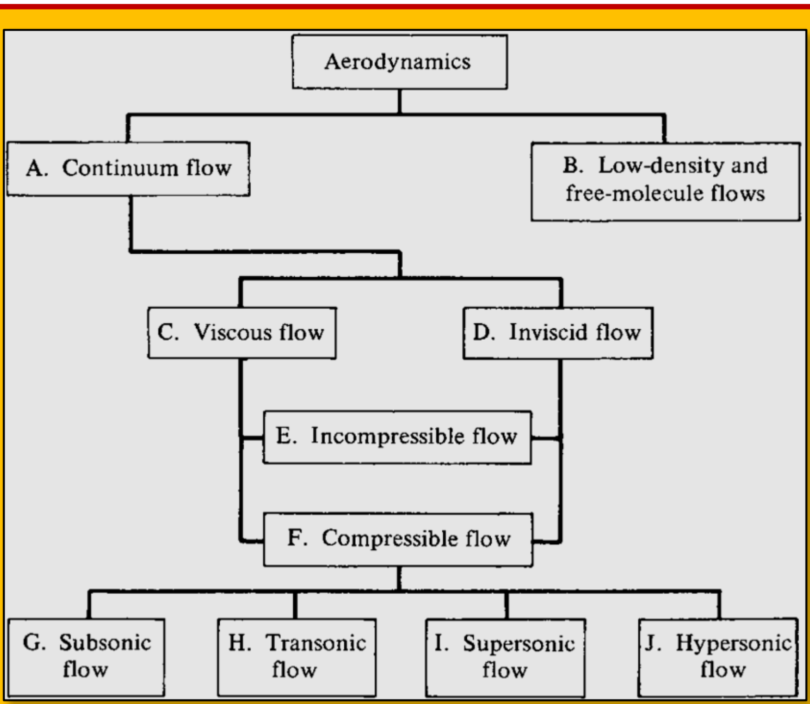

Figure 3.9.2 Block Diagram Categorizing the Types of Aerodynamic Flows (Courtesy of John D. Anderson)

3.9.1 Flow Regions Based on Mach Number

Looking at the whole field simultaneously, ***four*** different speed regimes can be identified using Mach number as the criterion:

3.9.1.1 Subsonic Flow (M < 1 everywhere)

A flow field is defined as ***subsonic*** if the Mach number is less than 1 at every point. Subsonic flows are characterized by smooth streamlines (no discontinuity in slope), as sketched in **Figure 3.9.3 a**. Moreover, since the flow velocity is everywhere less than the speed of sound, disturbances in the flow (say, the sudden deflection of the trailing edge of the airfoil in **Figure 3.9.3 a**) propagate both upstream and downstream, and are felt throughout the entire flow field. Note that a freestream Mach number M_∞ less than 1 does not guarantee a totally subsonic flow over the body. In expanding over an aerodynamic shape, the flow velocity increases above the freestream value, and if M_∞ is close enough to 1, the local Mach number may become supersonic in certain regions of the flow. This gives rise to a rule of thumb that $M_\infty < 0.8$ for subsonic flow over slender bodies. For blunt bodies, M_∞ must be even lower to ensure totally subsonic flow. (Again, emphasis is made that the above is just a loose rule of thumb and should not be taken as a precise quantitative definition). Also, we will show later that incompressible flow is a special limiting case of subsonic flow where $M \to 0$.

---

[69] John D. Anderson, Jr, Professor Emeritus University of Maryland, "*Fundamentals of Aerodynamics*", 5th edition, The McGraw-Hill Companies, Inc., 1221 Avenue of the Americas, New York, NY 10020, 2011.

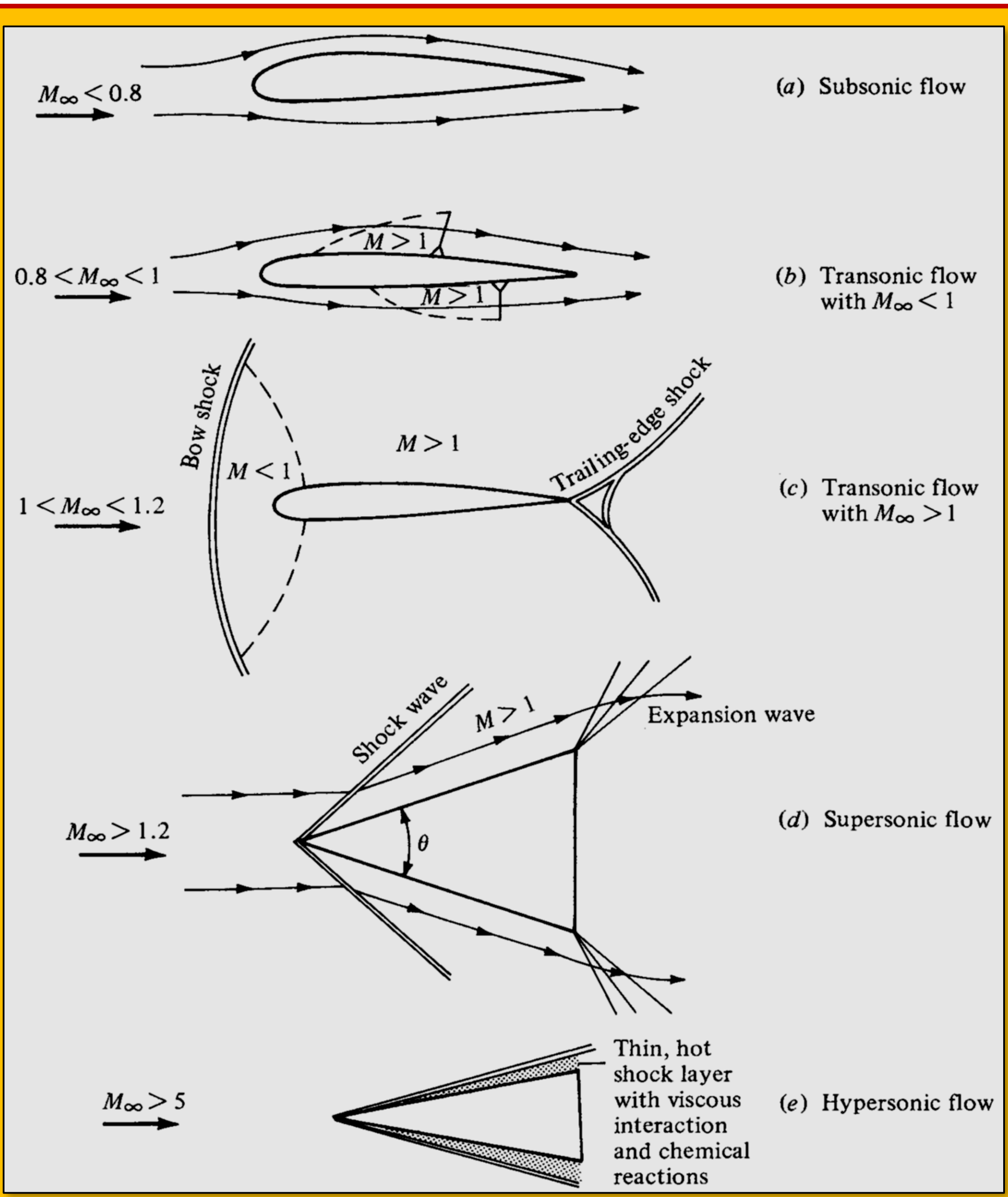

Figure 3.9.3 Different Regimes of Flow (Courtesy of John D. Anderson)

3.9.1.2 Transonic Flow (Mixed Regions Here M < 1 and M > 1)

As stated above, if M_∞ is subsonic but is near unity, the flow can become locally supersonic (M > 1). This is sketched in **Figure 3.9.3 b**, which shows pockets of supersonic flow over both the top and bottom surfaces of the airfoil, terminated by weak shock waves behind which the flow becomes subsonic again. Moreover, if M is increased slightly above unity, a bow shock wave is formed in front of the body; behind this shock wave the flow is locally subsonic, as shown in **Figure 3.9.3 c**. This subsonic flow subsequently expands to a low supersonic value over the airfoil. Weak shock waves are usually generated at the trailing edge, sometimes in a "fishtail" pattern as shown in **Figure 3.9.3 c**. The flow fields shown in **Figure 3.9.3 b** and **c** are characterized by mixed subsonic-supersonic flows and are dominated by the physics of both types of flow. Hence, such flow fields are called ***transonic flows***. Again, as a rule of thumb for slender bodies, transonic flows occur for freestream Mach numbers in the range $0.8 < M < 1.2$.

3.9.1.3 Supersonic Flow ($M > 1$ Everywhere)

A flow field is defined as ***supersonic*** if the Mach number is greater than 1 at every point. Supersonic flows are frequently characterized by the presence of shock waves across which the flow properties and streamlines change discontinuously. This is illustrated in **Figure 3.9.3 d** for supersonic flow over a sharp-nosed wedge; the flow remains supersonic behind the oblique shock wave from the tip. Also shown are distinct expansion waves, which are common in supersonic flow. (Again, the listing of $M_\infty > 1.2$ is strictly a rule of thumb. For example, in **Figure 3.9.3 d,** if θ is made large enough, the oblique shock wave will detach from the tip of the wedge and will form a strong, curved bow shock ahead of the wedge with a substantial region of subsonic flow behind the wave. Hence, the totally supersonic flow sketched in **Figure 3.9.3 d** is destroyed if θ is too large for a given M_∞. This shock detachment phenomenon can occur at any value of $M_\infty > 1$, but the value of θ at which it occurs increases as M_∞ increases. In turn, if θ is made infinitesimally small, the flow field in **Figure 3.9.3 d** holds for $M_\infty \geq 1.0$. The above discussion clearly shows that the listing of $M_\infty > 1.2$ in **Figure 3.9.3 d** is a very tenuous rule of thumb and should not be taken literally.) In a supersonic flow, because the local flow velocity is greater than the speed of sound, disturbances created at some point in the flow ***cannot*** work their way upstream (in contrast to subsonic flow). This property is one of the most significant physical differences between subsonic and supersonic flows. It is the basic reason why shock waves occur in supersonic flows, but do not occur in steady subsonic flow[70].

3.9.1.4 Hypersonic Flow ($M \geq 5$)

Refer again to the wedge in **Figure 3.9.3 d**. Assume θ is a given, fixed value. As M increases above 1, the shock wave moves closer to the body surface. Also, the strength of the shock wave increases, leading to higher temperatures in the region between the shock and the body (the shock layer). If ***M is sufficiently large, the shock layer becomes very thin, and interactions between the shock wave and the viscous boundary layer on the surface occur***. Also, the shock layer temperature becomes high enough that chemical reactions occur in the air. The O_2 and N_2 molecules are torn apart; that is, the gas molecules dissociate. When M_∞ becomes large enough such that viscous interaction and/or chemically reacting effects begin to dominate the flow (**Figure 3.9.3 e**), the flow field is called ***hypersonic***. (Again, a somewhat arbitrary but frequently used rule of thumb for hypersonic flow is $M_\infty > 5$). Hypersonic aerodynamics received a great deal of attention during the period 1955 –1970 because atmospheric entry vehicles encounter the atmosphere at Mach numbers between 25 (ICBMs) and 36 (the Apollo lunar return vehicle). Again during the period 1985–1995, hypersonic flight received a great deal of attention with the concept of air-breathing supersonic-combustion ramjet-powered trans atmospheric vehicles to provide single-stage-to-orbit capability. Today, hypersonic aerodynamics is just part of the whole spectrum of realistic flight speeds[71].

3.9.1.4.1 Characteristics of Hypersonic Atmosphere [72]

Hypersonic flight has special traits, some of which are seen in every hypersonic flight. Presence of these particular features during a flight is highly dependent on type of trajectory, configuration etc. In short it is the mission requirement which decides the nature of hypersonic atmosphere encountered by the flight vehicle. Some missions are designed for high deceleration in outer

---

[70] John D. Anderson, Jr, Professor Emeritus University of Maryland, "*Fundamentals of Aerodynamics*", 5th edition, The McGraw-Hill Companies, Inc., 1221 Avenue of the Americas, New York, NY 10020, 2011.

[71] See Previous.

[72] Nptel Online courses.

atmosphere during reentry. Hence, those flight vehicles experience longer flight duration at high angle of attacks due to which blunt nosed configuration are generally preferred for such aircrafts. On the contrary, some missions are centered on low flight duration with major deceleration closer to earth surface hence these vehicles have sharp nose and low angle of attack flights. Reentry flight path of hypersonic vehicle is thus governed by the parameters called as ballistic parameter and lifting parameter. These parameters are obtained by applying momentum conservation equation in the direction of the flight path and normal to it. Velocity-altitude map of the flight is thus made from the knowledge of these governing flight parameters, weight and surface area. Ballistic parameter is considered for non-lifting reentry flights like flight path of Apollo capsule, however lifting parameter is considered for lifting reentry trajectories like that of space shuttle. Therefore hypersonic flight vehicles are classified in four different types based on the design constraints imposed from mission specifications.

1. **Reentry Vehicles (RV):** These vehicles are typically launched using rocket propulsion system. Reentry of these vehicles is controlled by control surfaces. Large angle of attack flight of blunt nosed configurations is the need of these flights. Space shuttle (US), BURAN (Russian), HOPE (Japan) and HERMES (European) are some examples of these kind vehicles.
2. **Cruise and Acceleration Vehicle (CAV):** Slender configurations with low angle of attack flights are main features of these flights. These vehicles are prepared for high heating loads with ablative cooling system. Air breathing propulsion system of ram or scramjet type is generally preferred for these vehicles. Sanger, which is a two stage (TSTO) hypersonic vehicle, has first stage with air breathing propulsion and second stage is propelled with rocket. Hence first stage of Sanger falls in CAV category for which separation takes place at Mach 7.
3. **Ascent and Reentry Vehicles (ARV):** These vehicles have opposing requirements of their design due to dual duty of ascent, which is dominated by fuel requirements, and reentry by aero-braking. Rocket or air breathing propulsion systems can be preferred for these flights. NASP or National Aerospace Plane of US, Space Plane by Japan and HOTOL are some examples of these vehicles.
4. **Aero assisted Orbit Transfer Vehicle (AOTV):** This is one more class in which hypersonic vehicles are classified. Ionization and hence presence of plasma in the vicinity of the spacecraft is the major concern of these vehicles.

Each of these vehicles faces different flight challenges based on their missions and flight configurations. These challenges form the topic of research in the field of hypersonic aerodynamics.

3.9.1.4.2 Physics of Hypersonic Flow Regime

Definition of flow regime is based on the Mach number of the flow. If Mach number is below unity then the flow is called as subsonic. Sonic flow has Mach number exactly equal to one however flow in the narrow range of Mach number ($0.8 \leq M \leq 1.2$) is called as transonic flow. When the flow Mach number exceeds beyond 1 then flow is called as supersonic flow. As per the thumb rules, when flow speed exceeds five times the sound speed, it is treated as hypersonic flow. However hypersonic flow has certain characteristics which when experienced in the flow, should then only be termed as hypersonic. These characteristics of hypersonic flow are mentioned below:

- **Thin Shock Layers**

  Region between shock and the body (flight vehicle) is named as shock layer. From the relations between shock angle, Mach number and flow deflection angle or wedge angle, it would be clear that, for same flow deflection angle, shock angle decreases with increase in Mach number. Hence the thickness of the shock layer decreases with increase in Mach number for the same flow deflection angle. Therefore hypersonic flows have thin shock layer. This interpretation of shock layer thinness for calorically perfect gas is also applicable for thermally perfect gas and chemically reacting flow. However, complexity of flow field increases due to thin shock layer where the boundary layer thickness and shock layer thickness become comparable.

- **Entropy Layer**

  One of the main properties of the curved shock waves in that, each streamline passing through the shock faces differential entropy rise where stronger portion of shock leads to higher entropy rise than the weaker portion. Therefore, a layer of entropy variation getting formed downstream of the shock is termed as entropy layer. Analysis of hypersonic flow becomes further troublesome with consideration of this entropy layer since according to Croco's principle the entropy layer leads to vorticity. As it was evident that the shock layer thickness decreases with increase in Mach number and shock comes closer to the sharp leading edge configurations like wedge or cone, it is also obvious that shock detachment distance decreases with increase in Mach number for blunt bodies. Hence the entropy layer exhibits strong gradient of entropy which leads to higher vorticity at higher magnitudes of Mach numbers. Due to presence of entropy layer it becomes difficult to predict the boundary layer properties and properties at the edge of the boundary layer of hypersonic flow due to interaction of boundary layer vorticity and entropy layer vorticity. This interaction is termed as vorticity interaction.

- **Viscous Interaction**

  As we know, formation of boundary layer takes place near the wall due to no-slip property of the viscous fluid flow. Formation of this boundary layer takes place across enormous loss of kinetic energy at hypersonic speeds. This kinetic energy necessarily gets converted in to thermal energy which leads to increase in temperature of the flow in the vicinity of the wall. This phenomenon is called as viscous dissipation. Viscous dissipation leads to increase in boundary layer thickness due to increase in viscosity coefficient with temperature. This situation can also be interpreted from boundary layer theory where pressure is considered to be constant across the boundary layer. This thickened boundary layer displaces outer inviscid flow hence freestream hypersonic flow encounters an inflated object which changes the shock shape and intern boundary layer parameters along with surface pressure, wall heat flux, skin friction etc. This interaction or communication loop between viscous boundary layer and outer inviscid flow is called as viscous interaction. As a result of this interaction aerodynamic parameters such as lift, drag etc deviate a lot from their base value without interaction. Hence it becomes mandatory to treat viscous interaction for hypersonic flights since whole shock layer tends to become viscous due to this interaction.

- **High-Temperature Flows**

  As we know, viscous dissipation leads to higher boundary layer thickness and temperature of the boundary layer fluid. Therefore any hypersonic flight experiences presence of high temperature fluid in the vicinity of the flight vehicle. Apart from this, blunt nosed configurations encounter very high temperatures due to normal shock present at the stagnation point. Therefore at these elevated temperatures, treatment of fluid as calorically perfect or with constant thermodynamic properties leads to unrealistic estimations. Hence it becomes essential to take in to account the dependence of specific heats and their ratio as function of temperature for rational estimates.

  The dependence of thermodynamic properties on temperature mainly comes from microscopic changes in the fluid due to increase in internal energy of the fluid by the virtue of loss of kinetic energy. Increased internal energy leads initially to vibrational excitation followed by dissociation and finally ionization according to the extent of increase in internal energy. As per the order of magnitude estimate, vibrational excitation of air takes place at around 800K. Oxygen dissociation starts at around 2000 K and completes at 4000 K. At around 4000 K nitrogen dissociation commences and completes at 9000 K. Ionization of this high temperature air or mixture of gases starts from 9000 K temperature. Hence the initial air with atmospheric composition becomes plasma after 9000 K. As a result of all these reactions, hypersonic vehicle gets engulfed by reacting boundary layer and high temperature plasma. Therefore treatment of air or any fluid flowing with hypersonic speed over any configuration should be done properly by incorporating all the microscopic changes which essentially leads to change in thermodynamic properties with temperature. This dependence is highly non-linear, hence analysis or prediction of flow field becomes tougher in this flow regime. Therefore two types of assumptions are generally made about the flow conditions for high temperature fluid as equilibrium flow and non-equilibrium flow. If the microscopic changes or reactions are at faster rate than the movement of the fluid, then it is treated as equilibrium flow otherwise it is treated as non-equilibrium flow which is difficult to analyze. All these difficulties are collectively termed as ‘real gas effects'.

Some consequences of presence of high temperature reacting fluid or plasma in the vicinity of the flight vehicle include, influence on aerodynamic parameters, aerodynamic heating and communication block-out. Flight parameters like pitch, roll, drag, lift, defection of control surfaces get largely deviated from their usual estimate of calorically perfect gas. Presence of hot fluid near the cold vehicle surface induces heat transfer not only through convection but also through radiation. Communication waves which are necessarily radio waves get absorbed by free electrons formed from ionization of atmospheric fluid. This phenomenon is called as communication block-out where on board and ground communication gets terminated.

- **Low-Density Flow**

Hypersonic flights at higher altitudes experience very low density flows. The governing non-dimensional parameter for these regimes is called as Knudsen number which is defined as the ratio of mean free path to the characteristic length of the object. Here mean free path is termed as the mean distance traveled by the fluid molecule between two successive collisions with other molecules. Since density of air is very high on the earth's surface, therefore Knudsen number is close to zero for standard dimensions of hypersonic flights. However if we consider any standard hypersonic flight taking off from earth surface, it becomes clear that, the flight vehicle is going to encounter change in density with increase in altitude. Validation of continuum assumption and in turn the usage of usual governing equations remains intact till the altitude of around 90 km from earth surface where Knudsen number is below 0.3. Above this altitude, till 150 km from earth surface, density becomes lower as a effect of which fluid velocity and temperature at the surface do not remain in equilibrium with the surface. Therefore flow for Knudsen number in range 0.3 to 1 is treated in the transitional regime where slip wall boundary conditions should be used along with the usual governing equations based on continuum assumption. However above 150 km from earth's surface, density of air becomes very low therefore this region is called as free molecular flow where Knudsen number becomes more than or equal to unity. Thus need for change in governing equations arise in this regime. Hence kinetic theory of gases finds its application for hypersonic flights at such altitudes.

From these specifications of hypersonic flow regime, it is clear that Mach number to be very much greater than one is the formal definition of hypersonic flow. Higher density ratio is also one of the definitions of hypersonic flow. Density ratio across normal shock would reach 6 for calorically perfect gas (air or diatomic gas) at very high Mach numbers. If concerned fluid is chemically reacting mixture or even thermally perfect then this ratio increases to value more than 20, which was reached in Apollo flight. For density ratio to reach more than 20, the specific heat ratio should decrease and reach a value close to one for air. In actual flight conditions, hypersonic flow field can be reached with increasing the flight velocity without altering thermal properties of surrounding fluid. However, it is difficult to achieve this flow in ground testing with very high kinetic energy and high Mach number without change in thermal properties the fluid. Therefore there are many challenges for experimental simulation of hypersonic flow. One solution for this problem is the use of different gases to simulate the low specific heat ratio condition. Tetrafluoroethane is used for specific heat ratio of 1.2 and hexafluoroethane for 1.1. Understanding the challenges faced by hypersonic flight and derived solutions for some of those problems are the themes of this subject.

3.10 Case Study 2 - A Data Fusion Method using Combined Variable Fidelity Modeling and Space Mapping for Aerodynamic Database

Authors : *MuKyeom Kim, Maxim Tyan, Vinh Pham, Nadhie Juliawan, Sangho Kim, Jae-Woo Lee*
Affiliations : *120 Neungdong-ro, Gwangjin-gu, Seoul 05029, Republic of Korea*
Title of Paper : *A Data Fusion Method using Combined Variable Fidelity Modeling and Space Mapping for Aerodynamic Database*
Citation : *(MuKyeom, et al., 2018)*
Bibliography : *MuKyeom, K., Maxim, T., Vinh, P., Nadhie, J., Sangho, K., & Jae-Woo, L. (2018). A Data Fusion Method using Combined Variable Fidelity Modeling and Space Mapping for Aerodynamic Database. China: APISAT2018.*

Aerodynamic database is an important component of flight simulation, propeller blade analysis, aircraft loads analysis, and other types of engineering analysis (MuKyeom, et al., 2018). Construction of such database may require the use of multiple sources of data and analysis at the same time. ***A data fusion method is pro-posed which is an efficient trade-off between computationally costly high-fidelity methods and cheap but less accurate low fidelity***. The proposed data fusion method uses combination of variable fidelity modeling with space mapping algorithm. The variable fidelity modeling uses scaling factor to approximate the differences between high and low fidelity functions. Space mapping makes correction to the input variables by adjusting peak point to reduce nonlinearity of a scaling function. Aerodynamic table of 2D airfoil is constructed to demonstrate the proposed method and compare to the original one. The result demonstrates that the proposed method has absolute maximum prediction error of 0.0361, com-paring with 0.1035 using original variable fidelity modeling.

3.10.1 Introduction

Nowadays, the importance of flight simulation is increasing. From flight simulation for entertaining content to simulation for aviation certification, the importance of simulation is increasing. One of the key components for creating a simulation is aerodynamic database. In flight simulation for fun, precision of aerodynamic database is not that important. On the other hand, accuracy of aerodynamic for pilot training or aviation certification is very important. In the aerospace field, the most popular and relatively accurate way to analyze aerodynamic characteristic is Wind Tunnel Test (WT) and (CFD). Someone who performs WT test or CFD can face the limitation of such jobs. One of the problems is that it takes too much time to calculate or the cost for WT could be expensive. In CFD, it can be taking more than a week to calculate for just one flight condition with one angle of attack. And in WT case, WT needs model to perform tests, also need WT itself. Those ones cost so much and perhaps we could need a building for WT. In such situation, there were several attempts to reduce such time and expense while maintaining accuracy of analysis.

Here, high fidelity data prediction with combined method between Variable Fidelity Modeling (VFM) and Space Mapping (SM) was performed. Both methods have been developed for reducing calculation time and expense. Case of VFM, the goal is to obtain reliable full data set in the design area by combining large amounts of low fidelity data which can get fast and cheap with a small number of high fidelity data set. In the case of SM, it is used as a method to overcome the prediction limit which is caused by converting 2d into 1d when using only VFM[73].

3.10.2 High & Low Fidelity Data for Numerical Example

Clark Y airfoil aerodynamic data were used for numerical examples. Java Foil was used as a low fidelity analysis tool which is based on panel method. Java Foil calculates the velocity distribution at the surface and then computes the flow at the boundary layer based on the result. However, since

---

[73] Ping Jiang, Tingli Xie, Qi Zhou, Xinyu Shao, Jiexiang Hu, and Longchao Cao, *A space mapping method based on Gaussian process model for variable fidelity metamodeling, Simulation Modeling Practice and Theory*, 2018.

the flow separation is not considered, the accuracy is low where the stall occurs. As a high fidelity analysis tool, *ANSYS Fluent*® with RANS solver was used to solve 301 by 100 structured C type mesh. Y^+ is equal to 1.0 and *Spalart-Allmaras* model was used as turbulence model. For ***low fidelity*** data you can see **Figure 3.10.1**, represented by the wire-frame surface, the analysis results from Clark Y airfoil using Java foil at Mach number 0.1 to 0.9 with 0.1 deg intervals and angle of attach -20 to 20 degrees with interval 1deg. For ***high fidelity*** data, represented by dot in **Figure 3.10.1**, using *ANSYS Fluent* tools result at Mach number 0.1, 0.5 and 0.8, and -20 to 20 degrees with intervals of 2degree.

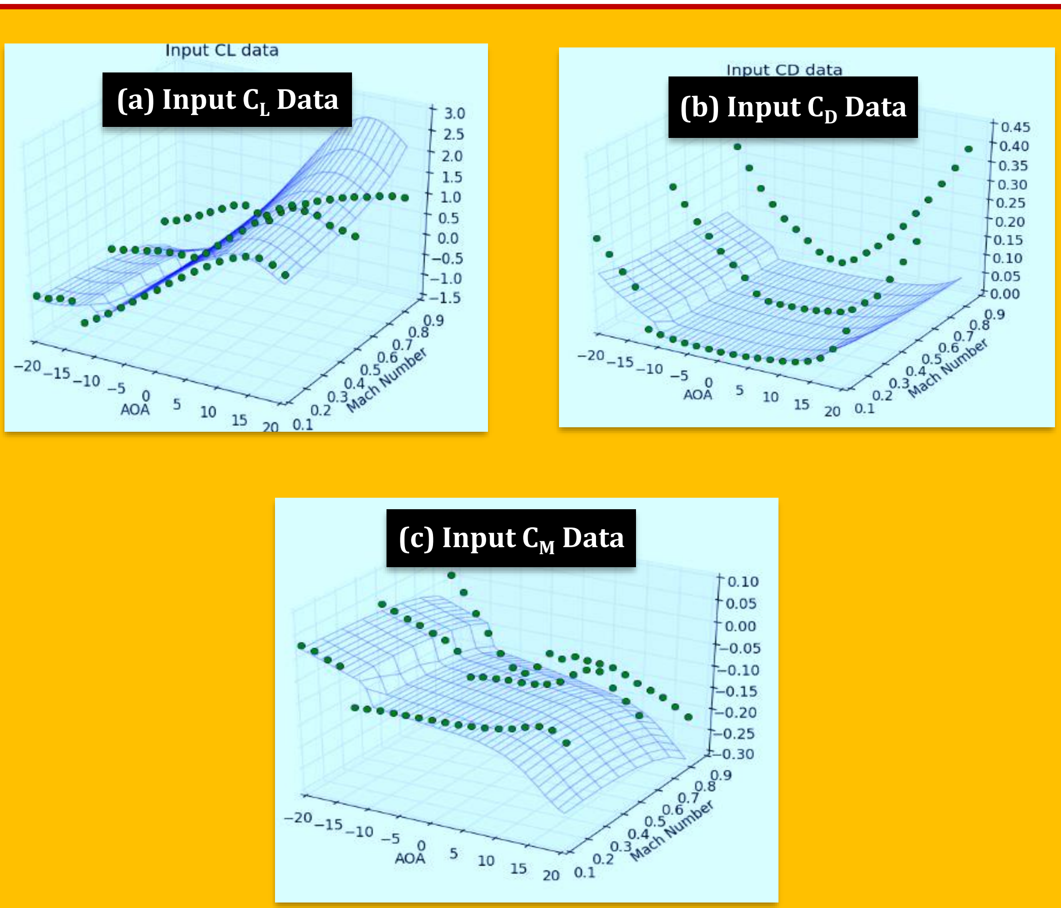
(a) Input C_L Data

(b) Input C_D Data

(c) Input C_M Data

Figure 3.10.1 Inputs of Coefficients for Numerical Examples, lift(a), Drag (b), Moment (c)

3.10.3 VFM Airfoil Prediction

Compared to input data, prediction data are close to high fidelity data. Mean Absolute Error (MAE) and maximum error locations of the data predicted by high fidelity data and Data Fusion are as **Table 3.10.1**. As evidence from the above table, MAE is quite low, but maximum error looks like too large to use as a coefficient. Generally, this large error can be a problem because lift, drag, and moment coefficients are originally very small values. However, it should be noted that not only the magnitude of maximum error is large, but also the location of

	MAE	Max. Error [%]	[AOA, Mach]
C_L	5.35 × 10−2	0.2972 [39.6%]	[2.0, 0.7]
C_D	0.6124 × 10−2	0.0296 [18%]	[14.0, 0.6]
C_M	0.7716 × 10−2	0.0592 [81.2%]	[-6.0, 0.7]

Table 3.10.1 Prediction Error

maximum error occurs. It can be confirmed that all errors occur in the transonic region and location of peak point as you can see below figure. This is because, in the case of low fidelity data, there is a smooth transition from subsonic to supersonic due to the limitations of the analysis tool, whereas in the case of high fidelity data, there is a sudden change in the same area due to the effect of more accurate analysis result.

This kind of problem is caused by big difference between low fidelity and high fidelity data. Besides, it caused by problem of Gaussian Process in VFM method. It seems like that Gaussian Process has difficulty to predict scaling function if the model has too much non-linear trend such as the location of peak points like $C_{L,max}$ point or $C_{m,min}$ point. For this reason, it is necessary to reduce the non-linearity of scaling factor function between low fidelity and high fidelity data in the transonic and peak point region before performing VFM. See **Figure 3.10.2**.

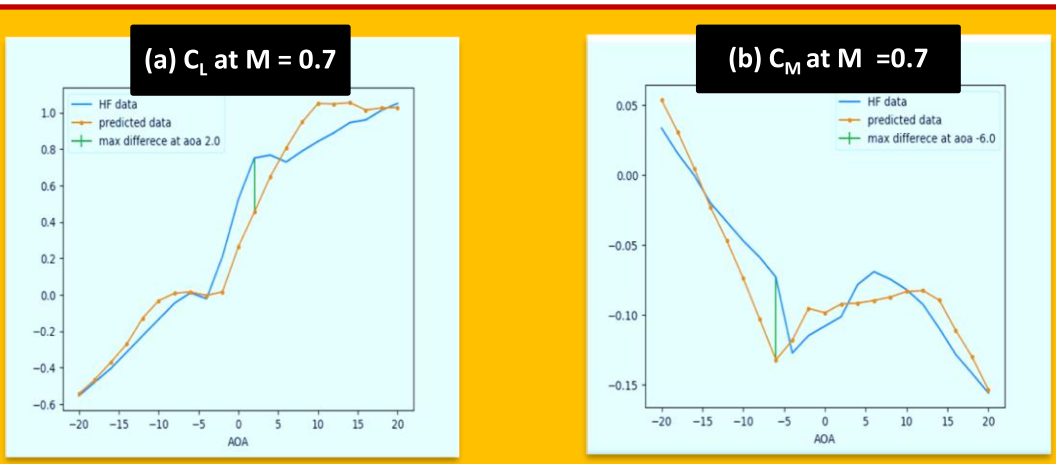
(a) C_L at M = 0.7

(b) C_M at M =0.7

Figure 3.10.2 Lift and Moment Coefficients Maximum Error Location

3.10.4 SM and VFM Combined Airfoil Prediction

So, SM was performed to reduce such non-linearity. VFM was performed after SM to overcome big error in transonic region and peak point. We performed SM before VFM based on peak point C_L max point. So, SM moved C_L max point of low fidelity to same point with high fidelity cl max point. As you can see above, SM + VFM result is quite similar to VFM only result. But in the peak points like $C_{L\ max}$ point or cl min point, it decreased maximum error. Maximum error is changed from 0.10353 (VFM only) to 0.03615 (SM+VFM) of error value, numerically about 68% decreased. See **Figure 3.10.3**.

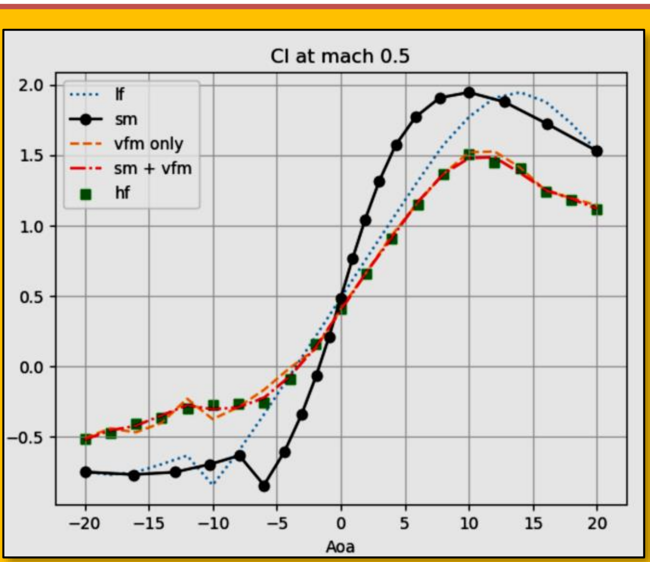

Figure 3.10.3 SM+VFM Method Lift Coefficient Prediction

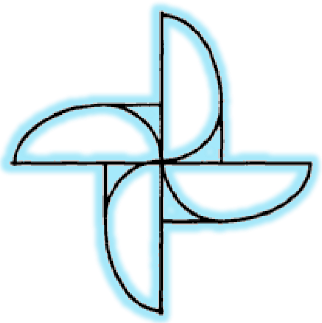

4 Shock Waves

4.1 Preliminaries

A shock wave is a very thin region in a supersonic compressible flow across which there is a large variation in the flow properties. Because there variation occur in such a short distance, viscosity and heat conductivity play a dominant role in the structure of shocks. These will be revisited later while **Figure 4.1.1** displays shock wave for different flow regions as applicable to a jet fighter. Another examples in detecting of shocks would be the concentration of contour lines. As a discontinuity in the flow field, the contour line of Mach number, pressure, density and temperature all concentrate near the shock wave. For slip plane and contact discontinuity, pressure contour lines do not concentrate. **Figure 4.1.2** displays contour lines of all relevant of flow features exemplifying a bow shock in presence of blunt body, in supersonic flow[74].

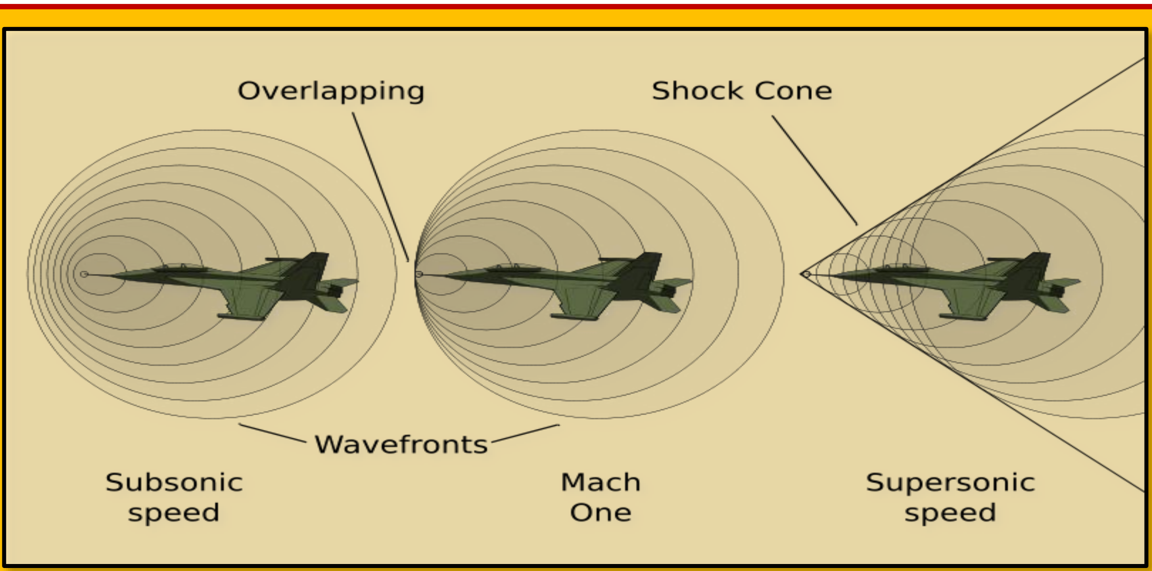

Figure 4.1.1 Evolution of Shock Wave

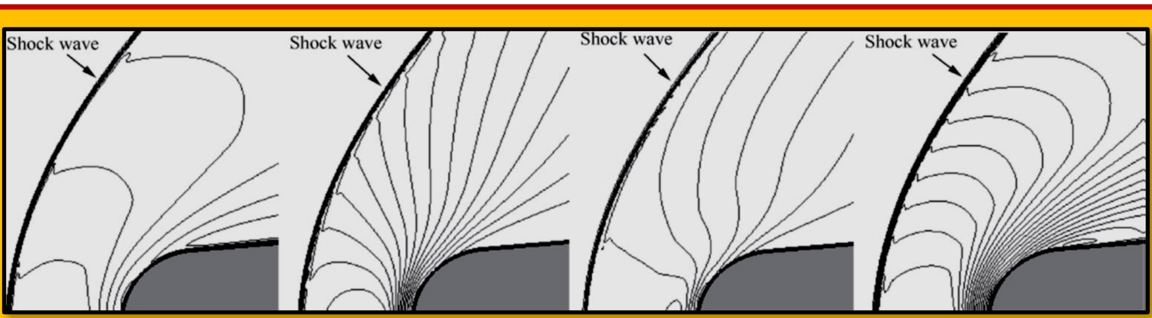

Figure 4.1.2 Contour Concentration Examples at M = 5 ; From Left to Right ; (a) Mach number (b) Pressure (c) Density (d) Temperature

As a intriguing example, **Figure 4.1.3** shows two *U.S. Air Force Test Pilot School T-38* aircraft fly in formation, approximately 30 feet apart, at supersonic speeds, or faster than the speed of sound, producing shockwaves that are typically heard on the ground as a sonic boom. The images, originally

---

[74] Wu Ziniu , Xu Yizhe, Wang Wenbin, Hu Ruifeng, "*Review of shock wave detection method in CFD post-processing*", Chinese Journal of Aeronautics, 2013.

monochromatic and shown here as colorized composite images, were captured during a supersonic flight series flown in part to better understand how shocks interact with aircraft plumes, as well as with each other[75].

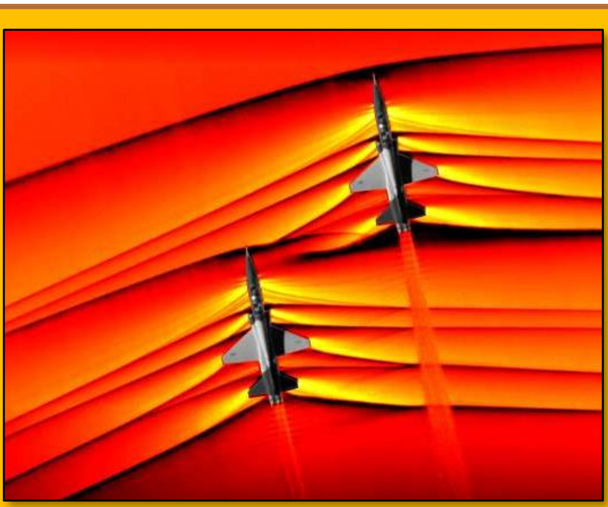

Figure 4.1.3 Two U.S. Air Force Test Pilot School T-38 Aircraft Fly in Formation

4.2 Difficulties for Shock Wave Detection

There exist several difficulties for shock detection from CFD result:

- ➢ The numerical dissipation and oscillation in CFD may cause some shock waves to be undetected. The numerical dissipation smears the discontinuity in the flow field, and makes weak shock waves undetectable.
- ➢ The numerical oscillation produces structures similar to weak shock waves just near real shock wave, and thus may lead to false detection results.
- ➢ The similarity among shock waves and other discontinuous flow structures like slip lines can lead to incorrect detection results.
- ➢ The graphical display of shock detection result is also a problem for three-dimensional and multiple shock waves.

4.3 Traditional Shock Detection Methods

According to investigation by [Ziniu, et al.][76], traditionally, through the contour lines one may detect shock waves since near shock waves the contour lines are concentrated. While pressure, density, temperature and Mach number contour lines all concentrate near shock waves, only pressure contour is recommended for shock detection, because the others cannot distinguish shock wave from slip line, shear layer or contact discontinuity. However, it is still difficult to get a clear view of the shock wave structure from pressure contour. Also contour method cannot give a direct way to display shock surfaces in three-dimensional flow field. These disadvantages highly restrict the use of this contour shock detection method. Another traditional shock detection method is to plot the iso-surface of Mach number. It is convenient to approximate the shock surface around the vehicle by displaying a Mach number iso-surface just a little lower than the freestream Mach number. This method can yield a full shock wave surface in three-dimensional flow field. However, it may produce too many surfaces other than desired shock wave surfaces, and become helpless to detect shock wave except the leading shock wave.

In numerical solutions of fluid flow with discontinuities (shock wave) by the shock-capturing method. The shock wave can be smoothed by low-order scheme or there are spurious oscillations near shock surface by high-order scheme[77], as shown in **Figure 4.3.1,** where solid lines represent analytical solution, and dotted lines represent computed result. In the classical boundary shock-fitting method, shock wave must be introduced explicitly as outer flow boundary, which depends on experimental, theoretical or numerical-based knowledge on shock shape and location. While in the

---

[75] Photo released March 22, 2019. NASA/Handout via Reuters.

[76] see Previous.

[77] Toro EF. "*Riemann solvers and numerical methods for fluid dynamics*". 3rd Edition, Berlin: Springer; 2009.

floating shock-fitting method proposed by Moretti[78], shock waves are detected through ***Rankine–Hugoniot*** jump condition and the method of characteristics, which may be applicable to shock detection in post-processing.

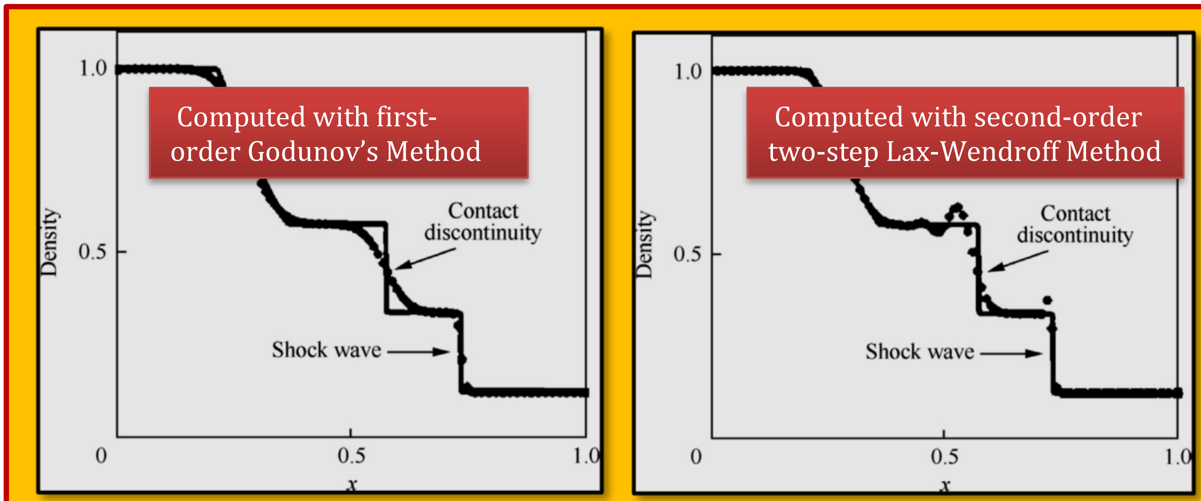

Figure 4.3.1 Solution of Shock Capturing for Euler Equations

4.4 Compressible 1D Shock Waves Relations

An undesirable side effect to supersonic, compressible flow is the phenomena called ***shock wave*** that almost always associated with aerodynamic losses and should be avoid. A shock wave is a thin region across which flow properties exhibit a large gradient[79]. On molecular level, the disturbance due to an obstacle is propagated upstream via molecular collisions (momentum) at approximately the local speed of sound. If the upstream flow is subsonic, the disturbances have no problem working their way upstream, thus giving the incoming flow plenty of time to move out of way of obstacle. On the other hand, if upstream flow is supersonic, the disturbances cannot work their way upstream, but rather at some finite distance from the obstacle. This disturbance wave pile up and coalesce, forming a thin standing wave in front of the body. Hence, the physical generation of shocks and expansion wave is due to propagation of information via molecular collisions and due to the fact that in

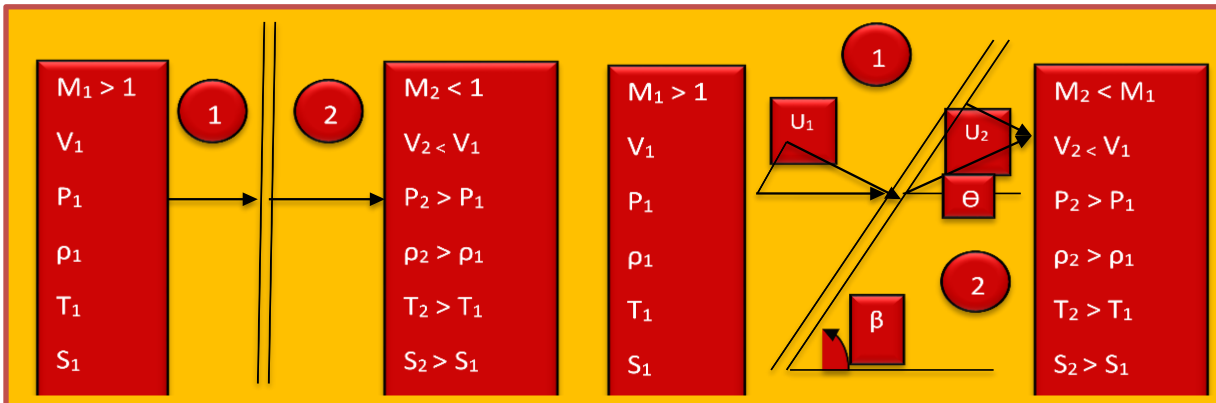

Figure 4.4.1 Qualitative Depiction of 1D Flow Through Normal and Oblique Shocks

---

[78] Moretti G. "*Experiments in multi-dimensional floating shock fitting*". Polytechnic Institute of Brooklyn, Brooklyn, NY, PIBAL, Report No. 73–18, 1973.

[79] Anderson, John D. 1984: "*Fundamentals of Aerodynamics*", McGraw Hills Inc.

supersonic flow this information cannot work its way into certain region of supersonic flow. The shock wave is usually at an oblique angle to the flow, attached or detached, however, there are many cases that it could be the stronger normal type. In both cases, the pressure increases almost discontinuously across the wave.

Figure 4.4.1, the qualitative changes across the wave is noted, for region 1 ahead, and region 2 behind, with normal shock (left), and oblique shock (right). The pressure, density, temperature, and entropy increases across the shock, whereas the total pressure, Mach number, velocity decreases. Since the flow across the shock is adiabatic (no external heating), the total enthalpy is constant across. Behind the oblique shock the flow remain usually supersonic, but weaker. For normal shock, the downstream flow is always subsonic. U_1 and U_2 are normal component of velocity. The quantities downstream could be directly evaluated by upstream values[80]. Another relation vital to oblique shock wave is the relations between deflection angle θ and wave angle β in relation to upstream Mach number (M_1) as

$$\tan\theta = 2\cot\beta\frac{M_1^2\sin^2\beta - 1}{M_1^2(\gamma + \cos 2\beta) + 2}$$

Eq. 4.4.1

This is an important relationship between upstream Mach number, M_1, deflection angle θ, wave deflection β, and should be analyzed thoroughly. Using known Θ we could obtain the ***tangential*** velocity components (U_{t1}, U_{t2}), and use of previously relationship to obtain the downstream values as:

$$\rho_1 U_1 = \rho_2 U_2 \quad , \quad p_1 + \rho_1 U_1^2 = p_2 + \rho_2 U_2^2 \quad , \quad U_{t1} = U_{t2} \quad , \quad h_1 + \frac{U_1^2}{2} = h_2 + \frac{U_2^2}{2}$$

Eq. 4.4.2

Other consideration in obtaining Θ include:

1. For any upstream Mach number, M_1, there exists a maximum deflection angle, θ_{max}, where there is no solution exists for straight oblique shock. Instead, nature establishes a curved shock wave, ***detached*** from the body.
2. For any values less than θ_{max}, there are two straight oblique shock solutions, denoting to *weak* and ***strong*** shock solutions.
3. If θ=0, then β=90 degrees and therefore normal shock results.
4. For a fixed θ, increasing the upstream Mach number M_1, causes the shock becomes stronger and closer to the body (β decreases). This would cause stronger dissipative effects near surface (shear and thermal conductivity), clearly an undesirable effect in thermal management of body.

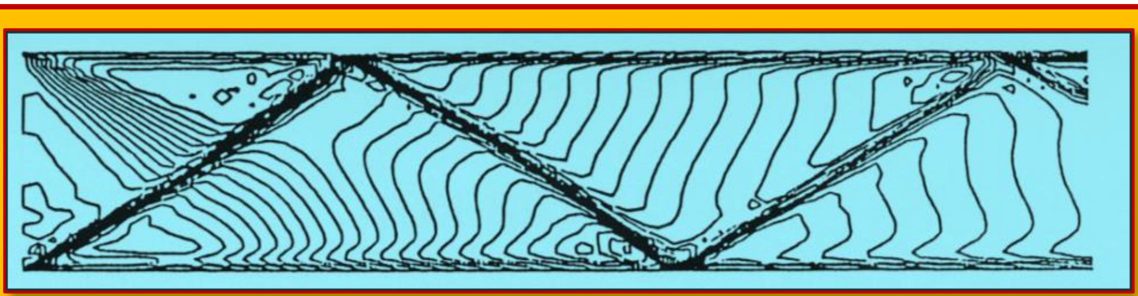

Figure 4.4.2 Oblique Shock Reflections on a Channel Flow (M = 2 AoA = 15˚)

---

[80] Anderson, John D. 1984: "*Fundamentals of Aerodynamics*", McGraw Hills Inc.

The physical effects of oblique shock discussed above are very important. Yet another feature is the shock interactions and reflections. An impinging oblique shock on a surface would not simply disappear but rather weakens and reflects, provided the flow on the surface preserves the tangential quantities. **Figure 4.4.2** exhibits the reflection of oblique shock wave on an in-viscid channel flow, generated by its edges with free-stream Mach number of 2.0, AOA = 15° and slip wall boundary conditions.

4.5 Quasi -1D Correlation Applied to Variable Area Ducts

Following the trend developed for 1D shock relations, and expanding on the idea that the area could change A = A(x). But the area variations are moderate and the components in y and z are small relative to x, enabling p = p(x), ρ = ρ(x), u = u(x), etc. Most supersonic wind tunnels could fall within such assumption. Where the momentum equation is seen previously as Euler's equation holding along a stream line. Now we see that holds for quasi 1-D flow. Manipulating the continuity relation with some help from momentum, yield an important relation between velocity and area called the area-velocity relation as:

$$\frac{dA}{A} = (M^2 - 1)\frac{du}{u}$$

Eq. 4.5.1

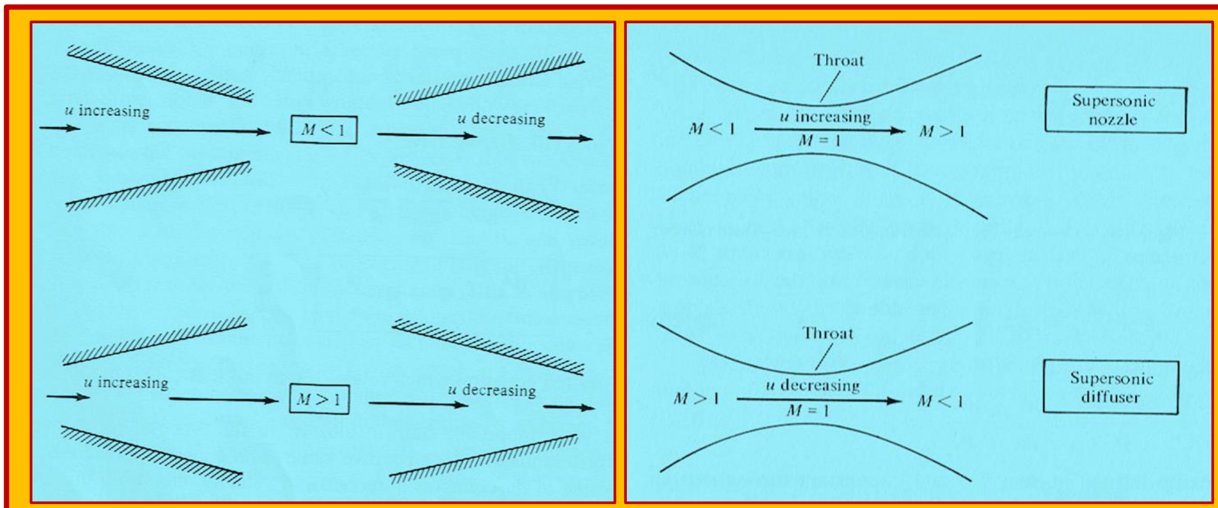

Figure 4.5.1 Compressible Flow in Converging-Diverging Ducts (Nozzles and Diffusers)

Depending the character of coefficient (M^2 - 1), and assuming positive values u and A meant an increase in du or dA, following observations could be made,

1. For subsonic flows (M < 1), the coefficient in parentheses is negative. Hence an increase in velocity (positive du) is associated with a decrease in area (negative dA). Likewise, a decrease in velocity (negative du) is associated with an increase in area (positive dA). Clearly for a subsonic compressible flow, to increase the velocity, we must have a convergent duct and to decrease, the velocity, must have a divergent duct. Similar to incompressible flow.
2. For supersonic flows (M > 1), the coefficient is positive. Therefore, an increase in velocity (positive du) is associated with an increase in area (positive dA). Inversely, a decrease in velocity (negative du), cause a decrease in area (negative dA). For supersonic flows, to increase the velocity we must have a divergent duct, and decease the velocity must have a convergent duct.

3. For M = 1 or sonic flow, it can be shown that dA = 0 which corresponds mathematically to local max/min in area. Physically, it represents the minimum area (throat).

These findings for converging-diverging duct, could best illustrated using the following **Figure 4.5.1** and by introduction to concepts of nozzle and diffuser. Where a nozzle is designed to achieve supersonic flow at is exit, conversely a diffuser tries to bring the flow down to subsonic. Nozzles are equipment used for controlling the flow rate, flow direction and increasing the velocity. We can see the nozzles in gas jets, fluid jets, hydro jets, jet engines, sprays, vacuum cleaner, etc. one of the most popular nozzles is converging diverging nozzle which has a converging section, throat and diverging section. Converging and diverging nozzles are used in many different systems such as propulsion systems, rackets and jet engines and steam turbines. The relationship for oblique shock and comparison with theory is given be where incident Mach number ($M_\infty = 3$) is plotted against the theory[81] as depicted in **Figure 4.5.2.**

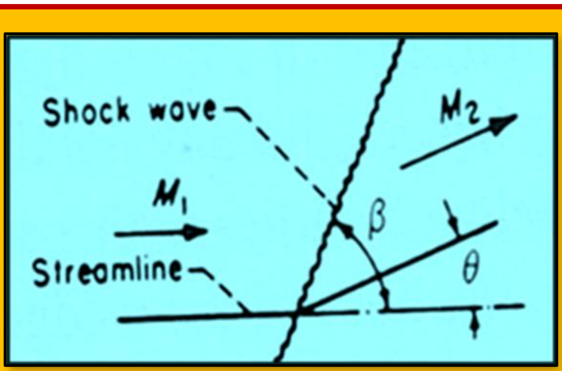

$$M_{n,1} = M_1 \sin\beta$$

$$M_{n,2}^2 = \frac{1 + [(\gamma - 1)/2] M_{n,1}^2}{\gamma M_{n,1}^2 - (\gamma - 1)/2}$$

$$M_2 = \frac{M_{n,2}}{\sin(\beta - \theta)} \quad \text{with } \gamma = 1.4$$

$M_{n,1}$ $M_{n,2}$ up stream/down stream normal component of Mach numbers

Figure 4.5.2 Oblique Shock Relationship

4.6 Oblique Shock Crossing Interaction

Oblique crossing shock interactions in steady flows with conditions in the dual-solution domain were examined both numerically and experimentally[82]. Two and 3D simulations were compared with the measured Mach-stem heights determined from flow visualization. Hysteresis in the shock-reflection configuration was demonstrated for two-dimensional solutions with the same limits of the hysteresis loop observed by both participating research groups. The transition from regular to Mach reflection occurs very near the theoretical detachment condition, while for decreasing flow deflection angles the transition from Mach to regular reflection occurs before the flow deflection angle has decreased to the Neumann condition. Both the two and three-dimensional solutions show reasonable agreement between the numerical and experimental Mach-stem heights on the interaction centerline. Additionally, the 3D simulations closely predict the span-wise variation of the Mach-stem height observed in the experiments.

While numerical simulations of the oblique crossing shock interaction appear to predict the shock structure with reasonable accuracy, the question of which reflection configuration (Mach or regular) is correct for flows in the dual-solution domain remains an issue. Computations of these interactions accurately predict the resulting flow as long as the correct initial conditions (either Mach or regular reflection) are employed. Outstanding questions remain regarding which configuration should be expected in real flows within the dual solution domain and what initial conditions should be employed to ensure prediction of the same shock structure observed in real flows.

---

[81] ©2012 Mentor Graphics Corporation.

[82] S. Walker and J.D. Schmisseur, "*CFD Validation of Shock-Shock Interaction Flow Fields*", RTO-TR-AVT-007-V3.

4.6.1 Experimental Data

Experimental data for evaluation of the two-dimensional numerical simulations of crossing oblique shock interactions were collected by the Ivanov group in tunnel T313 at ITAM, Novosibirsk. A schematic of the experimental geometry is shown in . The wedges could be rotated symmetrically about the trailing edges. The freestream Mach number was 5 and the Reynolds number, based on the wedge compression surface length, w, was 2 million. The wedge aspect ratio was b/w = 3.75, while the distance between the trailing edge of the wedge and the plane of symmetry was g/w = 0.42. The theoretical compression and shock angles for the Neumann and detachment conditions are listed in **Table 4.6.1** where θ is the flow deflection angle and α is the resulting shock-wave angle. (See also **Figure 4.5.2**).

Mach Number	θ_D	α_D	θ_N	α_N
5	27.7	39.3	20.9	30.9

Table 4.6.1 Theoretical Detachment D and Neumann N Conditions Q the Flow Deflection Angle and a is the Shock-Wave Angle

4.6.2 Case Study 1 – 2D Oblique Shock Crossing Numerical Simulations

2D simulations for the geometry and flow conditions defined above were performed by the *Ivanov Group at the Institute for Theoretical and Applied Mechanics (ITAM), Novosibirsk, Russia* and *[Schmisseur and Gaitonde] at the United Stated Air Force Research Laboratory (AFRL)*. Both groups used upwind-biased schemes to compute the flows and a common procedure for incorporating changes in the wedge angle. The converged solution at a previous wedge angle was used as the initial condition for the next solution with an incremental change in wedge angle. The computations of the Ivanov Group were carried out with a multi-block shock capturing Euler TVD code using MUSCL reconstruction of the HLLE (Harten-Lax-van Leer-Einfeldt) solver. Time integration was accomplished with a third-order Runge-Kutta scheme. In the computations of [Schmisseur and Gaitonde], two different methods are considered for the discretization of the inviscid components of the governing equations, the Roe scheme and the van Leer scheme. The upwind-biased MUSCL method is used for reconstruction. The viscous fluxes in the governing equations are evaluated with

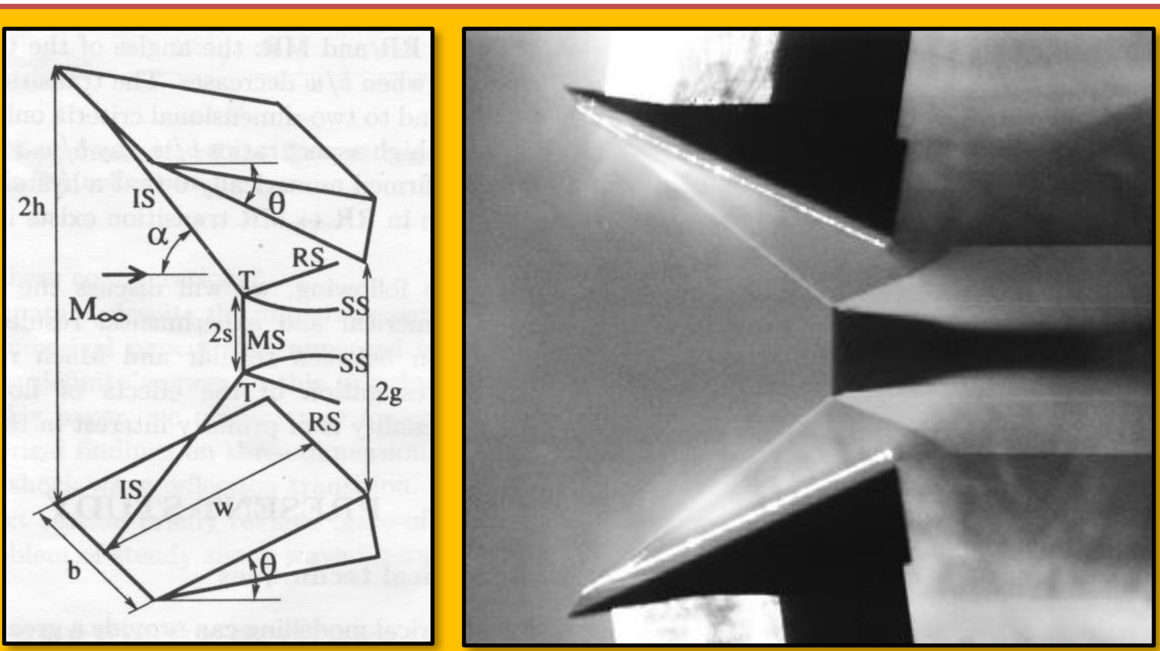

Figure 4.6.1 Schematic of the Experimental Configuration used by the Ivanov Group and Sample Laser Light-Sheet Visualization from the same M = 4, α =37 degrees, b/w =3.75, g/w =0.3

standard second-order central differences. The equations are integrated in time with an implicit approximately-factored scheme. Newton-like sub-iterations are incorporated to accelerate convergence.

4.6.2.1 Discussion

Hysteresis in the shock-reflection configuration for solutions in the dual-solution domain was verified by computing a sequence of solutions with first gradually increasing and then gradually decreasing compression wedge angles. For a few of the solutions where the wedge angle was gradually increased from an (Regular Reflection) RR solution, uniform flow initial conditions were employed. In terms of the final solution attained, for the demonstration of hysteresis, this approach was similar to that in which the initial condition was a converged RR solution at a lesser wedge angle. (When starting from a uniform flow initial condition the developing shock system propagates away from the fin surface and reflects regularly in the initial transient). See the discussion in [Ivanov, et al.][83]. All solutions for decreasing fin angles utilized the previous solution for the higher angle as an initial condition to obtain the new solution at the lower angle. The phenomenon of hysteresis is seen in **Figure 4.6.1** which shows the shock structure computed by [Schmisseur & Gaitonde] for two sets of computations with g/w = 0.42 and g/w = 0.34. In the dual-solution domain, when the initial condition was a regular reflection or uniform flow the RR configuration persisted until the theoretical value of the detachment condition. As may be seen in **Figure 4.6.2**, for the cases with g/w = 0.42 the transition from RR to (Mach Reflection) MR occurred for a flow deflection angle between 27 and 28

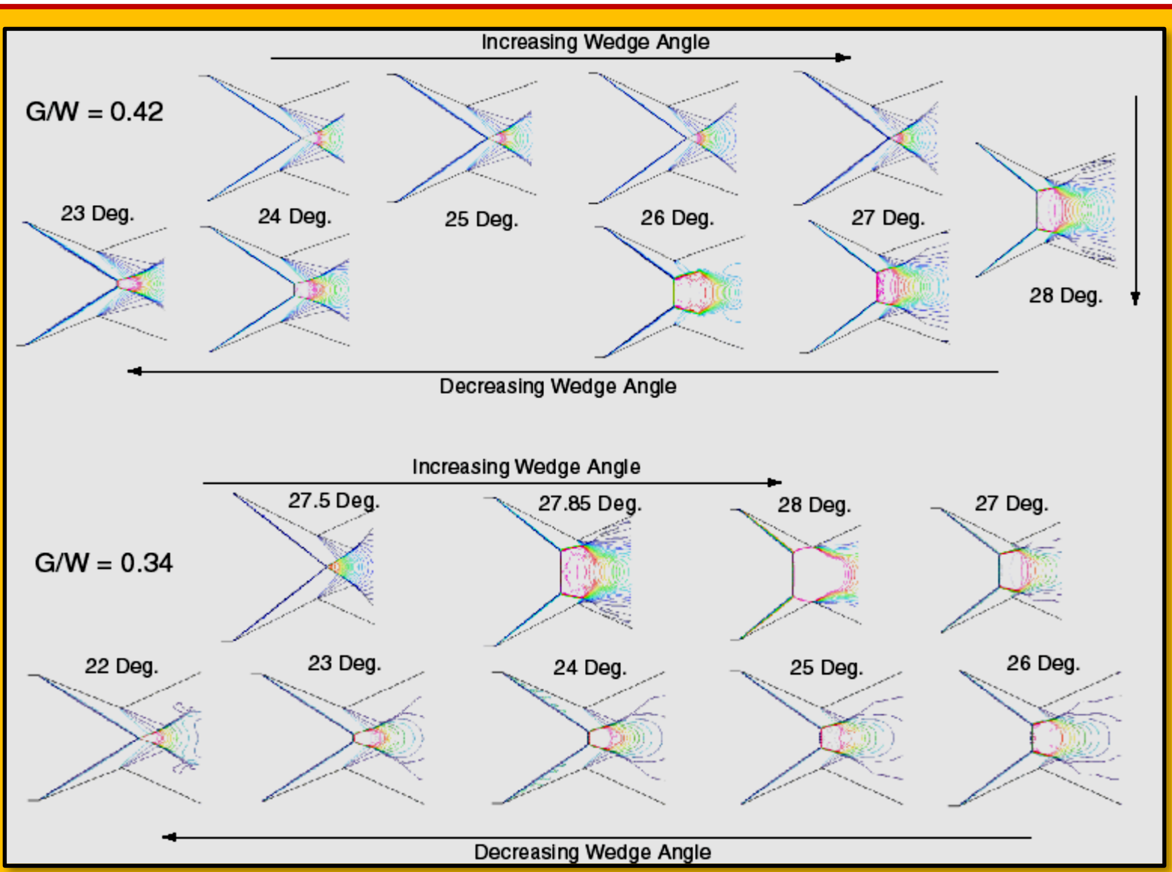

Figure 4.6.2 Isobars Demonstrating Hysteresis in 2D Simulations of (Schmisseur and Gaitonde)

---

[83] Ivanov M.S., Markelov G.N., Kudryavtsev A.N., and Gimelshein S.F., "*Numerical analysis of shock wave reflection transition in steady flows*", *AIAA Journal*, Vol. 36, No. 11, 1998.

degrees. For the cases with g/w = 0.34 smaller wedge angle increments were employed and the range for transition from RR to MR was narrowed to wedge angles between 27.5 and 27.85 degrees. This range of values is in close agreement with the theoretical value for detachment, 27.7 degrees. For solutions with MR initial conditions the MR pattern persists through much of the dual solution space, but transitions to an RR configuration before the Neumann condition is reached. For complete analysis and discussion, please consult the paper by [Walker and Schmisseur][84].

4.6.3 Case Study 2 - Unsteady 3D Numerical Study of Laminar Flow in Sudden Expansion Channel (Effect of Aspect Ratio)

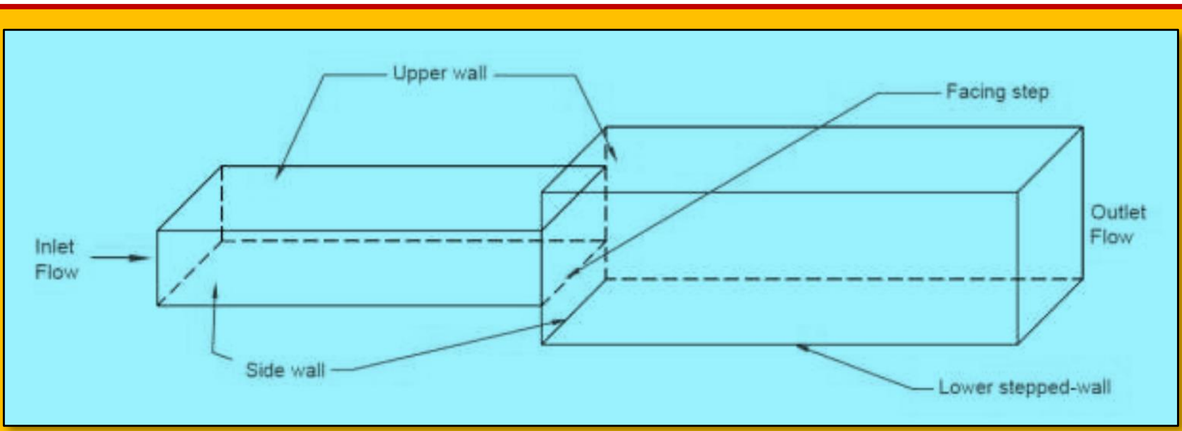

Figure 4.6.3 Schematic of Sudden Expansion with the Boundary Condition

Authors : *Ahmed N. Naeyyf[1] and Qais A. Rishack[2]*
Affiliations : *[1]Post Graduate Student, Engineering College Mechanical Engineering Department, Basra Iraq, [2]Lecture Engineering College Mechanical Engineering Department, Basra Iraq*
Citation : *(MuKyeom, et al., 2018)*
Bibliography : *Naeyyf, A. N., & Rishack, Q. A. (2019). Unsteady Three-Dimensional Numerical Study of Laminar Flow in Sudden Expansion Channel (Effect of Aspect Ratio). Journal of Mechanical Engineering and Technology (IJMET).*

As an example, 3D, Unsteady Laminar Flow through Sudden Expansion Channel has been studied numerically by (Naeyyf & Rishack, 2019). They used rectangular and symmetric sudden expansions (ER = H/h) with different aspect ratio (AR = Wch/h) as described in **Figure 4.6.3**. From the results founded the time steady state increase with the increasing of the aspect ratio and this effects become more clearly at the high of Reynolds numbers and the aspect ratio, so founded high effect of the time on the hydrodynamic parameters, behavior of the flow, recirculation region and the velocity profile, and this effect was clearly at high of Reynolds numbers. Also observed the increasing both the Reynolds numbers and

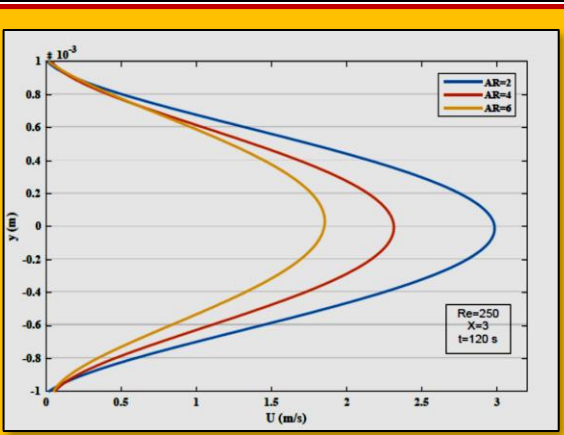

Figure 4.6.4 Velocity Profile with the High of Channel at Different Aspect Ratio

---

[84] S. Walker* and J.D. Schmisseur, "*CFD Validation of Shock-Shock Interaction Flow Fields*", RTO-TR-AVT-007-V3

aspect ratio leaded to increase the recirculation zone and stream wise velocity, the pressure drop increase with Reynolds number increase but reduce with increasing the aspect ratio, the results of the numerical study were compared with the other research and obtained acceptable convergence. **Figure 4.6.4** shows the effect of the aspect ratio on the distribution of the velocity profile with the z axis, the center of channel and at position x = 2, observed the value of velocity decrease with the increasing of aspect ratio this for 30% of the first width after this the velocity will increase with aspect ratio increasing, that's mean the flow will become two dimensional velocities due the large of aspect ratio.

4.6.4 Case Study 3 – Unsteady Phenomena in Supersonic Nozzle Flow Separation

---

Authors : *Dimitri Papamoschou and Andrew Johnson*
Affiliations : *University of California, Irvine, Irvine, CA 92697-3975*
Title of Paper : *Unsteady Phenomena in Supersonic Nozzle Flow Separation*
Adapted From : *AIAA 2006-3360*
Citation : *(Papamoschou & Johnson, 2006)*
Bibliography : *Papamoschou, D., & Johnson, A. (2006). Unsteady Phenomena in Supersonic Nozzle Flow Separation. AIAA Fluid Dynamics Conference & Exhilbit. San Francisco.*

4.6.4.1 Abstract

The work by (Papamoschou & Johnson, 2006) considers the instability of the jet plume from an over expanded, shock containing convergent-divergent nozzle and attempts to correlate this instability to internal shock-induced separation phenomena. Time resolved wall pressure measurements and Pitot measurements are used as primary diagnostics. For the conditions of this study flow separation is asymmetric resulting in a large separation zone on one wall and a small separation zone on the other wall. Correlations of wall pressures indicate a low-frequency, piston-like shock motion without any resonant tones. Correlations of Pitot pressure with wall pressures indicate strong coherence of shear-layer instability with the shock motion. The likely source of the plume instability is the interaction of unsteady waves generated past the main separation shock with the shear layer of the large separation region. In order to facilitate further, a nomenclature is given in **Table 4.6.2**.

A	Cross Sectional Area	Subscripts	
C	Coherence	a	Ambient
f	Frequency	e	Exit
h	Nozzle Height	o	Total
NPR	Nozzle Pressure Ratio = p_{res}/p_a	res	Reservoir
P	Pressure	rms	Root Mean Square
R	Normalized Correlation	t	Throat
S	Spectrum	1	lower wall transducer
U	Velocity	2	upper wall transducer
σ	Standard Deviation	3	dynamic Pitot probe

Table 4.6.2 Nomenclature for Unsteady Phenomena in Supersonic Nozzle Flow Separation

4.6.4.2 Background and Literature Survey

Supersonic flow separation in a convergent-divergent nozzle results in instability of the plume exiting the nozzle. This can be used to enhance mixing of the nozzle flow. Alternatively, the instability can be used as an excitation means to destabilize a flow adjacent to the nozzle. Potential applications include fuel injection, ejectors, and thermal signature reduction from jet engines. The instability phenomenon was initially observed in cannular jet experiments at the University of California, Irvine[85], where an arbitrary primary jet surrounded by a secondary jet from a convergent-divergent nozzle showed substantial improvements in mixing compared to the case where the secondary nozzle was simply convergent. **Figure 4.6.5** presents a visual example of such instability. This has been investigated in round and rectangular jets at NASA Glenn Research Center[86].

A typical result is that the length of the potential core is reduced by 50% and the velocity past the potential core decays at a much faster rate than for the equivalent jet without MESPI. For a nozzle with a given expansion ratio, the range of nozzle pressure ratios over which the instability occurs coincides with the range of nozzle pressure ratios for which a shock was located inside the nozzle. Therefore, the phenomenon of supersonic nozzle flow separation was deemed responsible for the observed instability. Numerous past studies have investigated supersonic nozzle flow separation [87-88], but their focus was on the internal flow phenomena and not so much on the unstable plume that emerges from the separation shock. A related effort has focused on the phenomenon of transonic resonance in convergent-divergent nozzles[89]. Transonic resonance appears to occur in relatively small nozzles where the boundary layer before the shock is laminar. For large nozzles with a turbulent boundary layer, such as those investigated here, there is no evidence of ringing phenomena.

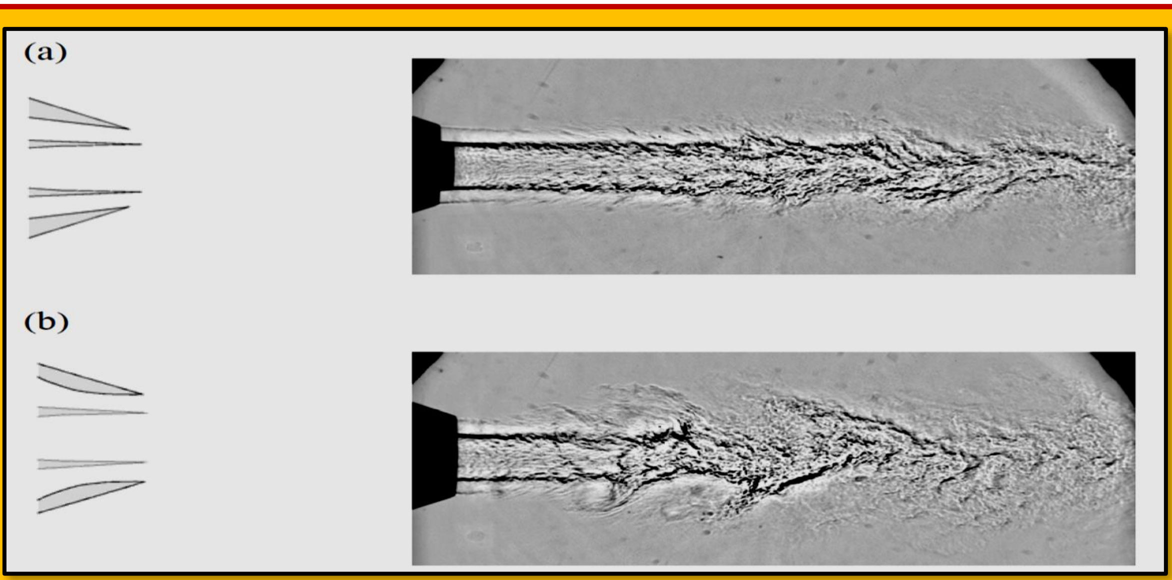

Figure 4.6.5 Primary Jet Flow at Mach 0.9 Surrounded by an annular secondary flow at Nozzle Pressure Ratio NPR =1.7 (a) Secondary Nozzle is Convergent; (b) Secondary Nozzle is Convergent-Divergent – (Courtesy of [36])

To better understand the phenomenon of nozzle flow separation and its connection to flow instability, a fundamental experimental effort was started at UCI using a specially designed facility, to be described later in this report. shows a picture of nozzle flow separation obtained in this facility [90]. As is evident from the photograph, the phenomenon is very complex and much more intricate than

---

[85] Papamoschou, D., "*Mixing Enhancement Using Axial Flow,*" AIAA Paper 2000-0093, Jan 2000.

[86] Zaman, K.B.M.Q, and Papamoschou, D., "*Study of Mixing Enhancement Observed with a Co-Annular Nozzle Configuration,*" AIAA Paper 2000-0094, Jan. 2000.

[87] Morrisette, E.L., and Goldberg, T.J., "*Turbulent Flow Separation Criteria for Over expanded Supersonic Nozzles*," NASA TP 1207, Aug. 1978.

[88] Romine, G.L., "*Nozzle Flow Separation,*" AIAA Journal, Vol. 36, No.9, 1998, pp. 1618-1625.

[89] Zaman, K.B.M.Q., Dahl, M.D., Bencic, T.J., and Loh, C.Y., "Investigation of a Transonic Resonance with Convergent- Divergent Nozzles," *Journal of Fluid Mechanics*, Vol. 263, 2002, pp. 313-343.

[90] Papamoschou, D., Zill, A., "*Fundamental Investigation of Supersonic Nozzle Flow Separation*," AIAA Paper 2004-1111.

one would expect from quasi-one dimensional theory. The illustration of **Figure 4.6.6 (Top)** highlights some key features of the flow, but it is by no means complete. The shock in the viscous case takes on a bifurcated structure consisting of an incident shock and a reflected shock merging into a Mach stem. This is commonly referred to as a lambda foot, and the point at which the three components meet is called the triple point. The Mach stem is essentially a normal shock producing subsonic outflow. For the range of conditions of interest here, the incident and reflected shocks are of the "weak" type resulting in supersonic outflow past both. The adverse pressure gradient of the incident shock causes the boundary layer to separate and detach from the wall as a shear layer that bounds the separation (recirculation) region.

Emerging from the triple point is a slipstream forming a sonic throat that acts to reaccelerate the subsonic region. The reflected portion of the main shock structure will then emerge from the separation shear layer as an expansion fan that is then transmitted through the slipstream toward the other separation shear layer where it is reflected again into compression waves, this pattern repeating with downstream distance. Therefore the separation "jet" that emerges from the shock contains a series of alternating compression and expansion waves. In nozzles with straight or convex walls subjected to nozzle pressure ratios above about 1.4, separation is asymmetric wherein one lambda foot is larger than the other (see for example **Figure 4.6.6 (Bottom)**). The asymmetry does not flip during an experiment but may change sides from one experiment to the next. A recent computational effort by [Xiao et al.][91] also predicted asymmetric separation. This asymmetry has been recognized as a key factor for mixing enhancement. [Papamoschou and Zill][92] discovered large eddies forming in the shear layer of the large separation region, sometimes occupying over half the test section height. It was suspected that these eddies were due to the unsteady nature of the main shock. The objective of this paper is to investigate possible connections between the oscillation of the main shock and the occurrence of large-scale turbulent fluctuations downstream of the shock.

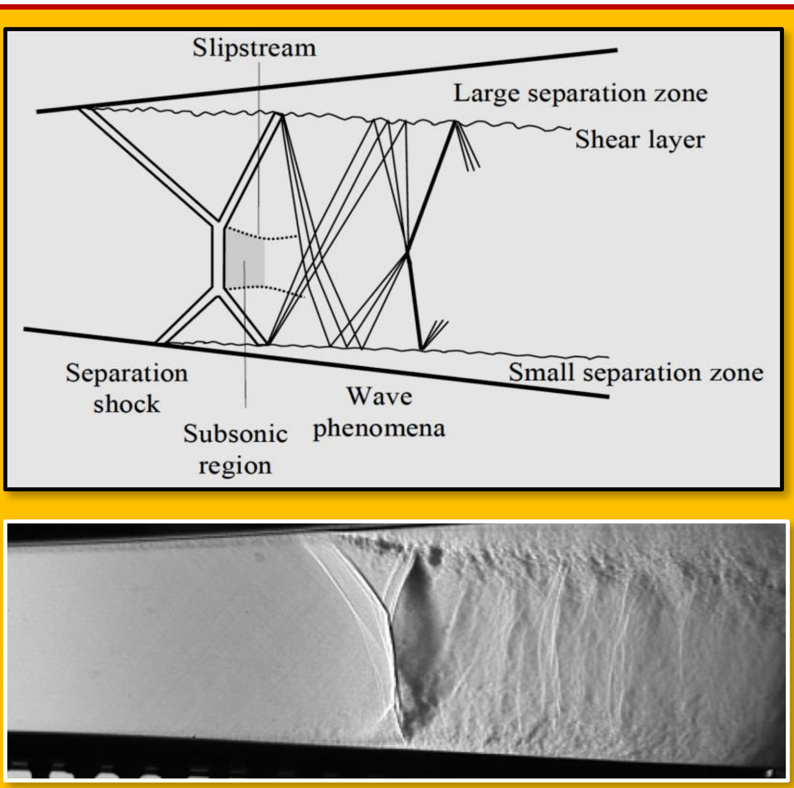

Figure 4.6.6 Schematic of Supersonic Nozzle Flow Separation (Top), vs. *schlieren* Image (Bottom) , (Courtesy of Papamoschou, D., Zill) – (Courtesy of [36])

4.6.4.3 Experimental Setup for Flow Facility

The experiments used a facility designed specifically for studying flow separation in nozzles of

---

[91] Xiao, Q., Tsai, H.M., and Papamoschou, D., "*Numerical Investigation of Supersonic Nozzle Flow Separation*," AIAA Paper 2005-4640, June 2005.

[92] Papamoschou, D., Zill, A., "*Fundamental Investigation of Supersonic Nozzle Flow Separation*," AIAA 2004.

various shapes as described by [Papamoschou and Zill][93]. The nozzle apparatus consists of two flexible plates that can be shaped using two sets of actuators to form the upper and lower walls. One set of actuators controls the transverse force applied to the plates and the other controls the moment applied, allowing variations in nozzle area ratio, nozzle contour and exit angle. The nominal test section dimensions are 22.9 mm in height, 63.5 mm in width, and 117 mm in length from throat to exit. The sidewalls of the nozzle incorporate large optical windows for visualization of the entire internal flow, from the subsonic converging section to the nozzle exit. The apparatus is connected to a system of pressure-regulated air capable of nozzle pressure ratios as high as 3.5. The nozzle pressure ratio (NPR) ranged from 1.2 to 1.8 resulting in ideally-expanded velocities U_e ranging from 170 m/s to 320 m/s. The Reynolds number prior to the shock, based on axial distance from the throat, was typically 2.5×10^6. This indicates a fully-turbulent boundary layer.

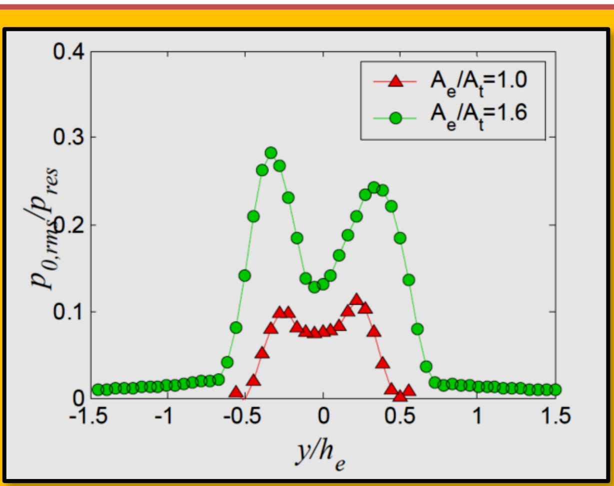

Figure 4.6.7 RMS Total Pressure Profile of Jet Plume at $x/h_e = 0.5$ for Straight Nozzle (A_e/A_t=1) and Convergent-Divergent Nozzle (A_e/A_t=1.6) – (Courtesy of [36])

4.6.4.4 Results of Plume Pitot Pressure

A parametric investigation of the jet plume versus nozzle shape and pressure ratio has shown significant increase in turbulence fluctuations levels as the exit-to-throat area ratio increases. The fluctuations are quantified in terms of the pressure p_3 measured by the Dynamic Pitot Probe (DPP), which for the experiments discussed here equals the local total pressure p_0. **Figure 4.6.7** shows the distribution of p_3,rms a short distance from the nozzle exit and the threefold increase in rms fluctuation levels as the nozzle area ratio changes from A_e/A_t =1 (straight) to A_e/A_t =1.6 (converging-diverging).

4.6.4.5 Wall Pressure Statistics

Before attempting correlations of the shock motion with plume fluctuations, it is helpful to understand the behavior of the oscillating shock as well as the nature of the unsteady flow in its vicinity. To measure the fluctuations in the entire neighborhood of the shock, the nozzle was held at a fixed area ratio of A_e/A_t =1.6 and the nozzle pressure ratio was gradually increased pushing the shock from upstream to downstream of the wall transducers.

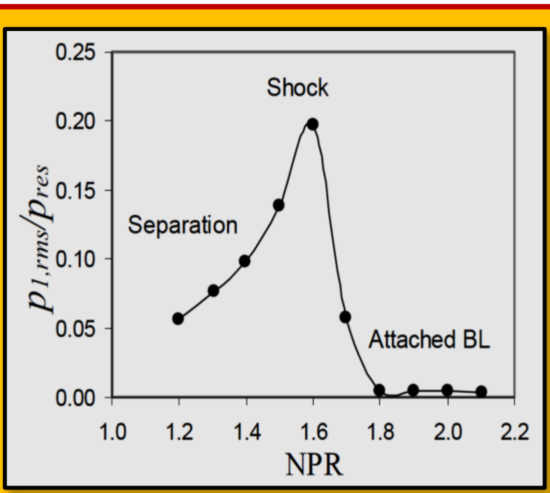

Figure 4.6.8 RMS Wall Static Pressure Fluctuation vs. Nozzle Pressure Ratio Presenting Different Flow Regimes – Courtesy of [36]

Figure 4.6.8 shows the variation of p_1, rms with nozzle pressure ratio. The resulting curve shows the relative magnitude of the wall pressure fluctuations in the various regions around the shock. At higher NPR, corresponding to when the wall transducers are measuring the attached boundary layer upstream of the shock, the fluctuations are comparatively small in

---

[93] See Previous.

magnitude. At the nozzle pressure ratio where the shock begins to influence the pressure transducer, there is a steep increase in p_1, rms as a consequence of the large pressure jump across the shock. At lower nozzle pressure ratios, where the transducers are located in the separated region, the fluctuations are larger than in the attached boundary layer but significantly smaller than when the shock is over the transducer. The spectrum of the fluctuations in the attached boundary layer is significantly lower in intensity than the spectra in the two other regimes. It is reasonable to assume that the attached boundary layer plays little or no role on the shock motion. The spectral levels in the separated region are substantial and match those of the shock motion for $f_{he}/U_e > 0.3$. Therefore, the fluctuations in the separation zone are likely to have an effect on the shock motion.

4.6.4.6 Correlations Between Wall Pressure Ports

The cross correlation and coherence of the two wall transducers illuminate some important characteristics of the unsteady phenomena in supersonic nozzle flow separation. **Figure 4.6.9** show the cross correlation and coherence, respectively, of the two wall transducers situated upstream, downstream and at the location of the shock. As one might expect, in the attached boundary layer there is no correlation between the upper and lower wall since the fluctuations are a result of random turbulent eddies. There is a significant correlation when measuring the shock itself, implying that the shock oscillates in a "piston-like" manner. The coherence plot confirms the relatively low frequency of the shock motion.

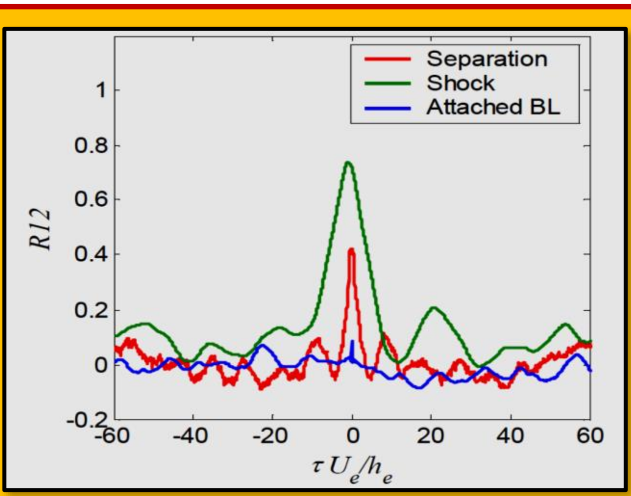

Figure 4.6.9 Cross Correlations of Upper and Lower Wall Transducers for Various Flow Regimes – Courtesy of [36]

4.6.4.7 Correlations Between Wall Pressure Ports and Dynamic Pitot Probe

Several experiments were conducted at area ratio $A_e/A_t = 1.6$, taking simultaneous measurements of the DPP and the wall mounted transducers. Initially the DPP was held at fixed positions in both the large and small separation zones and the nozzle pressure ratio was varied. Later the NPR was fixed at 1.6 and the DPP was translated along certain paths inside and outside the nozzle. For studying the effect of NPR on the coherence between wall pressures and DPP, we consider the case of the DPP being situated near the upper wall where the large separation zone occurs for NPR > 1.4. **Figure 4.6.11** plots the nces for NPR = 1.2 and 1.6. For NPR = 1.2, separation occurs fairly symmetrically and the wall probes are in the separated region. There is no significant coherence between the DPP and either of the wall probes. At NPR =1.6, the shock sits over the wall probes and separation is asymmetric. We observe significant coherence between the DPP and the wall probes, the coherence between the DPP and lower wall (small separation zone) exceeding the coherence between the DPP and upper wall (large separation zone) at low frequencies. The coherences drop when the NPR increases further, pushing the shock downstream and locating the wall probes in the attached region. This experiment suggests that the best correlations between wall probes and DPP occur when the shock sits in the vicinity of the wall probes. It also suggests that asymmetric separation may amplify those correlations, although this is still speculative. also plots the coherence between the two wall probes, which remains large as the shock moves upstream of the probes. Having established that the best correlations between wall probes and DPP occur for NPR = 1.6 (shock sits over wall ports), the next step was to conduct a search for the locations of DPP where the correlations were maximized.

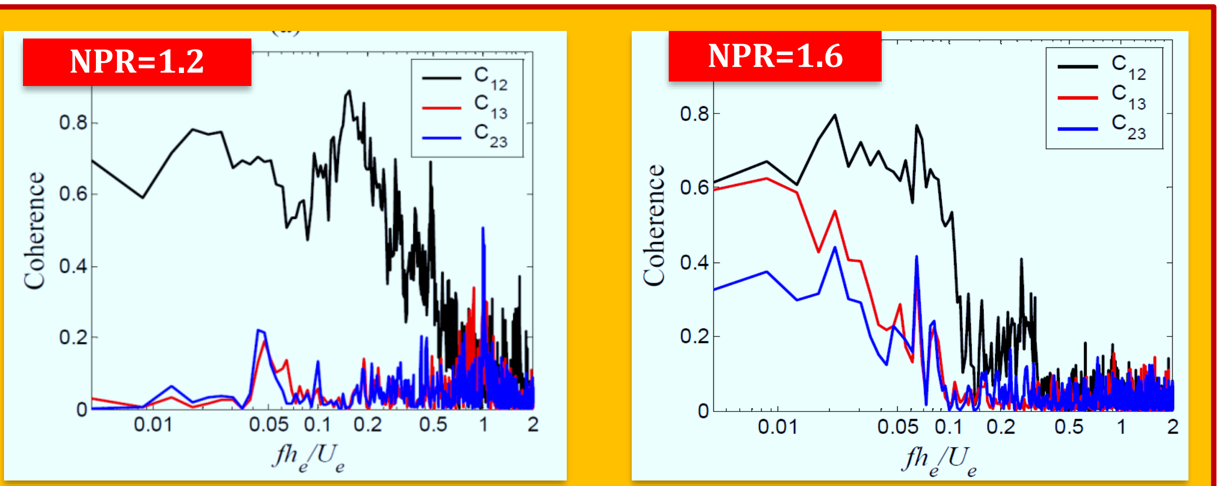

Figure 4.6.11 Coherence Between Upper and Lower Walls (C_{12}), DPP and Lower Wall (C_{13}), and DPP and Upper Wall (C_{23}) – Courtesy of [36]

The search pattern is shown in **Figure 4.6.10**. For a rapid assessment of the trends of the correlations versus DPP position, see[94]. Close to the shock, the correlations peak when the DPP is in the large separation zone (upper wall). There is consistently better correlation of DPP with the lower wall probe that with the upper wall probe. As we exit the nozzle, the DPP remains significantly correlated with the wall probes, and this correlation becomes rather insensitive with the transverse position of the DPP. This is probably because the instability excites the entire plume so it does not matter where the DPP sits. Interestingly, the better correlation of the DPP with the lower wall probe persists even as the DPP moves outside the nozzle. This suggests that instability eddies are created through an interaction between the expansion reflected from the smaller lambda foot and the shear layer of the larger separation. To provide further details, please consult the work by [Papamoschou & Johnson][95].

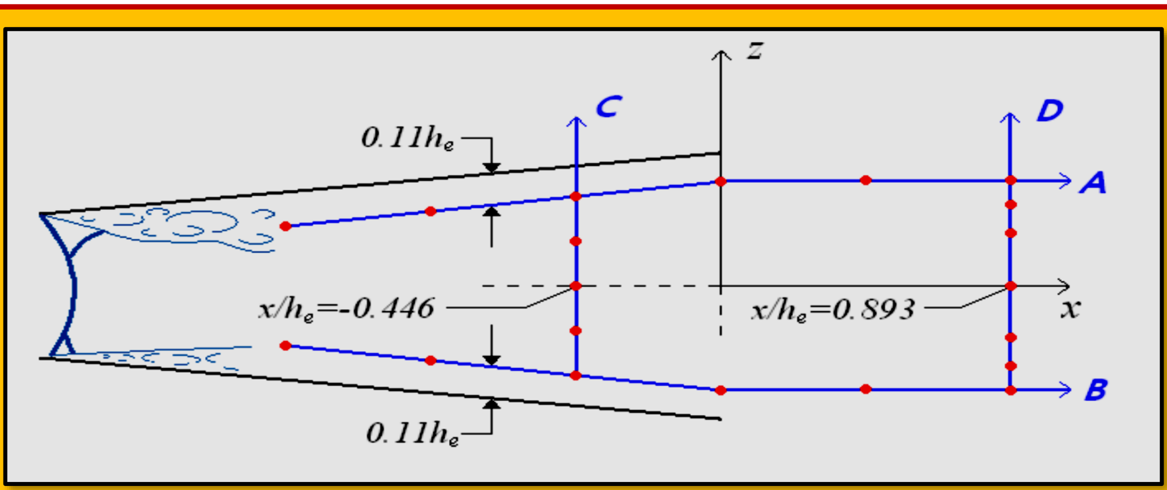

Figure 4.6.10 Translation Paths of Dynamic Pitot Probe. Red Points Indicate Measurement Locations – Courtesy of [36]

---

[94] Dimitri Papamoschou and Andrew Johnson, "*Unsteady Phenomena in Supersonic Nozzle Flow Separation*", AIAA 2006-3360, 36th AIAA Fluid Dynamics Conference and Exhibit, 5 - 8 June 2006, San Francisco, California.

[95] Dimitri Papamoschou and Andrew Johnson, "*Unsteady Phenomena in Supersonic Nozzle Flow Separation*", AIAA 2006-3360, 36th AIAA Fluid Dynamics Conference and Exhibit, 5 - 8 June 2006, San Francisco, California.

4.6.4.8 Concluding Remarks

An investigation has been conducted into the source of plume instability from over expanded convergent divergent nozzles. The effect of internal shock phenomena on the plume unsteadiness was a particular focus. Time resolved measurements of wall static pressures and total pressure in the plume were correlated. A summary of the key findings is as follows:

- For nozzle pressure ratios that give rise to shock formation inside the nozzle, increasing the nozzle area ratio from 1 (straight nozzle) to 1.6 (convergent-divergent nozzle) results in a three-fold increase in the rms total pressure fluctuations near the nozzle exit. Spectra indicate that most of the instability energy is contained at low to moderate frequencies.
- For the conditions of this study, the separation shock is asymmetric. This gives rise to a large separation region on one wall and a small separation region on the other wall.
- The coherence and cross correlation of pressures measured on the upper and lower nozzle walls indicate that the shock oscillates in a piston-like manner with no noticeable rotational motion. The oscillation is a low-frequency phenomenon without any resonant tones.
- There are substantial correlations between the wall pressures caused by the shock motion and the total pressure inside the large separation zone. The frequency content of the total pressure fluctuation is similar to that of the shock motion.
- There is consistently better coherence between the total pressure in the large separation zone and the pressure on the wall opposite that zone. This suggests that the instability mechanism is due to an interaction between the expansion fan reflected from the smaller lambda foot with the shear layer of the larger separation zone.

4.7 Effect of Heating Loads on Shock-Shock Interaction in Hypersonic Flows

The heating rates generated by shock-shock interactions can result in some of the most severe heating loads imposed on the thermal protection systems of hypersonic lifting bodies and air-breathing propulsion systems, as investigated by [Walker and Schmisseur][96]. In regions near a leading edge heating levels up to 30 times those encountered in an undisturbed stagnation flow can be generated. In these regions the strong gradients, unsteadiness and transitional nature of the flow combine to make accurate prediction of the flow field a challenging endeavor. The severe heating loads developed in a shock-shock interaction were first studied in detail following the X-15 scramjet program where shock-shock heating resulted in a structural failure in the pylon supporting the scramjet engine[97]. A series of studies were conducted in the late 1960s where the main focus was the interaction between a shock wave and vertical fin. The studies by [Edney][98] of shock interactions on spherical configurations, coupled with his analysis of various interaction geometries that can be developed over cylinders and struts, provided the basic groundwork for the semi-empirical prediction of these flows. Another similar study conducted by [Chettle et al.][99] where hypersonic research engine model was attached to the underside of the aircraft, and the oblique shock generated by the wing of the X-15 interacted with the bow shock of the engine support pylon[100]. This resulted in catastrophic damage to the pylon and incineration of part of the protective skin. This damage was due to an increase in the peak heat transfer and pressure at the surface of the pylon, as a simple demonstration of an overall schlieren image in **Figure 4.7.1**.

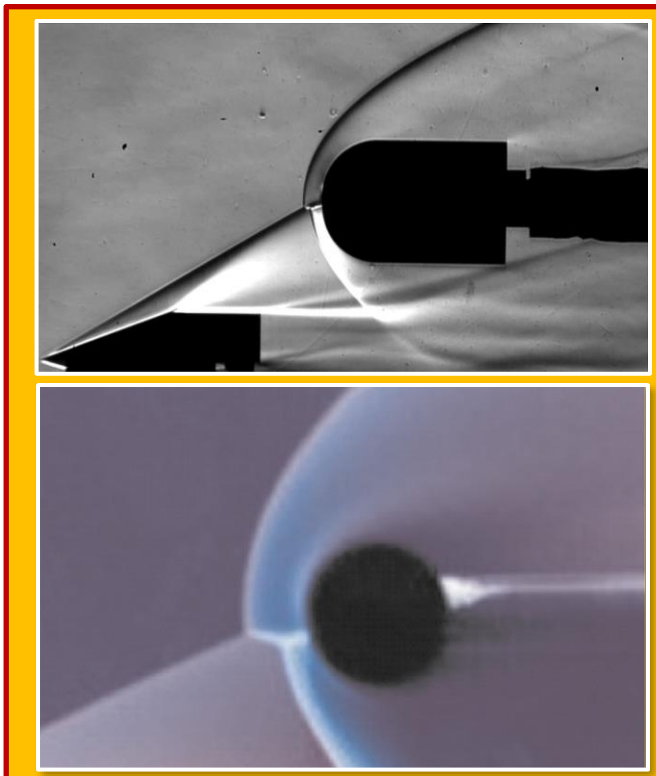

Figure 4.7.1 Schematic of Edney Type IV Shock-Shock Interaction

Understanding and controlling these interactions is a key part of moving forward in creating and maintaining a viable hypersonic program. A review of these earlier studies together with measurements of heat transfer and pressure distribution in regions of shock-shock interaction over cylindrical leading edges in laminar, transitional and turbulent interaction regions were presented by [Holden et al.][101]. Historically, the empirical

---

[96] See Previous.

[97] Watts J.D., "*Flight experience with shock impingement and interference heating on the X-15-2 research airplane*", NASA TM X-1669, 1968.

[98] B. Edney, Anomalous heat transfer and pressure distributions on blunt bodies at hypersonic speeds in the presence of an impinging shock. Rep. 115, Flygtekniska Forsoksanstalten (The Aeronautical Research Institute of Sweden), Stockholm, 1968.

[99] A. Chettle1, E. Erdem1, and K. Kontis, "*Edney IV Interaction Studies at Mach 5*", Conference Paper · July 2013.

[100] J. Watts, "*Flight experience with shock impingement and interference heating on the X-15-2 research airplane*", NASA Technical Reports, NASA TM (X-1669), (1968).

[101] Holden M.S., Moselle J.R., Lee J., Weiting A.R., and Glass C., "*Studies of aerothermal loads generated in regions of shock-shock interaction in hypersonic flow*", NAS1-17721, 1991.

modeling of these flows has been based on defining a small stagnation region downstream of a jet like flow such as that observed in the Type IV interaction.

However, experiments have revealed that it is extremely difficult to distinguish between the heating loads generated by the various flow field elements such as the strong viscous effects or transitional nature of the shear layer[102]. It has been observed that the heating rates derived from an Edney IV shock-shock interaction vary widely depending on whether the flow is laminar, transitional or turbulent as well as whether the gas is considered perfect or real. In laminar flow, both Navie.r-Stokes and DSMC predictions have compared well with experiments if well-defined grid resolution studies are performed. When the shear layers or the boundary layers in the reattachment region become transitional a significant increase in the heating load results. Edney also demonstrated that the jet like model proposed for the Type IV interaction was highly sensitive to the specific heat ratio and the freestream Mach number through the sensitivity of the compression processes to these parameters. Specifically, he concluded that real gas effects could lower specific heat ratio, and result in significant increases in heating in these regions. Experimental studies of this have yielded conflicting results and computational techniques, both Navier-Stokes and DSMC, have shown 50% increases in peak heating rates over ideal gas heating predictions[103].

In summary, the Edney IV shock-shock interaction flow field is a complex shock-shock interaction relevant to high-speed airframe-propulsion system. Given the geometric simplicity of the shock generators and the numerical challenges associated with accurate simulation of the resulting flow field, it is an excellent test case for CFD validation studies for propelled vehicles in hypersonic flight.

4.7.1 Case Study – University of Buffalo Research Center (CUBRC) Test Case

[Holden][104] at the *Calspan-University of Buffalo Research Center (CUBRC)* developed the second ***Edney IV shock-shock interaction*** test case. Flow conditions, experimental setup, and detailed measurements are reported in[105]. CUBRC conducted an extensive series of studies over a range of Mach numbers from 10 to 16 to define the aerothermal loads generated in regions of shock-shock interaction from the rarefied to the fully continuum turbulent flow regimes. Detailed heat transfer and pressure measurements were made in the 48-inch, 96-inch and LENS shock tunnels. The results of these studies were analyzed to provide guidance to predict the heating enhancement factors in laminar, transitional, and turbulent flows. The experimental data presented in this section are for fully laminar flows. The CUBRC model configuration is shown in **Figure 4.7.2**. The regions

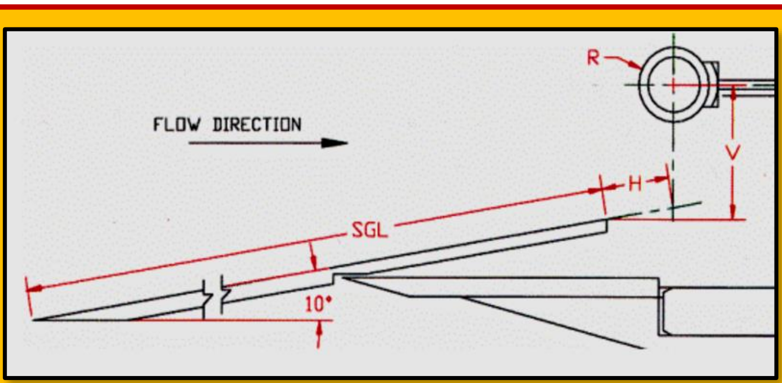

Figure 4.7.2 Schematic of the CUBRC Edney IV Interaction Generator (Courtesy of Holden)

---

[102] S. Walker and J.D. Schmisseur, "*CFD Validation of Shock-Shock Interaction Flow Fields*", RTO-TR-AVT-007-V3.

[103] Carlsen A.B. and Wilmoth R.G., "*Monte Carlo simulation of a near-continuum shock-shock interaction problem", *AIAA 27th Thermo-physics Conference, Nashville, TN, 1992.

[104] Holden M.S.," *A review of the aerothermal characteristics of laminar, transitional, and turbulent shock-shock interaction regions in hypersonic flows*", AIAA 98-0899, 1998.

[105] Holden M.S., "*Database of aerothermal measurements in hypersonic flow for CFD validation*", CUBDAT Version 2.2 CDROM, Calspan-University of Buffalo Research Center, 1999.

of shock-shock interaction studied were generated over a series of cylindrical leading edge configurations with nose radii of 0.351, 0.953, and 3.81 cm. Each of these leading edges was densely instrumented with heat transfer instrumentation placed to have a circumferential resolution less than 1 degree. The thin-film instrumentation was deposited on a low conductivity surface to minimize measurement errors associated with lateral conduction in the large heat transfer gradients generated in the region of peak heating. The high-frequency response of the thin-film instrumentation was also a key factor in accurately determining the heating distribution for shock-shock interactions, which exhibited intrinsic flow unsteadiness. The flow conditions for this study produced perfect gas, planar flow field, laminar flow shock-shock interactions. For the exact flow conditions of test runs 38, 43, 44, and 105, (please see **Table 4.7.1**). The experimental data includes surface temperature, heat transfer, pressure distributions and ***Schlieren*** photographs.

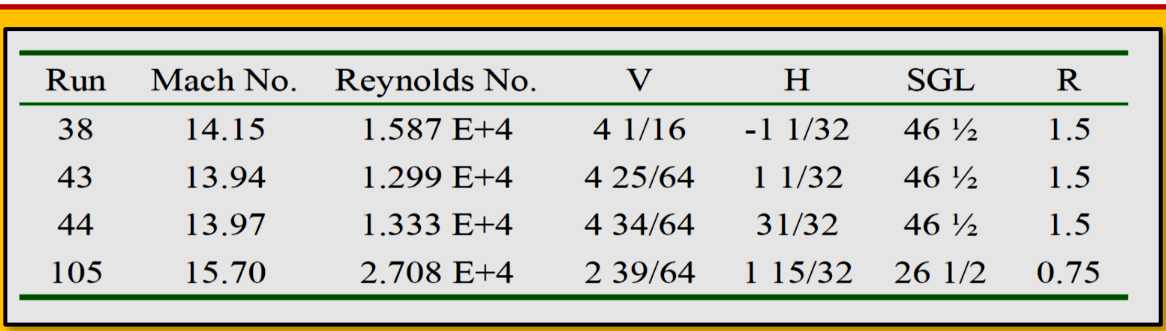

Run	Mach No.	Reynolds No.	V	H	SGL	R
38	14.15	1.587 E+4	4 1/16	-1 1/32	46 ½	1.5
43	13.94	1.299 E+4	4 25/64	1 1/32	46 ½	1.5
44	13.97	1.333 E+4	4 34/64	31/32	46 ½	1.5
105	15.70	2.708 E+4	2 39/64	1 15/32	26 1/2	0.75

Table 4.7.1 CUBRC Test Conditions (V, H, SGL, R in inches)

4.7.1.1 Computational Contributions

The three contributors for this test case were Dr Domenic D'Ambrosio, Politecnico di Torino, Torino, Italy, Dr Graham Candler, University of Minnesota, Minneapolis, MN, and Dr. Iain Boyd, University of Michigan, Ann Arbor, MI. D'Ambrosio's numerical technique was the same as that described above for the *ONERA* test case. Results were obtained using a coarse (75 X 150) and a fine (250 X 300) grid. Candler's computations were performed with a CFD code that uses second-order accurate modified Steger-Warming flux vector splitting and an implicit parallel time integration method. The grid consisted of 382 points in the circumferential direction, and 256 points normal to the cylinder surface. The grid was exponentially stretched from the surface, and care was taken to have sufficient near-wall resolution to capture the large flow gradients at the surface. Because of the relatively low enthalpy conditions of the experiments, chemical reactions were not considered, however ibrational relaxation of the gas was allowed. A vibrational equilibrium free-stream was assumed. Standard transport property models were used for the gas as in [Candler and Mac Cormack]. Candler computed post-shock conditions using the experimental free-stream conditions and the 10 degree turning angle of the shock generator. The post-shock conditions were then used as inflow conditions everywhere below a specified distance from the cylinder centerline. This distance was adjusted until the maxima in the heat transfer rate and surface pressure were located at the same point on the cylinder as in the experiments. This approach was required since very slight differences in the location of the shock generator relative to the cylinder result in large differences in the structure of the shock interaction.

The *DSMC* solutions provided by Boyd were performed using the *MONACO* code: a general, object-oriented, cell-based, parallelized implementation of the *DSMC* method developed by Dietrich and

[Boyd][106]. *MONACO* employs the Variable Soft Sphere (VSS) collision model of [Koura et al][107], a variable rotational energy exchange probability model of [Boyd][108] and the variable vibrational energy exchange probability model of [Vijayakumar et al.][109] . The flow conditions here do not involve chemical reactions. Simulations of particle/wall interaction employ accommodation and momentum reflection coefficients of 0.85. The present simulations employ grids of 512 by 512 cells (Run 105) and 1024 by 1024 cells (Run 43), which give maximum sizes of 2 local mean free paths. The time step employed in both simulations is $(10)^{-9}$ sec and this is less than the local mean time between collisions everywhere. The total numbers of particles employed is 2 million (Run 105) and 8 million (Run 43). This allows the minimum number of particles per cell to be everywhere greater than 4.

4.7.1.2 Computational Results

A comparison of the numerical results with the measured CUBRC Run 38 data of Holden is shown in **Figure 4.7.3.** Both surface pressure and surface non-dimensional heat transfer are plotted in angular coordinates around the cylinder. Inspection reveals that both the calculated pressure coefficient and heat transfer ratio are severely over-predicted. In a similar manner as described above, D'Ambrosio corrected this over-prediction by averaging his CFD results over the experimental measurement resolution. However, for the CUBRC experiments, this resolution was undetermined at the time of the computations. If similar averaging schemes were utilized, improved agreement between simulation and experiment resulting from the CFD averaging process would suggest that the experiment is highly unsteady and that the data are actually average quantities of an unsteady, oscillating impinging jet.

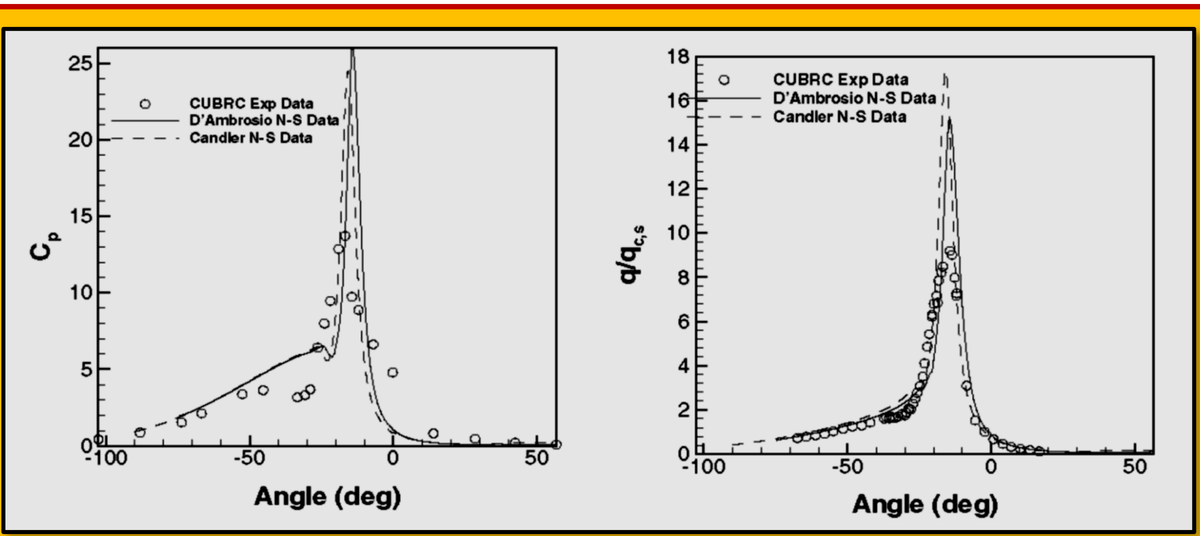

Figure 4.7.3 Experimental and Numerical Results for the Conditions of CUBRC Run #38

The sensitivity of the solutions to the shock impingement location may have an important effect on the interpretation of the experimental data. Slight variations in the free-stream conditions result in changes in the shock impingement location, which substantially change the surface quantities. Thus,

---

[106] Dietrich, S. and Boyd, I. D., "*Scalar optimized parallel implementation of the direct simulation Monte Carlo method*", *Journal of Computational Physics*, Vol. 126, pp. 328-342, 1996.

[107] Koura, K. and Matsumoto, H., "*Variable soft sphere molecular model for air species*", Physics of Fluids A, Vol. 4, pp. 1083-1085, 1992.

[108] Boyd, I. D., "*Analysis of rotational non-equilibrium in standing shock waves of Nitrogen*", AIAA Journal, Vol. 28, pp. 1997-1999, 1990.

[109] Vijayakumar, P., Sun, Q. and Boyd, I. D., "*Detailed models of vibrational-translational energy exchange for the direct simulation Monte Carlo method*", Physics of Fluids, Vol. 11, pp. 2117-2126, 1999.

it is possible that the experimental results represent some averaging of the shock impingement location. This would tend to broaden the peaks and reduce their magnitudes, as seen in the comparison between the computations and experiments. Another reason may be that because the cylinders are small in diameter, and the pressure instrumentation is limited, there are some cases where the actual peak pressure falls between two transducers and is not fully recorded. This may be the case, especially with Run 43, where there is almost no experimental peak pressure coefficient. (In Run 105, the cylinder was too small to incorporate any pressure sensors, so there is no experimental pressure data available for this case). The off-peak surface pressure coefficient beneath the interaction location is not well predicted by either Navier-Stokes or DSMC for Run 43, while the heat transfer ratio comparisons are much better. The good off peak heat transfer comparisons may be a function of the better resolution of heat transfer instrumentation.

Also, both Navier-Stokes and DSMC methods required several milliseconds to reach steady-state solutions and for some shock impingement locations, the solutions never did stabilize. Run 43 is a particularly strong interaction, and the supersonic jet impinging on the surface is likely to be unstable. Of course, the capacity for the present CFD simulations to accurately capture this unsteadiness is suspect. The translational temperature contours for both Navier-Stokes and DSMC are shown in **Figure 4.7.4 (a, b)**. Both methods predict similar flow fields. Overall, considering both peak and off-peak regions, Run 44 represents the best that DSMC and Navier-Stokes methods can offer. However, it is still apparent that there are many inconsistencies between the computational methods and the experimental data that need to be resolved.

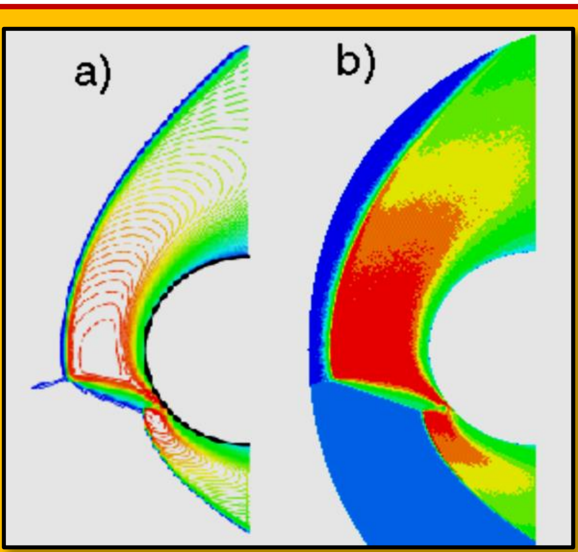

Figure 4.7.4 Contours of Constant Translational Temperature for; a) Navier-Stokes and b) DSMC Solutions for CUBRC Run #44

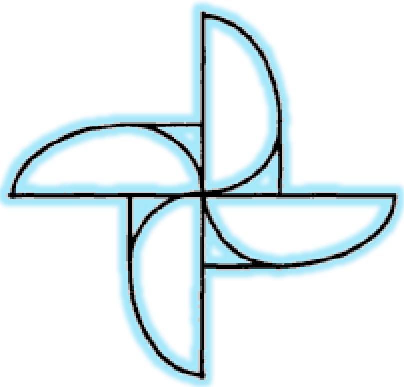

5 Airfoil Aerodynamics

5.1 Preliminaries

Aerodynamics, is the study of motion of air, particularly as interaction with a solid object, such as an airplane wing. It is a sub-field of fluid dynamics and gas dynamics, and many aspects of aerodynamics theory are common to these fields. The term aerodynamics is often used synonymously with ***gas dynamics***, the difference being that "gas dynamics" applies to the study of the motion of all gases, and is not limited to air. The formal study of aerodynamics began in the modern sense in the 18th century, although observations of fundamental concepts such as aerodynamic drag were recorded much earlier. Most of the early efforts in aerodynamics were directed toward achieving heavier-than-air flight, which was first demonstrated by [Otto Lilienthal][110] in 1891. Since then, the use of aerodynamics through mathematical analysis, empirical approximations, wind tunnel experimentation, and computer simulations has formed a rational basis for the development of heavier-than-air flight and a number of other technologies. Recent work in aerodynamics has focused on issues related to compressible flow, turbulence, and boundary layers and has become increasingly computational in nature[111].

Figure 5.1.1 indicates a hierarchy of models at different levels of simplification which have proved useful in practice. Inviscid calculations with boundary layer corrections can provide quite accurate predictions of lift and drag when the flow remains attached. The current main CFD tool of the Boeing Commercial Airplane Company is *TRANAIR*, which uses the transonic potential flow equation to

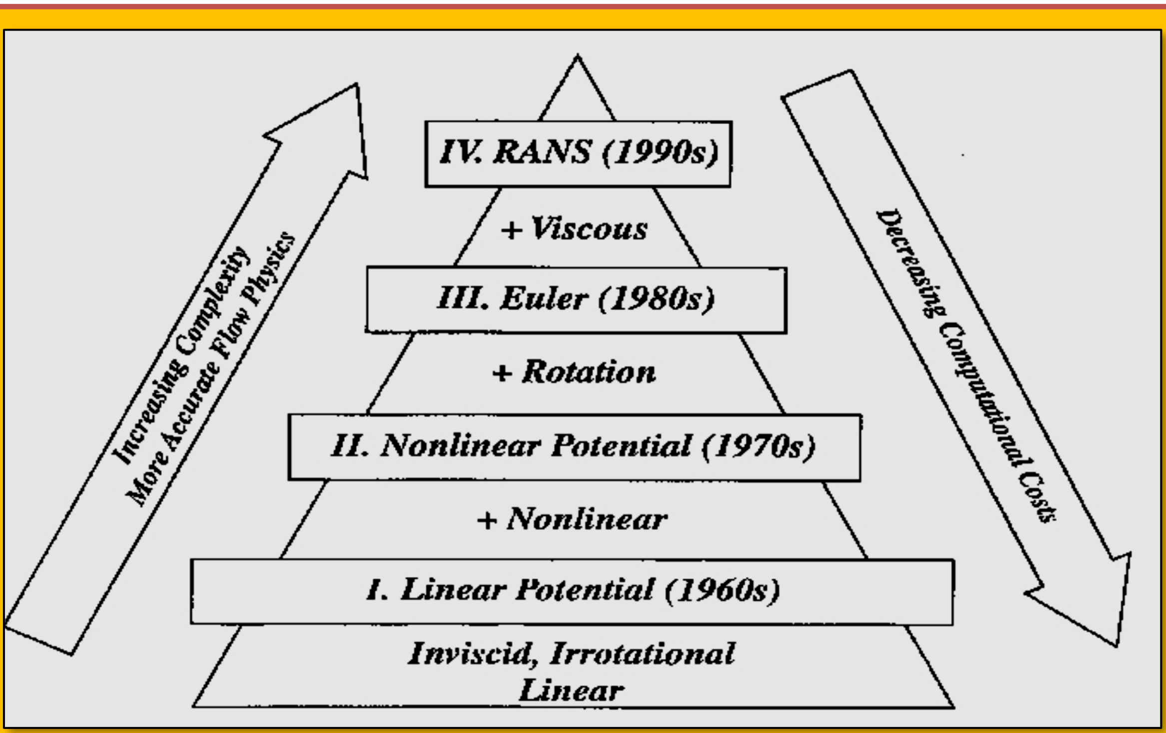

Figure 5.1.1 Hierarchy of Models for Industrial Flow Simulations – Courtesy of *Antony Jameson and Massimiliano Fatica*

---

[110] *"How the Stork Inspired Human Flight".* flyingmag.com.

[111] Wikipedia.

model the flow. Procedures for solving the full viscous equations are needed for the simulation of complex separated flows, which may occur at high angles of attack or with bluff bodies. In current industrial practice these are modeled by the Reynolds Average Navier-Stokes (RANS) equations with various turbulence models[112].

5.2 Airfoil[113]

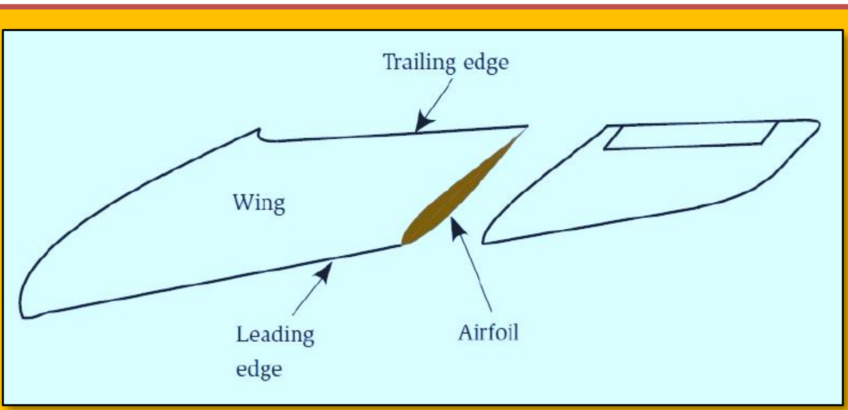

Figure 5.2.1 Airfoil Section

An airfoil is the shape of a wing or blade (of a propeller, rotor or turbine) or sail (see **Figure 5.2.1**). An airfoil shaped body moved through a fluid produces an aerodynamic force. The component of this force perpendicular to the direction of motion is called lift. The component parallel to the direction of motion is called drag. Subsonic flight airfoils have a characteristic shape with a rounded leading edge, followed by a sharp trailing edge, often with asymmetric camber.

The lift on an airfoil is primarily the result of its shape (in particular its camber) and its angle of attack. When either is positive, the resulting flow field about the airfoil has a higher average velocity on the upper surface than on the lower surface. This velocity difference is necessarily accompanied by a pressure difference via Bernoulli's principle for incompressible in viscid flow, which in turn produces the lift force. The lift force can also be related directly to the average top or bottom velocity difference, without involving the pressure, by using the concept of circulation and the ***Kutta-Joukowski theorem***.

5.2.1 Basic Nomenclature of Airfoil

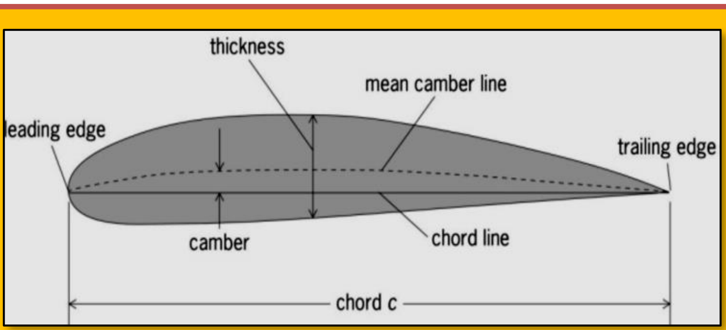

Figure 5.2.2 Basic Nomenclature of Aerofoil

The various terms related to airfoils are defined below:

- The suction surface (upper surface) is generally associated with higher velocity and thus lower static pressure.
- The pressure surface (lower surface) has a comparatively higher static pressure than the suction surface. The pressure gradient between these two surfaces contributes to the lift force generated for a given airfoil.

---

[112] Antony Jameson and Massimiliano Fatica, "*Using Computational Fluid Dynamics for Aerodynamics*", Stanford University.

[113] *Design, Fabrication and Numerical Analysis on NACA 642-215*, 2015.

The geometry of the airfoil is described with a variety of terms. A key characteristic of an airfoil is its chord. We thus define the following concepts:

- The leading edge is the point at the front of the airfoil that has maximum curvature.
- The trailing edge is defined similarly as the point of maximum curvature at the rear of the airfoil.
- The chord line is a straight line connecting the leading and trailing edges of the airfoil.
- The chord length, or simply chord (c) is the length of the chord line and is the characteristic dimension of the airfoil section.

The shape of the airfoil is defined using the following concepts:

- The mean camber line is the locus of point midway between the upper and lower surfaces. Its exact shape depends on how the thickness is defined.
- The thickness of an airfoil varies along the chord. It may be measured in either of two ways:
    - Thickness measured perpendicular to the camber line. This is sometimes described as the "American convention".
    - Thickness measured perpendicular to the chord line. This is sometimes described as the "British convention".

Two key parameters to describe an airfoil's shape are its maximum thickness (expressed as a percentage of the chord), and the location of the maximum thickness point (also expressed as a percentage of the chord). Finally, important concepts used to describe the airfoil's behavior when moving through a fluid are:

- The aerodynamic centre which is the chord-wise length about which the pitching moment is independent of the lift coefficient and the angle of attack.
- The centre of pressure which is the chord-wise location about which the pitching moment is zero.

5.3 Physics of Lift in Airfoils

Author : *Ed Regis has written 10 science books, including Monsters: The Hindenburg Disaster and the Birth of Pathological Technology (Basic Books, 2015). He has also logged 1,000 hours flying time as a private pilot. Credit: Nick Higgins.*
Original Appearance : *This article was originally published with the title "The Enigma of Aerodynamic Lift" in Scientific American 322, 2, 44-51 (February 2020).*
Source : *doi:10.1038/scientificamerican0220-44*

In Brief

- **On a strictly** mathematical level, engineers know how to design planes that will stay aloft. But equations don't explain why aerodynamic lift occurs.
- **There are two** competing theories that illuminate the forces and factors of lift. Both are incomplete explanations.
- **Aerodynamicists** have recently tried to close the gaps in understanding. Still, no consensus exists.

In December 2003, to commemorate the 100th anniversary of the first flight of the Wright brothers, the *New York Times* ran a story entitled "*Staying Aloft; What Does Keep Them Up There*?" The point of the piece was a simple question: What keeps planes in the air? To answer it, the *Times* turned to John D. Anderson, Jr., curator of aerodynamics at the National Air and Space Museum and author of several textbooks in the field.

What Anderson said, however, is that there is actually no agreement on what generates the aerodynamic force known as lift. “There is no simple one-liner answer to this,” he told the *Times*. People give different answers to the question, some with “religious fervor.” More than 15 years after that pronouncement, there are still different accounts of what generates lift, each with its own substantial rank of zealous defenders. At this point in the history of flight, this situation is slightly puzzling. After all, the natural processes of evolution, working mindlessly, at random and without any understanding of physics, solved the mechanical problem of aerodynamic lift for soaring birds eons ago. Why should it be so hard for scientists to explain what keeps birds, and airliners, up in the air?

Adding to the confusion is the fact that accounts of lift exist on two separate levels of abstraction: the technical and the nontechnical. They are complementary rather than contradictory, but they differ in their aims. One exists as a strictly mathematical theory, a realm in which the analysis medium consists of equations, symbols, computer simulations and numbers. There is little, if any, serious disagreement as to what the appropriate equations or their solutions are. The objective of technical mathematical theory is to make accurate predictions and to project results that are useful to aeronautical engineers engaged in the complex business of designing aircraft.

But by themselves, equations are not explanations, and neither are their solutions. There is a second, nontechnical level of analysis that is intended to provide us with a physical, commonsense explanation of lift. The objective of the nontechnical approach is to give us an intuitive understanding of the actual forces and factors that are at work in holding an airplane aloft. This approach exists not on the level of numbers and equations but rather on the level of concepts and principles that are familiar and intelligible to non-specialists.

It is on this second, nontechnical level where the controversies lie. Two different theories are commonly proposed to explain lift, and advocates on both sides argue their viewpoints in articles, in books and online. The problem is that each of these two nontechnical theories is correct in itself. But neither produces a complete explanation of lift, one that provides a full accounting of all the basic forces, factors and physical conditions governing aerodynamic lift, with no issues left dangling, unexplained or unknown. Does such a theory even exist?

5.3.1 Two Competing Theories

By far the most popular explanation of lift is Bernoulli’s theorem, a principle identified by Swiss mathematician ***Daniel Bernoulli*** in his 1738 treatise, *Hydrodynamica*. Bernoulli came from a family of mathematicians. His father, Johann, made contributions to the calculus, and his Uncle Jakob coined the term “integral.” Many of Daniel Bernoulli’s contributions had to do with fluid flow: Air is a fluid, and the theorem associated with his name is commonly expressed in terms of fluid dynamics. Stated simply, Bernoulli’s law says that the pressure of a fluid decreases as its velocity increases, and vice versa. Bernoulli’s theorem attempts to explain lift as a consequence of the curved upper surface of an airfoil, the technical name for an airplane wing. Because of this curvature, the idea goes, air traveling across the top of the wing moves faster than the air moving along the wing’s bottom surface, which is flat. Bernoulli’s theorem says that the increased speed atop the wing is associated with a region of lower pressure there, which is lift.

5.3.2 The Flawed Classics[114]

On a commonsense, everyday basis, two theories have been advanced to explain what keeps an airplane aloft. One is **Bernoulli's theorem***, which associates lift with the area of higher speed and lower pressure atop the wing. The other is the* **Newtonian principle of action and reaction***, which explains lift as an upward push on the wing from the moving air below. Each of these theories is correct in its way, and neither one contradicts the other, although proponents of each theory argue their viewpoints with a zeal bordering on mania. Still, neither theory by itself provides a complete explanation of lift, nor*

---

[114] L-Dopa

do both of them together, because each leaves something out. A complete explanation must account for all the forces and factors acting on the wing, with no issue, major or minor, left dangling.

5.3.2.1 Bernoulli's Theorem

As applied to an airplane wing, technically called an airfoil **Bernoulli's theorem** *attempts to explain lift as a consequence of the wing's curved upper surface. The idea is that because of this curvature, the air traveling across the top of the wing moves faster than the air moving along the wing's bottom surface, which is flat. Bernoulli's theorem says that the increased speed atop the wing is associated with a region of lower pressure there, which is lift.*
BUT...
Although Bernoulli's theorem is largely correct, there are several reasons that the principle does not constitute a complete explanation of lift. It is a fact of experience that air moves faster across a curved surface, but the theorem alone does not explain why this is so or why the higher velocity atop the wing brings lower pressure along with it. And practically speaking, an airplane with wings that have a curved upper surface, or even flat surfaces on top and bottom, is capable of flying inverted, so long as the airfoil meets the oncoming wind at an appropriate angle.

5.3.2.2 Newton's 3rd Law

Air has mass. Therefore, Newton's third law would say that the wing's downward push results in an equal and opposite push back upward. This Newtonian account of lift applies to wings of any shape, curved or flat, symmetrical or not, and it holds for aircraft flying inverted or right-side up (the critical feature being a suitable angle of attack). For these reasons, it is a more comprehensive and universally applicable explanation of lift than Bernoulli's.
BUT...
Taken by itself, the principle of action and reaction still fails to explain the lower pressure atop the wing, which exists in that region irrespective of whether the airfoil is cambered or not.

Mountains of empirical data from streamlines (lines of smoke particles) in wind-tunnel tests, laboratory experiments on nozzles and Venturi tubes, and so on provide overwhelming evidence that as stated, ***Bernoulli’s principle*** is correct and true. Nevertheless, there are several reasons that Bernoulli’s theorem does not by itself constitute a *complete* explanation of lift. Although it is a fact of experience that air moves faster across a curved surface, Bernoulli’s theorem alone does not explain why this is so. In other words, the theorem does not say how the higher velocity above the wing came about to begin with.

5.3.3 New Ideas of Lift[115]

Today's scientific approaches to aircraft design are determined by computational fluid dynamics (CFD) simulations, as well as equations that take full account of the actual viscosity of real air. Although we still do not have a singular and satisfying physical, qualitative explanation of lift, some recent attempts may have gotten us a bit closer.

5.3.3.1 Co-Dependency of Lift's Four Elements

As applied to an airplane wing technically called an airfoil Bernoulli's theorem attempts to explain lift as a consequence of the wing's curved upper surface. The idea is that because of this curvature, the air traveling across the top of the wing moves faster than the air moving along the wing's bottom surface, which is flat. Bernoulli's theorem says that the increased speed atop the wing is associated with a region of lower pressure there, which is lift.
BUT...
Although McLean says the reduced pressure above and increased pressure below result from the airfoil being "completely surrounded by flowing air," this doesn't explain how the reduced pressure up top got there initially.

---

[115] See Previous

How Low Pressure Forms Above The Wing

Mark Drela, an expert on fluid dynamics, has attempted to address what evaded Newton and Bernoulli: how the low-pressure zone, or partial vacuum, above the wing comes into existence. The air above the wing momentarily flows straight back forming a void or vacuum. This vacuum will then strongly pull the air back down : , filling in and thus eliminating most but not all of the vacuum. Just enough vacuum remains to pull the air into the curved path that follows the wing.

There are plenty of bad explanations for the higher velocity. According to the most common one—the "equal transit time" theory—parcels of air that separate at the wing's leading edge must rejoin simultaneously at the trailing edge. Because the top parcel travels farther than the lower parcel in a given amount of time, it must go faster. The fallacy here is that there is no physical reason that the two parcels must reach the trailing edge simultaneously. And indeed, they do not: the empirical fact is that the air atop moves much faster than the equal transit time theory could account for.

There is also a notorious "demonstration" of Bernoulli's principle, one that is repeated in many popular accounts, YouTube videos and even some textbooks. It involves holding a sheet of paper horizontally at your mouth and blowing across the curved top of it. The page rises, supposedly illustrating the Bernoulli effect. The opposite result ought to occur when you blow across the bottom of the sheet: the velocity of the moving air below it should pull the page downward. Instead, paradoxically, the page rises.

The lifting of the curved paper when flow is applied to one side "is not because air is moving at different speeds on the two sides," says [Holger Babinsky], a professor of aerodynamics at the University of Cambridge, in his article "How Do Wings Work?" To demonstrate this, blow across a straight piece of paper, for example, one held so that it hangs down vertically and witness that the paper does not move one way or the other, because "the pressure on both sides of the paper is the same, despite the obvious difference in velocity."

The second shortcoming of Bernoulli's theorem is that it does not say how or why the higher velocity atop the wing brings lower pressure, rather than higher pressure, along with it. It might be natural to think that when a wing's curvature displaces air upward, that air is compressed, resulting in increased pressure atop the wing. This kind of "bottleneck" typically slows things down in ordinary life rather than speeding them up. On a highway, when two or more lanes of traffic merge into one, the cars involved do not go faster; there is instead a mass slowdown and possibly even a traffic jam. Air molecules flowing atop a wing do not behave like that, but Bernoulli's theorem does not say why not.

The third problem provides the most decisive argument against regarding Bernoulli's theorem as a complete account of lift: An airplane with a curved upper surface is capable of flying inverted. In inverted flight, the curved wing surface becomes the bottom surface, and according to Bernoulli's theorem, it then generates reduced pressure *below* the wing. That lower pressure, added to the force of gravity, should have the overall effect of pulling the plane downward rather than holding it up. Moreover, aircraft with symmetrical airfoils, with equal curvature on the top and bottom—or even with flat top and bottom surfaces are also capable of flying inverted, so long as the airfoil meets the oncoming wind at an appropriate angle of attack. This means that Bernoulli's theorem alone is insufficient to explain these facts.

The other theory of lift is based on Newton's third law of motion, the principle of action and reaction. The theory states that a wing keeps an airplane up by pushing the air down. Air has mass, and from Newton's third law it follows that the wing's downward push results in an equal and opposite push back upward, which is lift. The Newtonian account applies to wings of any shape, curved or flat, symmetrical or not. It holds for aircraft flying inverted or right-side up. The forces at work are also familiar from ordinary experience for example, when you stick your hand out of a moving car and tilt it upward, the air is deflected downward, and your hand rises. For these reasons, ***Newton's third law*** is a more universal and comprehensive explanation of lift than Bernoulli's theorem.

But taken by itself, the principle of action and reaction also fails to explain the lower pressure atop the wing, which exists in that region irrespective of whether the airfoil is cambered. It is only when an airplane lands and comes to a halt that the region of lower pressure atop the wing disappears, returns to ambient pressure, and becomes the same at both top and bottom. But as long as a plane is flying, that region of lower pressure is an inescapable element of aerodynamic lift, and it must be explained.

5.3.4 Historical Understanding

Neither Bernoulli nor Newton was consciously trying to explain what holds aircraft up, of course, because they lived long before the actual development of mechanical flight. Their respective laws and theories were merely repurposed once the Wright brothers flew, making it a serious and pressing business for scientists to understand aerodynamic lift.

Most of these theoretical accounts came from Europe. In the early years of the 20th century, several British scientists advanced technical, mathematical accounts of lift that treated air as a perfect fluid, meaning that it was incompressible and had zero viscosity. These were unrealistic assumptions but perhaps understandable ones for scientists faced with the new phenomenon of controlled, powered mechanical flight. These assumptions also made the underlying mathematics simpler and more straightforward than they otherwise would have been, but that simplicity came at a price: however successful the accounts of airfoils moving in ideal gases might be mathematically, they remained defective empirically.

In Germany, one of the scientists who applied themselves to the problem of lift was none other than ***Albert Einstein***. In 1916 Einstein published a short piece in the journal *Die Naturwissenschaften* entitled “Elementary Theory of Water Waves and of Flight,” which sought to explain what accounted for the carrying capacity of the wings of flying machines and soaring birds. “There is a lot of obscurity surrounding these questions,” Einstein wrote. “Indeed, I must confess that I have never encountered a simple answer to them even in the specialist literature.”

Einstein then proceeded to give an explanation that assumed an incompressible, frictionless fluid—that is, an ideal fluid. Without mentioning Bernoulli by name, he gave an account that is consistent with Bernoulli’s principle by saying that fluid pressure is greater where its velocity is slower, and vice versa. To take advantage of these pressure differences, Einstein proposed an airfoil with a bulge on top such that the shape would increase airflow velocity above the bulge and thus decrease pressure there as well.

Einstein probably thought that his ideal-fluid analysis would apply equally well to real-world fluid flows. In 1917, on the basis of his theory, Einstein designed an airfoil that later came to be known as a cat’s-back wing because of its resemblance to the humped back of a stretching cat. He brought the design to aircraft manufacturer LVG (Luftverkehrsgesellschaft) in Berlin, which built a new flying machine around it. A test pilot reported that the craft waddled around in the air like “a pregnant duck.” Much later, in 1954, Einstein himself called his excursion into aeronautics a “youthful folly.” The individual who gave us radically new theories that penetrated both the smallest and the largest components of the universe nonetheless failed to make a positive contribution to the understanding of lift or to come up with a practical airfoil design.

5.3.5 Toward a Complete Theory of Lift

Contemporary scientific approaches to aircraft design are the province of computational fluid dynamics (CFD) simulations and the so-called Navier-Stokes equations, which take full account of the actual viscosity of real air. The solutions of those equations and the output of the CFD simulations yield pressure-distribution predictions, airflow patterns and quantitative results that are the basis for today’s highly advanced aircraft designs. Still, they do not by themselves give a physical, qualitative explanation of lift.

In recent years, however, leading aerodynamicist Doug McLean has attempted to go beyond sheer mathematical formalism and come to grips with the physical cause-and-effect relations that account for lift in all of its real-life manifestations. McLean, who spent most of his professional career as an engineer at Boeing Commercial Airplanes, where he specialized in CFD code development, published his new ideas in the 2012 text *Understanding Aerodynamics: Arguing from the Real Physics*.

Considering that the book runs to more than 500 pages of fairly dense technical analysis, it is surprising to see that it includes a **section (7.3.3)** entitled "A Basic Explanation of Lift on an Airfoil, Accessible to a Nontechnical Audience." Producing these 16 pages was not easy for McLean, a master of the subject; indeed, it was "probably the hardest part of the book to write," the author says. "It saw more revisions than I can count. I was never entirely happy with it."

McLean's complex explanation of lift starts with the basic assumption of all ordinary aerodynamics: the air around a wing acts as "a continuous material that deforms to follow the contours of the airfoil." That deformation exists in the form of a deep swath of fluid flow both above and below the wing. "The airfoil affects the pressure over a wide area in what is called a ***pressure field***," McLean writes. "When lift is produced, a diffuse cloud of low pressure always forms above the airfoil, and a diffuse cloud of high pressure usually forms below. Where these clouds touch the airfoil they constitute the pressure difference that exerts lift on the airfoil."

The wing pushes the air down, resulting in a downward turn of the airflow. The air above the wing is sped up in accordance with Bernoulli's principle. In addition, there is an area of high pressure below the wing and a region of low pressure above. This means that there are four necessary components in McLean's explanation of lift: a downward turning of the airflow, an increase in the airflow's speed, an area of low pressure and an area of high pressure.

But it is the interrelation among these four elements that is the most novel and distinctive aspect of McLean's account. "They support each other in a reciprocal cause-and-effect relationship, and none would exist without the others," he writes. "The pressure differences exert the lift force on the airfoil, while the downward turning of the flow and the changes in flow speed sustain the pressure differences." It is this interrelation that constitutes a fifth element of McLean's explanation: the reciprocity among the other four. It is as if those four components collectively bring themselves into existence, and sustain themselves, by simultaneous acts of mutual creation and causation.

There seems to be a hint of magic in this synergy. The process that McLean describes seems akin to four active agents pulling up on one another's bootstraps to keep themselves in the air collectively. Or, as he acknowledges, it is a case of "circular cause-and-effect." How is it possible for each element of the interaction to sustain and reinforce all of the others? And what causes this mutual, reciprocal, dynamic interaction? McLean's answer: ***Newton's 2nd law of motion***.

Newton's second law states that the acceleration of a body, or a parcel of fluid, is proportional to the force exerted on it. "Newton's 2nd law tells us that when a pressure difference imposes a net force on a fluid parcel, it must cause a change in the speed or direction (or both) of the parcel's motion," McLean explains. But reciprocally, the pressure difference depends on and exists because of the parcel's acceleration. Aren't we getting something for nothing here? McLean says no: If the wing were at rest, no part of this cluster of mutually reinforcing activity would exist. But the fact that the wing is moving through the air, with each parcel affecting all of the others, brings these co-dependent elements into existence and sustains them throughout the flight.

5.3.6 Turning on the Reciprocity of Lift

Soon after the publication of *Understanding Aerodynamics*, McLean realized that he had not fully accounted for all the elements of aerodynamic lift, because he did not explain convincingly what causes the pressures on the wing to change from ambient. So, in November 2018, McLean published a two-part article in *The Physics Teacher* in which he proposed "a comprehensive physical explanation" of aerodynamic lift.

Although the article largely restates McLean's earlier line of argument, it also attempts to add a better explanation of what causes the pressure field to be nonuniform and to assume the physical shape that it does. In particular, his new argument introduces a mutual interaction at the flow field level so that the nonuniform pressure field is a result of an applied force, the downward force exerted on the air by the airfoil.

Whether McLean's section 7.3.3 and his follow-up article are successful in providing a complete and correct account of lift is open to interpretation and debate. There are reasons that it is difficult to produce a clear, simple and satisfactory account of aerodynamic lift. For one thing, fluid flows are more complex and harder to understand than the motions of solid objects, especially fluid flows that separate at the wing's leading edge and are subject to different physical forces along the top and bottom. Some of the disputes regarding lift involve not the facts themselves but rather how those facts are to be interpreted, which may involve issues that are impossible to decide by experiment.

Nevertheless, there are at this point only a few outstanding matters that require explanation. Lift, as you will recall, is the result of the pressure differences between the top and bottom parts of an airfoil. We already have an acceptable explanation for what happens at the bottom part of an airfoil: the oncoming air pushes on the wing both vertically (producing lift) and horizontally (producing drag). The upward push exists in the form of higher pressure below the wing, and this higher pressure is a result of simple Newtonian action and reaction.

Things are quite different at the top of the wing, however. A region of lower pressure exists there that is also part of the aerodynamic lifting force. But if neither Bernoulli's principle nor Newton's third law explains it, what does? We know from streamlines that the air above the wing adheres closely to the downward curvature of the airfoil. But why must the parcels of air moving across the wing's top surface follow its downward curvature? Why can't they separate from it and fly straight back?

Mark Drela, a professor of fluid dynamics at the Massachusetts Institute of Technology and author of *Flight Vehicle Aerodynamics*, offers an answer: "If the parcels momentarily flew off tangent to the airfoil top surface, there would literally be a vacuum created below them," he explains. "This vacuum would then suck down the parcels until they mostly fill in the vacuum, i.e., until they move tangent to the airfoil again. This is the physical mechanism which forces the parcels to move along the airfoil shape. A slight partial vacuum remains to maintain the parcels in a curved path."

This drawing away or pulling down of those air parcels from their neighboring parcels above is what creates the area of lower pressure atop the wing. But another effect also accompanies this action: the higher airflow speed atop the wing. "The reduced pressure over a lifting wing also 'pulls horizontally' on air parcels as they approach from upstream, so they have a higher speed by the time they arrive above the wing," Drela says. "So the increased speed above the lifting wing can be viewed as a side effect of the reduced pressure there."

But as always, when it comes to explaining lift on a nontechnical level, another expert will have another answer. Cambridge aerodynamicist Babinsky says, "I hate to disagree with my esteemed colleague Mark Drela, but if the creation of a vacuum were the explanation, then it is hard to explain why sometimes the flow does nonetheless separate from the surface. But he is correct in everything else. The problem is that there is no quick and easy explanation."

Drela himself concedes that his explanation is unsatisfactory in some ways. "One apparent problem is that there is no explanation that will be universally accepted," he says. So where does that leave us? In effect, right where we started: with John D. Anderson, who stated, "There is no simple one-liner answer to this."

5.3.6.1 NACA Four-Digit Series Airfoils

Earliest NACA airfoils were designated as four-digit series[116]. The thickness distribution was based on successful *RAE & Gottigen* airfoils. It is given as:

$$\pm y_t = \frac{t}{20}\left[0.2969\sqrt{x} - 0.1260\text{x} - 0.3516\text{x}^2 + 0.2843\text{x}^3 - 0.1015\text{x}^5\right]$$

---

[116] Sadrehaghighi, I., *Conceptual Aero-Design for CFD Analysis*", 1.87.2.

Eq. 5.3.1

where, t = maximum thickness as fraction of chord. The leading radius is : $r_t = 1.101$. It is a symmetrical airfoil by design. The maximum thickness of all four-digit airfoils occurs at 30% of chord. In the designation of these airfoils, the first two digits indicate that the camber is zero and the last two digits indicate the thickness ratio as percentage of chord. The camber line for the four-digit series airfoils consists of two parabolic arcs tangent at the point of maximum ordinate. The expressions for camber(y_c) are

$$y_c = \frac{m}{p^2}[2px - x^2] \quad , x \leq x_{ycmax} = \frac{m}{(1 - p)^2}[(1 - 2p) + 2px - x^2] \quad x > x_{ycmax}$$

Eq. 5.3.2

Where m = maximum ordinate of camber line as fraction of chord and p = chord wise position of maximum camber as fraction of chord. The camber lines obtained by using different values of m & p are denoted by two digits, e.g. NACA 64 indicates a mean line of 6% camber with maximum camber occurring at 40% of the chord. A cambered airfoil of four-digit series is obtained by combining mean line and the thickness distribution as described in the previous subsection. For example, NACA 2412 airfoil is obtained by combining NACA 24 mean line and NACA 0012 thickness distribution. This airfoil has (a) maximum camber of 2% occurring at 40% chord and (b) maximum thickness ratio of 12%.

5.3.6.2 NACA Five-Digit Series Airfoils

During certain tests it was observed that C_{Lmax} (Max. Lift Coefficient) of the airfoil could be increased by shifting forward the location of the maximum camber. This finding led to development of five-digit series airfoils. The new camber lines for the five-digit series airfoils are designated by three digits. The same thickness distribution was retained as that for NACA four-digit series airfoils. The camber line shape is given as :

$$y_c = \frac{1}{6}k_1[x^3\text{-}3mx^2 + m^2(3 - m)x] \qquad 0 < x \leq m$$

$$= \frac{1}{6}k_1 m^3[1 - x] \quad m < x < 1$$

Eq. 5.3.3

The value of 'm' decides the location of the maximum camber and that of k_1 the design lift coefficient. A combination of m = 0.2025 and $k_1 = 15.957$ gives li C = 0.3 and maximum camber at 15% of chord. This mean line is designated as NACA 230. The first digit '2' indicates that $C_L = 0.3$ and the subsequent two digits (30) indicate that the maximum camber occurs at 15% of chord. A typical five-digit cambered airfoil is NACA 23012. The digits signify : First digit(2) indicates that li $C_L = 0.3$. Second & third digits (30) indicate that maximum camber occurs at 15% of chord. Last two digits indicate that the maximum thickness ratio is 12%.

5.3.6.3 Six Series Airfoils

As a background to the development of these airfoils the following points may be mentioned. In 1931 [Theodorsen] presented 'Theory of wing sections of arbitrary shape' NACA TR 411, which enabled calculation flow past airfoils of general shape. Around the same time the studies of [Tollmien and Schlichting] on boundary layer transition, indicated that the transition process, which causes laminar boundary layer to become turbulent, depends predominantly on the pressure gradient in the flow around the airfoil. A turbulent boundary layer results in a higher skin friction drag coefficient as compared to when the boundary layer is laminar. Hence, maintaining a laminar boundary layer over a longer portion of the airfoil would result in a lower drag coefficient. Inverse methods, which could permit design of mean line shapes and thickness distributions, for prescribed pressure distributions were also available at that point of time. Taking advantage of these developments, new series of airfoils called low drag airfoils or laminar flow airfoils were designed. These airfoils are designated as 1-series, 2-series,……..,7-series. Among these the six series airfoils are commonly used airfoils. When the airfoil surface is smooth, these airfoils have a C_{Dmin} which is lower than that for four-and five-digit series airfoils of the same thickness ratio. Further, the minimum drag coefficient extends over a range of lift coefficient. This extent is called drag bucket. The thickness distributions for these airfoils are obtained by calculations which give a desired pressure distribution. Analytical expressions for these thickness distributions are not available. However, the camber lines are designated as : a = 0, 0.1, 0.2 …., 0.9 and 1.0. For example, the camber line shape with a = 0.4 gives a uniform pressure distribution from x/c = 0 to 0.4 and then linearly

Family	Advantages	Disadvantages	Applications
4-Digit	1. Good stall characteristics 2. Small center of pressure movement across large speed range 3. Roughness has little effect	1. Low maximum lift coefficient 2. Relatively high drag 3. High pitching moment	1. Low maximum lift coefficient 2. Relatively high drag 3. High pitching moment
5-Digit	1. Higher maximum lift coefficient 2. Low pitching moment 3. Roughness has little effect	1. Poor stall behavior 2. Relatively high drag	1. General aviation 2. Piston-powered bombers, transports 3. Commuters 4. Business jets
16-Series	1. Avoids low pressure peaks 2. Low drag at high speed	1. Relatively low lift	1. Aircraft propellers 2. Ship propellers
6-Series	1. High maximum lift coefficient 2. Very low drag over a small range of operating conditions 3. Optimized for high speed	1. High drag outside of the optimum range of operating conditions 2. High pitching moment 3. Poor stall behavior 4. Very susceptible to roughness	1. Piston-powered fighters 2. Business jets 3. Jet trainers 4. Supersonic jets
7-Series	1. Very low drag over a small range of operating conditions 2. Low pitching moment	1. Reduced maximum lift coefficient 2. High drag outside of the optimum range of operating conditions	Seldom used
8-Series	Unknown	Unknown	Very seldom used

Table 5.3.1 Summary of Different Types of NACA Airfoils

decreasing to zero at x/c = 1.0. If the camber line designation is not mentioned, ‘a’ equal to unity is implied. It is obtained by combining NACA 662 – 015 thickness distribution and a = 1.0 mean line.

5.3.6.4 NASA Airfoils

NASA has developed airfoil shapes for special applications. For example GA(W) series airfoils were designed for general aviation aircraft. The ‘LS’ series of airfoils among these are for low speed airplanes. A typical airfoil of this category is designated as LS(1) - 0417. In this designation, the digit ‘1’ refers to first series, the digits ‘04’ indicate C_{LOPT} of 0.4 and the digits ‘17’ indicate the thickness ratio of 17%. For the airfoils in this series, specifically designed for medium speed airplanes, the letters ‘LS’ are replaced by ‘MS’. NASA NLF series airfoils are ‘Natural Laminar Flow’ airfoils. NASA SC series airfoils are called ‘Supercritical airfoils’. These airfoils have a higher critical Mach number. **Table 5.3.1** displays Summary of different types of NACA Airfoils in use.

5.3.7 Forces on Airfoil

A total aerodynamic force is generated when a stream of air flows over and under an airfoil that is moving through the air. The point at which the air separates to flow about the airfoil is called the point of impact. A high-pressure area or stagnation point is formed at the point of impact. Normally the high-pressure area is located at the lower portion of the leading edge, depending on angle of attack. This high-pressure area contributes to the overall force produced by the blade. **Figure 5.3.1** shows airflow lines that illustrate how the air moves about the airfoil section. Notice that the air is deflected downward as it passes under the airfoil and leaves the trailing edge. By Newton's third law which states "every action has an equal and opposite reaction". Since the air is being deflected downward, an equal and opposite force must be acting upward on the airfoil. This force adds to the total aerodynamic force developed by the airfoil. At very low or zero angles of attack, the deflection force or impact pressure may exert a zero positive force, or even a downward or negative force. Air passing over the top of the airfoil produces aerodynamic force in another way. The shape of the airfoil causes a low pressure area above the airfoil according to Bernoulli's Principle, and the decrease in pressure on top of the airfoil exerts an upward aerodynamic force. Pressure differential between the upper and lower surface of the airfoil is quite small, in the vicinity of 1 percent. Even a small pressure differential produces substantial force when applied to the large area of a rotor blade.

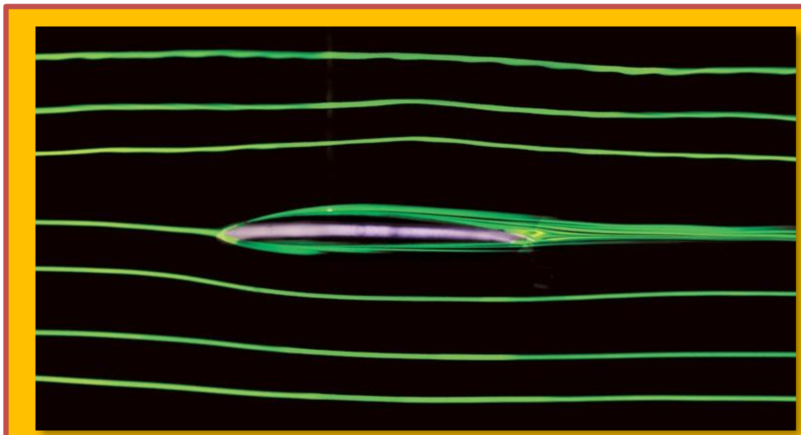

Figure 5.3.1 Flow Around an Airfoil (Courtesy of AMS Research Center)

The total aerodynamic force, sometimes called the resultant force, may be divided into two components called ***lift*** and ***drag***. Lift acts on the airfoil in a direction perpendicular to the relative wind. Drag is the resistance or force that opposes the motion of the airfoil through the air. It acts on the airfoil in a direction parallel to the relative wind. Many factors contribute to the total lift produced by an airfoil. Increased speed causes increased lift because a larger pressure differential is produced between the upper and lower surfaces. Lift does not increase in direct proportion to speed, but varies as the square of the speed. Thus, a blade traveling at 500 knots has four times the lift of the same blade traveling at only 250 knots. Lift also varies with the area of the blade. A blade area of 100 square

feet will produce twice as much lift as a blade area of only 50 square feet. Angle of attack also has an effect on the lift produced. Lift increases as the angle of attack increases up to the stalling angle of attack. Stall angle varies with different blades and is the point at which airflow no longer follows the camber of the blade smoothly. Air density is another factor that directly influences lift.
Two design factors, Airfoil Shape and Airfoil Area are primary elements that determine how much lift and drag a blade will produce. Any change in these design factors will affect the forces produced. Normally an increase in lift will also produce an increase in drag. Therefore, the airfoil is designed to produce the most lift and the least drag within normal speed ranges.

5.3.8 Stalling Region of Airfoil

Stall is an undesirable phenomenon in which the aircraft wings produce an increased air resistance and decreased lift, which may cause an aircraft to crash. The stall occurs when the airflow separates from the upper wing surface. It happens when a plane is under too great an ***Angle of Attack (AoA)***. For light aircraft, without high-lift devices, the critical angle is usually around 16°. A stall is a condition in aerodynamics and aviation wherein the angle of attack increases beyond a certain point such that the lift begins to decrease. The angle at which this occurs is called the critical angle of attack. (see **Figure 5.3.2)**. Flow separation begins to occur at small angles of attack while attached flow over the wing is still dominant. As angle of attack increases, the separated regions on the top of the wing increase in size and hinder the wing's ability to create lift. At the critical angle of attack, separated flow is so dominant that further increases in angle of attack produce less lift and vastly more drag.

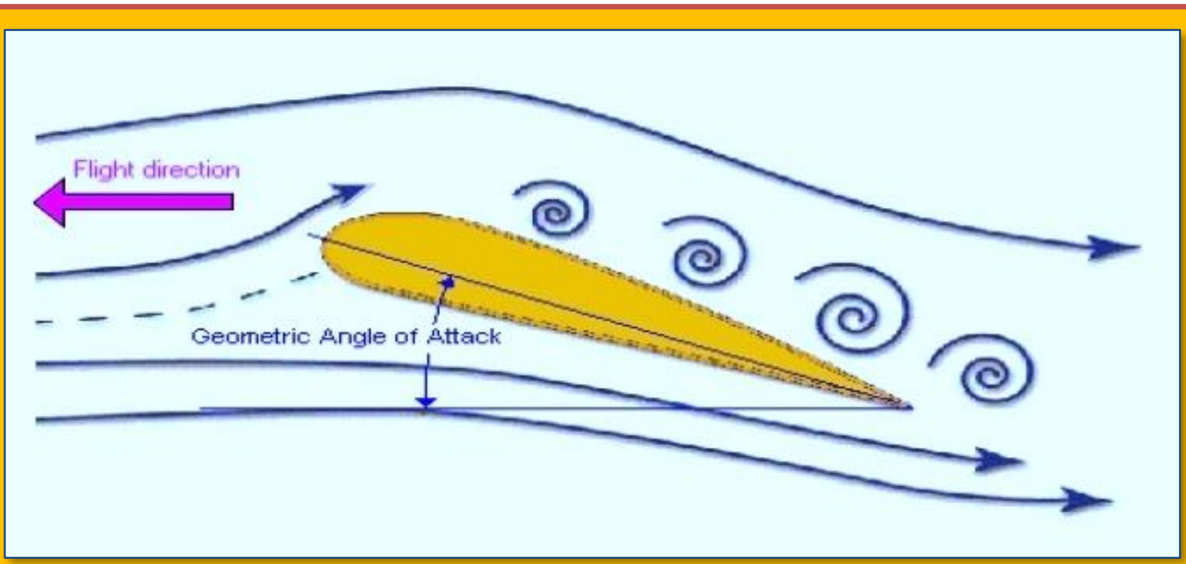

Figure 5.3.2 The Stalled Airfoil

5.3.9 Case Study - A CFD Database for Airfoils and Wings at Post-Stall Angles of Attack

Authors : Justin Petrilli[1], Ryan Paul[2], Ashok Gopalarathnam[3], and Neal T. Frink[4]
Affiliations : [1,2,3]*Department of Mechanical and Aerospace Engineering North Carolina State University, Raleigh, NC 27695-7910*
[4]*NASA Langley Research Center, Hampton, Virginia, 23681*
Title : *A CFD Database for Airfoils and Wings at Post-Stall Angles of Attack*
Citation : *(Petrilli, Paul, Gopalarathnam, & Frink, 2013)*
Bibliography : *Petrilli, J., Paul, R., Gopalarathnam, A., & Frink, N. T. (2013). A CFD Database for Airfoils and Wings at Post-Stall Angles of Attack. AIAA Applied Aerodynamics Conference. San Diego, CA.*

5.3.9.1 Abstract

This paper presents selected results from an ongoing effort to develop an aerodynamic database from Reynolds-Averaged Navier-Stokes (RANS) computational analysis of airfoils and wings at stall and post-stall angles of attack (Petrilli, Paul, Gopalarathnam, & Frink, 2013). The data obtained from this effort will be used for validation and refinement of a low-order post-stall prediction method developed at NCSU, and to fill existing gaps in high angle of attack data in the literature. Such data could have potential applications in post-stall flight dynamics, helicopter aerodynamics and wind turbine aerodynamics. An overview of the NASA *TetrUSS* CFD package used for the RANS computational approach is presented. Detailed results for three airfoils are presented to compare their stall and post-stall behavior. The results for finite wings at stall and post-stall conditions focus on the effects of taper-ratio and sweep angle, with particular attention to whether the sectional flows can be approximated using two-dimensional flow over a stalled airfoil. While this approximation seems reasonable for un swept wings even at post-stall conditions, significant spanwise flow on stalled swept wings preclude the use of 2D data to model sectional flows on swept wings. Thus, further effort is needed in low-order aerodynamic modeling of swept wings at stalled conditions.

5.3.9.2 Introduction

Airfoil lift and moment data in the low angle of attack regime is readily available from a multitude of sources- from Abbott and von Doenhoff [1] and those from the University of Stuttgart [2] and University of Illinois at Urbana-Champaign [3,4,5], to modern computational approaches designed to predict sectional aerodynamic characteristics based on arbitrary input geometry, such as XFOIL [6]. For many applications, data in this linear regime is sufficient. However, fields such as wind turbine aerodynamics, helicopter aerodynamics and post-stall flight dynamics of fixed wing aircraft require data to extend beyond aerodynamic stall. Efforts have been made in the wind turbine community and the helicopter aerodynamics community to extend airfoil data into the post-stall regime. In both wind turbine and helicopter aerodynamics, local blade sections close to the root of the rotor may experience very high angles of attack.

Models for airfoil force and moment coefficients at high angle of attack conditions have been developed experimentally [7, 8], which has led to researchers proposing empirical models based on flat plate theory [9]. The empirical models developed from experiment require that both the maximum C_l and the corresponding *_stall* at which this lift coefficient occurs be known reliably before theoretical flat plate data may be fitted to extend the data well into post-stall. Very little data exists in the literature covering the stall behavior of finite wings, especially that which extends deep into post-stall. Published work in post-stall wing aerodynamics often covers general stall behavior, dependent on factors such as planform, without providing detailed force and moment data beyond initial stall [10]. Some studies propose empirical methods based on theory to extend existing force and moment coefficient data-sets deep into post stall taking into account 3D effects with some correction for aspect ratio [8]. An interesting, purely experimental study, that covers the stall of both a 2D airfoil section and 3D wings of various aspect ratios was performed by Ostowari and Naik in

1985 [11]. The study presented consistent lift coefficient versus angle of attack data for various NACA 44XX series airfoils and 3D rectangular wings with a range of aspect ratios having the same airfoils as cross sections.

A database of post-stall airfoil and wing data, with a similar scope to the Ostowari and Naik study, was desired partly to address this dearth of data in the literature, but primarily to support a local effort within the Applied Aerodynamics Group at North Carolina State University. The ongoing effort involves developing a low-order model of post-stall aerodynamics for finite wings via use of existing linear low-order methods (VLM, Weissinger or LLT) corrected for nonlinear sectional airfoil behavior. Corrections are accomplished via a de cambering approach used to mimic the nonlinear aerodynamics caused by flow separation. Details of the development of the low-order method may be found in Ref. [12], with the current status pertaining to its use in real-time simulation of aircraft flight dynamics described in Ref. [13]. In addition to geometry information, the low-order post-stall model requires sectional 2D airfoil data as input for each of the control points. This sectional input data ($C_l-\alpha$, $C_d-\alpha$, and $C_m-\alpha$ curves) defines the convergence criteria for the low-order post-stall calculation for finite wings. Outputs include the total aerodynamic force and moment coefficients and spanwise distributions of these coefficients.

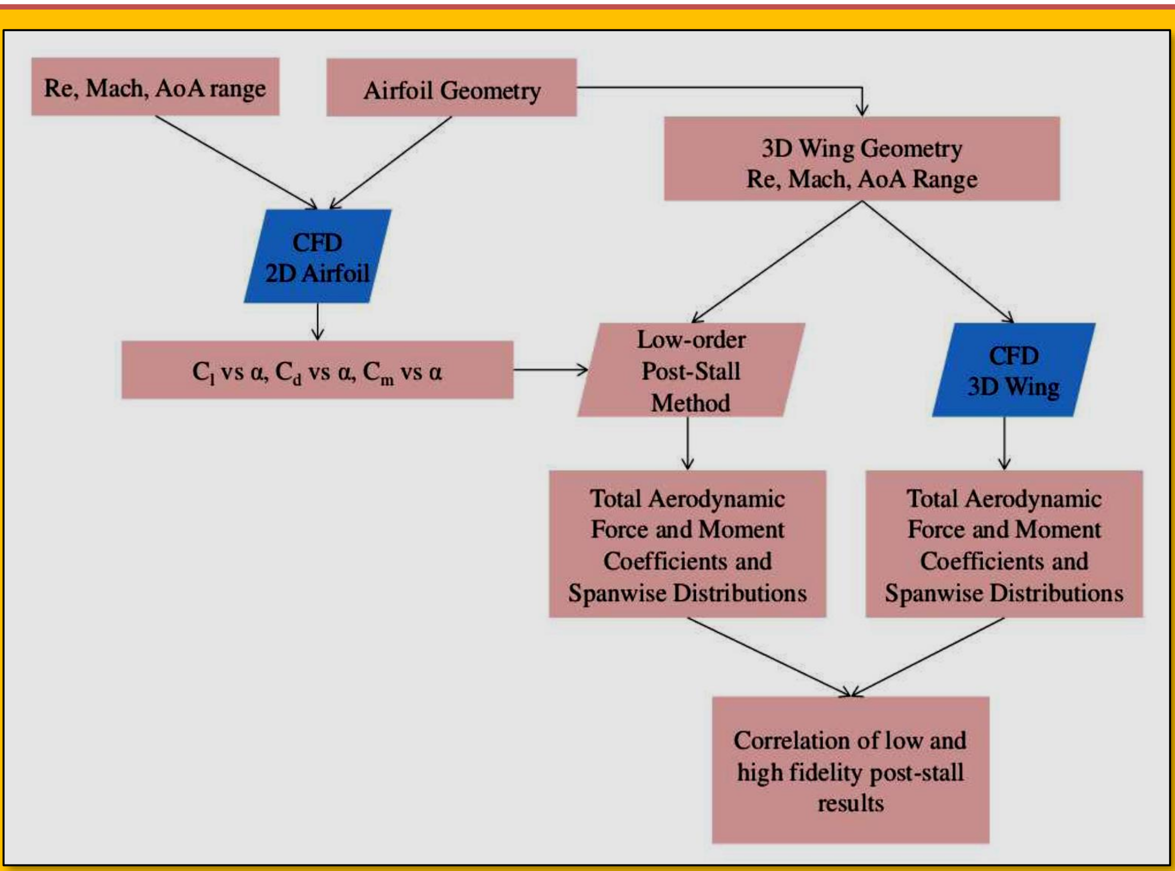

Figure 5.3.3 Approach for using CFD for initial validation and further refinement of the low-order method. Blue emphasizes that a consistent grid spacing is used with the 2D and 3D CFD discretization.

Figure 5.3.3 describes the relationship between the low-order method and the higher order Computational Fluid Dynamics (CFD) effort, and how the results from the latter are to be used for initial validation and further refinement of the former. Two dimensional CFD is performed on airfoil sections, and the outputs are used as inputs to the low-order method. The 3D geometries utilizing the same 2D cross section are run in both CFD and the low-order method. The results are then compared on the basis of total force/moments and spanwise force/moment distributions. CFD solutions and accompanying flow visualizations allow for further development and refinement of the low-order method. Comparisons between the low-order method and CFD are beyond the scope of this paper. This paper aims to discuss the methodology used in generating CFD solutions of airfoils and wings in post-stall angles of attack and to present the results in this regime as dependent on geometry and flow conditions.

This paper begins by describing the CFD software package that was chosen to generate consistent flow solutions for airfoils and wings. The methodology developed to effectively use the CFD package is presented next – from generating usable geometry, creating a suitable grid over the computational domain, running the flow-solver, checking solution convergence, and post-processing to extract desired quantities from the outputs. The 2D and 3D results are presented which show effects from geometry, including wing sweep, and flow parameters. Selected results are shown in more detail using flow visualization and/or spanwise local lift coefficient distributions.

5.3.9.3 Background: NASA Tetrahedral Unstructured Software System

The NASA Tetrahedral Unstructured Software System (*TetrUSS*) [14] is a package of loosely integrated software, developed to allow rapid aerodynamic analysis from simple to complex problems. The system has its origins in 1990 at the NASA Langley Research Center and has won the NASA Software of the Year Award twice. *TetrUSS* has been used on high priority NASA programs such as Constellation and the new Space Launch System for aerodynamic database generation along with work in the Aviation Safety Program. The component software packages are assembled such that a user follows a systematic process during each application of *TetrUSS*. There are software packages for preparing geometries for grid generation (*GridTool*), generating unstructured surface and volume grids (VGRID) and calculating flow solutions (USM3D). Post-processing the solutions with *TetrUSS* can be done using the included *SimpleView* software or by easily converting for use with other commercial packages (eg *Tecplot*, *EnSight* etc.). For preparing geometries for grid generation, *GridTool* is used to generate the necessary *VGRID* [15] input files.

GridTool can read ***Non-uniform Rational B-Spline (NURBS)*** curves and surfaces through an Initial Graphics Exchange Specification (IGES) file, as well as PLOT3D point cloud surface definitions. The geometric surfaces are then defined by way of surface patch construction. Each patch has a specified boundary condition such as a viscous or inviscid surface and a family definition for users to group related patches together. Grid spacing parameters are also defined and controlled within *GridTool*. Sources are placed in three dimensional space by a user in order to control the size and growth rates of the tetrahedral cells. Numerous classes of sources are available to control the grid topography. Nodal sources and line sources are typically used in most cases, while volume sources are available for use in specific cases requiring control over a large volume of the domain. Other parameters defined in *GridTool* are the viscous layer spacing parameters and the maximum and minimum tetrahedral sizes. VGRID is the unstructured grid generation tool used in the *TetrUSS* Package. Viscous layer generation is accomplished via the ***Advancing Layers Method (ALM)*** [16]. Tetrahedral cells are generated in an orderly manner, "marching" nodes away from the surface. The size and growth of these cells is controlled by **:**

$$\Delta z_{i+1} = \Delta z_1 \left[1 + a(1+b)^i\right]^i$$

Eq. 5.3.4

In this equation, the height of the *ith* layer is determined by an initial spacing parameter, Δz_1, and two stretching/growth factors *a* and *b*. Once the height of the *ith* layer reaches the size of the background sources specified by the user in *GridTool*, no more cells are formed and viscous layer generation is complete. After the viscous layers are generated, VGRID then utilizes the Advancing Front Method (AFM) [17] for the generation of the inviscid portion of the volume grid. VGRID cannot always close the grid completely. When this occurs, a slower but more robust auxiliary code called *POSTGRID* is used to complete the formation of the remaining tetrahedral cells. The flow solver at the core of the *TetrUSS* package is *USM3D* [18]. *USM3D* is a parallelized, tetrahedral cell centered, finite volume Reynolds Averaged Navier-Stokes (RANS) flow solver. It computes the finite volume solution at the centroid of each tetrahedral cell and utilizes several upwind schemes to compute inviscid flux quantities across tetrahedral faces. USM3D has numerous turbulence models implemented for use; the *Spalart-Allmaras* (SA) one equation model and ***Menter Shear Stress Transport*** (SST) two equation model were used in this study. Some additional capabilities that *USM3D* has implemented are dynamic grid motion and overset grids.

5.3.9.4 Methodology: Developing the Aerodynamic Database

The aerodynamic database is desired to have high fidelity flow solutions for a wide variety of 2D airfoils and 3D geometries. Flow solutions would include a large range of angles of attack to encompass pre-stall, stall and post-stall flow regimes. The data gained from these simulations will be vital in assisting the further development and validation of the low-order method mentioned in the introduction as well as to fill gaps in the currently available high angle of attack aerodynamic data for arbitrary geometries. An efficient process to go from a geometry to a converged flow solution was developed and is discussed in the following sub-sections.

5.3.9.4.1 Geometry Generation

Traditional ***Computer Aided Design (CAD)*** software would be more than adequate for the creation of the desired geometries, however these tools are not geared specifically towards the modeling of wings and airfoils. Understanding this, the recently released parametric modeling tool, Open Vehicle Sketch Pad (*OpenVSP*) [19], was chosen as the geometry generation tool. A flow chart showing the process of geometry generation can be seen in **Figure 5.3.4**. *OpenVSP* is a modeling package developed and released by NASA Langley Research Center in Hampton, Virginia. The unique concept that *OpenVSP* provides is that it allows a user to drag and drop generic aircraft components (such as a wing) into the modeling area, and directly manipulate familiar geometric parameters. Consequently, it is simple to insert a wing, change its root chord, tip chord, span, etc. and view the resulting geometry in real time. Aerodynamic reference quantities can also be automatically calculated for the user. Airfoils cross section generation is also simplified. A user can select any 4 or 5 digit series NACA airfoil or load in a formatted airfoil coordinate file for use on any lifting surface.

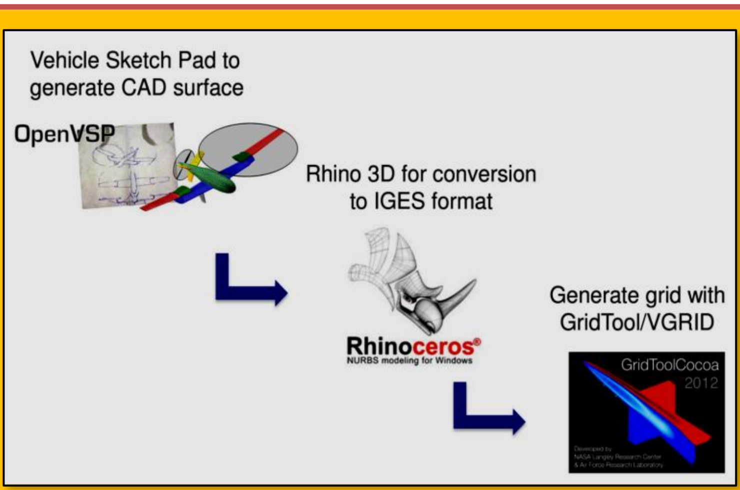

Figure 5.3.4 Process of Geometry Generation To Grid Generation

The 3D wing and corresponding airfoil for each case to be analyzed were generated in *OpenVSP*. In order to read the geometry into *GridTool*, the file must be in the IGES format. Vehicle Sketch Pad does not output IGES files, thus each geometry must be exported as a *Rhino3D* formatted file. The Rhinoceros NURBS modeling package was used to convert the geometry into the necessary IGES file as well as make small modifications to the geometry. Some grid generation failures were encountered due to how *OpenVSP* closes the trailing edge of the wing/airfoil geometries (it always forces a sharp trailing edge). In some cases the sharpness had to be removed to ensure successful grid generation.

5.3.9.4.2 Grid Generation

Grid generation parameters were generalized such that, between different geometries, parameters such as source placement and viscous spacing had minimal required changes. This meant that from initial geometry generation to a completed grid would require only a matter of hours. Establishing this commonality and routine for grid generation enabled the generation of adequate grids for many configurations in a short time span. An example placement of sources for a simple tapered wing is shown in **Figure 5.3.5**. A series of line sources are utilized, in the spanwise direction of each wing at differing chord-wise locations. Anisotropic stretching [20] as high as 10:1 was used near the root of the wing, transitioning to isotropic cells near the wing tips. For viscous tetrahedral layer generation, the height of the first layer (Δz_1) is Reynolds number dependent. A viscous layers spacing tool called *USGUTIL*, was used to determine the height of the initial viscous layer. In order to have adequate number of cells in the viscous layers, the $y+$ of the first node was set to be 3, this would ensure that the $y+$ of the first cell center would be less than 1 (approx. 0.75) as is required for a fully viscous Navier-Stokes solution. The values used for the grid growth parameters (a and b) in **Eq. 5.3.4** were 0.15 and 0.02 respectively [20]. A grid sensitivity study was performed on a rectangular wing with aspect ratio of 12 to determine adequate grid sizing. It was found that a grid sizing of 5–9 M[117] tetrahedral cells showed changes in $C_{L,max}$ of approximately 0.02 between the grids. This method of grid generation was applied to all 3D wing geometries with the typical grids averaging between 9–12 M tetrahedral cells.

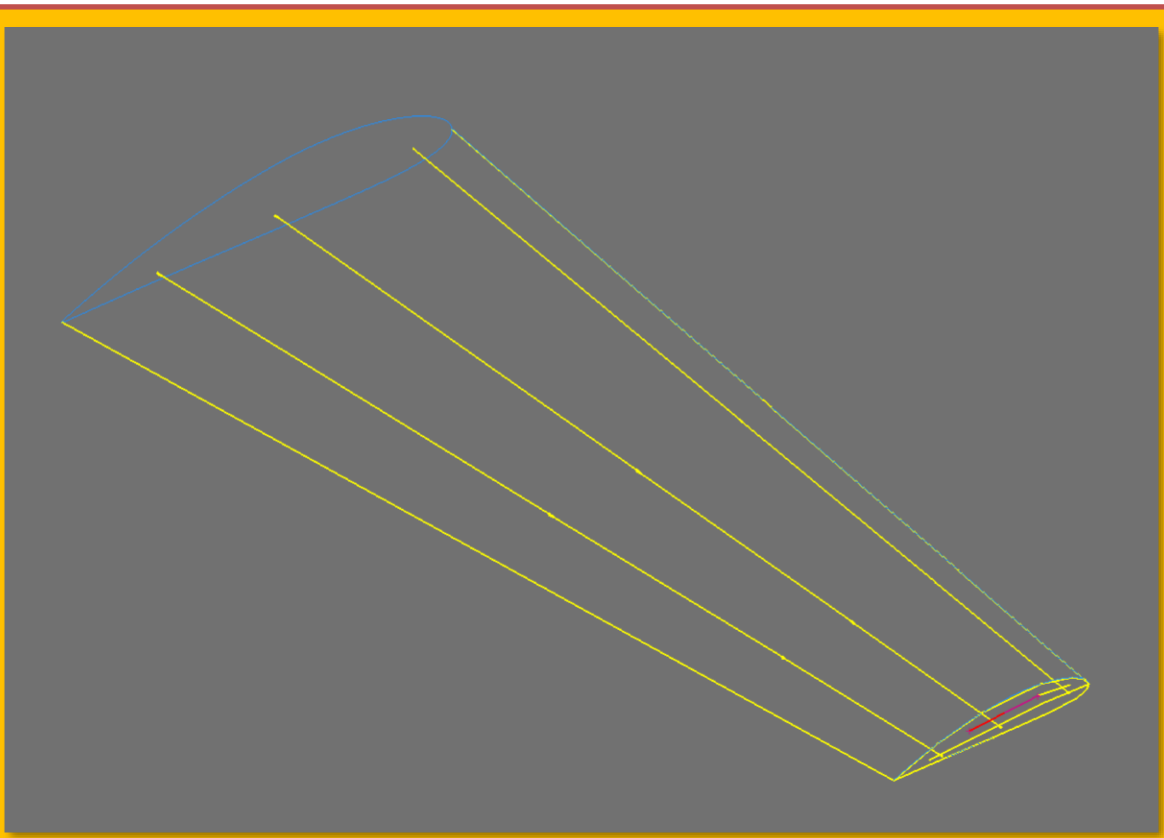

Figure 5.3.5 Screen Capture of *Gridtool* Source Placement On A Tapered Wing

---

[117] M = million

For airfoil calculations, a quasi 2D grid was generated on a constant-chord, short-span wing, between two reflection plane boundary condition patches. **Figure 5.3.6** shows a completed grid for an NACA 0012 airfoil. A general goal was set to maintain very similar grid density between the 3D wing grids and the airfoil grids. This is necessary because the airfoil results were being used as input data into the low-order method discussed in the introduction while the 3D wing results from *USM3D* were being used to assess the accuracy of the low-order method (**Figure 5.3.3**). Therefore a separate grid sensitivity study was not performed specifically for airfoils. Typical airfoil grids were on the order of 300,000 tetrahedral cells and were generated using a nearly identical source placement as the 3D wing.

5.3.9.4.3 Flow Solution Generation

All solutions with the USM3D solver were computed with time-accurate Reynolds-Averaged Navier-Stokes (RANS). The limitations of RANS for modeling massively separated flows are well known. The more preferred ***Detached Eddy Simulation*** (DES) modeling will provide better physical representation of 3D separated flow, but with an order-of magnitude more expense. Since this investigation requires generation of many flow solutions, the initial focus is to determine if time-accurate RANS can provide sufficient engineering accuracy for capturing the salient aerodynamic characteristics of wings at stall and post-stall conditions. Furthermore, a consistent modeling is desired between the 2D airfoils and 3D wings.

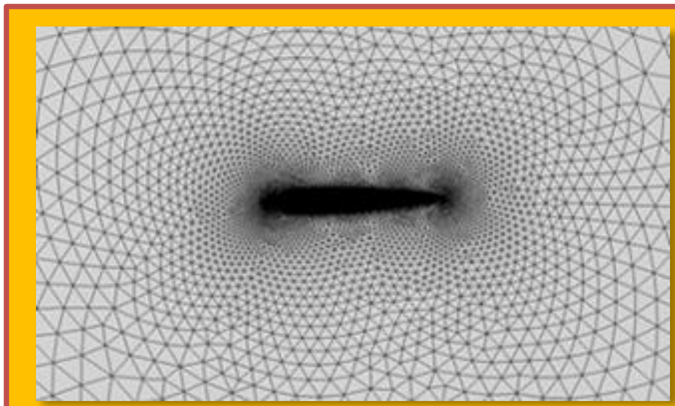

Figure 5.3.6 Screen Capture of Airfoil Grid

All computations were advanced at a characteristic time step of $\Delta t^* = \Delta t \bullet U_\infty/C_{ref} = 0.02$ using a second order time-accurate scheme with three-point backward differencing and physical time stepping. The number of sub iterations for each time step was set to between 10 and 15 to ensure

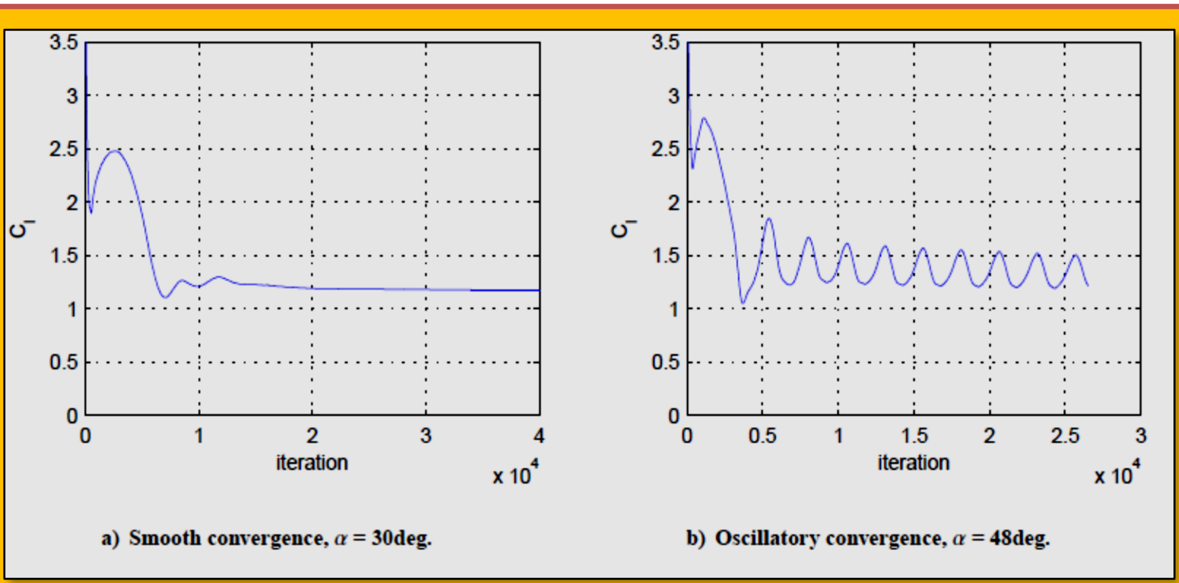

a) Smooth convergence, $\alpha = 30$deg.

b) Oscillatory convergence, $\alpha = 48$deg.

Figure 5.3.7 Typical *USM3D* convergence of lift coefficient for an airfoil. NACA 4415, *USM3D*/SA, Re = 3×10^6, $M_\infty = 0.2$

adequate sub-iteration convergence. The *Spalart-Allmaras* (SA) [21] one equation turbulence model was used almost exclusively, however some simulations were performed with the two equation SST turbulence model to understand the difference in final solution quantities. The solver was run on both a NASA Langley computer cluster and the North Carolina State University High Performance Computing (NCSU HPC) cluster. Making use of *USM3D's* parallel computation capabilities, each grid was partitioned into 28-64 equal zones which could be loaded onto 28–64 individual processors, reducing calculation times significantly. To further increase productivity, a series of Unix scripts were developed to generate the required input files for job submission and minor post-processing of completed jobs.

5.3.9.4.4 Solution Convergence

Convergence of the solutions was monitored by generating convergence plots such as that seen in the **Figure 5.3.7**. Unix scripts were used to compile all of the convergence information contained in the *USM3D* output files into a *Tecplot* format. Each plot showed the logarithm of the residual over each iteration and the changes in the aerodynamic coefficients. The criteria for a fully converged solution was for each plot to show a leveling off of the quantities under consideration. These plots allowed for rapid determination of whether any given solution had reached a converged state (**Figure 5.3.7 a**) or if the solution had attained an unsteady solution shown by oscillatory convergence (**Figure 5.3.7 b**).

5.3.9.4.5 Post-Processing

After solution convergence was verified, the data is processed so that total forces and moments, the spanwise distribution of forces and moments, and flow visualization may be studied. As was previously mentioned, in some cases an oscillatory solution develops rather than single steady-state values for the forces and moments. This has only been observed for 2D airfoil solutions at very high angles of attack. To handle such cases, a method had to be developed in order to address these oscillations.

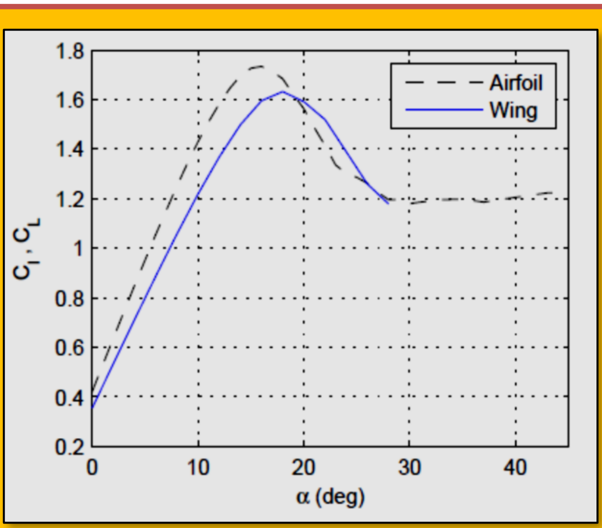

Figure 5.3.8 Comparison of lift coefficients for 2D airfoil (NACA 4415) and AR = 12 rectangular wing at RE = 3 million.

1. Forces and moments acting on the entire wing/configuration

The first outputs of interest are the total force and moment coefficients acting on a wing/configuration. A script was used to extract the body-axis force and moment coefficients [C_X C_Y C_Z C_{Mx} C_{My} C_{Mz}], defined parallel and perpendicular to the body coordinate system, and stability-axis coefficients [C_L C_D], defined parallel and perpendicular to the free-stream velocity. **Figure 5.3.8** shows an example of lift coefficient results for a 2D airfoil and a 3D wing which used the same airfoil cross section.

2. Span-wise distribution of forces on a surface

The other output of interest is the span-wise distribution of force coefficients, particularly the span-wise lift coefficient. The *PREDISC* utility [22], was used for extracting this information. *PREDISC* simultaneously loads the grid files containing the surface grid and a converted *TetrUSS* solution file containing only surface data. Data extraction planes can be arbitrarily defined (see **Figure 5.3.9**) and *PREDISC* will output surface pressure and skin friction coefficients, C_p and C_f

respectively, along the surface discretized according to a fine mesh of x/c, y/c locations. The surface pressure and skin friction coefficients are integrated to approximate body-axis force coefficients. An example lift coefficient distribution obtained by integrating the C_p and C_f values at each extraction plane is shown in **Figure 5.3.9**.

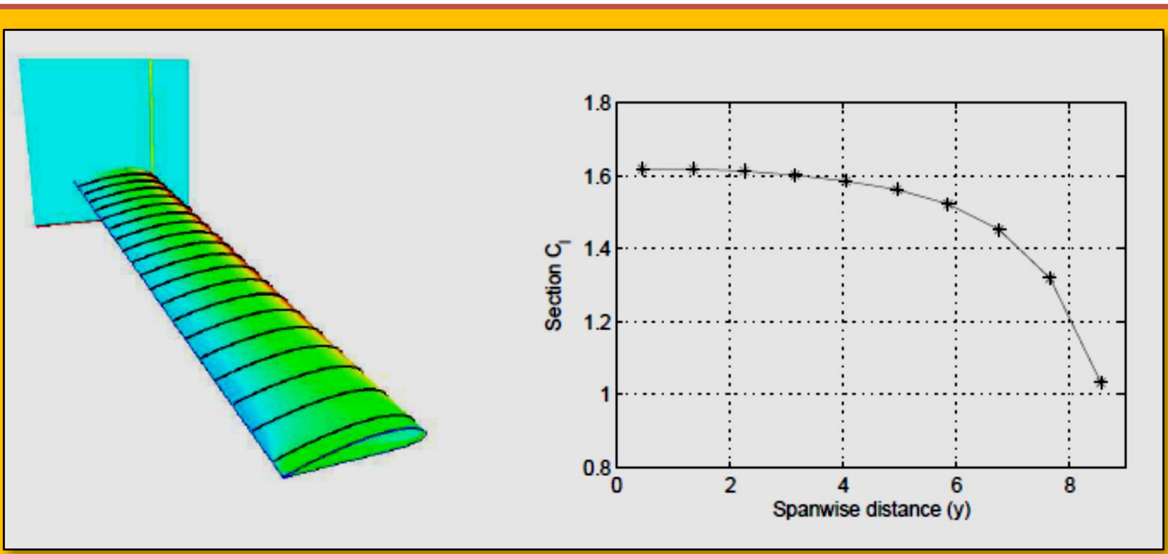

Figure 5.3.9 Screen shot of *PREDISC* code (left) showing defined data extraction planes and a plot of the extracted spanwise C_l distribution (right) on a rectangular wing AR = 12.

5.3.9.5 Results

The results shown in this section represent the current level of development of the CFD database. The results from analysis of 2D airfoil CFD solutions for cambered, symmetric and thin airfoils will be presented along with 3D wing solutions with rectangular, tapered and swept planforms.

5.3.9.5.1 2D Airfoil Results

Three different airfoils have been studied and added to the CFD aerodynamic database to date. Additional airfoils will be added as needed for further development of the database and as required for validation of the low-order post-stall method discussed previously. The airfoils chosen exhibit different stall and post-stall behavior and offer insight on how certain airfoil geometries will tend to behave at high angles of attack. Results for a symmetric airfoil (NACA 0012), a cambered airfoil (NACA 4415) and a very thin airfoil (NACA 63006) are shown in this section. The geometries of the airfoils are shown in **Figure 5.3.10.**

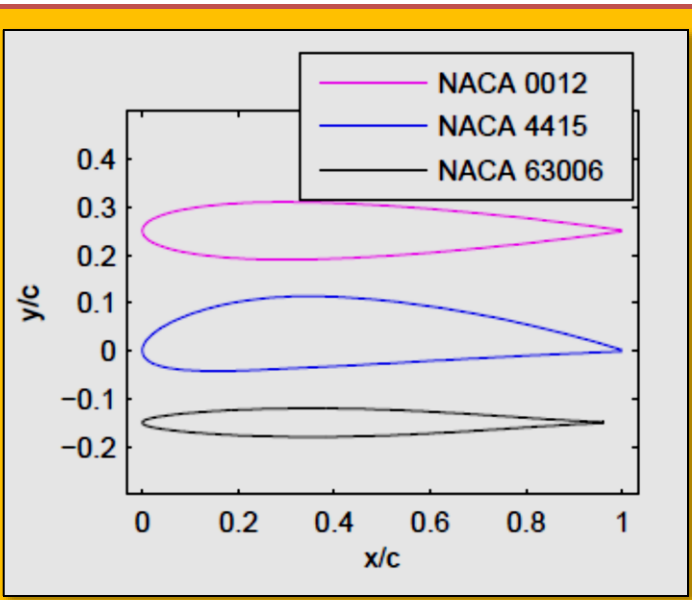

Figure 5.3.10 Comparison of Airfoil Geometry For The Three Cases Studied

One interesting phenomenon that was encountered while developing the airfoil database, was the tendency for the airfoil solutions to exhibit oscillatory behavior in the force and moment convergence histories at angles of attack of approximately 40 degrees and above. The cause of these oscillations was determined using flow visualization which revealed periodic vortex shedding from the upper surface of the airfoil. A process to average the oscillatory behavior and determine peak to peak amplitudes was established. A post-processing MATLAB script was developed to read all of the force and moment history files for an airfoil and detect the oscillatory behavior. For any angle of attack that displayed this behavior, the script identified two complete cycles at the end of the convergence history and determined the mean value along with the peak to peak amplitude. The plots in **Figure 5.3.11** illustrate the approach used for the processing of the raw CFD data with this code.

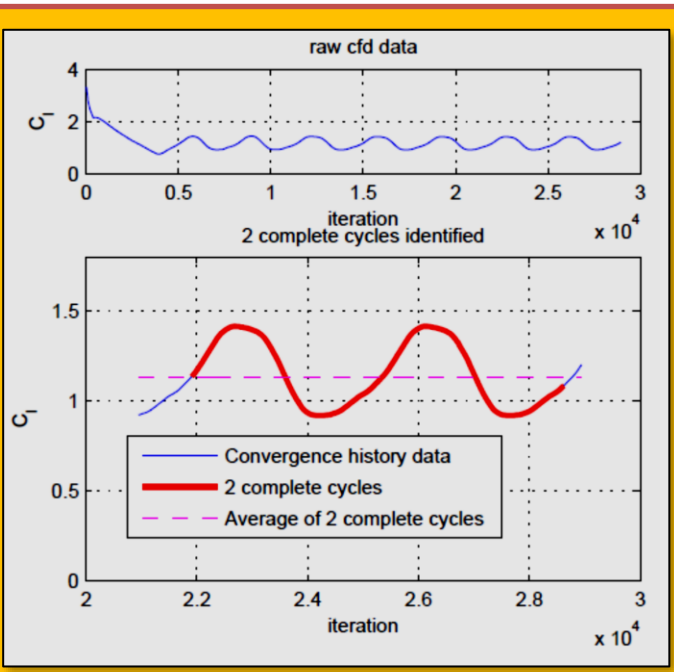

Figure 5.3.11 Illustration of approach used for averaging oscillator airfoil CFD convergence history

1. Reynolds Number Effects Through Post-Stall

The general effects of Reynolds number on the aerodynamic quantities, specifically $C_{l,max}$, are known and have been observed with the current work as well. However, it is important to extend this to the post-stall region. **Figure 5.3.12** shows a comparison of the lift curves for the NACA 4415 airfoil at three different Reynolds numbers (3, 6 and 10 M[118]). The increased maximum lift coefficient with increased Reynolds number is expected. In the post stall region between angle of attack of 40 and 70 degrees, an additional effect of the Reynolds number is seen. The region falls directly where the oscillatory solutions develop; the values shown in **Figure 5.3.12** are the averaged values from any oscillating data. After this recovery region, the solutions tend to follow a similar path out to 90 degrees.

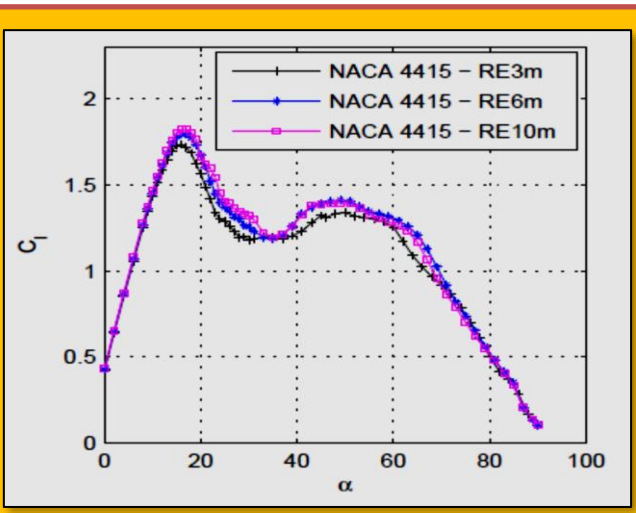

Figure 5.3.12 Effect of Reynolds number on lift coefficient for an NACA 4415 airfoil. USM3D/SA, M_∞ = 0.2

2. Sharp vs. Blunt Trailing Edge Geometries

It has been noted by Hoerner [23], that the trailing edge shape of an airfoil has a distinguishable effect on the C_l vs. _ curve. When comparing an airfoil with a sharp trailing edge with the same airfoil but with a blunt trailing edge, it is found the

---

[118] M = million

maximum lift coefficient is seen to be higher for the blunt trailing edge airfoil. The plot in **Figure 5.3.13** displays results for an NACA 4415 airfoil with both a sharp and blunt trailing edge at a Reynolds number of 3 M. The blunt TE geometry was generated by removing the final one percent of the chord of the sharp trailing edge geometry, thus no other alterations to the geometry are present. The expected trend is seen with the blunt trailing edge case having a higher maximum lift coefficient. It is interesting to see that this effect seems to continue all the way past stall and through to approximately α = 70 degrees, after which the lift curves coincide. The flow mechanism that allows for this all the way through post stall is not readily apparent from the CFD at this time, but warrants further investigation.

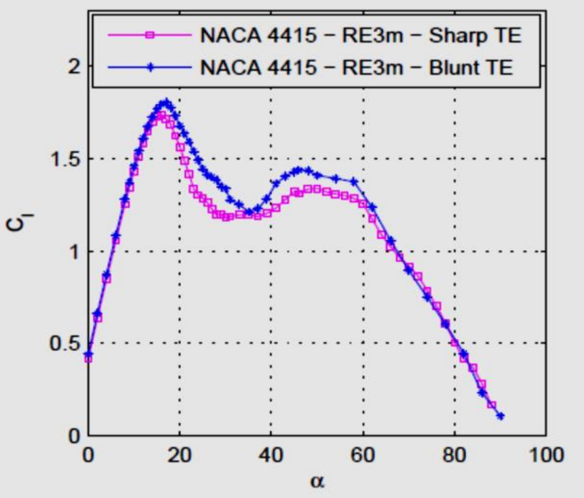

Figure 5.3.13 Effects of trailing-edge sharpness for an NACA 4415 airfoil. USM3D/SA, Re = 3 million, $M\infty$ = 0.2

3. Comparison of Post-Stall Characteristics of Three Airfoil Geometries

Airfoils that exhibit different characteristics in terms of maximum lift coefficient and stall behavior were analyzed for addition to the post-stall database. In **Figure 5.3.14-a**, lift curves for three airfoils are shown from 0 to 90 degrees angle of attack. A cambered airfoil (NACA 4415), a symmetric airfoil (NACA 0012) and a very thin airfoil (NACA 63006) are compared in the figure. The NACA 4415 and NACA 0012 both exhibit trailing edge stall behavior. That is, flow separation begins at the trailing edge and progresses towards the leading edge as the angle of attack increases.

This can be seen in the lift curves as both the airfoils have a relatively "gentle" stall. It is interesting to note that although the NACA 4415 airfoil has a higher $C_{l,max}$ as compared to the NACA 0012, the two airfoils have very similar maximum recovery lift coefficients at approximately 50 degrees angle of attack. The NACA 63006 produced a much more unusual lift curve. This airfoil is categorized as

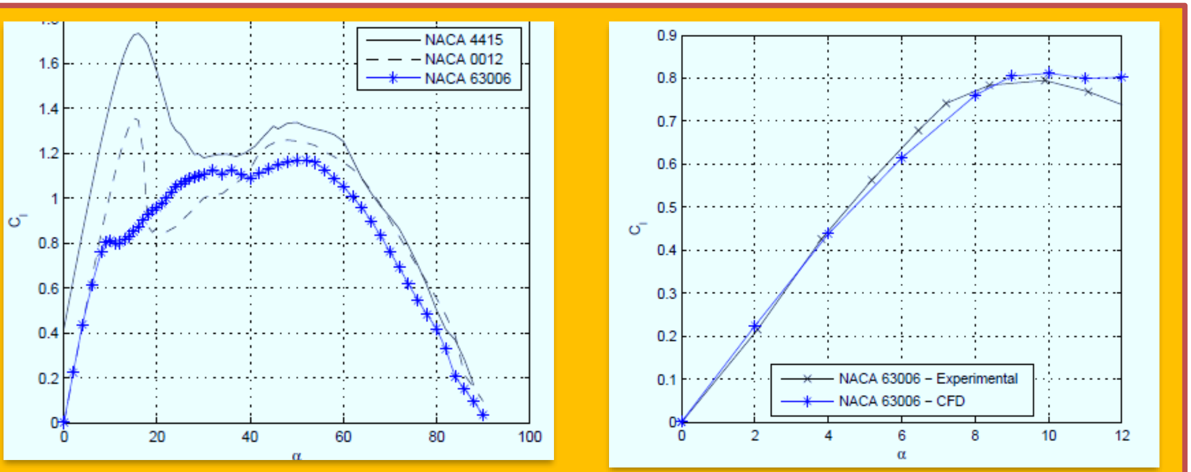

(a) 3 airfoil types. USM3D/SA, Re = 3 M, M_∞ = 0.2

(b) CFD and experiment for the NACA 63006 thin airfoil.

Figure 5.3.14 Comparison of C_l vs. α

having "thin airfoil" stall characteristics. Due to the presence of a severe adverse pressure gradient around the leading edge at even low angles of attack, the flow over the upper surface completely separates. This sudden onset of flow separation can been seen by the sudden leveling of the lift coefficient at around 10 degrees. After this initial "stall", the airfoil recovers past the initial stall lift coefficient and reaches nearly the same maximum recovery C_l at $\alpha = 50$ degrees as the NACA 4415 and NACA 0012. The differences seen between these three airfoils in the 40 to 60 degree range can mainly be attributed to thickness, camber and leading-edge radius effects.

An enlarged plot of the NACA63006 in the region of incipient stall is shown in **Figure 5.3.14-b** with comparison to experimental data obtained from Abbott and von Doenhoff [1] and also noted by Hoerner [23]. It should be noted that since the CFD solutions were fully turbulent (no transition model was used) no evidence or effects of a laminar separation bubble near the leading edge were modeled, a phenomenon noted by Leishman and in other studies of similar airfoils [24].

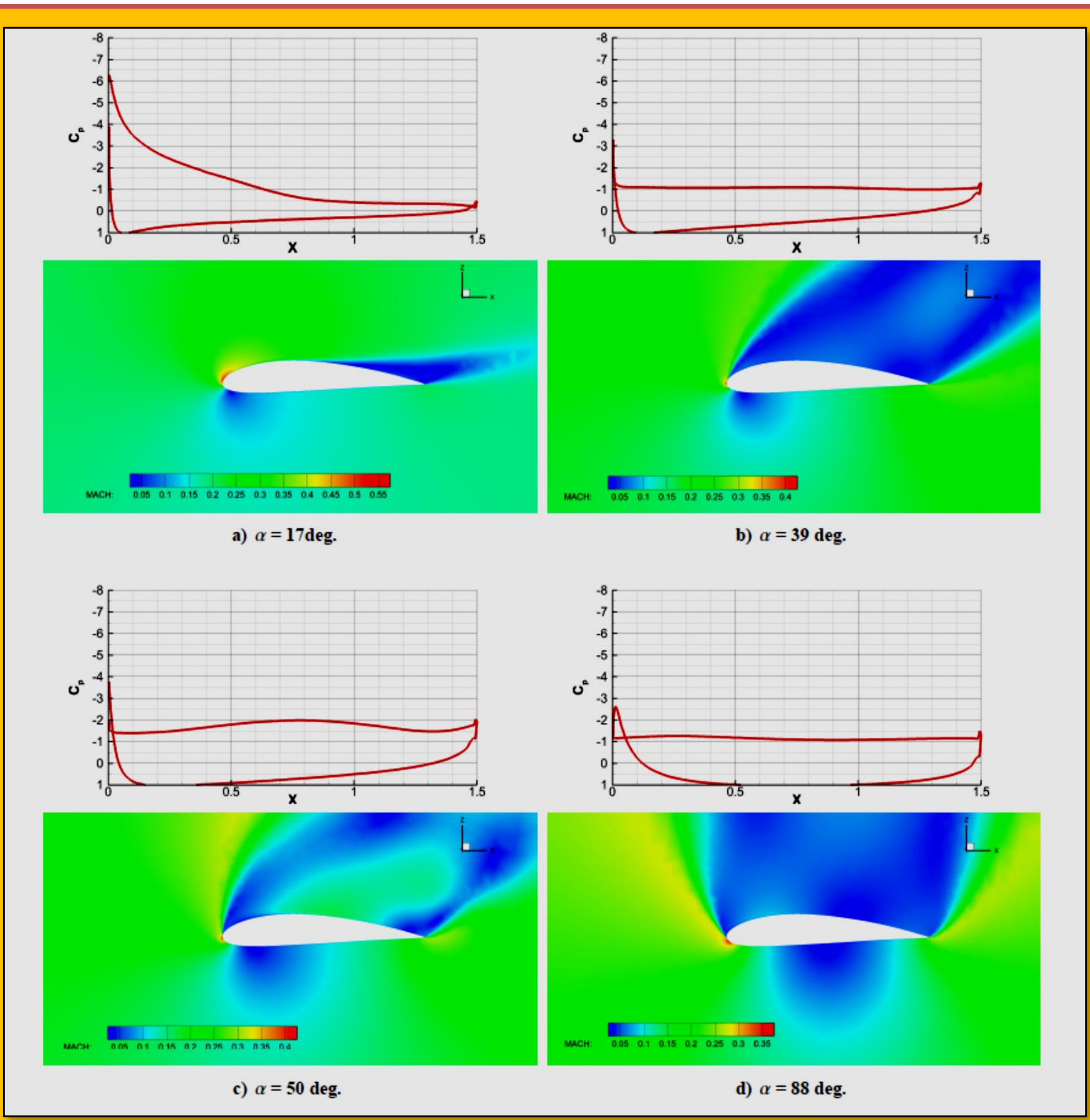

a) $\alpha = 17$deg.

b) $\alpha = 39$ deg.

c) $\alpha = 50$ deg.

d) $\alpha = 88$ deg.

Figure 5.3.15 Mach contours and C_p distribution for a NACA 4415 airfoil. USM3D/SA, Re = 3 M, $M_\infty = 0.2$

Figure 5.3.15 and **15** show Mach number contour plots along with surface C_p distributions for the NACA 4415 and NACA 63006 airfoils at different stages along their respective lift curves. The NACA 4415 flow visualization in **Figure 5.3.15** at α = 17 degrees. ($C_{l,max}$) shows the presence of trailing edge stall propagating forward along the chord. This is also evident in the C_p distribution. As the angle of attack is extended above stall and into post-stall, a large wake region is seen to develop accompanied by a loss of much of the suction peak. At α = 50 deg a snapshot of the Mach contours and C_p distribution show the unsteady behavior that exists. At α = 88 degrees the solution shows massively separated flow typical of bluff bodies. A small suction peak is still generated around the leading edge resulting in a small amount of lift generation.

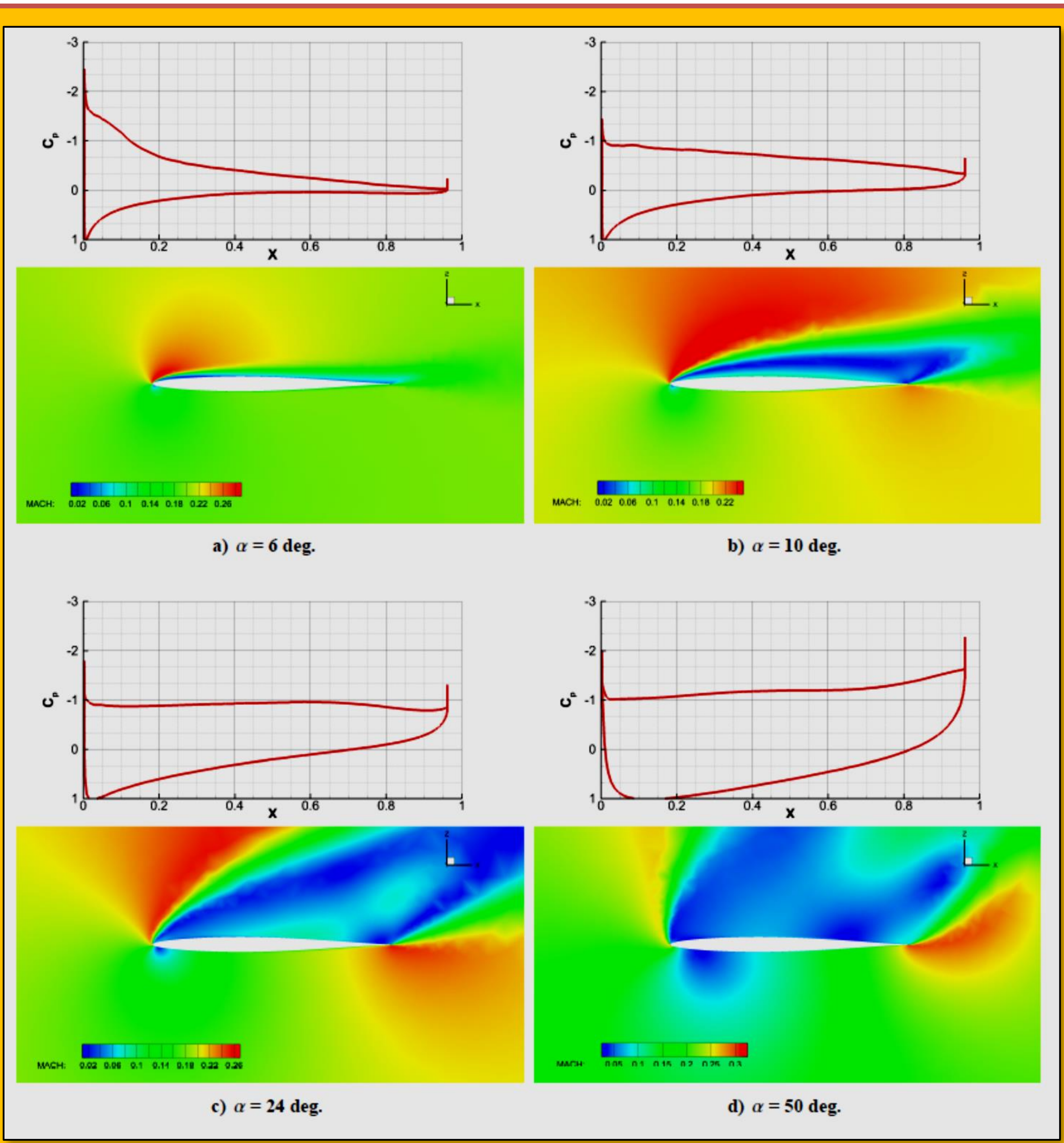

a) $\alpha = 6$ deg.

b) $\alpha = 10$ deg.

c) $\alpha = 24$ deg.

d) $\alpha = 50$ deg.

Figure 5.3.16 Mach contours and *Cp* distribution on a NACA 63006 airfoil. USM3D/SA, Re = 3M, M_∞ = 0.2

The flow visualization of the NACA 63006 CFD solutions in **Figure 5.3.16** provides an interesting view of thin-airfoil stall behavior. It can be seen from **Figure 5.3.16** that, at $\alpha = 6$ degrees, there is a significant suction peak followed by a steep adverse gradient. The leading edge at this angle of attack shows a small area of separated flow. Looking back at **Figure 5.3.14**, a slight change in the slope of the lift curve can be identified in this region. At 10 degrees angle of attack, the flow on the upper surface is completely separated; this corresponds with the maximum lift coefficient prior to the airfoil entering into the recovery region in post-stall. The C_p distribution at 24 degrees angle of attack shows a larger internal area signaling an increase in the normal force generated, the majority of which still falls along the lift direction. The airfoil reaches another "$C_{l,max}$" at approximately 50 degrees and also shows unsteady characteristics.

5.3.9.5.2 3D Wing Results

Results of various 3D wing geometries are presented in the following subsection. The plots in **Figure 5.3.17 (a-b)** display the lift curves for multiple wing planform geometries. Only a subset of the geometries have been run completely to 90 degrees due to the extensive run time of the solutions and the limited availability of computing nodes. The effects of both taper and sweep have been studied. The database will eventually include wing geometries that have a combination of both sweep and taper, similar to civilian transport aircraft. This data will be of interest to continuing efforts aimed at improving safety of transport aircraft. Detailed spanwise load distributions and surface streamline flow visualizations are presented in this paper for three wings of AR = 12 with rectangular, tapered and swept planforms.

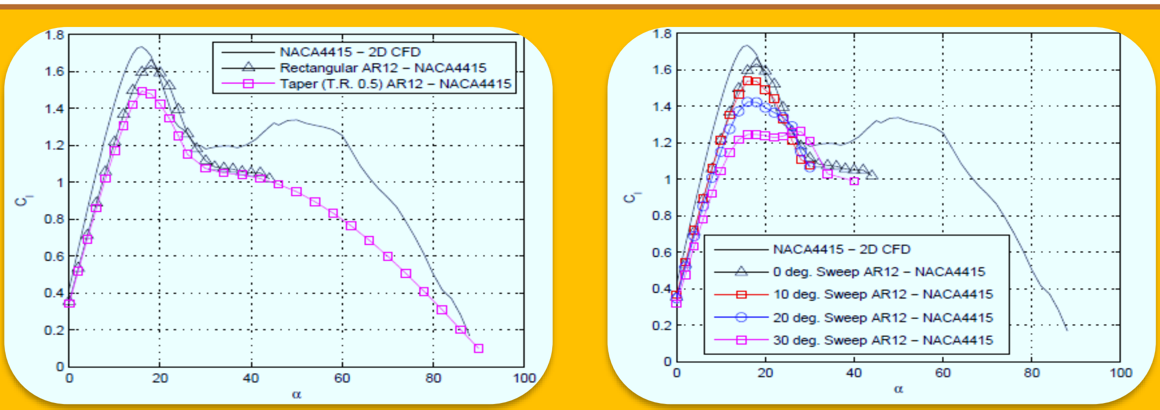

(a) Effect of taper on unswept wings

(b) Effect of sweep on constant-chord wings

Figure 5.3.17 C_L vs. α USM3D/SA, Re = 3 M , $M_\infty = 0.2$

1. Rectangular Wing

The results presented are for a rectangular wing with an aspect ratio of 12 and an NACA 4415 airfoil cross section. The solutions for this case were produced for a Reynolds number of 3 M based on the chord and a Mach number of 0.2. The plots in **Figure 5.3.18** show a snapshot of the spanwise C_L distributions calculated from the time-accurate CFD solutions for angles of attack near stall and into post-stall. It is seen that at an angle of attack of 18 degrees, a sawtooth pattern in the C_L distribution is present. The extent of this sawtooth pattern seems to grow at 22 degrees and 28 degrees. Correlating these load distributions with flow visualization at the same angles of attack enlightened the reason for the sawtooth patterns. Through the use of surface streamlines it can be seen in **Figure**

5.3.19 that as the angle of attack increases, reversed flow is seen aft of the separation line and shows the presences of multiple stall cells forming along the semi-span of the wing. This causes certain sections along the wing to have more attached flow than others, generating the oscillations in the local lift coefficients going from the root to the tip. This stall cell formation eventually dissipates as the flow over the upper surface becomes fully separated and the region of reversed flow reaches the

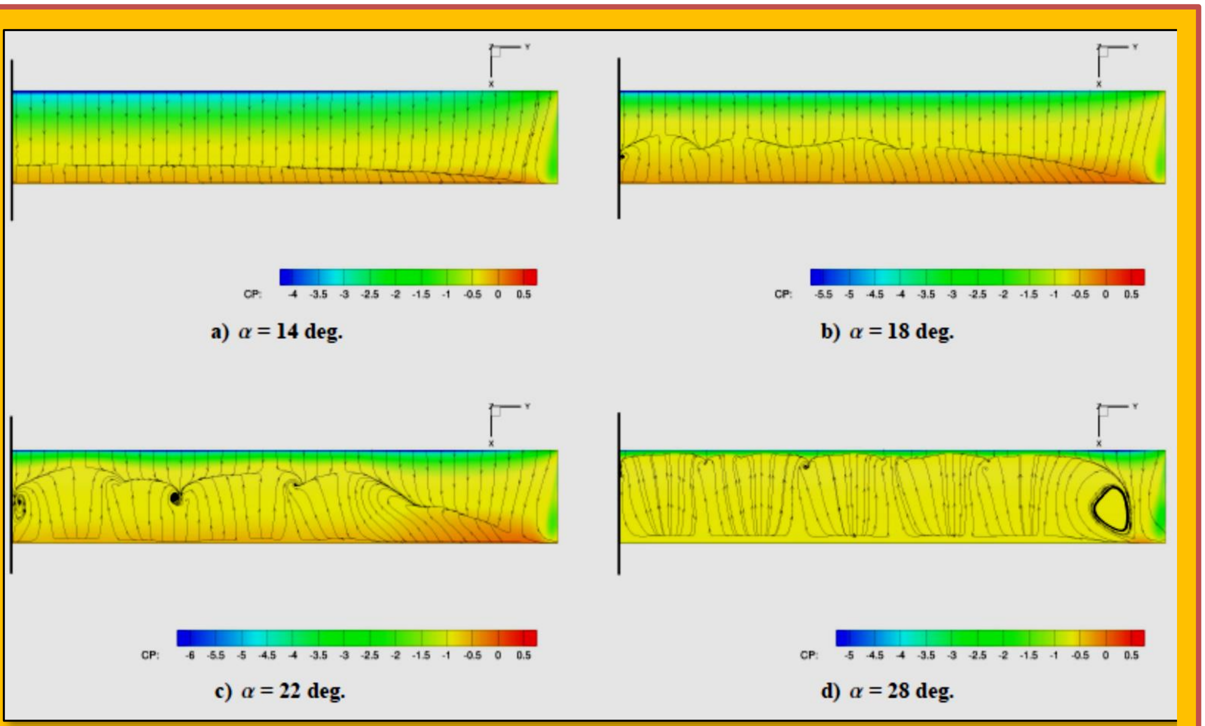

Figure 5.3.18 Cp contours and surface streamlines on a tapered wing, λ = 0.5, AR = 12, symmetry plane indicated by black line. USM3D/SA, Re = 3 M, M_∞ = 0.2.

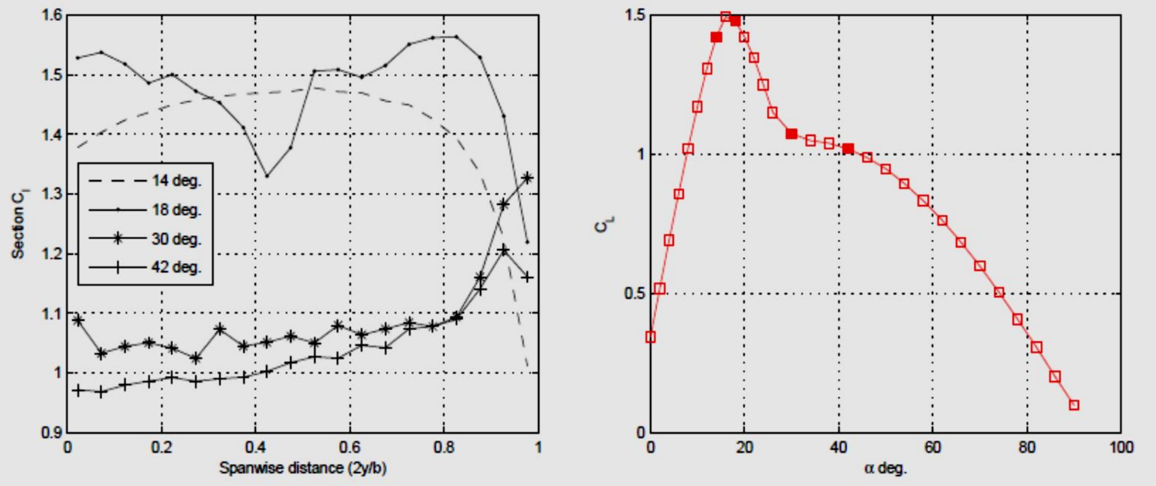

a) Local C_l distribution at various angles of attack

b) Corresponding points on C_L vs. α curve

Figure 5.3.19 Comparison of local Cl distribution at varying angles of attack for a tapered wing, λ= 0.5 and AR = 12. USM3D/SA, Re = 3 M, M∞ = 0.2.

leading edge of the wing as can be seen at 28 degrees. The streamlines in **Figure 5.3.19** seem to suggest that even in high angle of attack situations the surface flow is still relatively in the chord-wise direction for the majority of the semi-span. There are some variations near the borders of stall cells and near the wing tip as would be expected due to the influence of the tip vortex.

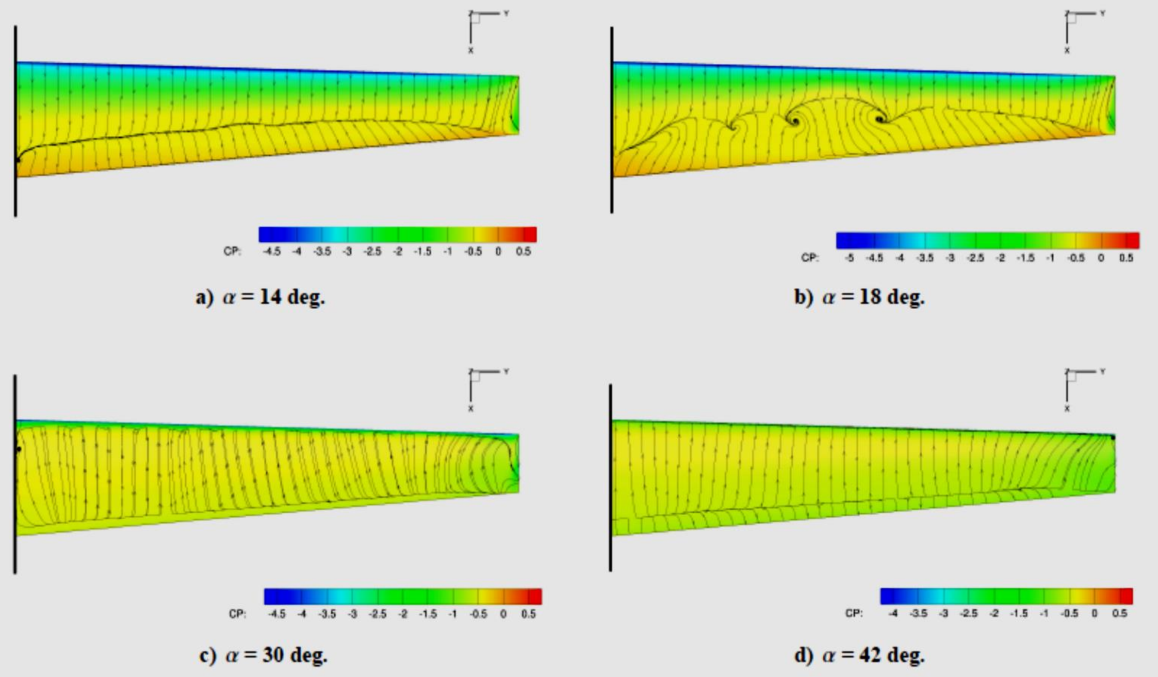

a) $\alpha = 14$ deg.

b) $\alpha = 18$ deg.

c) $\alpha = 30$ deg.

d) $\alpha = 42$ deg.

Figure 5.3.20 Comparison of local Cl distribution at varying angles of attack for a tapered wing, λ = 0.5 and AR = 12. USM3D/SA, Re = 3 M, M∞ = 0.2

2. Tapered Wing

Results for a tapered wing with a taper ratio of 0.5 and aspect ratio of 12 are presented in **Figure 5.3.20** and **Figure 5.3.21**. This wing also has the same NACA 4415 airfoil cross section and the solutions were generated for a Mach number of 0.2 and Reynolds number of 3 M based on the mean aerodynamic chord. The C_l distributions in **Figure 5.3.20** show that the highest C_l is seen near the middle of the semi-span at 14 degrees angle of attack.

Such increases in local span C_l can be an indicator of impending stall in that region. As anticipated, a stall cell develops near this high C_l area of the semi-span at 18 degrees, which is denoted by the severe drop in the local lift coefficients. Looking at the surface streamlines in **Figure 5.3.21** shows the existence of the stall cell as predicted by CFD. Similar to the rectangular case, these stall cells disappear once the angle of attack is high enough that the flow on the upper surface is entirely separated. Chord-wise reversed flow is still seen along the majority of the semi-span at highly separated conditions.

3. 30 Degree Swept Wing

Results are presented for a swept wing case with 30 degrees of sweep, an aspect ratio of 12 and an NACA 4415 cross section parallel to the plane of symmetry. The solutions were generated at a Mach number of 0.2 and Reynolds number of 3 M. Spanwise C_l distributions are shown in **Figure 5.3.22**

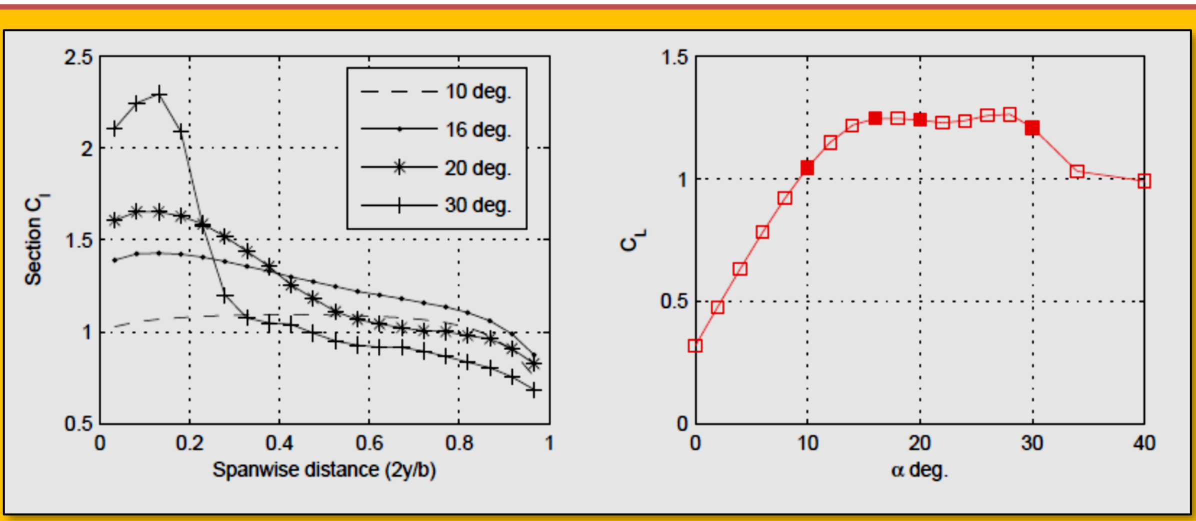

Figure 5.3.21 Comparison of local Cl distribution at various angles of attack on a swept wing, Λ = 30 deg., AR = 12. USM3D/SA, Re = 3 M, M_∞ = 0.2

Stall progression from near the tip of the wing towards the inboard sections of the wing is evident and expected. As the angle of attack increases to 30 degrees the inboard local lift coefficients (calculated here based on a streamwise section, not chord-wise) are well above observed maximum lift coefficient seen for the NACA 4415 2D airfoil CFD solutions (app. 1.75). This phenomenon however has been observed in past studies of swept wings. Hunton and James [25] as well as Harper and Maki [10] note this same behavior, which is most pronounced at inboard sections near the root, but can occur along most of the semi span.

They describe this as an effect of a ”natural boundary-layer control” that delays stall on the inboard section of a swept wing. It should also be noted that the percent increase in the local sectional $C_{l,max}$ goes up with the sweep angle. Evidence of this delayed stall near the root of the 30 degree swept wing can be seen in **Figure 5.3.23**. The inboard section does not show significant flow separation even at 30 degrees angle of attack, while the rest of the wing is fully separated.

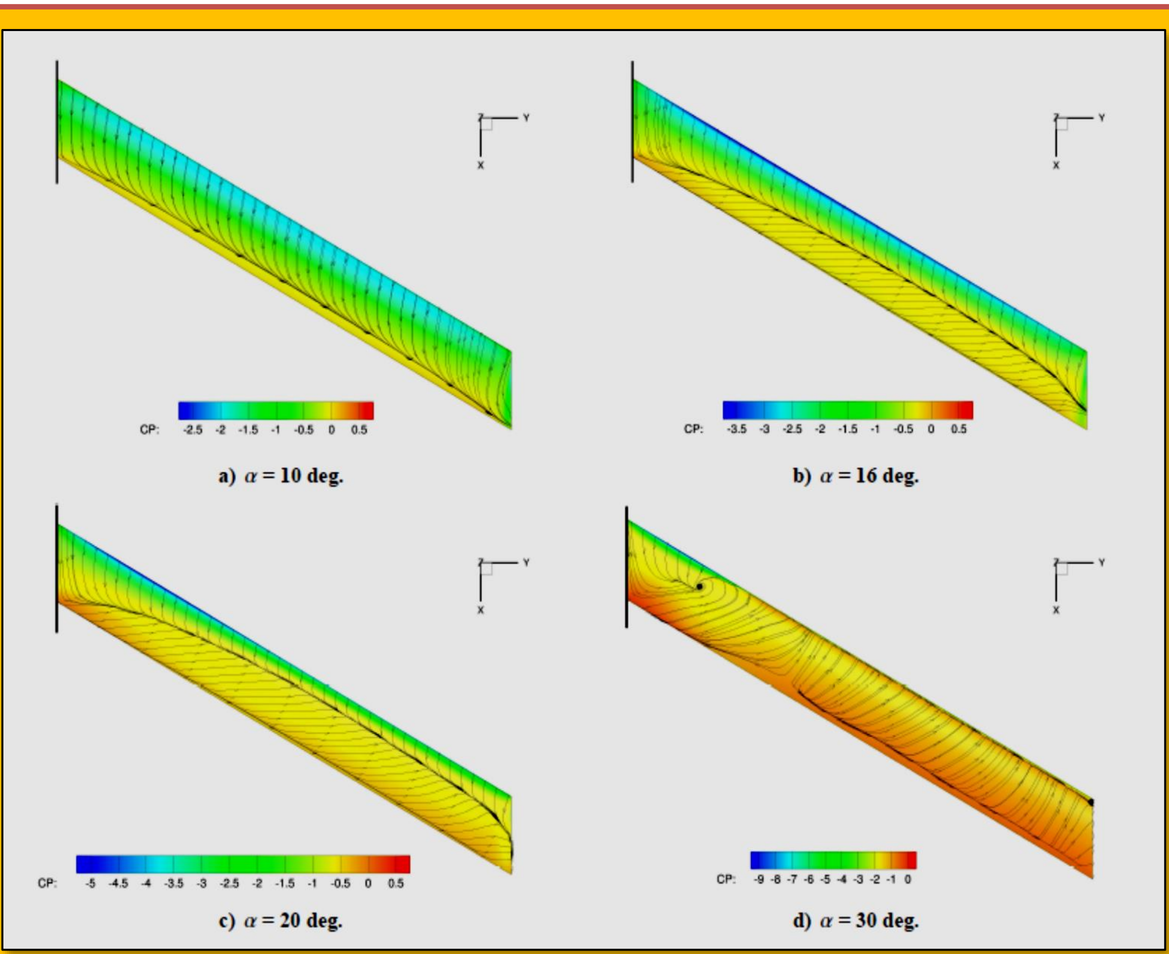

Figure 5.3.22 Cp contours and surface streamlines on a swept wing, Λ = 30 deg., AR = 12, symmetry plane indicated by black line. USM3D/SA, Re = 3 M, M_∞ = 0.2.

5.3.9.6 Conclusions

This paper presents on-going research related to the development of an aerodynamic database of airfoils and wings through post-stall angles of attack. Such data has potential for use in modeling post-stall flight dynamics of fixed wing and rotary-wing aircraft, and for prediction of wind turbine performance. Except for a few sources, however, there is a dearth of post-stall aerodynamic data from experimental or computational studies. One objective of the current work is in filling this gap in the knowledge. Further motivation behind developing this database is that it is expected to be of use in the validation and refinement of a low-order post-stall aerodynamics prediction method being developed for wings and aircraft configurations. The current approach to the development of this database is to use the NASA *TetrUSS* CFD package to analyze the geometries using Reynolds Averaged Navier Stokes equations. The CFD analyses enables flow solutions to be generated for various geometries (both 2D and 3D) in a more rapid fashion than would be possible with experimental work, besides providing detailed spanwise lift coefficients, and separation patterns that are not easily available from experimental studies.

In this paper, results are first presented for three airfoils that exhibit different stall and post-stall behaviors. The results for these and other airfoils will be used as input data for the low-order post-stall prediction method for finite wings. Another objective in obtaining these results is that studying the post-stall behavior of these airfoils may lead to the development of a rapid method of generating airfoil force and moment curves from 0 to 90 degrees angle of attack using a combination of results from XFOIL and other simplified models such as the flat plate theory for very high angles of attack. Next the paper presents results for finite wings to illustrate the effects of taper ratio and sweep angles on stall and post-stall behavior. The results for the rectangular and tapered un swept wings show that the flow along wing sections is nominally two-dimensional even at post-stall conditions. The nominally two-dimensional flow provides confidence in the use of sectional data in modeling post-stall aerodynamics of finite wings. However, there is noticeable variation in the shape of the upper-surface flow separation line, resulting in saw tooth oscillations in the spanwise lift-coefficient distributions. It is not clear if these saw tooth oscillations have any correspondence with similar oscillations seen in the results predicted by the low-order post-stall method.

In contrast to the results for un swept wings, the results for swept wings are seen to be highly three dimensional, as expected. At and beyond stall, there is significant spanwise flow on the upper surface. As a result of this spanwise flow (resulting from spanwise pressure gradients) and the higher lift coefficients on the outboard portions of the wing in pre-stall conditions, the outboard portions of the swept wings stall first while the root portion maintains lift coefficients much higher than the maximum lift coefficient in two-dimensional flow. The consequences of such behavior for aircraft stall characteristics, namely tip stall with associated rolling moment and pitch-up moment at stall, are well known. In the context of the low-order modeling, the significant three-dimensional flow on swept wings at and beyond stall poses serious stumbling blocks. It remains to be seen how these effects can be captured correctly and efficiently in a low-order aerodynamic model that can be used in real-time flight dynamics simulation.

The benefit of such CFD studies, however, is that the detailed results do provide the very type of sought-after information for developing phenomenological augmentation of low-order approaches even when the flow is not entirely two dimensional. In follow-on work, continued expansion of the database will progress with the addition of more airfoil and wing geometries. Studies of wing-tail geometries and effects of angular velocities are also planned.

5.3.9.6.1 Acknowledgments

The CFD portion of the effort was supported by a grant from the NASA Langley Research Center under the Vehicle Systems Safety Technologies project. We thank technical monitor Gautam Shah for the support and collaboration. Justin Petrilli gratefully acknowledges the guidance and mentoring from Neal Frink of NASA Langley in the use of the TetrUSS CFD software. Ryan Paul gratefully acknowledges support from the National Science Foundation Graduate Research Fellowship Program.

5.3.9.7 References

[1] Abbott, I. H. and von Doenhoff, A. E., *Theory of Wing Sections*, Dover, New York, 1959.

[2] Althaus, D. and Wortmann, F. X., *Stuttgarter Profilkatalog I*, Friedr. Vieweg & Sohn, Braunschweig, 1981.

[3] Selig, M. S., Guglielmo, J. J., Broeren, A. P., and Gigu`ere, P., *Summary of Low-Speed Airfoil Data, Vol. 1*, SoarTech Publications, Virginia Beach, Virginia, 1995.

[4] Selig, M. S., Lyon, C. A., Gigu`ere, P., Ninham, C. N., and Guglielmo, J. J., *Summary of Low-Speed Airfoil Data, Vol. 2*, SoarTech Publications, Virginia Beach, Virginia, 1996.

[5] Lyon, C. A., Broeren, A. P., Gigu`ere, P., Gopalarathnam, A., and Selig, M. S., *Summary of Low-Speed Airfoil Data, Vol. 3*, SoarTech Publications, Virginia Beach, Virginia, 1998.

[6] Drela, M., “XFOIL: An Analysis and Design System for Low Reynolds Number Airfoils,” *Low Reynolds Number Aerodynamics*,
edited by T. J. Mueller, Vol. 54 of *Lecture Notes in Engineering*, Springer-Verlag, New York, June 1989, pp. 1–12.
[7] Critzos, C. C., Heyson, H. H., and Jr., R. W. B., “Aerodynamic Characteristics of NACA 0012 Airfoil Section at Angles of Attack From 0◦ to 180◦,” NACA Technical Note 3361, January 1955.
[8] Tangler, J. L., “Insight into Wing Turbine Stall and Post-stall Aerodynamics,” *Wind Engineering*, Vol. 7, 2004, pp. 247–260.
[9] Lindenburg, C., “Aerodynamic Airfoil Coefficients at Large Angles of Attack,” IEA Symposium Paper ECN-RX–01-004, 2001.
[10] Harper, C. W. and Maki, R. L., “A Review of the Stall Characteristics of Swept Wings,” NASA TN D-2373, 1964.
[11] Ostowari, C. and Naik, D., “Post Stall Studies of Untwisted Varying Aspect Ratio Blades with an NACA 4415 Airfoil Section—Part 1,” *Wind Engineering*, Vol. 8, No. 3, 1984, pp. 176–194.
[12] Mukherjee, R. and Gopalarathnam, A., “Post stall Prediction of Multiple-Lifting-Surface Configurations Using a De cambering Approach,” *Journal of Aircraft*, Vol. 43, No. 3, May–June 2006, pp. 660–668.
[13] Gopalarathnam, A., Paul, R., and Petrilli, J., “Aerodynamic Modeling for Real-Time Flight Dynamics Simulation (Invited),” AIAA Paper 2013-0969, January 2013.
[14] Frink, N. T., Pirzadeh, S., Parikh, P., and Pandya, M., “The NASA Tetrahedral Unstructured Software System (TetrUSS),” *The Aeronautical Journal*, Vol. 104, No. 1040, 2000, pp. 491–499.
[15] Pirzadeh, S., “Three-Dimensional Unstructured Grids by the Advancing Layer Method,” *AIAA Journal*, Vol. 33, No. 1, 1996, pp. 43–49.
[16] Pirzadeh, S., “Unstructured Viscous Grid Generation by the Advancing-Layers Method,” *AIAA Journal*, Vol. 32, No. 8, 1994, pp. 1735–1737.
[17] Lohner, R. and Parikh, P., “Three-dimensional grid generation by the advancing front method,” *International Journal for Numerical Methods in Fluids*, Vol. 8, No. 10, 1988, pp. 1135–1149.
[18] Frink, N. T., “Tetrahedral Unstructured Navier-Stokes Method for Turbulent Flows,” *AIAA Journal*, Vol. 36, No. 11, 1998, pp. 1975–1982.
[19] Fredericks, W. J., Antcliff, K. R., Costa, G., Deshpande, N., Moore, M. D., Miguel, E. A. S., and Snyder, A. N., “Aircraft Conceptual Design Using Vehicle Sketch Pad,” AIAA Paper 2010-658, 2010.
[20] Frink, N. T., Pirzadeh, S. Z., Atkins, H. L., Viken, S. A., and Morrison, J. H., “CFD Assessment of Aerodynamic Degradation of Subsonic Transport Due to Airframe Damage,” AIAA Paper 2010-500, 2010.
[21] Spalart, P. and Allmaras, S., “One-Equation Turbulence Model for Aerodynamic Flows,” AIAA Paper 92-0429, 1992.
[22] Pandya, M. J., Khaled S. Abdol-Hamid, R. L. C., and Frink, N. T., “Implementation of Flow Tripping Capability in the USM3D Unstructured Flow Solver,” *AIAA Journal*, , No. 2006-0919, January 2006.
[23] Hoerner, S. and Borst, H., *Fluid-Dynamic Lift*, Hoerner Fluid Dynamics, 1985.
[24] Li, D., “Numerical Simulation of Thin Airfoil Stall By Using a Modified DES Approach,” *International Journal For Numerical Methods In Fluid*, Vol. 54, 2007, pp. 325–332.
[25] Hunton, L. W. and James, H. A., “Use of Two-Dimensional Data In Estimating Loads on a 45*o* Sweptback Wing with Slats and Partial-Span Flaps,” NACA TN 3040, 1953.

5.4 Surface Roughness

Surface roughness can be used to control separation and increase performance at low Re numbers. Experimental observations have shown that a "***rough***" airfoil surface will perform better than a "***smooth***" airfoil surface at low Re values, as shown in **Figure 5.4.1**, adapted from [McMasters and Henderson][119]. This is why small birds and insects have rough wing surfaces. Flow over the surface of an airfoil at low Re numbers (40 - 50000) was laminar and remains laminar over the airfoil. Laminar fluid moves in layers and follows the curved surface of an airfoil. The closer the fluid layers are to the airfoil surface, the slower they move [Simpson][120].

Generally, the static pressure increases as the flow moves across a surface, small disturbances in the laminar flow are amplified and the flow turns turbulent. Static pressure decreases over the surface, disturbances in laminar flow are damped out and the flow remains laminar. Over an airfoil, the static pressure decreases from the leading edge to the point of maximum thickness. Thus, in this region, laminar flow was encouraged. However, the static pressure increases toward the trailing edge and laminar flow is hindered. In this laminar flow regime the airflow separates from the surface of the airfoil due to the unfavorable pressure gradients in the flow field. This causes a loss in performance of the airfoil, and the airfoil was said to "stall", causing loss of lift and a large increase in drag. In contrast at higher Re numbers, the airflow is turbulent. Turbulent flow over the same airfoils was shown to resist separation[121]. This provides a good reason for separation control by means of encouraging a transition from laminar to turbulent flow.

As seen in **Figure 5.4.1**, surface roughness affects a body in a flow field. Surface roughness can cause the flow near the body to go from laminar to turbulent. The Re number and surface roughness both contribute to the determination of the laminar to turbulent transition. Low Re number flow will be laminar even on a rough surface and a very high Re number flow will be turbulent even on a smooth surface. This prompted research into devices which generated turbulence and hence aided in the transition from laminar to turbulent flow. The turbulence promoting devices ranged from static mechanical roughness elements such as strips and bumps to dynamic methods such as acoustic excitation and surface vibration. The methods disturb the flow and are generally hard to analyze.

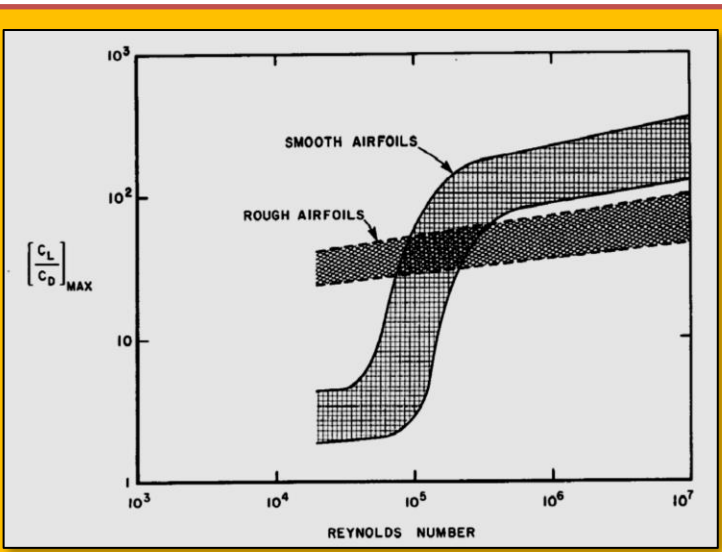

Figure 5.4.1 L/D versus Re ratio [2]

The NACA reports are some of the earliest research studies on the effects of surface roughness on airfoil performance. The research placed protuberances of different shapes and sizes in a range of chord-wise locations. The reports observed that the loss of lift was directly proportional to the height of protuberances. At higher angles of attack, the protuberances had an adverse effect, especially when moved closer to the leading edge. Other work examined the effects of ice on the surface of

---

[119] J.H. McMasters and M.L. Henderson. *Low-speed single element airfoil synthesis*. Technical Soaring, 1980.

[120] Simpson, Andrew D., "*Design And Evaluation Of Inflatable Wings For UAVs*" (2008). *University of Kentucky Doctoral Dissertations.* Paper 589. http://uknowledge.uky.edu/gradschool_diss/589

[121] M. Gad-El-Hak. *Flow control: The future*. Journal of Aircraft, 38:402-418, 2001.

wings. It was observed that bigger protuberances showed slightly better performance than thinner protuberances, and simple 2D protuberances provided the same benefits as 3D protuberances.

The effects of large distributed surface roughness on airfoil boundary layer development and transition to turbulence has been investigated for Re values of 0.5, 1.25 and 2.25 M by [Kerho et al.][122]. They observed that the roughness promoted the growth of a transitional boundary layer, which required substantial chordwise extent (downstream of the roughness) to become fully turbulent. The fluctuating streamwise velocity and turbulence intensity in the roughness-induced boundary layer was found to be lower than the smooth case. In general, the longer the chordwise extent of the roughness and larger the roughness dimensions, the more the length of the transitional region was found to decrease.

Error! Reference source not found. shows the variation in L/D performance for various airfoils versus Re as determined by [McMasters and Henderson]. Note that at low Re (in the range of birds, insects, µAVs, and UAVs), "smooth" airfoils perform worse than "rough" airfoils. However, the performance of smooth airfoils greatly improves at Re $\sim 10^5$ and exceeds that of rough airfoils. This is primarily due to the difference in the underlying physics at low and high Re and needs to be discussed further here. The variation in the L/D ratio with respect to Re for rough and smooth airfoils is described. However, the effect of the transition location with respect to L/D ratio is not described. As noted earlier, surface roughness and Re affect boundary layer development and the transition to turbulence. The effect of changing the initial trip location on L/D was examined. By altering the location of the transition point we can examine the effect of surface perturbations' positions on the performance of the airfoil. The location of the perturbations or the transition point, the Re number, and the characteristics of the airfoil and set-up affect the airfoils' performance.

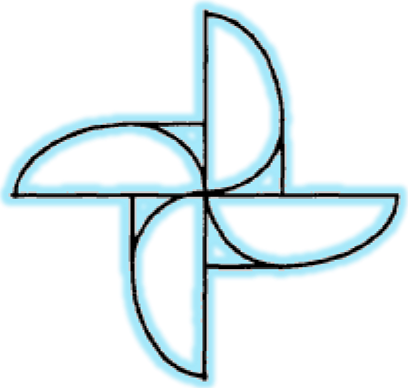

---

[122] Michael F. Kerho and Michael B. Bragg. *Airfoil boundary layer development and transition with large leading-edge roughness.* AIAA Journal, 35(1):75-84, 1997.

6 Case Studies Specific to Airfoil Aerodynamics

6.1 Case Study 1 - Aerodynamic Analysis of NACA 0012 With Different Turbulence Models

---

Authors : *Amit Kumar Saraf[1], Mahendra Pratap Singh[2], Tej Singh Chouhan[3]*
Affiliations : *[1-2]Department of Mechanical Engineering, Jagannath University Jaipur, India, [3]Rajdhani Engineering College, Jaipur India*
Title of Paper : *Aerodynamic Analysis of Naca0012 Airfoil Using CFD*
Citation : *(Saraf, SINGH, & CHOUHAN, 2017)*
Bibliography : *Saraf, A. K., SINGH, M. P., & CHOUHAN, T. S. (2017). Aerodynamic Analysis of Naca0012 Airfoil Using CFD. International Journal of Mechanical And Production Engineering.*

6.1.1 Abstract

Analysis of the two dimensional airfoil was done with the help of CFD Software. The target of the work is to come across the most suitable turbulent model in calculation of Governing Equations. The Governing Equations were solved using CFD software. Since two dimensional and three dimensional airfoil shows the equivalent result that is why the two dimensional airfoil was used. NACA0012 airfoil is a non-cambered airfoil and it is used in various aeronautical applications. Flow on this airfoil was analyzed for different angle of attack and compared practical data with simulated data for different turbulent models. Calculations were done at low Reynolds number keeping a constant velocity for altered angle of attack. During calculation grid independence test was done to show the accuracy of result by changing in grid size or nodes. As the number of nodes increases, the lift coefficient is also increased. But as soon as we reached 102180 nodes, the lift coefficient becomes stagnate.

6.1.2 Introduction

Computational Fluid Dynamics is the technique for analyzing and simulation where fluid flow involved. This technique has multiple uses in Industrial and Non industrial application areas. This technique reduces the cost of working and gives good agreement with practical results. The CFD contains three main elements which are Preprocessor, Solver and Post Processor[123]-[124]. During flow, viscous effect dominates the entire fluid flow field. The fluid exerts pressure force perpendicular to the surface and there is another force which is parallel to the surface of the body and along the outer surface of the body is known as shear force. Resultant of pressure force and shear force is the area of interest. Normal component of the resultant is known as lift force and component which acts in flow direction is called drag force[125]. The drag force can be subdivided into two parts skin drag and pressure drag. Frictions drag force having relation with the position of the body and the amount of the wall shear stress. Friction drag also varies with the viscosity of the fluid. As we know that Reynolds number is inversely proportional to the total viscosity. Frictions Drag also depends on the surface area. In case of laminar flow friction drag is independent of the roughness of the surface but in turbulent flow it plays a chief role.

---

[123] Versteeg, H. K., & Malalasekera, W. (2012). *An Introduction To Computational Fluid Dynamics*. New Delhi India: Pearson Education, Ltd.

[124] Cengel, Y. A., & Cimbala, J. M. (2008). *Fluid Mechanics*. New Delhi India: Tata Mcgraw-Hill Publishing Company Limited, New Delhi India.

[125] Cengel, Y. A., & Cimbala, J. M. (2008). *Fluid Mechanics*. New Delhi India: Tata Mcgraw-Hill Publishing Company Limited, New Delhi India.

6.1.3 Literature Review

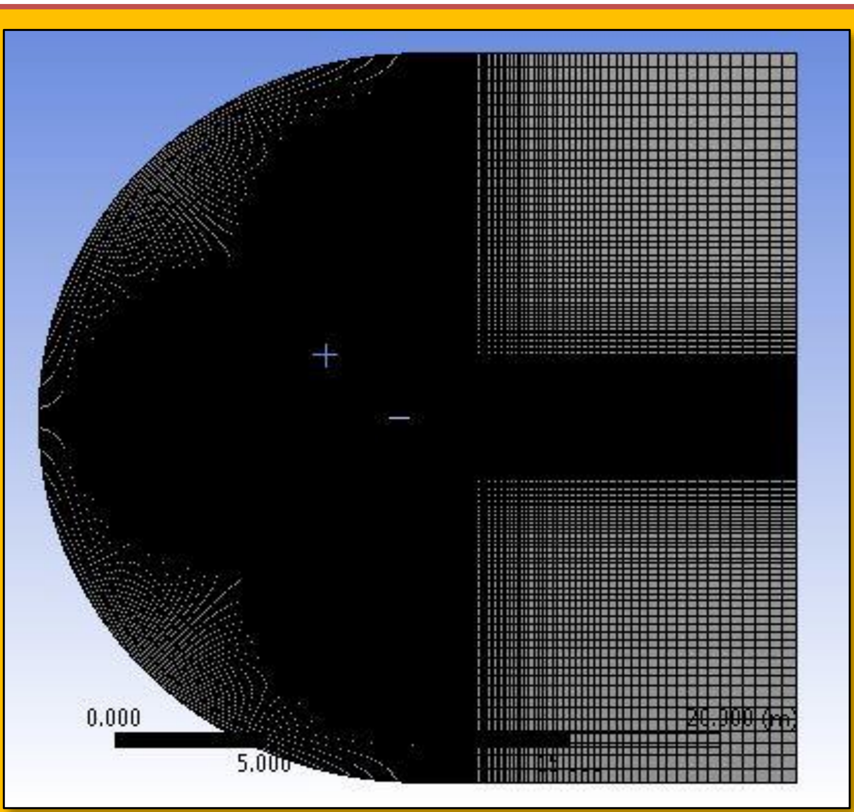

Figure 6.1.1 NACA 0012 C-Type Mesh

2D & 3D models of airfoil with far field was created in *GAMBIT* and analyzed using *FLUENT* [126] . 3D model consumes much amount of time and requires high memory computer while 2D model gives the identical results. Author tested NACA 0012 airfoil at different Reynolds Number on 2D and 3D models of airfoil. Accuracy of FLUENT was not up to the mark for values of above 10° angle of attack. Simulation was done with inviscid and Spalart-Allmaras turbulent models [127] . Blade Element Momentum Theory (BEM) can be used to explore the Horizontal Axis Wind Turbine Blades. Here S-809 Blade was used[128]. Breakaway at a point on the surface is known as separation point & such phenomenon is called separation. In this report author found that detachment location is significantly independent on turbulent intensity & vibration but it is dependent on pressure distribution[129]. There are many turbulent Models available but these three Models were used included (Realizable and RNG k-Reynolds and Reynolds Stress Model (RSM)). Here aerodynamic behavior of the airfoil with different turbulent models has been studied[130]. A symmetrical airfoil was used to study the trailing edge separation on trailing edge. Here the low Reynolds numbers were used. RANS equations were solved with finite volume method on airfoil SD8020. κ-ω SST turbulent model were used to simulate the problem. It was noticed at small angles of attack laminar separation happens on both sides of airfoil while at high angles of attack, the separation reattach to the trailing edge.

---

[126] Logsdon, N. (2006). *A Procedure For Numerically Analyzing Airfoils And Wing Sections*. Columbia: University Of Missouri.

[127] Kulunk, E., & Yilmaz, N. (2009*). Computer-Aided Design And Performance Analysis Of Hawt Blades*. 5th International Advanced Technologies Symposium (Iats'09) (P. .). Karabuk, Turkey: Iats'09, Karabük University, Karabük, Turkey.

[128] Potter, J. L., Barnet, R. J., Fisher, C. E., & Costas. (1986). *The Influence Of Free-Stream Turbulence On Separation Of Turbulent Boundary Layers In Incompressible, Two-Dimensional Flow*. Department Of Mechanical Engineering. Nashville Tn 37235: Vanderbilt University.

[129] Agrawal, M., & Saxena, G. (2013). *Analysis Of Wings Using Airfoil Naca 4412 At Different Angle Of Attack*. International Journal Of Modern Engineering Research , 1467-1469.

[130] Juanmian, L., Feng, G., & Can, H. (2013). *Numerical Study Of Separation On The Trailing Edge Of A Symmetrical Airfoil At Allow Reynolds Number*. Chinese Journal Of Aeronautics , 918-925.

6.1.4 Turbulent Model

The turbulent kinetic energy and rate of dissipation of κ-ε is solved by κ-ε turbulent model. This model has good convergence rate compared to other models and requires low memory computers. Though this model is suitable for bluff and streamlined body, different analysis needs to be done for different geometric models. The specific rate of dissipation of kinetic energy is solved by k-ω turbulent models. This model requires higher memory computers for the computation. It is quite sensitive and has difficulty in converging. This model is useful if κ-ε model is not suitable. For details about airfoil sensitivity w.r.t different turbulence models, please confer with [Saraf et al.][131].

6.1.5 Grid Independence Test

The Grid distribution scheme suffers from some important drawbacks[132]. There is no control on the magnitude of global error. Though the local error may be redistributed well, the computed solution may not possess the desired accuracy due to insufficient number of nodes. This problem can be resolved by solving the problem repeatedly with different mesh size and finally we can get accurate results. The result changed with respect to the size of the grid or number of nodes, grid independency test was done to get much accurate result. Though it increases the time of simulation but tends towards an accurate result. The Grid independence test was done using CFD Software. In this test first the simulation was done with coarse mesh, after that the meshing was converted into finer mesh and simulation was done in order to get a more accurate result. In order to get dense grid, number of nodes has to be increased.

6.1.6 Computation Method

A NACA0012 airfoil was used to study various turbulent models and here 102180 nodes used. The airfoil models was first prepared and then exported into *ANSYS* where far filed and meshing was done as shown in **Figure 6.1.1**. Here the air was made to flow at a constant velocity at 7.3 m/s and density of the air was taken 1.225 kg/m^3. Temperature of air was taken as 300K. This site was used to validate the practical data[133]. Practical data were compared with the simulated data at different turbulent models.

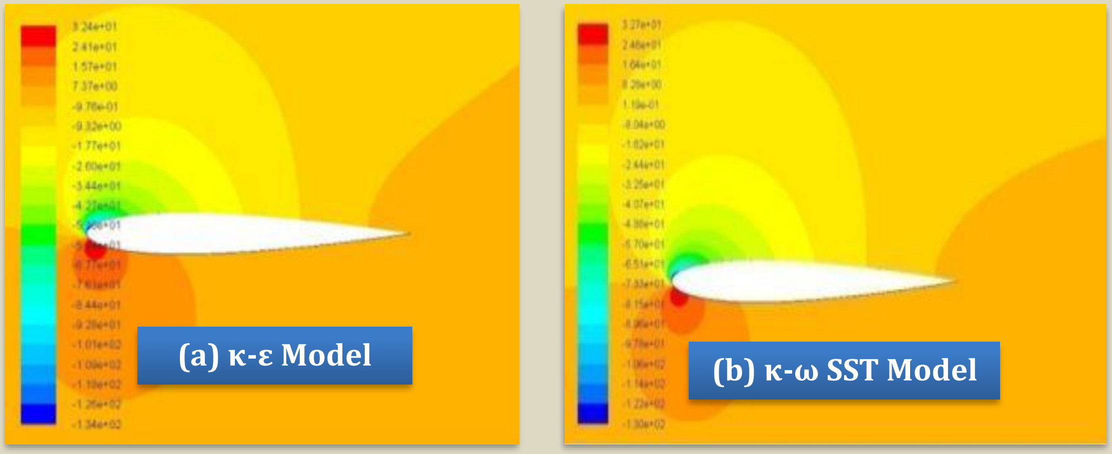

Figure 6.1.2 Contours of Pressure at 10° Angle of Attack for Different Turbulence Models

---

[131] Amit Kumar Saraf, Mahendra Pratap Singh, Tej Singh Chouhan, "*Aerodynamic Analysis of NACA 0012 Airfoil Using CFD*", International Journal of Mechanical and Production Engineering, 2017.

[132] Agrawal, M., & Saxena, G. (2013). *Analysis Of Wings Using Airfoil Naca 4412 At Different Angle Of Attack.* International Journal Of Modern Engineering Research , 1467-1469.

[133] Airfoiltools.Com. (2016). Http://Airfoiltools.Com/Polar/Details?Polar=Xf-N0012-Il-500000.

6.1.7 Simulation Outcomes

6.1.7.1 Pressure Contours

Figure 6.1.2 (a-b) exhibits of pressure contours for κ-ε and κ-ω SST turbulence models. (see [Saraf][134] for additional models). It can be seen that upper surface having lower pressure and lower surface has higher pressure. This situation shows that pressure on lower side tries to lift the body and hence increases the lift coefficient. In the given figure of pressure contours it is shown that at the leading edge of the upper side there is a greenish color and on the lower side the color is reddish, where red color indicates a higher value of pressure and greenish color indicates a lower value. As the angle of attack increases, the coefficient of lift also increases but after 15^{o}-16^{o} of angle of attack it starts decreasing.

6.1.7.2 Velocity Contours

The same thing can be seen in velocity contours (not shown here) that the upper surface of the airfoil is shown in a reddish color while lower surface is shown in bluish color where a reddish color indicates higher velocity and according to Bernoulli's Theorem it will have a lower pressure. Near the trailing edge there is huge gape amongst the velocity vectors which means that flow starts to separate near the trailing edge.

6.1.8 Result

The Coefficient of lift (C_L), increases with the angle of attack. Three models are presented here and all models show approximately same results (see **Figure 6.1.3**). Stall condition comes near 15^{o} angle of attack. But while all graphs presented on the single sheet there seems to be a difference amongst all the graph

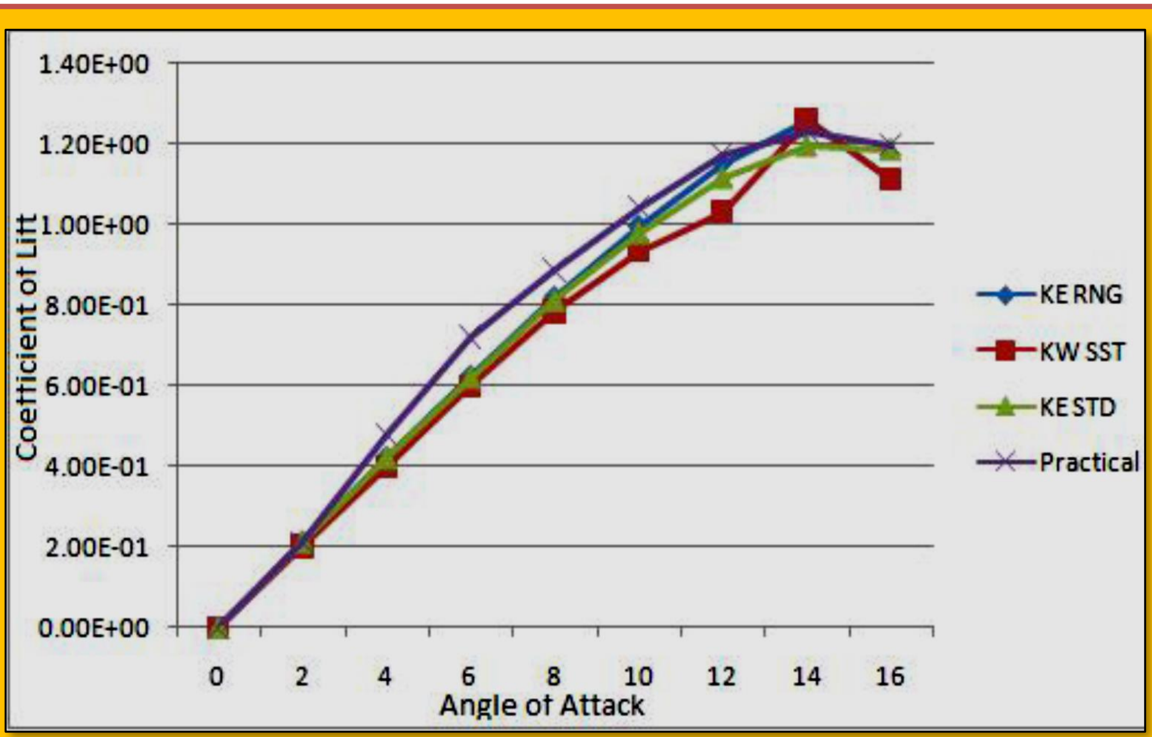

Figure 6.1.3 Comparison of C_L for Various Turbulent Models

---

[134] See Prevuis.

6.1.9 Conclusion

It was noticed that all the graphs shows similar results but while compared with practical data it shows that there is some deviation among all the graphs. From the figures of the graph it is seen that k-ε standard model and k-ε RNG give a good approximation. Though k-ω SST turbulent model is also a good model but here it is not as good as the others. All the models show similar result at lower angle of attack but near angle of stall the deviation in graphs starts showing.

6.2 Case Study 2 - Aerodynamic Performance of NACA 0015 Flapped Airfoil

An analysis of 2D subsonic flow over an NACA 0015 airfoil with a 30% trailing edge flap at a constant Re = 10^6 for various incidence angles and a range of flap deflections is provided by [Obeid et al, 2017][135]. The steady-state governing equations of continuity and momentum conservation are solved combined with the realizable κ-ε turbulence model using a leading commercial code. The primary objective of the study is to provide a comprehensive understanding of flow characteristics around the NACA 0015 airfoil as a function of the angle of attack and flap deflection.

6.2.1 Background & literature Survey

The aerodynamic shape of lifting objects is one of their most important design parameters. This parameter affects the amount of the lift and the drag forces that the airfoil can generate. Aircraft wings are mainly intended to provide the maximum value of the lift-to-drag ratio L/D. The L/D ratio is deemed as a measure of the efficiency of an aircraft and can be stated as the amount of power (thrust) that is required to force an aircraft of a certain weight. The aircraft wing performance is seriously impaired if flow separation occurs. Commonly, flow separation results in a loss of lift, an increase of drag, diminished pressure recovery, etc. Therefore, a considerable amount of research effort has been devoted to the control of flow separation, and many methods to attain separation control have been suggested. Among the most promising active flow control approaches are suction, blowing, synthetic jet actuation and wall movement. Proper flow control methods have the ability to reduce skin friction and form drag, increase lift and improve flight controllability. The potential benefits of flow control include enhanced range and payload, short runway landing capability, improved ecological compliance and savings in overall fuel consumption. For instance, maintaining laminar flow over the entire wing surface can reduce total aircraft drag by as much as 15% [136].

Recently, there has been considerable interest in flow control, especially in the field of aerodynamics with the intent of increasing lift and decreasing the drag of airfoils. To allow landing and take-off from short runways at reduced ground speeds, some modern airplanes are equipped with multi-element high-lift devices that generate the required high lift. Slat and single or multiple flaps are typical examples of such devices. Multi-element wing designs, however, are found unfavorable from a weight and complexity point of view. That is the reason for replacing the multi-element flap with a single-hinged flap in the current designs to reduce the complexity while increasing the efficiency of the wing. While reducing the complexity of the wing, the single-hinged flap increases the chance for flow separation on the flap at large deflection angles. To prevent or at least to minimize the effects of flow separation, the air flowing over the wing near the surface must be energized so that it could overcome the effects of the adverse pressure gradient encountered along the flap.

In recent years, the possible application of trailing edge flaps as a potential vibration and noise control tool has gained considerable attention for application to the helicopter blades and wind turbines. Applications of trailing edge flap systems in helicopter rotors have been the subject of much research, both in the context of individual blade control[137]. The employment of plain flaps in wind turbines has been also a topic of interest to many researchers. The efficacy of plain flaps in wind turbines is considered favorable both in relation to load alleviation, as well as power generation. Furthermore, small flap deflections could delay the laminar-turbulent transition[138].

A wide range of engineering applications utilize airfoils operating at relatively low and medium chord Reynolds numbers ranging from 10^4 to 10^6. As noted before, helicopter rotor blades, small-to-

---

[135] Sohaib Obeid, Ratneshwar Jha, and Goodarz Ahmadi, "*RANS Simulations of Aerodynamic Performance of NACA 0015 Flapped Airfoil*", Fluids 2017, 2, 2; doi:10.3390/fluids2010002.

[136] Schrauf, G. "*Application of laminar flow technology on transport aircraft*", Proceedings of the CEAS Drag Reduction Conference, Potsdam, Germany, 19–21 June 2000.

[137] Ham, N.D., "*Helicopter individual blade control research at MIT 1977–1985".* Vertica 1987, 11, 109–122.

[138] Somers, D.M. "*Effect of Flap Deflection on Section Characteristics of S813 Airfoil (Period of Performance: 1993–1994)";* NREL/SR-500–36335; National Renewable Energy Laboratory: Golden, CO, USA, 2005.

medium-scale wind turbines and unmanned aerial vehicles are typical examples[139] . In this Reynolds number range, the boundary layer on the upper surface of an airfoil is prone to experience flow separation, even at a low incidence angle. While there is a number of published works on airfoil performance at low Reynolds numbers, still there are not many studies, either experimentally or numerically, that cover the range of Re = 10^6. In addition, despite numerous publications on the lift and drag of NACA airfoils, better understanding of airfoils with one hinged flap is still of interest. Symmetric NACA airfoils with a thickness range from 9% to 18% also have many applications in industry and for demonstration purposes[140]. [Gault][141] classified the stalling characteristics of the low speed NACA airfoil sections into: thin airfoil stall, leading edge stall, trailing edge stall and a combination of leading edge and trailing edge stall. Based on this classification, the NACA 0015 airfoil was selected for this study as it is classified as a medium thickness airfoil, which is susceptible only to trailing edge stall at Re = 10^6.

Numerical studies of the aerodynamic performance of the NACA 0015 airfoil with an integral-type trailing edge flap were reported by Hassan[142] using the 2D Navier–Stokes flow solver developed at the NASA Ames Research Center. [Zhang et al.] [143] studied the aerodynamic performance of the NACA 0015 airfoil at different speeds. They reported the flow patterns pressure distributions, velocity vector fields and turbulence intensities around the airfoil. Numerical studies for plain (un-flapped) airfoils were presented by [Srinivasan et al.] [144] . They investigated various turbulence models for unsteady flows around a NACA 0015 oscillating airfoil. The main objective of the numerical simulations presented here is to provide a thorough understanding of flow features around the NACA 0015 airfoil as a function of both angle of

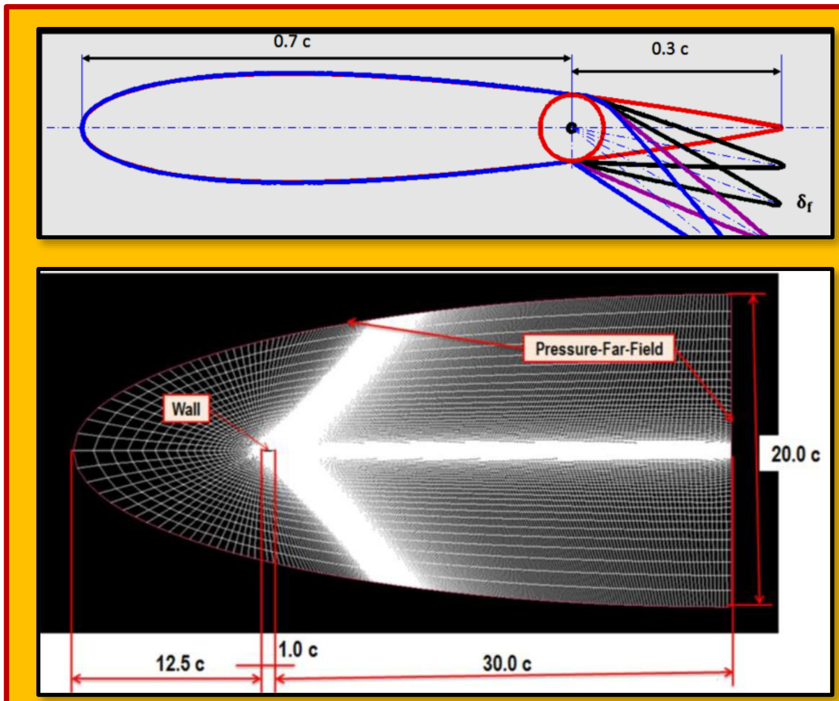

Figure 6.2.1 Geometry of the NACA 0015 Airfoil with a 30% Trailing Edge Deflected Flap (Top) and Domain of Calculations and Boundary Conditions (Bottom) - Courtesy of [Obeid et al.].

---

[139] McCroskey, W.J. "*A Critical Assessment of Wind Tunnel Results for the NACA 0012 Airfoil*"; NASA Technical Memorandum 100019; NASA Technical Reports Server (NTRS): Hampton, VA, USA, 1989.

[140] Gerakpoulos, R.; Boutier, M.S.H.; Yarusevych, S. "Aerodynamic characteristics of NACA 0018 airfoil at low reynolds numbers", Proceedings of the 40th Fluid Dynamic Conference and Exhibit, Chicago, IL, USA, 2010.

[141] Gault, D.E. "*A Correlation of Low-Speed, Airfoil-Section Stalling Characteristics with Reynolds Number and Airfoil Geometry*", NACA Technical Note 3963; NACA Technical: Washington, DC, USA, 1957.

[142] Hassan, "*A Predicted Aerodynamic Characteristics of a NACA 0015 Airfoil Having a 25% Integral Type Trailing Edge Flap*", NACA CR/-1999–209328; NASA Technical Reports Server (NTRS): Hampton, VA, USA, 1999.

[143] Zhang, G.; Jiang, J.; Liu, C. ,"*Numerical simulation of aerodynamic performance for wind turbines*". J. E. China Electric Power 2009, 37, 449–452.

[144] Srinivasan, G.R.; Ekaterinaris, J.A.; McCroskey, W.J. "*Evaluation of turbulence models for unsteady flows of an oscillating airfoil*". Computer Fluids 1995, 24, 833–861.

attack and flap deflection at fixed (Re = $10^{6)}$. The other objective is to validate the computational model by comparison of the results with the experimental data and earlier numerical simulation results. The flow problem here is of a boundary layer nature; therefore, the fluid motions near the airfoil surfaces are of interest.

6.2.2 Computational Domain and Boundary Conditions

To facilitate the grid generation process, as well as the analysis, similar to the earlier study of Hassan, the airfoil with the deflected trailing edge flap is treated as a single-element airfoil with no gap between the flap's leading edge and the base of the forward portion of the airfoil. For deflecting the flap, solid body rotations were assumed, and a four-point spline smoothing was made for the resulting airfoil at the chord-wise position corresponding to the location of the flap hinge point. Geometry of the NACA 0015 Airfoil with a 30% Trailing Edge Deflected Flap (Top) and Domain of Calculations and Boundary Conditions (Bottom) - Courtesy of [Obeid et al.]. **Figure 6.2.1** shows the schematic geometry of the NACA 0015 with various trailing edge flap deflections, as well as detailed mesh. The grids constructed for this study have about 104K cells with a four-node quadrilateral element. To simulate the wake area correctly, [Dolle][145] recommended using a fine grid with quadrilateral cells in these areas rather than other type of cells. Therefore, refined quadrilateral cells were placed on top of the boundary layer grid on the upper side and lower side of the airfoil outline. The pressure far-field boundary is a non-reflecting boundary condition based on "Riemann invariants" used to model a free-stream condition at infinity, with the free-stream Mach number and static conditions being specified. At the wall, the standard wall function boundary condition was used. The calculation procedures at the pressure far-field boundaries, as well as the shear-stress calculations at wall**.** The boundary conditions for this simulation were the pressure far-field at the computational domain periphery and stationary wall condition at the airfoil surface. The pressure far-field boundary is a non-reflecting boundary condition based on "***Riemann invariants***" used to model a free-stream condition at infinity, with the free-stream Mach number and static conditions being specified. At the wall, the standard wall function boundary condition was used. The calculation procedures at the pressure far-field boundaries, as well as the shear-stress calculations at wall boundaries were described in[146]. In some cases, the mesh is adapted based on the static pressure gradient, using the default mesh adaptation control settings, so the solver periodically refines the mesh in the regions of high pressure gradients.

6.2.3 Setting Up of the Numerical Simulation Parameters

Time independent ***pressure-based*** solver is used. The realizable k-ω turbulence model is selected for analyzing the boundary layer flow over the airfoil. The airflow is assumed to be incompressible. A simple scheme with the Green-Gauss cell-based gradient implicit formulation of pressure velocity coupling is utilized. For spatial discretization, the second order upwind differencing scheme which offers several advantages over a central-differencing formulation for computing viscous flows is used. A convergence criterion of $1\text{x}10^{-8}$ was used for the continuity, x-velocity, y-velocity, k and ω. All solutions converged with the standard interpolation scheme for calculating cell-face pressure and second order up-wind density, momentum, turbulent kinetic energy, turbulent dissipation rate and energy interpolation schemes for turbulent flow.

---

[145] Dolle, T.J.A. ,"*Flap Performance Improvement by Surface Excitation*". Master's Thesis, Aerospace Engineering, Delft University of Technology, The Netherlands, 2009; pp. 23–27.

[146] ANSYS, Inc. Introduction to ANSYS FLUENT 12.0. "*Lecture 5 Solver Setting*" ANSYS, Release 13; ANSYS, Inc.: Canonsburg, PA, USA, 2010; pp. 8–30.

6.2.4 Mesh Independence Tests

To ensure that the simulation results are independent of grid size, different computational meshes were inspected. This is done by running cases with increasing number of grid cells until the simulation results did not change with the use of progressively finer grids. **Table 6.2.1** lists the properties of six different grids with varying density that have been inspected for the flow pattern around the NACA 0015 airfoil with zero flap deflection. It also provides maximum, minimum, and average values of non-dimensional normal distance from the wall, y+, for each grid. It is observed that all of the grids inspected have considerably low y+ values, particularly Grids III–VI, to sufficiently resolve the viscous sub-layer. The mesh size near the airfoil surface is a critical parameter for proper simulation of boundary layer flow properties. The size of the first cell height near the wall Δy was estimated based on the physical properties of the fluid used and the selected values of the non-dimensional normal distance from the wall y^+. The last step in the grid convergence inspection was focused on the analysis of the distribution of the pressure coefficient along the airfoil chord, as well as the velocity profiles on the upper surface of the airfoil in some selected sections. For detailed information, reader are encourage to consult [Obeid et al.][147].

Grid	No. of Cells	Max y+	Min y+	Aver y+
I	24,910	32.5 4	4.8	13.85
II	53,040	16.5	3.4	06.55
III	76,128	12	1	05.50
IV	103,192	9.2	0.8	04.20
V	141,168	8.8	0.7	04.05
VI	367,235	1.01	0.01	0.500

Table 6.2.1 Details of Grids used in Mesh Sensitivity Testing

6.2.5 NACA 0015 Airfoil with Zero Flap Deflection Results

The airflow properties around the NACA 0015 with zero flap deflection are first studied, and the corresponding distributions of static pressure and velocity magnitude at different incidence angles are evaluated and compared with the published numerical results and/or experimental data. **Figure 6.2.2** shows the static pressure and velocity magnitude contours around the NACA 0015 airfoil for a few selected incidence angles. As NACA 0015 is a symmetric airfoil, at zero incidence angle, the static pressure and velocity distribution over the airfoil are symmetric, which results in zero lift force and a stagnation point, exactly at the nose of the airfoil. There are regions of accelerated flows over and under the airfoil that reach the highest speed at the airfoil maximum thickness point. The velocity is high (marked by red spots) in the low pressure region and vice versa. The maximum pressure occurs at the stagnation point when the velocity is zero. At an incidence angle of 5 degree, the contours of static pressure over the airfoil become asymmetric; the pressure on the upper surface becomes lower than the pressure on the lower surface; regions of high pressure on the airfoil lower surface become dominant; and a lift coefficient of 0.531 is generated due to the pressure imbalance.

Figure 6.2.3 shows that as the angle of attack increases, the stagnation point is shifted towards the trailing edge on the bottom surface; hence, it creates a low velocity region at the lower surface of the airfoil and a high velocity region on the upper side of airfoil. Thus, the pressure on the upper side of the airfoil is lower than the ambient pressure, whereas the pressure on the lower side is higher than the ambient pressure. Therefore, increasing the incidence angle is associated with the increase of the lift coefficient, as well as the increase of the drag coefficient. This increase in the lift coefficient continues up to a maximum, after which the lift coefficient decreases. It is also seen that the flow field around the airfoil varies markedly with the incidence angle.

---

[147] Sohaib Obeid, Ratneshwar Jha, and Goodarz Ahmadi, "*RANS Simulations of Aerodynamic Performance of NACA 0015 Flapped Airfoil*", Fluids 2017, 2, 2; doi:10.3390/fluids2010002.

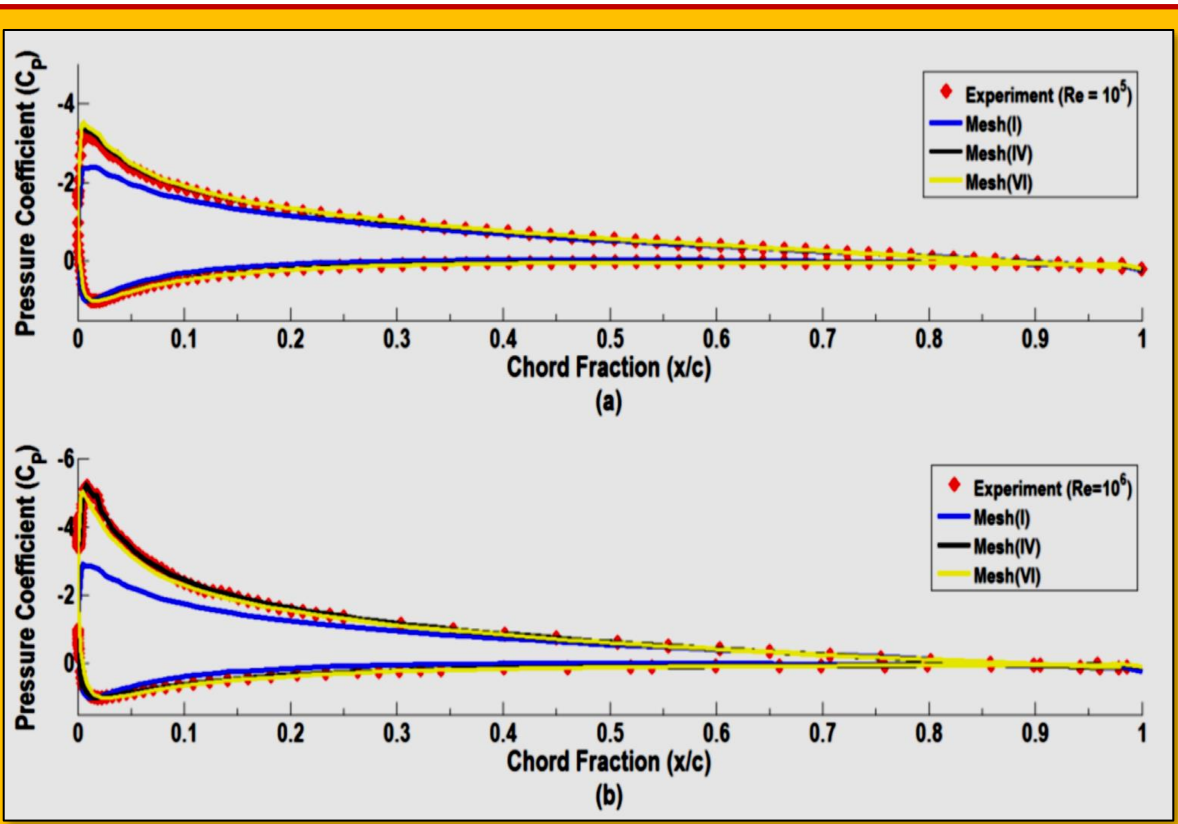

Figure 6.2.2 C_p Around NACA 0015 Airfoil for a Few Selected Incidence Angles- (Courtesy of Obeid et al.)

In addition to the changes in velocity and pressure distributions, the properties of the boundary layer flow along the airfoil surface also change. At low incidence angles up to about 12 degrees, the boundary layer is fully attached to the surface of the airfoil, and the lift coefficient increases with angle of attack, while the drag is relatively low. With the increase of incidence angle, the boundary layer is thickened. When the incidence angle of the airfoil is increased to about 13 degree or larger, the adverse pressure gradient imposed on the boundary layers become so large that separation of the boundary layer occurs. A region of recirculating flow over the entire upper surface of the airfoil forms, and the region of higher pressure on the lower surface of the airfoil becomes smaller. Consequently, the lift decreases markedly, and the drag increases sharply. This is a typical condition in which the airfoil is stalled.

For a further increase of the airfoil incidence angle to 20 degree, the stagnation point shifts significantly further towards the trailing edge on the bottom surface. The recirculating flow region becomes dominant and covers the entire upper surface of the airfoil, and the airflow is fully separated from the upper surface of the airfoil. This leads to further reduction of the lift force and a severe increase of the drag force. The air flowing along the top of the airfoil surface experiences a change in pressure, moving from the ambient pressure in front of the airfoil, to a lower pressure over the surface of the airfoil, then back to the ambient pressure behind the airfoil. The region where fluid must flow from low to high pressure (adverse pressure gradient) could cause flow separation. If the adverse pressure gradient is too high, the pressure forces overcome the fluid inertial forces, and the flow separates from the airfoil upper surface. As noted before, the pressure gradient increases with incidence angle, and there is a maximum angle of attack for keeping the flow attached to the airfoil. If the critical incidence angle is exceeded, separation occurs, and the lift force decreases sharply.

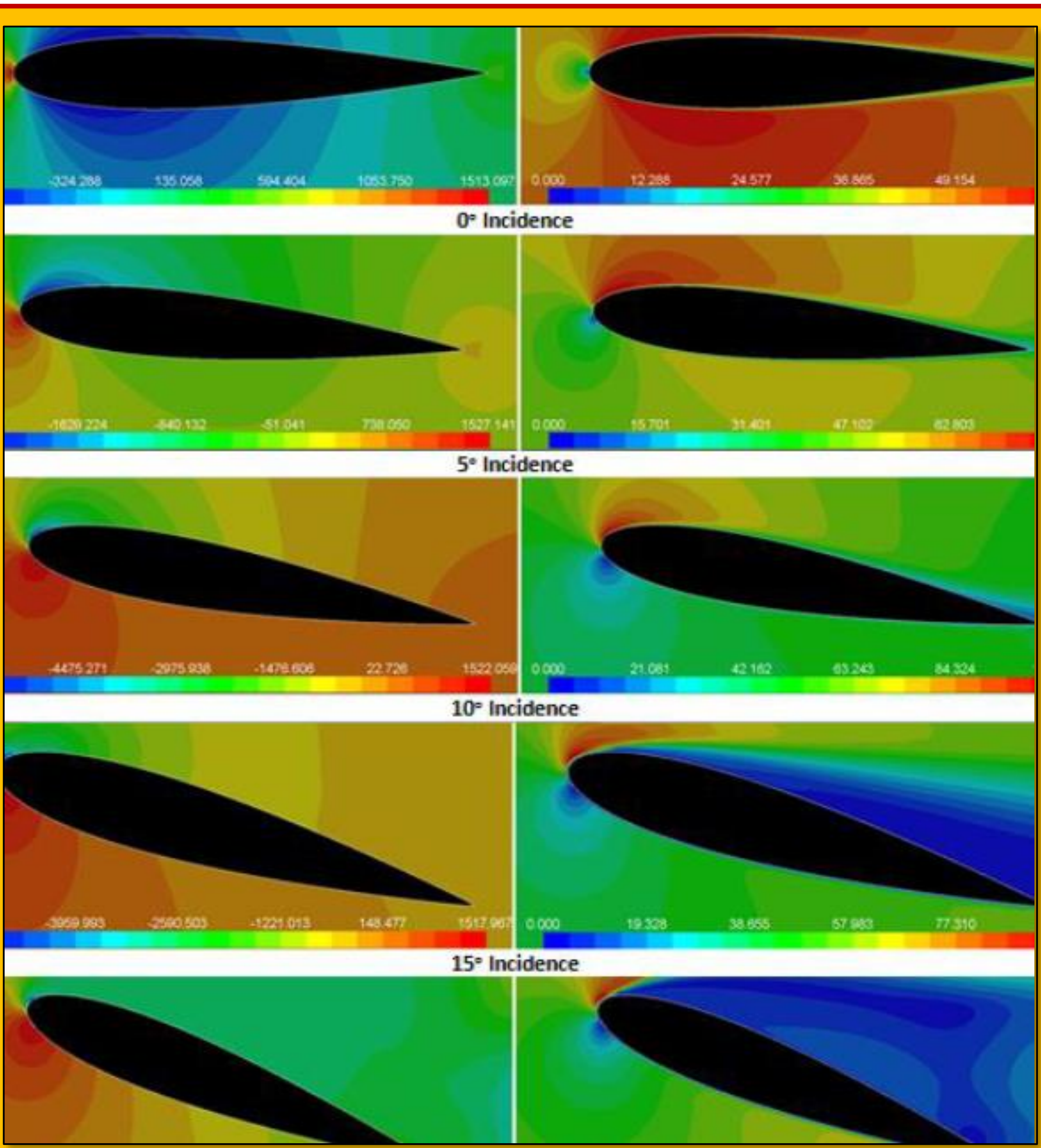

Figure 6.2.3 C_p (left) and velocity magnitude contours(right) around the NACA 0015 airfoil at different incidence angles - Courtesy of [Obeid et al.]

Figure 6.2.4 presents the chord wise distributions of the pressure coefficient (C_p) profile for the airfoil at some selected incidence angles. For small angles of attack, the C_p distribution is characterized by a negative pressure peak near the leading edge on the suction side. Beyond this point, the Cp value gradually increases along the chord of the airfoil. On the pressure side of the airfoil, the Cp value reaches a maximum of Cp = 1 at the stagnation line. This point is near the leading edge, but shifts slightly depending on the incidence angle. Further down the chord length of the airfoil, the pressure side Cp value increases gradually until it equals the suction side value at the trailing edge. **Figure 6.2.4** also shows that the flow remains attached to the suction surface up to $\alpha = 13$ degree after which flow begins to separate. The separation line starts near the trailing edge and

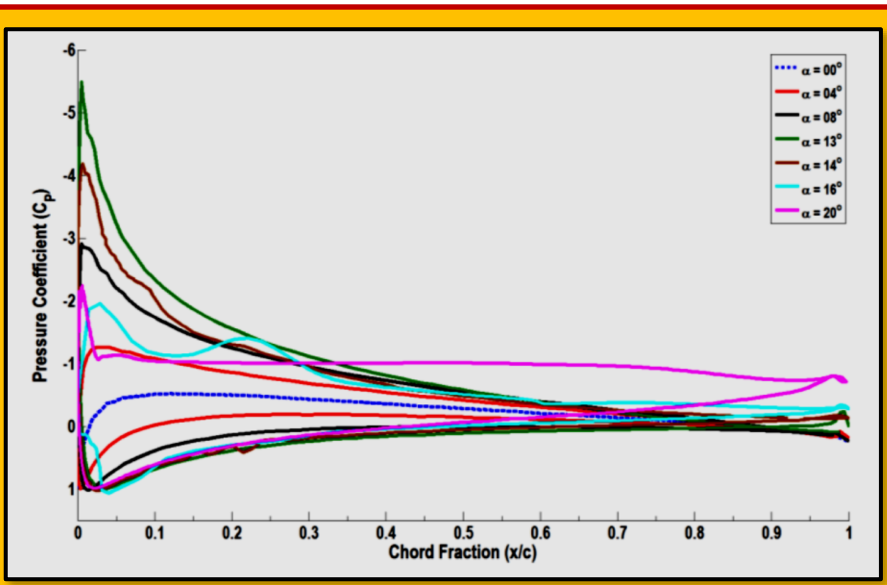

Figure 6.2.4 Pressure Coefficients along the Upper and Lower Surfaces of the Airfoil with 0 Degree Flap – (Courtesy of [Obeid et al.])

moves forward toward the leading edge as incidence increases. The flow becomes fully separated over almost the entire chord of the airfoil for α greater than 15 degrees. For α > 13, the maximum C_p negative value decreases on the airfoil upper side, and a pronounced shift of the stagnation position toward the trailing edge is found. This situation continues until α = 17, at which the C_p value starts to vary in an irregular manner. For better understanding of the airflow characteristics around the airfoil, variations of the skin friction coefficient are evaluated for selected incidence angles. The skin friction coefficients increase with the incident angle and also show a smooth variation for angles of attack equal to or smaller than 13 degrees. The skin friction coefficient

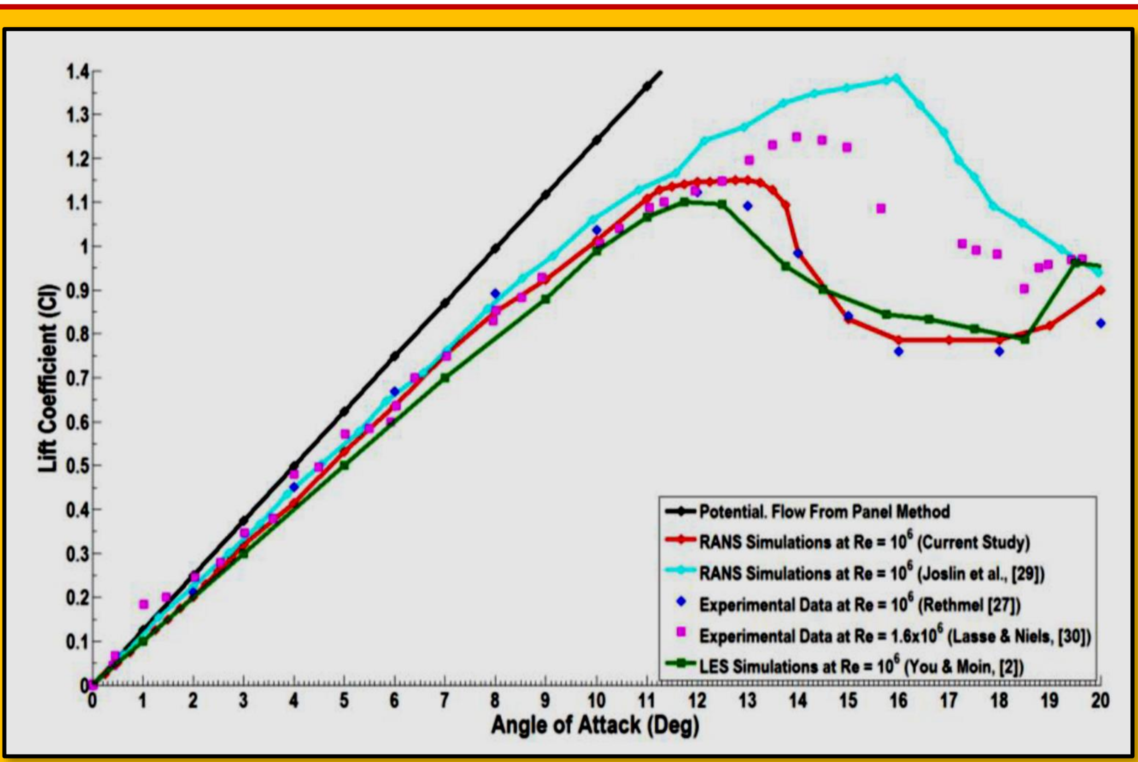

Figure 6.2.5 Comparison of Lift Coefficient C_L values of the Airfoil at 0° flap Deflection as a Function of (α) at Chord Re = 10^6 with Experimental and Numerical Results – (Courtesy of [Obeid et al.])

curve at $\alpha = 16$ shows an irregular variation, which is a typical trend for the cases when there are some separation zones.

Figure 6.2.5 shows the variation of the lift coefficient (C_L) with the incidence angle (α) at free stream conditions corresponding to a Re = 10^6. The lift and drag coefficients were calculated, and the results for the lift coefficient are shown. It is seen that the lift coefficient increases with the angle of attack up to about 13° and then decreases. The lift coefficient obtained from 2D potential flow analysis using the panel method, the RANS simulation results of [Joslin et al.][148] and the large eddy simulation results of [You and Moin][149] are also shown in this figure for comparison. Further and detailed analyses can be obtained from [Obeid et al.][150].

6.2.6 NACA 0015 Airfoil with Flap Deflection Results

The effect of downward flap deflection on the aerodynamic performance of the airfoil is studied for eight different flap positions of 10, 30 and 40 degrees. For zero AoA, the static pressure and velocity contours for different flap deflections (δ_f) are presented in **Figure 6.2.6**. The comparison of the static pressure contours for zero flap deflection and for the deflected flap at the same angle of attack shows that the flap deflection increases the negative pressure over the entire upper surface of the main airfoil and increases the positive pressure on the lower surface near the trailing edge. The

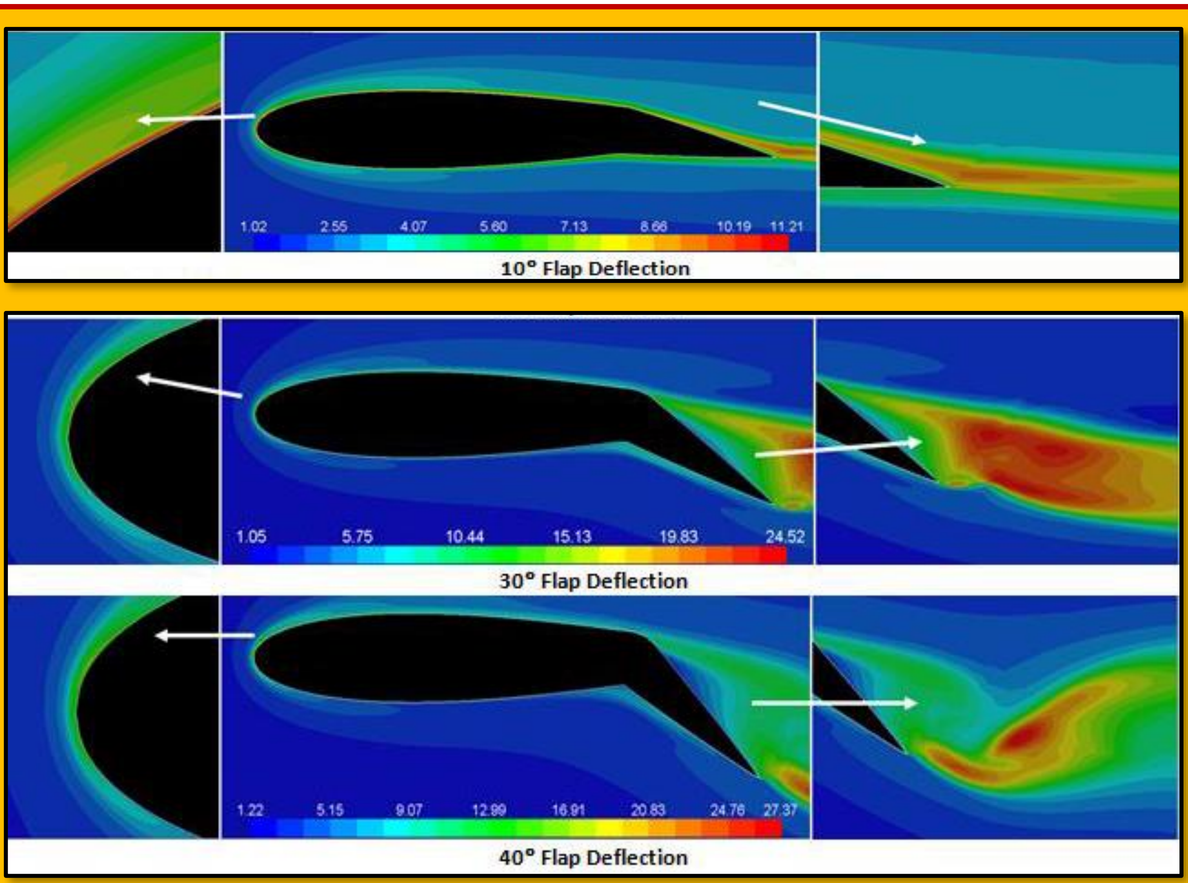

Figure 6.2.6 Turbulence Intensity (δ_f) Around the a Flapped Airfoil – (Courtesy of [Obeid et al.]

---

[148] Joslin, R.D.; Horta, L.G.; Chen, F.J. "*Transiting action control to application*", Proceedings of the 30th AIAA Fluid Dynamics Conference, Norfolk, VA, USA, 1999.

[149] You, D., Moin, P. "*Active control of flow separation over an airfoil using synthetic jets*", 2008.

[150] Sohaib Obeid, Ratneshwar Jha, and Goodarz Ahmadi, "*RANS Simulations of Aerodynamic Performance of NACA 0015 Flapped Airfoil*", Fluids 2017, 2, 2; doi:10.3390/fluids2010002.

pressure on the lower surface increases rapidly with flap deflection, while the pressure on the upper surface increases gradually. The pressures on both the upper and the lower surfaces of the flap increase with flap deflection. One other interesting observation is the progressive increase of the velocity magnitude over the upper surface of the main airfoil as the flap deflection increases. The flap deflection changes the velocity and pressure distributions on the airfoil upper and lower surfaces, causing higher pressure to be built over the rear portion, generating a net lift force at AoA = 0, and increases the airfoil maximum lift coefficient. The flap deflection also moves the zero lift angle-of-attack of the airfoil to a lower negative value and greatly increases the drag force.

The turbulence intensity contours of the flow around the flapped airfoil at some selected deflection angles and zero incidence are also evaluated. **Figure 6.2.6** presents the contours of turbulence intensity (δ_f) at 10, 30 and 40 degrees and for zero incidence angle. It is observed that at the zero incidence angle, the flap deflection has a pronounced influence on the turbulence intensity around the flapped airfoil. Even a small deflection in flap angle disturbs the flow and creates regions of high turbulence intensity in the upper surface of the flapped airfoil. These regions expand with increasing of the flap deflection and shift from the main airfoil towards the flap section. For $\delta_f \leq 15$, the realizable κ-ε model predicts that the peak turbulence intensity occurs in the boundary layer near both the upper and lower surfaces of the main airfoil close to the leading edge and with a lower level of turbulence intensity in the wake region. For $\delta_f > 15$, however, the maximum turbulence intensity occurs in the wake region close to the flap in addition to the boundary layer regions. This is due to the fact that the region with recirculating flow becomes larger as the wake width increases with the flap deflection. At high flap deflections, the flow separates from the flap, and high pressure acting on the pressure side of the flapped airfoil and consequently marked increase in the drag occur compared to situations where the flow remains attach to the surface. [Obeid et al.][151].

---

[151] Sohaib Obeid, Ratneshwar Jha, and Goodarz Ahmadi, "*RANS Simulations of Aerodynamic Performance of NACA 0015 Flapped Airfoil*", Fluids 2017, 2, 2; doi:10.3390/fluids2010002.

6.3 Case Study 3 - Dynamic Stall Investigation of 2D Vertical Axis Wind Turbine Blades Using CFD

Vertical axis wind turbines (VAWTs) are a type of wind turbines, mainly useful for urban and residential areas to produce electricity. It has some advantages over Horizontal axis wind turbines in terms of costs and maintenances. Dynamic Stalling is a common feature of these VAWTs in unsteady flow conditions. In fact, dynamic stalling is regarded as one of the prior obstructions for the ***improved aerodynamic features*** of VAWTs. Thus, it is important to understand the effects of dynamic stalling on it. This paper aims to present the dynamic stall investigation of a two-dimensional VAWT blade, i.e. NACA 0012 at the low-speed condition. The phenomenon was simulated using computational fluid dynamics (CFD) techniques to capture the leading-edge vortex (LEV) and trailing edge vortex on the airfoil due to unsteady flow conditions. *ANSYS FLUENT©* with manually hooked UDF subroutine was used to simulate the numerical results which were later compared to experimental data. ***Unsteady Reynold Average Navier Stokes (URANS) SST $k-\omega$ modeling was used to capture the dynamic stalling in a more detailed fashion.***

6.3.1 Introduction

The energy crisis has become one of the major problems for humanity. With the consumption of fossil fuel and other resources, the world's climate is changing dramatically. So, environment-friendly energy resources like wind energy have become an auspicious choice for engineers and scientist. Developed countries are now relying more on clean energy than conventional fossil fuels. For instance, in UK, total energy from total wind generation increased by more than one third, offshore wind energy increased by 27 percent (20.9 TWh)[152] vertical axis wind turbines (VAWTs) has some conveniences over the Horizontal axis wind turbines (HAWTs) for the built environment such as low sound emission, better aesthetic view, its insensitivity to yaw wind direction, and increased power output in the skewed form[153]-[154]. However, VAWT experiences dynamic stall when the tip speed ratio (λ) is low (generally $\lambda < 5$). So, it's essential to have a clear understanding of dynamic stall at a low Reynolds number. Modeling of VAWTs in dynamic stall faces some bold challenges[155]:

- Unsteady flow requires a time, accurate model.
- The rotor geometry does not allow for importing time grid simplification.
- A large amount of shed vorticity shows that model could be sensitive to numerical dissipation.
- The development of shed vorticity must be modeled correctly inside the rotor diameter. To avoid numerical dissipation, the spatial resolution of the grid must be very fine.
- The variation of the angle of attack of the blade with the azimuthal angle implies a varying relation
- between lift and drag force. Use of the correct turbulence model and near wall model is essential for this situation.

Figure 6.3.2-b is schematic of a straight-bladed fixed-pitch VAWT, which is an example of ***Darrieus*** type VAWTs. Relative velocity faces by the blade always changes with the change of azimuthal angle. **Figure 6.3.2-a** shows the rotating VAWT blade for a given azimuthal angle θ. In the counter-

---

[152] *UK Energy In Brief*, Department of Business, Energy & Industrial Strategy, London, 2018.

[153] Mertens, S., van Kuik, G. and van Bussel, G.. *Performance of an H-Darrieus in the skewed flow on a roof.* Journal of solar energy engineering, 125(4), pp.433-440, 2003.

[154] Ferreira, C.J.S., Van Bussel, G.J. and Van Kuik, G.A., 2006. *Wind tunnel hotwire measurements, flow visualization and thrust measurement of a VAWT in skew*. Journal of Solar Energy Engineering, 128(4).

[155] Ferreira, C.S., Bijl, H., Van Bussel, G. and Van Kuik, G., 2007. *Simulating dynamic stall in a 2D VAWT: modeling strategy, verification and validation with particle image velocimetry data*. Journal of physics: conference series (Vol. 75, No. 1, p. 012023). IOP Publishing.

clockwise direction, the angle θ is increased. The relationship between the angle of attack α, the tip speed ratio λ and the azimuthal angle θ can be expressed as flows:

$$\tan\alpha = \frac{U_\infty \sin\theta}{\Omega R - U_\infty \cos\theta} = \frac{\sin\theta}{\lambda - \cos\theta} \quad \rightarrow \quad \alpha = \arctan\left(\frac{\sin\theta}{\lambda - \cos\theta}\right)$$

Eq. 6.3.1

When the angle of attack is significantly beyond the static stall angle, an airfoil or wing faces dynamic stall under the unsteady motion. This dynamic stall usually followed by some events like larger lift for a short period of time and pitching moment. This phenomenon is associated with the motion of helicopter rotor blades, wind turbines, jet engine compressor blades, highly maneuvering air fighter.

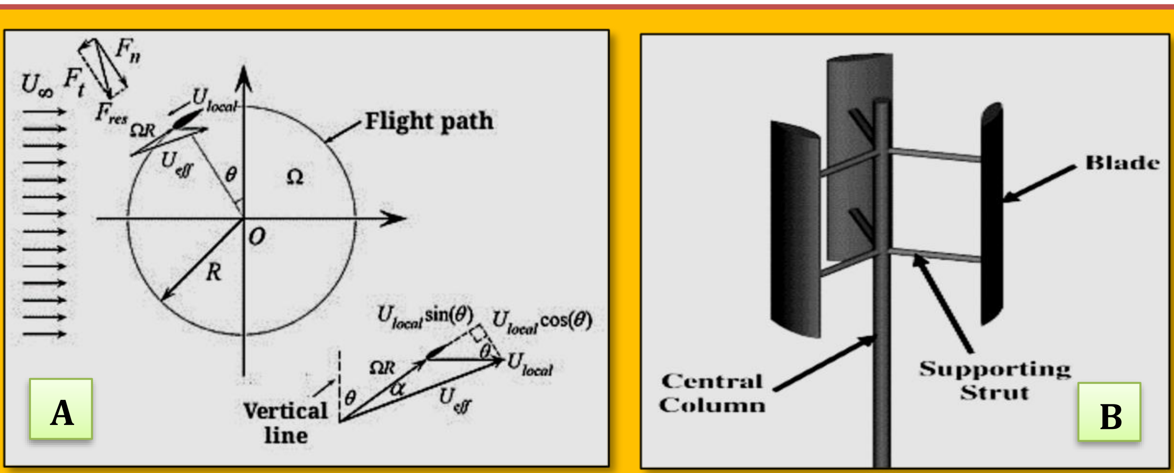

Figure 6.3.2 (a) Flow velocities of a straight-bladed Darrieus type VAWT [5] (b) Fixed pitch straight-bladed VAWT[6]

The stalled process has four parts: attached flow, development of the LEV, post stall vortex shedding, and the reattachment of flow. The Darrieus motion of blade is similar to sine curve and so, in a rotational frame of reference fixed on the turbine blade, the blade will experience a cyclic sinusoidal motion in the effective air velocity. Keeping that in mind, we choose a sinusoidal motion of the turbine blade as its pitching motion.

6.3.2 Model Geometry and Numerical Technique

The geometry of this model is a 2D setup of an experimental investigation of [Wernert et al] [156]. The blade executes an oscillatory motion around a fixed pivot point and follows a sinusoidal mode as described in the introduction. The function

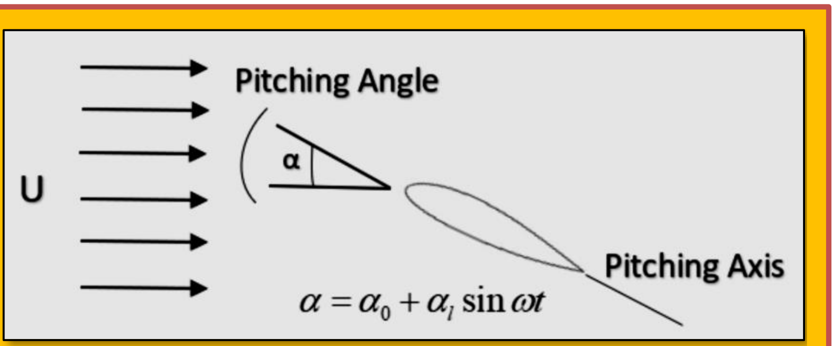

Figure 6.3.1 A Blade in the Pitching Motion [5]

---

[156] Wernert, P., Geissler, W., Raffel, M. and Kompenhans, J., 1996. *Experimental and numerical investigations of dynamic stall on a pitching airfoil.* AIAA journal, 34(5), pp.982-989.

for the angle of attack motion is:

$$\alpha = \alpha_0 + \alpha_1 \sin\omega t$$

Eq. 6.3.2

Where α_0 the mean angle of attack is, α_1 is the pitching magnitude, ω is the angular velocity. The pitched motion of the blade is shown in **Figure 6.3.1**. We have used NACA 0012 with a cord length of 0.20 meter and having a Reynolds number of 3.73 × 10^5. The case specification for the dynamic stall is shown in **Table 6.3.1**.

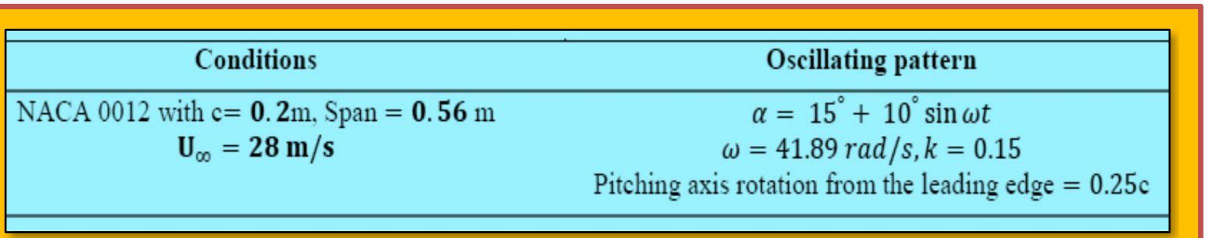

Conditions	Oscillating pattern
NACA 0012 with c= $\mathbf{0.2}$m, Span = $\mathbf{0.56}$ m $U_\infty = \mathbf{28\ m/s}$	$\alpha = 15^\circ + 10^\circ \sin \omega t$ $\omega = 41.89\ rad/s, k = 0.15$ Pitching axis rotation from the leading edge = 0.25c

Table 6.3.1 Case Specification for Dynamic Stall

6.3.3 Dynamic Mesh and Oscillating Pattern

Dynamic mesh technique is used here to simulate the sinusoidal pitching motion. The mesh consists of two domains: one is the fixed mesh zone and other is the dynamic mesh zone. ***Dynamic mesh*** zone was further divided it into two sections: sub-grid *I* and sub-grid II in order to get a better solution of the flow near the blade. We used the C-type mesh grid for sub-grid I. The circular shape zone oscillates like a rigid body while the fixed mesh zone is kept stationary. A UDF (user defined function) is developed and hooked up with fluent to control the dynamic mesh motion. Slip boundary condition is used for the simulation. Upper and lower boundary is 16*c* and 12*c* away from the blade respectively so that they have no boundary effects on the flow near the blade. The inlet and outlet are placed 8*c* upstream and 45*c* downstream from the blade respectively. The value of $y+$ is less than 1 so that the boundary wall behavior is accurately resolved. For further discussion. see [Hasan et al.][157]. Our point of interest is in the domain of C mesh (sub-grid I) which is coarser than sub-grid II. The turbulent process is still less understood phenomena in fluid mechanics. Turbulence models used in modern day are either algebraic type, turbulence energy equation type or second order closure type[158].

Large Eddy Simulation (LES), Direct Numerical Simulation (DNS), and Reynolds-Averaged Navier-Stokes (RANS) are the most used turbulence simulation methods. URANS (Unsteady Reynolds-Averaged Navier-Stokes) is employed here because of its acceptable computational cost with reasonable accuracy. To solve the governing equations, *ANSYS Fluent* © is used. Pressure based solver is used for the incompressible flow. The calculations have been carried out using standard $k\!-\!\omega$ model.

6.3.4 Results and Discussions

The objective of the work is to show the effect of dynamic stall on an airfoil having a Darrieus motion. For this case, SST $k\!-\!\omega$ model is used. Streamlines are computed numerically for a particular angle of attack. The airfoil mostly completes 15° upstroke and then it retreats. **Figure 6.3.4** shows the streamline velocity vector for α = 15° upstroke. **Figure 6.3.4-b** represents both experimental PIV

---

[157] Mahdi Hasan, Asif Kabir and Yeasir Mohammad Akib, "*Dynamic Stall Investigation of Two-Dimensional Vertical Axis Wind Turbine Blades Using Computational Fluid Dynamics*", AIP Conference Proceedings, (2019).

[158] Allet, A., Hallé, S. and Paraschivoiu, I., 1999. *Numerical simulation of dynamic stall around an airfoil in Darrieus motion.* Journal of solar energy engineering, 121(1), pp.69-76.

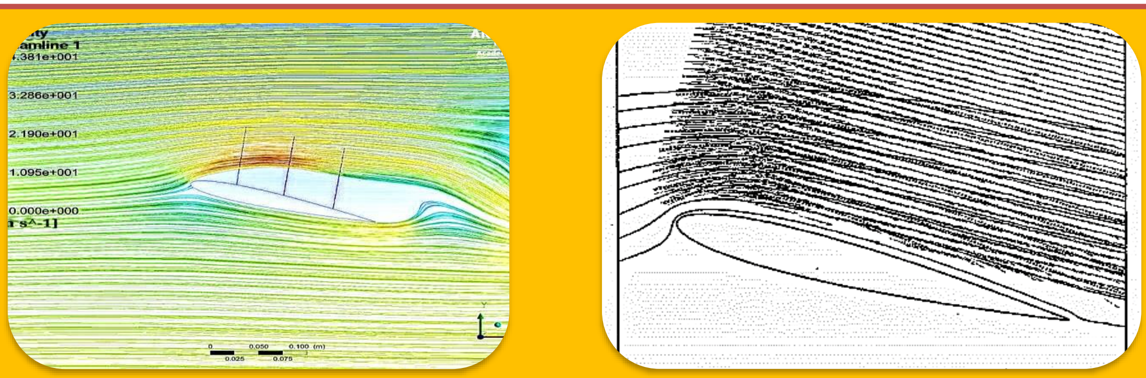

(a) **(b)**

Figure 6.3.3 Comparison Between Streamline Velocity (a) Numerical (for α = 15°, upstroke) (b) Experimental Data [7] (for α = 15°, upstroke)

(particle image velocimetry) and numerical streamlines calculated by [Wernert et al][159]. The computed streamline by using SST $k{-}\omega$ (**Figure 6.3.4-a)** is moderately matched with the experimental data shown in **Figure 6.3.4-b.** [Spentzos et al,][160] calculated the streamline velocity vectors (for α = 22°, upstroke) in **Figure 6.3.3** which is taken in three chord wise locations x/c = 0.25, 0.5, 0.75, (see [Hasan et al.][161].

Computed non-dimensional velocity at three different chord wise location (x/c = 0.25) is compared with the experimental data. At location x/c = 0.25 and x/c = 0.5, our numerical data (**Figure 6.3.4-a**) matches nicely with the experimental data. (**Figure 6.3.4-b**). The conclusion can be drawn by the comparison between numerical and experimental results, shown in **Figure 6.3.4** is that the same trend in velocity along the three-particular chord length location is observed.

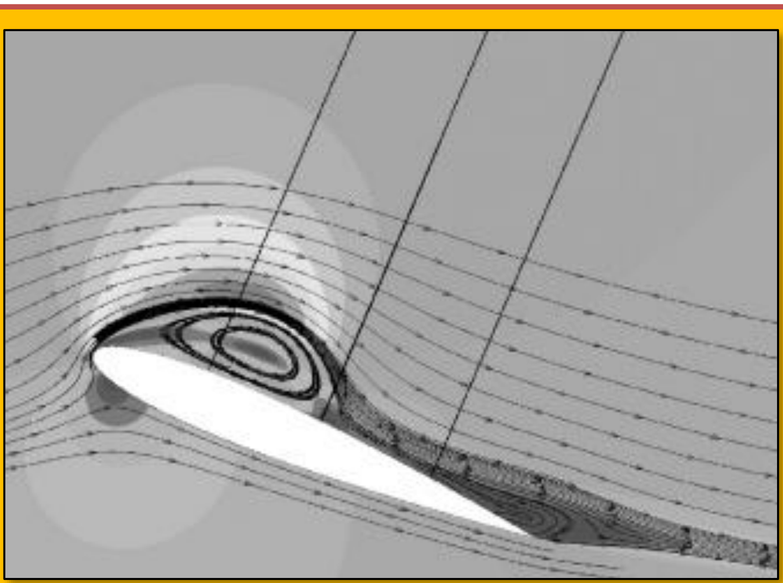

Figure 6.3.4 Streamline Velocity for α = 22°, Upstroke [Spentzoset al.]

---

[159] Wernert, P., Geissler, W., Raffel, M. and Kompenhans, J., 1996. *Experimental and numerical investigations of dynamic stall on a pitching airfoil*. AIAA journal, 34(5), pp.982-989.

[160] Spentzos, A., Barakos, G.N., Badcock, K.J., Richards, B.E., Wernert, P., Schreck, S. and Raffel, M., 2005. *Investigation of three-dimensional dynamic stall using computational fluid dynamics*. AIAA journal, 43(5).

[161] Mahdi Hasan, Asif Kabir and Yeasir Mohammad Akib, "*Dynamic Stall Investigation of Two-Dimensional Vertical Axis Wind Turbine Blades Using Computational Fluid Dynamics*", AIP Conference Proceedings, (2019).

For a full pitching cycle**, Figure 6.3.6** shows the vorticity fields for different angles of attack. For the angles of attack α = 5° and α = 9° flow remains attached with the airfoil (**Figure 6.3.6-a**). Small laminar separation occurs at the leading edge after α = 14° (**Figure 6.3.6-b)**. Counter-rotating vortices are observed in **Figure 6.3.6-c** and a LEV (leading Edge Vortex). As well as trailing edge vortex is produced. When the blade retreats, some counter-rotating vortices is observed (**Figure 6.3.5-d**). Then the vortices began to detach (**Figure 6.3.5-e-f)** from the blade and another counter-rotating vortex appear.

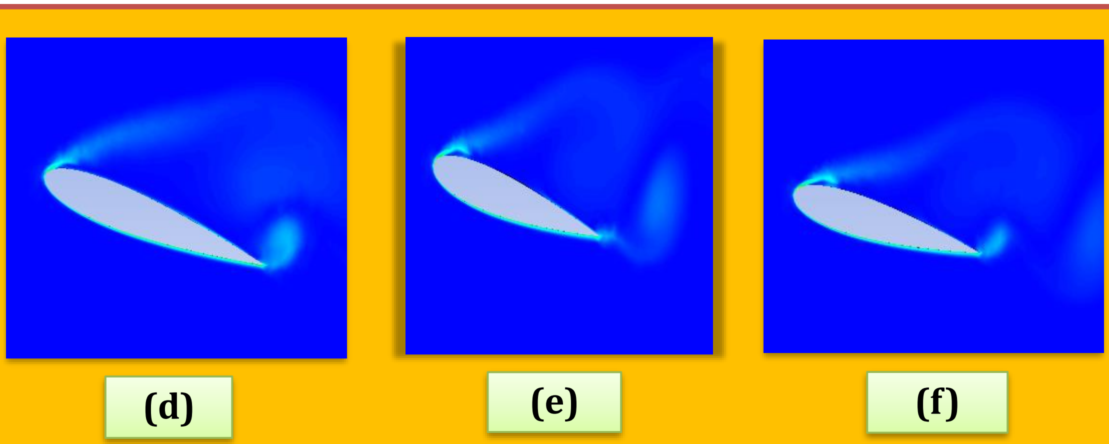
(d) **(e)** **(f)**

Figure 6.3.5 Vorticity for the Upstroke Pitching Phase Using (d) $\alpha = 10°$, downstroke (e) $\alpha = 7.5°$, downstroke (f) $\alpha = 6.5°$ downstroke

6.3.5 Conclusion

here, we studied and simulated the sinusoidal pitching motion of vertical axis wind turbine (VAWT) blade i.e. NACA 0012 to observe the dynamic stalling effects. ***Unsteady Reynold Average Navier Stokes (URANS) SST k-ω modeling*** was used to simulate the blade under low Reynolds number. The results are compared with experimental values and the results showed the same trend that we expected. The leading and trailing edge vortices found in the result is the key features in a pitching

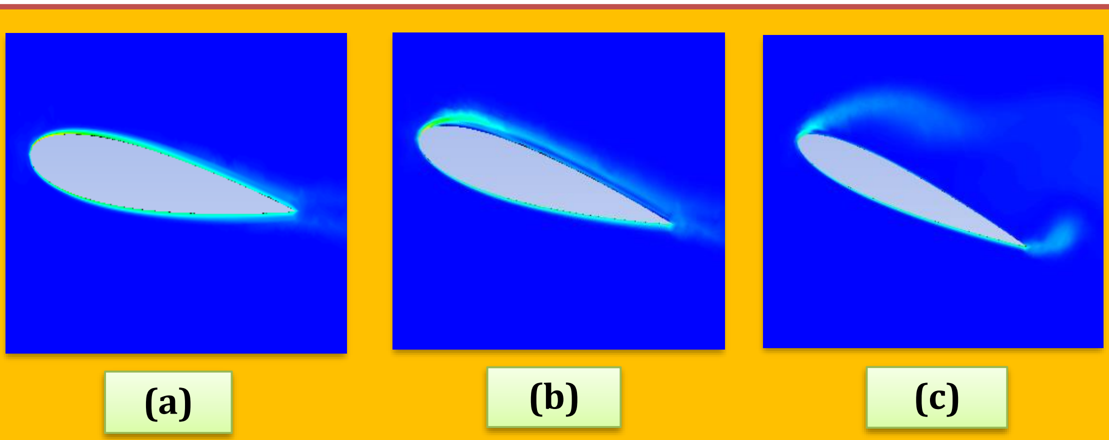
(a) **(b)** **(c)**

Figure 6.3.6 Vorticity for the Upstroke Pitching Phase Using (a) α = 5°, upstroke (b) α = 9°, upstroke (c) α = 14°

blade under the dynamic stall. From the study, it is observed that a more detailed feature of the blade can be compared with a higher pitching angle than the present study. To get the full understanding of the dynamic stall of the VAWTs, new simulations with high fidelity solvers like LES or DNS can be deployed instead of URANS. In order to do so, our present work can be a good guide to compare the results and draw a full-fledged conclusion on dynamic stalling effects of VAWT blades.

6.4 Case Study 4 - Numerical Investigation of Turbulent Flow Around an Stepped Airfoil at High Reynolds Number

Authors : *Masoud Boroomand and Shirzad Hossienverdi*
Affiliations : *AmirKabir University of Technology, Tehran, Iran*
Title of Paper : *Numerical Investigation of Turbulent Flow Around a Stepped Airfoil at High Reynolds Number*
Citation : *(Boroomand & Hossienverdi, 2009)*
Bibliography : *Boroomand, M., & Hossienverdi, S. (2009). Numerical Investigation Of turbulent Flow Around A stepped Airfoil at High Reynolds Number. ASME 2009 Fluids Engineering Division Summer Meeting FEDSM2009. Vail, Colorado USA.*

6.4.1 Abstract

This study presents the numerical simulation of flow development around NACA 2412 airfoil which utilized the backward facing step to explore the possibility of enhancing airfoil aerodynamic performance by trapped vortex lift augmentation (Boroomand & Hossienverdi, 2009). This article concentrate on the effect of separated flow and following vortex formation which is created by backward facing step on pressure distribution and subsequently on lift and drag coefficient. Reynolds number that based on the free stream velocity and airfoil chord is 5.7×10^6. The two equation shear stress transport (SST) k-ω turbulence model of Menter is employed to determine accurately turbulent flow, as well as the recirculation pattern along the airfoil. The ***Reynolds Averaged Navier Stokes (RANS)*** equations are solved numerically using finite volume based solution with second order upwind Roe's scheme. Steps are located on both suction side and pressure side of the airfoil, at different locations, different length s and various depth s in order to determine their effects on lift, lift to drag ratio and near stall behavior. The modeling results showed that all stepped airfoil cases studied experienced higher drag compared to the base airfoil. Considerable lift enhancement was found for airfoil with backward facing step o n pressure side at all values of angle of attack because of trapped vortex. The results suggest that the steps on the lower surface that extended back to trailing edge can lead to more enhancement of lift to drag ratio for some angles of attack; while the rear locations for the step on upper surface was found to have negative effect on lift to drag ratio. Based on this study , the backward facing step on suction surface offers no discernable advantages over the conventional airfoil but showed some positive effect on delaying stall

6.4.2 Introduction

The aerodynamic design of various airfoil sections continues today as an elegant yet practical engineering design problem. Theoretical studies of airfoil design led to the decomposition of airfoil geometric characteristic into thickness, camber, trailing edge and angle of attack. Much of the early design studies dealt with the proper combination of thickness shapes and camber shapes required to achieve some aerodynamic goals. This subject is not only important in external flow; but also it is very vital in internal flow such as the flow within the blade passage of a turbo machine.

For example, if one can design a blade that allows making a low mass flow zones in high angles, hence expects an increase in the working range or operating range of compressors. This article investigates separated flow developments around an airfoil that incorporate a backward facing step. The step is employed to generate a vortex over its vicinity, which increase the momentum of special regions on blade or airfoil and cause the moving of flow over it that may produce favorable effects in some flight conditions. The origin of this concept in airfoil design is attributed to a two artists in 1985 that published a book entitled "***The Ultimate Paper Plane***" in which they introduced the concept of a stepped airfoil[162]. A Kline Fogelman airfoil configuration such as this was reported to have vastly improved the performance of their paper creations and was expected to have a similar effect on real

---

[162] Kline R, *The ultimate paper plane.* Simon and Schuster, New York, N.Y, 1985.

aircraft. Stepped airfoils were claimed to possess excellent near stall properties and being capable of *"utilizing drag"* to achieve improved aerodynamic efficiency. A similar NASA sponsored study on the Kline Fogelman airfoil was carried out in 1974 at the University of Tennessee[163]. However, the cross section carefully examined in the study had a wedge like geometry lifted directly from the patent an d kind of missed the point.

[Fertis][164] reported considerable enhancement of the aerodynamic characteristics for a three dimensional wing model in terms of lift, drag, and stall angle[165]. Lift and the lift to drag ratio were greatly improved for specific geometries and angle of attack ranges. Against above studies that have done in low Reynolds number this work has been done in a high Reynolds number flow (5.7×10^{6}). The airfoil was simulated with the variations of following parameters: step location, step depth, step configuration and with the step on either the upper or lower surface. A standard NACA-2412 airfoil was used for simulation because of the availability of experiment data in the literature[166].

The present study aims on investigating the aerodynamic characteristic such as lift, drag and near stall behavior of stepped airfoil configuration. The stepped airfoil parameters such as airfoil chord, angle of attack, location of step, length and depth of upper and/or lower surface step are shown in **Figure 6.4.1**. In the first phase of the present research, the results of two dimensional flows are presented. Three dimensional studies are also under construction that its results will present in future report.

Nomenclature

C	Airfoil chord
C_L	Lift coefficient, $L/q_\infty C$
C_D	Drag coefficient, $D/q_\infty C$
C_P	Pressure coefficient, $(p-p_\infty)/q_\infty$
D_S	Step depth
K	Turbulent kinetic energy
L_R	Reattachment length
L_S	Step length
Re	Reynolds number, $U_\infty C/\nu$
X_S	Step location
t	Airfoil local thickness
U_i	Mean velocity component
U_∞	Free stream velocity

Greek Symbols

α	Angle of attack
μ	Molecular viscosity
μ_t	Turbulent viscosity
ρ	Density
ω	Specific dissipation rate
σ_k, σ_ω	Turbulent model constant

Subscript

L	Lower
R	Reattachment
S	Step
T	Turbulent property
U	Upper
∞	Free stream value

---

[163] Lumsdaine E, Johnson W.S, Fletcher L.M, Peach J.E, *Investigation of the Kline-Fogleman Airfoil Section for Rotor Blade Application*.1974, NASA, AE-74-1054-1

[164] Fertis D. G, *New airfoil design concept with improved aerodynamic characteristics*. J Aerospace Eng. ASCE, 1994; 7:328-339.

[165] See Previous..

[166]] Abbot I. H, Von Doenhoff A. E, *Theory of Wing Sections*. McGraw-Hill Book Company, New York, 1949.

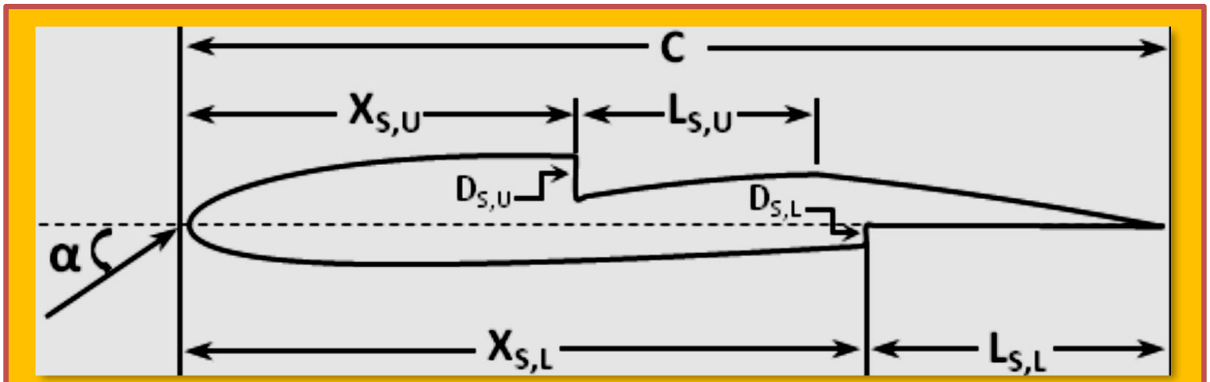

Figure 6.4.1 Stepped Airfoil Geometrical Parameters

6.4.3 Governing Equations

6.4.3.1 Reynolds-Averaged Navier-Stokes (RANS) Equations

For two dimensional flows, the time-averaged continuity equation and Navier-Stokes equations along with energy equation, in conjunction with the isotropic turbulent viscosity hypothesis, are written in a tensor form:

$$\frac{\partial \rho}{\partial t} + (\rho u_i)_j = 0$$

$$\frac{\partial \rho u_i}{\partial t} + \left(\rho u_i u_j + p\delta_{ij} - \tau_{ij}\right)_j = 0$$

$$\frac{\partial \rho e_0}{\partial t} + \left[(\rho e_0 + P)u_j + q_i - u_i\tau_{ij}\right]_j = 0$$

Eq. 6.4.1

The fluid is assumed to be perfect gas and obey the equation of state for calculation of pressure

$$p = (\gamma - 1)\left(\rho e_0 - \frac{1}{2}u_k u_k - \rho k\right)$$

Eq. 6.4.2

Shear stress tensor is

$$\tau_{ij} = \tau_{ij}^{Lam} + \tau_{ij}^{Turb}$$

Eq. 6.4.3

Where the laminar and turbulent stress are

$$\tau_{ij}^{Lam} = \mu\left(u_{i,j} + u_{ji} - \frac{2}{3}\rho u_k u_k \delta_{ij}\right)$$

$$\tau_{ij}^{Turb} = \mu_t\left(u_{i,j} + u_{ji} - \frac{2}{3}\rho u_k u_k \delta_{ij}\right) - \frac{2}{3}\rho k \delta_{ij}$$

Eq. 6.4.4

Similarly, the conductive heat transfer rate is

$$q_i = q_i^{Lam} + q_i^{Turb}$$

$$q_i^{Lam} = \frac{-\gamma}{\gamma - 1}\frac{\mu}{Pr}\left(\frac{p}{\rho}\right)_i$$
$$q_i^{Turb} = \frac{-\gamma}{\gamma - 1}\frac{\mu_t}{Pr_t}\left(\frac{p}{\rho}\right)_i$$

Eq. 6.4.5

The fluid is assumed air with a Prandtl number of 0.7 and turbulent Prandtl number of 0.9.

6.4.3.2 Turbulence Modelling

Among the several variations of widely used two-equation turbulence models, the shear-stress transport (SST) k-ω turbulence model of Menter[167]-[168] is adopted to properly resolve the complex flow over the stepped airfoil. This model is a two-equation eddy-viscosity model which merges the k-ω model of Wilcox with a high Reynolds number k-ε model (transformed into the k-ω formulation). The transport equations for the turbulent kinetic energy and the specific dissipation rate of turbulent in cartesian coordinate, along with their coefficients, develop in [Boroomand & Hossienverdi][169] and will not be repeated here.

6.4.3.3 Boundary Conditions

The boundary conditions applied to the computational domain are as follows:
No slip boundary conditions are enforced on the airfoil surface.

$$u_w = v_w = \kappa_w = 0 \qquad , \qquad \omega = \frac{60\nu}{\beta_1 d_1^2}$$

Eq. 6.4.6

Where, d_1 denotes the normal distance of the first node (cell centroid) from the airfoil surface. Pressure is based on a second-order extrapolation from within the flow field. Adiabatic wall boundary condition is used for temperature.
The far-field boundary conditions follow from the Riemann invariants. Depending on the sign of the eigenvalues of convective flux Jacobians, the information is transported out of or into the computational domain along the characteristic. The values of *k* and ω at the far-field boundary are calculated from the following equations:

$$\kappa = \frac{3}{2}(T_i \times u_\infty)^2 \qquad , \qquad \omega = \frac{1.82k^{0.5}}{L_m}$$

Eq. 6.4.7

Where T_i is turbulence intensity and less than 0.1 %, L_m is the length scale constant and is the order of 0.001.

6.4.4 Numerical Solution Procedure

The above equations are solved by finite-volume method in a non-uniform orthogonal body-fitted grid. The inviscid flux terms are approximated by Roe's method with MUSCL treatment to achieve

---

[167] Menter F. R, Zonal *Two Equation k-ω Turbulence Models for Aerodynamic Flows*. AIAA Paper 1993; 93-2906.

[168]] Menter F. R, *Two-Equation Eddy-Viscosity Turbulence Models for Engineering Applications*. AIAA Journal, 1994; 32: 269-289.

[169] Masoud Boroomand, Shirzad Hossienverdi, *Numerical Investigation Of turbulent Flow Around A stepped Airfoil at High Reynolds Number,* Proceedings of the ASME 2009 Fluids Engineering Division Summer Meeting FEDSM2009 August 2-6, 2009, Vail, Colorado USA.

second-order accuracy (2nd order upwind), and viscous terms are approximated by second-order gradient theorem. The time derivative–terms are discretized using first-order backward Euler implicit scheme.

6.4.5 Validation Test & Grid Independency Study

The major difficulty of model validation in the present case is the lack of adequately detailed experimental data. In view of this, model validation is focused on flow over unmodified airfoil of NACA-2412. **Figure 6.4.2** represented the lift and drag coefficient for the current case at Reynolds number of 5.7×10^6 in wide range of angles of attack in which the experimental data are plotted as symbols, and the solid and dashed lines represent the transitional and fully turbulent models, respectively. The figure highlights the improvement achieved for drag coefficient (C_D) when using the transitional model where the corresponding curve is consistently closer to experimental data from the one obtained the fully turbulent model. The comparison of lift coefficients are in an excellent agreement with the experimental. The lift coefficient results are the same for the both of the models. The location of maximum lift coefficient (C_L) predicted very well by means of k-ω (SST).

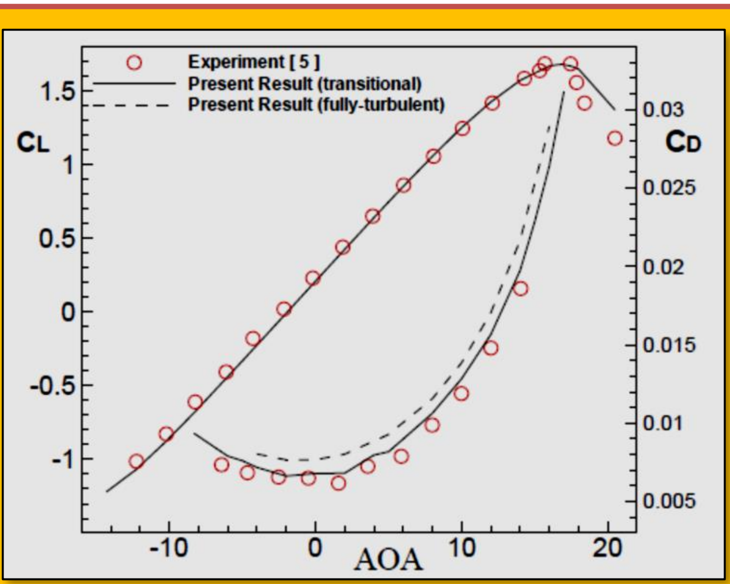

Figure 6.4.2 Validation of C_L and C_D for NACA 2412 Airfoil

The discretized equations are solved in C-grid system. The distance of the first cell adjacent to the airfoil surface was taken to be 1.5×10^{-5} chord which is sufficient to resolve the laminar sub layer, ($y^+\approx1$). The computational domain extends 35 chords away from the airfoil. A grid-independent study is shown in **Figure 6.4.3**, for stepped airfoil which $X_{S,U}/C=0.4$, $D_{S,U}/t = 0.2$. Three levels of grid refinement have been used. In every refinement, number of total grid is about 1.5 times more and third one with 30000 grid nodes is selected to be sure of grid independency.

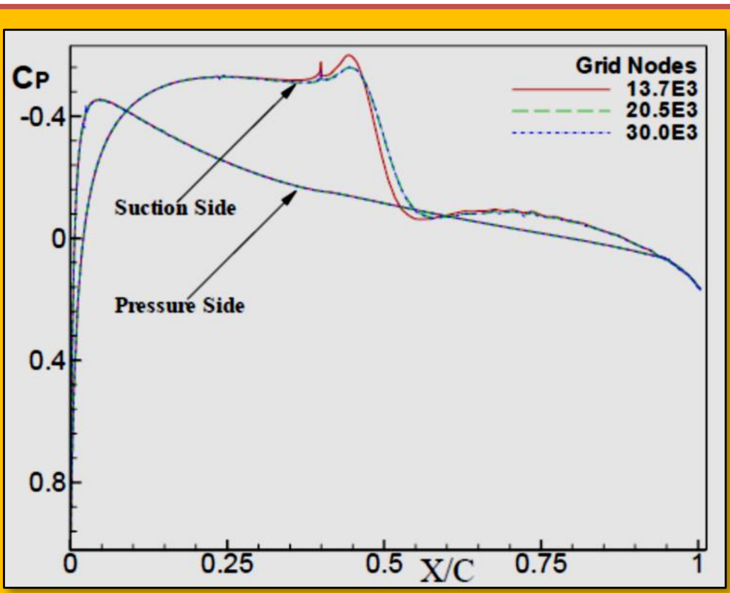

Figure 6.4.3 Grid Independency Study of Stepped Airfoil

6.4.6 Results & Discussion

Numerical solutions are presented in three parts and results are produced in Reynolds number of 5.7×10^6 but at four different angles of attack, (-2°, 0°, 5°, 10°).

6.4.6.1 Effect of Step Location

For studying of influence of step location on aerodynamic behavior of airfoil, step front is moving toward the leading edge while the whole step extended back to the trailing edge, ($L_S = CX_S$). In all of the cases, the ratio of step depth (D_S) to the airfoil local thickness (t) is kept constant, and equals 0.2 ($D_S/t = 0.2$). Step location varies between 0.2C to 0.5C. The calculations are done for both upper and lower step separately**.** The step shapes are shown in **Figure 6.4.4**. Note in this part the ratio of D_S/t is constant, but D_S varies with moving of step location. For the upper and lower step, with the moving forward from $X_S/C = 0.5$ to X_S/C =0 .3, step depth, D_S, increases and from $X_S/C = 0.3$ to $X_S/C = 0.2$, decreases. Before detailed discussions of pressure distributions and corresponding lift and drag coefficients are presented, it seems necessary to introduce the reattachment length that this length is the indication of circulation region. The air stream over the backward facing step produces a separated flow containing a circulation zone and shear layer which the flow will be attached again after a length of LU (Reattachment length). This phenomenon is shown in **Figure 6.4.5**. Reattachment length definition and velocity profile over the step corner have to be introduced as it is that shown in **Figure 6.4.5.** Reattachment length equals distance between the points that skin friction coefficient is zero to the step location.

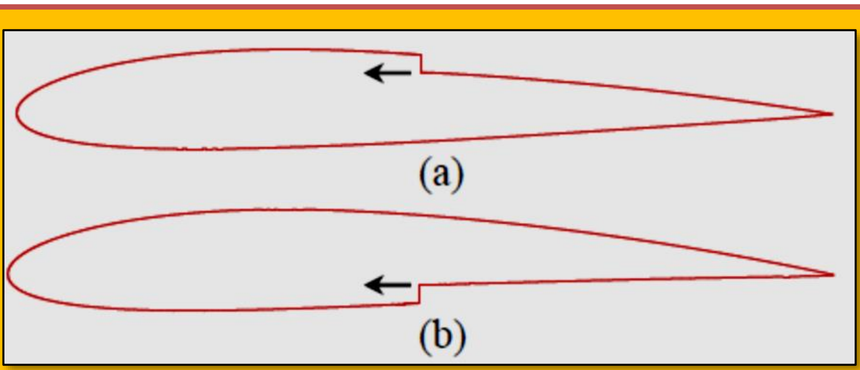

Figure 6.4.4 Step Shapes a) Upper, b) Lower Stepped Airfoil

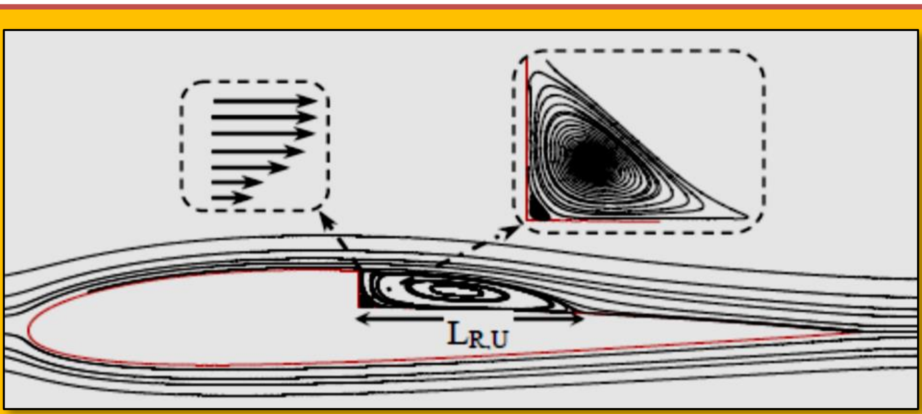

Figure 6.4.5 Velocity Profile Over the Top Step Corner and Reattachment

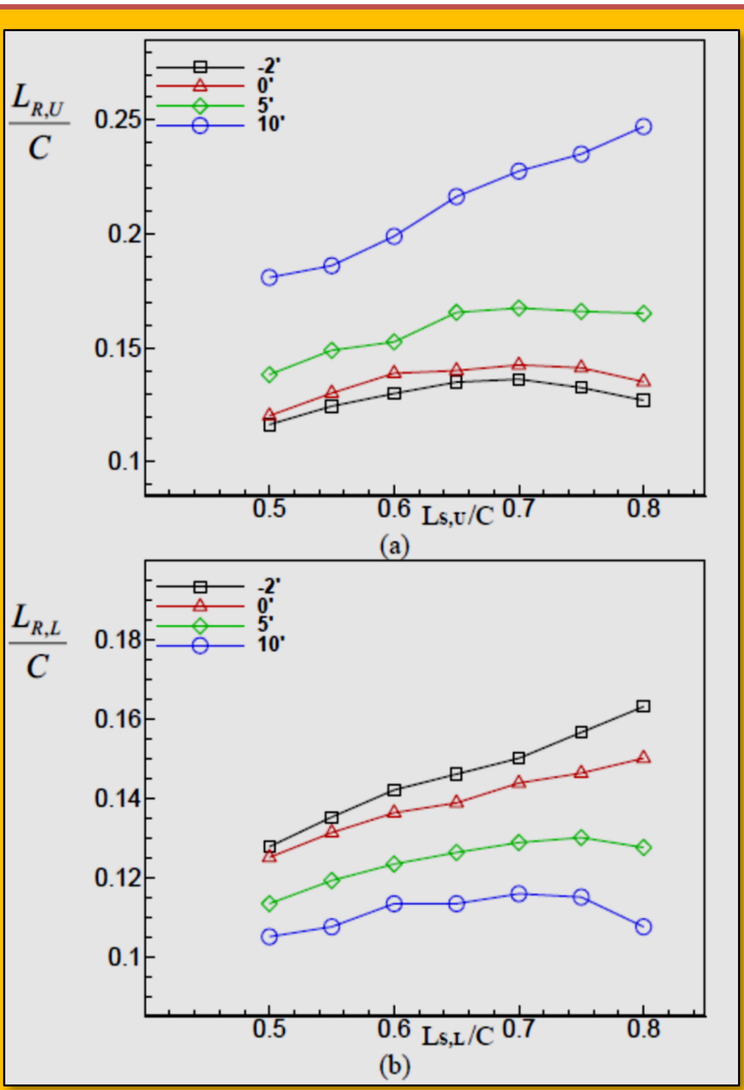

Figure 6.4.6 Variation of Re-Attachment Length Versus Step Length for Upper, b) Lower Stepped Airfoils

This length has significant impact on the variation of the lift and drag coefficient. Therefore variations of this length for upper and lower stepped airfoils for this part are studied in detail. There are two important factors which influence the reattachment length [170] - [171] - [172]. The first parameter is step depth and the second parameter is the velocity profile over the step corner. The former parameter will also vary with angle of attack. If both of them increase, then reattachment length will increase. The decreased of both of them will eventually reduce the reattachment length. The variations of reattachment length against the step length for upper stepped airfoils are displayed in **Figure 6.4.6-(a)**. Keeping constant step location, the reattachment length is increased with the increasing of angle of attack. This is due to the higher velocity above the step. Moreover, considering constant angle of attack, when the step front is moved toward to the leading edge from $X_{S,U}/C = 0.5$ to $X_{S,U}/C = 0.3$. It means that the step length increased to $L_{S,U}/C = 0.7$, the reattachment length increases, because of the both mention factors increased, but when the step front is moved from $X_{S,U}/C = 0.30$ to $X_{S,U}/C = 0.20$ ($0.7 < L_{S,U}/C < 0.8$) the reattachment length ($L_{R,U}/C$) stayed without change or a little reduction at $\alpha = -2^{\circ}$ and 0° angles of attack. It is resulting from reduction in step depth; also velocity increment over the step is negligible.

Figure 6.4.6-(b) shows the same result for lower stepped airfoils. Similar the above explanation, in the fixed step location ($X_{S,L}/C$ = Cte), as angles of attack increased, the reattachment length ($L_{R,L}/C$) decreases with it, against the upper stepped airfoils, this is due to the velocity over the step

---

[170] Adams E. W, Johnston J. P, Eaton J. K, *Experiments on the structure of turbulent reattaching flow*. 1984, Report MD-43, Department of Mechanical Engineering, Stanford University.

[171] Armaly B. F, Durst F, Pereira J. C. F, Schonung B, *Experimental and theoretical investigation of backward-facing step flow*. J. Fluid Mech, 1983: 127:473-496

[172] Thangam S, Knight D. D, *Effect of step height on the separated flow past a backward facing step*. Phys, Fluids, 1989; 3:604-606.

decreased. The trend of change in the reattachment length in the fixed angle of attack for lower stepped airfoil is similar to the upper stepped airfoil but at 5^{o} and 10^{o} angles of attack, the $L_{R,L}/C$ is stayed constant or a little reduction. Because of the velocity increment over the step is negligible and step depth decreases.

Figure 6.4.7(a) shows the surface pressure distribution over upper stepped airfoils at 0o angle of attack for various step locations. For upper stepped airfoils, only the pressure distribution of upper surface is shown here. The distribution for the unmodified lower surface reminded the same regardless of step. **Figure 6.4.7(b)** shows the same results for lower stepped airfoils. Also for lower stepped airfoil, the lower surface pressure distribution is shown here only and the unmodified upper surface pressure stays without change.

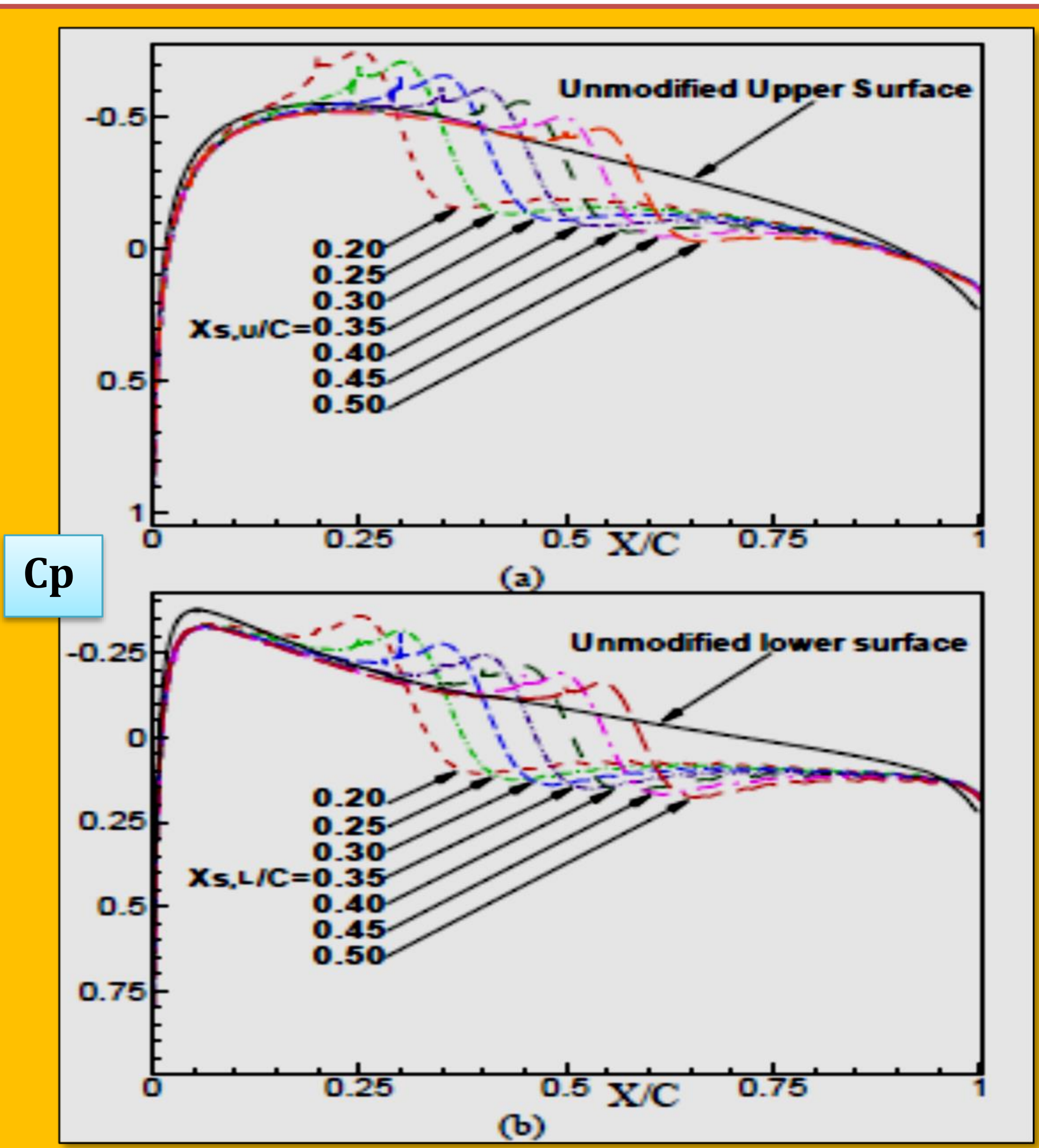

Figure 6.4.7 Pressure Distribution at $\alpha = 0$ Angle of Attack for a) Upper, b) Lower Stepped Airfoils

As evidence, significant changes in the pressure distribution occurs because of the presence of the step. Step on the upper side of the airfoil increases the level of pressure distribution above the airfoil in LR,U comparison with unmodified upper airfoil surface. The same results show the level of pressure for airfoil with step on pressure side increase in the lower surface with regard to the unmodified lower airfoil surface.

The location of minimum pressure is placed somewhere in the near of the center of circulation zone. By extracting the reattachment length from **Figure 6.4.6** for angle of attack of 0.0, it can be shown that, the location of maximum pressure occurs about at the point that the flow is reattach again.

Figure 6.4.8 (a) shows the change in the lift coefficient, ΔCL, as a function of step length for the upper stepped airfoils. Value of ΔC_L represents the difference in lift coefficient between an unmodified airfoil and a stepped airfoil. A positive value indicates an enhancement in C_L and negative value indicates a reduction in C_L with respect to the lift coefficient of unmodified airfoil.

For upper step, when the step is moved forward, it means that XS,U/C is decreased consequently the step length ($L_{S,U}/C$) is increased, ΔC_L is getting more negative. The reason can be seen in **Figure 6.4.7(a)**, because the high pressure zone on the upper surface increases, hence C_L drops more. But in higher angles of attack (50 and 100) the extent of drop is more, because the circulation zone over upper surface is larger.

For lower stepped airfoil, because of presence of step on lower surface, as expected, the lift coefficient is enhanced. This is illustrated by the positive value of ΔC_L in **Figure 6.4.8(b)**. In this case, the high pressure zone in lower surface increases as can be seen in **Figure 6.4.7(b)**. Therefore, it is concluded that the enhancement of lift coefficient is more when the step is moved forward. At higher angle of attacks (50 & 100) this increment is less than lower angle of attacks because the circulation zone in lower surface is smaller.

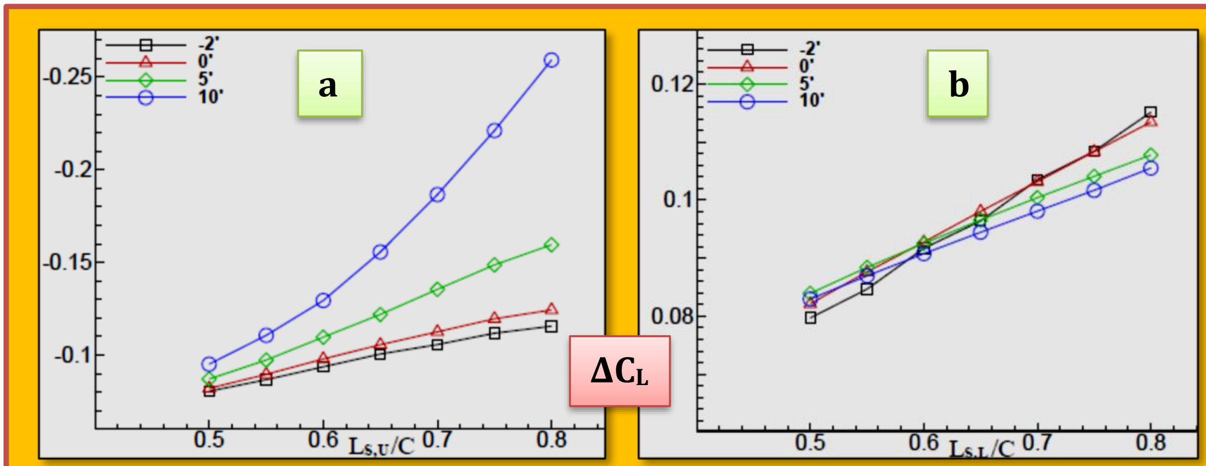

Figure 6.4.8 Change in Lift Coefficient versus Step Length for a) Upper, b) Lower Stepped Airfoils

Change in drag coefficient for upper and lower stepped airfoils are shown in **Figure 6.4.10(a)** and **(b).** The first object that can be found in these figures is that the all stepped airfoils with different step lengths, experienced higher drag coefficient in compared to the base airfoil. The other subject that is the worthy of note is the trend of variation in drag coefficient. Comparison of the behavior of drag coefficient increment (ΔC_D) in **Figure 6.4.10(a) (b)** with the extend of the reattachment length in **Figure 6.4.6(a) & (b)** for upper and lower stepped airfoils respectively, it's found that they have the same procedure particularly for upper stepped airfoil.

This means that as reattachment length is more, change in drag coefficient (ΔC_D) is also getting more, as reattachment length stayed constant; ΔC_D is also stayed without change. Drag increment for lower stepped airfoil is less than the upper stepped airfoil drag at the same angle of attack and step length. This is due to the higher reattachment length of upper stepped airfoil compared to the lower stepped airfoil. For further information, such as effect of C_L/C_D, please refer to the development in [Boroomand and Hossienverdi][173].

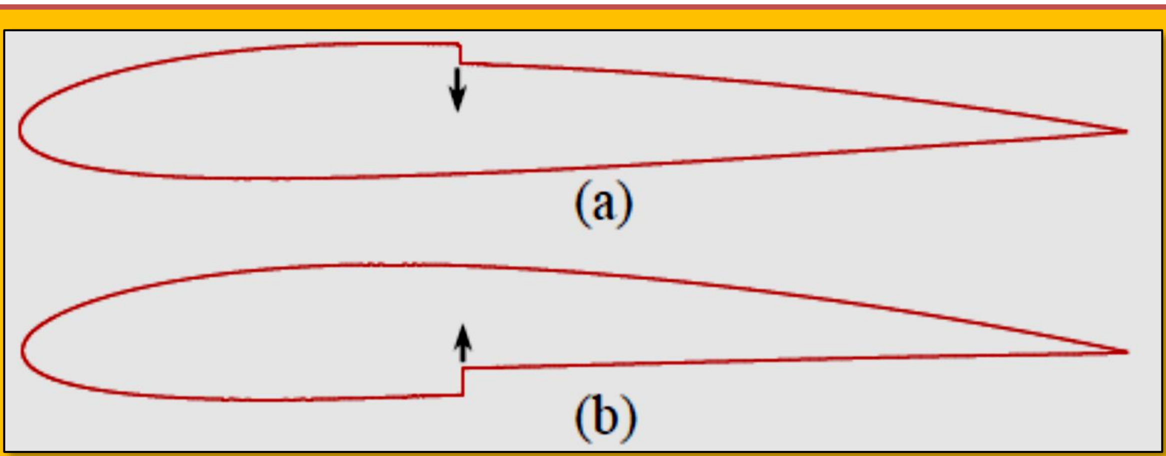

Figure 6.4.9 Step Shapes for a)Upper, b) Lower Stepped Airfoils

6.4.6.2 Effect of Step Depth

The second parameter which is studied is step depth. In this case, the step location is kept constant at 0.4 chord ($X_S/C = 0.4$). The step depth, DS is varied in a range between 0 (airfoil without step) and 0.4 airfoil local thickness (t). The step configurations are displayed in **Figure 6.4.9**. As a previous part, the step extends back to the trailing edge. The effect of circulation zone (reattachment length)

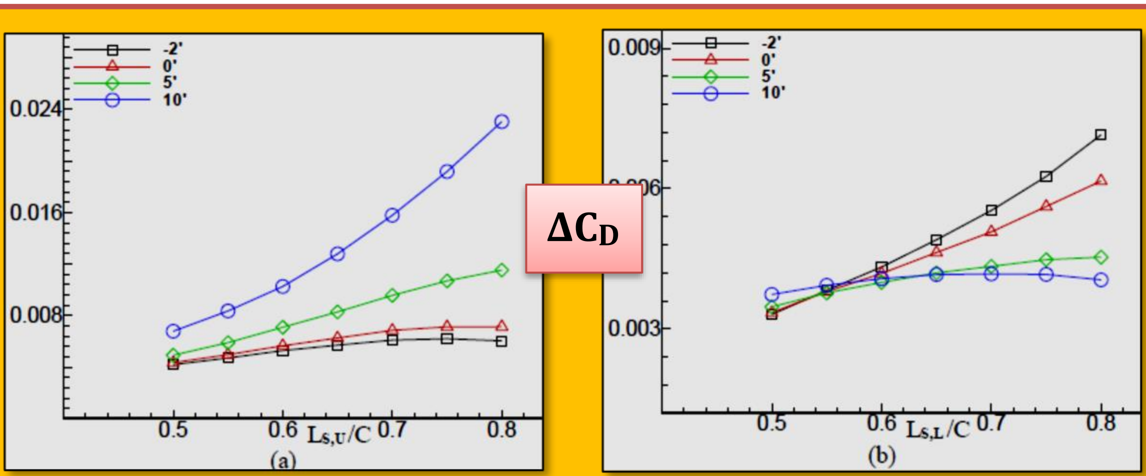

Figure 6.4.10 Change in Drag Coefficient vs Step Length a) Upper b) Lower Step Airfoil

---

[173] Masoud Boroomand, Shirzad Hossienverdi, *Numerical Investigation Of turbulent Flow Around A stepped Airfoil at High Reynolds Number,* Proceedings of the ASME 2009 Fluids Engineering Division Summer Meeting FEDSM2009 August 2-6, 2009, Vail, Colorado USA.

on the variation of lift and drag coefficient is similar to the previous investigated. Then they are not discussed in detailed again.

Upper surface pressure distributions of upper stepped airfoils are shown in **Figure 6.4.11 (a)**. The increased in pressure caused by reattachment of the flow can also be seen in this figure. As step depth increased, a downstream migration of the disturbance was observed for upper stepped airfoils. This indicates that the circulation zone (reattachment length) increased with increased of step depth. Also pressure recovery became stronger. The similar trend is seen in **Figure 6.4.11 (b)** for lower surface of lower stepped airfoils.

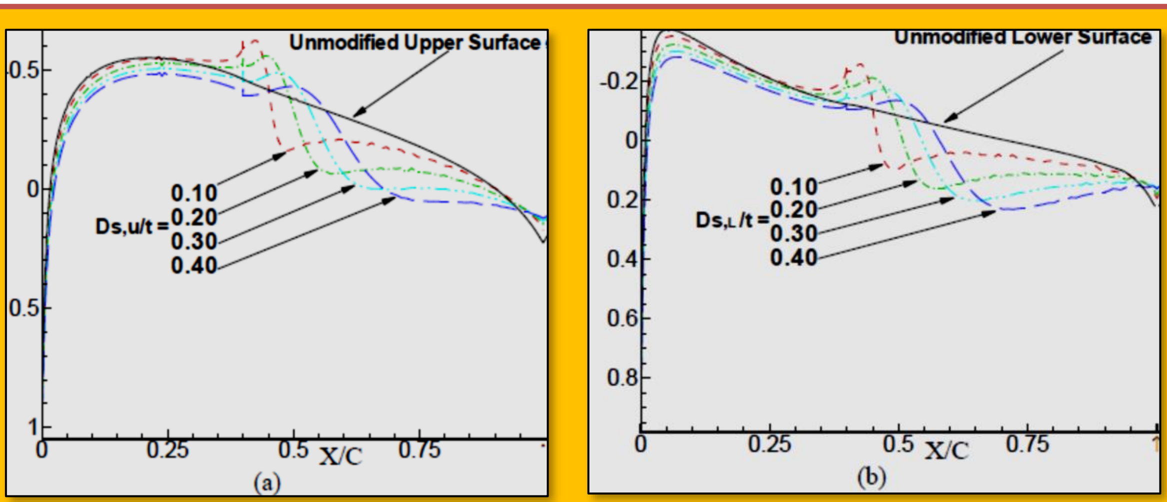

Figure 6.4.11 C_P Distribution at α = 0 (a) Upper (b) Lower Stepped Airfoil

The variation of lift to drag ratio with the step depth for upper stepped airfoils in are shown [Boroomand and Hossienverdi][174], and not repeated here. With increasing of step depth, reduction in C_L/C_D happened at all angles of attack. At higher angles of attack (5°, 10°), reduction is significant.

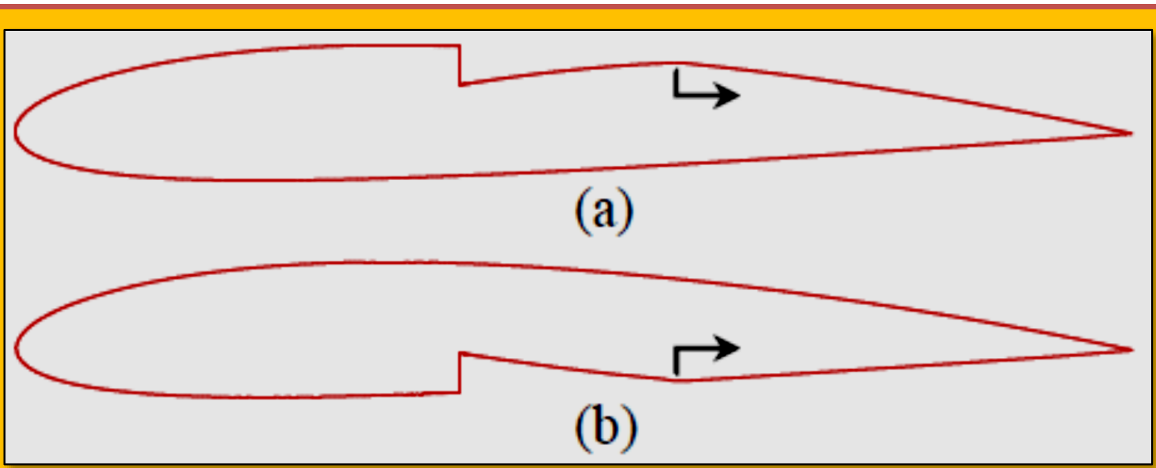

Figure 6.4.12 Step Shapes for (a) Upper, (b) Lower Stepped Airfoils

---

[174] Masoud Boroomand, Shirzad Hossienverdi, *Numerical Investigation of turbulent Flow Around A stepped Airfoil at High Reynolds Number,* Proceedings of the ASME 2009 Fluids Engineering Division Summer Meeting FEDSM2009 August 2-6, 2009, Vail, Colorado USA.

6.4.6.3 Effect of Step Configuration

In order to study the step configuration especially because the previous studies used a different form [175]; it was decided to compare different configurations. In this section, the step location and step depth are constant and equal $X_S/C = 0.4$, $D_S/t = 0.3$, but against the previous parts, that step extend back to the trailing edge, step cuts the intermediate upper or lower airfoil surface, and the cut point varies from X/C = 0.5 to X/C = 1. The step shapes are shown in **Figure 6.4.12**.

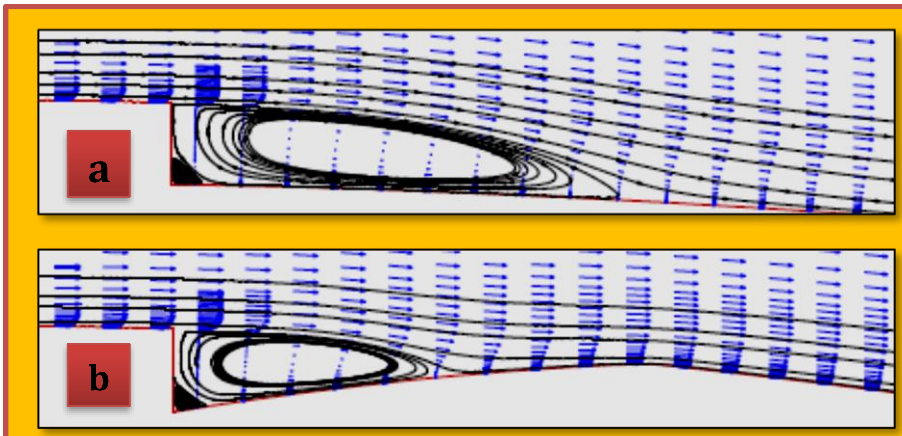

Figure 6.4.13 Velocity Vectors and Stream Line Within the Step Region at α = 0°

Before discussion of pressure distribution for these cases, it seems logical to show sample of velocity vector and stream line around a airfoils with step on upper surface with close up on the step region.

As can be seen in **Figure 6.4.13 (a)**, for upper stepped airfoil which step extended be back completely to the trailing edge, a circulation zone formed over the step, as indicated by the stream line, which also show the flow reattachment some distance downstream the step.

Another flow visualize over the upper stepped airfoil is shown in **Figure 6.4.13 (b)**, but against the above sample, the step cuts the intermediate upper surface of airfoil. As expected, flow reattachment occurs at the shorter length. Because of the convex shape of the region, flow accelerates as indicated in **Figure 6.4.13 (b)** by the increases in lengths of the velocity vectors near the convex location. Both of these stepped airfoils have the same step location at $X_{S,U}/C = 0.4$ and step depth of $D_{S,U}/t = 0.3$.

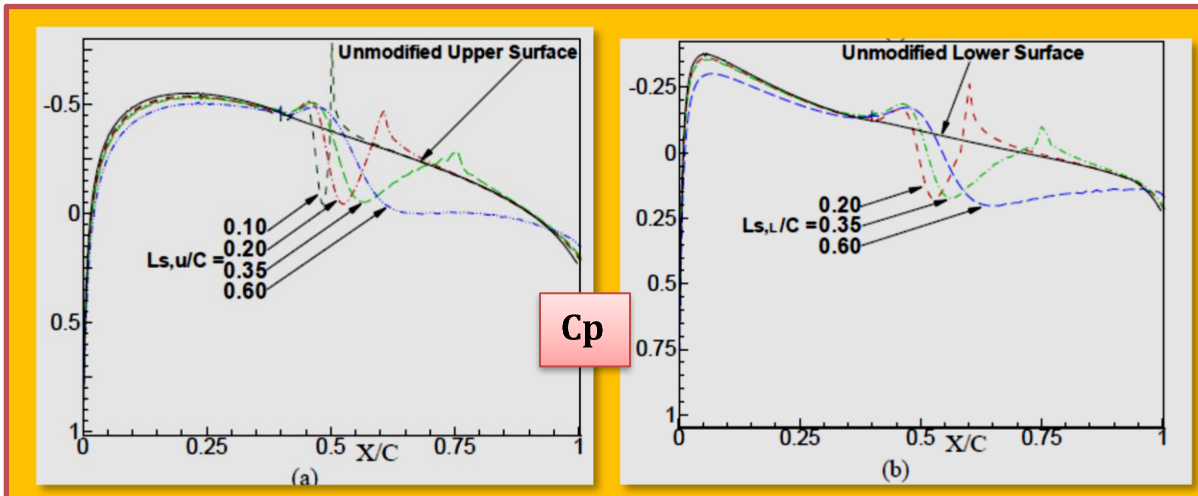

Figure 6.4.14 Pressure Distribution at α = 0 (a) Upper (b) Lower

---

[175] Finaish F, Witherspoon S, *Aerodynamic performance of an airfoil with step-induced vortex for lift augmentation*. J Aerospace Eng, ASCE, 1998; 7:9-16

Figure 6.4.14 (a) and **(b)** show the surface pressure distributions of upper and lower stepped airfoils respectively. The results indicate that there are some differences between these pressure distributions with the previous cases studied. This discrepancy is due to the presence of convex region on upper and lower surface. Existence of the convex region caused that flow accelerated and ensuing pressure drop causes spikes, which can be seen near the X/C = 0.5, 0.6 and 0.75 for upper stepped airfoil and X/C = 0.6 and 0.75 for lower stepped airfoil. The blue dashed lines exhibit the stepped airfoils which step extended back completely to the trailing edge and they did not have the spikes in own pressure distribution.

Variation of the lift to drag ratio of upper and lower stepped airfoils are displayed in[176]. For upper stepped airfoils, similar the previous upper stepped airfoils investigated, the lift to drag ratio drop, but for step which cut the intermediate upper surface, the reduction is less. For lower stepped airfoil, at α=-2° the lift to drag ratio increased compared to the unmodified airfoil as expected, but the gain in lift to drag ratio is more for lower stepped airfoil which step stretched back entirely.

However, the reduction of lift to drag ratio at higher angles of attack (5°, 10°) is less for stepped airfoil which the step cut the intermediate lower airfoil surface. Improvement in stall condition is more for upper stepped airfoils which step on upper surface stretched back to the trailing edge**.** Enhancement of lift coefficient for lower stepped airfoils are more for step which extended back to the trailing edge entirely,

6.4.7 Conclusion

Numerical simulation of turbulent flow round NACA-2412 airfoil which utilized a backward-facing step on upper and lower surface is reported. Based on the observation of the effects of step-induced vortex on aerodynamic performance of stepped airfoil at Reynolds number of 5.7×10^6, the following conclusion can be made:

1. Drag coefficient experienced higher at all angles of attack in all cases. When step front is moved toward the leading edge which it means step length increased or step depth increased, drag also increased for both of upper and lower stepped airfoils. Drag increment for lower stepped airfoil is less than the upper stepped airfoil drag at the same angle of attack, step depth and step length.
2. Incorporating backward-facing step on upper surface caused a reduction of lift coefficient and lift to drag ratio at all angles of attack. Therefore the presence of step on upper surface offers no advantages over unmodified airfoil but showed some positive effects on delaying the stall point. The improvement of stall angle of attack is increased with the increases of step length and depth. From the geometric point of view of the step, it is recommended that the step on upper surface should not be extended back completely to the trailing edge, but step cuts the intermediate upper airfoil surface in order to reduce the negative effect of reduction in lift and lift to drag ratio.
3. For lower stepped airfoil, lift coefficient was higher at all angles of attack. In some angle of attack a better ratio of lift to drag is achieved. This means that airfoils with step on lower surface have a potential for more improvement.

Against the previous conclusion for upper stepped airfoil, step on lower surface that extended back to the trailing edge can lead to more enhancement of lift to drag ratio. In conclusion, based on this study one concluded that a single configuration is not, and cannot be, the best configuration at every angle of attack.

---

[176] Masoud Boroomand, Shirzad Hossienverdi, *Numerical Investigation of turbulent Flow Around A stepped Airfoil at High Reynolds Number,* Proceedings of the ASME 2009 Fluids Engineering Division Summer Meeting FEDSM2009 August 2-6, 2009, Vail, Colorado USA.

6.5 Case Study 5 - Computational Study of Flow Around a NACA 0012 Wing Flapped at Different Flap Angles with Varying Mach Numbers

Authors : *Tousif Ahmed, Md. Tanjin Amin, S.M. Rafiul Islam & Shabbir Ahmed*
Affiliations : *University of Engineering and Technology, Bangladesh*
Original Appearance : *Global Journals Inc. (USA)*
Online ISSN : *2249-4596 Print ISSN: 0975-5861*
Citations : *Tousif Ahmed, Mohammad Tanjin Amin, S.M. Rafiul Islam & Shabbir Ahmed.*

6.5.1 Abstract

The analysis of two dimensional (2D) flow over NACA 0012 airfoil is validated with NASA Langley Research Center validation cases. The k-ω shear stress transport (SST) model is utilized to predict the flow accurately along with turbulence intensities 1% and 5% at velocity inlet and pressure outlet respectively. The computational domain is composed of 120000 structured cells. In order to enclose the boundary layer method the enhancement of the grid near the airfoil is taken care off. This validated simulation technique is further used to analyses aerodynamic characteristics of plain flapped NACA 0012 airfoil subjected to different flap angles and Mach number. The calculation of lift coefficients (C_L), drag coefficients (C_D) and C_L/C_D ratio at different operating conditions show that with increasing Mach number (M) C_L increases but C_D remains somewhat constant. Moreover, a rapid drastic decrease is observed for C_L and an abrupt upsurge is observed for C_D with velocity approaching to the sonic velocity. In all cases range and endurance are decreased, as both values of C_L/C_D and $\sqrt{C_L}/C_D$ are declined.

Keywords: NACA 0012 airfoil; lift coefficient (C_L); drag coefficient (C_D); lift curve; drag polar; flap angle (δ); range (R); endurance (E); Mach number (M); k-ω shear stress transport (SST) model.

Nomenclature

C_L	Lift coefficient	M	Mach Number
W_1	Final weight of plane	W	Plane weight
C_D	Drag coefficient	E	Endurance
W_0	Initial weight of plane	S	Frontal area
δ	Flap angle	R	Range
C_t	Thrust-specific fuel consumption	ρ_∞	Density
L	Lift	V_∞	Free-stream velocity
A	Angle of Attack (AoA)	M	= million
D	Drag		

6.5.2 Introduction

CFD study of airfoils to predict its lift and drag characteristics, visualization and surveillance of flow field pattern around the body, before the endeavor of the experimental study is almost patent. In the present study aerodynamic characteristics of a well-documented airfoil, NACA 0012, equipped with plain flap is investigated. Wing with flap is usually known as high lift device. This ancillary device is fundamentally a movable element that supports the pilot to change the geometry and aerodynamic characteristics of the wing sections to control the motion of the airplane or to improve the performance in some anticipated way.

CFD facilitates to envisage the behavior of geometry subjected to any sort of fluid flow field. This fast progression of computational fluid dynamics (CFD) has been driven by the necessity for more rapid and more exact methods for the calculations of flow fields around very complicated structural configurations of practical attention. CFD has been demonstrated as an economically viable method of preference in the field of numerous aerospace, automotive and industrial components and processes in which a major role is played by fluid or gas flows. In the fluid dynamics, For modelling flow in or around objects many commercial and open source CFD packages are available. The computer simulations can model features and details that are tough, expensive or impossible to measure or visualize experimentally.

Some high lift devices are illustrated in **Figure 6.5.1**. These devices are primarily used to improve the maximum lift coefficients of wings with changing the characteristics for the cruising and high-speed flight conditions. As a result, it is very important to understand the characteristics of the wing having different flap angles (δ) at different Mach number (M). Operating the aircraft at optimum flap angle at optimum velocity may result significant amount of fuel saving. The B-17 Flying Fortress, Cessna 152 and the helicopter Sikorsky S-61 SH-3 Sea King as well as horizontal and vertical axis wind turbines use NACA 0012 airfoil which place this specific airfoil under extensive research and study.

This study does not provide any experimental data for the flow over the flapped airfoil. Therefore, to reduce the skepticism associated the results obtained, the simulation process for the study is validated instead.

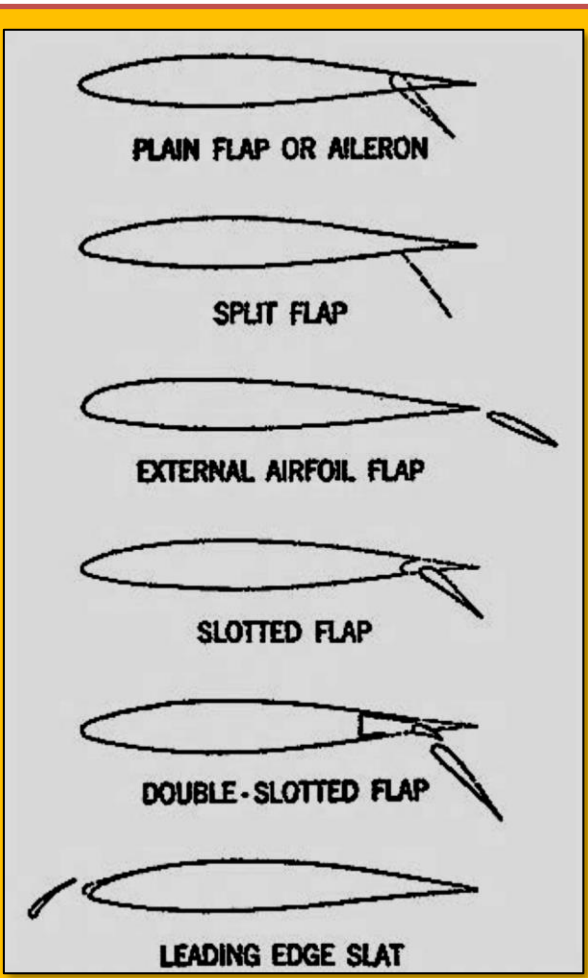

Figure 6.5.1 Typical high lift devices

In the validation course the results for flow over no flapped NACA 0012 is compared with published standard data by NASA [1], as nearly same computational method is used to study flapped NACA 0012 airfoil. Many researchers have studied aerodynamic characteristics of NACA 0012 using different methods and operating conditions. The Abbott and von Doenhoff data [7] were not tripped. The Gregory and O'Reilly data [10] were tripped, but were at a lower Re of 3 M. Lift data are not affected too significantly between 3 M and 6 M, but drag data are [11].

Selecting a proper turbulence model, the structure and use of a model to forecast the effects of turbulence, is a crucial undertaking to study any sorts of fluid flow. It should model the whole flow condition very accurately to get satisfactory results. Selection of wrong turbulence model often results worthless outcomes, as wrong model may not represent the actual physics of the flow. Turbulent flow dictates most flows of pragmatic engineering interest. Turbulence acts a key part in the determination of many relevant engineering parameters, for instance frictional drag, heat transfer, flow separation, transition from laminar to turbulent flow, thickness of boundary layers and wakes.

Turbulence usually dominates all other flow phenomena and results in increasing energy dissipation, mixing, heat transfer, and drag. In present study flow is fully developed turbulent and Reynolds number (Re) is set to 6×10^6. Spallart-Allmaras, k-ε realizable, k-ω standard and k-ω Shear Stress Transport (SST) are primarily used to model viscous turbulent model. However, these specific models are suitable for specific flow cases. Douvi C. Eleni [2] studied variation of lift and drag coefficients for different viscous turbulent model. His study shows that for flow around NACA 0012 airfoil k-ω Shear Stress Transport (SST) model is the most accurate.

6.5.3 Theoretical Background

Lowest flight velocities are encountered by an airplane at takeoff or landing, two phases that are most Perilous for aircraft safety. The stalling speed $V_{stall}$is defined as the slowest speed at which an airplane can fly in straight and level flight. Therefore, the calculation of V_{stall}, as well as aerodynamic methods of making V_{stall} as small as possible, is of vital importance. The stalling velocity is readily obtained in terms of the maximum lift coefficient, as follows. From the definition of C_L,

$$L = q_\infty S C_L = \frac{1}{2}\rho V_\infty^2 S C_L \quad \text{where} \sqrt{\frac{2w}{\rho_\infty S C_L}}$$

$$\text{and for steady level flight } L = W$$

Eq. 6.5.1

Examining **Eq. 6.5.1,** we find that the only alternative to minimize V_∞ is by maximizing C_L for an airplane of given weight and size at a given altitude. Therefore, stalling speed resembles to the angle of attack that yields $C_{L,max}$:

$$V_{stall} = \frac{2w}{\rho_\infty S C_{L,max}}$$

Eq. 6.5.2

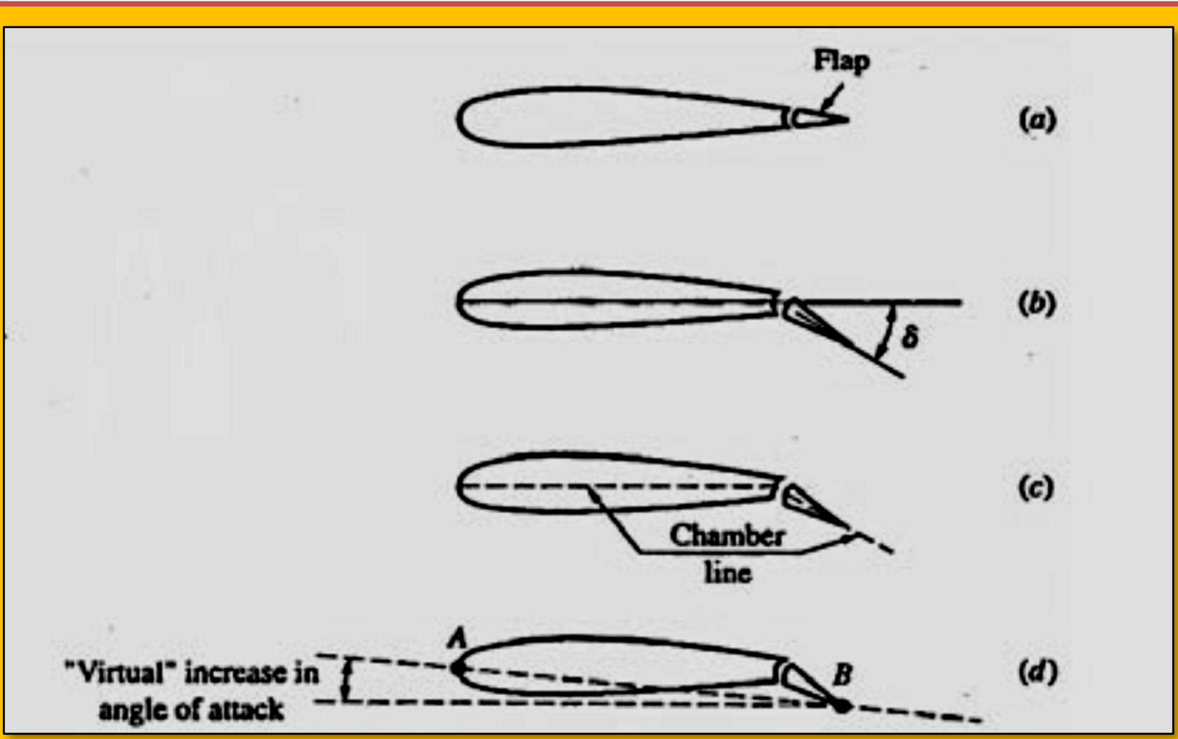

Figure 6.5.2 When a plain flap is deflected, the increase in lift is due to an effective increase in camber and a virtual increase in angle of attack

When a plain flap is deflected, the increase in lift is due to an effective increase in camber and a virtual increase in angle of attack In order to decrease V_{stall}, $C_{L,max}$ must be increased. However, for a wing with a given airfoil shape, $C_{L,max}$ is fixed by nature, that is, the lift properties of an airfoil, including maximum lift, depend on the physics of the flow over the airfoil. To assist nature, the lifting properties of a given airfoil can be greatly enhanced by the use of "artificial" high-lift devices. The most common of these devices is the flap at the trailing edge of the wing, as sketched in **Figure 6.5.2**. When the lap is deflected downward through the angle δ, as sketched in **Figure 6.5.2b**, the lift coefficient is increased for the following reasons:

- The camber of the airfoil section is effectively increased, as sketched in **Figure 6.5.2c**. The more camber an airfoil shape has at a given angle of attack, the higher the lift coefficient.
- When the flap is deflected, we can visualize a line connecting the leading edge of the airfoil and the trailing edge of the lap, points A and B, respectively, in **Figure 6.5.2d.** Line AB constitutes a virtual chord line, rotated clockwise relative to the actual chord line of the airfoil, making the airfoil section with the deflected lap see a "virtual" increase in angle of attack. Hence, the lift coefficient is increased.

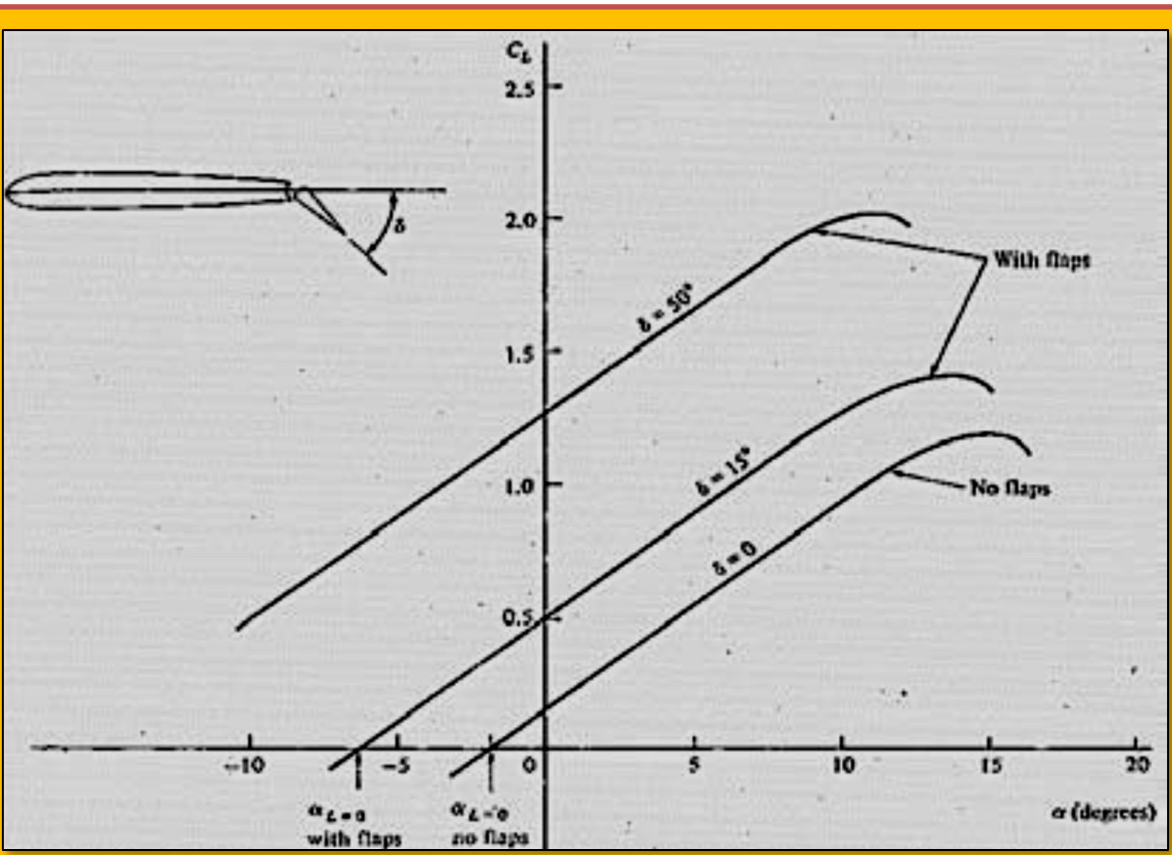

Figure 6.5.3 Illustration of the effect of flaps on the lift curve. The numbers shown are typical of a modern medium-range jet transport

For these reasons, when the flap is deflected downward through the flap deflection angle δ, the value of $C_{L,max}$ is increased and the zero-lift angle of attack is shifted to a more negative value, as shown in **Figure 6.5.3**. In **Figure 6.5.3**, the lift curves for a wing with and without laps are compared. Note that when the flaps are deflected, the lift curve shifts to the left, the value of $C_{L,max}$ increases, and the stalling angle of attack at which $C_{L,maxis}$ achieved is decreased. However, the lift slope remains unchanged; trailing-edge laps do not change the value $\partial C_L/\partial\alpha$

6.5.3.1 Range (R) and Endurance (E)

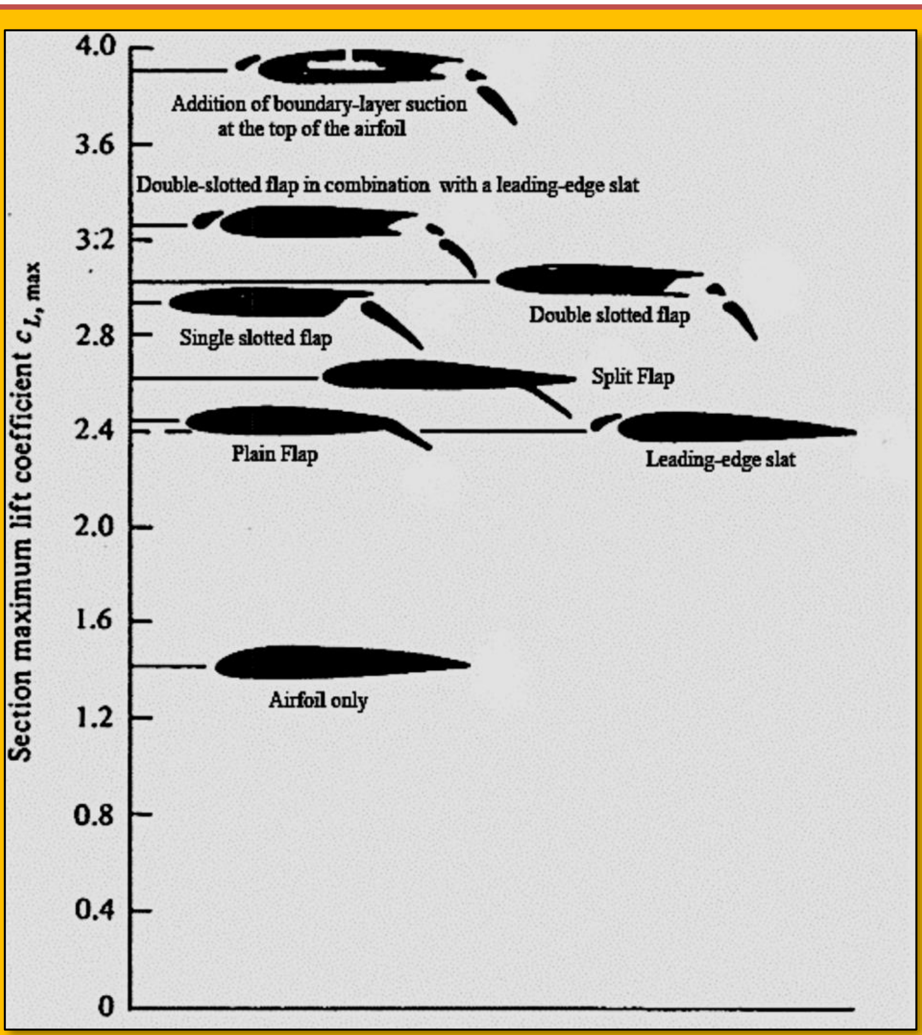

Figure 6.5.4 Typical values of airfoil maximum lift coefficient for various types of high-lift devices

Range (R) is characterized by the maximum distance that an aircraft can travel with a full tank of fuel. Range is technically defined as the total distance (measured with respect to the ground) traversed by the airplane on a tank of fuel. All the way through 20th century aviation, range has been avital design factor, especially for transcontinental and transoceanic conveyors and for tactical bombers for the army. The range formula for jet airplane which gives a quick, practical estimate for range and which is generally accurate to within 10 to 20 percent is given by

$$R = 2\sqrt{\frac{2}{\rho_\infty S}}\frac{1}{c_t}\frac{\sqrt{C_L}}{C_D}\left(\sqrt{W_0}-\sqrt{W_1}\right)$$

Eq. 6.5.3

From **Eq. 6.5.3** that to obtain maximum range for a jet airplane, we want the following:

- Minimum thrust-specific fuel consumption c_t.
- Maximum fuel weight W_f.
- Flight at maximum $C_L^{1/2}/C_D$.
- Flight at high altitudes, that is, low ρ_∞.

Endurance (E) is defined as the entire time that an airplane stays in the air on a tank of fuel. In different applications, it may be desirable to maximize one or the other of these characteristics. The parameters that maximize range are different from those that maximize endurance. The formula for endurance is given by

$$E = \frac{1}{c_t}\frac{C_L}{C_D}\ln\frac{W_0}{W_1}$$

Eq. 6.5.4

From **Eq. 6.5.4** that for maximum endurance for a jet airplane, we want:

- Minimum thrust-specific fuel consumption ct.
- Maximum fuel weight W_f.
- Flight at maximum C_L/C_D.

6.5.3.2 Mathematical Formulation of Turbulence Model

Equations for mass and momentum are solver by the solver for all flows. In case of turbulent flow transport equations are also solved additionally. The equation representing the conservation of mass or continuity equation, can be written as follows:

$$\frac{\partial \rho}{\partial t} + \boldsymbol{\nabla}\,.\,(\rho\mathbf{u}) = S_m$$

Eq. 6.5.5

This equation is valid for incompressible as well as compressible flows which is the general form of the mass conservation equation. S_m is the source of the mass added to the continuous phase from the dispersed second phase (for instance, due to vaporization of liquid droplets) and any user-defined sources. Momentum conservation in an inertial reference frame can be described by

$$\frac{\partial(\rho\mathbf{u})}{\partial t} + \nabla.(\rho\mathbf{u}\mathbf{u}) = -\nabla p + \nabla.\boldsymbol{\tau} + \rho\mathbf{g} + \mathbf{F}$$

Eq. 6.5.6

where p is the static pressure, $\boldsymbol{\tau}$ is the stress tensor (expressed below) and $\rho\boldsymbol{g}$ and $\boldsymbol{F}$ are the gravitational body force and external body forces, respectively. $\boldsymbol{F}$ contains additional model-dependent source terms like porous-media and user-defined sources as well. The stress tensor $\boldsymbol{\tau}$ is given by:

$$\boldsymbol{\tau} = \mu\left[(\nabla\mathbf{u} + \nabla\mathbf{u}^{T}) - \frac{2}{3}\right]\boldsymbol{\nabla}.\mathbf{u}_{I}$$

Eq. 6.5.7

Where, μ is the molecular viscosity, I is the unit tensor, and the second term on the right hand side is the consequence of volume dilation. *Fluent* facilitates with various turbulent model having various characteristics suitable for various specific field of study. As stated earlier, no single turbulence model is generally recognized as being superior for all courses of problems. Choice of turbulence model depends on contemplations such as the physics incorporated in the flow, the conventional practice for a definite sort of problem, the level of exactness required, the obtainable computational resources, and the amount of time offered for the simulation. To make the most apposite choice of model for required work, one requires to comprehend the competencies and limitations of the various options. However, Douvi C. Eleni [2] shows in his study that the most accurate among Spalart-Allmaras Model, k- ε realizable Model and k - ω Shear Stress Transport (SST) Model, is k - ω SST Model for 2D NACA 0012 airfoil simulation process. Therefore, for this study k - ω SST Model is employed.

6.5.3.3 The k-*ω* shear stress transport (SST) model

The k -ω shear-stress transport (SST) model was proposed and developed by Menter [9] to effectively blend the vigorous and precise formulation of the k - ω standard model in the near-wall region with the free-stream liberation of the k - ω standard model in the far field. This is achieved by the conversion of the k -ω model into a k - ω formulation. The k - ω SST model is comparable to the standard k - ω model, but following enhancements are included:

- A blending function was multiplied to both of the standard k -ω model and the transformed k - ω model and then added together. In the near-wall region the blending function is one activating the standard k-ω model. Away from the surface it is zero, which activates the transformed k - ω model.
- A damped cross-diffusion derivative term is incorporated in the ω equation of SST model.
- The modified definition of the turbulent viscosity is used to account for the transport of the turbulent shear stress.
- The constants of modeling are made different.

These features make the SST k - ω model more accurate and reliable for a wider class of flows (e.g., adverse pressure gradient flows, airfoils, transonic shock waves) than the standard k - ω model. The SST k - ω model has a similar form to the standard k - ω model. For detailed regarding the SST k - ω formulation, please refer to [Tousif A. et al.]).

6.5.4 Computational Method

The well documented airfoil, NACA 0012, is utilized in this study. As NACA 0012 airfoil is symmetrical, theoretical lift at zero angle of attack, AoA (α) is zero. In order to validate the present simulation process, the operating conditions are mimicked to match the operating conditions of NASA Langley Research Center validation cases [1]. Reynolds number for the simulations is $Re=6x10^6$, the free Stream temperature is 300 K, which is the same as the ambient temperature. The density of the air at the given temperature is $\rho = 1.225 kg/m^3$ and the viscosity is $\mu=1.7894\times10^{-5}$ kg/ms. Flow for this Reynolds number can be labelled as incompressible.

This is a supposition close to reality and there is no necessity to resolve the energy equation. A segregated, implicit solver, *ANSYS Fluent 12*, is utilized to simulate the problem. The airfoil profile is engendered in the Design Modeler and boundary conditions, meshes are created in the pre-processor ICEM-CFD. Pre-processor is a computer program that can be employed to generate 2D and 3D models, structured or unstructured meshes consisting of quadrilateral, triangular or tetrahedral elements. The resolution and density of the mesh is greater in regions where superior computational accuracy is needed, such as the near wall region of the airfoil.

As the first step of accomplishing a CFD simulation the influence of the mesh size on the solution results should be investigated. Mostly, more accurate numerical solution is obtained as more nodes are used, then again using added nodes also escalates the requisite computer memory and computational time. The determination of the proper number of nodes can be done by increasing the number of nodes until the mesh is satisfactorily fine so that further refinement does not change the results. **Figure 6.5.6** depicts the variation

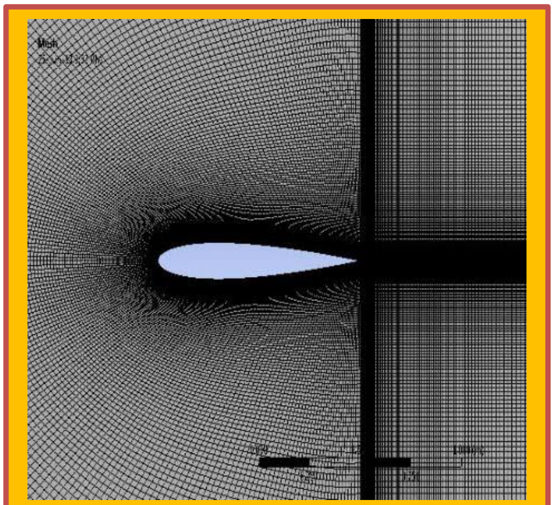

Figure 6.5.5 Mesh of the computational domain around NACA 0012 airfoil

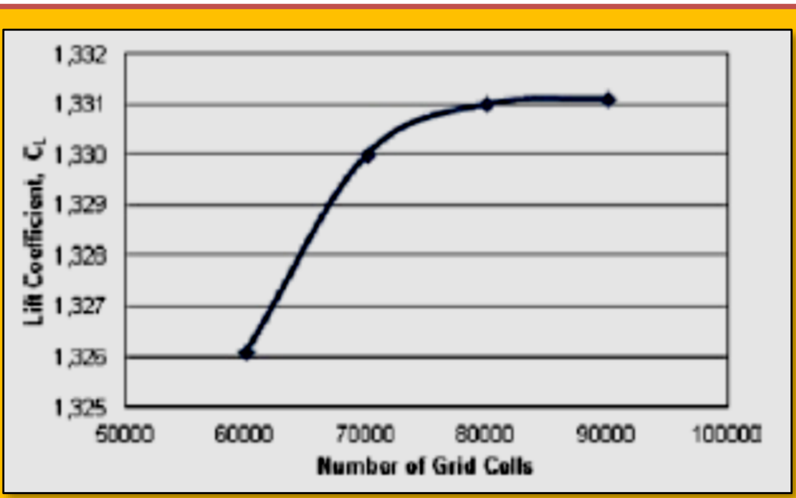

Figure 6.5.6 Variation of lift coefficient with number of grid cells [2]

of coefficient of lift with number of grid cells at stall angle of attack (16°). 120000 quadrilateral cells with C-type grid topology is applied to establish a grid independent solution (**Figure 6.5.5**). From **Figure 6.5.3** it is evident that 120000 cells are quite sufficient to get a stable and accurate result. Moreover, Douvi C. Eleni [2] was able to generate accurate results using only 80000 cells. The domain height and length is set to approximately 25 chord lengths. This computational model is very small compared to that of NASA's validation cases (**Figure 6.5.7**). To minimize problems concomitant with the effect of far-field boundary (which can particularly influence drag and lift levels at high lift conditions), the far-field boundary in the grids provided have been located almost 500 chords away from the airfoil. But then again, simulation of NASA's specification of the large computational domain requires very high computer memory. Furthermore, far-field boundary contributes very little on the result. Ansys recommends turbulence intensities ranging from 1% to 5% as inlet boundary conditions. In this study it is assumed that inlet velocity is less turbulent that pressure outlet.

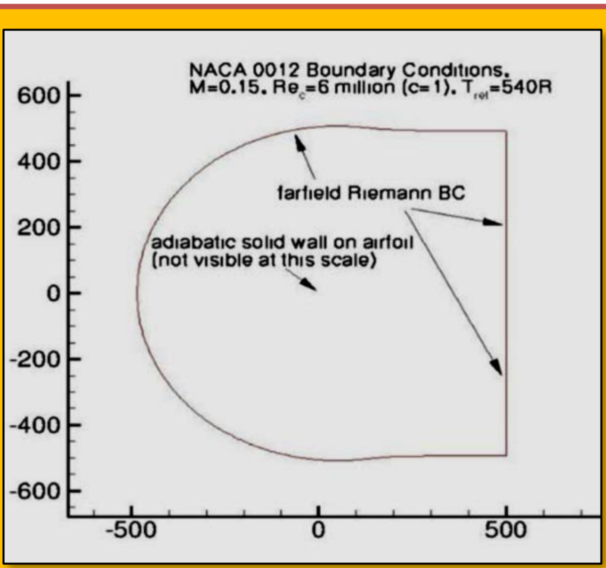

Figure 6.5.7 Actual computational domain under NASA's experiment [1]

Hence, for velocity inlet boundary condition turbulence intensity is considered 1% and for pressure outlet boundary5%. In addition, Ansys also recommends turbulent viscosity ratio of 10 for better approximation of the problem. For accelerating CFD solutions two methods were employed on the solver. The pressure based coupled solver (PBCS) introduced in 2006, reduces the time to overall convergence, by as much as five times, by solving momentum and pressure-based continuity equations in a coupled manner. In addition, hybrid solution initialization (**Figure 6.5.8(a) and (b)**), a collection of recipes and boundary interpolation methods to efficiently initialize the solution based purely on simulation setup, is employed, so the user does not need to provide additional inputs for initialization.

The method can be applied to flows ranging from subsonic to supersonic. It is the recommended method when using PBCS and DBNS (density-based coupled solver) for steady-state cases in *ANSYS Fluent 13.0*. This initialization may improve the convergence robustness for many cases [6].

6.5.5 Validation of the Simulation Process

To validate the computational method stated earlier, results obtained by the 2D simulation of NACA 0012 for zero flap angle (δ) is compared with NASA's result. The lift curve, drag polar, pressure coefficient (CP) curve (AoA 0, 10 and 15 degree) for present study is obtained and overlapped on the standard curves provided in NASA's website [1] to observe the fit of current study data. As NASA recommended the definition of the NACA 0012 airfoil is slightly altered so that the airfoil closes at chord = 1 with a sharp trailing edge. To do this, the exact NACA 0012 formula is used, then the airfoil is scaled down by 1.008930411365. Moreover, fully developed turbulent flow is simulated in *Fluent* to match NASA's criteria. Variation of lift coefficient (C_L) with angle of attack (α) for the simulation can be observed from **Figure 6.5.9**. From-16 degree AoA to 16 degree AoA the lift curve is almost linear. Throughout this regime no separation occurs and flow remains attached to the airfoil. At stall AoA lift coefficient is reduced drastically due to intense flow separation generation. Slight deviation from Abbott and Von Doenhoff's [7] unstripped experimental

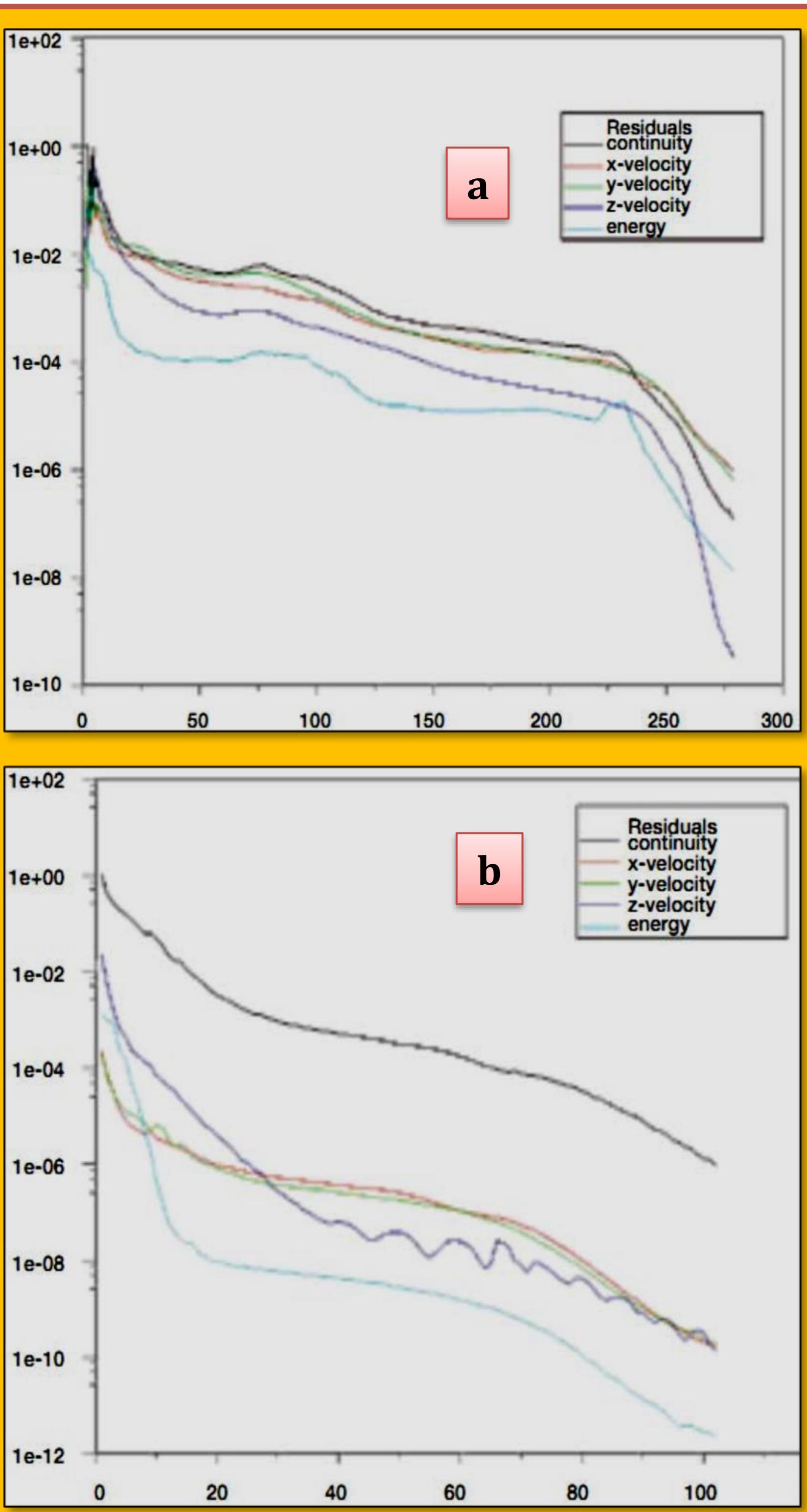

Figure 6.5.8 (a) Standard Initialization, 279 Iterations (b) Hybrid Initialization, 102 Iterations [6]

results occurs (almost 3%), as the computational domain of the current study is nearly 1/20th of the original computational domain under experiment of NASA.

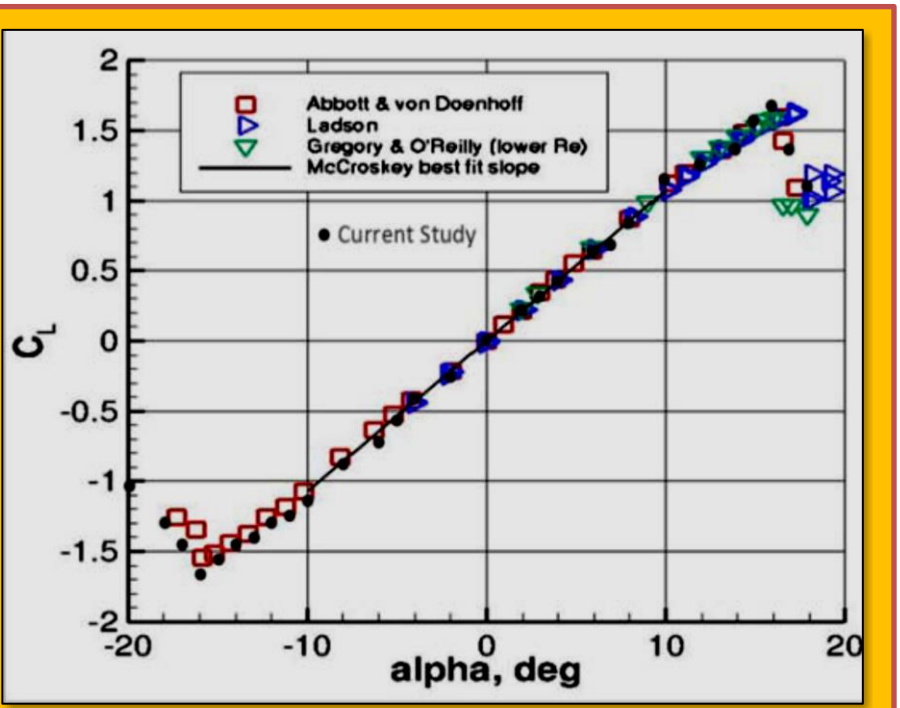

Figure 6.5.9 Lift curve of NACA 0012 airfoil

At zero angle of attack (AoA) surface pressure coefficients matches with all experimental data particularly well having slender deviations at the trailing edge of the airfoil (**Figure 6.5.10**). However, surface pressure coefficients for flow having AoA 10 degree and 15 degree appear to (see [Tousif A. et al.] ; **fig. 12** and **fig. 13**) conform to data of experiment conducted by Ladson et al [8]. Leading edge upper surface pressure peak do not appear to resolve well in both cases. Additionally, present study depicts higher pressure than Ladson study [8] on the lower surface on the leading edge of the airfoil primarily due to assuming zero surface roughness of the wall.

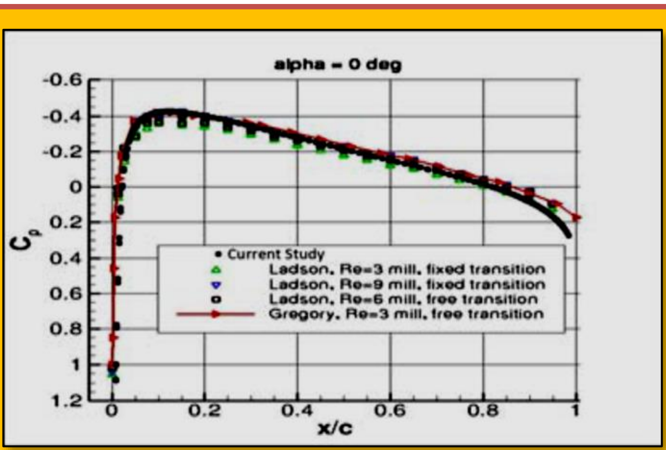

Figure 6.5.10 Variation of pressure coefficient (CP) for 0 degree AoA

Pressure and velocity contours along with streamlines for different AoA (α) are presented in a tabular form in **fig. 15** (see appendix). As NACA 0012 is a symmetric airfoil, for zero AoA it can be observed that velocity profile, pressure profile and streamlines are also same on both upper surface and lower surface of the airfoil. As a consequence, lift generation is also zero for this case (**Figure 6.5.9**). However, with changing AoA the position of stagnation point also changes (see [Tousif A. et al.]).

At stagnation point pressure is maximum and velocity is zero which is characterized by distinct red point on the velocity contour plots. It is also apparent that with positive AoA stagnation point moves toward trailing edge on the lower surface of the airfoil. This pressure deviation on the upper and lower surface of the airfoil principally creates significant amount of positive lift. Moreover, separation of flow is also evident at high angle of attack (α). In turn this flow separation phenomenon creates another source of aerodynamic drag, called pressure drag due to separation. That is why high lift usually associates with high drag. Two major significances of separated low over the airfoil can be noted. The first is the loss of lift. The aerodynamic lift is derived from the net component of a pressure distribution in the vertical direction. When the flow is separated higher pressure is created on the top surface pushing the airfoil downward, thus creating less lift.

6.5.6 Results and Discussion

NACA 0012 airfoil having different flap angles (δ) was subjected to flow of varying Mach number (M). Flow having Mach number greater than 0.3 is considered compressible. Density based solver utilizing k-ω Shear Stress Transport (SST) modeling *Fluent* facilitates mimicking compressible flow over the body under experimentation very accurately. The resultant forces are typically resolved into two forces and moments. The component of the net force acting normal of the airfoil is lift force (F_L) and acting horizontal to the airfoil is drag force (F_D). The curves showing variation of lift coefficient (C_L) and drag coefficient (C_D) with different flap angles (δ) and Mach number (M) are analyzed to realize the aerodynamic behavior of plain flapped NACA 0012 airfoil. Curves of C_L/C_D and $\sqrt{C_L}/C_D$ are analyzed further, as these are crucial factors affecting range (R) and endurance (E) of aircrafts. However, flow at high flap angles (δ) (i.e. 30, 40 and 50 degrees) are very unstable and it remains un converged even after 5000 iteration in *Ansys Fluent* flow solver. Hence, flow for flap angle (δ) 30, 40 and 50 degrees are slightly erratic.

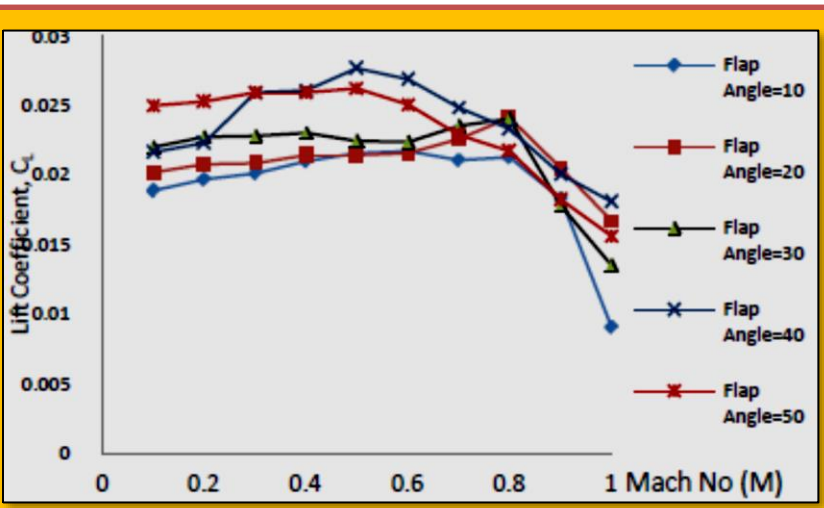

Figure 6.5.11 Variation of Lift Coefficient (C_L) with Mach number (M) for different flap angle (δ)

At **Figure 6.5.11** variation of lift coefficient (C_L) with Mach number (M) can be observed. Higher lift coefficient (C_L) is obtained for higher flap angles (δ) at any Mach number (M). However, a typical behavior of the curves are evident at increasing Mach number (M). Lift coefficient (C_L) escalates with increasing Mach number (M) but a dramatic downslope is obtained at free-stream velocity (V_∞) approaching to sonic velocity.

When Mach number (M) is in between 0.8 to 1.2, the flow is said to be transonic which is characterized by some very complex effects. This problem of drastic increasing in drag coefficient (C_D) (**Figure 6.5.12** and **Figure 6.5.13**) and decreasing in lift

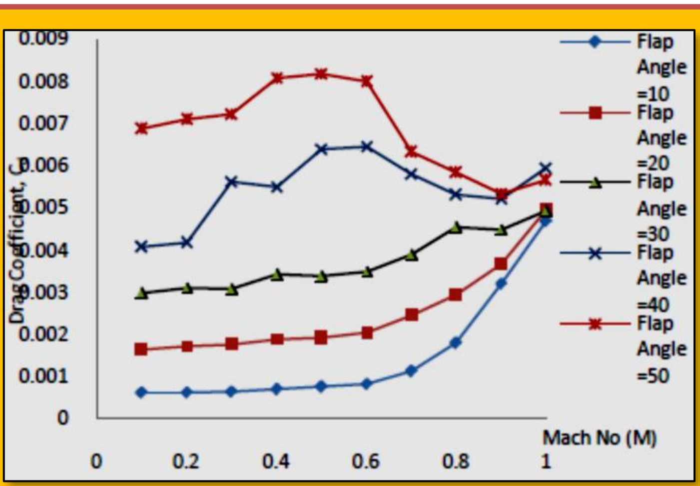

Figure 6.5.12 Variation of Drag Coefficient (C_D) with Mach number (M) for different flap angle (δ)

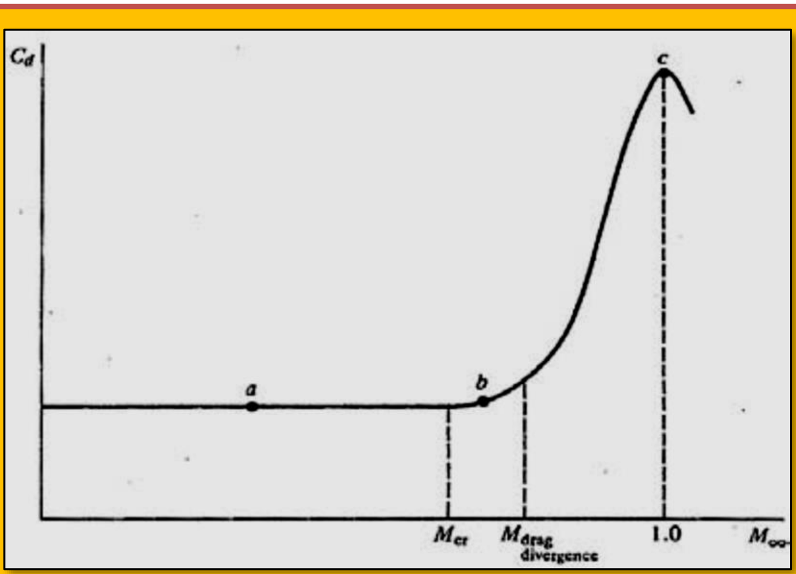

Figure 6.5.13 Variation of Drag Coefficient (C_D) with Mach number (M)

coefficient (C_L) can be dealt by using thin airfoil or supercritical airfoil. A rise in critical Mach number (M_{cr}) usually means an upsurge in the drag divergence Mach number. Hence, before encountering drag divergence a transonic airplane having a thinner airfoil can fly at a higher Mach number if everything else being equal. The drag coefficient (C_D) remains somewhat constant at low Mach number (M). But, very sudden and dramatic escalation is observed when Mach number (M) approaches to unity (**Figure 6.5.12**). This phenomenon can be also observed in **Figure 6.5.13** which depicts variation of drag coefficient (C_D) with Mach number (M). However, **Figure 6.5.13** is attained for zero angle of attack (AoA). As in this study flap angle (δ) is varied, the virtual AoA is also changed (**Figure 6.5.2**). As a result, **Figure 6.5.12** gives dissimilar outcomes form **Figure 6.5.13** to some extent.

The airfoil subjected to the flow passes through three distinct phases with Mach number (M) represented by point a, b and c in the **Figure 6.5.13**. At point a, free stream Mach no is characterized by $M_\infty < M_{cr}$. The physical mechanism in this flow condition can be observed from **Figure 6.5.14-a**. Maximum velocity occurs on the upper surface of the airfoil which is well less than the sonic velocity. Usually in these cases, for zero AoA, drag coefficient remains constant, but flap angle of 10 degrees causes slight separation at the trailing edge of the NACA 0012 airfoil. This results rise in drag coefficient with Mach number (M) even at low Mach number (M) flow condition.

In **Figure 6.5.13,** point b is the point where M is increased slightly above M_{cr} and drag coefficient starts to escalate very rapidly. A supersonic bubble forms on the upper surface of the airfoil having Mach number (M) greater that unity (**Figure 6.5.14-b**) and surrounding by minimum pressure point. However, even at this point drag coefficient remains reasonably low.

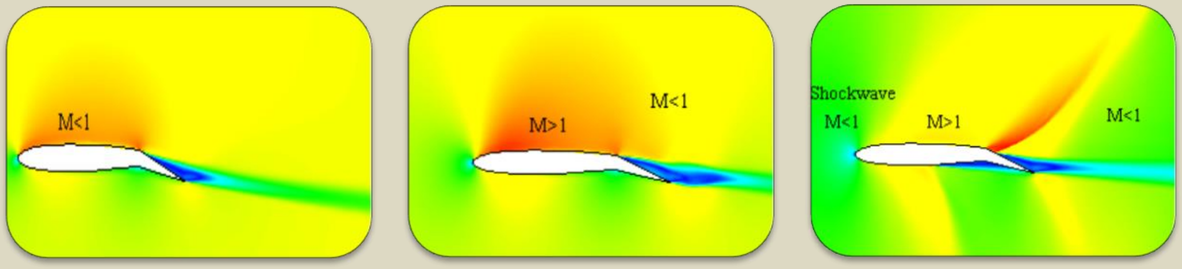

(a) (b) (c)

Figure 6.5.14 Physical mechanism of drag divergence in Figure 6.5.12 for 20 degrees of flap angle (δ) (a) Flow field at point, a (b) Flow field at point, b (c) Flow field at point, c

Physical mechanism of drag divergence in **Figure 6.5.12** for 20 degrees of flap angle (δ) (a) Flow field at point, a (b) Flow field at point, b (c) Flow field at point, c **Figure 6.5.12** suggests for flow around airfoil having flap angle (δ) 10, 20 and 30 degrees maximum drag coefficient happens at sonic velocity (i.e. M = 1.0). **Figure 6.5.13** also depicts the same trend at point c. The physical mechanism can be well perceived from **Figure 6.5.14-c** where presence of shockwave is depicted. Shock waves themselves are dissipative occurrences, which results in an escalation in drag on the airfoil. Moreover, sharply increase of pressure across the shock waves creates an adverse pressure gradient, causing the flow to separate from the surface. This flow separation also contributes to the drag substantially. However, with high flap angles (δ) (i.e. 40 and 50) this trend occurs somewhere at Mach 0.5 (**Figure 6.5.12**). This is mainly due to increasing flap angle (δ) associates with increasing frontal area of the airfoil.

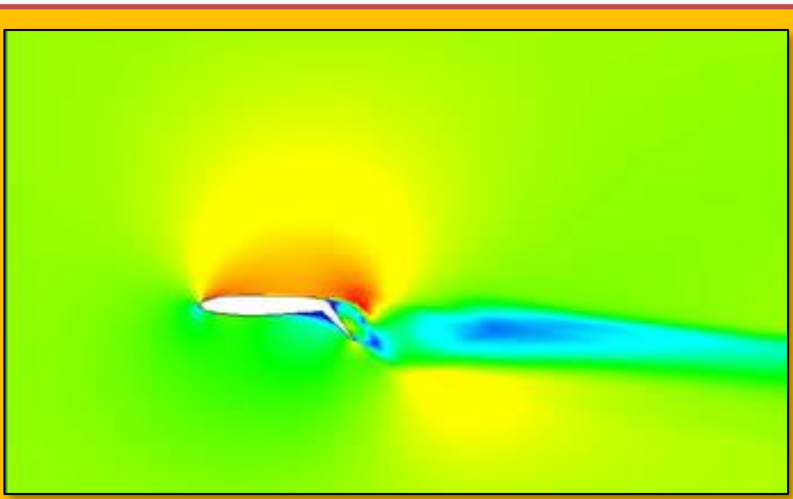

Figure 6.5.15 Velocity contour for 50 degrees of flap angle (δ) at 0.5 Mach number (M)

Due to this reason very intense amount of flow separation occurs even at low Mach number (M) (**Figure 6.5.15**). Moreover, the increase in flap angle also increases the effective thickness of the airfoil. Hence, airfoil having higher flap angle experiences drag divergence even at lower Mach number (M) (**Figure 6.5.16**). This depicts variation of Critical Mach number (M_{cr}) with thickness of airfoil. Thick airfoil encounters critical

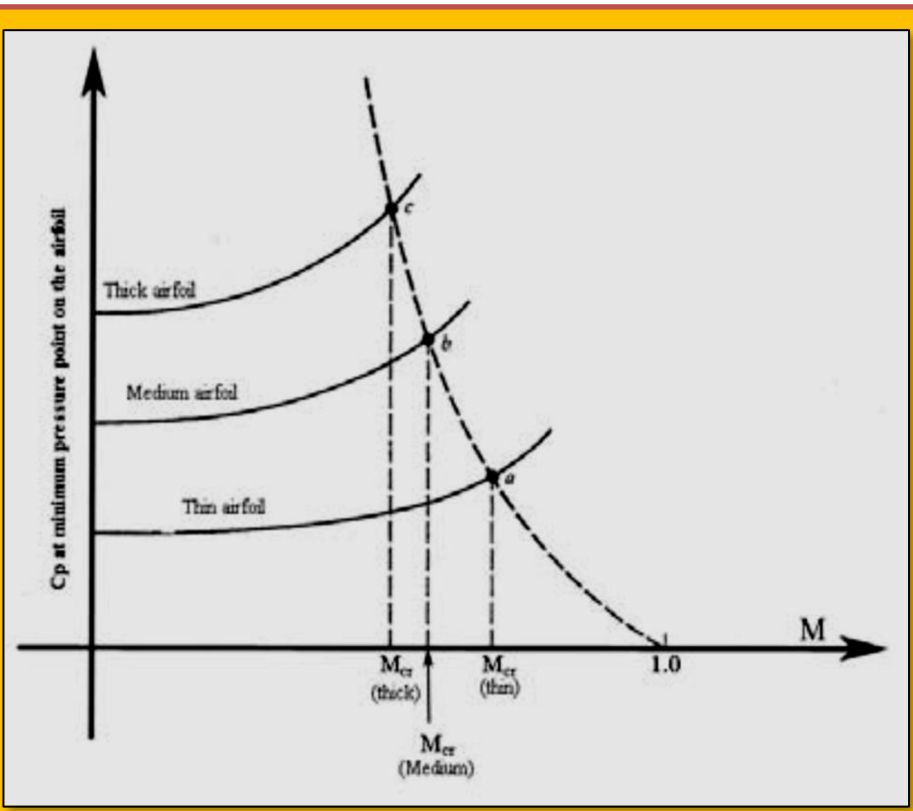

Figure 6.5.16 Critical Mach number (M_{cr}) for airfoils of different thickness

Mach number (M_{cr}) which is well less than M_{cr} for thin airfoil. Hence, the point where rapid increase of drag coefficient (C_D) occurs is well before the Mach number 1.0 for thick airfoils.

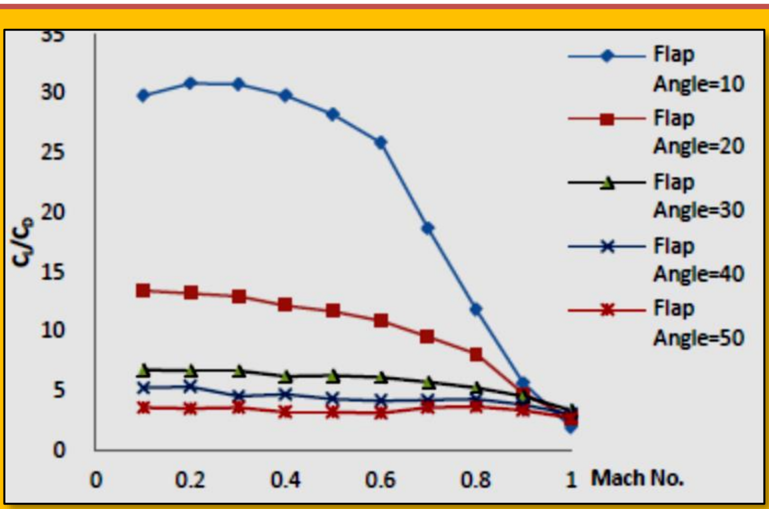

Figure 6.5.17 Variation of C_L/C_D with Mach number (M) for different flap angle (δ)

The alteration of C_L/C_D with Mach number (M) can be observed from **Figure 6.5.17**. As, variation of $\sqrt{C_L}/C_D$ with Mach number (M) is patently same as **Figure 6.5.17**, it has not shown here. For a definite flap angle (δ) higher range (R) and endurance (E) are attainable at low Mach number (M), as C_L/C_D is decreasing with increasing Mach number (**Eq. 6.5.3** & **Eq. 6.5.4**). However, for higher flap angle range (R) and endurance (E) remains somewhat constant or fluctuates in a negligible manner. At a certain Mach number (M) higher range (R) and endurance (E) is available at lower flap angle. At lower flap angles (δ) separation of flow is relatively low compared to higher flap angles (δ) which results a greater lift coefficient (C_L) corresponding to a lower drag coefficient (C_D).

6.5.7 Conclusions

Present study divulges behavior of NACA 0012 airfoil at different flap angles (δ) and Mach numbers (M). The k - ω Shear Stress Transport (SST) model is used to simulate NACA 0012 non-flapped and plain flapped airfoil, as it was mostly recommended by Douvi C. Eloeni [2] for airfoil study. Using the methodology of current study with 120000 cells, a very negligible deviation of 2% -3% from NASA validation cases are obtained. High flap angles (δ) results higher lift but it also increases drag very significantly. Study shows increased flap angle increases effective thickness. Hence, drag divergence ensues at considerably lower Mach number (M) for wing having high flap angles which further results a speed limitation for aircrafts during lift-off. Moreover, it is also evident that range (R) and endurance (E) increases with decreasing flap angles (δ). Moreover, for each flap angle (δ) range (R) and endurance (E) decrease with increasing Mach number (M).However, for higher flap angles somewhat constant range and endurance is obtained for increasing Mach number. This comprehensive study will facilitate efficient design of wing sections of aircrafts and an optimized flight.

6.5.8 References

1. 2D NACA 0012 Airfoil Validation Cases available at: http://turbmodels.larc.nasa.gov/naca0012_val.html.
2. Eleni, Douvi C., Tsavalos I. Athanasios, and Margaris P. Dionissios. "Evaluation of the turbulence models for the simulation of the flow over a National Advisory Committee for Aeronautics (NACA) 0012 airfoil." Journal of Mechanical Engineering Research 4.3 (2012): 100-111.
3. Information on k-ω SST model available at: http://turbmodels.larc.nasa.gov/sst.html.
4. Fluent 2013 Theory Guide.
5. John D Anderson, Jr. "Introduction to flight" 5th edition, McGraw-Hill.
6. Mark Keating, "Accelerating CFD Solutions-Several recent enhancements in ANSYS Fluent solver capabilities accelerate convergence and reduce solution time," ANSYS, Inc.
7. Abbott, I. H. and von Doenhoff, A. E., "Theory of Wing Sections," Dover Publications, NY, 1959.

8. Ladson, C. L., Hill, A. S., and Johnson, Jr., W. G., "Pressure Distributions from High Reynolds Number Transonic Tests of an NACA 0012 Airfoil in the Langley 0.3-Meter Transonic Cryogenic Tunnel," NASA TM 100526, December 1987.
9. Menter, F. R., "Two-Equation Eddy-Viscosity Turbulence Models for Engineering Applications," AIAA Journal, Vol. 32, No. 8, August 1994, pp. 1598-1605.
10. Gregory, N. and O'Reilly, C. L., "Low-Speed Aerodynamic Characteristics of NACA 0012 Aerofoil Sections, including the Effects of Upper-Surface Roughness Simulation Hoar Frost," NASA R&M 3726, Jan 1970.
11. W. J. McCroskey, "A Critical Assessment of Wind Tunnel Results for the NACA 0012 Airfoil." NASA Technical Memorandum 1987. Computational Study of Flow Around a NACA 0012 Wing Flapped at Different Flap Angles with Varying Mach Numbers

6.6 Case Study 6 - Aerodynamic Characteristics of Thick Airfoils in High Reynolds and Moderate Mach Numbers

---

Authors : *John M Prospathopoulos[1], Giorgos Papadakis[1] Giorgos Sieros[2], Spyros G Voutsinas[1], Takis K Chaviaropoulos[2] and Kostas Diakakis[1]*

Affiliation : *[1] Laboratory of Aerodynamics, Department of Mechanical Engineering, National Technical University of Athens, Athens, Greece*
[2] Wind Energy Department, Centre for Renewable Energy Sources and Saving, Pikermi Attiki Greece

Title : *Assessment of the aerodynamic characteristics of thick airfoils in high Reynolds and moderate Ma numbers using CFD modeling*

Source : *doi:10.1088/1742-6596/524/1/012015*

Citation : *Citation John M Prospathopoulos et al 2014 J. Phys.: Conf. Ser. 524 012015 - © The Science of Making Torque from Wind 2014 (TORQUE 2014) IOP Publishing Journal of Physics: Conference Series 524 (2014) 012015 doi:10.1088/1742-6596/524/1/012015*

6.6.1 Abstract.

The aerodynamic characteristics of thick airfoils in high Reynolds number is assessed using two different CFD RANS solvers: *the compressible MaPFlow and the incompressible CRES-flowNS-2D* both equipped with the k-ω SST turbulence model. Validation is carried out by comparing simulations against existing high Reynolds experimental data for the NACA 63-018 airfoil in the range of -10° to 20°. The use of two different solvers aims on one hand at increasing the credibility in the results and on the other at quantifying the compressibility effects. Convergence of steady simulations is achieved within a mean range of -10° to 14°, which refers to attached or light stall conditions. Over this range the simulations from the two codes are in good agreement. As stall gets deeper, steady convergence ceases and the simulations must switch to unsteady. Lift and drag oscillations are produced which increase in amplitude as the angle of attack increases. Finally in post stall, the average C_L is found to decrease up to ~24° or 32° for the FFA or the NACA 63-018 airfoils respectively, and then recover to higher values indicating a change in the unsteady features of the flow.

6.6.2 Motivation and Scope

One of the main objectives of the FP7 Innwind.EU Project is to design low solidity rotors for offshore applications that operate at relatively high tip speeds. High tip speed implies higher (than usual) Mach numbers so that compressibility effects need to be considered in the design of the outer blade region. At large sizes high tip speeds also result in very high Reynolds numbers (up to 12 million for the Innwind.EU 10 MW rotor) for which, airfoil behavior has not been studied to sufficient extent. Finally, low solidity implies that thicker airfoils will be used, which sets the design further beyond current know-how. In support of this design activity, the aerodynamic behavior of three FFA airfoils of different thickness is assessed using CFD modelling.

Two different URANS finite volume solvers are applied: the compressible *MaPFlow* and the incompressible *CRES-flowNS-2D* both equipped with the k-ω SST turbulence model. A wide range of angle of attacks (AOAs) from -32o to 32o is considered so as to cover both power production and extreme conditions. Depending on the AOA, the flow can exhibit inherent unsteadiness so the simulation set-up must be accordingly adapted. The turning point will depend on the airfoil shape, so at first an investigation is needed in order to determine the range of AOAs that allow steady simulations. Next, the convergence rate to either a steady or a periodic state is examined. Validation is carried out in comparison to wind tunnel measurements for the NACA 63-018 airfoil [1]. The C_L-C_D polar plots are produced for the FFA airfoils and the different trends in the linear and post-stall regions are discussed. Finally, the dependence on the Reynolds and Mach numbers is investigated for the FFA-W3-301 and the FFA-W3-241 airfoils respectively.

6.6.3 Methods and Numerical Specifications

6.6.3.1 Solvers

MaPFlow is a multi-block MPI enabled compressible solver equipped with preconditioning in regions of low Mach flow developed at NTUA [2]. The discretization scheme is cell centered and makes use of the Roe approximate Riemann solver for the convective fluxes. In space the scheme is 2nd order accurate defined for unstructured grids and applies the Venkatakrishnan's limiter. The time scheme is also 2nd order and implicit introducing dual time stepping for facilitating convergence. The solver is equipped with the Spalart-Allmaras (SA) and the k-ω SST eddy viscosity turbulence models. *CRESFlowNS-2D* is an incompressible solver developed at CRES [3]. The code utilizes a restarting *GMRES* method for pressure correction. The k-ω SST model is used for turbulence closer. The code can be used for steady state calculations or transient calculations, where additional pseudo-time steps are introduced. A structured grid is used for the solution with various grid types (C-type, O-type) implemented.

6.6.3.2 Numerical Specifications

All simulations used the grids provided by DTU Wind in the context of InnWind project [4]. They are structured O-type grids with 513x257 cells. The distance of the first node from the surface of the airfoil corresponded to a y+ of the order of 10^{-4}. Also in all simulations the k-ω SST model was used assuming fully turbulent flow. Steady simulations were performed starting from the zero AOA and proceeded to higher (or lower angles) with a step of 2 degrees. Beyond a certain value of AOA, the simulations failed to converge to a steady solution indicating the onset of unsteadiness in the flow. So the simulations switched to unsteady simulations.

In order to accelerate convergence the CFL in *MaPFlow* is allowed to gradually increase from 1 to its final value within a certain number of iterations (or time steps). For the simulations of the FFA airfoils maximum CFL was set equal to 10, which was attained after 200 iterations. Higher maximum CFL values were tested but since they caused convergence difficulties at high AOAs, 10 was retained in all simulations for the sake of uniformity. The time step was set to 0.002 (dimensionless) and 10 dual steps per iteration were performed. In general, convergence was slow for all airfoils of the FFA family, especially as the AOA increased. For the simulations of the NACA 63-018 airfoil, a higher maximum CFL value of 30 was achieved for all angles of attack. The higher CFL value along with the smaller airfoil thickness led to a faster convergence as compared to the FFA airfoils.

Similarly, the simulations with *CRESFlowNS-2D* in steady flow mode beyond a certain angle of attack resulted in unnatural low-frequency variations in lift and drag. The time step was set to 0.001 (dimensionless). In general, convergence was slow for all airfoils of the FFA family, especially as the AOA increased

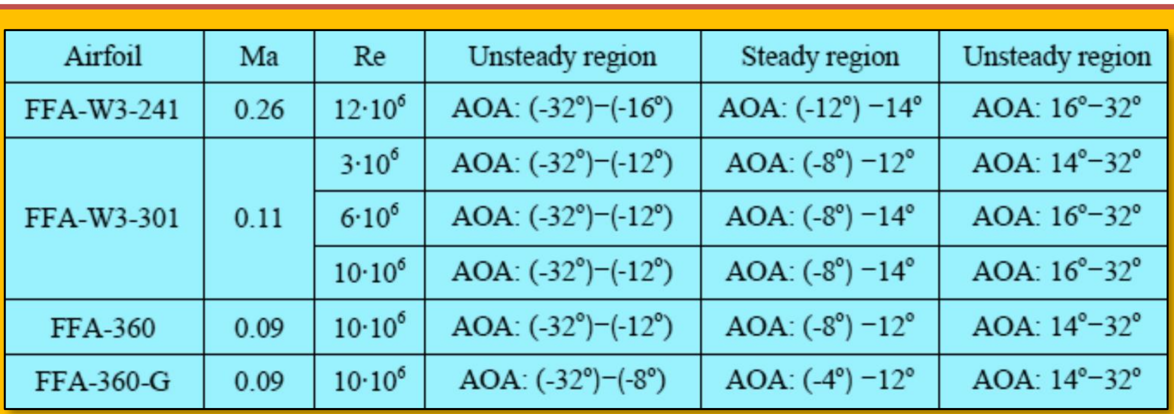

Airfoil	Ma	Re	Unsteady region	Steady region	Unsteady region
FFA-W3-241	0.26	$12\cdot10^6$	AOA: (-32°)−(-16°)	AOA: (-12°) −14°	AOA: 16°−32°
FFA-W3-301	0.11	$3\cdot10^6$	AOA: (-32°)−(-12°)	AOA: (-8°) −12°	AOA: 14°−32°
		$6\cdot10^6$	AOA: (-32°)−(-12°)	AOA: (-8°) −14°	AOA: 16°−32°
		$10\cdot10^6$	AOA: (-32°)−(-12°)	AOA: (-8°) −14°	AOA: 16°−32°
FFA-360	0.09	$10\cdot10^6$	AOA: (-32°)−(-12°)	AOA: (-8°) −12°	AOA: 14°−32°
FFA-360-G	0.09	$10\cdot10^6$	AOA: (-32°)−(-8°)	AOA: (-4°) −12°	AOA: 14°−32°

Table 6.6.1 AOA range for steady and unsteady state simulations of the FFA airfoils

6.6.4 Results

For the FFA airfoils, steady and unsteady state calculations were performed depending on the AOA according to **Table 6.6.1**. For the NACA 63-018 airfoils, convergence in steady mode was achieved for AOAs from -10° to 14°. Then up to 20° the simulations were switched to unsteady mode. The onset of unsteadiness in the flow appeared at AOAs around 14°–16° (depending on the shape of the airfoil and the Reynolds number) and was combined with the formation of a von Karman street like wake (**Figure 6.6.1**). As the AOA increased, the intensity of the shed vortices also increased and the shaping of compact vortices was faster. The wave length increased resulting in a decreasing Strouhal number as shown in **Table 6.6.2**, where the amplitude and the Strouhal number of the converged periodical C_L variation, as predicted by the compressible code *MaPFlow*, are presented for the various AOAs in the case of the FFA-W3-241 airfoil.

FFA-W3-241 Re=12·10^6 Ma=0.26	AOA	-32°	-28°	-24°	-20°	-16°	20°	24°	28°	32°
	ΔC_L	0.355	0.295	0.236	0.083	0.016	0.035	0.288	0.342	0.403
	St	0.366	0.549	0.793	1.099	1.648	1.16	0.732	0.488	0.366

Table 6.6.2 Amplitudes and Strouhal numbers of the converged C_L variation for the FFA-W3-241 airfoil. Unsteady calculations performed by *MaPFlow*

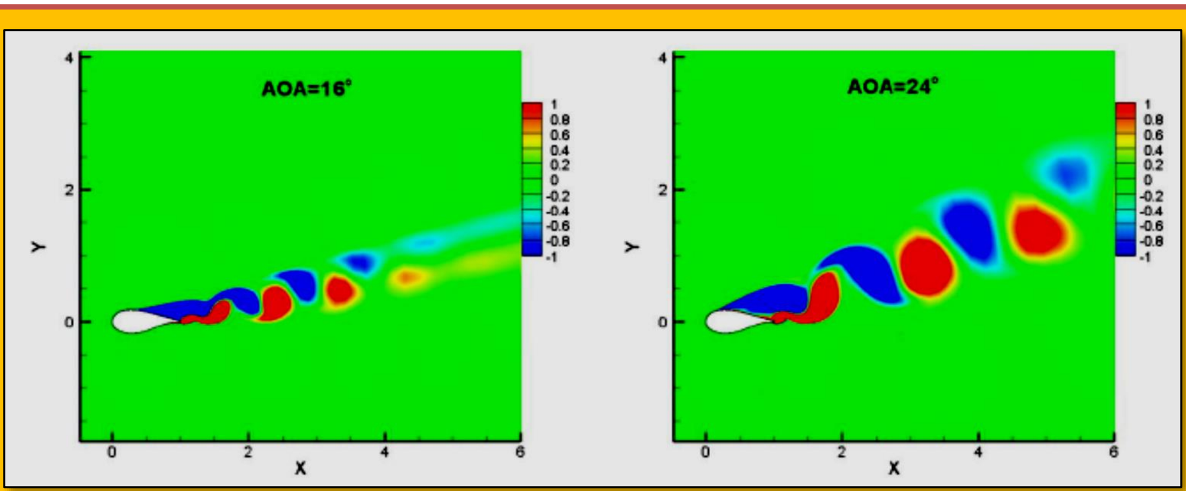

Figure 6.6.1 Vorticity contours in the wake of the FFA-W3-241 airfoil at Re = $12x10^6$. Left: AOA=16°. Right: AOA=24°. Predictions obtained with MaPFlow

6.6.4.1 Convergence.

Simulations for FFA airfoils required at least 20000 iterations in order to achieve convergence of the steady state or a variation in mean CL less than 3%. On the contrary a significantly smaller number of times steps was sufficient in the NACA airfoil simulations. In **Figure 6.6.3,** the convergence history for both FFA and NACA airfoils at AOA=10o is depicted as predicted by *MaPFlow*. It seems that convergence is slower as the airfoil thickness increases. Therefore, the faster convergence in the NACA airfoil simulations can be attributed to its smaller thickness (18%) as well as to the higher CFL used in comparison to the FFA simulations. The convergence history of C_L at AOA = 20° is represented in Figure 3 of source [J. M. Prospathopoulos et al][177].

---

[177] John M Prospathopoulos et al 2014 J. Phys.: Conf. Ser. 524 012015

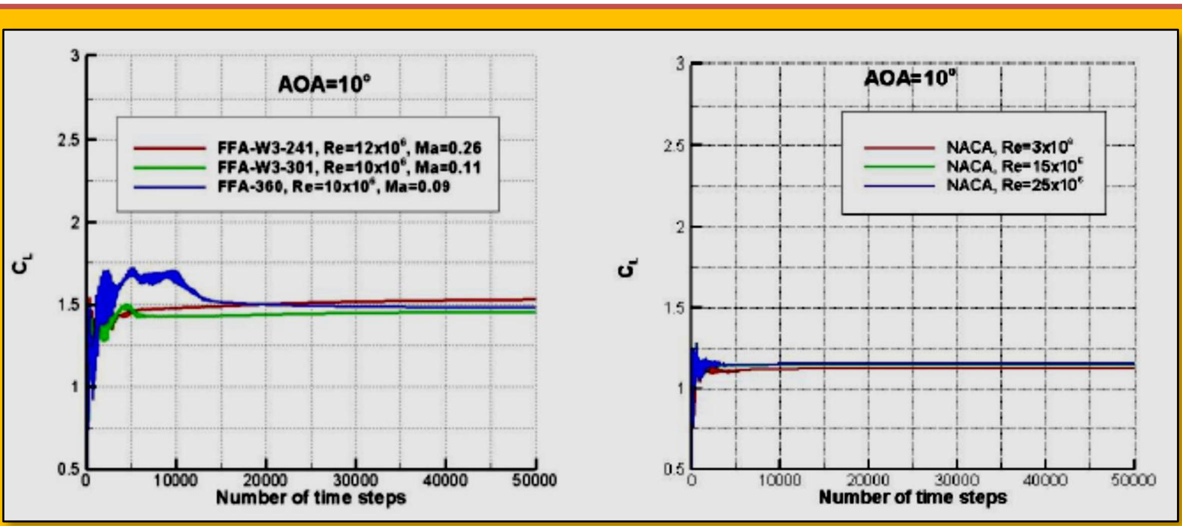

Figure 6.6.3 Convergence of C_L for AOA=10°. Left: FFA airfoils. Right: NACA 63-018 airfoil. Predictions obtained with *MaPFlow*

For the FFA airfoils, as expected, the amplitude of the attained periodic state increased with airfoil thickness. In Figure 4 of [J. M. Prospathopoulos et al][178], the convergence histories of the two CFD solvers are compared. At AOA = 0°, for which a steady state is obtained, both *MaPFlow* and *CRES-flowNS-2D* converge to the same C_L value. At AOA = 16°, both solvers give a periodic response with the same Strouhal number. However, the mean value, as well as the amplitude, is different. Such differences are attributed to the presence of acoustic waves in compressible simulations that change the pressure level at the suction side as shown in **Figure 6.6.2**.

For the high AOAs (24°, 28°, 32°), the flow phenomena due to the deep stall are too complex. So, in order to obtain grid independent solutions, fine meshes and small time steps are required. A thorough parametric investigation of the numerical parameters is not the focus of the present work, so the same fine mesh with a minimum y+ of the order of 10^{-4} is used in all simulations. However, it must be noted that a sufficiently small time step is required in order to ensure that the vortex shedding is properly captured. In **Figure 6.6.4** the C_L time history and the corresponding error convergence are shown for two time steps in the case of the FFA-360 at AOA = 32°. For dt = 0.002, although a periodic state is obtained, the error in the u-

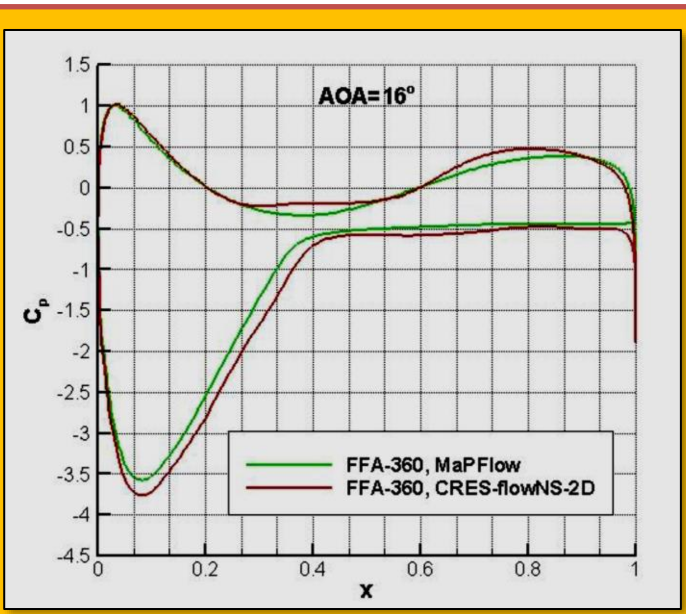

Figure 6.6.2 Comparison of pressure coefficient plots between *MaPFlow* and *CRES-flowNS-2D* for the FFA-360 airfoil at AOA=16°, Re =10^7, M =0.09. The higher pressure at the suction side predicted by *CRES-flowNS-2D* is the reason for the higher C_L value in Figure 4

---

[178] See Previous

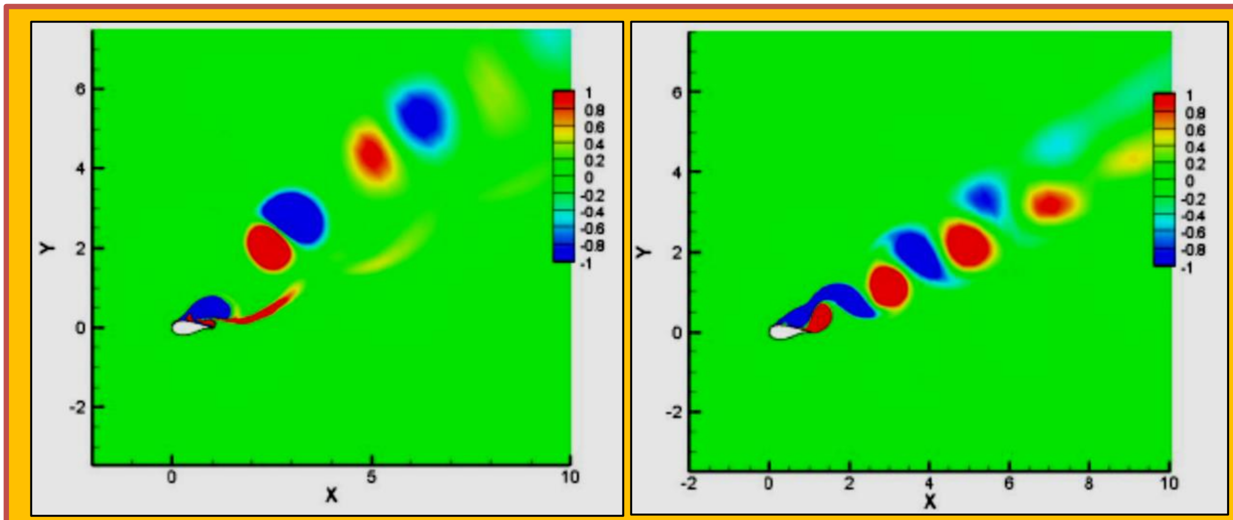

Figure 6.6.4 Vorticity contours of the flow around the FFA-360 airfoil for AOA =32°, Re =10^7, M =0.09. Left: Time step=0.002. Right: Time step=0.001. Predictions obtained with *MaPFlow*

momentum equation diverges. On the contrary when dt = 0.001 is used, clear convergence is attained. The corresponding flows are compared in **Figure 6.6.5**. In the dt = 0.002 simulation, the flow exhibits an unnatural vortex pairing at higher frequency while the trajectory of the wake vortices follows a higher slope that that defined by the AOA. On the contrary the pattern in the dt = 0.001 case is reasonable, having the expected von Karman structure.

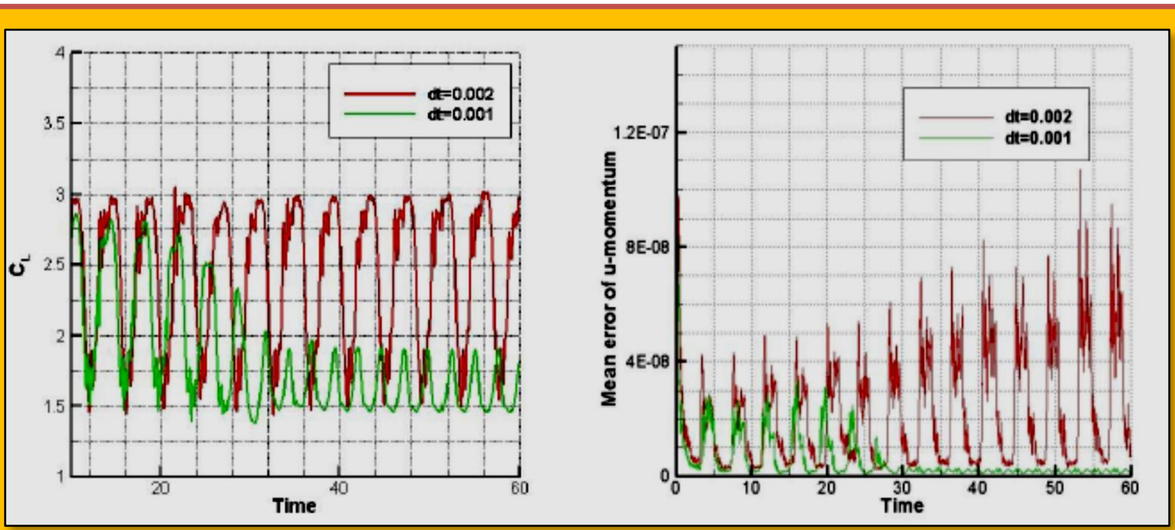

Figure 6.6.5 Unsteady calculation of the FFA-360 airfoil at AOA =32° for different time steps, Re =10^7, M = 0.09. Left: Time history of C_L. Right: Mean error of the u-momentum equation

6.6.4.2 C_L-C_D Polar

The compressible *MaPFlow* was used for most of the subsequent computations for two reasons: First, it is valid for the whole range of Mach number and second, it is faster due to the fact that implements parallel processing. Validation of the *MaPFlow* predictions was performed using the existing measurements for the NACA 63-018 airfoil [1]. Comparison of the mean polar for the various Reynolds numbers is shown in **Figure 6.6.6**. A good agreement is observed in the linear region. In the post-stall region predictions overestimate measurements, but the overall trend is reproduced. As Re increases both measurements and simulations show that max convergences to a limiting upper value.

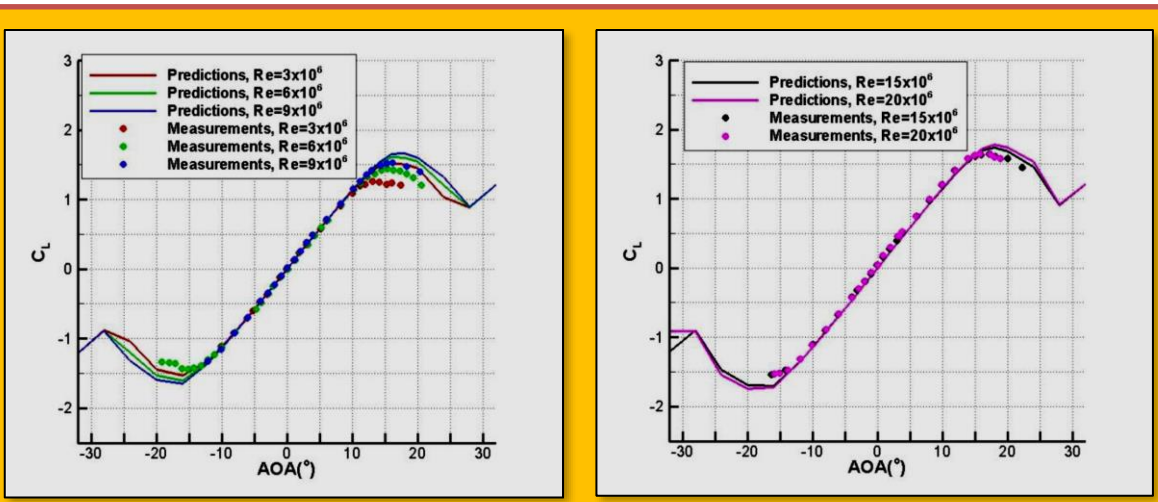

Figure 6.6.6 polar plots for the NACA 63-018 airfoil. Left: Re=3, 6, 9 x10^6. Right: Re=15, 20x10^6. Predictions obtained with *MaPFlow*

In the measurements, convergence to that limiting value is slower and so the largest difference is seen in the smaller Re number of 3x10^6. Also the angle of attack corresponding to max is higher in the simulations indicating a delay is stall, which could be attributed to the turbulence modelling. Furthermore, is found to decrease up to ~28° and then recovers to higher values indicating a change in the unsteady features of the flow. A similar lift recovery has been also reported for the NACA 63-

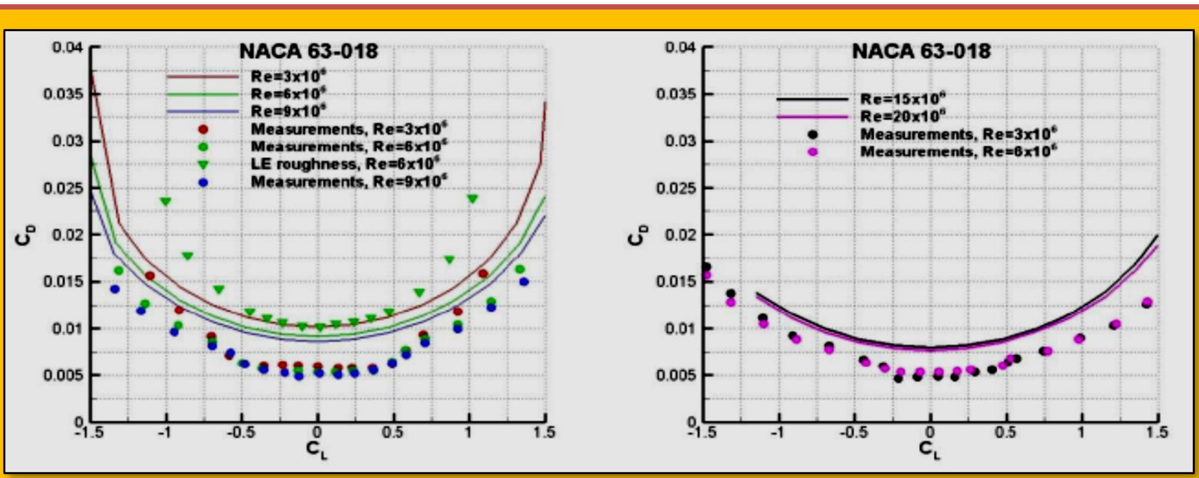

Figure 6.6.7 C_D polar plots for the NACA 63-018 airfoil. Left: Re=3, 6, 9x10^6. Right: Re=15, 20 x10^6. Predictions obtained with *MaPFlow*

215 and 4418 airfoils on the basis of wind tunnel tests [5]. Regarding drag, the difference in between predictions and measurements at AOA = 0^o is 0.005 (**Figure 6.6.7**). Such a difference is justified by the fact that the CFD predictions are fully turbulent. It should be mentioned that for Re =6x10^6 measurements with leading edge roughness are also available in [1]. In that case, the measured at AOA = 0^o is in better agreement with the predicted value as shown in **Figure 6.6.7(left).**

In **Figure 6.6.8**, the predicted C_L- C_D polar plots for the different FFA airfoils are presented. As expected, stall appears at lower AOA as thickness increases. In addition, the increase in thickness results in lower C_L and higher C_D in the post-stall region. Attention should be paid to the effect of the Gurney flap (FFA-360-G airfoil) that gives a significant increase in the slope of C_L over the linear range as well as higher max . In the post-stall region, a recovery of lift is found similar to that already observed in the NACA airfoils. The turning point depends on the airfoil thickness. As thickness increases from 24% to 36%, this characteristic AOA is reduced from 28^o to ~18^o. Due to airfoil camber, the variation of C_L is different at negative AOAs. For increasing thickness onset of separation appears earlier.

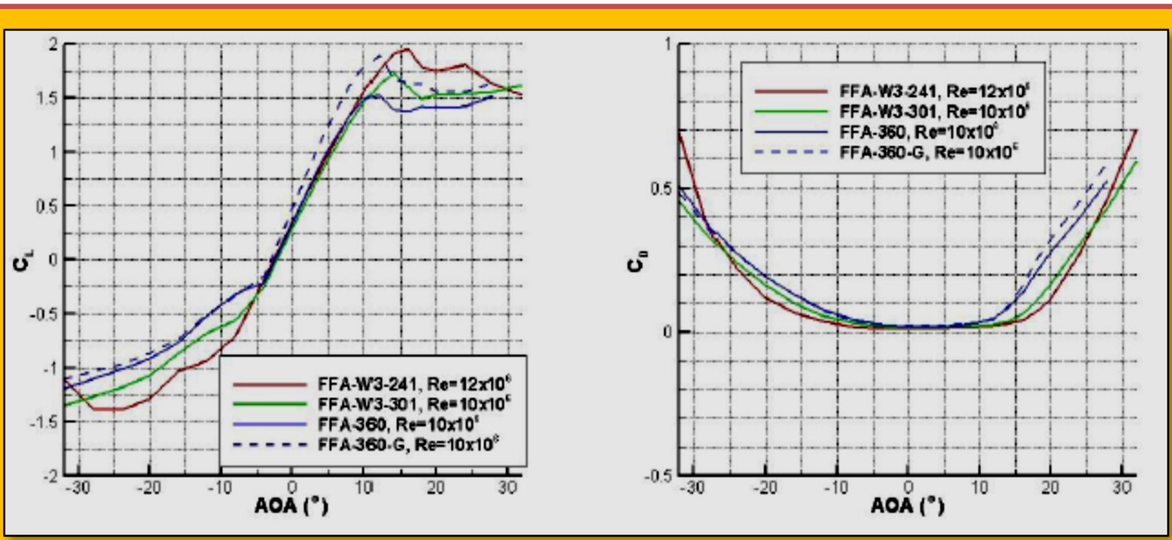

Figure 6.6.8 C_L- C_D polar plots for the FFA airfoils. Comparison of airfoils with different thickness. Predictions obtained with *MaPFlow*

The post stall (negative) slope after max is more or less the same indicating similar aerodynamic damping characteristics in case of vibrations. Slightly higher values are observed for the Gurney flap airfoil. The dependence of C_L, C_D predictions on the Reynolds number is shown in [Figure 11 of J. M. Prospathopoulos et al][179] for the FFA-W3-301 airfoil. As expected, the increase of Reynolds number delays flow separation and leads to higher C_L and lower C_D values in the region of separated flow. Finally, the effect of Mach number was studied for the FFA-W3-241 and FFA-360 airfoils in the linear region of C_L, C_D. Figures 12, 13 of [J. M. Prospathopoulos et al][180] show that by increasing the Mach number, lift increases and drag decreases. For the thicker airfoil FFA-360 the effect of Mach number appears stronger at high AOAs. The reason is the stronger effect of compressibility on the pressure

---

[179] John M Prospathopoulos et al 2014 J. Phys.: Conf. Ser. 524 012015

[180] John M Prospathopoulos et al 2014 J. Phys.: Conf. Ser. 524 012015

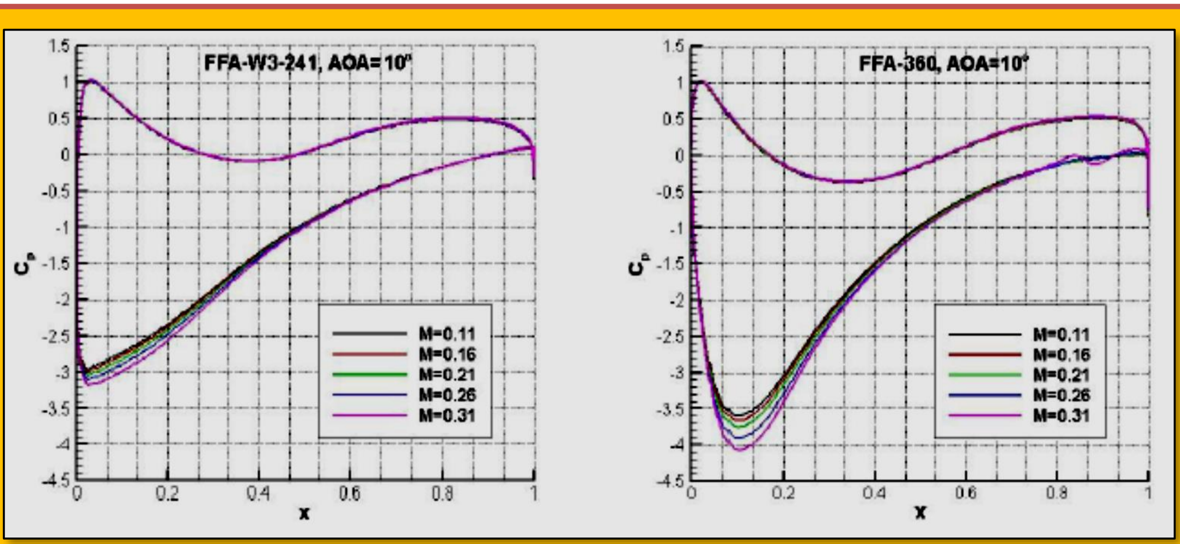

Figure 6.6.9 C_P plots at different Mach numbers, AOA=10°, for the FFA-W3-241 and the FFA-360 airfoils. Predictions obtained with *MaPFlow*

at the suction side as depicted in the C_p plots (**Figure 6.6.9**). The increase in lift with respect to Mach number is in accordance with ***Ackeret's linear theory*** for airfoils [6].

The comparison between the predictions of the *MaPFlow* and *CRES-flowNS-2D* codes is presented in Figure 15 of of [J. M. Prospathopoulos et al][181]. *MaPFlow* simulations were also performed at M = 0.09, so that comparison with the incompressible *CRES-flowNS-2D* be possible. A fairly good agreement is observed at the linear region for both FFA-W3-241 and FFA-360 airfoils. For the thicker FFA-360 airfoil *MaPFlow* predicts stall at a lower AOA as also mentioned above (see **Figure 6.6.8**). It is not clear if *CRES-flowNS-2D* presents the same trend since convergence was not possible in the 12°-20° range for FFA-W3-241. However, the predictions at 12° and 20° show that the comparison between the two codes is worse as we move away from the linear region. This is further supported by the comparison of the C_p plots in **Figure 6.6.10**, which shows better agreement at 8° than at 12°.

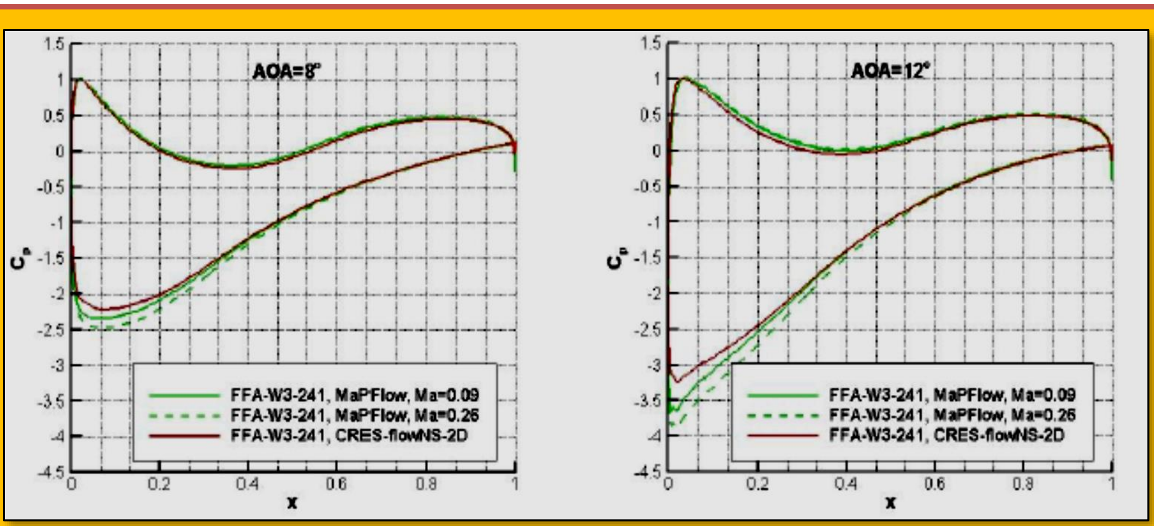

Figure 6.6.10 Comparison of pressure coefficient plots between *MaPFlow* and *CRES-flowNS-2D* for the FFA-W3-241 airfoil, Re=$12x10^6$. Left: AOA=8°. Right: AOA=12°

---

[181] John M Prospathopoulos et al 2014 J. Phys.: Conf. Ser. 524 012015

In the same figure the difference in the predictions of *MaPFlow* for M = 0.09 and M = 0.26 also shows the effect of the compressibility.

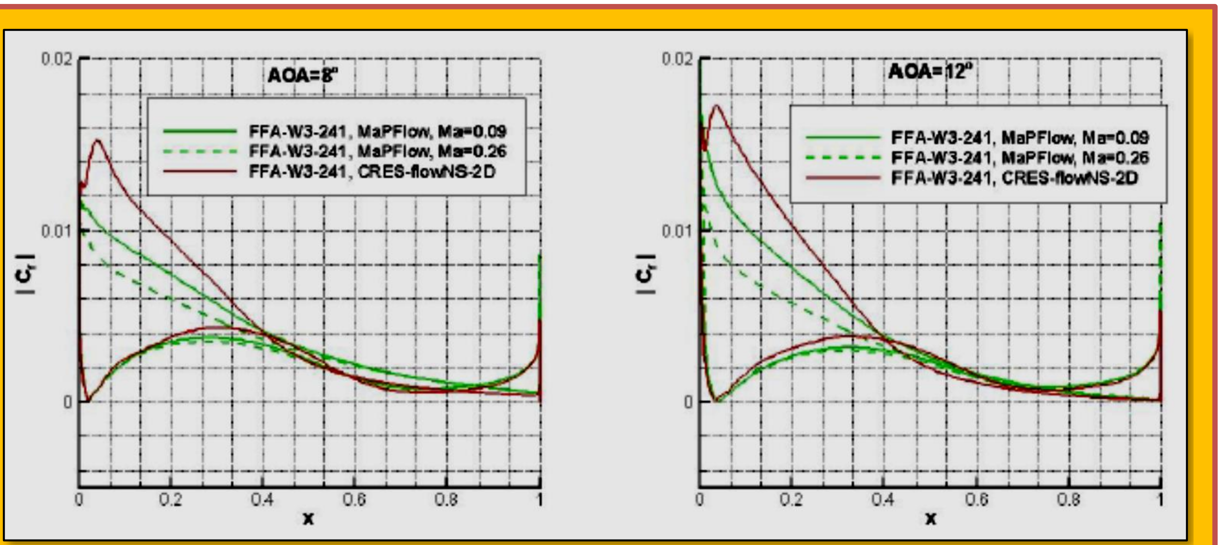

Figure 6.6.11 Comparison of skin friction coefficient plots between *MaPFlow* and *CRES-flowNS-2D* for the FFA-W3-241 airfoil, Re=12x10^6. Left: AOA=8°. Right: AOA=12°

In order to explain the deviation of the predictions between the two codes at high AOAs the skin friction coefficient are plotted in **Figure 6.6.11**. *CRES-flowNS-2D* predicts a sudden peak in skin friction at the suction side close to the leading edge, which is not observed in the *MaPFlow* predictions. As a result the pressure at the suction side is reduced and produces a continuously lower lift as the AOA increases.

This peak in skin friction is not observed in CRES-flowNS-2D predictions for the 36% airfoil as shown in **Figure 6.6.12** at AOA = 10°. Therefore, the two codes predict similar pressure and lift coefficients,

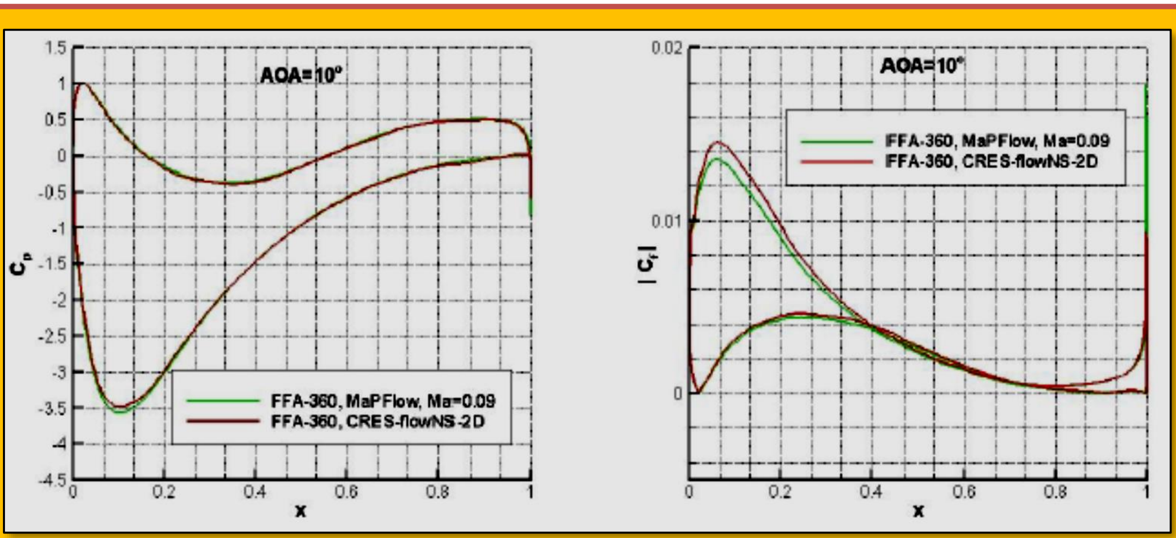

Figure 6.6.12 Comparison between *MaPFlow* and *CRES-flowNS-2D* predictions for the FFA-360 airfoil, Re = 10^6, AOA=10°. Left: Pressure coefficient. Right: Skin friction coefficient.

even in the post-stall region as shown in Figure 15 of [J. M. Prospathopoulos et al][182]. It seems that the skin friction predicted by the incompressible code is sensitive to surface curvature especially as the AOA increases. The difference in the behavior of the two codes may be also related to the way velocity fluctuations are treated (in a compressible code velocity fluctuations are filtered through the density equation); however a clear explanation could not be found and further investigation is required.

6.6.5 Discussion

In order to assess the aerodynamic performance of thick airfoils at high Reynolds numbers and increased Mach numbers, CFD simulations were performed on three FFA airfoils in a wide range of AOAs. First, a numerical investigation was performed focusing on: the distinction between steady and unsteady calculations; the convergence; and the choice of the proper time step. Steady state simulations were found adequate for a range of AOAs approximately between -8° and 14°. For higher AOAs, steady state simulations failed to give a converged mean value of C_L, C_D, indicating the onset of unsteady flow phenomena. Unsteady calculations converged to a periodic variation of C_L, C_D, which is driven by the frequency of vortex shedding. A number of 20000 time steps proved to be sufficient for most of the simulated cases. For AOAs higher than 24° it was observed that a sufficiently small time step must be used, otherwise the wake structure may be lost leading to non-physical simulated flows.

After tuning the numerical parameters, CFD predictions were validated against the wind tunnel measurements of the NACA 63018 airfoil in a wide range of Reynolds number from $3x10^6$ to $20\ x10^6$. Good agreement was obtained for in the linear region, whereas onset of stall was predicted at higher AOAs and resulted in a lift overestimation in the post-stall region. The overall trend of the curve was well predicted. Regarding drag, CFD predictions exhibited a shift at zero AOA justified by the fact that calculations were fully turbulent. A similar shift was presented in the measurements when surface roughness was added at the leading edge.

Next, the effects of thickness, Reynolds and Mach numbers on the aerodynamic characteristics of the FFA airfoils were investigated. A higher thickness reduced the lift and increased the drag at "high" AOAs; namely outside the linear region. For the studied FFA airfoils, the linear region lied approximately between -5° and 10°. In the post-stall region there was a certain value of the AOA, dependent on the airfoil thickness, at which the C_L-AOA curve changed trend, denoting a change in the unsteady features of the flow. The same trend has been observed in the wind tunnel measurements of the NACA 63-215 and 4418 airfoils. Changing the Reynolds number from $3x10^6$ to $10x10^6$ gave a considerable increase in the maximum C_L (16%), but the increase over the linear region was much smaller (3-5%). A similar effect in the linear region was caused by the increase of the Mach number from 0.11 to 0.31.

Finally, a comparison was made between the predictions of the compressible and the incompressible CFD solvers. The two codes showed good agreement in the linear region for both 24% and 36% airfoils. As the AOA increased, the incompressible code predicted a lower pressure at the suction side of the 24% airfoil resulting in a lower lift This is attributed to the prediction of a peak in the skin friction close to the leading edge. Such a peak is not present in the 36% airfoil predictions and the agreement between the two codes becomes better even in the post-stall region. Further investigation is required in order to better understand whether the airfoil thickness has a physical or numerical effect on the prediction of the skin friction.

6.6.6 Conclusion

CFD predictions are capable of predicting the basic flow features around thick airfoils at high Reynolds numbers. However, the occurrence of strong unsteady phenomena at high AOAs demands unsteady calculations with small time steps leading to a significant increase of the computational

---

[182] See Previous

cost. ***As thickness increases, unsteady vorticity structures become more complex and appear at lower AOAs.*** Therefore, a proper tuning of the numerical parameters is necessary in order to achieve a fast convergence without losing the complex unsteady flow features.

6.6.7 References

[1] Loftin LK and Bursnall WJ "The Effect of Variations in Reynolds Number between 3x106 and 25x106 upon the Aerodynamic Characteristics of a Number of NACA 6-Series airfoil sections", NACA Report 964

[2] Papadakis G., Voutsinas S., Sieros G., Chaviaropoulos P. 2012 "CFD aerodynamic analysis of non-conventional airfoil sections for very large rotor blades", In Proceedings of *The Science of Making Torque from Wind,* October 9-11, Oldenburg, Germany.

[3] Chaviaropoulos PK. and Douvikas DI. 1998 "Mean-flow-field Simulations over Complex Terrain Using a 3D Reynolds Averaged Navier–Stokes Solver", *Proceedings of ECCOMAS '98*, 1(2), pp. 842-848.

[4] Zahle F, Riziotis V, Bergami L, Madsen HA 2013 "Benchmarked aerodynamic-structural design methods, Part B: Benchmarking of aerodynamic and aeroelastic models", Deliverable D 2.21, Innwind.EU FP7 project

[5] Timmer WA 2010 "Aerodynamic Characteristics of Wind Turbine Airfoils at High Angles of Attack", Proceedings of *The Science of Making Torque from Wind,* June 28-30, Crete, Greece

[6] Ackeret J. 1925. "Luftkräfte auf Flügel, die mit größerer als Schallgeschwindigkeit bewegt werden. Zeitschrift für Flugtechnik und Motorluftschiffahrt", 16, pp.72-74.

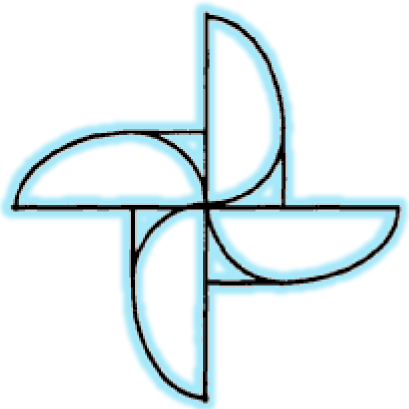

7 Case Studies Involving Wing Aerodynamics

7.1 Case Study 1 - Numerical Study of 3D Flow Around the Wing Airfoil E562 With Forward and Rearward Wingtip Fence

---

Authors : *Setyo Hariyadi Suranto Putro, Sutardi and Wawan Aries Widodo*
Citation : *AIP Conference Proceedings 2187, 020017 (2019)*
Source : *https://doi.org/10.1063/1.5138272*

Airfoil is an aerodynamic model that is widely used both on aircraft wings, ***Unmanned Aerial Vehicle (UAV)*** and fluid machines such as pumps, compressors, and turbines (Putro, Sutardi, & Widodo, 2019). The airfoil on aircraft wings with the resulting lift force is used to lift the entire aircraft. Therefore, the researchers concentrate more on wing modification so that the resulting lift is more optimal. Increased performance of the airfoil on the wing can be done in various ways, one of which is adding a winglet to reduce drag. It is hoped that a large enough lift and drag ratio will improve aircraft performance. This research was conducted by numerical simulation using *Ansys 19.0.* with turbulent model k-ω SST [Putro et al.][183]. The velocity flow rate used is 10 m/s (Re = 2.3×10^4) with $\alpha = 0^o, 2^o, 4^o, 6^o, 8^o, 10^o, 12^o, 15^o, 16^o, 17^o, 19^o$ and 20^o. The test model is an *Eppler 562 (E562)* airfoil with and without a winglet. From this study, tip vortex was seen in plain wings, forward wingtip fence and rearward wingtip fence with lower speeds. In the area that has been separated (wake) which is indicated by a lower speed in the three configurations x = 1c. In the z = 1.5c area, it is shown that there is a path line pattern difference between the three configurations. It is shown that the influence of the three-dimensional flow on the rearward wingtip fence where there is a higher velocity in the upper surface area. In the trailing edge, z = 1.9 shows that there is a path line from the lower surface to the upper surface in the plain wing and rearward wingtip fence. Keywords: wing, *Eppler 562*, winglet, tip vortex, forward wingtip fence, rearward wingtip fence.

7.1.1 Research Methodology

This research was conducted by numerical simulation using Ansys 19.0 with turbulent model K-ω SST. The freestream flow rate used is 10 m/s (Re = 2.34×10^4) with α = 0, 2, 4, 6, 8, 10,12,15, 16,17,19 and 20 degrees. The model specimen is an *E562 airfoil* with variations in the use of winglets. The winglet that will be used is a forward and rearward wingtip fence. The Reynolds Number is determined based on the length of the chord. In this case, the chord length used is 20 cm. **Figure 7.1.1** represents the simulation domain and the boundary conditions used in the simulation. The test configuration is shaped in the form of an *Eppler 562 type* airfoil with and without a winglet in the form of

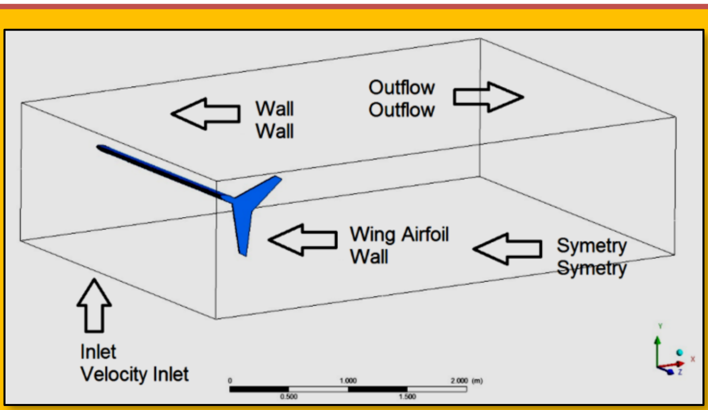

Figure 7.1.1 Simulation domain and boundary conditions

---

[183] Setyo Hariyadi Suranto Putro, Sutardi and Wawan Aries Widodo, "*Numerical study of three-dimensional flow characteristics around the wing airfoil E562 with forward and rearward wingtip fence*", AIP Conference Proceedings 2187, 020017 (2019.

a wingtip fence as shown in and the dimensions of the modeling dimensions in [7]. While the meshing used in this simulation study is shown in **Figure 7.1.4**.

(a) Forward Wingtip Fence

(b) Rearward Wingtip Fence

Figure 7.1.2 Specimens Model

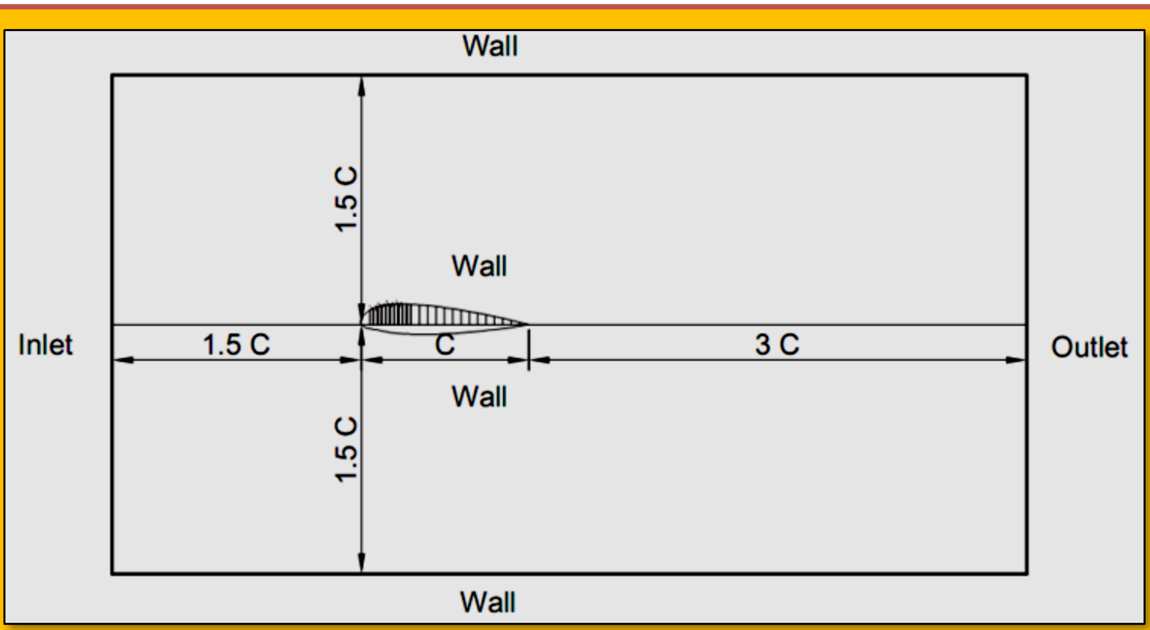

Figure 7.1.3 Modeling Dimensions and Background Conditions

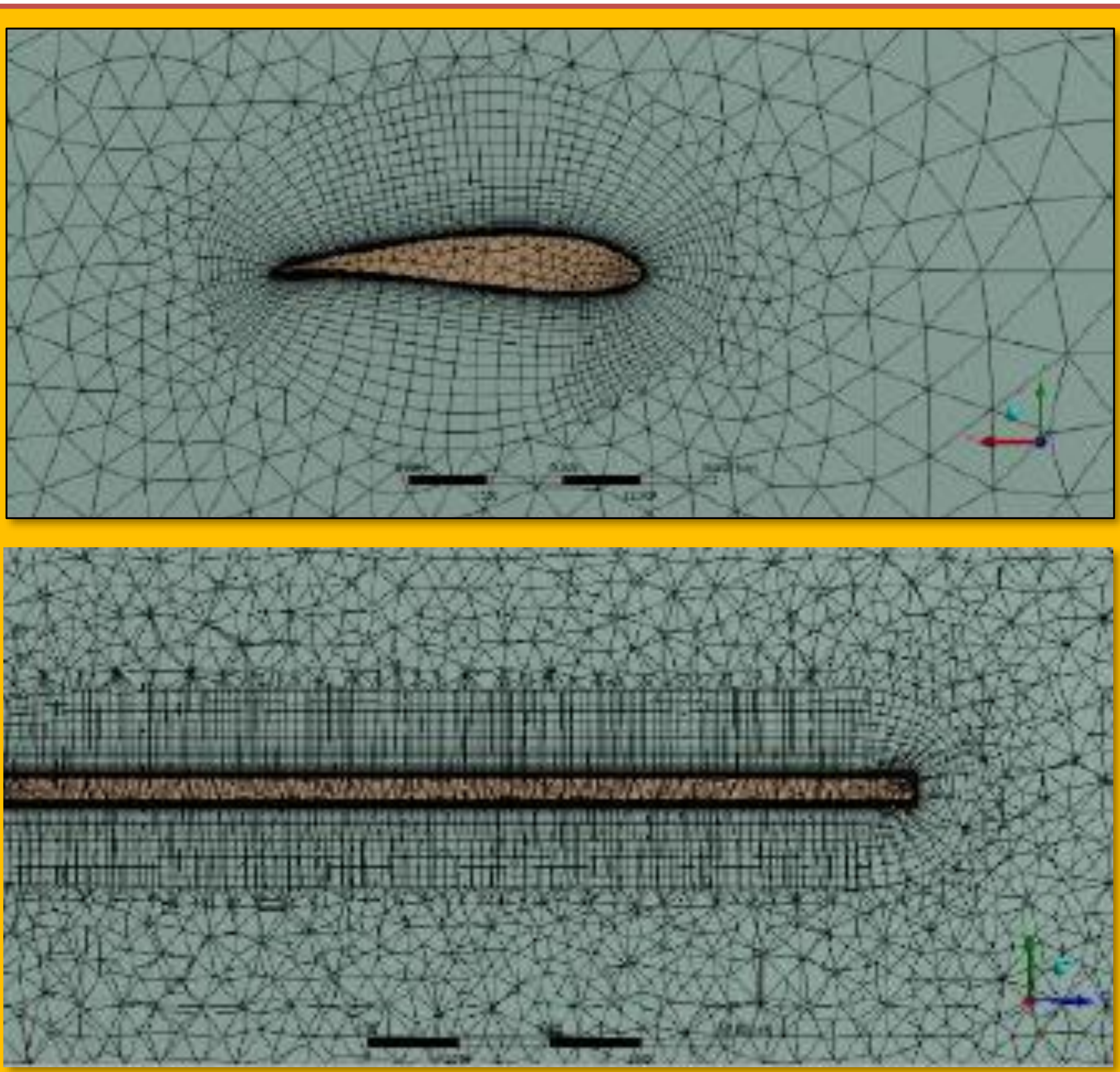

Figure 7.1.4 Geometry and Meshing

7.1.2 Grid Independency

The use of simulation software requires data accuracy both in the pre-processing and post-processing steps. The grid independence step is needed to determine the level and structure of the most efficient grids so that the modeling results are close to true. Grid independence is done to get the amount of meshing that tends to be constant so that it can be obtained in this independence grid, the number of meshing is divided into 4 types, then from this type of meshing we will look for the smallest difference in value of each meshing by comparing the numerical C_D graph. The C_D and y+ value of the grid independency in the numerical simulation is shown in **Table 7.1.1** where it shows the meshing variations of the three dimensional grid independency of the test model at the Reynolds number 2.34 x10^4. To get more complete information on the area around the wall, it requires the calculation of *y+* on each meshing. In addition to the calculation of *y+*, the inflation layer is needed so that the area around the wall uses a type of quadrilateral meshing so that information around the wall is more accurate. To calculate the smaller number of nodes, the area far from the wall will use meshing tetrahedrons.

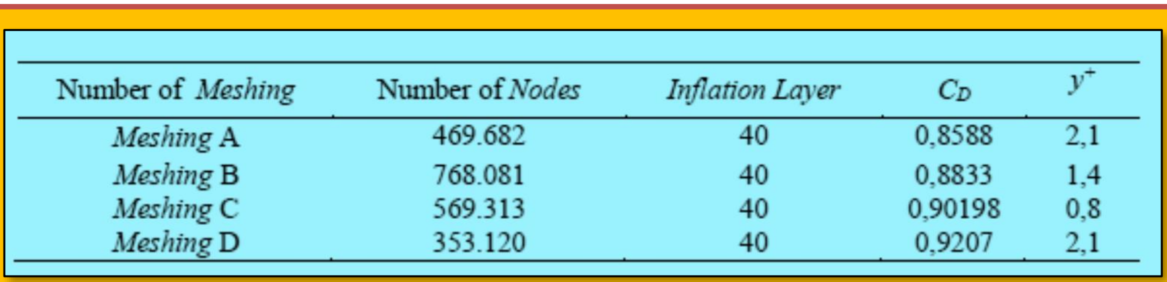

Number of *Meshing*	Number of *Nodes*	*Inflation Layer*	C_D	y^+
Meshing A	469.682	40	0,8588	2,1
Meshing B	768.081	40	0,8833	1,4
Meshing C	569.313	40	0,90198	0,8
Meshing D	353.120	40	0,9207	2,1

Table 7.1.1 Analysis of the Three-Dimensional E562 Grid Model Without Winglets

In this study, to get the best results, the $y+$ used is less than 1, as was done in the [Kontogiannis] research. Based on **Table 7.1.1**. C_D values that tend to be smaller occur in Meshing C. One of the considerations in using numerical simulations is the time and memory used, then the meshing used for comfortable simulations is Meshing C. In this modeling, the flow characteristics step, including the selection of the solver model and determining the turbulence model are used. The solver model used is unsteady. The turbulence model used for this airfoil is the k-ω SST model. The k-ω SST model developed by *Menter* to combine the formulation of a stable and accurate k-ω standard model in the area near the wall with the k-ε model which has advantages in freestream flow. To achieve this, a k-ω SST model was made. (10)

7.1.3 Result and Discussion

7.1.3.1 Velocity Vector

In **Figure 7.1.5,** it is shown that velocity vector visualization comparison of the plain wing, forward wingtip fence, and rearward wingtip fence. When the velocity moves from an angle of 90^{o} to 270^{o}, the velocity strength is higher. But when velocity moves from 270o to 90o it has a lower value. In **Figure 7.1.5 (a)** it is shown that the plain wing has a high velocity density value at x = 0.5c. In **Figure 7.1.5 (b)** it is shown that at x = c, the velocity density has decreased but still has a high value. This is indicated by the resulting velocity vector length. In **Figure 7.1.5 (c)**, the forward wingtip fence cant angle 90^{o} produces The forward wingtip fence cant angle 90^{o} produces velocity vector that congregates around the fence and the vector density is more tightly than the plain wing. A similar phenomenon occurs in **Figure 7.1.5 (d)** which shows the velocity vector decreases. However, at rearward wingtip fence cant angle 90^{o} at $\alpha = 17^{o}$, it produces the lowest velocity pattern compared to plain wing and forward wingtip fence. This is possible because there is a flow leak around the leading edge that is larger than the forward wingtip fence. This flow leakage not only causes a decrease in speed around the rearward wingtip fence but also causes an irregular flow pattern as shown in **Figure 7.1.5 (e).** In **Figure 7.1.5 (f)** it can be seen that irregular flow patterns behind the wing into the direction of the wingspan. The flow pattern from the bottom side controverts with the airflow from the top side. This results in a decrease in the velocity value at the rearward wingtip fence.

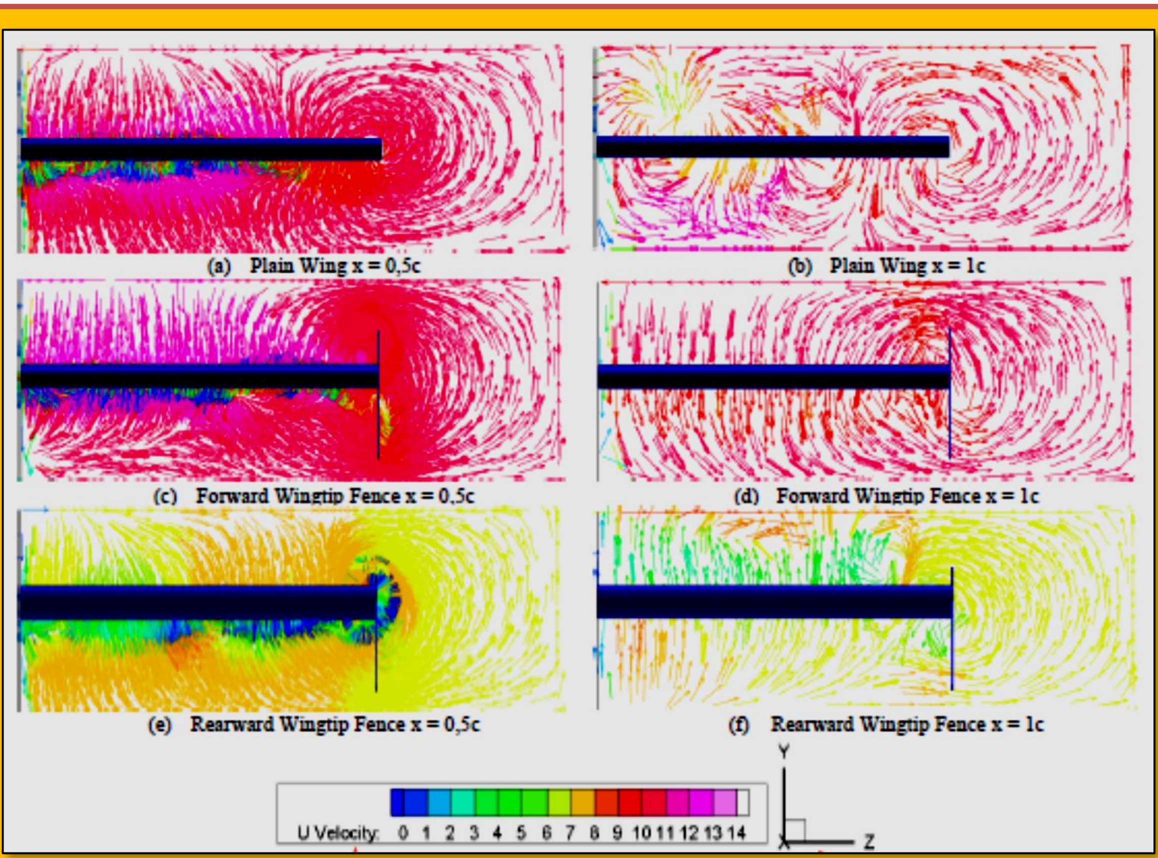

Figure 7.1.5 Velocity Vector y and z on Wing Airfoil α = 17°

7.1.3.2 Velocity Path Line

Figure 7.1.6 shows the velocity contour along with the path line of the flow passing through the plain *wing Eppler 562* and with the winglets, at α = 17o. It is seen from the cut in the midspan and the area near the tip (z/s = 0.9). It can be seen that the visualization of the velocity path line and contours value in each variation show a certain pattern.

At α = 17°, there is a difference in the phenomenon of flow passing through the airfoil midspan. On the *Eppler 562* airfoil with a forward wingtip fence (**Figure** 7.1.6 **(c)**) it has a wake phenomenon that occurs slightly smaller than the plain wing *Eppler 562* (**Figure** 7.1.6 **(a)**). Rearward wingtip fence configuration has a smaller wake region than forward wingtip fence configuration but larger than the plain wing. (**Figure** 7.1.6 **(e)**). However, the plain wing and rearward wingtip fence have a slight velocity path line that collides with the wake. It is suspected that this is the effect of leaps in fluid flow from the lower surface to the upper surface. The effect of this fluid flow jump is seen in the z = 0.9 area both on the plain wing (**Figure** 7.1.6 **(b))** and on the rearward wingtip fence (**Figure** 7.1.6 **(f)**). But this does not occur in the forward wingtip fence. This shows that the influence of fluid flow jumps from the lower surface to the upper surface is felt up to the midspan region. But the result of the flow jump is influenced by the shape of the end wall in the wingtip area.

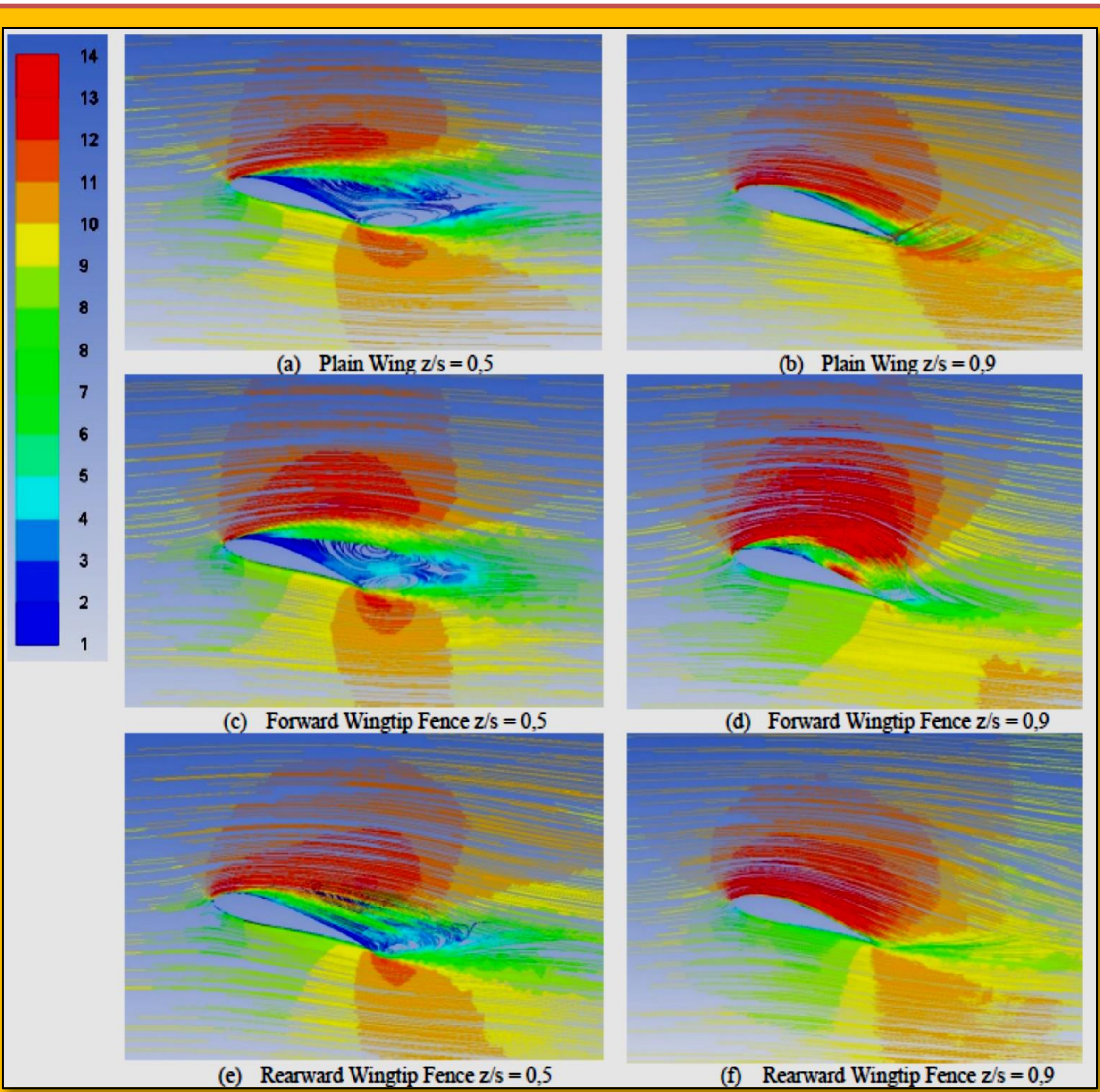

(a) Plain Wing z/s = 0,5

(b) Plain Wing z/s = 0,9

(c) Forward Wingtip Fence z/s = 0,5

(d) Forward Wingtip Fence z/s = 0,9

(e) Rearward Wingtip Fence z/s = 0,5

(f) Rearward Wingtip Fence z/s = 0,9

Figure 7.1.6 Velocity Path Line on Wing Airfoil α = 17°

7.1.3.3 Velocity Magnitude

To observe the flow phenomenon in the tip region, velocity contours are observed in an isometric view of a particular y-z plane. It can be seen from **Figure 7.1.7** that tip vortex develops when the flow is at greater x/c. This is the following numerical studies conducted by Wells (2009). To facilitate the analysis of the vortex tip phenomenon in each configuration, the contours are only compared to x/c = 1, 1.5, and 2. In addition to facilitating analysis, all configurations show the same pattern where the magnitude of the tip vortex is greater at a large x/c. The illustration also displays velocity magnitude in the y and z directions to clarify the tip vortex phenomenon. **Figure 7.1.7** gives information on the airflow of the trailing edge that moves from the lower side to the upper side. The airflow forms a vortex called the tip vortex. This is caused by pressure magnitude value on the upper side is smaller than the lower side so that the fluid jump to the tip of the wing. In the plain wing, it is pointed out that the tip vortex phenomenon is relatively larger than two other configurations. The tip vortex then shrinks at a greater distance from the wing. Similar tip vortex phenomena also occur in other configurations. Tip Vortex was arisen a small size develop with the shape of the end wall. However, in the forward wingtip fence and rearward wingtip fence, it can be seen that the contour is redder (velocity increases) around the airfoil in addition to the wake area. In areas that have been dispersed (wake), the area with blue color increases. This phenomenon indicates that the wake region is getting bigger when the angle of attack is raised.

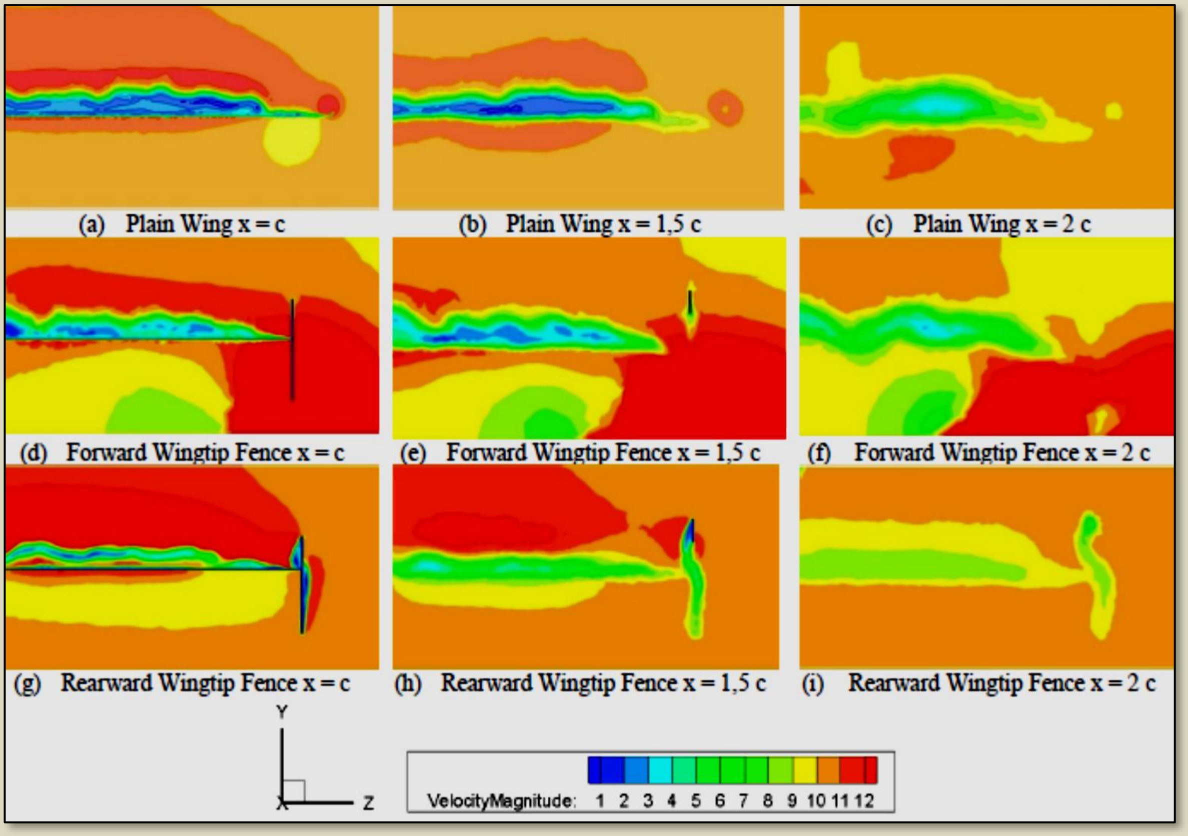
(a) Plain Wing x = c
(b) Plain Wing x = 1,5 c
(c) Plain Wing x = 2 c
(d) Forward Wingtip Fence x = c
(e) Forward Wingtip Fence x = 1,5 c
(f) Forward Wingtip Fence x = 2 c
(g) Rearward Wingtip Fence x = c
(h) Rearward Wingtip Fence x = 1,5 c
(i) Rearward Wingtip Fence x = 2 c

Figure 7.1.7 Velocity Magnitude on Wing Airfoil α = 17°

7.1.4 Conclusion

This study shows the influence of the use of winglets significantly on fluid flow patterns. The difference in flow patterns is seen in the midspan and the area near the winglet. The velocity vector and velocity path line contours show this effect. From the numerical simulation, several fluid characteristics are shown, including:

- Fluid flow leaps affect the velocity vector value and density patterns. The geometry configuration of the rearward wingtip fence causes a decrease in the value and density of the velocity vector compared to the plain wing and forward wingtip fence.
- The plain wing has the highest velocity vector value and density compared to other geometric configurations.
- The effect of a fluid flow jump (tip vortex) has an impact that reaches the fold including in the form of the wake. Wake formed from plain wing shows the lowest value and wider area compared to other configurations. The use of winglets can reduce wake wide, especially in midspan areas. In the wingtip region, the fluid flow jumps from the lower surface to the upper surface.

- The addition of winglets influences the size of the wake in the midspan area and the size of the vortex tip behind the wingtip. Adding winglets will reduce wake size and tip vortex.
- The reduction in wake means reducing the induced drag generated from the E562 airfoil.

7.1.5 References

1. Kody F, Bramesfeld G, Schmitz S. *An Efficient Methodology for Using a Multi-Objective Evolutionary Algorithm for Winglet Design.* Tech Soar. 2013;37(3), pp.45–56.
2. El Haddad N. *Aerodynamic and Structural Design of a Winglet for Enhanced Performance of a Business Jet* Scholarly Commons Citation. 2015;112. Available from: https://commons.erau.edu/edt/265
3. Hossain A, Rahman A, Hossen J, Iqbal P, Shaari N, Sivaraj GK. *Drag reduction in a wing model using a bird feather like winglet.* Jordan J Mech Ind Eng. 2011;5(3),pp.267–72.
4. Amendola G, Dimino I, Concilio A, Andreutti G, Pecora R, Cascio M Lo. *Preliminary design process for an adaptive winglet*. Int J Mech Eng Robot Res. 2018;7(1),pp.83–92.
5. Wei Z, Meijian S. *Design optimization of aerodynamic shapes of a wing and its winglet using modified quantum behaved particle swarm optimization algorithm.* Proc Inst Mech Eng Part G J Aerosp Eng. 2014;228(9):1638–47.
6. Panagiotou P, Efthymiadis M, Mitridis D, Yakinthos K. *A CFD-aided investigation of the morphing winglet concept for the performance optimization of fixed-wing MALE UAVS.* 2018 Applied Aero. Conf. 2018,pp.1–14.
7. Setyo Hariyadi SP, Sutardi, Widodo WA, Mustaghfirin MA. *Aerodynamics analysis of the wingtip fence effect on UAV wing*. Int Rev Mech Eng. 2018;12(10).
8. Mulvany N, Chen L, Tu J, Anderson B. *Steady-State Evaluation of Two-Equation RANS (Reynolds-Averaged Navier-Stokes) Turbulence Models for High-Reynolds Number Hydrodynamic Flow Simulations*. Dep Defense, Aust Gov [Internet]. 2004;1–54. Available from: http://oai.dtic.mil/oai/oai?verb=getRecord&metadataPrefix=html&identifier=ADA426359
9. Kontogiannis SG, Mazarakos DE, Kostopoulos V. *ATLAS IV wing aerodynamic design: From conceptual approach to detailed optimization*. Aero. Sci Technol [Internet]. 2016;56:135–47. Available from: http://dx.doi.org/10.1016/j.ast.2016.07.002
10. Harinaldi, Budiarso, Tarakka R, Simanungkalit SP. *Effect of active control by blowing to aerodynamic drag of bluff body van model*. Int J Fluid Mech Res. 2013;40(4):312–23.

7.2 Case Study 2 - Zonal Structure of Unbounded Flow Domains

Authors : *L. Q. Liu, L. L. Kang and J. Z. Wu*
Title : *Zonal structure of unbounded external-flow and aerodynamics*
Appeared in : *Fluid Dynamics Research · November 2016*
Source : *DOI: 10.1088/1873-7005/aa79d0*

It was argued by [Liu et al.][184] that the well-known algebraic decay of disturbance velocity as derived kinematically is too conservative. Once the kinetics is taken into account by working on the fundamental solutions of far-field linearized Navier-Stokes equations, it is proven that the furthest far-field zone adjacent to the uniform fluid at infinity must be unsteady, viscous and compressible, where all disturbances degenerate to sound waves that decay exponentially. But this optimal rate does not exist in some commonly used simplified flow models, such as steady flow, incompressible flow and inviscid flow, because they actually work in true subspaces of the unbounded free space, which are surrounded by further far fields of different nature. This finding naturally leads to a zonal structure of externally-unbounded flow field. The significance of the zonal structure is demonstrated by its close relevance to existing theories of aerodynamic force and moment in external flows, including the removal of the difficulties or paradoxes inherent in the simplified models.

7.2.1 Introduction

A fundamental issue in all studies of externally unbounded flows is the asymptotic behavior of velocity field as $\mathbf{r} \equiv |\mathbf{x}| \to \infty$ (x is the position vector). This is a necessary prerequisite for not only prescribing far-field boundary conditions for external-flow problems, but also ensuring the convergence of relevant integrals over the entire externally unbounded space with the fluid in uniform state at infinity (below we use the word `free space' for short) or arbitrarily large external boundary. This issue has long been an important subject for mathematicians working on the existence and uniqueness of the solutions of Navier-Stokes (NS) or Euler equations. But in the field of applied fluid dynamics and aerodynamics, when conducting the theoretical analysis or numerical computation of a specific external-flow problem, one seldom asks, in that problem, what the `infinity' means (does it really reach the uniform fluid at the `true' infinity?) and what the decay rates of various disturbances are (do they decay algebraically as $O(r^{-m})$ or exponentially as $O(e^{-rk})$, with m, k > 0 ?). The answer to these questions actually varies from one flow model to another, for example from steady to unsteady flows, from incompressible to compressible flows, and from inviscid to viscous flows. In the present paper we address this fundamental issue by using far-field analysis, both kinematically and kinetically. Here, kinematics is referred to as the study of motions of themselves apart from considerations of mass and force, and kinetics is referred to as the study of changes of motions produced by forces (Webster 1953). The results provide a precise estimate of the disturbance decay rates and associated concept of `infinity' as used in different flow models.

Specifically, it is well known that if the vorticity and dilatation fields are physically compact (i.e., they are significant only in a finite zone, say V_c, outside which they decay exponentially), then the far-field velocity must be irrotational and incompressible, which decays only algebraically (Batchelor 1967). But the assumed decay rate of vorticity and dilatation itself needs a proof. This can only be done by entering kinetics. As one of the major findings of the present paper, we shall not only confirm that assumption, but also further prove that the algebraic decay rule of velocity only represents an upper bound and is too conservative. Kinetically, it can be sharpened to exponential decay of all disturbance quantities (including velocity), if and only if the ow is unsteady, viscous and compressible. Evidently, exponential decay ensures a smooth transition to uniform fluid status at infinity and the convergence of various integrals over arbitrarily large domain.

---

[184] L. Q. Liu, L. L. Kang and J. Z. Wu, "*Zonal structure of unbounded external-flow and Aerodynamics*", Fluid Dynamics Research · November 2016, DOI: 10.1088/1873-7005/aa79d0

Unfortunately, all other simplified flow models (e.g., incompressible flow, steady flow, and inviscid flow, etc.) do not enjoy the nice feature of expontial decay. But this situation by no means implies that unsteady, viscous and compressible flow is an exception; rather, it just reflects the inherent physical incompleteness of those models, namely they only work in some true subspaces of the free space. Thus, in these models when one talks about some far field conditions as $r \to \infty$, the `infinity' there cannot really reach the uniform fluid at infinity in free space, while only the `infinity' in unsteady, viscous and compressible flow can. This observation naturally leads to a physical picture of the far fields for the first time: they form a zonal structure. Some long-standing or new puzzles or paradoxes concerning far-field behavior can thereby be well clarified. For further discussion, please see by [Liu et al.][185].

7.2.2 Far-Field Asymptotic and Decay Rate

The decay behavior of far-field velocity in externally unbounded domain, denoted by V_1 here and after, can be studied kinematically and kinetically. To orient our approach, it is necessary to compare these two methods first. This is done for the first time in 7.2.2.1, which shows that only kinetic method can obtain a complete description of the far-field decay rate. Then, the linearized NS equations are reduced in **sec 7.2.2.2**, of which the fundamental solutions of decoupled type and coupled type are carefully studied in 7.2.2.3 and **x 2.4 (see the source)**, respectively, both proving that the far-field disturbances decay exponentially and the result obtained by kinematic method is only an upper bound. This result is crucial for the constructing of a complete zonal structure.

7.2.2.1 From Kinematics To Kinetics

Batchelor (1967) has given a clear presentation of the kinematic method for estimating the far-field velocity decay rate. By the classic Helmholtz decomposition of velocity field

$$u = u_{\phi} + u_{\psi} = \nabla\phi + \nabla \times \psi \quad , \qquad \nabla . \psi = 0$$

Eq. 7.2.1

where ϕ and ψ are scalar and vector potentials, respectively, one has Poisson's equations

$$\vartheta \equiv \nabla . u = \nabla^2 \phi \quad , \quad \omega \equiv \nabla \times u = -\nabla^2 \psi$$

Eq. 7.2.2

Their fundamental solutions in V_1 yield the familiar generalized Biot-Savart law (Wu 2005, Wu et al 2006, Wu et al 2015), to which Batchelor applied the Taylor expansion and proved that the far-field ow must be incompressible and irrotational, which decays algebraically in space. The only assumption is that ! and # should be physically compact, so that the Taylor expansion is convergent. This assumption itself was not proved. Nevertheless, since this method is purely kinematic, it has been regarded as universally true, no matter whether the ow is steady or unsteady, compressible or incompressible, laminar or turbulent, etc.

In our view, however, this kinematic estimate can hardly describe the true far-field asymptotic of externally unbounded flow. Rather, it only gives an upper bound of the velocity decay rate and is too conservative, because the Poisson equation only considers the spatial effect without any temporal evolution of the flow field where kinetic effects such as viscosity must enter. To obtain the optimal estimate of the far-field asymptotic decay rate, therefore, it is necessary to go into kinetics, based on the NS equations (??) below.

The first effort toward this goal was made by Wu (1982), who used the vorticity transport equation of incompressible flow to prove that ω is indeed compact as Batchelor (1967) assumed. He then used the Biot-Savart law to confirm Batchelor's estimate: u decays as r^{-n}, where $n = 2$, 3, … is the

---

[185] L. Q. Liu, L. L. Kang and J. Z. Wu, "*Zonal structure of unbounded external-flow and Aerodynamics*", Fluid Dynamics Research · November 2016, DOI: 10.1088/1873-7005/aa79d0

dimensionality of the space. Following the same strategy of Wu (1982), Liu et al (2014) proved that ω and ϑ of compressible flow must be compact. Then, using the generalized Biot-Savart law they obtained the same result as that for incompressible flow. However, for compressible ow this result is still not optimal: for an observer standing outside the reach of the first sound wave front generated by the body motion, the fluid should keep undisturbed and thus the velocity decays arbitrarily fast, say exponentially.

Instead of appealing to Poisson's equation, the most thorough approach to this problem would be directly deriving the far-field asymptotic from the NS equations. But, since the flow is critically dependent on the initial and boundary conditions, for example, under the same nonlinear NS equations with specified initial and boundary conditions the flow can be either laminar or turbulent, it is impossible to determine the far-field behavior by the full NS equations. To bypass this difficulty, we assume that there exists a far-field zone neighboring the uniform fluid at infinity, where the governing equations can be linearized and the effects of the initial and boundary conditions can be mimicked by proper source terms. Thus, the fundamental solution of the linearized NS equations obtained by Lagerstrom et al (1949) can be applied.

Intuitively, the assumed existence of linearized far field should be a physical fact since the flow at infinity always recovers to the uniform state and before that the disturbances of the flow must have decayed arbitrarily small. Actually, Lagerstrom (1964) has clearly stated that a linear zone should exist in viscous flow around a finite-size object. Although this assertion has not been mathematically proven for general NS ow, in our case the assumed existence of linear far field can be checked after the linearized solutions are obtained.

At this stage, the expressions of the equivalent source terms need to be carefully treated. This is relatively simple for steady flow, where the mass and energy sources are absent and the momentum source can be simplified to an impulsive force of unit mass fixed on the space,

$$\mathbf{f} = \frac{\delta(\mathbf{x})}{\rho_0}\mathbf{F}$$

Eq. 7.2.3

where **F** is the total force experienced by the body, $\delta(\mathbf{x})$ is the Dirac delta function, and suffix 0 denotes the uniform constant value at infinity. Under these assumptions, Liu et al (2015) have obtained the far-field asymptotic expression of the velocity in two-dimensional (2D) steady flow region, say V_{st}, which decays algebraically for both incompressible and compressible flows. In particular, both in the vortical wake and along the primary shock waves, the disturbance velocity u' decays as $r^{-1/2}$. This estimate can by no means be reached by purely kinematic method, since the steady vortical wake must extend to downstream and finally escape from V_{st}, making ω noncompact. The same approach has been applied to three-dimensional (3D) steady flow, by which we found that u' decays as r^{-1} in the vortical wake and $r^{-5/4}$ along the primary shock waves (Liu 2016). However, for more general case where the object is allowed to move and deform arbitrarily, the expressions of the source terms can hardly be obtained.

This difficulty is likely associated with the very fact that in the formula for total force **F** there must be a volume integral of $(\rho u)_t$ due to local flow unsteadiness (see **Eq. 7.2.6** below), making it impossible to express **F** by boundary integrals only, which however is the prerequisite of expressing **F** by linearized far-field variables. But incompressible flow is a pleasant exception, where for calculating the force (not the moment) one has transformation (Saffman 1992, Noca et al 1999, Wu et al 2005)

$$\int_V \mathbf{u}_t dV = \int_{\partial V} \boldsymbol{x}(\mathbf{u}_t.\mathbf{n})dS \quad \text{if } \nabla.\mathbf{u} = 0$$

Eq. 7.2.4

Nevertheless, this limitation for flow incompressibility occurs only in the study of aerodynamic force. It does not affect the compactness of sources in estimating the far-field decay rate of unsteady compressible and viscous flow. For the latter purpose, the fundamental solution of linearized equations can still lead to the desired correct results.

7.2.2.2 The linearized NS Equations

Consider a body B moving and deforming arbitrarily in a canonically perfect gas externally unbounded and at rest at infinity. The continuity equation, NS equation per unit volume, and energy equation read (Liu et al 2014):

$$\frac{D\rho}{Dt} = \rho_t + \mathbf{u}\,.\nabla\rho = -\rho\vartheta$$

Eq. 7.2.5

$$\rho\,\frac{D\mathbf{u}}{Dt} = (\rho\mathbf{u})_t + \boldsymbol{\nabla}.(\rho\mathbf{u}\mathbf{u}) = -\boldsymbol{\nabla}\boldsymbol{\Pi} - \boldsymbol{\nabla}\times(\mu\boldsymbol{\omega})$$

Eq. 7.2.6

$$\rho T\frac{Ds}{Dt} = \rho T s_t + \rho T u\,.\boldsymbol{\nabla} s = \Phi + \boldsymbol{\nabla}.(k\nabla T)$$

Eq. 7.2.7

and the equation of state is

$$p = \rho R T$$

Eq. 7.2.8

Here ρ; p; T; s are the density, pressure, temperature and entropy, respectively, $\prod = p - \mu_\theta\vartheta$ is the viscous modified normal stress, $\boldsymbol{\vartheta} = \bar{\nabla}.\mathbf{u}$ the dilatation, μ; μ_θ ; k the dynamic transport coefficients of shear, compressing and heat conduction, respectively, _ the viscous dissipation, R the gas constant, subscript t denotes the time derivative, and D/Dt is the material derivative. Because NS equations **Eq. 7.2.5**, **Eq. 7.2.6**, **Eq. 7.2.7** are nonlinear and have infinite degrees of freedom, it is still impossible to obtain its analytical solutions in the general case. However, since in unbounded external-flow there must be a uniform region, we can properly assert that there must be a linear region adjacent to the uniform fluid. In this region, **Eq. 7.2.5**, **Eq. 7.2.6**, **Eq. 7.2.7** can be linearized, making it hopeful to get some significant results. Let $\epsilon \ll 1$ be a small dimensionless parameter, and denote

$$\begin{array}{rcl} s = c_p(\epsilon s' + \cdots) & , & \rho = \rho_0\,(1 + \epsilon\rho' + \cdots) \\ p = p_0(1 + \epsilon p' + \cdots) & , & T = T_0\,(1 + \epsilon T' + \cdots) \\ \mathbf{u} = \epsilon\mathbf{u}' + \cdots & , & \mu = \mu_0\,(1 + \epsilon\mu' + \cdots) \\ \mu_\theta = \mu_{\theta 0}(1 + \epsilon\mu_0' + \cdots) & , & k = k_0\,(1 + \epsilon k' + \cdots) \end{array}$$

Eq. 7.2.9

where c_p is the specific heat at constant pressure, subscript 0 refers to the uniform constant value at infinity, and prime ʻ denotes disturbance quantity, which is $O(1)$. Substitute **Eq. 7.2.9** into **Eq. 7.2.5**, **Eq. 7.2.6**, **Eq. 7.2.7** and **Eq. 7.2.8**, there is

$$\rho_t' + \nabla.u' = m$$

Eq. 7.2.10

$$\mathbf{u}_t' + \frac{a^2}{\gamma}\nabla p' - \nu_\theta\nabla(\nabla\times\mathbf{u}') + \nu\nabla\times(\nabla\times\mathbf{u}') = \mathbf{f}$$

Eq. 7.2.11

$$s_t' + \alpha\nabla^2 T' = Q$$

And

$$p' = \rho' + T' = \gamma(\rho' + s')$$

Eq. 7.2.12

In the above equations

$$a^2 = \gamma \frac{p_0}{\rho_0} \quad , \quad \alpha^2 = \frac{k}{\rho_0 c_p} \quad , \quad \nu_\theta = \frac{\mu_{\theta 0}}{\rho_0} \quad , \quad \nu = \frac{\mu_0}{\rho_0}$$

Eq. 7.2.13

are the speed of sound and kinematic transport coefficients of shear, compressing and heat conduction, respectively, where is the specific heat ratio. To make **Eq. 7.2.10**, **Eq. 7.2.11**, **Eq. 7.2.12** more universal, three source terms are added, namely, m; **f** ; Q, which denote sources of mass, momentum, and heat, respectively. They can be regarded as either the remanent nonlinear terms after the linearization of the original NS equations, or the equivalent source terms which represent the contributions of the nonlinear region (including the body) to the linear region. For the former, **Eq. 7.2.10**, **Eq. 7.2.11**, **Eq. 7.2.12** are strictly valid in the entire flow region; while for the latter, they are valid only in the linear flow region. In this paper, we call equations **Eq. 7.2.10**, **Eq. 7.2.11**, **Eq. 7.2.12** and **Eq. 7.2.13** the linearized NS equations.

7.2.2.3 Fundamental Solutions and Decay Rate of The Decoupled Fields

Before exploring the fundamental solution of the linearized NS equations, we first consider a much simpler case where the flow field can be completely decoupled into a longitudinal field and a transversal field. Assume all sources are absent (m = Q = 0; **f** = 0) and introduce the Helmholtz decomposition (**Eq. 7.2.1**) but with **u** replaced by **u**'. Then **Eq. 7.2.10**, **Eq. 7.2.11**, **Eq. 7.2.12** can be completely split into a transverse field (Lagerstrom et al 1949)

$$(\partial_t - \nu\nabla^2)u_\psi = 0$$

Eq. 7.2.14

and a longitudinal field

$$\rho'_t + \nabla^2\phi = 0$$

Eq. 7.2.15

$$(\partial_t - \nu_\theta\nabla^2)\phi = -\frac{a^2 p'}{\gamma}$$

Eq. 7.2.16

$$s'_t - \alpha\nabla^2 T' = 0$$

Eq. 7.2.17

Eliminate the thermodynamic variables in **Eq. 7.2.15**, **Eq. 7.2.16**, **Eq. 7.2.17** , we obtain

$$a^2(\partial_t - \alpha\nabla^2)\nabla^2\phi = \quad (\partial_t - \nu_\theta\nabla^2)\,(\partial_t - \gamma\alpha\nabla^2)\,\partial_t\phi$$

Eq. 7.2.18

If we further assume (Mao et al 2010)

$$\alpha\,,\nu_\theta = O(\delta) \quad , \quad \epsilon \ll 1$$

Eq. 7.2.19

After manipulation outlined in [Liu et al.][186], we obtain

---

[186] L. Q. Liu, L. L. Kang and J. Z. Wu, “*Zonal structure of unbounded external-flow and Aerodynamics*”, Fluid Dynamics Research · November 2016, DOI: 10.1088/1873-7005/aa79d0

$$(\partial_t^2 - \alpha^2\nabla^2)\phi = b\nabla^2\,\partial_t\phi \quad \text{where} \quad b \equiv (\gamma - 1)\alpha + \nu_\theta$$

Eq. 7.2.20

is the sound diffusion coefficient (Lighthill 1956). Evidently, both the decoupled equations (**Eq. 7.2.14**) and (**Eq. 7.2.20**) are of parabolic type, making the exponential decay rate possible. Specifically, (**Eq. 7.2.14**) is a standard second-order parabolic partial differential equation (PDE), which describes the processes that behave like heat diffusion through a solid and is valid for any transversal variables. In contrast, (**Eq. 7.2.20**) is a third-order PDE of parabolic type, which is also valid for ϕ , ϑ and s'.

The same equation of (**Eq. 7.2.20**) was obtained by Lagerstrom et al (1949) without considering the heat transfer so that $b = \nu_\theta$. Later, Wu (1956) also obtained the same equation with heat transfer included but under assumption $Pr_\theta = \nu_\theta/\alpha = 1$, which is very close to the value of ordinary gases. With these facts we conclude that, if Q is negligible small, which is the usual case as we are considering, then (**Eq. 7.2.17**) of the generalized Stokes equations can be omitted and its effect can be represented by replacing ν_θ by b in (**Eq. 7.2.16**) (see also Mao et al 2010). Thus, the fundamental solution of the linearized NS equations without heat transfer given by Lagerstrom et al (1949) can be directly applied to explore the far-field asymptotic of unsteady compressible and viscous external-flow. For additional discussion, please refer to [Liu et al.][187].

7.2.3 Zonal Structure of Unbounded Flow Domains

The decay rates of disturbances in far field estimated in the preceding section should have been optimal, as they are established both kinematically and kinetically. We have seen that the furthest far-field flow adjacent to the uniform fluid at infinity is unsteady, viscous and compressible, where all disturbances degenerate to viscous sound waves and damp out exponentially. This is consistent with the fact that only sound waves can propagate themselves without external forces and thus travel furthest (Lighthill 1978). They are annihilated there not by nonlinear dissipation but by dispersion (Lighthill1956). At the same time, we have also encountered some concepts of `infinity' and decay rate in various externally unbounded flow models, which are not exponential.

This situation suggests a zonal structure of flow domains used by different theoretical models in near and far field, such as incompressible ow, steady ow, and inviscid flow effect., of which a thorough clarification as we attempt below may strengthen and deepen our physical understandings on the overall picture of this type of flow. This zonal structure has somewhat analogy with the various wall regions and layers in turbulent boundary layer, where the mean velocities satisfy different approximate rules, say, linear law in viscous sublayer and log-law in log-law region, which are crucial for the high-accurate modeling of turbulent flow. Although how to apply the zonal structure into modern computational fluid dynamics (CFD) is not clear yet, its importance can never be ignored. In addition, with the help of the zonal structure, we can easily discriminate the advantages and disadvantages of various aerodynamic theories and clarify some paradoxes concerning far-field behavior.

In this section, the zonal structure is illustrated first. As before, the externally unbounded flow is assumed to be caused by a finite body moving through it, and the flow plus body fulfills the entire free space V_∞ with fluid rest or in uniform status at infinity. We add that the body and fluid are initially at rest at $t \le 0$, and let the airfoil start moving at $t = 0$, reaching its final state $u_B = Ue_x$ at $t = t_s$. Then a preliminary zonal structure is shown in **Figure 7.2.1**, which for the sake of illustration only describes the disturbance development caused by the low-speed or subsonic flight of an airfoil. This figure is yet incomplete; some further classification will be introduced below. But since the far-field

---

[187] L. Q. Liu, L. L. Kang and J. Z. Wu, "*Zonal structure of unbounded external-flow and Aerodynamics*", Fluid Dynamics Research · November 2016, DOI: 10.1088/1873-7005/aa79d0

decay law of viscous, unsteady and compressible flow has been fully clarified, no more discussion on it is needed.

Adjacent to the uniform fluid at infinity, there must be a zone where the disturbance intensity E decays sufficiently small, say $E = O(\varepsilon)$ with $\varepsilon \ll 1$, so that the governing equations can be linearized. We call this zone the linear zone or linear far-field, and denote it by V_L. This linear zone encloses a nonlinear zone V_{NL}. While the disturbance intensity in the latter is $E = O(\varepsilon^0)$, in the former it is $E = O(\varepsilon^m)$, $m > 1$. Thus, V_L should locate between the nonlinear zone VNL and uniform zone (i.e. the zone between the solid loop and dashed loop in **Figure 7.2.1**). Although the existence of this linear far-field is assumed based on physical intuition and a mathematical rigorous proof is still lacking, one can check the existence from the behavior of obtained analytical solutions of linearized equations. On the other hand, although the details of how the flow transforms from V_{NL} to V_L is of great interest, it is beyond the scope of this paper.

7.2.3.1 Nonlinear Near Field, Steady or Unsteady

We start from the most inner zone enclosed by the solid loop in **Figure 7.2.1**. Since the viscous fluid has to satisfy the no-slip and no-penetration conditions on a solid wall, thus in the region very close to the wall, such as the viscous sublayer of boundary layer and initial segments of free shear layer, either laminar or turbulent, the flow must be rotational with strong effect of viscosity. Once leaving the body surface, the flow quickly evolve nonlinearly as the characteristic feature of near-field flow. The flow can be either incompressible or compressible, and either intrinsically unsteady, or steady viewed in the reference frame fixed to the body.

Denote by c the length scale of the body, say the chord length of the airfoil, then the nonlinear zone surround the body occupies a volume $V_{NL} = O(c^n)$. Obviously, in V_{NL} the flow exhibits its full complexity, in particular at large Reynolds numbers and Mach numbers. The governing equation in

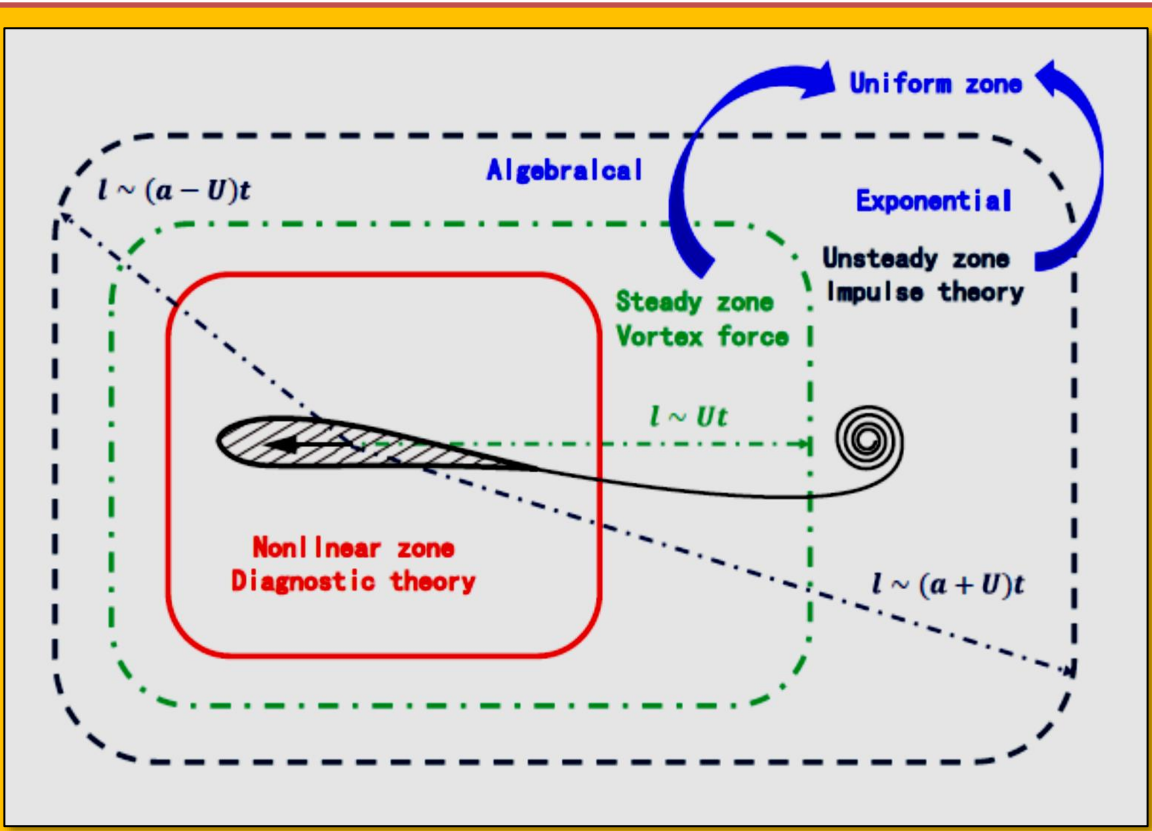

Figure 7.2.1 Sketch of Zonal Structure of Unbounded External-Flow

V_{NL} is the fully nonlinear NS equations of infinity degrees of freedom, and it is almost impossible to find its analytical or asymptotic solution in general case. This is the major place where CFD and advanced experimental techniques show their full power in revealing the detailed complex flow structures and processes. In the computation, the flow conditions at the external boundary of computational domain have to be prescribed, which depends on what far-field zone it will be right outside the domain.

7.2.3.2 Steady Far Field

Return to the airfoil motion in **Figure 7.2.1**. The transient dynamic process and causal mechanisms from the airfoil starts motion to the establishment of its lift, along with a starting vortex shedding downstream to ensure total-circulation conservation, has been addressed in detail by [Zhu et al (2015)] and references therein, so our concern here is only the zonal structures of the flow field after the airfoil has reached or almost reached its final state.

As time goes on, the starting vortex continually moves away to sufficiently large distance behind the airfoil, such that its effect on the flow field near the airfoil is negligible. Actually, such a distance needs not to be very large; for the starting problem of 2D thin airfoil, [von Karman and Sears (1938)] have theoretically proven that a few chord lengths will be enough. Therefore, if we shift the reference frame from the one fixed to the still fluid at infinity to that fixed to the airfoil, when this distance satisfies the condition $l \sim U_t \gg c$ (see **Figure 7.2.1**), there can be a zone which excludes the starting vortex and in which the flow is steady or statistical steady, with uniform incoming flow velocity $U = Ue_x$. We call such a zone the steady zone and denote it by V_{st} (i.e. the zone enclosed by the dashed-dotted loop in **Figure 7.2.1**). In subsonic flow, when $t \geq t_s$, although the total amount of vorticity shedding off the airfoil is zero [Liu et al 2015, Liu 2016], there is always vorticity with the same magnitude but different signs shedding off the upper and lower airfoil surfaces, respectively. This region where the vorticity itself is nonzero but its total flux is zero is called the steady wake, which connects the starting vortex and airfoil's boundary layers.

The above overall picture will have some modification for transonic or supersonic incoming flow, where the specific near-field flow structures can be very complicated due to the appearance of shock waves not shown in **Figure 7.2.1**, which can make the total vorticity flux no longer be zero [Liu et al 2015)]. However, this complexity does not change the corresponding zonal structures, provided that the fluid is viscous. Owing to the fact that part of vortical wake must be inevitably excluded from V_{st} in both incompressible and compressible flows, the transverse Oseen equation indicates that as $r \to \infty$ in V_{st} the velocity can only decay algebraically (Liu et al 2015, Liu 2016). Evidently, V_{st} must be a true subspace of V_1.

7.2.3.3 Unsteady Far Field, Incompressible

If one needs to investigate the above airfoil flow in an exceedingly large region that encloses the starting vortex, the whole disturbance zone V_1 enclosed by the dashed loop in **Figure 7.2.1** has to be taken into consideration, and then the flow must be intrinsically unsteady. [Wu (1981, 2005)] was one of the first to emphasize this relationship between steady and unsteady flows by thorough physical discussion. But this issue has not yet become trivial. More awareness of and attention to it are needed in aerodynamics community.

Unsteady incompressible far field, however, is not yet able to enjoy exponential decay. This has been explicitly shown, because the longitudinal **Eq. 7.2.20** degenerates to a Laplace equation for ϕ. In fact, incompressibility assumption is incompatible with the furthest zone at far field. Specifically, as stressed by [Landau & Lifshitz (1987)], for steady flow to be regarded as incompressible, the familiar condition $lul \ll a$ is sufficient; but for unsteady flow, a further condition has to be added: if t and l are the temporal and special scales over which the flow undergoes significant changes, then there should be $t \gg l/a$. Now the first condition can always be satisfied as along as u_B keeps small enough. But the second one cannot as the truly far-field asymptotic $r \to \infty$ is reached where $l \sim V_\infty^{1/n}$, although it can at near and middle fields. Therefore, the incompressible flow zone, say V_{inc}, is also a true subspace of V_1.

Here we recall a classic paradox that the total momentum of unbounded Incompressible fluid has only conditional convergence, and the total angular momentum diverges. Evidently, the paradox will disappear at once as one realizes the incompressibility domain cannot reach the true infinity, but is surrounded by a viscous, compressible, unsteady and linear zone with exponential decay. Furthermore, ignoring this fact has also caused the well-known paradox of the same root as the poor behavior of total momentum and angular momentum for incompressible flow: there must be $\mathbf{I}/n$ ($\mathbf{I}$ is the impulse, see **Eq. 7.2.22** below) portion of total momentum escaping out of a spherical domain of arbitrarily large radius, although the flow there is irrotational. The paradox was removed by [Landau & Lifshitz (1987)], who pointed out that the far-field flow is compressible and the escaped momentum is carried away by sound wave, see also [Saffman (1992)].

Actually, unsteady near-field incompressible flow surrounded by compressible far field has been a well-known and effective model in the field of aeroacoustics ever since [Lighthill (1952)] constructed the acoustic analogy theory. In that theory the source of sound (say an unsteady vorticity field) can be treated incompressible in a compact region, which emits sound as very weak disturbance waves to far field but is not affected by the waves.

7.2.3.4 Role of Viscosity

As said before, very near the body surface the fluid viscosity plays a key role for the satisfaction of the adherence condition and the motion inside the boundary layer. At large Reynolds number Re, the explicit viscous effect outside the strong shear layers can often be neglected. As a common concept, the viscosity can then be neglected all the way till the far field. But once again this concept is incorrect. Without viscosity the far-field sound waves cannot be annihilated to ensure the smooth exponential transition to the uniform fluid at infinity. More specifically, [Liu et al (2015)] have shown that, although in subsonic regime the leading-order far-field behavior of the flow is still of inviscid nature, in transonic and supersonic flow regimes no linear far field can exist without viscosity. Their numerical simulation has confirmed the analytically obtained asymptotic behavior and location of the viscous linear far field in high-speed flow regime.

7.2.4 Relevance To External-Flow Aerodynamics

The zonal structure of externally unbounded flow bears close relevance to aerodynamics, of which the central concern is the force and moment acted to the moving body by the fluid. In this section we examine how the zonal structure influences aerodynamic problems formulated by various flow models. Once again the viscous and compressible unsteady flow does not need to be discussed; it is just a perfect model with which other flow models are to be compared.

Aerodynamic theory has been developed along two approaches, far-field and near-field, in a combined manner. The former uses linearized far-field equations and can obtain concise, accurate and universal force formulas, but leaving the determination of the value of the key variable thereof to the latter for specific problems. For example, the famous ***Kutta-Joukowski*** (KJ) theorem $L = \rho U\Gamma$, the first cornerstone of modern aerodynamics, was first derived by Joukowski (1906) using steady far-field approach (for its version in modern language see Batchelor 1967, pp. 406-407). But the value of circulation Γ has to be fixed by near-field theory under prescribed specific body geometry and flow condition, including the ***Kutta condition*** for inviscid flow model. Conversely, a nonlinear near-field theory can check the far-field results by taking its leading-order approximation as $r \to \infty$. Below we organize our discussion based on this classification of far- and near-field approaches and their combination.

7.2.4.1 Near-Field Low-Speed Aerodynamics

Among classic low-speed aerodynamic theories developed before computer era, we consider the vortex-force theory for steady flow and impulse theory for unsteady flow as two most brilliant pearls due to their neatness in form, physical insight implied thereby, and generality in their respective zones. Here we use these theories to demonstrate the importance of identifying the proper ow zones to which different aerodynamics theories can apply.

We remark that both these theories belong to near-field type effective in nonlinear zone V_{NL}, since they involve inherently nonlinear domain integrals. Fortunately, due to the rapid development of CFD it has become a routine task to solve the NS equation numerically. Thus, the main task of corresponding modern aerodynamics theory should be switched from finding analytical solutions to identifying the key quantitative contribution of specific flow structures and dynamic processes to the aerodynamic performance. We call such a theory the diagnosis theory of complex flows. Namely, except a few special cases where the flow is fully attached and force formulas can be simplified by small perturbation techniques, the power of these theories could only be fully appreciated when they are used to diagnose detailed flow-field data already obtained experimentally or numerically.

In the steady zone V_{st} as shown in **Figure 7.2.1**, the most significant low-speed flow structure is the boundary layer and vortical wake. Accordingly, the most beautiful aerodynamic theory is the vortex-force theory (Prandtl 1918, Saffman 1992), which was originally formulated for inviscid ow or at the limit Re → ∞. In this theory, the force and moment are expressed by the integrals of the Lamb vector $\boldsymbol{\omega} \times \mathbf{u}$ and its moment $\mathbf{x} \times (\boldsymbol{\omega} \times \mathbf{u})$, respectively. For example, with _0 being constant reference density, the force reads

$$\mathbf{F} = -\rho_0 \int_{V_{st}} \boldsymbol{\omega} \times \mathbf{u}\, dV$$

Eq. 7.2.21

which not only has excellent convergence property and clear asymptotic form as r → ∞, but also can reveal the specific contributions of the ow structures to the force. In particular, in 2D **Eq. 7.2.21** degenerates to the KJ formula $L = \rho U \Gamma$ (Prandtl 1918, von Karman & Burgers 1935), while in 3D it contains reduced drag with its linearized approximation leading to Prandtl's lifting-line theory. Now the vortex-force theory has been generalized to viscous and unsteady flow, by adding a wake-plane integral to account for the form drag and a domain integral of $\mathbf{x} \times \boldsymbol{\omega}_t$ to account for the flow unsteadiness (Wu et al 2007, Wu et al 2015).

On the other hand, in the unsteady zone V_∞ as shown in **Figure 7.2.1**, the most significant flow structure in low-speed aerodynamics is also the boundary layer and vortical wake, but now the unsteady motion of the starting vortex is included. In this case the most beautiful aerodynamic theory is the impulse theory or vorticity-moment theory (Burgers 1920, Wu 1981, Lighthill 1986), in which the force and moment are expressed by the time rate of the integrals of $\mathbf{x} \times \boldsymbol{\omega}/(n-1)$ and $r^2\boldsymbol{\omega}/2$ for n = 2; 3, respectively. For example, For fluid occupying V_f , which extends to infinity and bounded internally by body surface ∂B, the total force reads (Wu 1981)

$$\mathbf{F} = -\rho_0 \frac{d\mathbf{I}}{dt} + \rho_0 \frac{d}{dt}\int_B \mathbf{u}_B\, dV \quad , \quad I = \frac{1}{n-1}\int_{V_\infty} \mathbf{x} \times \boldsymbol{\omega}\, dV$$

Eq. 7.2.22

The nonlinearity and kinetic content of the theory will show up once the time-rate operator d/dt is shifted into the integral (Saffman 1992, Wu et al 2015). Since vorticity is physically compact, the impulse theory is very suitable for the forces acted on bodies that have arbitrary motion and deformation of the body at any Reynolds numbers. In particular, it has now been the primary choice in the force analysis of animal locomotion; for a recent example see Meng & Sun (2015).

To fit the need for using the theory in practical experiments and computations, one may shrink the domain boundary in impulse theory to a finite one to explore its full generality. The result is exactly the recovery of the force formula of the generalized vortex-force theory. However, the concept of impulse was introduced as an artifact that is `applied to a limited portion of the fluid in order to generate the whole of the given motion from rest' (Batchelor 1967, p. 518). The impulse I does not really equal the total momentum; their difference is an integral, say S, over the outer boundary of flow domain. The very neat **Eq. 7.2.22** holds only if the vortex system under study is compact and at its outer boundary the flow is irrotational. It can be proven that once the domain boundary cuts the vortical wake as is inevitable for steady flow, the term d**S**/dt will immediately become very complicated and **Eq. 7.2.22**.no longer holds. In this case, the artificial splitting of the total momentum into **I** and **S** is physically meaningless.

Actually, the best one can do with the finite-domain impulse theory is requiring the vortex system under study is compact so at the boundary the flow remains irrotational, which is fortunately the case for those animal motions that generate a series of nearly compact vortex rings in the wake.

7.2.4.2 Near-Field High-Speed Aerodynamics

The above remark on near-field low-speed aerodynamic theories on their nonlinearity also applies to near-field high-speed aerodynamics. But the latter is much more complicated than the former, due to longitudinal process caused by compressibility and entropy change associated with shocks. Thus, classic high-speed aerodynamics can only rely on further theoretical models which are oversimplified in two aspects, implying that it has less generality compared to its low-speed counterpart. First, the inviscid-flow assumption is made except in attached boundary layers. Second, the full NS equations are mostly replaced by small disturbance potential-flow equations. In modern aerodynamics, as one's major concern has become complex flows with steady or unsteady flow separation and separated flows with free shear layers, shocks and vortices, the framework of classic high-speed aerodynamics with these oversimplifications has inevitably made it far behind the need of modern numerical and physical experiments. On the first oversimplification, it has been addressed in 7.2.3.4 that the neglect of viscosity makes it impossible to construct linear far-field theory, especially for transonic and supersonic flows. As a remedy of this lacking, Cole & Cook (1986) have to introduce nonlinearity to inviscid transonic `far field'. But the corresponding result is evidently neither smooth nor truly far field. In fact, while modern CFD scheme for high-speed aerodynamics can resolve the flow structure in shear layers at the scale of $O(Re^{-1/2})$, it is not yet able to resolve viscous shock layers at the scale of $O(Re^{-1})$ (laminar flow for example). Thus, at large Reynolds numbers, away from thin boundary layers and vortical wake, the global external flow can indeed be assumed inviscid plus shock discontinuity. However, the viscosity has to be recovered in the far field to ensure the exponential decay of all disturbance quantities, and to construct physically correct far-field theory. The recovery of viscosity in far field but retaining inviscid assumption in `middle field' is quite similar to the recovery of compressibility in far field but retaining incompressible assumption elsewhere in low-speed aerodynamics. A recently developed far-field theory for viscous and compressible steady flow will be highlighted in the next subsection.

To remove the second oversimplification of classic high-speed aerodynamics as well as to include viscous effects, one finds that besides the Lamb vector there is a new longitudinal term, namely the gradient of the density (Chang et al 1998, Wu et al 2006, Xu et al 2010), which can be further split into two parts, namely the Mach-number weighted Lamb vector and the gradient of the Mach-number weighted temperature, of which the latter represents the contribution of the longitudinal process to the force and moment (Liu et al 2014, Liu 2016). The resulted longitudinal-transverse force theory matches CFD perfectly as they are based on the same full NS equations.

Following the same tactics of Wu (1981), Huang (1994) has attempted to generalize the impulse theory to compressible flow, by replacing the vorticity by the `dynamic vorticity' $\boldsymbol{\omega}^* \equiv \nabla \times (\rho \mathbf{u})$. Not mentioned by Huang is that, the linearized governing equation of $\boldsymbol{\omega}^*$ is the same as that of $\boldsymbol{\omega}$ multiplied by a constant ρ_0 when the frame is fixed on the infinity still fluid. Thus, we can dynamically prove that $\boldsymbol{\omega}^*$ has the same compactness as that of $\boldsymbol{\omega}$, making the compressible impulse theory be rigorous. Unfortunately, there is still no direct application of this theory to practical diagnosis of complex compressible flows.

7.2.4.3 Steady Far-Field Aerodynamics

A necessary condition for the construction of complete far-field aerodynamic force theories is that the total force and moment can be solely expressed by control-surface integrals. As remarked in **7.2.2.1**, this cannot be fulfilled for unsteady flow in general case due to the volume integral of $(\rho u)_t$. Thus, the far-field force theory is still uncompleted. However, the total forces of steady flow and incompressible flow are two pleasant exceptions, where for the former the unsteady term disappears automatically while for the latter (and force only) it can be transformed to a related boundary-integral (Noca et al 1999, Wu et al 2005).

For the flow in V_L, the governing equation can be reduced to its linearized form. In specific, when the frame of reference is fixed to still fluid at infinity, the linearized equation is the linearized NS equations **Eq. 7.2.15**, **Eq. 7.2.16**, **Eq. 7.2.17** and **Eq. 7.2.18**; while when the frame of reference is fixed on the body, it is the steady/unsteady Oseen equation. Though these two equations are fully equivalent in physics, they have their individual advantages and disadvantages in specific problems. For example, in steady zone V_{st}, the Oseen equation is more convenient (Liu et al 2015); while in the unsteady zone, especially when the speed of the object is time-dependent, $U = U(t)$, the linearized NS equations are more convenient.

Using the far-field method, Liu et al. (2015) obtained a universal theory for the aerodynamic lift and drag on a body in 2D, steady, viscous and compressible external flow, effective from incompressible all the way to supersonic regimes. Two sets of total-force formulas have been derived. In the first set, the lift L and drag D are given exactly and universally by the contour integrals of velocity scalar potential ϕ and vortical stream-function ψ, respectively:

$$\mathbf{F} = \rho\left(\mathbf{U} \times \boldsymbol{\Gamma}_{\phi} + \mathbf{U} Q_{\psi}\right)$$

Eq. 7.2.23

$$\boldsymbol{\Gamma} = \int_S \mathbf{n} \times \boldsymbol{\nabla}\phi dS \quad , \quad Q_V \equiv -\int_S (\mathbf{n} \times \boldsymbol{\nabla}).\psi \, dS$$

Eq. 7.2.24

where S is an arbitrary contour enclosing the body, which may even lie in V_{NL}, the highly nonlinear zone around the body. This result has the same form as but significantly generalizes the classic KJ inviscid lift formula (Joukowski 1906) and Filon's (1926) viscous drag formula for incompressible flow to any viscous and compressible flow.

However, the universality of this set of formulas is at the expense that ϕ and ψ are not directly testable by experiment or computation. Thus, the second set of formulas was derived in terms of the physically testable quantities only, which is the asymptotic approximation of the first set and holds only in V_L. The most remarkable feather of this set is that L and D are solely expressed in terms of far-field vorticity integral even if the flow is supersonic. On the (x, z)-plane with $\boldsymbol{\omega} = (0 , \omega , 0)$ and $\boldsymbol{\psi} = (0 , \psi , 0)$, the result reads

$$L = \lim_{r\to\infty} \int_{V_{st}} \omega dV = \llbracket \phi \rrbracket \quad , \quad D = \lim_{r\to\infty} \int_{W} z\omega dz = \llbracket \psi \rrbracket$$

Eq. 7.2.25

where W is a far-field wake plane and [[.]] denotes the jump of potentials due to the double-connectivity of 2D flow domain. Therefore, no matter how many interacting processes could appear in a nonlinear complex near-field flow, only the vorticity field has the furthest downstream extension as the sole signature of the complex flow in far field, of which the distribution can faithfully capture the total aerodynamic force. In addition, Liu et al (2015) have also proven that the far-field velocity of viscous and compressible flow (including subsonic, transonic and supersonic flows) decays algebraically as $r \to \infty$ in V_{st} (**Figure 7.2.1**), and have given a direct evidence of the existence of linear zone, by comparing the theoretical estimates of the location of the linear zone with the results obtained by numerical simulation. Following the same strategy of Liu et al (2015), the above result has been extended to 3D by Liu (2016).

7.2.4.4 Unsteady Far-Field Theory

For an externally unbounded incompressible ow over an arbitrarily moving and deforming body B with prescribed velocity distribution $u_B(x; t)$ at its surface ∂B, Wu et al (2005) have obtained an exact total-force formula solely in terms of boundary integrals over ∂B and a control surface $\sum$. It can be written as

$$\mathbf{F} = -\rho\left[\frac{d}{dt}\int_{\partial B}\mathbf{x}(\mathbf{u_B}.\mathbf{n})\,dS + \int_{\Sigma}\mathbf{x}(\mathbf{u}.\mathbf{n})dS\right] - \frac{\rho}{n-1}\frac{d}{dt}\int_{\Sigma}\mathbf{x}\times(\mathbf{n}\times\mathbf{a})\,dS + \int_{\Sigma}(\rho\boldsymbol{\sigma}+\boldsymbol{\tau})dS$$

Eq. 7.2.26

where **a** = d**u**/dt is the material acceleration, **σ** = ∂**ω**/∂n is the vorticity diffusion flux, and **τ** = μ**ω** x **n** is the shear stress. At far field this formula can be linearized, but similar convergence difficulty as **r** → ∞ remains as the total momentum for incompressible flow. Once again, the way out should be the recovery of compressibility at far field.

The 2D version of **Eq. 7.2.26** was derived independently by Iima (2008) via complex-variable approach. Interestingly, Iima raised a paradox of hovering insects in space: insects maintaining their bodies in a particular position cannot, on average, generate hydrodynamic force if the induced ow is temporally periodic and converges to rest at infinity. Evidently, the same paradox could also true for 3D flow. As a demonstration of how to apply our preceding results, let us resolve this paradox. For convenience we further assume that the insect's body volume can be omitted. Then the momentum source reduces to (**Eq. 7.2.4**) but with a time-dependent **F**(t):

$$\mathbf{f}(\mathbf{x},t) = \frac{\delta(\mathbf{x})}{\rho_0}\mathbf{F}(t)$$

Eq. 7.2.27

Then, by substituting **Eq. 7.2.27** into [(39) – see [Liu et al.][188]] there is

$$\phi = \frac{1}{\rho_0}\nabla G_\phi \, . \int_0^t \mathbf{F}(\tau)d\tau$$

Eq. 7.2.28

It is now clear that although the total force **F** can be assumed to be periodic, the corresponding far-field flow cannot. Rather, there must be a constant term in **F** which balances the weight of the body, e.g., **F**(t) = -m**g** + **F**(t), where m is the mass of the insect, **g** is the gravitational acceleration, and **F**(t) is a periodic function whose time-average is zero. Then, from **Eq. 7.2.28** there must be a term which is proportional to time, making the far-field flow be non-periodic. In particular, if we omit the term **F** (t), which may be small compared to mg, then **Eq. 7.2.28** reduces to

$$\phi = \frac{t}{\rho_0}m\mathbf{g}.\nabla G_\phi$$

Eq. 7.2.29

---

[188] L. Q. Liu, L. L. Kang and J. Z. Wu, "*Zonal structure of unbounded external-flow and Aerodynamics*", Fluid Dynamics Research · November 2016, DOI: 10.1088/1873-7005/aa79d0

It should be pointed out that the above argument is based on two conditions. First, since we have omitted the volume of the body or the term $d/dt\int_B \mathbf{u}dV$, to ensure mg to be dominant the density of the insect body must be much larger than that of the fluid. In other words, Iima's periodic assumption can be valid for fish swimming. Second, since there will be some terms proportional to t^2 in the nonlinear term $\mathbf{u}.\bar{\nabla}\mathbf{u}$, which for large enough time $t \gg 1$ must prevail other terms in the full NS equations (the viscous term is put aside), to ensure the linear assumption there must be

$$t \ll \mathbf{r}^{n+1}$$

Eq. 7.2.30

namely, the nonlinear term is much smaller than other terms.

7.2.5 Conclusions

This paper studies the asymptotic behavior of velocity field as r → ∞, a fundamental issue in all unbounded external-flow problems. Our analysis is based on the assumption that for viscous flow over a finite body, between the innermost nonlinear near field VNL and uniform fluid at infinity there must be a linear field V_L where the Navier-Stokes equations can be linearized, leading to a pair of coupled linear, longitudinal and transverse equations. While this assumption is not yet generally proven in mathematic consistency, the existence of linear far field can be checked by physical behavior of the analytical solutions obtained thereby. Using this linear far-field analysis both kinematically and kinetically, we found that:

- The furthest far-field zone adjacent to the uniform fluid at infinity must be unsteady, viscous and compressible, where all disturbances degenerate to viscous sound waves that decay exponentially. The well-known algebraic decay of velocity field (e.g., Batchelor 1967) is only a kinematic result which, although holds universally, is too conservative and only serves as an upper bound.
- All flow models simplified from unsteady, viscous and compressible flow, as commonly used in various theoretical and computational studies, fail to satisfy the above exponential decay rule, since they are effective only in certain true subspaces of the free space V_1. Thus, instead of just assuming the flow to become uniform as r → ∞ in these models, there is a zonal structure at far field. Specifically, in formulating outer conditions in these models, it should be born in mind that:

    - The steady flow zone V_{st} must be surrounded by an unsteady far field;
    - The incompressible flow zone V_{inc} must be surrounded by a compressible far field;
    - The inviscid flow zone V_{inv} must be surrounded by a viscous far field.

- The far-field zonal structure is of close relevance to external-flow aerodynamics.

It is demonstrated why aerodynamic theories derived from the above simplified models encounter some difficulties or lead to paradoxes, and how to remove them in terms of the zonal structure.

7.2.5.1 Acknowledgments

This work was partially supported by NSFC (Grant No. 10921202, 11472016) of China. The authors are very grateful to Profs. Weidong Su and Yipeng Shi, Dr. Jinyang Zhu, Messrs. Shufan Zou and Ankang Gao for their valuable discussions. Special thanks are given to Prof. Zhensu She, who pointed out the analogy between zonal structure in unbounded external-flow and various wall regions in turbulent boundary layer.

7.2.6 References

Batchelor G K 1967 An Introduction to Fluid Dynamics (Cambridge Univ.)

Burgers J M 1920 On the resistance of fluids and vortex motion Proceedings of the Koninklijke Akademie Van Wetenschappen Te Amsterdam 23 774-782

Chang C C, Su J Y and Lei S Y 1998 On aerodynamic forces for viscous compressible flow Theoretical Com. Fluid Dyn.mics10 71-90

Cole J D and Cook L P 1986 Transonic Aerodynamics (North-Holland)

Filon L N G 1926 The forces on a cylinder in a stream of viscous fluid Proc. R. Soc. Lond. A 113 7{27

Huang G C 1994 Unsteady Vortical Aerodynamics: Theory and Applications (Shanghai Jiaotong Univ., in Chinese)

Iima M 2008 A paradox of hovering insects in two-dimensional space J. Fluid Mech. 617 207-229

Joukowski N E 1906 On annexed vortices Proc. of Physical Section of the Natural Science Society.

Lagerstrom P A 1964 Laminar Flow Theory (Princeton Univ.)

Lagerstrom P A, Cole J D and Trilling L 1949 Problems in the theory of viscous compressible fluids Tech. Rep. 6. GALCIT Rept.

Landau L D and Lifshitz E M 1959 Fluid Mechanics (Pergamon Press)

Lighthill M J 1952 On sound generated aerodynamically. I. General theory Proc. R. Soc. London.

Lighthill M J 1956 Viscosity Effects in Sound Waves of Finite Amplitude. (in Surveys in Mechanics, ed. Batchelor G K and Davies R M, Cambridge Univ.)

Lighthill M J 1978 Waves in Fluids (Cambridge Univ.)

Lighthill M J 1986 An Informal Introduction to Theoretical Fluid Mechanics (Clarendon Press)

Liu L Q 2016 Unified Theoretical Foundations of Lift and Drag in Viscous and Compressible External Flows Doctor thesis, Peking University (in Chinese)

Liu L Q, Shi Y P, Zhu J Y, Su W D, Zou S F and Wu J Z 2014 Longitudinal-transverse aerodynamic force in viscous compressible complex flow J. Fluid Mech. 756 226-251

Liu L Q, Wu J Z, Shi Y P and Zhu J Y 2014 A dynamic counterpart of Lamb vector in viscous compressible aerodynamics Fluid Dyn. Res. 46 061417

Liu L Q, Zhu J Y and Wu J Z 2015 Lift and drag in two-dimensional steady viscous and compressible flow J. Fluid Mech. 784 304-341

Mao F, Shi Y P and Wu J Z 2010 On a general theory for compressing process and aeroacoustics: linear analysis Acta Mech. Sin. 26 355-364

Meng X G and Sun M 2015 Aerodynamics and vortical structures in hovering fruities Phys. Fluids.

Noca F, Shiels D and Jeon D 1999 Lift and drag in two-dimensional steady viscous and compressible flow J. Fluids Structures 13 551-578

Prandtl L 1918 Nachrichten von der gesellschaft der wissenschaften zu gottingen, mathematischphysikalische klasse Tragflugeltheorie. I. Mitteilung 451-477

Saffman P G 1992 Vortex Dynamics (Cambridge Univ.)

von K_arm_an Th and Burgers J M 1935 General Aerodynamic Theory | Perfect Fluids. (In Aerodynamic Theory Vol. II, ed. Durand W F, Dover)

von Karman and Sears W R 1938 Airfoil theory for non-uniform motion J. Aero. Sci. 5 (10) 379{390

Webster 1987 Webster's Ninth New Collegiate Dictionary (Merriam-Webster Inc. Publishers)

Wu J C 1981 Theory for aerodynamic force and moment in viscous flows AIAA J. 19 432-441

Wu J C 1982 Problems of general viscous flow In Developments in Boundary Element Method (ed. P. K. Benerjee)

Wu J C 2005 Elements of Vorticity Aerodynamics (Tsinghua Univ. & Springer)

Wu J Z, Lu X Y and Zhuang L X 2007 Integral force acting on a body due to local flow structures J. Fluid Mech. 576 265-286

Wu J Z, Ma H Y and Zhou M D 2006 Vorticity and Vortex Dynamics (Springer)

Wu J Z, Ma H Y and Zhou M D 2015 Vortical Flows (Springer)

Wu J Z, Pan Z L and Lu X Y 2005 A comparison of methods for evaluating time-dependent fluid dynamic forces on bodies, using only velocity fields and their derivatives Phys. Fluids 17 098102

Wu T Y 1956 Small perturbations in the unsteady flow of a compressible, viscous and heat-conducting

Fluid J. Math. Phys. 35 13-27
Xu C Y, Chen L W and Lu X Y 2010 Large-eddy simulation of the compressible ow past a wavy cylinder J. Fluid Mech. 665 238-273
Zhu J Y, Liu T S, Liu L Q, Zou S F and Wu J Z 2015 Causal mechanisms in airfoil-circulation formation Physics of Fluids 27 (12) 123601

7.3 Case Study 3 - Active Flow Control for External Aerodynamics

Authors : *Oriol Lehmkuhl[1], Adrian Lozano-Duran[2], Ivette Rodriguez[3]*
Affiliations : *[1] Dpt. of Computer Applications in Science and Engineering, Barcelona Supercomputing Center, Spain*
[2] Center for Turbulence Research, Stanford University, USA
[3] Dpt. of Heat Engines, Universitat Politecnica de Catalunya, Spain
Title : *Active flow control for external aerodynamics: from micro air vehicles to a full aircraft in stall*
Original Appearance : *Journal of Physics: Conference Series 1522 (2020) 012017*
Source : *doi:10.1088/1742-6596/1522/1/012017*

7.3.1 Abstract

We investigate the aerodynamic performance of active flow control of airfoils and wings using synthetic jets with zero net-mass flow [Lehmkuhl et al.][189]. The study is conducted via wall-resolved and wall-modeled large-eddy simulation using two independent CFD solvers: *Alya*, a finite-element based solver; and *charLES*, a finite-volume-based solver. Our approach is first validated in a NACA4412, for which numerical and experimental results are already available in the literature. The performance of synthetic jets is evaluated for two ow configurations: a SD7003 airfoil at moderate Reynolds number with laminar separation bubble, which is representative of Micro Air Vehicles, and the high-lift configuration of the JAXA Standard Model at realistic Reynolds numbers for landing. In both cases, our predictions indicate that, at high angles of attack, the control successfully eliminates the laminar/turbulent recirculation located downstream the actuator, which increases the aerodynamic performance. Our efforts illustrate the technology readiness of large-eddy simulation in the design of control strategies for real-world external aerodynamic applications.

7.3.2 Introduction

The overall performance of an aircraft wing is significantly affected by boundary-layer flow separation, specially at the high angles of attack (AoA) typically encountered during take-off and landing operations. In these situations, there is a loss of momentum across the boundary layer, which eventually leads to flow detachment. Thus, keeping the ow attached to the wing surface by supplementing additional momentum might improve the aerodynamic performance of the wing. In the quest for controlling or modifying the boundary layers over wings, different flow control strategies have been studied in the past years, namely, vortex generators, plasma actuators, synthetic jets, etc. (see the reviews in Refs. [1, 2, 3]). Here, we focus on the investigation of ***active flow control (AFC)*** of airfoils and wings for external aerodynamics via synthetic jets, which have been successful in reducing the fuel burnt during the operations of take-off and landing [4].

Significant advances have been achieved in the past years in the context of AFC in airfoils (see, for instance, [5, 6, 7, 8]), but whether such improvements are applicable to a full aircraft configuration remains an open question. A large body of studies have been conducted recently to explore the capabilities of AFC in high-lift devices. Shmilovich and Yadlin [9] studied different AFC strategies of a high-lift profile in the conditions of take-off and landing using the Reynolds Averaged Navier-Stokes equations (RANS). Bauer et al. [10] conducted experiments on a two element wing with unsteady AFC near the leading edge and showed that stall can be delayed.

Lin et al. [11] addressed different strategies in the ap of a high-lift profile comprising steady suction and blowing, and periodic excitation of the boundary layer. Several of these AFC strategies are planned to be tested experimentally by NASA for increasing lift to drag ratios (L/D) in take-off configurations [12]. Recently, Andino et al. [13] tested fluidic actuators in a generic tail at low speeds

---

[189] Oriol Lehmkuhl, Adrian Lozano-Duran, Ivette Rodriguez, "*Active flow control for external aerodynamics: from micro air vehicles to a full aircraft in stall*", Fourth Madrid Summer School on Turbulence Journal of Physics: Conference Series **1522** (2020) 012017.

and demonstrated that a modest increase of the momentum coefficient can result in important increments of the side force.

In the present work, we explore AFC of boundary layers in moderate-Reynolds-number airfoils and the wing of a full aircraft in high-lift configuration. The simulations are carried on using wall-resolved (WR) and wall-modeled (WM) large-eddy simulations (LES). The control approach adopted entails synthetic jets with zero net mass flux, in which the fluid necessary to alter the boundary layer is intermittently injected through an orifice driven by the motion of a diaphragm located on a sealed cavity below the surface [3]. Previous studies have shown that the periodic excitation introduced at the boundary layer by the jet has the potential to significantly change the lift and drag forces on airfoils and wings.

This paper is organized as follows. In **x2**, the modeling strategy is presented and validated with results in the literature for the NACA4412 at a chord-based Reynolds number of $Re_c = U_0C/\nu = 10^6$ and AoA = 5^o [14,15]. Two different cases with AFC are proposed with increasing complexity. In **x3**, a SD7003 airfoil at $Re_c = 6 \times 10^4$ is studied with different actuations by means of wall-resolved LES. The objective is to understand the ow control of laminar separation bubbles, which is relevant for micro air vehicles and aps of high-lift aircraft wings. In **x4**, the JAXA high-lift configuration Standard Model (JSM) is selected to investigate the performance of AFC on a full aircraft in stall conditions. A landing configuration with the high-lift devices (slat and ap) deployed in the absence of nacelle/pylon is considered at $Re_c = 1.93 \times 10^6$ and Mach number $M_\infty = 0.15$. Ten different actuations strategies are explored to assess the impact of the different control parameters. Finally, conclusions are offered in **x5**.

7.3.3 Mathematical Modelling

The spatially filtered incompressible N-S equations using SGS model are presented in [Lehmkuhl et al.][190] and will not be repeated here.

7.3.4 Simulation

The simulations are performed using two independent solvers. The first code, Alya [18], is a parallel multi-physics/multi-scale simulation code developed at the Barcelona Supercomputing Centre to run efficiently on high-performance computing environments. The convective term is discretized using a Galerkin finite element (FEM) scheme recently proposed [19], which conserves linear and angular momentum, and kinetic energy at the discrete level. Both second- and third-order spatial discretization are used. Neither up winding nor any equivalent momentum stabilization is employed. In order to use equal-order elements, numerical dissipation is introduced only for the pressure stabilization via a fractional step scheme [20], which is similar to those approaches used for pressure-velocity coupling in unstructured, collocated finite volume codes [21]. The set of equations is integrated in time using a third-order Runge-Kutta explicit method combined with an eigenvalue-based time-step estimator [22]. This approach is significantly less dissipative than the traditional stabilized FEM approach [23].

A second set of simulations are conducted using the code *charLES* with a Voronoi mesh generator (Cascade Tech., Inc). The solver integrates the compressible LES equations using a 2nd order accurate finite volume formulation. The SGS model is the static-coefficient Vreman model. The numerical discretization relies on a flux formulation that is approximately entropy preserving in the inviscid limit, thereby limiting the amount of numerical dissipation added into the calculation. The time integration is performed with a 3rd order Runge-Kutta explicit method. The mesh generator is based on a Voronoi hexagonal close packed (HCP) point-seeding method which automatically builds high-quality meshes for arbitrarily complex geometries with minimal user input. First, the surface

---

[190] Oriol Lehmkuhl, Adrian Lozano-Duran, Ivette Rodriguez, "*Active flow control for external aerodynamics: from micro air vehicles to a full aircraft in stall*", Fourth Madrid Summer School on Turbulence Journal of Physics: Conference Series **1522** (2020) 012017.

geometry of the aircraft is provided to describe the computational domain. Second, the coarsest grid resolution is set to uniformly seeded HCP points.

7.3.5 Wall Modeling and Validation

To overcome the restrictive grid-resolution requirements to resolve the small-scale flow motions in the vicinity of the walls, we utilize a wall model. The no-slip boundary conditions at the walls are replaced instead by a wall-stress boundary condition. The wall-shear stress from the an algebraic equilibrium wall model is imposed as the wall boundary condition, and the wall is assumed to be isothermal. In the case of *Alya*, a finite element extension [24] of the wall law of Reichardt [25] is used:

$$u^+ = \frac{1}{\kappa}\ln(1+\kappa y^+) + 7.8\left(1 - e^{-\frac{y^+}{11}} - \frac{y^+}{11}e^{-0.33y^+}\right)$$

Eq. 7.3.1

where $u_\tau = \tau^{1/2}{}_w$, $y^+ = yu_\tau/\nu$ and $u^+ = u/u_\tau$. For *charLES*, we use a simple algebraic wall model derived from the integration of the one-dimensional equilibrium stress model along the wall-normal direction,

$$u^+(y^+) = \begin{cases} y + a_1(y^+)^2 & \text{for } y^+ > 23 \\ \frac{1}{\kappa}\ln y^+ + B & \text{otherwise} \end{cases}$$

Eq. 7.3.2

where B = 5.2 and a_1 is computed to ensure C^1 continuity. In *charLES,* the matching location for the wall model is the first off-wall grid cell of the LES mesh, and temporally filtered LES data are provided to the wall model as suggested by Yang et al. [26] to avoid the log-layer mismatch (LLM). *Alya* uses the exchange location suggested by Ref. [27]. The Navier-Stokes characteristic boundary condition for subsonic non-reflecting outflow is imposed at the outflow and top planes [28]. In all cases, we impose a uniform plug flow as the inflow boundary condition. Prior to the investigation of AFC strategies, we perform WMLES of a NACA 4412 airfoil at $Re_c = U_0C/\nu = 10^6$ and AoA = 5° in order to validate the current modelling approach.

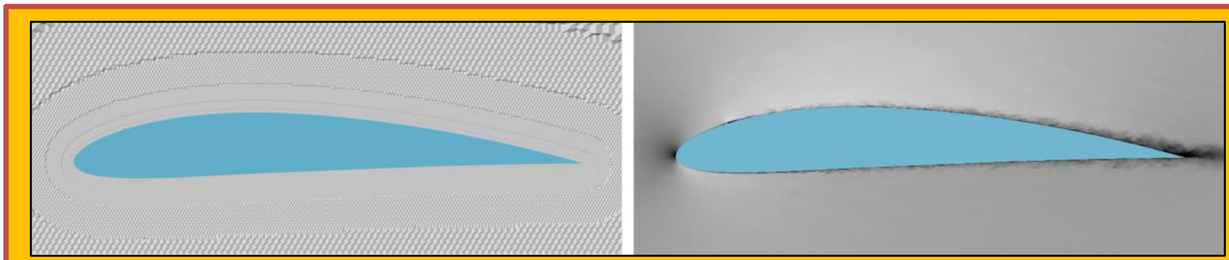

Figure 7.3.1 NACA4412 at $Re_c = 10^6$ and AoA = 5°. Left: Voronoi grid. Right: instantaneous velocity magnitude. Results for *charLES*

The Reynolds number is defined in terms of the free-stream velocity U_0 and the airfoil chord C. This particular configuration has been recently studied by Vinuesa et al. [14] by means of wall resolved LES using the spectral-element code Nek5000 and 2.28 B[191] grid points. Hence, the current case is a convenient testbed for LES under mild adverse pressure gradients (APG). We compare our results (the wall shear stress, boundary layer (BL) profiles, and pressure coefficient distribution) with Vinuesa et al. [14] and the experimental data available [15].

---

[191] B = billion

The simulations with *Alya* are carried out with a mesh of 6 million grid points, which is representative of WMLES [29]. The first off-wall grid point located at y+ ≈ 30, yielding roughly 10 elements within the BL region. Additionally, a bump of the size comparable to the BL thickness (δ) is placed at x/C = 0.1 to trigger the transition to turbulence similarly to previous experiments [15] and LES [14]. The ILSA SGS model [16] is used as eddy viscosity. For *charLES*, the mesh contains about 12 M degrees of freedom (DoF), and the SGS model selected is the Vreman model [17] with a constant coefficient equal to 0.1. A visualization of the Voronoi grid and the velocity magnitude for *charLES* is included in **Figure 7.3.1**.

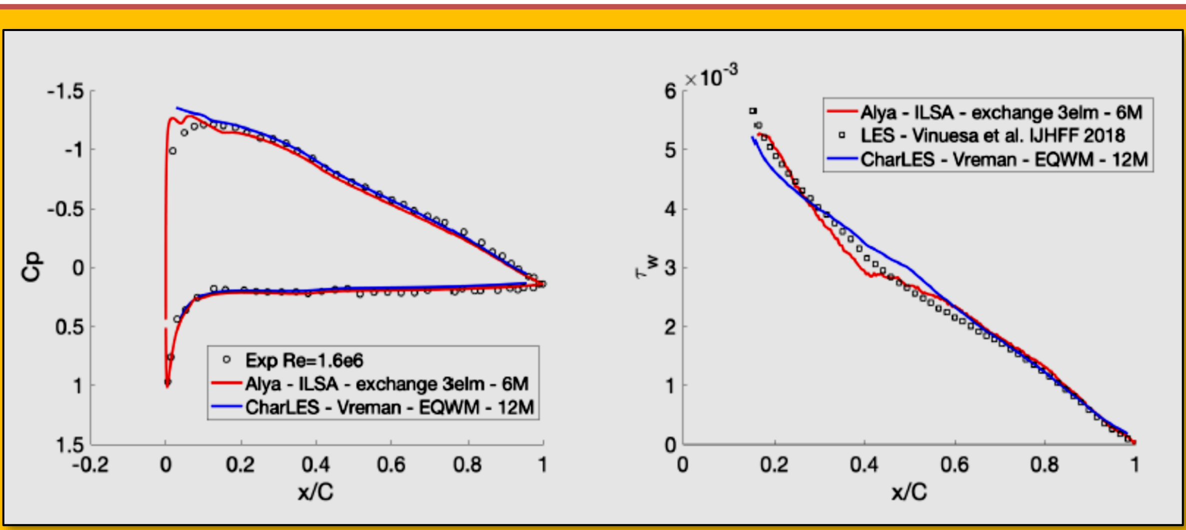

Figure 7.3.2 NACA4412 at Rec = 106 and AoA = 5o. left) Non-dimensional pressure at the airfoil surface, WMLES results vs. experimental data [15]. right) Wall shear stress at the suction side, WMLES results vs wall resolved results from Vinuesa et al. [14].

The results for the wall-shear stress and the pressure coefficient are presented in **Figure 7.3.2**. No apparent differences are observed for the predictions obtained with WMLES compared to the experimental data [15]. Similar conclusions apply to the wall shear stress at the suction side. Although the results from WMLES do not show a fully turbulent BL until x/C = 0.6, the error relative to the wall resolved data is below 10% along the full chord. This outcome demonstrates the capabilities of WMLES in the presence of APG, even when equilibrium assumptions derived from mean zero-pressure-gradient boundary layers are invoked to model the near-wall region [30, 31]. The results from *Alya* based, on an exchange location between WM and LES at the 3rd off grid node, shows an excellent agreement with the wall resolved data of Vinuesa et al. [14]. The results from *charLES* also show a good prediction of the mean velocity profile, although they exhibit a slight mismatch at the first grid points, which does not affect the prediction of the log layer further from the wall. Larger discrepancies are observed for the fluctuating velocities. The results from *charLES* are in fair agreement with the WRLES, but the results from *Alya* show a noticeable over prediction near the wall. These differences might be attributed to the coarser grid resolution used in the simulations with Alya (6M vs. 12 M DoF) [32]. Although they could also be due to the exchange location method utilized by *Alya* [27] in constant to the time filtering approach from *charLES* [26], or differences in the SGS model. A further assessment will be made in future works in order to clarify this issue.

7.3.6 Active Flow Control of Airfoils With Laminar Separation Bubbles

In this section, we focus on airfoils operating at moderate Reynolds numbers, which is of interest for the development of Micro Air Vehicles such as drones. To that end, we study the performance of different actuation mechanisms on the boundary layer of a SD7003 airfoil at Re = U_0C/ν = 6 x 10^4. The Reynolds number is defined in terms of the free-stream velocity U0 and the airfoil chord C. At the present moderate Re, the formation of a laminar separation bubble (LSB) may have a dominant effect on the flow field and thus, it is of prime importance to understand the role of the actuation on the reduction or suppression of the LSB along with the post-stall behavior. We consider three AoAs equal to 4°, 11°, and 14°.

The first AoA results in a large laminar separation bubble, the second is close to the maximum lift, while the last one corresponds with the flow in full stall. For this part of the study we employ the solver Alya. Giving the moderate Reynolds number, the flow is simulated using wall-resolved LES. The dimensions of the computational domain are 15C x 16C x 0.2C, with the leading edge of the airfoil placed at (0; 0; 0). The boundary conditions at the inflow consist of a uniform velocity profile (u; v;w) = (U_0 cos(AoA); U_0 sin(AoA); 0). For the outflow, we impose a pressure-based boundary condition. No-slip conditions on the airfoil surface are prescribed, and periodic boundary conditions are used in the spanwise direction. For the actuated cases, we impose the inlet velocity

$$(u, v, w)_{act} = A_p U_0 \sin(2\pi f t) \sin(2\pi \tau z) \left(\sin(AoA, \cos(AoA)\,, 0\right)$$

Eq. 7.3.3

Here, A_p is the maximum amplitude of the jet such that $U_{max} = ApU_0$; f is the actuator frequency which defines $F^+ = f\,U_0 = x_{TE}$, with x_{TE} the distance from the actuator to the trailing edge; and τ is the spanwise period of the signal with τ = $0.5L_z$. In the present simulations, a momentum coefficient $c_\mu = h(\rho U^2_{max}) = (C\rho U^2_0\ ) = 3 \times 10^{-3}$ (with h the actuator width) and a non-dimensional frequency of $F^+ = 1$ are

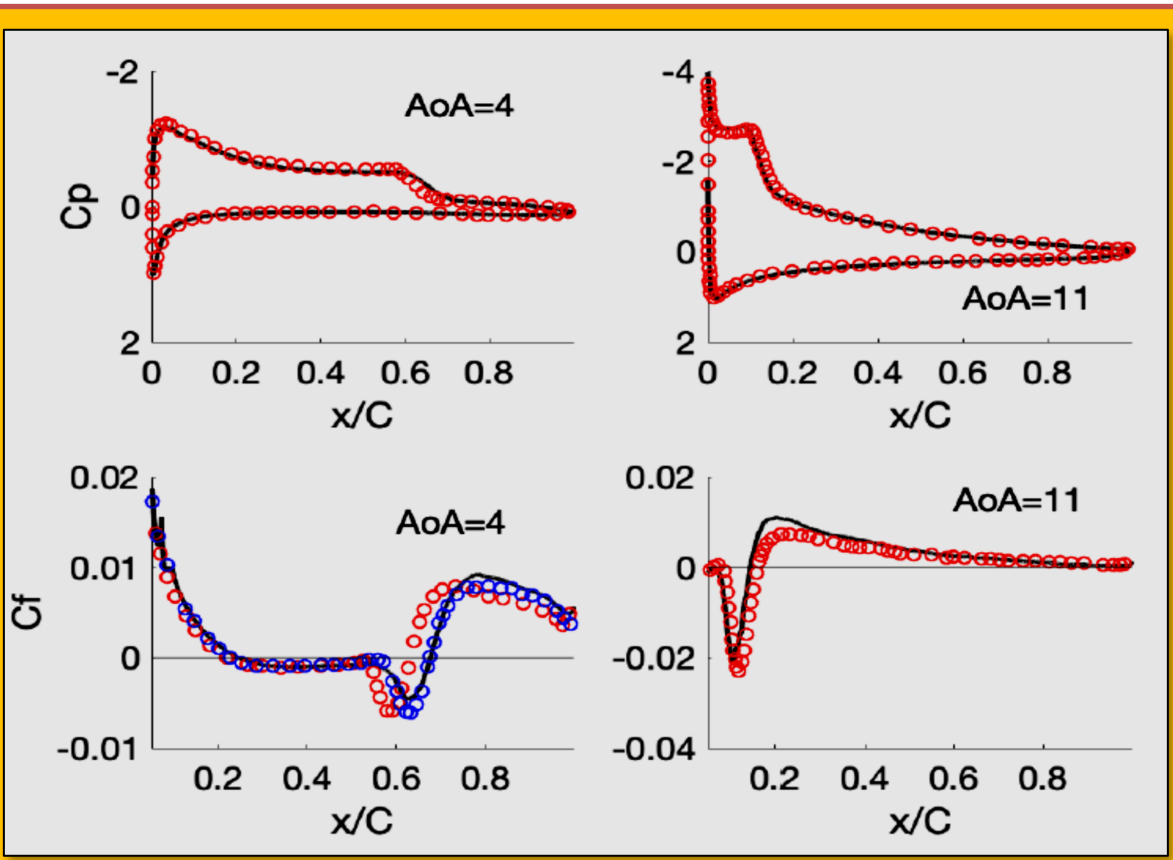

Figure 7.3.3 SD7003 at Re_c = 6 x 10^4. Comparison with the literature. (solid line) present results. (blue circle) LES [34], (red circles) ILES [33]

considered. The actuator outlet is located at 0.01C. The computational meshes used for both the baseline and actuated cases are unstructured grids of about 30 M DoF. The meshes are obtained by extruding an unstructured two-dimensional mesh in N elements along the spanwise direction. The meshes are constructed to attain a wall normal resolution of $\Delta y+ \approx 1$ in the near wall region. The number of elements in the spanwise direction in all computations is 64.

With the aim of validating the current numerical set-up, the un-actuated case is compared with the available data in the literature obtained by Galbraith and Visbal [33] using implicit LES (ILES) with a computational grid of about 5.7 M grid points. A detailed comparison of the pressure coefficient and skin friction at AoA = 4° and 11° is presented in **Figure 7.3.3**. In both cases, our results are in good agreement with Galbraith and Visbal [33], which provides confident in our current approach. The lift and drag coefficients for both the actuated and baseline cases at AoA = 4°; 11°, and 14° are considered in **Figure 7.3.4**. Moreover, the instantaneous vortical structures represented by means of Q-iso surfaces for the baseline and the actuated cases are depicted in **Figure 7.3.5**.

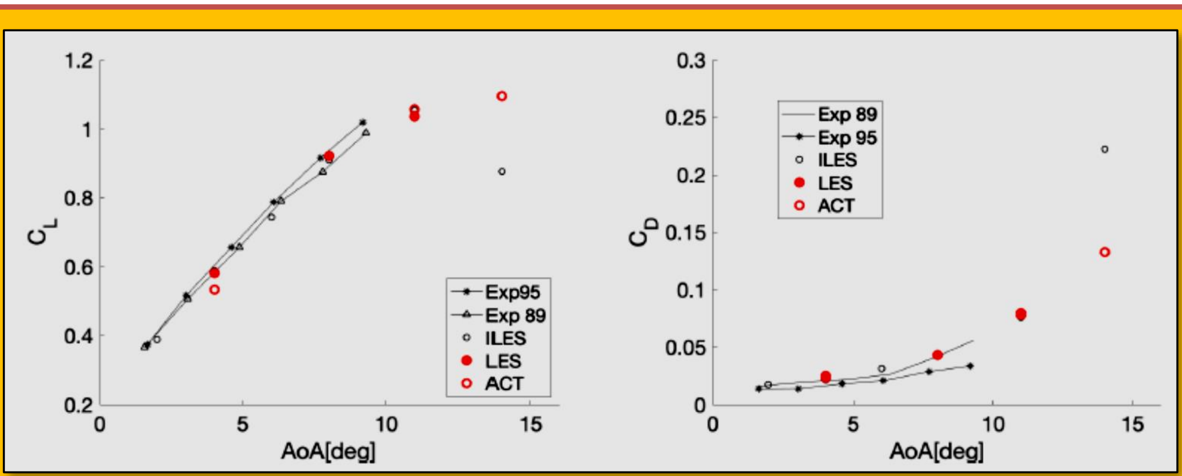

Figure 7.3.4 SD7003 at Rec = 6 _ 104. Lift and drag coe_cients for the controlled cases. Comparison with the baseline cases and with the literature.EXP95[35], EXP89[36], ILES[33].

For an AoA lower than the point of maximum lift (i.e. AoA = 11°), the actuation successfully eliminates the laminar separation bubble and triggers the transition to turbulence right after the location of the actuator (see **Figure 7.3.5**). However, the new flow configuration offers no advantages from the airfoil efficiency point of view. Conversely, the airfoil efficiency increases considerably for the stall condition at AoA = 14°: the actuation increases the lift coefficient 19%, whereas the reduction in the drag forces is about 67%, thus increasing the airfoil efficiency by 98%. As can be seen from the **Figure 7.3.5**, in the baseline case for AoA = 14°, the flow massively separates from almost the leading edge of the airfoil and fails to reattach, producing a large recirculation bubble and momentum deficit in the suction side of the airfoil. As a consequence of the large detachment of the flow, the airfoil is stalled and its efficiency drops. When the actuator is activated, the jet transfers momentum to the flow and produces three-dimensional instabilities in the shear layer which trigger the transition to turbulence. The added momentum forces the shear layer to reattach to the airfoil surface for most of the airfoil chord. This results in a reduction in the separated zone of the airfoil and the increase in the airfoil efficiency.

7.3.7 Active Flow Control of A Full Aircraft In High-Lift Configuration at Realistic Reynolds Numbers

The JAXA Standard Model (JSM) in high-lift configuration, which was the experimentally studied at JAXA [37], is selected to investigate AFC strategies at realistic Reynolds numbers for a full aircraft. A landing configuration with the high-lift devices (slat and flap) deployed is considered at Re_c = 1.93 x

10^6 and $M_\infty = 0.15$. The nacelle/pylon components are not included in the simulations. This geometry was the subject of study in the recent 3rd AIAA CFD High Lift Prediction Workshop [38], where various RANS-based methodologies were challenged to predict the onset of stall and maximum lift. The conclusions from the workshop pointed out the high sensitivity of the lift and drag results at high angle of attacks: RANS-based approaches exhibit multiple solutions given different initial conditions and they have difficulties to predict the lift coefficient at high AoA.

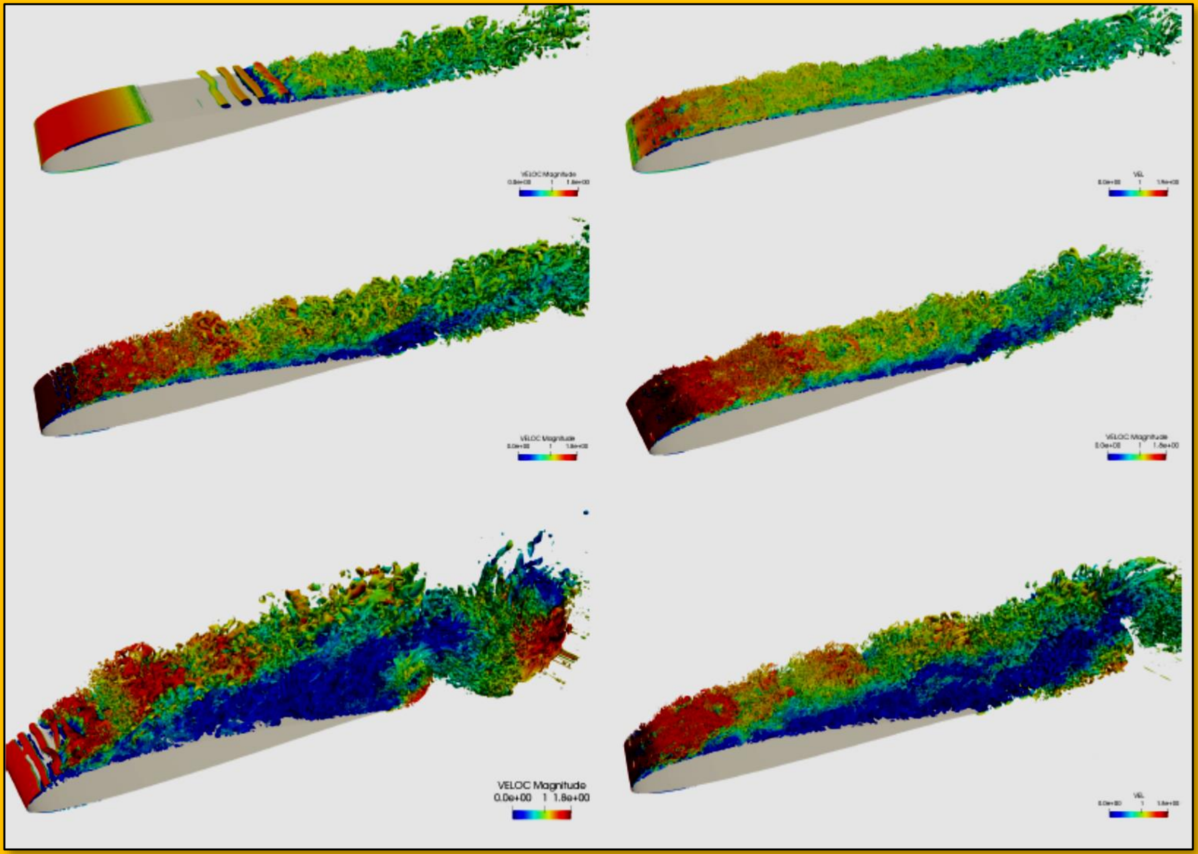

Figure 7.3.5 SD7003 at $Re_c = 6 \times 10^4$. Q iso-surfaces for the different configurations considered. Top left)AoA = 4_ baseline; top right) AoA = 4_ actuated; middle left) AoA = 11_ baseline; middle right) AoA = 11° actuated; bottom left) AoA = 14° baseline; and bottom right) AoA = 14° actuated.

The study is mainly performed using *Alya*, and the most successful case is cross validated using *charLES*. The performance of WMLES in the JSM configuration has been previously assessed by Lehmkuhl et al. [39] at AoAs pertaining to the linear-lift regime, maximum lift, and stall conditions (4, 10, 18.58, and 21.57 degrees). The results from the previous and the current validation exercise (**Figure 7.3.6**) reveal that the lift coefficient is in good agreement with the experimental results. The predicted drag is over estimated compared to the experimental measurements, although this may be due the geometric differences between the simulations and experimental set-up.

For the actuated cases, only the AoA = 21.57° is considered in order to make the study computationally affordable. The meshes adopted are similar to those reported in Lehmkuhl et al. [39]. For *Alya*, the mesh consist of 180 M of finite elements, and is composed of anisotropic wedge/prism layers near the wall and tetrahedra elsewhere. Additionally, dedicated mesh density zones are designed to provide a proper mesh resolution in the wakes of the slant, ap, and main wings. For *charLES*, the mesh is generated using a Voronoi grid with 60 M control volumes and refinement close to the solid boundaries. The meshes are refined in the near-wall regions so that the number of

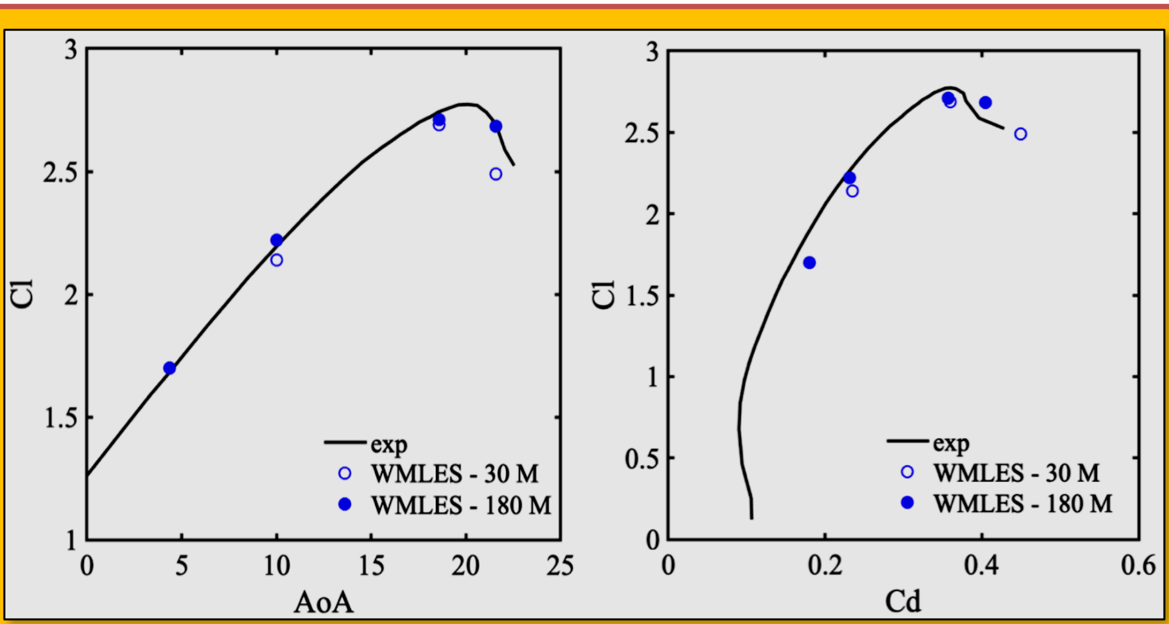

Figure 7.3.6 JSM high lift at $Re_c = 1.93 \times 10^6$. Averaged integral forces: WMLES vs experimental data[37, 40] (see Lehmkuhl et al. [39] for more details).

grid cells across the local boundary layer thickness ranges from 5 to 10. The boundary conditions at the inflow consist of a uniform velocity profile (u; v; w) = (U_0 cos(AoA); 0; U_0 sin(AoA)). At outlet, a pressure-based boundary condition is imposed, while at the surface of the aircraft a wall stress boundary condition is imposed using the equilibrium model. Homogeneous Neumann boundary conditions are used in the symmetry plane. The reader is referred to Lehmkuhl et al. [39] for more information about the current numerical set-up. The actuation is imposed in the main wing and in the aps as shown in the right panel of **Figure 7.3.7x**. The actuation is located at x/C = 0.5 for the

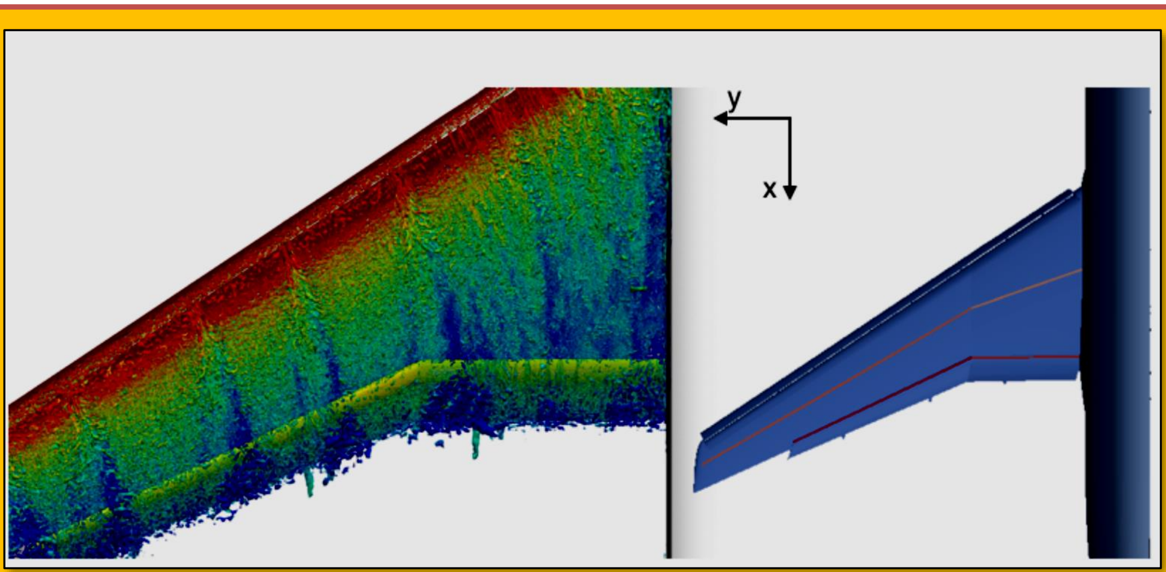

Figure 7.3.7 JSM high lift at Re_c = 1:93 x 10^6 and AoA = 21.57°. Left) Q iso-surfaces at the wing of JSM geometry colored by velocity magnitude (baseline case); right) x-y view: location of the synthetic jets (main at x/c = 0.5 and ap at x/c = 0.1)

main wing, and at x/C = 0.1 for the flap. Across the actuator area, we prescribe the jet velocity in x-, y- and z-direction as,

$$(u, v, w)_{act} = V_{max}\sin(2\pi f t)\sin\left(2\pi\tau_y y\right)(\cos\alpha, \sin\alpha, 1)(\sin\phi, \sin\phi, \cos\phi)$$

Eq. 7.3.4

where f is the actuator frequency $F^+ = f\,C/U_0$, τ_y is the spanwise period of the signal (0 in 2D actuations and $N_{jet}=L_y$ in 3D), V_{max} is obtained from

$$C_\mu = \frac{(\rho V_{max}^2)A_{act}}{(\rho V_0^2)A_{ref}}$$

Eq. 7.3.5

and α is the angle with respect to the y-axis (see **Figure 7.3.7 right**) and ϕ is the angle respect to the wing surface normal. The number of jets in the wing span(N_{jet}) is adjusted to have a $\tau_y = 0.1$. The main goal of the actuation is to control both the separation induced by the brackets connecting the slant and main wing, and the laminar separation bubbles in the flap region.

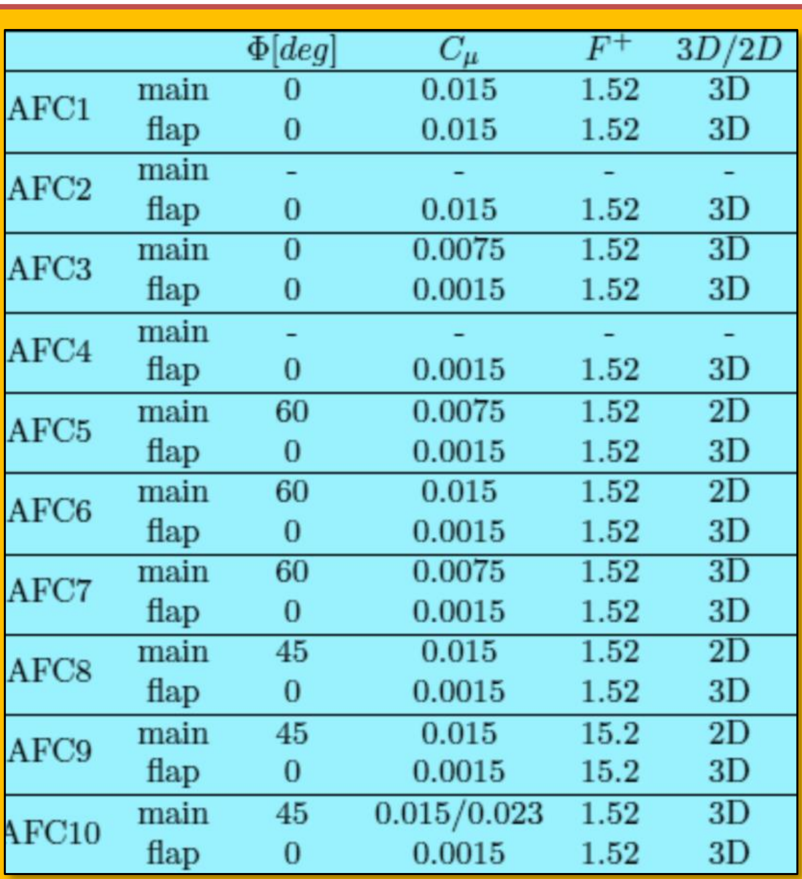

		$\Phi[deg]$	C_μ	F^+	$3D/2D$
AFC1	main	0	0.015	1.52	3D
	flap	0	0.015	1.52	3D
AFC2	main	-	-	-	-
	flap	0	0.015	1.52	3D
AFC3	main	0	0.0075	1.52	3D
	flap	0	0.0015	1.52	3D
AFC4	main	-	-	-	-
	flap	0	0.0015	1.52	3D
AFC5	main	60	0.0075	1.52	2D
	flap	0	0.0015	1.52	3D
AFC6	main	60	0.015	1.52	2D
	flap	0	0.0015	1.52	3D
AFC7	main	60	0.0075	1.52	3D
	flap	0	0.0015	1.52	3D
AFC8	main	45	0.015	1.52	2D
	flap	0	0.0015	1.52	3D
AFC9	main	45	0.015	15.2	2D
	flap	0	0.0015	15.2	3D
AFC10	main	45	0.015/0.023	1.52	3D
	flap	0	0.0015	1.52	3D

Table 7.3.1 JSM high-lift at $Re_c = 1.93 \times 10^6$ and AoA = 21.57°. Considered AFC parameters

Ten actuation conditions are studied by varying the momentum coefficient, the actuation frequency, and the angle of actuator with respect to the normal direction to the surface. The complete test matrix is reported in **Table 7.3.1**. Three jet angles in the main wing are considered: normal (AFC1, AFC2, AFC3 and AFC4), tangential (AFC5, AFC6 and AFC7), and semi tangential (AFC8, AFC9 and AFC10). The flap is always actuated with a jet in the normal direction to the surface. No actuation in the main wing is considered in AFC2 and AFC4.

Following Shmilovich and Yadlin [9], the value of F+ is set equal to 1.52. In AFC9, we select $F^+ = 15.2$ to assess the effects of the frequency on the efficiency of the control. The impact of 2D actuation (constant Cμ) over the main wing is explored in cases AFC5, AFC6, AFC8 and AFC9. Finally a variable Cμ over the main wing to compensate for the change of spanwise area is assessed in AFC10.

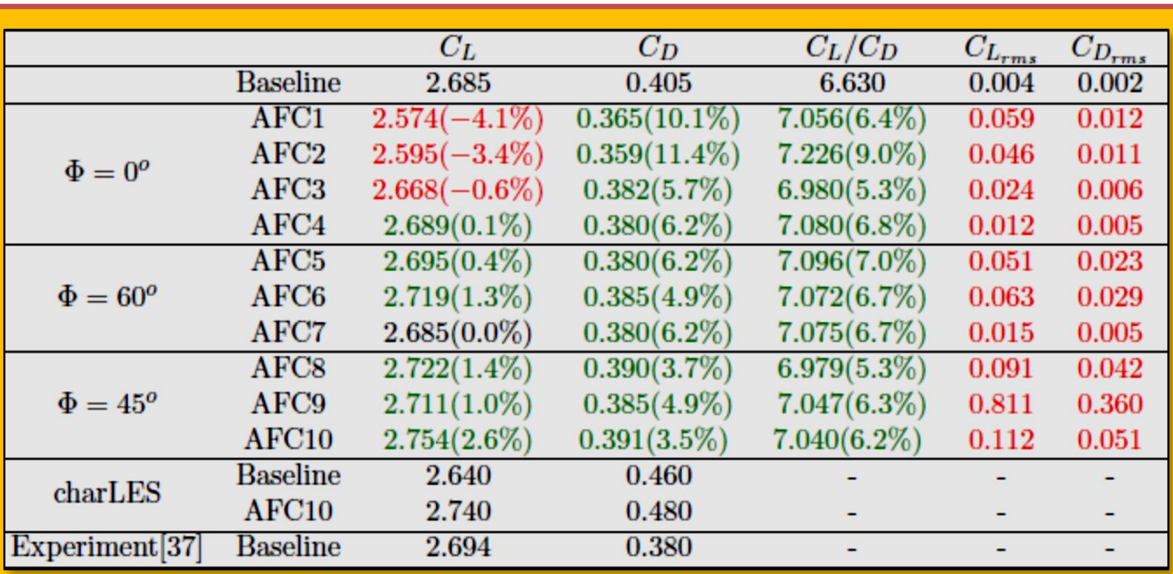

		C_L	C_D	C_L/C_D	$C_{L_{rms}}$	$C_{D_{rms}}$
	Baseline	2.685	0.405	6.630	0.004	0.002
$\Phi = 0^o$	AFC1	2.574(−4.1%)	0.365(10.1%)	7.056(6.4%)	0.059	0.012
	AFC2	2.595(−3.4%)	0.359(11.4%)	7.226(9.0%)	0.046	0.011
	AFC3	2.668(−0.6%)	0.382(5.7%)	6.980(5.3%)	0.024	0.006
	AFC4	2.689(0.1%)	0.380(6.2%)	7.080(6.8%)	0.012	0.005
$\Phi = 60^o$	AFC5	2.695(0.4%)	0.380(6.2%)	7.096(7.0%)	0.051	0.023
	AFC6	2.719(1.3%)	0.385(4.9%)	7.072(6.7%)	0.063	0.029
	AFC7	2.685(0.0%)	0.380(6.2%)	7.075(6.7%)	0.015	0.005
$\Phi = 45^o$	AFC8	2.722(1.4%)	0.390(3.7%)	6.979(5.3%)	0.091	0.042
	AFC9	2.711(1.0%)	0.385(4.9%)	7.047(6.3%)	0.811	0.360
	AFC10	2.754(2.6%)	0.391(3.5%)	7.040(6.2%)	0.112	0.051
charLES	Baseline	2.640	0.460	-	-	-
	AFC10	2.740	0.480	-	-	-
Experiment[37]	Baseline	2.694	0.380	-	-	-

Table 7.3.2 JSM high-lift at Re$_c$ = 1.93 x 10^6 and AoA = 21:57o. AFC results

The time-averaged aerodynamic forces are presented in **Table 7.3.2**. Since no experimental results are available from the current control cases, we carried out an additional simulation of case AFC10 using *charLES* with a mesh of 60 M control volumes. The predictions of C_L from *Alya* and *charLES* differ less than 1%, which cross validates the present approach using different numerical and modelling set-ups as described in section 2.1. Nonetheless, larger drag forces are predicted with *charLES*. This trend has been observed in the baseline configuration in previous

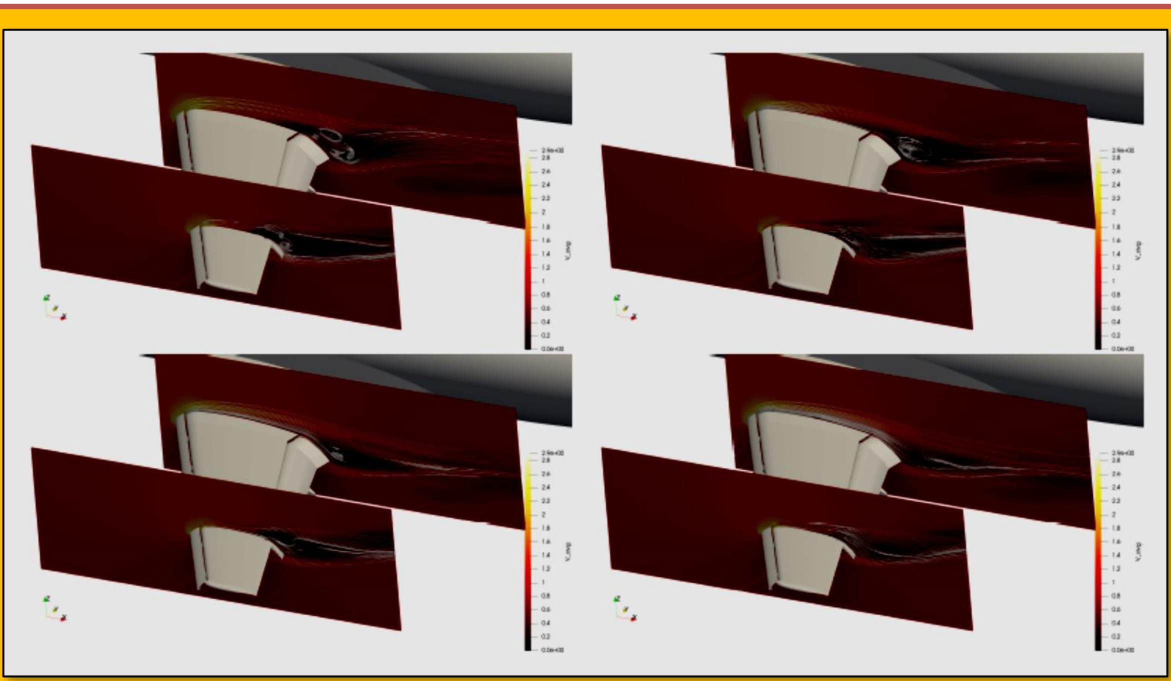

Figure 7.3.8 JSM high-lift at Rec = 1.93 x 10^6 and AoA = 21:57^o. 2D streamlines at different span-wise locations: baseline case vs different actuator jet angles. Top left) baseline; top right) AFC3(ϕ = 0o); bottom left) AFC6 (ϕ = 60o); and bottom right) AFC8(ϕ = 45o).

simulations for the same JSM baseline flow configuration [39].

According to the results presented in **Table 7.3.2**, drag forces are reduced for all the proposed actuations at least by a 5%, while lift forces are improved only in AFC4, AFC5, AFC6, AFC8, AFC9 and AFC10. Even if the efficiency is improved by all the actuations considered, it is worth noting that, as a result of the periodic jets, the fluctuations in the drag and lift forces are considerably enhanced in all cases. This is accentuated for the case AFC9 ($F^+ = 15.2$), i.e., the periodic suction and blowing of the boundary layer produces a wave-like flow that alters the instantaneous values of the aerodynamic forces by more than one order of magnitude. To understand the effect of the actuation on the main wing, we inspect the flow patterns in the presence and absence of actuation.

Figure 7.3.8 shows the mean streamlines for the un-actuated base flow and for cases AFC3, AFC6, and AFC8. The visualizations suggest that the main losses in the lift forces are due to the formation of large separated zones. In the uncontrolled case, a large recirculation region occurs behind the flap, which lifts up the boundary layer in the rear end of the main wing right after the flow changes direction as induced by the flap deployment. For actuated cases with $\phi = 0^\circ$ (AFC1 and AFC3), the turbulent boundary layer is vertically displaced, which decreases the lift coefficient. When the actuation in the main wing is suppressed, the variations in the lift is very small, and the jet located at the flap can barely act on the recirculation zone. The present results suggest that $\phi = 0^\circ$ is not a viable option to improve the lift forces, and the most efficient actuations are in the tangential direction with angles between $\phi = 45^\circ$ and $\phi = 60^\circ$. For $\phi = 45^\circ$, the jet is injected directly into the main boundary layer, enhancing mixing and preventing separation.

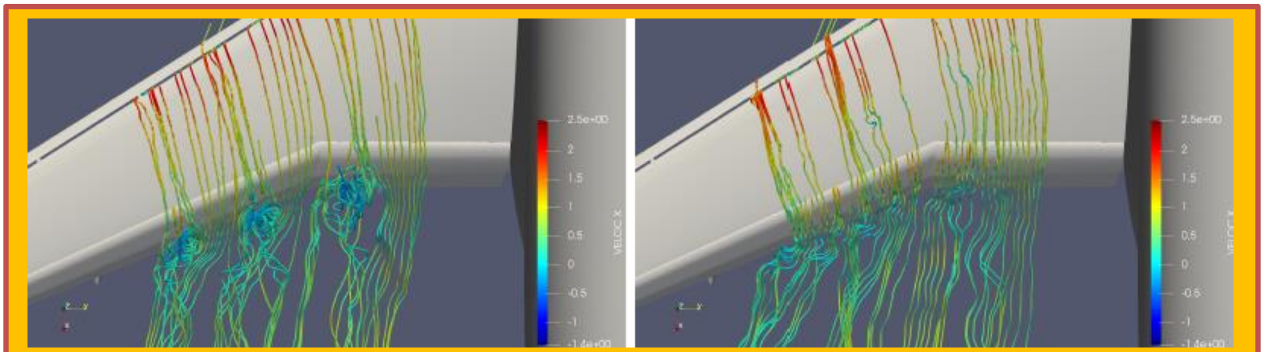

Figure 7.3.9 JSM high-lift at Rec = 1:93 _ 106 and AoA = 21:57o. Streamlines colored by nondimensional streamwise velocity at the JSM high-lift wing: left) baseline configuration; right) AFC10.

The actuation strategies which approximates the best the ideal linear behavior of C_L are AFC8 and AFC10, with a slight improvement for case AFC10. In both cases, the large recirculation zone behind the flap is almost suppressed and the streamlines evolve parallel to each other behind the flap (see **Figure 7.3.8** bottom right and **Figure 7.3.9**). Therefore, the actuator with spanwise-varying C_τ along the wing is effective in compensating for the geometrical changes in the wing.

7.3.8 Conclusions

Since the early days of aviation, many efforts have been devoted to the design of devices capable of providing the required lift, while reducing the associated drag of the device, such as slotted flaps or other high-lift mechanisms. Among the various approaches, active flow control via synthetic jets has emerged as a versatile technology for a broad range of applications at moderate and high Reynolds numbers. However, the use of CFD in the design of active flow control strategies for real-world applications has been hampered by the prohibitive computational cost associated with the computation of all the scales of the motions typically encountered in turbulent flows.

Here, we have investigated the impact of active flow control on the aerodynamic performance of actuated airfoils and wings. To make the problem tractable, the methodology employed has been wall-resolved and wall-modeled LES. Most of the simulations are carried out using the finite-element-based solver, *Alya*. To quantify the sensitivity of the results to the numerical discretization scheme, several cases have been simulated using a finite-volume-based solver, *charLES*.

Prior to the investigation of AFC with synthetic jets, we have validated the modelling capabilities of wall-modeled LES in a NACA 4412 airfoil at $Re_c = 10^6$ and AoA = 5^o, for which high-fidelity CFD and experiments results are available in the literature. The simulation are carried out using both solvers, *Alya* and *charLES,* with 6 M[192] DoF in the former and 12 M control volumes in the latter. Consistent with previous analysis, our results show that WMLES enables a faithful prediction of the most relevant figures of merit in external aerodynamics such as the pressure coefficient and skin friction, together with an accurate estimation of the mean velocity profile at multiple chord locations. The turbulence intensities are also correctly captured in the outer layer of the boundary layer, although they are overpredicted in the near-wall region with *Alya*. It was argued that several factors might be responsible for the overprediction of turbulence kinetic energy (grid resolution, wall-model matching location, SGS model,...), and future studies will be devoted to clarify this issue.

The effects of AFC in Micro Air Vehicles has been evaluated selecting as a representative case a SD7003 airfoil at $Re = U_0C/\nu = 6 \times 10^4$. This flow configuration is characterized by a large separation bubble anchored at the leading edge of the airfoil, which is responsible for a degraded aerodynamic performance. The calculations are performed with *Alya* using wall-resolved LES with 30 M DoF. It is shown that actuating the airfoil in the vicinity to the leading edge at high AoA provides the necessary additional linear momentum to induce the breakdown of the laminar separation bubble. The new flow configuration is turbulent across the full chord of the airfoil, which improves considerably the aerodynamic performance. At lower AoAs, the synthetic jet is still able to suppress the laminar separation bubble, but with marginal improvements in terms of the aerodynamic performance.

The capabilities of AFC for a full aircraft in high-lift configuration at realistic Reynolds numbers is tackled by WMLES of the JAXA Common Research Model at AoA = 21:57o and $Re_c = 1.93 \times 10^6$. A systematic study of the effect of synthetic jets is addressed by performing a campaign of WMLESs varying the jet inclination angle relative to the solid boundary, the value of the momentum coefficient, actuating jet frequency, and the number of actuation lines (flaps or wing + flaps). The simulations are performed using *Alya*. The most successful case is also computed using *charLES* to provide cross-validation between different CFD solvers. Both *Alya* and *charLES* utilize the constant-coefficient Vreman SGS model and the algebraic equilibrium wall-model. The comprehensive matrix of cases provides rich information about the impact of the AFC on the flow. The most effective control in terms of aerodynamic performance (with 6.2% improvement) is achieved for jets with 45 degrees inclination angles, frequencies of $F^+ = 1.52$, and variable spanwise momentum coefficient along the wing. Interestingly, cases where the actuation is limited to the flaps reveal that the additional momentum injected into the boundary layer occurs too late downstream flow to efficiently remove the recirculation pattern.

The present analysis demonstrates the capabilities of LES to quantify the effects of active flow control for external aerodynamics. This ability to accurately predict turbulent flows without the necessity of empirical adjustments renders LES a promising methodology for arbitrary new geometries, as opposed to traditional Reynolds-Averaged Navier-Stokes (RANS) techniques which, require calibration according to the flow configuration.

7.3.9 Acknowledgment

This work is funded in part by the Coturb program of the European Research Council. O. L. acknowledges the financial support by the Ministerio de Economa y Competitividad, Secreta_a de Estado de Investigacion, Desarrollo e Innovacion, Spain (ref. TRA2017-88508-R) and the European Union's Horizon 2020 research and innovation programmed (INFRAEDI-02-2018, EXCELLERAT- The European

---

[192] M = million

Centre Of Excellence For Engineering Applications H2020.). We also acknowledge Red Espanola de Super computation and Barcelona Supercomputing Center for awarding us access to the MareNostrum IV machine based in Barcelona, Spain (FI-2018-3-0021, FI-2018-2-0015, FI-2018-1-0022, FI-2017-3-0024). We acknowledge Prof. R. Vinuesa for the discussions and data analysis of the NACA4412. A.L.-D. acknowledges the support of NASA Transformative Aeronautics Concepts Program (Grant No. NNX15AU93A) and the Office of Naval Research (Grant No. N000141712310).We thank Prof. Philipp Schlatter for reading the manuscript and for his valuable suggestions.

7.3.10 References

[1] T. C. Corke, C. L. Enloe, and S. P. Wilkinson. Dielectric barrier discharge plasma actuators for flow control. Ann. Rev. Fluid Mech., 42:505{529, 2010.

[2] L. N. Cattafesta and M. Sheplak. Actuators for active flow control. Ann. Rev. Fluid Mech, 2011.

[3] A. Glezer. Some aspects of aerodynamic flow control using synthetic-jet actuation. Phil. T. Roy. Soc. A, 369:1476-1494, 2011.

[4] P. M. Hartwich, A. Shmilovich, D. S. Lacy, E. D. Dickey, A. J. Scalafani, P. Sundaram, and Y. Yadlin. Refined AFC-enabled high-lift system integration study. Technical Report NASA/CR-2016.

[5] D. C. Mccormick. Boundary layer separation control with directed synthetic jets. In 38th AIAA Aerospace Sciences Meeting & Exhibit, number 2000-0519, 2000.

[6] M. Amitay and A. Glezer. Role of actuation frequency in controlled flow reattachment over a stalled airfoil. AIAA J., 40:209{216, 2002.

[7] J. L. Gilarranz, L. W. Traub, and O. K. Rediniotis. A new class of synthetic jet actuators{Part I: Design, fabrication and bench top characterization. J. Fluids Eng., 127:367{376, 2005.

[8] D. You and P. Moin. Active control of flow separation over an airfoil using synthetic jets. J. Fluids Struct., 24:1349-1357, 2008.

[9] A. Shmilovich and Y. Yadlin. Active flow control for practical high-lift systems. J. Aircraft, 46:1354{1364, 2009.

[10] M. Bauer, J. Lohse, F. Haucke, and W. Nitsche. High-lift performance investigation of a two-element configuration with a two-stage actuator system. AIAA J., 52:1307{1313, 2014.

[11] J. C. Lin, L. G. Pack Melton, S. Viken, M. Y. Andino, M. Koklu, J. Hannon, and V. N. Vatsa. High Lift Common Research Model for Wind Tunnel Testing: An Active Flow Control Perspective. In 55th AIAA Aerospace Sciences Meeting, number 2017-0319, 2017.

[12] J. C. Lin, L. G. Pack Melton, J. Hannon, M. Y. Andino, M. Koklu, K. Paschal, and V. N. Vatsa. Wind tunnel testing of active flow control on the high-lift common research model. In AIAA Aviation 2019 Forum, number 2019-3723, 2019.

[13] M. Y. Andino, J. C. Lin, S. Roman, E. C. Gra_, M. Gharib, E. A. Whalen, and I. J. Wygnanski. Active flow control on vertical tail models. AIAA J., 57:3322{3338, 2019.

[14] R. Vinuesa, P.S. Negi, M. Atzori, A. Hani_, D.S. Henningson, and P. Schlatter. Turbulent boundary layers around wing sections up to Rec = 1000000. Int. J. Heat Fluid Flow, 72:86{99, 2018.

[15] R. C. Hastings and B. R. Williams. Studies of the flow field near a NACA 4412 airfoil at nearly maximum lift. Aeronaut. J., 91(901):29{44, 1987.

[16] O. Lehmkuhl, U. Piomelli, and G. Houzeaux. On the extension of the integral length-scale approximation model to complex geometries. Int. J. Heat Fluid Flow, 78:108422, 2019.

[17] A. W. Vreman. An eddy-viscosity sub grid-scale model for turbulent shear flow: Algebraic theory and applications. Phys. Fluids, 16:3670-3681, 2004.

[18] A. M. Vazquez, G. Houzeaux, S. Koric, A. Artigues, J. Aguado-Sierra, R. Aris, D. Mira, H. Calmet, F. Cucchietti, H. Owen, E. Casoni, A. Taha, E. D. Burness, J. M. Cela, and M. Valero. Alya: Multiphysics engineering simulation towards exascale. J. Comput. Sci., 14:15{27, 2016.

[19] S. Charnyi, T. Heister, M. A. Olshanskii, and L. G. Rebholz. On conservation laws of Navier-Stokes Galerkin discretization . J. Comput. Phys., 337:289 { 308, 2017.

[20] R. Codina. Pressure stability in fractional step finite element methods for incompressible flows. J. Comput. Phys., 170:112-140, 2001.
[21] L. Jofre, O. Lehmkuhl, J. Ventosa, F.X. Trias, and A. Oliva. Conservation properties of unstructured finite-volume mesh schemes for the Navier-Stokes equations. Num. Heat Tr. B{Fund., 65:53-79, 2014.
[22] F. X. Trias and O. Lehmkuhl. A self-adaptive strategy for the time integration of Navier-Stokes equations. Num. Heat Tr. B{Fund., 60:116{134, 2011.
[23] O. Lehmkuhl, G. Houzeaux, H. Owen, G. Chrysokentis, and I. Rodriguez. A low-dissipation finite element scheme for scale resolving simulations of turbulent flows. J. Comp. Phys., 390:51 - 65, 2019.
[24] H. Owen, G. Chrysokentis, M. Avila, D. Mira, G. Houzeaux, R. Borrell, J. C. Cajas, and O. Lehmkuhl. Wall-modeled large-eddy simulation in a _nite element framework. Int. J. Num. Meth. Fluids, 2019.
[25] H. Reichardt. Vollstandige darstellung der turbulenten geschwindigkeits- verteilung in glatten leitungen. ZAMM-Z. Angew. Math. Me., 31:208-219, 1951.
[26] X. I. A. Yang, G. I. Park, and P. Moin. Log-layer mismatch and modeling of the fluctuating wall stress in wall-modeled large-eddy simulations. Phys. Rev. Fluids, 2:104601, 2017.
[27] S. Kawai and J. Larsson. Wall-modeling in large eddy simulation: Length scales, grid resolution, and accuracy. Phys. Fluids, 24(015105), 2012.
[28] T. J. Poinsot and S. K. Lele. Boundary conditions for direct simulations of compressible viscous flows. J. Comp. Phys., 101:104 - 129, 1992.
[29] A. Lozano-Duran and H. J. Bae. Error scaling of large-eddy simulation in the outer region of wall-bounded turbulence. J. Compt. Phys., 392:532-555, 2019.
[30] J. Larsson, S. Kawai, J. Bodart, and I. Bermejo-Moreno. Large eddy simulation with modelled wall stress: recent progress and future directions. Mech. Eng. Rev., 3, 2016.
[31] S. T. Bose and G. I. Park. Wall-modeled large-eddy simulation for complex turbulent flows. Ann. Rev. Fluid Mech., 50:535-561, 2018.
[32] H. J. Bae, A. Lozano-Duran, S. T. Bose, and P. Moin. Turbulence intensities in large-eddy simulation of wall-bounded ows. Phys. Rev. Fluids, 3:014610, 2018.
[33] M. Galbraith and M. Visbal. Implicit large eddy simulation of low Reynolds number ow past the SD7003 airfoil. In 46th AIAA Aerospace Sciences Meeting and Exhibit, number 2008-225, 2008.
[34] S. Schmidt and M. Breuer. Hybrid LES-URANS methodology for the prediction of non-equilibrium wall bounded internal and external flows. Comp. Fluids, 96:226-252, 2014.
[35] M. S. Selig, J. J. Guglielmo, A. P. Broeren, and P. Giguere. Summary of low-speed airfoil data. Technical report, University of Illinois, 1995.
[36] M. S. Selig, J. F. Donovan, and D. B. Fraser. Airfoils at low speeds. Technical report, UoI, 1989.
[37] Y. Yokokawa, M. Murayama, M. Kanazaki, K. Murota, T. Ito, and K. Yamamoto. Investigation and improvement of high-lift aerodynamic performances in low speed wind tunnel testing. AIAA 2008.
[38] C. L. Rumsey, J. P. Slotnick, and A. J. Sclafani. Overview and summary of the Third AIAA High Lift Prediction Workshop. AIAA Pap., (2018-1258. Also, https://hiliftpw.larc.nasa.gov/), 2018.
[39] O. Lehmkuhl, G. Park, S.T. Bose, and P. Moin. Large-eddy simulation of practical aeronautical flows at stall conditions. In Center Tur. Res.{Proc. Summer Prog., pages 87-96, 2018.
[40] Y. Yokokawa, M. Murayama, H. Uchida, K. Tanaka, T. Ito, and K. Yamamoto. Aerodynamic influence of a half-span model installation for high-lift configuration experiment. AIAA Pap., (2010-684), 2010.

7.4 Case Study 4 - Aerodynamics of High-Subsonic Blended-Wing-Body (BWB) Configurations

---

Authors : *Dino Roman, Richard Gilmore and Sean Wakayama*
Affiliation : *The Boeing Company, Huntington Beach, CA 92647*
Title of Paper : *Aerodynamics of High-Subsonic Blended-Wing-Body Configurations*
Source & URL : *AIAA 2003-554; https://doi.org/10.2514/6.2003-554*
Citation : *Dino Roman, Richard Gilmore and Sean Wakayama ; Aerodynamics of High-Subsonic Blended-Wing-Body Configurations 41st Aerospace Sciences Meeting and Exhibit. AIAA 2003-554. January 2003.*
Adaptation : *Only for Formatting*

7.4.1 Abstract

A Mach 0.93 Blended-Wing-Body (BWB) configuration was developed using *CFL3DV6*, a Navier-Stokes computational fluid dynamics (CFD) code, in conjunction with the Wing Multidisciplinary Optimization Design (*WingMOD*) code, to determine the feasibility of BWB aircraft at high subsonic speeds. Excluding an assessment of propulsion airframe interference, the results show that a Mach 0.93 BWB is feasible, although it pays a performance penalty relative to Mach 0.85 designs. A Mach 0.90 BWB may be the best solution in terms of offering improved speed with minimal performance penalty.

7.4.2 Introduction

By integrating the functions of wing and fuselage, the Blended-Wing-Body (BWB) achieves a clean aerodynamic and efficient structural design that offers tremendous potential for reduced fuel burn, weight, and cost (Refs. 1-3). With the announcement of the Sonic Cruiser, a 0.95 to 0.98 Mach number configuration, Boeing expressed a new emphasis on increased speed. While the BWB had previously been studied as a Mach 0.85 configuration, the new emphasis motivated a study to determine if the advantages of the BWB could be maintained at higher speeds. The natural area ruling of the BWB indicated that this might be possible. Area ruling is important when considering the wave drag for a body, which is governed by the following equation:

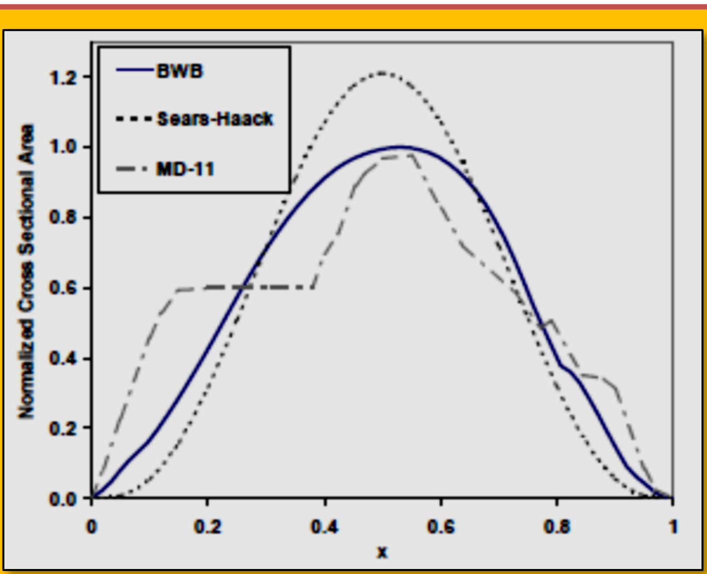

Figure 7.4.1 Area Distribution

$$D \approx q_0 \left[\frac{1}{2\pi} \int_0^1 \int_0^1 S''(x) S''(\xi) \log \frac{1}{|x-\xi|} \, dx d\xi \right]$$

Eq. 7.4.1

This equation shows that wave drag varies with the second derivative of cross-sectional area, implying that breaks in the area distribution result in high wave drag. Such breaks can be seen in the area distributions of conventional aircraft, like the MD-11, shown in **Figure 7.4.1** along with the area distributions of the BWB and the theoretical minimum wave drag Sears-Haack body.

The conventional airplane has a very non-smooth area distribution, with sharp breaks where the wing and empennage meet the fuselage. To solve this increased wave drag problem when going to higher subsonic speeds, conventional airplanes often use an area ruled, or “coke-bottle,” fuselage. This modification results in a manufacturing cost penalty associated with changing from a pressure vessel with constant cross section to one with varying cross section. Unlike a conventional airplane, the BWB has a smooth area distribution that is similar to the Sears-Haack distribution. Since the BWB is already area ruled, there is no additional cost penalty for changing the character of the pressure vessel, suggesting that the BWB may perform at lower cost than a conventional airplane when increasing to higher subsonic speeds.

7.4.3 Tools

7.4.3.1 Navier-Stokes Computational Fluid Dynamics (CFD) and Inverse Design

Due to the unconventional nature of the BWB (large inboard chords, thick airfoils with large trailing edge closure angles, and extreme blending), results from standard drag build-up methods based on flat plate friction and empirical form factors are suspect, especially at chord Reynolds Numbers as high as 300 million. Navier-Stokes analysis, however, is well suited to represent the three-dimensional physics involved. To conduct the CFD analysis presented in this study, *CFL3D*, with the Spalart-Allmaras one–equation turbulence model, was used. *CFL3D* (Ref. 4) is a NASA-developed Reynolds-averaged Navier-Stokes code. It incorporates an upwind differencing scheme, which is better at capturing shocks and avoiding excessive numerical dissipation than a central differencing scheme.

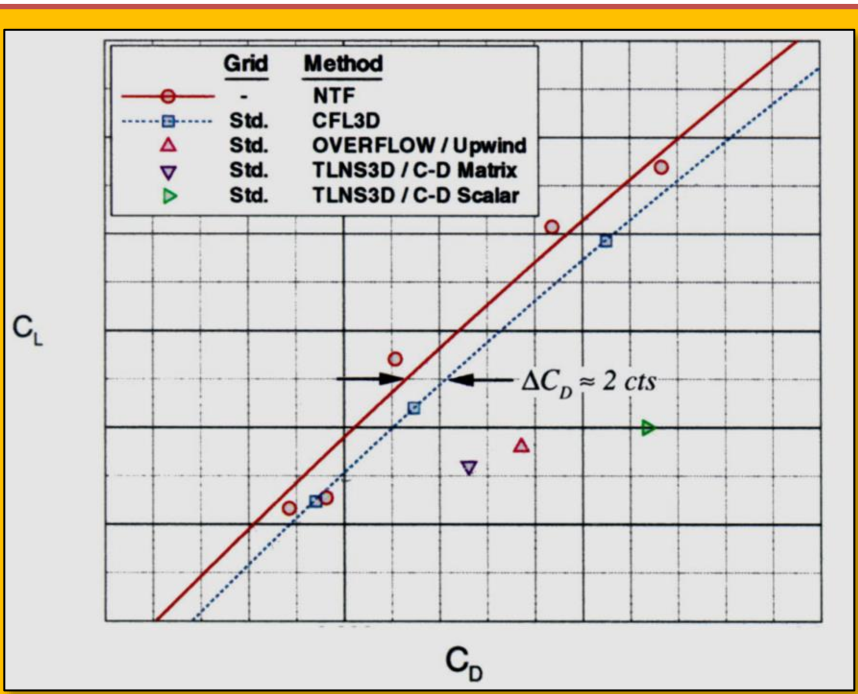

Figure 7.4.2 C_L and C_D results from multiple CFD codes, compared to NTF results. M = 0.85, Re = 25M

Figure 7.4.2 shows NTF wind tunnel results for a first generation BWB configuration compared to results from multiple CFD codes (Ref. 5). *CFL3D* provides a better drag estimate than other popular CFD codes at cruise conditions, matching the drag within 2 counts at constant C_L. **Figure 7.4.3** shows almost perfect agreement in variation of lift coefficient with angle of attack, and only a small discrepancy in pitching moment variation with angle of attack. The magnitude of the pitching moment coefficient discrepancy is about 0.01 at its maximum, but the pitching moment break still occurs at nearly the same C_L, an important consideration for buffet prediction. Pressure distributions on an inboard and outboard airfoil are shown in **Figure 7.4.4** for both the mid-cruise C_L and the buffet-onset C_L. Buffet is assumed to occur at or near the pitching moment break. Again, the *CFL3D* results agree well with the NTF wind tunnel results. The chordwise shock locations and magnitudes are captured. Excellent accuracy in drag, lift, pitching moment and pressure distributions is obtained with under one million grid points. The airfoil stacks for the various wings designed in this study were extensively modified using a NASA Langley-developed constrained inverse design capability, (Ref. 6). Within *CDISC*, the user specifies a pressure distribution and the code determines the geometry necessary to achieve those pressures under user specified geometric and aerodynamic constraints. Coupled to *CFL3D* with specified constraints on airfoil thickness, leading edge radius, trailing edge closure angle, pressure vessel height, shock strength, pitching moment, and span load, CDISC allows for realistic tailoring of the pressures to achieve a smooth chordwise and spanwise distribution with weakened shocks and less aggressive trailing edge pressure recoveries. *CFL3D* coupled to the *CDISC* inverse design capability proved to be an extremely valuable tool for BWB clean wing design.

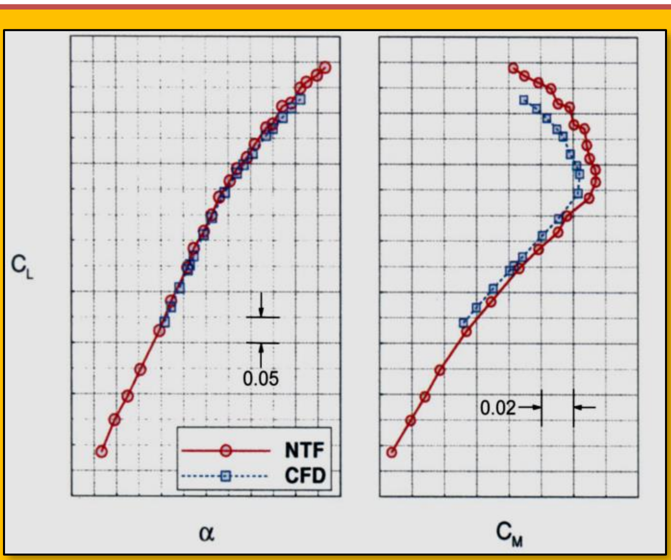

Figure 7.4.3 C_L variation with angle of attack and C_M. NTF results compared to *CFL3D*. M = 0.85, Re = 25M.

7.4.3.2 Multidisciplinary Design Optimization (MDO)

The Wing Multidisciplinary Optimization Design (*WingMOD*) tool was used to perform the MDO portion of the current study. As described in Refs. 7-8, WingMOD models the BWB with a simple vortex lattice code and monocoque beam analysis, coupled to give static aeroelastic loads. The model is trimmed at several flight conditions to obtain load and induced drag data. Profile and compressibility drag are evaluated at stations across the span of the wing with empirical relations using the lift coefficients obtained from the vortex lattice code. The compressibility drag model is calibrated to CFD results. Structural weight is calculated from the maximum elastic loads encountered through a range of flight conditions, including

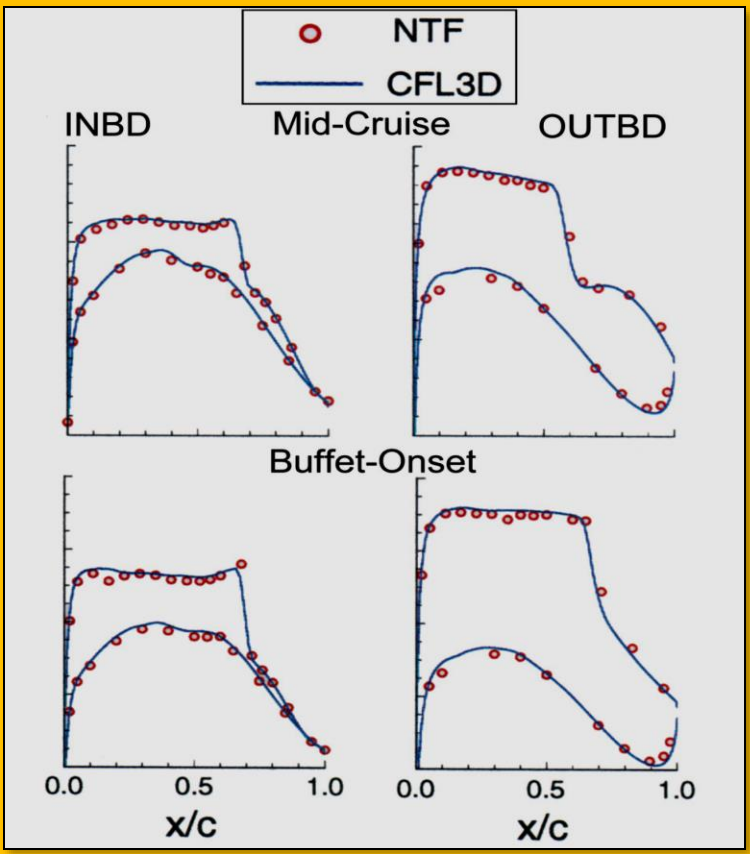

Figure 7.4.4 Chordwise pressure distributions on an inboard and outboard airfoil, at mid-cruise and buffet-onset C_L. NTF results compared to *CFL3D*. M=0.85, Re=25M.

maneuver, vertical gust, and lateral gust. The structure is sized based on bending strength and buckling stability considerations. Maximum lift is evaluated using a critical section method that declares the wing to be at its maximum useable lift when any section reaches its maximum lift coefficient, which is calculated from empirical data.

These analysis modules are linked to a non-linear gradient-based optimizer. The optimizer is flexible and allows the user to designate any analysis input as a design variable and any database variable as a constraint. In typical wing planform optimizations, as described in Ref. 9, a wide variety of constraints is applied. Mission constraints such as payload, range, and approach speed are applied as well as design constraints like maximum running loads and buffet characteristics. These design constraints are put in place to ensure that the optimizer designs a practical configuration that can be refined later using higher fidelity methods.

7.4.4 Approach

CFD and MDO were used in conjunction to develop a Mach 0.93 BWB configuration. While CFD can accurately capture compressibility and other aerodynamic effects, a CFD-based design does not consider constraints such as balance and structural sizing. Additionally, while a CFD-designed configuration may be aerodynamically efficient, it is not necessarily low weight. Therefore, MDO was incorporated in the current study to satisfy non aerodynamic constraints and optimize for minimum take-off weight. The study consisted of a four-step process:

1. Design an aerodynamically efficient configuration using CFD.
2. Calibrate the MDO tool (*WingMOD*) to CFD results.
3. Using MDO, optimize a BWB for minimum take-off weight.

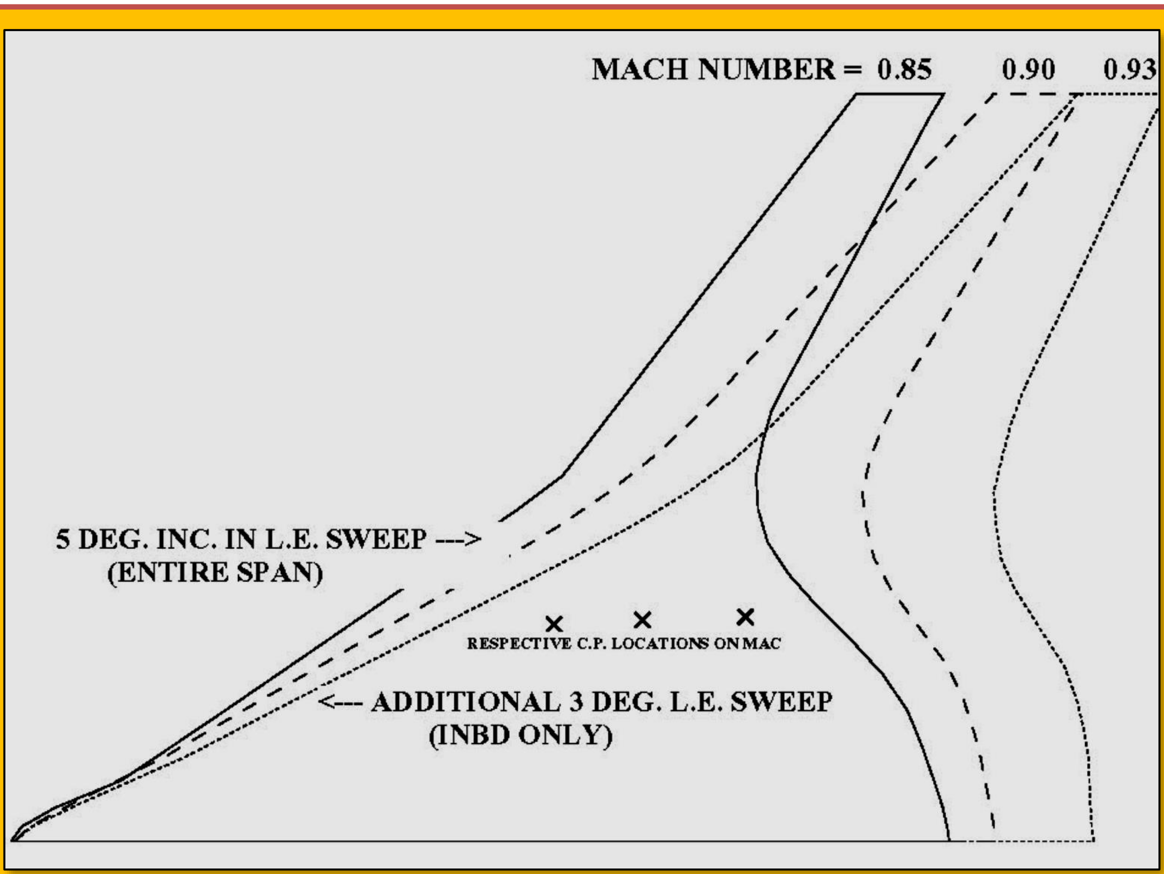

Figure 7.4.5 Planform change with increasing Mach number

4. Verify and refine the resultant configuration aerodynamics in CFD.

7.4.4.1 Initial CFD-Based Aerodynamic Design

Because aerodynamic performance must be evaluated using the lower order, but much faster, methods in the MDO tool, starting from an efficient aerodynamic design at the desired Mach number would result in a better overall configuration with acceptable aerodynamic performance. Even though *WingMOD* was calibrated to CFD at various Mach numbers, straying too far from an initial design could lead to overly-optimistic aerodynamic performance. Several design cycle iterations between *WingMOD* and CFD revealed the advantages of starting with an aerodynamically efficient configuration.

Starting from a well-established 0.85 Mach configuration, new wings were developed at 0.90 and 0.93 Mach with the goal of maximizing L/D at each Mach number, with consideration given to various design constraints. In particular, each wing design was driven by the requirement to enclose the pressurized passenger and cargo cabin, maintain a reasonable buffet boundary and achieve acceptable post-buffet characteristics (i.e. avoid severe post-buffet pitch-up).

A description of the additional multi-disciplined interdependent real-world constraints affecting aerodynamic design particular to a BWB are described in detail in Ref. 10. Although these additional constraints were not specifically tracked or evaluated during the initial CFD phase of the study, they did play a secondary role in limiting some of the plan form design choices made. All of these constraints were addressed by the subsequent *WingMOD* optimizations.

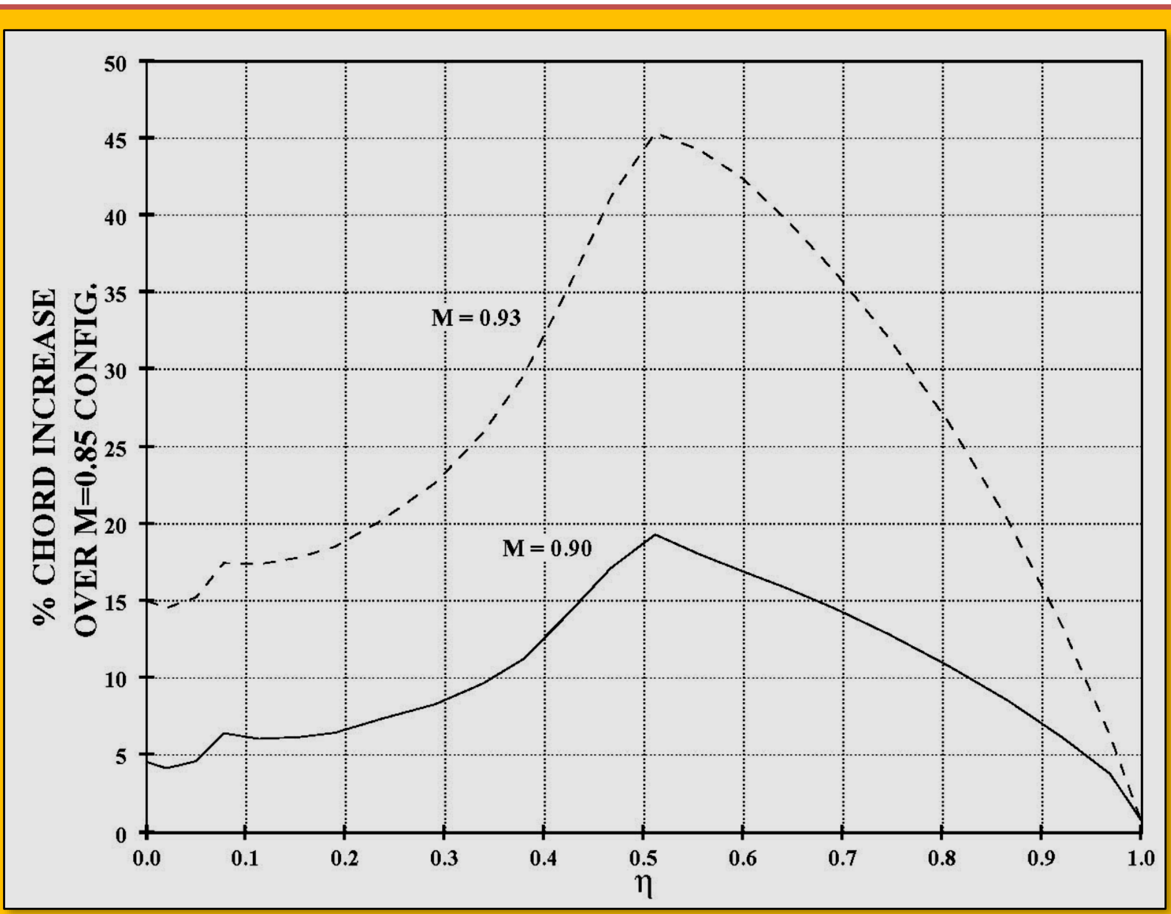

Figure 7.4.6 Spanwise chord increase with increasing Mach number

While the span was held fixed, the sweep and chord length of the baseline 0.85 Mach design were systematically varied (effectively reducing *t/c* for fixed thickness) to minimize wave drag associated with wing thickness effects, and to maintain acceptable buffet margin and characteristics. The resulting planforms are shown in **Figure 7.4.5**, compared to the baseline 0.85 Mach design. The sweep increased to minimize wing thickness effects on wave drag. Because the inboard wing thickness was driven by the height of the pressure vessel, there is little one can do, apart from increasing sweep and chord, to reduce transonic thickness effects in this portion of the wing. The chord increases are shown in **Figure 7.4.6** as a percentage increase over the baseline 0.85 Mach configuration chords.

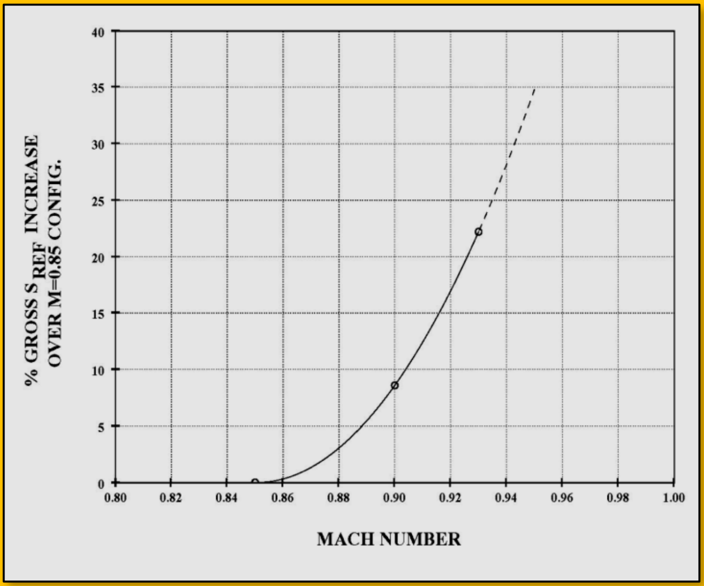

Figure 7.4.7 Planform area increase with Mach number

The inboard chord increases were mainly driven by thickness considerations while the outboard chords were driven by the requirement to maintain a reasonable span load and maintain acceptable buffet margin and characteristics. Increasing the chord length reduced the section lift coefficient for a given section loading, *ccl*, which gave more margin to the critical section buffet *cl*. Tailoring the chord lengths in the spanwise direction allowed the designer to locate the buffet-critical section at a spanwise location that did not aggravate post-buffet pitch-up characteristics. The increases in chord length lead to significant increases in wing area as Mach number increased, as shown in **Figure 7.4.7**. Note the steepening slope with Mach number.

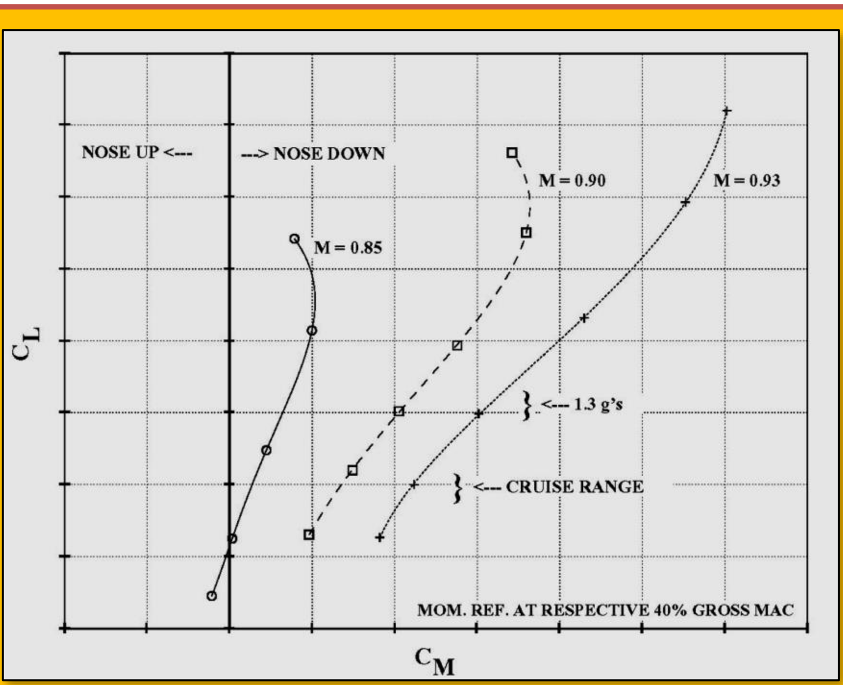

Figure 7.4.8 Pitching moment curves with increasing Mach number

Figure 7.4.8 shows the pitching moment curve for the three wings at their respective Mach numbers. Improvement in buffet margin and pitch-up characteristics were seen as Mach number increased. This is partly due to the spanwise wing chord distribution, but also due to the natural tendency of the wing center-of-pressure location to move aft with

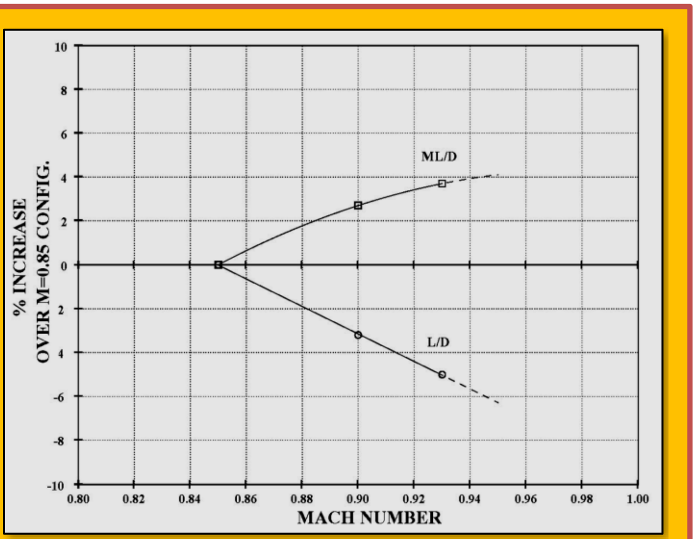

Figure 7.4.9 L/D and ML/D change with Mach number

Mach number, leading to a more stable design. Note that other than the baseline 0.85 Mach configuration, the wings were not trimmed, an issue later resolved using MDO.

The airfoil stack for each wing was designed using *CDISC* coupled to *CFL3D* as described earlier. The resulting aerodynamic performance of the higher Mach number wings is shown in **Figure 7.4.9** compared to the baseline 0.85 Mach number wing. While L/D decreased with Mach number as expected (due to compressibility effects), ML/D showed a significant improvement. It is important to note, however, that these are purely aerodynamic, untrimmed wing-alone results. The many non-aerodynamic constraints not addressed by the CFD designs (e.g. trim, balance, structures) were later addressed by MDO. With proper calibration, the MDO tool emulated the CFD results, and there was confidence that it could capture the important aerodynamic effects during planform optimizations.

7.4.4.2 Drag Calibration

In analyzing BWB configurations at Mach numbers going up to 0.95, there is concern that the simple *WingMOD* models may not capture significant transonic effects. This concern was addressed by calibrating the *WingMOD* models to *CFL3D* Navier-Stokes CFD results for a number of BWB configurations, comparing calibrated *WingMOD* and CFD results, and performing CFD design and analysis on the final *WingMOD* optimized configuration.

Figure 7.4.10 and **Figure 7.4.11** show the *WingMOD* compressibility drag model. Compressibility drag is determined on a section-by-section basis. For each section, a thickness to chord ratio and lift coefficient are evaluated perpendicular to the effective sweep line, which is determined from a source-sink thickness model described in Ref. 11. These properties are then input to a function represented in **Figure 7.4.10** to determine the section crest-critical

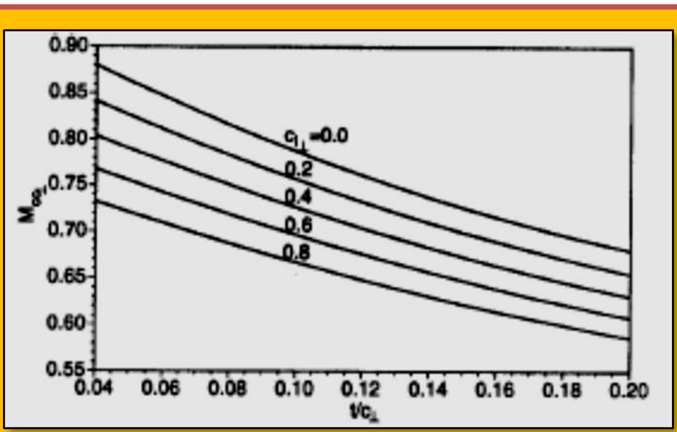

Figure 7.4.10 Crest critical Mach number as a function of *t/c* and *cl*.

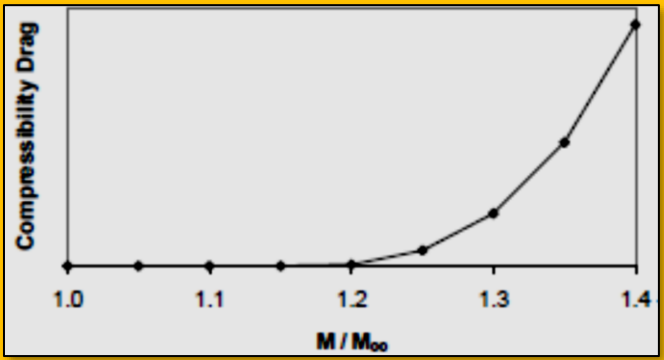

Figure 7.4.11 Sectional compressibility drag curve

Mach number (M_{cc}). M_{cc} is described as the freestream Mach number at which the local flow at the crest of the airfoil, the location where the surface is tangent to the freestream direction, becomes sonic (Ref. 12). Once M_{cc} is determined, compressibility drag can be derived. For each section, compressibility drag is related to the ratio of freestream Mach number to crest-critical Mach number, as shown in **Figure 7.4.11**. The curve shown is represented by a spline that can be manipulated by the *WingMOD* optimizer during calibration.

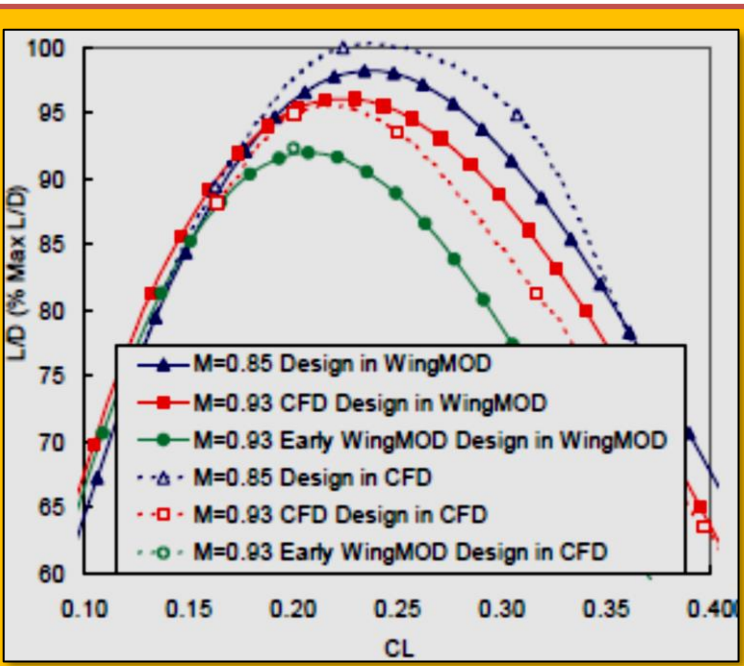

Figure 7.4.12 Comparison of CFD and *WingMOD* lift to drag ratios

To calibrate for the current study, a Mach 0.85 BWB configuration and two Mach 0.93 BWB configurations were analyzed in both *WingMOD* and *CFL3D*. To match *WingMOD* and CFD representations, *WingMOD* span loads were tailored to match CFD, and the configurations were analyzed without nacelles, pylons, or winglets. The *WingMOD* compressibility drag model was then adjusted, via the coefficients for the spline shown in **Figure 7.4.11**, to minimize the error in compressibility drag over all three configurations.

Procedures described in Ref. 13 for linking variables were used to enable a simultaneous optimization over the three configurations to calibrate the compressibility drag model. **Figure 7.4.12** compares lift to drag ratio (L/D) for the three configurations relative to the maximum L/D of the Mach 0.85 configuration, analyzed both in CFD and in *WingMOD* after the calibration. *WingMOD* L/D levels are within 5% of CFD and show similar trends in C_L. This is good agreement considering the *WingMOD* aerodynamic analysis runs in a fraction of a second. It is also possible that the less mature Mach 0.93 designs will improve relative to the Mach 0.85 design with further aerodynamic refinement in CFD, resulting in better agreement between *WingMOD* and CFD.

7.4.4.3 MDO Study

Starting from the Mach 0.93 CFD designed baseline, *WingMOD* was used to design and analyze a family of BWB configurations with Mach numbers of 0.85, 0.90, 0.93, and 0.95, and ranges of 7500 nmi and 8900 nmi (study described in detail in Ref. 14). Configurations were optimized for minimum take-off weight, with 154 design variables and 1,091 constraints specified, of which 134 were critical. This resulted in a system with 20 unconstrained degrees of freedom. Design variables included structural gauge thicknesses, structural layout parameters, geometry (chords, thicknesses, twist, etc.), control commands, control schedules, fuel distribution schedules, etc. *WingMOD* analyzed 28 different conditions, most of which were subject to trim and balance constraints. The resulting configurations met the mission requirements (i.e. range and payload) as well as satisfying trim, balance, performance, stability, maximum lift, buffet, structural sizing, and passenger cabin height constraints.

Figure 7.4.13 demonstrates some of what *WingMOD* accomplished by optimizing an aerodynamically efficient design. **Figure 7.4.13.a** shows the balance diagram for the CFD baseline design. The points represent c.g. locations for different conditions. The dashed lines represent the control limits of the aircraft. Several of the c.g. locations fall outside the limits, indicating the aircraft is not balanced. **Figure 7.4.13b** shows how *WingMOD* was able to balance this airplane using ballast. The addition of ballast increased operating empty weight (OEW) through increases in structural weight, in addition to the weight of the ballast itself. As the aircraft balanced at more-aft c.g. locations, *L/D* increased, improving fuel burn. Take-off weight (TOW) then increased less than OEW, because the fuel burn improvement partially offset the empty weight increase.

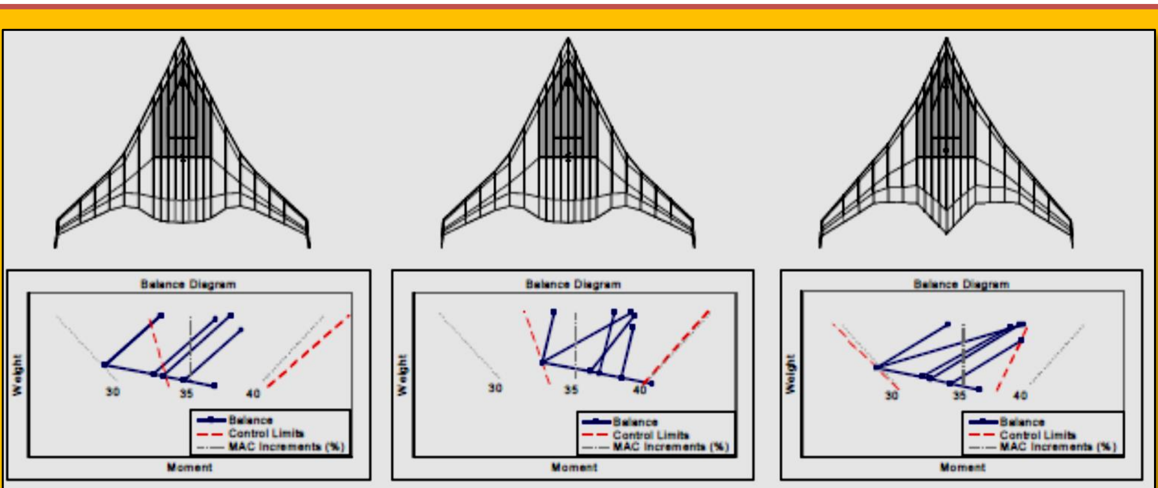

(a) CFD Baseline
Unbalanced
TOW: Base
OEW: Base

(b) Balanced CFD Baseline
Adds Aft Ballast
TOW: +2.1%
OEW: +4.2%

(c) Optimized Configuration
Planform Reshaped
TOW: -6.8%
OEW: -5.5%

Figure 7.4.13 *WingMOD* balance analysis

By reshaping the planform, *WingMOD* was able to solve the balance problem and reduce the TOW of the aircraft at the same time. The balance diagram for the optimized 0.93 Mach, 7,500 nmi configuration is shown in **Figure 7.4.13c**.

Figure 7.4.14 shows the Mach number times lift to drag ratio (ML/D) for each member of the optimized family, relative to the 7500 nmi Mach 0.85 configuration. Aerodynamically, a Mach 0.90 BWB configuration may be optimal, with the peak in ML/D occurring at that speed. The increase in ML/D over a Mach 0.85 geometry is a result of speed increasing faster than the lift to drag ratio (L/D) decreases. With the current study emphasizing speed, a Mach 0.93 design was selected for further study.

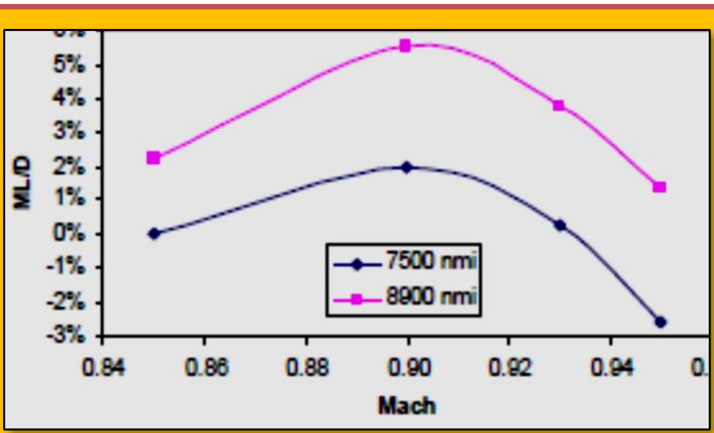

Figure 7.4.14 Average cruise Mach number times lift to drag ratio trend

7.4.4.4 CFD Aerodynamic Refinement

The Mach 0.93, 7500 nmi *WingMOD-optimized* configuration was the basis for the BWB-6-250B, shown in **Figure 7.4.15**. *CFL3D* coupled to *CDISC* inverse design was used to design the airfoil stack, as discussed earlier, and verify the aerodynamic performance of the wing. For simplicity of this design study the isolated BWB wing was considered without the added complications of modeling the winglet and nacelle and pylon. Whereas the winglet has a fairly localized effect at the wing tip, the nacelle and pylon can have a more pronounced effect and would need to be integrated in the design at whichever speed is deemed most appropriate from this initial study. Similar design techniques and tools as described earlier would be used to perform the propulsion/airframe and winglet integration. Without the nacelle and pylon, gridding the wing geometry became a simple task using readily available tools. Airfoil shape and camber were adjusted by *CDISC* to achieve a smooth chordwise and spanwise pressure distribution, limit shock strength, and achieve a center of pressure corresponding to the c.g. location determined by *WingMOD*. Additionally, this inverse design process was subject to constraints on airfoil thickness, leading edge radius, trailing edge closure angle, pressure vessel height, and span load.

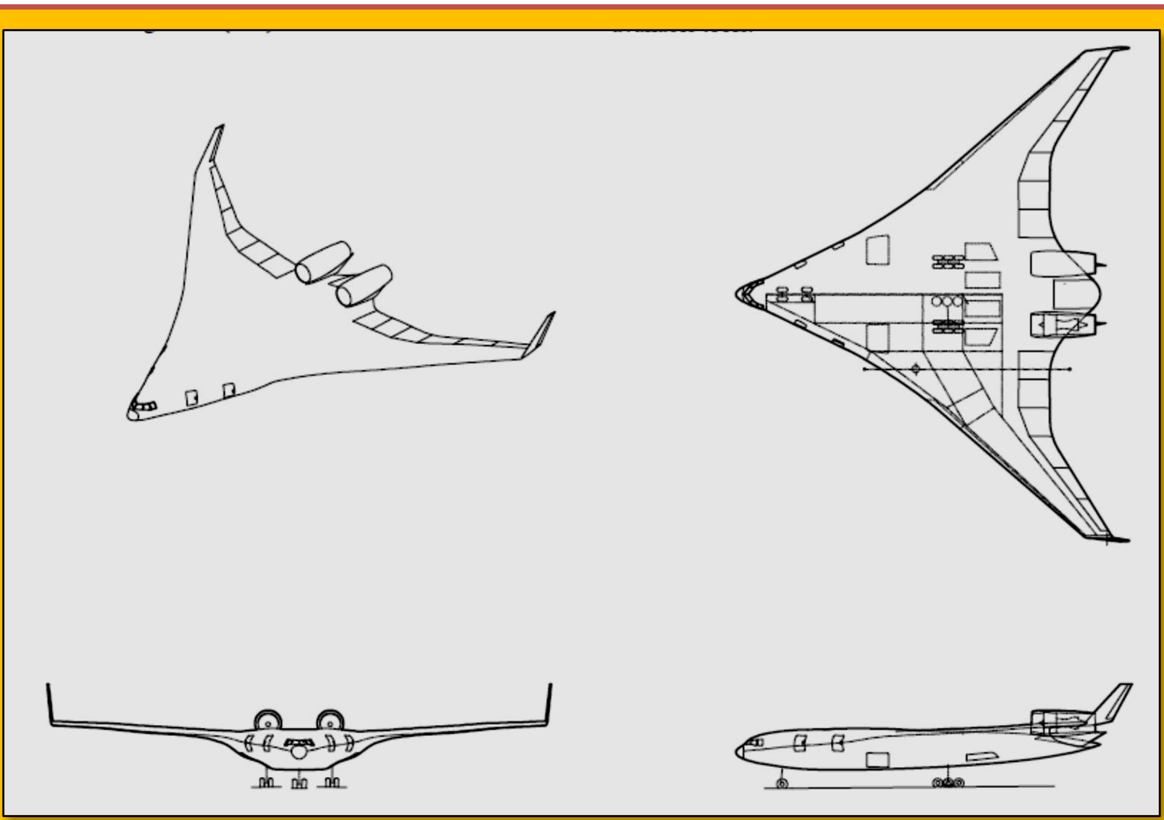

Figure 7.4.15 BWB 6-250B configuration

7.4.5 Results

Figure 7.4.16 shows *CFL3D* predicted pressure contours and chordwise pressure distributions for the wing. The pressure distributions show a very weak inboard shock well ahead of the engine inlet location with a more pronounced outboard shock and a tendency to double shock near the wing tip. The double shock tendency is typical of sections that are under loaded. The same techniques used thus far could be used to tailor the span load and airfoils to address this double shock, though judging from the L/D level, there does not seem to be a significant penalty associated with this characteristic

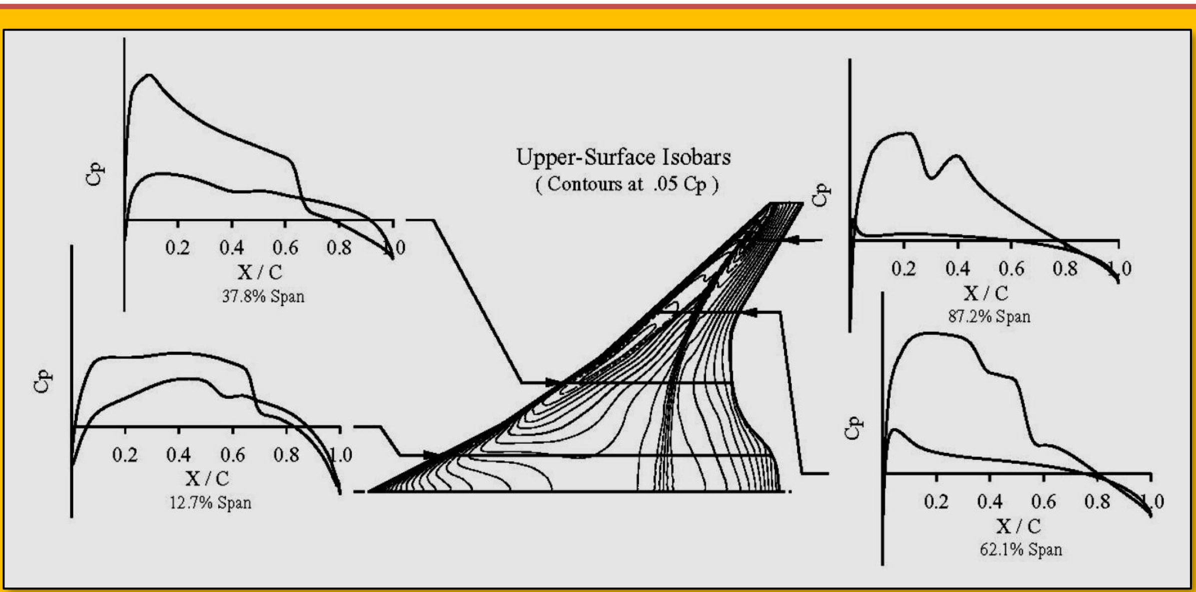

Figure 7.4.16 BWB 6-250B Pressure Contours. *CFL3DV6*, no N/P or winglet

at the tip. Pitching moment variation with C_L is shown in **Figure 7.4.17**. In the cruise C_L range, pitching moment is close to zero, as it should be for trimmed cruise. Buffet onset, as defined by the break in the pitching moment curve, does not occur until well beyond 1.3g's (1.3 times cruise C_L), and the pitch break is mild, indicating that post-buffet pitch-up characteristics will not be severe.

Figure 7.4.18 shows the ML/D of the configuration at Mach 0.93, 0.94, and 0.95 relative to a more refined Mach 0.85 BWB with a similar mission. At the design cruise Mach number of 0.93, the BWB 6-250B is at 92% of the peak ML/D of the Mach 0.85 configuration. As expected, the ML/D drops off as Mach number is increased beyond the cruise Mach number. This drag rise can be seen in **Figure 7.4.19**. As indicated, drag divergence, as defined by a slope of 0.05 of the drag rise curve, happens just beyond Mach 0.93, indicating that the wing is well designed to cruise at Mach 0.93.

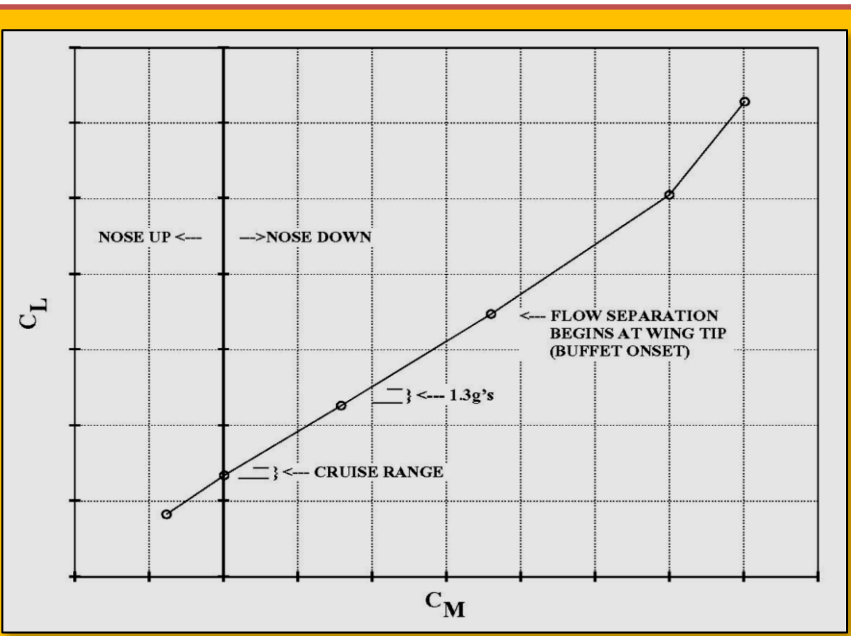

Figure 7.4.17 BWB 6-250B pressure contours. *CFL3DV6*, no N/P or winglet

7.4.6 Conclusions

A dual CFD/MDO design study was conducted to develop a Mach 0.93 BWB. *CFL3D* coupled to *CDISC* was used to create an aerodynamically efficient baseline design, which was then optimized in *WingMOD* for minimum take-off weight, subject to many non-aerodynamic constraints not considered in the baseline design. *CFL3D* with *CDISC* was again used to refine the *WingMOD* optimized design. Analysis of the final design indicated that it achieved reasonable L/D and a drag divergence Mach number just beyond 0.93. Although additional CFD work is needed to quantify drag stemming from propulsion airframe interference, the work done so far indicates good potential for creating a BWB that performs well at Mach 0.93.

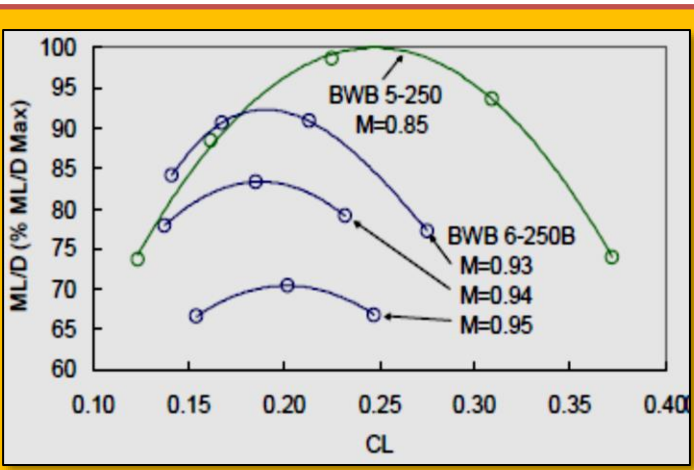

Figure 7.4.18 Mach times lift to drag ratio of BWB 6-250B versus 5-250. *CFL3DV6*, no N/P or winglet

Acknowledgement

The authors gratefully acknowledges the contributions of the BWB team, especially the following individuals who were directly involved with or contributed supporting data for the study described in this paper: Ron Fox, Antonio Gonzales, Ron Kawai, Roger Lyon, and Jennifer Whitlock.

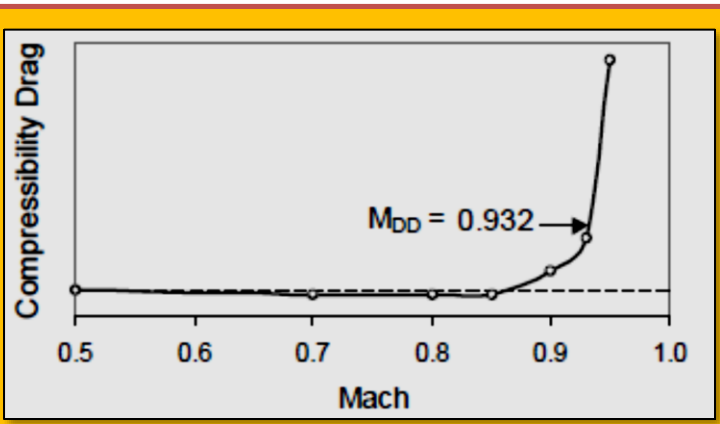

Figure 7.4.19 Compressibility drag Mach trend

1.1.1 References

[1] Liebeck, R. H., “Design of the Blended-Wing-Body Subsonic Transport,” 2002 Wright Brothers Lecture, AIAA Paper 2002-0002, Jan. 2002.

[2] Liebeck, R. H., Page, M. A., Rawdon, B. K., “Blended-Wing-Body Subsonic Commercial Transport,” AIAA Paper 98-0438, Jan. 1998.

[3] “Blended-Wing-Body Technology Study,” Final Report, NASA Contract NAS1-20275, Boeing Report CRAD-9405-TR-3780, Oct. 1997.

[4] http://cfl3d.larc.nasa.gov/Cfl3dv6/cfl3dv6.html

[5] Pelkman, R.A., “Key Findings and Conclusions from an NTF Wind Tunnel Test of an Initial Blended-Wing-Body Concept,” NASA Contract NAS1-20268, Boeing Report No. CRAD-9402-TR-3985, 1998.

[6] Campbell, R. L., “Efficient Viscous Design of Realistic Aircraft Configurations,” AIAA Paper 98-2539, June 1998.

[7] Wakayama, S., Kroo, I., “Subsonic Wing Planform Design Using Multidisciplinary Optimization,” *Journal of Aircraft*, Vol. 32, No. 4, Jul.-Aug. 1995, pp.746-753.

[8] Wakayama, S., *Lifting Surface Design Using Multidisciplinary Optimization*, Ph.D. Thesis, Stanford University, Dec. 1994.

[9] Wakayama, S., “Blended-Wing-Body Optimization Problem Setup,” AIAA Paper 2000-4740.

[10] Roman, D., Allan, J.B., Liebeck, R.H., “Aerodynamic Design Challenges of The Blended-Wing-Body Subsonic Transport,” AIAA Paper 2000-4335, June 2000.

[11] Wakayama, S., "Multidisciplinary Optimization of the Blended-Wing-Body," AIAA Paper 98-4938, Sep. 1998.

[12] Shevell, R.S., *Fundamentals of Flight*, 2nd Ed., Prentice Hall, Englewood Cliffs, New Jersey, 1989.

[13] Willcox, K., Wakayama, S., "Simultaneous Optimization of a Multiple-Aircraft Family," AIAA Paper 2002-1423, Apr. 2002.

[14] Gilmore, R., Wakayama, S., Roman, D., "Optimization of High-Subsonic Blended-Wing-Body Configurations," AIAA Paper 2002-5666, Sep. 2002.